REPORT DOCUMENTATION PAGE

DTIC FILE COPY

Form Approved
OMB No. 0704-0188

AD-A225 444

1. AGENCY USE ONLY (Leave blank)	2. REPORT DATE	3. REPORT TYPE AND DATES COVERED
	11 June 1990	Technical - 11-15 June 1990

4. TITLE AND SUBTITLE
(U) AFOSR/ONR Contractors Meeting - Combustion, Rocket Propulsion, Diagnostics of Reacting Flow

5. FUNDING NUMBERS
PE - 61102F
PR - 2308

(2)

6. AUTHOR(S)
M A Birkan, J M Tishkoff and G S Roy

7. PERFORMING ORGANIZATION NAME(S) AND ADDRESS(ES)
Air Force Office of Scientific Research
Building 410
Bolling AFB DC 20332-6448

Office of Naval Research, Arlington VA 22217-5000

8. PERFORMING ORGANIZATION REPORT NUMBER
AFOSR-TR- 90 0808

9. SPONSORING/MONITORING AGENCY NAME(S) AND ADDRESS(ES)
AFOSR/NA
Building 410
Bolling AFB DC 20332-6448

10. SPONSORING/MONITORING AGENCY REPORT NUMBER

11. SUPPLEMENTARY NOTES

12a. DISTRIBUTION/AVAILABILITY STATEMENT
Approved for public release; distribution is unlimited

12b. DISTRIBUTION CODE

13. ABSTRACT (Maximum 200 words)

Abstracts are given for research in airbreathing combustion, rocket propulsion, and diagnostics of reacting flow supported by the Air Force Office of Scientific Research and the Office of Naval Research.

14. SUBJECT TERMS
Instability, Flames, Proulsion, Gas Turbines, Combustion, Shear Layer, Supersonic, Soot, Sprays, Boron, Lasers, Fluorescence, Rocket, Scramjet, Nitramines, Turbulence

15. NUMBER OF PAGES

16. PRICE CODE

17. SECURITY CLASSIFICATION OF REPORT	18. SECURITY CLASSIFICATION OF THIS PAGE	19. SECURITY CLASSIFICATION OF ABSTRACT	20. LIMITATION OF ABSTRACT
Unclassified	Unclassified	Unclassified	UL

CONTRACTOR'S MEETING IN PROPULSION

Sponsored by

AIR FORCE OFFICE OF SCIENTIFIC RESEARCH

OFFICE OF NAVAL RESEARCH

And

THE GEORGIA INSTITUTE OF TECHNOLOGY

11-15 June 1990

THE GEORGIA INSTITUTE OF TECHNOLOGY

DEPARTMENT OF AEROSPACE ENGINEERING

ATLANTA, GEORGIA 30332

CONTRACTORS MEETING IN PROPULSION

sponsored by

AIR FORCE OFFICE OF SCIENTIFIC RESEARCH
OFFICE OF NAVAL RESEARCH
and
THE GEORGIA INSTITUTE OF TECHNOLOGY

COLONY SQUARE HOTEL, ATLANTA, GEORGIA
11-15 June 1990

TABLE OF CONTENTS

IIc. WEDNESDAY

IId. THURSDAY

AGENDA

AFOSR CONTRACTOR'S MEETING

11-15 JUNE 1990

MONDAY, 11 JUNE 1990
PLASMA PROPULSION

10:00 - 10:30	Welcome Research Highlights In Plasma Propulsion M A Birkan, AFOSR
10:30 - 11:15	Statistical Mechanics of Collective Phenomena In Plasmas J L Lebowitz, Rutgers University
11:15 - 11:45	Plasma Instabilities E Y Choueiri, Princeton University
11:45 - 12:15	New Diagnostic Opportunities At The Astronautics Laboratory J C Andrews/R A Spores, Astronautics Laboratory
12:15 - 13:30	LUNCH
	LOW PRESSURE PLASMA BASED PROPULSION
	Chair: J C Andrews Astronautics Laboratory
13:30 - 13:55	Nonequilibrium And Radiation In MPD Plasmas M Martinez-Sanchez, Massachusetts Institute of Technology
13:55 - 14:20	Fundamental Research On Erosion In MPD Thrusters V V Subramaniam, Ohio State University
14:20 - 14:45	Basic Processes of Plasma Propulsion H Schrade, University of Stuttgart
14:45 - 15:10	Ionized Cluster Beams for Space Propulsion R L Poeschel, Hughes Research Laboratories
15:10 - 15:40	BREAK
	HIGH PRESSURE PLASMA BASED PROPULSION
	Chair: R A Spores Astronautics Laboratory
15:40 - 16:05	Picosecond Laser Breakdown Thresholds In Gases D Keefer, University of Tennessee Space Institute

16:05 - 16:30	Plasma Scaling Mechanisms For CW Laser Propulsion H Krier, University of Illinois
16:30 - 16:55	Coupling Between gas Dynamics And Microwave Energy Absorption M M Micci, Pennsylvania State University
16:55 - 17:20	Transport Processes in Beamed - Energy Propulsion Systems R A Beddini, University of Illinois

TUESDAY, 12 JUNE 1990

INSTABILITY

Chair: J N Levine
Astronautics Laboratory

09:00 - 09:30	Welcome Research Highlights In Rocket Combustion Instability M A Birkan, AFOSR
09:30 - 10:00	Oscillatory Internal Flow In Solid Propellant Rockets G A Flandro, Georgia Institute of Technology R S Brown, United Technologies, CSD
10:00 - 10:30	Solid Rocket Combustion Phenomena D R Kassoy, University of Colorado
10:30 - 11:00	BREAK
11:00 - 11:30	Energy Exchange Between Mean And Acoustic Flow Fields J D Baum, SAI Corporation
11:30 - 12:00	Flame-Acoustic Wave Interactions During Axial Solid Rocket Instabilities B T Zinn, Georgia Institute of Technology
12:00 - 12:30	Distributed Combustion In Solid Propellants M W Beckstead, Brigham Young University
12:30 - 14:00	LUNCH

ROCKET COMBUSTION DYNAMICS

Chair: G Roy
Office of Naval Research

14:00 - 14:30	Fractal Image Compression of Rayleigh, Raman, LIF and LDV data in Turbulent Reacting Flow W C Strahle, Georgia Institute of Technology
14:30 - 15:00	Plume Technology D P Weaver, Astronautics Laboratory
15:00 - 15:30	Kinetic Studies of Metal Combustion In Propulsion A Fontijn, RPI
15:30 - 16:00	BREAK
16:00 - 16:30	Chemical Kinetics of Nitramines M Branch, University of Colorado
16:30 - 17:00	Structure, Property And Reactivity relationships Among Energetic Materials T B Brill, University of Deleware
17:00 - 17:30	High Pressure Combustion Kinetics of Propellants J T Edwards, Astronautics Laboratory

WEDNESDAY 13 JUNE 1990

08:15 - 08:30	Welcome and Administrative Announcements
	Chairman: Dr Erwin Lezberg **NASA Lewis Research Center** **Session Topic: Combustion Enhancement**
08:30 - 09:00	Initiation and Modification of Reaction by Energy Additions: Kinetic and Transport Phenomena F E Fendell and M-S Chou, TRW, Inc
09:00 - 09:30	Fundamental Studies of Laser Ignition and Kinetics in Reactive Systems A W Miziolek, U S Army Ballistic Research Laboratory
	Session Topic: Diagnostics
09:30 - 10:00	Detecting Microwave Emissions From Terrestrial Sources: A Feasibility Study T Ehlert and T K Ishii, Marquette University
10:00 - 10:30	Nonlinear Spectroscopy of Multicomponent Droplets and Two- And Three-Dimensional Measurements in Flames R K Chang, M B Long, and R Kuc, Yale University
10:30 - 11:00	BREAK
11:00 - 12:00	Upcoming Space Shuttle Mission Report Franklin Chang-Diaz, Lyndon B Johnson Space Center
12:00 - 01:15	LUNCH
	Chairman: Dr J T Edwards, **Astronautics Laboratory, AFSC** **Session Topic: Diagnostics**
01:15 - 02:00	Advanced Diagnostics for Reacting Flows Ron Hanson, Stanford University
02:00 - 02:30	CATCARS: Two-Dimensional Coherent Anti-Stokes Raman Scattering With Application To The Hydrogen Arcjet E J Beiting, Aerospace Corporation
02:30 - 03:00	Energy Conversion Device Diagnostics Bish Ganguly, WRDC/POOC-3
03:00 - 03:30	BREAK
03:30 - 04:00	Plasma Propulsion Diagnostics R Spores, AL/LSVE
04:00 - 04:30	Novel Nonlinear Laser Diagnostic Techniques D Huestis, G Faris, and J Jeffries, SRI International
04:30 - 05:00	Asynchronous Optical Sampling for Laser-Based Combustion Diagnostics in High-Pressure Flames G B King, N M Laurendeau, and F E Lytle, Purdue University
05:00	BUSINESS MEETING, Investigators in Dr Tishkoff's Programs Only

THURSDAY, 14 JUNE 1990

Chairman: Lt Col Larry Davis
AFOSR/NC
Session Topic: Boron

08:30 - 09:00	Production and Coating of Pure Boron Powders H F Calcote, AeroChem Research Laboratories, Inc
09:00 - 09:30	Coating of Boron Powders By Chemical Vapor Deposition C Senior, PSI Technology Company
09:30 - 10:00	Production and Coating of Pure Boron Powders C Criner, Mach I, Inc
10:00 - 10:30	Particle-Laden Combustion Flows K K Kuo, Pennsylvania State University
10:30 - 11:00	BREAK
11:00 - 11:30	Characterization of IR Emission from Boron Combustion K Annen, Aerodyne Research, Inc
11:30 - 12:00	Transport Phenomena and Interfacial Kinetics in Multiphase Combustion Systems D E Rosner, Yale University
12:00 - 12:30	Kinetic Studies of Metal Combustion in Propulsion A Fontijn, Rensselaer Polytechnic Institute
12:30 - 02:00	LUNCH
02:00 - 05:00	WORKSHOPS

Boron
(Lt Col Larry Davis, AFOSR)

Soot
(Dr Ken Brezinsky, Princeton University)

Sprays
(Dr Michael Winter, United Technologies Research Center)

Supersonic Combustion
(Dr G B Northam, NASA Langley Research Center)

Turbulent Reacting Flow
(Dr Werner Dahm, University of Michigan)

FRIDAY, 15 JUNE 1990

Chairman: Dr David Mann,
U S Army Research Office
Session Topic: Sprays

09:00 - 09:30	Fundamental Studies of Droplet Interactions in Dense Sprays W A Sirignano and S E Elghobashi, University of California, Irvine
09:30 - 10:00	Particle Dispersion In Turbulent Shear Flows I M Kennedy and W Kollmann, University of California, Davis
10:00 - 10:30	BREAK
10:30 - 11:00	Drop/Gas Interactions In Dense Sprays G M Faeth, University of Michigan
11:00 - 11:30	Investigations of the Applications of Laser-Induced Exciplex Fluorescence to Fuel Spray and Single Droplet Vaporization L A Melton, University of Texas, Dallas and M Winter, United Technologies Research Center
11:30 - 01:00	LUNCH

Chairman: Capt Wayne Chepren,
AFESC/RDV
Session Topic: Soot

01:00 - 01:30	Fuels Combustion Research I Glassman, Princeton University
01:30 - 02:00	The Determination of Rate-Limiting Steps During Soot Formation M B Colkett III, United Technologies Research Center
02:00 - 02:30	Soot Particle Inception and Growth Processes in Combustion R J Santoro, Pennsylvania State University
02:30 - 03:00	BREAK
03:00 - 3:30	Computer Modeling of Soot Formation Comparing Free Radical and Ionic Mechanisms M Frenklach, Pennsylvania State University
03:30 - 04:00	Computer Modeling of Soot Formation Comparing Free Radical and Ionic Mechanisms H F Calcote, AeroChem Research Laboratories, Inc
04:00 - 04:30	A Systematic Approach To Combustion Model Reduction and Lumping H Rabitz and F L Dryer, Princeton University
04:30	ADJOURN

ENERGY DISTRIBUTION IN ARCJET THRUSTERS

(AFOSR Grant/Contract No. 2308M4)

Ronald A. Spores
Air Force Astronautics Laboratory, Edwards Air Force Base, Ca. 93523

Summary/Overview

There is a strong need to improve our fundamental understanding of electrothermal arcjets with the ultimate goal of increasing both efficiency and specific impulse. A research effort using emission spectroscopy, two-color pyrometry and analytical modeling is being developed to better understand and minimize the major energy loss mechanisms in arcjet thrusters, for example: anode heat losses, viscous losses and frozen flow losses. Research in these areas will assist in optimizing the overall design configuration and thermal characteristics of arcjet propulsion devices. → 298 →

Discussion

Arcjet thrusters, which utilize electrothermal acceleration of the propellant, will be the next major advancement in the area of operational electric propulsion technology. The present maximum obtained specific impulse is slightly over 800 sec for a 30 KW ammonia arcjet and I_{sp}=450 sec for a 1 KW arcjet using hydrazine: these values represent major improvements over chemical combustion technology, however arcjets are still not well understood and substantial improvements are possible.

Many mechanisms of energy loss occur in these type of devices and typically only 40% of the initial input power is actually transferred to usable kinetic energy. Areas of energy loss include: ~15% of the input power is lost as heat to the anode while ~40% of the energy actually transferred to the propellant is lost as frozen flow, viscous losses or via improper nozzle expansion. This research effort, which would have benefits throughout the arcjet design, is directed towards improved understanding of the energy transport in the anode body and gas propellant.

The energy distribution throughout arcjet thrusters is a very interrelated issue. For example, one proposed project is to locally cool the tungsten anode in the region of the constrictor and arc attachment by passing the propellant fluid through cooling channels.

This will then allow the nozzle to run with higher wall temperatures increasing heat transfer to the nozzle boundary layer. The lower density will then reduce the viscous losses allowing for a longer nozzle design that would increase the available time for molecular recombination thus decreasing frozen flow losses and enhancing thruster efficiency. Using the propellant fluid to cool the anode in a regenerative fashion also utilizes the wasted thermal energy to preheat the propellant again leading to improved efficiency.

This research endeavor will be broken down into several projects each looking at a particular aspect of the overall effort:

1) The interior of the nozzle region will be investigated by both looking upstream along the axis of the engine and viewing the nozzle region off-axis using emission spectroscopy. Optical access will also be gained by peering through quartz filled viewing slits cut through the anode into the nozzle. Information pertaining to the mode of anode arc attachment and its temperature distribution will be obtained with these techniques. By focusing the optics farther upstream into the constrictor region, information about peak temperature of the plasma and thermal gradients to the constrictor wall can potentially be acquired. Temperature measurements of the internal walls can be investigated using two-color pyrometry observations through optical access windows immediately after the arc is extinguished.

Unfortunately, very little research has been directed towards obtaining internal plasma diagnostics in arcjets and an extensive effort to design the optical access windows and sealing techniques will probably be required.

2) Experimentally, the energy distribution in the excited and ionized states can be analyzed in the plume as a function of nozzle length with emission spectroscopy. The doppler shift of emission line profiles will also be analyzed as the nozzle shape and length are varied in order to better comprehend and reduce the radial and azimuthal velocity components in the exhaust plume.

3) The effectiveness of preheating the propellant will be determined by measuring inlet temperature via a thermocouple positioned just inside the injector port (if it survives) and observing how performance is affected by inlet propellant temperature. An alternate approach will be to observe the injector port through an optical access window getting temperature from two-color pyrometry; the injector port would be treated as a black body cavity with the incoming propellant assumed in equilibrium.

4) Increased operating pressure of the propellant has been shown to enhance thrust performance by reducing the mean free paths between atoms thus diminishing frozen flow losses. The other main approach to reduce frozen flow is to lengthen the nozzle. Unfortunately, the longer the nozzle the higher the viscous losses and thus a trade off study

of these loss mechanisms, as a function of nozzle pressure and nozzle wall temperature would be beneficial for optimum nozzle design. Anode voltage fall would be another interesting factor to investigate as a function of wall temperature. The anode wall temperature will be varied by using water-cooling through the anode body to control heat flux while an analytical model will be utilized to determine viscous drag losses in the boundary layer profiles.

NONEQUILIBRIUM IONIZATION IN PLASMA ACCELERATORS

AFOSR Grant No. 86-0119

M. Martinez-Sanchez
Massachusetts Institute of Technology
Cambridge, Massachusetts 02139, U.S.A.

Summary

Plasma accelerators operate under the influence of gasdynamic, kinetic, and electromagnetic processes. It is unlikely that equilibrium flow will be approached, due to the magnitude of the ratio power density/mass density in these thrusters. Nonequilibrium production rates between these levels and the continuum are used in an analysis of the steady and unsteady behavior of the plasma. The influence of radiation and diffusion on these rates is evaluated. We determine that only at small temperatures compared to the energy gap between the first excited state and the continuum is a multi-level model required.

Technical Discussion

We model an atom or ion by its electronically excited states, using lumped states to reduce computations as well as to facilitate analysis. Three species were of concern: the hydrogen and argon atoms and the argon ion. Given the structure of the atom or ion, a finite-rate model of the interactions amongst these levels and between the levels and the continuum is used. The processes to be included are:

- Electron-atom excitation/deexcitation collisions.
- Electron-atom ionization and electron-electron-ion recombination collisions.
- Net dexcitation due to radiative decay and its inverse.
- Net recombination due to radiative recombination and its inverse.

A classical approach is taken in writing net production rate equations for each of the levels and the continuum. The continuum equation is the sum of collisional ionization and losses from collisional recombination and radiative recombination:

$$\dot{n}_e = n_e \sum_k n_k S_{kc} - n_e^2 \sum_k (n_e S_{ck} + A_{ck}\beta_{ck}) \tag{1}$$

The rate equations for a level k are the sum of: excitation and dexcitation processes with other levels, recombination from the continuum minus ionization, the gain from radiative decays from higher levels minus the loss by radiative decay to lower levels, and radiative recombination:

$$\dot{n}_k = n_e[\sum_{j\neq k}(n_j S_{jk} - n_k S_{kj}) + n_e^2 S_{ck} - n_k S_{kc}] + \sum_{l>k} n_l A_{lk}\beta_{lk} - n_k \sum_{j<k} A_{kj}\beta_{kj} + n_e^2 A_{ck}\beta_{ck} \tag{2}$$

Where n_k is the number density of level k ($k = 1$ is the ground state, $k = 2$ the first excited state, and so on), the S_{jk} terms are collisional rate coefficients (calculated), the A_{kj} terms are the Einstein transition probabilities (for radiative decay; tabulated), and the $\beta = 1 - \frac{absorption}{emission}$ are the radiative escape factors (assumed based on estimates or calculated in cases where it may be critical).

In this model, the escape factors are varied somewhat, although, in general, experimental evidence seems to indicate that $\beta_{lk} \approx 0$ for $1 = k < l$, and $\beta_{lk} \approx 1$ for $1 < k < l$; ie., most plasmas are optically thick towards the ground state, but optically thin for all other inter-level transfers. For the radiative line between the first excited state and the ground, for example, the escape factor is on the order of 10^{-5} under typical conditions. For a channel of height $h = .02m$, then $n_e n_1 \leq 10^{32} m^{-6}$ for a significant β_{21}, which is either a very low number density or an ionization fraction which is either very small (for broadening due to collisions with electrons) or close to 1.

For the ambipolar loss, we use a model which assumes ion-attracting walls, a uniform loss rate (parabolic density profile), and requires that at the edge of the sheath ambipolar diffusion is balanced by direct ion loss to the wall,

$$n_e v_B = D_a \frac{dn_e}{dy}$$

where $v_B = \sqrt{\frac{k_B T_e}{m_i}}$ is the ion Bohm velocity and the ambipolar diffusion coefficient is:

$$D_a = (1 + \frac{T_e}{T_g}) \sqrt{\frac{\pi k_B T_g}{m_e}} \frac{1}{2 Q_{ne} n_{tot}}$$

Then the ambipolar diffusion rate to the walls is:

$$(\dot{n}_e)_{amb} = \frac{\frac{12 D_a n_e}{h^2}}{1 + \frac{6 D_a}{v_B h}}$$

The ion loss will be limited by direct ion loss to the walls for low values of the factor hn_{tot}, and limited by diffusion (i-n collisions) at high values. Most cases of interest for plasma accelerators are near to the transition point, $hn_{tot} \approx 7 \times 10^{18} m^{-2}$.

The rate equations can be rewritten through use of the microreversibility relationships between the collisional rate coefficients:

$$S_{kc} = \frac{n_e^2}{n_k^*} S_{ck} = S(k, T_e) S_{ck}$$

$$S_{jk} = \frac{n_k^*}{n_j^*} S_{kj}$$

where $S(k, T_e) = \frac{n_e^2}{n_k^*}$ is the Saha equilibrium factor for level k (superscript $*$ denotes the equilibrium value). The resulting equations deal directly with the effects of each level being out of equilibrium. Writing the ratio of a level's population to its equilibrium population as $b_k = \frac{n_k}{n_k^*}$, then $(b_k - 1) S_{ck}$ is the net ionization rate due to collisions from level k and $(b_j - b_k) S_{kj}$ is the net gain of level k atoms due to excitation/dexcitation processes involving k and another level j. Equations 1 and 2 become:

$$\dot{n}_e = n_e^3 (\sum (b_k - 1) S_{ck} - \frac{\sum A_{ck} \beta_{ck}}{n_e}) \tag{3}$$

$$\begin{aligned} \dot{n}_k &= n_e^3 [\sum_{j \neq k} \frac{(b_j - b_k) S_{kj}}{S(k, T_e)} - S_{ck} (b_k - 1)] \\ &+ n_e^2 [\sum_{l > k} \frac{(b_l - 1) A_{lk} \beta_{lk}}{S(l, T_e)} - \sum_{j < k} \frac{(b_k - 1) A_{kj} \beta_{kj}}{S(k, T_e)}] \\ &+ n_e^2 [A_{ck} \beta_{ck} + \sum_{l > k} \frac{A_{lk} \beta_{lk}}{S(l, T_e)} - \sum_{j < k} \frac{A_{kj} \beta_{kj}}{S(k, T_e)}] \end{aligned} \tag{4}$$

The collisional rate coefficients vary inversely with the energy gap between the levels involved in the transition. Therefore the collisional rates for the excited states are much higher than for the ground state,

due to the smaller gaps. For stationary or moving plasmas, then, we could assume that all the excited states have $\dot{n}_k = 0$, and that only the ground state rates are on the order of convective and diffusive terms in the continuity equation:

$$\frac{\partial n_e}{\partial t} + \nabla \cdot (n_e \vec{u}) = \dot{n}_e - (\dot{n}_e)_{diff}$$

In this case, equation 4 could be used to solve for all of the $b_k - 1$ as a function of the ground state, $b_1 - 1$ in a form:

$$(b_k - 1) = \chi_k(\bar{\beta}, n_e, T_e)(b_1 - 1) + \psi_k(\bar{\beta}, n_e, T_e)$$

where $\bar{\beta}$ represents the matrix of escape factors, and ψ_k is entirely due to radiation, coming from the last line of equation 4. Plugging this form into the continuum rate equation, 3, assume that $n_a \approx n_1$, and rewrite the equation as:

$$\dot{n}_e = n_e n_1 [S(1, T_e) \sum_k (\chi_k + \frac{1}{b_1}\psi_k) S_{ck} - n_e^3 \sum_k \chi_k S_{ck}] - n_e^2 \sum_k A_{ck}\beta_{ck} \tag{5}$$

We can compare this with the standard form of the equation for a two-level model, $\dot{n}_e = n_e n_a S_{ac} - n_e^3 S_{ca}$. The corresponding overall rate coefficients, neglecting the radiative recombination term, are ionization: $S_{ac} = S(1, T_e) \sum_k (\chi_k + \frac{1}{b_1}\psi_k) S_{ck}$, and recombination: $S_{ca} = \sum_k \chi_k S_{ck}$. It should be noted that, although the recombination terms, S_{ck} diverge as $k \to \infty$, the factors χ_k fall off fast enoughwith k so that the series will converge. Overall microreversibility, $\frac{S_{ac}}{S_{ca}} = S(1, T_e)$ only holds when the plasma is collisionally dominated (ψ_k negligible).

We can estimate the degree of nonequilibrium of the ground state, b_1 under simple conditions. In a steady state, nonconvecting plasma, ion production due to collisional and radiative processes is balanced by ambipolar diffusion/recombination at the wall:

$$\dot{n}_e = \frac{\frac{12 D_a n_e}{h^2}}{1 + \frac{6 D_a}{v_B h}}$$

Looking at a fairly high temperature case where the upper levels do not contribute significantly, and at a relatively high hn_{tot}, then the ground state can be determined from (using mks units):

$$b_1 - 1 = \beta_{c1} \frac{10^{21}}{n_e} + 17 \frac{10^{46}}{n_e^2}$$

The effects of the radiative processes are most significant below $n_e \approx 10^{21} m^{-3}$ and diffusion effects are strong whenever $n_e < 4 \times 10^{23} m^3$. S_{C1} is roughly proportional to $T_e \exp(\frac{eV_i}{k_B T_e})$, for the temperatures of interest here ($k_B T_e < eV_i$), S_{C1} increases with decreasing temperature. Thus equilibrium is most likely at high n_e and low T_e.

The kinetic approach is also used to simulate a two-component gas: either two different atomic species or the atom and ion of the same species. Two cases were simulated: a gas (here, argon) whicl has a relatively small concentration of a second gas (here, hydrogen) added to it and the argon atom and ion. As earlier, only electronic collisions are considered. It is further assumed that the time scale for electron-electron equilibrium (in a Maxwellian distribution at T_e) is short compared to all others so that only one electron temperature is necessary.

Figures 1-3 show how the net collisional ionization flux in argon, normalized by the ground state flux, varies with excited level. This is $\frac{(b_k - 1) S_{ck}}{(b_1 - 1) S_{c1}}$ or, for a collisionally dominated case, $\chi_k \frac{S_{ck}}{S_{c1}}$. Note that at low temperatures the flux comes mostly from a high level peak, at moderate temperatures most of the levels have fluxes at similar orders of magnitude, and at high temperatures the flux comes mostly from the ground state. Thus, only at relatively low temperatures (when the average electron kinetic energy is small compared to the gap between the first excited state and the continuum: $\frac{kT_e}{E_{\infty} - E_1} \ll 1$) are the excited levels critical; at high temperatures, at most the first excited state contributes. Figure 4 is a comparison of overall recombination coefficients, S_{ca}, from this model (both for hydrogen and argon) and the Hinnov-Hirshberg formulation.

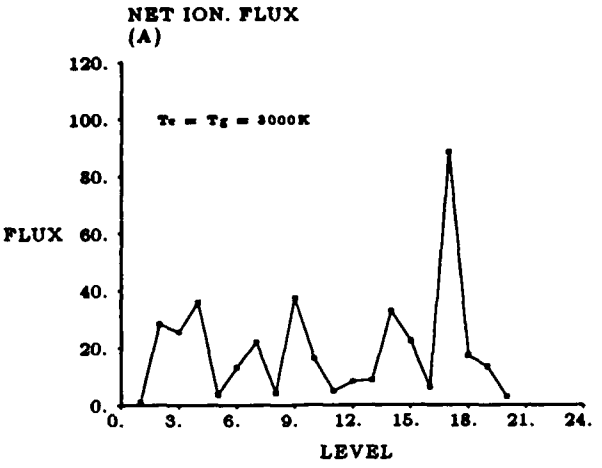

Figure 1: Net Ionization Flux vs. Level at 3000K

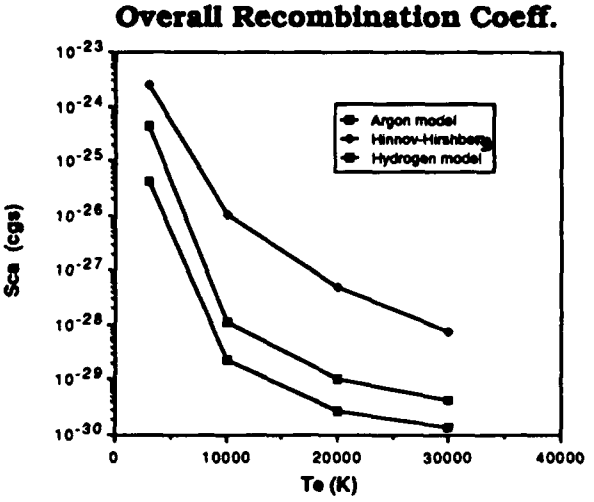

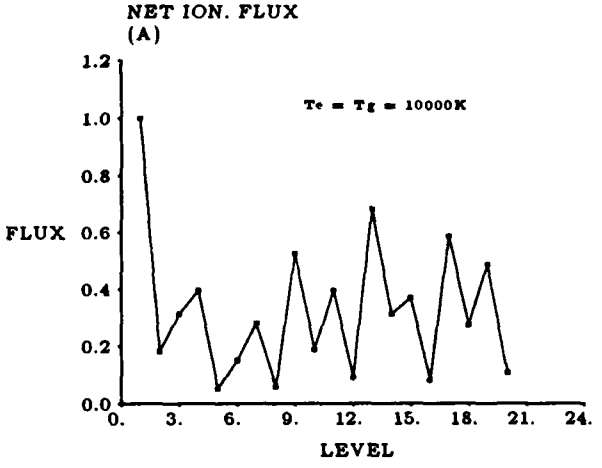

Figure 2: Net Ionization Flux vs. Level at 10000K

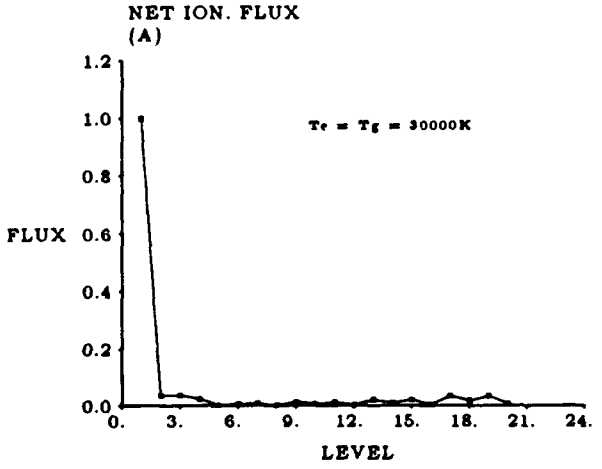

Figure 3: Net Ionization Flux vs. Level at 30000K

Fundamental Research on Erosion in Magnetoplasmadynamic Thrusters

(AFOSR Grant No. 87-0360)

Principal Investigators: V. V. Subramaniam and J. W. Rich

Department of Mechanical Engineering
The Ohio State University
Columbus, Ohio 43210

SUMMARY/OVERVIEW:

The purpose of this research is to understand and quantify the mechanisms responsible for erosion in steady state magnetoplasmadynamic (MPD) thrusters. This is an important step in being able to predict thruster lifetimes. A major if not dominant erosion mechanism in the diffuse mode, is evaporation. This analytical work aims to understand this mechanism in particular, its limits, and to provide quantitative models in order to estimate the electrode lifetimes.

TECHNICAL DISCUSSION

Erosion processes depend on a complex coupling between plasma discharge characteristics, plasma-wall interactions, and electrode phenomena. In particular, erosion rates depend on whether the current conduction is through localized spots, or via a diffuse (distributed) mode. Spots are detrimental to the electrode material because of their high erosion rates. Therefore, it is important to understand how and under what conditions they may be formed, and exactly when diffuse mode behaviour ends. Much of the focus of this research is on the cathode, although the anode has also been studied. The thermal response of the electrodes at steady state has been studied and for the first time, been coupled to existing models of the flowing plasma[1-5]. These will be briefly reviewed next, followed by a short summary of ongoing and planned research.

Recently developed simple models of the electrode-adjacent sheath have revealed a thermal runaway mechanism that can limit diffuse mode operation[1,2]. The thermal runaway is caused by a positive feedback between electron bombardment and thermionic emission. This is predicted to occur at high total currents for a given mass flow and thruster geometry, for both the anode and the cathode. Limits have been derived for both the minimum sheath voltage drops as well as the maximum local surface temperatures at which this thermal runaway occurs. The predicted critical temperatures for tungsten and thoriated tungsten (approximately 3200 K and 2850 K respectively) are well below the melting temperature. In addition to identifying limits to steady state operation, electrode surface temperatures and evaporative erosion rates have been predicted for a given steady state operating point. The

steady state electrode surface temperature is related to the global parameters such as electrode material, geometry, discharge current, and propellant mass flow rate. Once these quantities are specified, the profiles of current density, charged particle number density, and temperature versus distance along the electrode can be computed for the core flow far away from the walls. These are computed by solving the quasi one-dimensional non-equilibrium ionizing MPD equations[3,4], which subsequently serve as boundary conditions to an approximate two-temperature non-equilibrium ionizing viscous boundary layer model[5]. This boundary layer model is then able to predict the charged particle number densities near the electrode surfaces. Finally, coupling these solutions to the electrode-adjacent sheath serves to simultaneously determine the sheath voltage drop as well as the surface temperature. This overall strategy is an effective means of predicting evaporative electrode erosion rates for steady state MPD thrusters, as can be seen from a comparison between the shapes of the predicted and experimentally measured profiles (see Fig. 1 and Fig. 2).

Despite the apparent successes of our approximate models, two weaknesses remain. First, the behavior of the cathode sheath at conditions where the current densities are high (above $10^5\ A/m^2$) and the number densities are low (below $10^{20}\ m^{-3}$) is presently unknown. It is expected that the electron velocity distribution function will be substantially different from the Maxwellian distribution since the characteristic energy relaxation time is far greater than the momentum relaxation time. Consequently, the electrons in the near sheath region consist of two groups. These are the "slow" plasma electrons, and the "fast" electrons thermionically emitted from the electrode surface that gain substantial energy from the cathode fall. Based on this, a mechanism for enhanced ionization near emitting electrodes is being proposed and investigated. It is suggested that re-absorption of resonance radiation from the bulk of the flowing plasma produces a high density of excited states near the electrodes. These excited atoms are then subsequently ionized by electron impact from the thermionically emitted electrons when the sheath voltage drops reach levels on the order of the difference between the ionization potential and the energy of the first excited state. Second, the presence of these "fast" electrons in a region where only a few collisions take place, can excite large longitudinal oscillations[6]. This can lead to unsteady behavior in the terminal voltage which is observed at Onset. Future research is therefore aimed at studying transport of resonance radiation in the MPD plasma, and incorporating transient response in the sheath models.

References

(1) V. V. Subramaniam, and J. L. Lawless, "Thermal Instabilities of the Anode in an MPD Thruster", *J. Propulsion & Power*, Vol. 6, No. 2, pp. 221-224, March-April 1990.

(2) K. S. Hoyer, V. V. Subramaniam, and J. L. Lawless, "Limits on Steady Diffuse Mode Operation of the Cathode in an MPD Thruster", accepted for publication in *J. Propulsion & Power*.

(3) J. L. Lawless, and V. V. Subramaniam, "Theory of Onset in Magnetoplasmadynamic Thrusters", *J. Propulsion & Power*, Vol. 3, No. 2, pp. 121-127, March-April 1987.

(4) V. V. Subramaniam, and J. L. Lawless, "Onset in Magnetoplasmadynamic Thrusters with Finite Rate Ionization", *J. Propulsion & Power*, Vol. 4, No. 6, pp. 526-532, November-December 1988.

(5) V. V. Subramaniam, and J. L. Lawless, "Electrode-Adjacent Boundary Layer Flow in Magnetoplasmadynamic Thrusters", *Phys. Fluids*, Vol. 31, No. 1, pp. 201-209, January 1988.

(6) V. V. Subramaniam, and W. F. Hughes, "A Macroscopic Interpretation of Landau Damping", *J. Plasma Phys.*, Vol. 36, part 1, pp. 127-133, August 1986.

(7) R. M. Myers, N. Suzuki, A. J. Kelly, and R. G. Jahn, "Cathode Phenomena in a Low Power, Steady State MPD Thruster", paper AIAA-88-3206 presented at the AIAA/ASME/SAE/ASEE 24th Joint Propulsion Conference, Boston, Massachusetts, July 11-13, 1988,

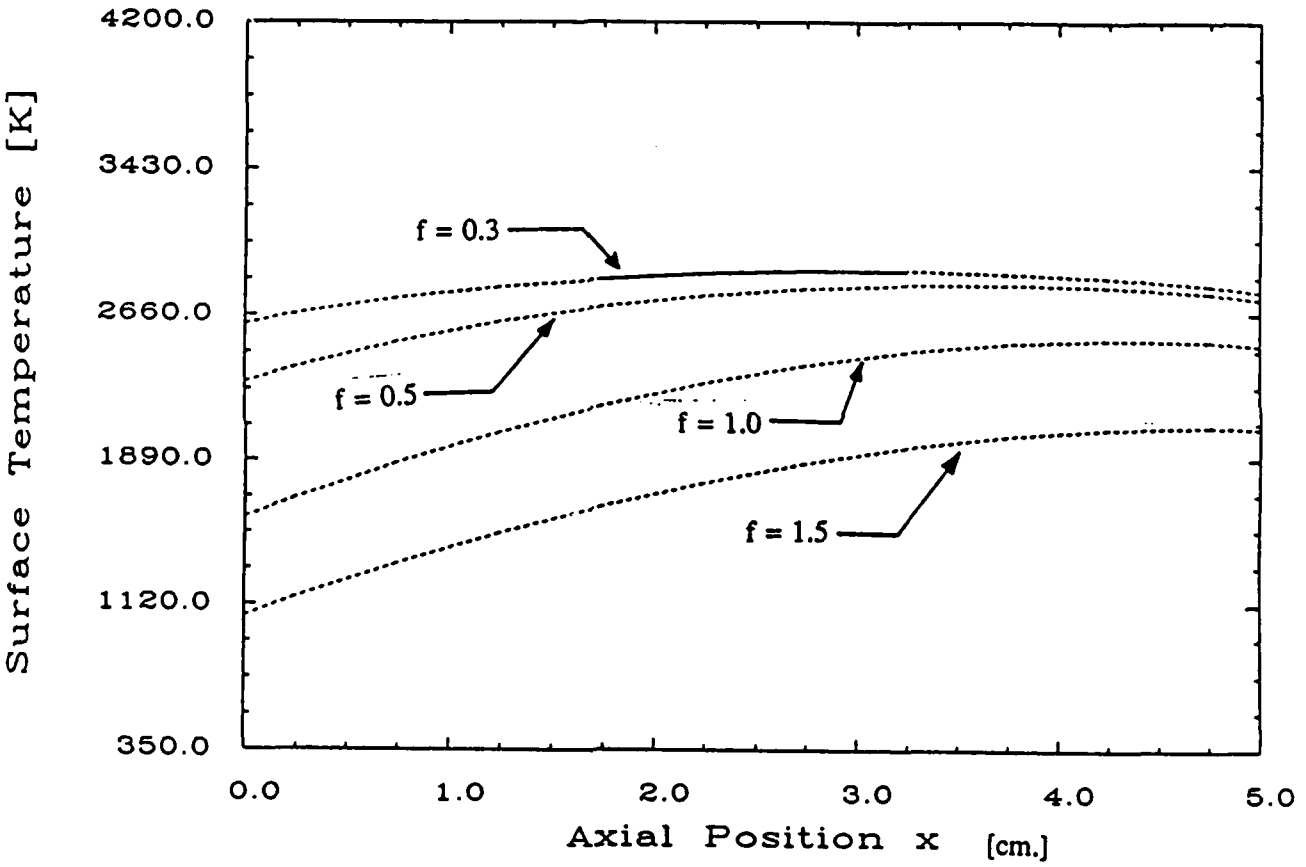

Fig. 1: Cathode surface temperatures versus distance along the cathode predicted by the present theory, are shown here for various values of the fraction of the ohmic heating removed via external cooling (f), for a total current of 2275 A and an argon mass flow rate of 0.1 g/s. This corresponds to the same value of $J^2/\dot{m}$ as for Fig. 2.

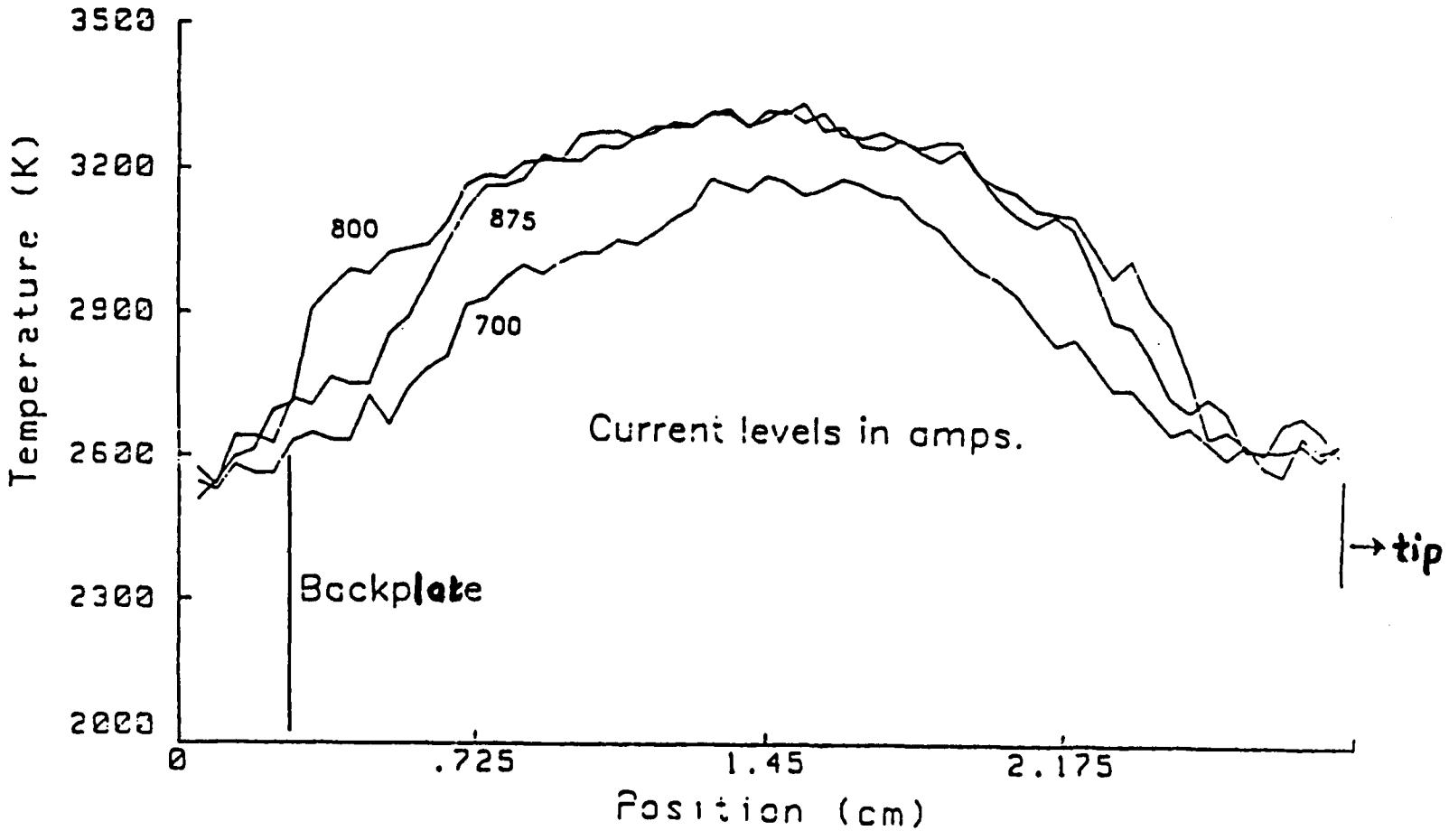

Fig. 2: Experimentally measured cathode surface temperatures versus distance along the cathode from ref. [7] are shown here for various total currents, for a nitrogen mass flow rate of 0.012 g/s.

BASIC PROCESSES OF PLASMA PROPULSION

AFOSR Grant No. 86-0337
Principal Investigator: Herbert O. Schrade

Institute for Space Systems
University of Stuttgart
Pfaffenwaldring 31
D-7000 Stuttgart 80
FRG

SUMMARY/OVERVIEW

The research work deals with critical, not fully understood problem areas in plasma thruster devices in order to assess and improve their performance and reliability. Major emphasis is placed on developing and improving of computational methods in order to predict thruster performance, on exploring plasma stability behaviour and on investigating electrode erosion effects and mechanisms in order to get a better understanding on the reliability and lifetime of plasma thrusters.

AUTHORS
H. O. Schrade
Chr. Sleziona

TECHNICAL DISCUSSION

Plasma thrusters like Arcjet- or Magnetoplasma-dynamic accelerators are for many space missions advantageous with respect to conventional chemical and even superior to the higher Isp ion engines. Despite of their fairly simple design, however, there is still the need to understand and to assess certain fundamental processes and problem areas in order to predict and improve the performance of these propulsion devices. The emphasis of this work is therefore placed on

a) developing and improving of computational methods for plasma thrusters.

b) exploring plasma stability in those devices

c) investigating of electrode erosion effects and arc cathode attachment mechanisms.

(a) Based on a previously developed semi two-dimensional MPD-code which distinguishes between the electron - and heavy particle temperature the influence of a geometrical change of the thruster on its performance has been determined. In Fig. 1 the constant electrical potential lines are plotted for these different constrictors and dischange chamber configurations of the Stuttgart nozzle type MPD thruster at m = 0,8 g/s Argon and I = 2000 A. With increasing constrictor diameters the voltage decreases which is in good agreement with the experimental findings. Development work on a fully two and even three dimensional MPD_Code based on a finite volume method is being continued. Within these codes one assumes that the plasma boundary is identical with the thruster contour. In reality escpecially at higher mass flow rates the boundary between the electrically heated plasma region and the unaffected surrounding cold gas flow becomes a free stream boundary the configuration of which must be determined. A first model calculation reveals that the discharge contour is beside the current a strong function of the ambient pressure (see view graphs).

(b) Plasma stability considerations have been continued. The original theory which allows to determine stable and instable current carrying plasma channels in a constant magnetic field is being extended in order to include also inhomogenous fields. Based on this theory typical onset effects observed in the nozzle type MPD-thrusters could be explained. One also can show that stable helical-shaped discharge channels are possible. This will be discussed in more detail as soon as the extended version of the stability theory is available.

(c) The cathode erosion experiments have been continued with different electrode materials like aluminum, copper, V_2A-steel and tungsten. By means of a PFN-capacitor battery and a trigger electrode the cathode is charged by a rectangular current puls of about 1400 A for about 2 ms. The measured erosion rate for tungsten electrodes at different ambient nitrogen pressure as as function of the number of pulses or accumulated electric charge is plotted in Fig. 2. One can see that with increasing pressure the erosion rate drops and that it asymptotically reaches its highest value after many pulses.

In Fig. 3 the maximum erosion rate is plotted as function of pressure. It shows a threshold drop when the ambient pressure increased above 100 Pa. This effect can be qualitatively explained by the recently developed spot theory. The arc traces left on the cathode surface are investigated by means of SEM pictures and show many separate and overlapping craters.

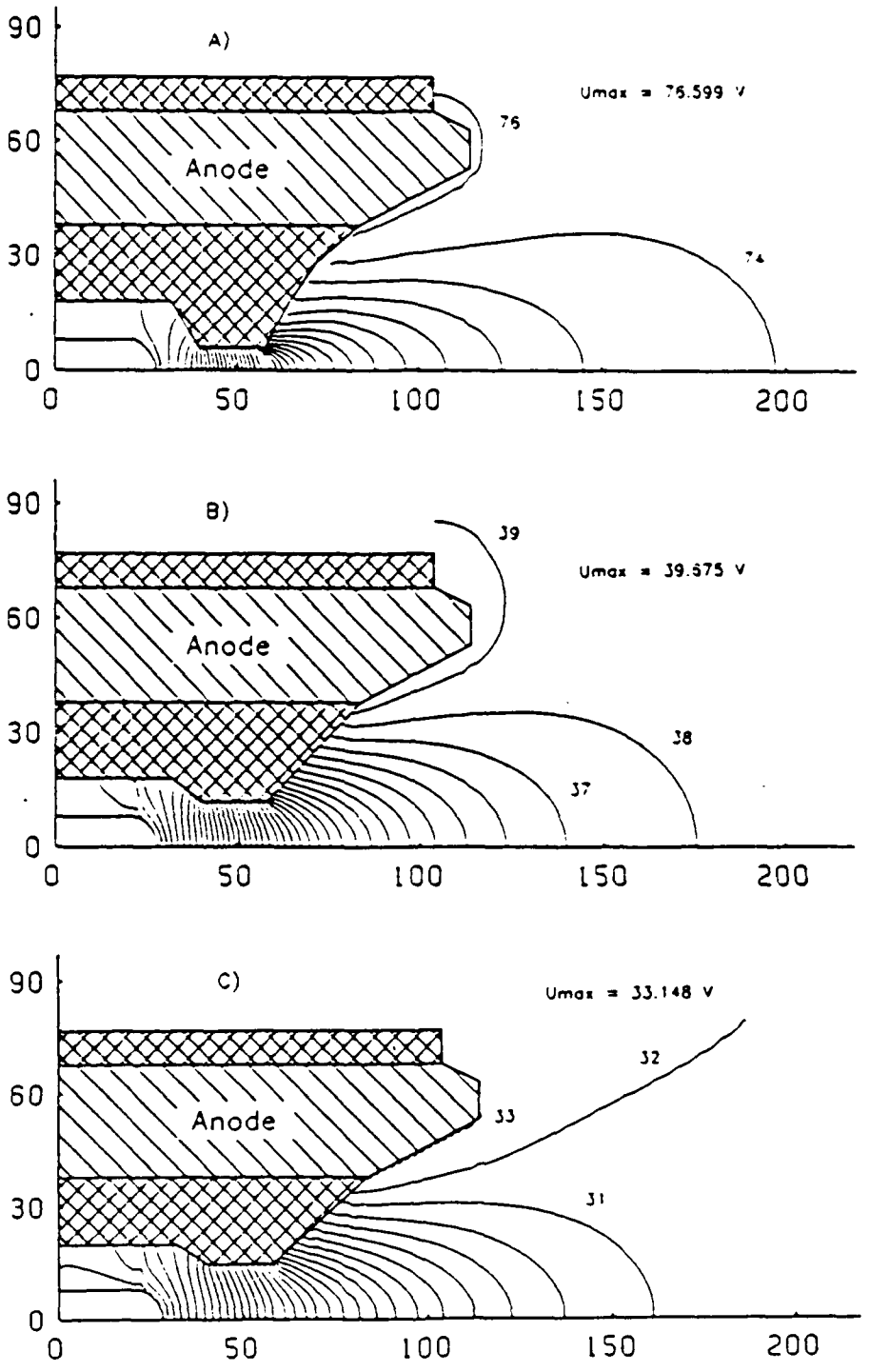

Fig.1 Lines of constant electric potential within three different MPD-thruster configurations (A, B, C) Massflowrate: 0,8 g/s argon Current: 2000 A.

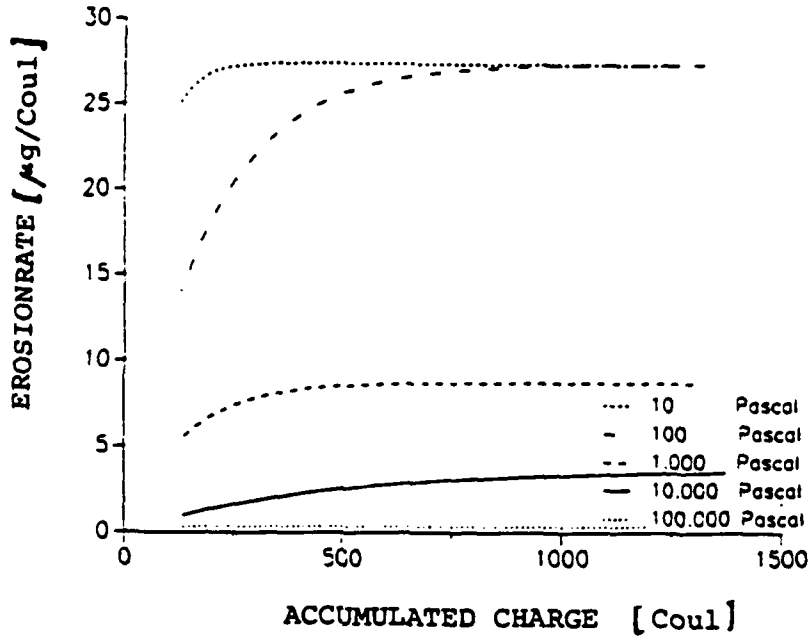

Fig.2 Erosionrate as function of the accumulated charge

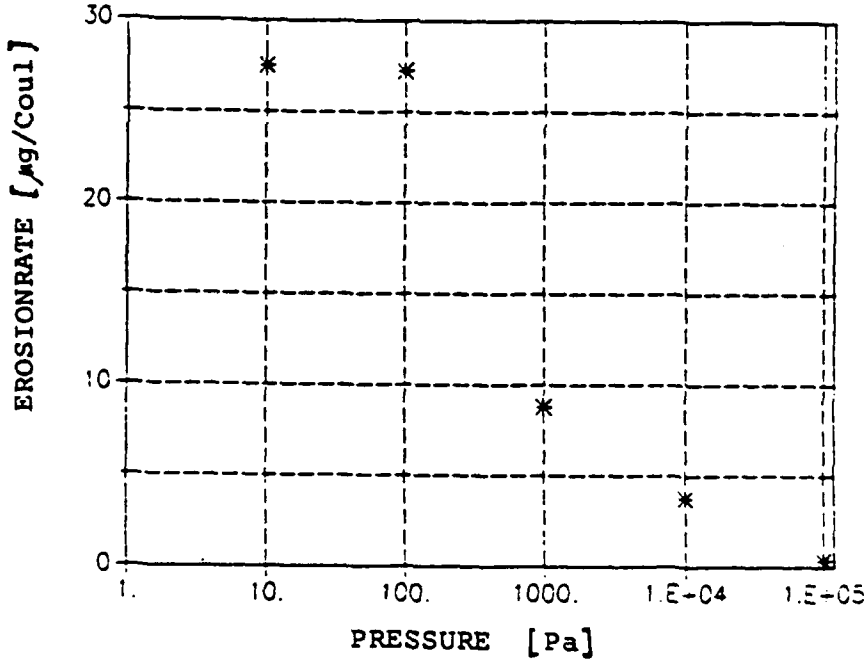

Fig.3 Asymptotic erosionrate as function of the ambient pressure of a tungsten cathode in a nitrogen atmosphere charged by rectangular currentpulses of 1400 A for 2 ms. (Pulsefrequency = 1 to 2 min^{-1})

IONIZED CLUSTER BEAMS FOR SPACE PROPULSION

AFOSR Contract to be awarded

Principal Investigator: Weldon S. Williamson

Hughes Research Laboratories
3011 Malibu Canyon Road
Malibu, CA 90265

SUMMARY/OVERVIEW:

Space propulsion systems must operate in the 1000 s < I_{SP} < 2000 s to make optimum use of foreseeable on-board electric power sources. Electrostatic ion thrusters operated with elemental materials cannot achieve practical thrust density in this range of operation because of space charge limitations. Operation of an electrostatic thruster with massive ions circumvents the space charge limitation, but raises the question of how to form massive ions. Researchers in the 1960's obtained good propulsion characteristics using large organic molecules, but were not able to overcome the difficulties associated with dispensing and ionizing organic materials. If clusters of inert-gas atoms can be formed and ionized efficiently, it may be possible to achieve the desired propulsion characteristics.

TECHNICAL DISCUSSION

In recent years, large clusters of atoms have been generated in the exhaust beam of gases expanded through supersonic nozzles into a vacuum[1]. These large clusters of atoms are bound together by Van der Waals forces, and the size is dependent on the nozzle geometry, the nozzle temperature, the gas species, and the stagnation pressure. Clusters of 200 atoms or more are quite stable, and can be ionized by electron bombardment without fragmentation. At Hughes Research Laboratories, we have studied cluster formation in some inert gases, and gas mixtures[2]. Hughes has developed relatively straightforward methods to generate clusters in the 1000 to 2000 atom range, and to reproducibly control the cluster size by controlling the gas pressure and nozzle temperature. In principle, it should be possible to tailor the mass of these Van der Waals clusters to fit the requirements of a propulsion system that could operate in the 1000 s < I_{sp} < 2000 s range. The feasibility of such a propulsion system depends on being able to form clusters efficiently and with the desired size.

Our approach is to form clusters using a mixture of two gases. These gases will be pre-mixed in specified proportion and when exhausted isentropically through a nozzle, one gas (which we

will call the thrust gas) will form clusters, and the other gas (which we will call the carrier gas) will serve as the medium for extracting the heat of condensation from the clusters. For this cluster-ion concept to be viable in a propulsion system, a major fraction of the thrust gas must form clusters of the desired size, and the mass of the carrier gas must be a relatively small fraction of the mass of the total gas mixture. Under our study, we plan to measure the cluster size distribution and the efficiency of cluster formation in gas mixtures of hydrogen, as the carrier gas, with an inert gas (xenon and/or argon), as the thrust gas. We will analyze the results of these measurements in terms of cluster applicability for use in an electrostatic thrust system, and we will calculate the thrust system performance as a function of mission parameters (power available, power source voltage, propellant requirements, etc.).

Figure 1 shows schematically how clusters are formed by isentropic expansion of gas at relatively high pressure through a supersonic nozzle into vacuum. All of the gas atoms and clusters in the central cone of the flow field are accelerated to the same velocity, and this velocity is a function only of the gas species and the nozzle temperature. To obtain an ionized cluster beam the nozzle is fitted with a skimmer and ionization cell as shown in Figure 2. The clusters and gas atoms are ionized by electron bombardment in the ionization cell. Electrons emitted by the filament are accelerated across the gas stream by the potential applied to G1 and eventually collected on the anode grid, G2. The drift velocity carries the ionized clusters and atoms to the extraction grid, G3, where they are accelerated by the electric field resulting from the voltage applied between grids G3 and G4.

Because the drift velocity, v_s, is the same for the clusters and gas atoms in the core of the expansion, it is possible to determine the cluster size distribution using the voltage-current (i.e. retarding potential) characteristic measured with a gridded Faraday cup collector (see Figure 2). Having obtained the cluster size distribution, the measured ion current and gas flow rates can be used to evaluate the efficiency of cluster formation.

REFERENCES

1. Hagena, O.F., and Obert, W., "Cluster formation in expanding supersonic jets: effect of pressure, temperature, nozzle size and test gas", J. Chem. Phys. 56, 1793-1802 (1972).

2. Knauer, W. and Poeschel, R.L., "Cluster Beam Studies", Final Technical Report for USAF Contract F49620-85-C-0125, AFOSR, April, 1988.

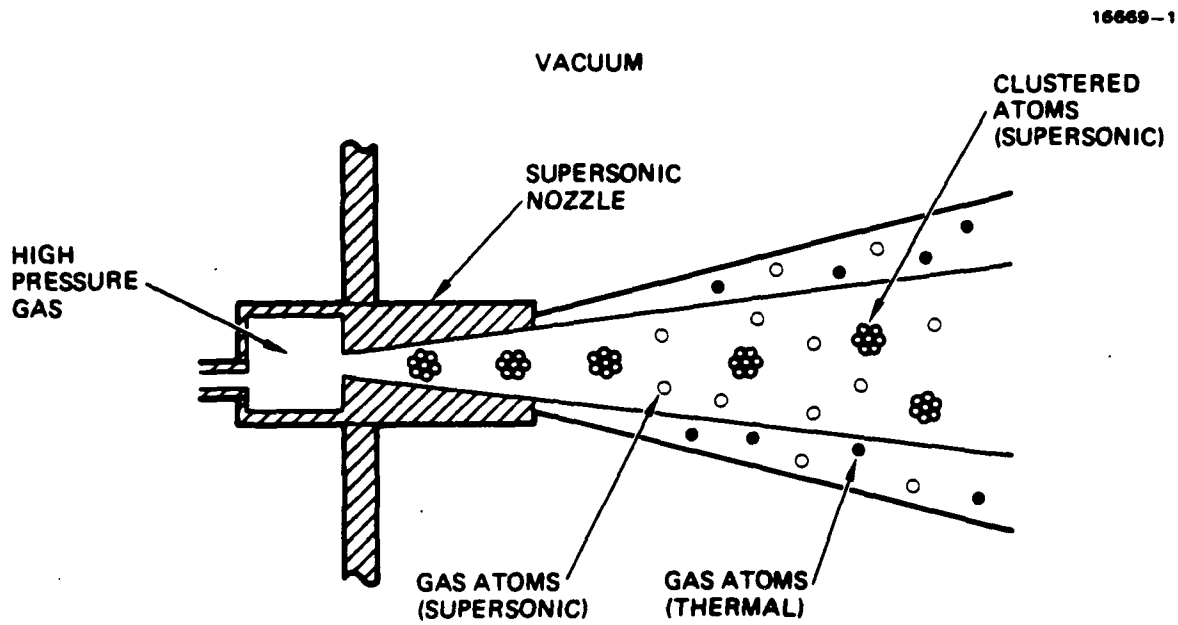

Figure 1. Illustration of cluster formation in gas expanded through a supersonic nozzle.

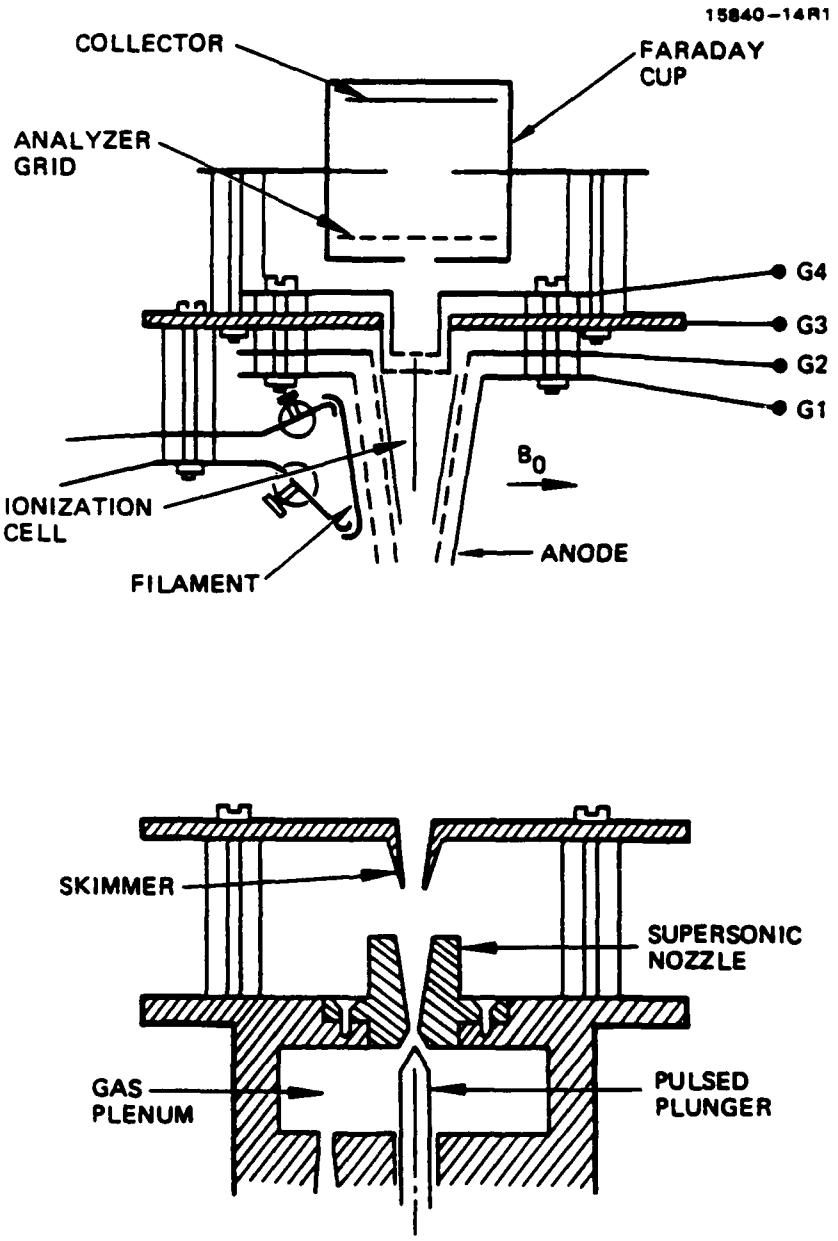

Figure 2. Ion cluster-beam experimental configuration.

PICOSECOND LASER BREAKDOWN THRESHOLDS IN GASES

AFOSR Grant No. AFOSR-86-00317

Principal Investigator: Dennis Keefer

Center for Laser Applications
University of Tennessee Space Institute
Tullahoma, TN 37388
615/455-0631

The objective of this research is to develop an understanding of the basic physical processes that control the interaction of plasmas sustained by laser beams in a flowing propellant gas. Previous experimental and theoretical studies have provided a reasonable understanding of these processes in flowing plasmas sustained by continuous lasers, and have shown that the absorption efficiency and radiation losses can be controlled through a combination of optical geometry, pressure and flow configuration. Practical beamed laser propulsion systems may require laser powers greater than one megawatt, and current laser development for other applications suggest that lasers capable of delivering average powers at these levels will be free electron lasers (FEL). The power from these free electron lasers will be pulsed, rather than continuous, and we have successfully sustained quasi-steady argon plasmas using the RF linac free electron laser at Los Alamos National Laboratory (LANL).

Attempts were made to initiate plasmas in both nitrogen and hydrogen using the same experimental procedures as for argon. These attempts were not successful, even though the pulse energy was an order of magnitude larger than our observed threshold for argon. This result is somewhat surprising, since predicted breakdown thresholds using 10.6 micron wavelength and 10 ps duration pulses for hydrogen and nitrogen are essentially the same as for argon.

In a plasma sustained by the absorption of power from a continuous laser, the power is absorbed primarily through inverse bremsstrahlung (free-free transitions in the electrons). The electrons are maintained in local thermodynamic equilibrium by electron-electron and electron-ion collisions, and the absorption coefficient can be accurately predicted using the Kramer-Unsöld theory. In free electron lasers, the pulse duration may be as short as a few picoseconds; a time similar to the electron collision time. Under these conditions it is unlikely that the electrons will maintain a Maxwellian distribution, and the absorption predicted by the Kramers-Unsöld theory may no longer apply. After the pulse terminates, the plasma will begin to decay from its nonequilibrium state through radiative and collisional processes, and may approach a local thermodynamic equilibrium prior to the arrival of the next pulse. If the time between pulses is sufficiently short, then subsequent pulses will be absorbed by the plasma remaining from the previous pulse, and a quasi-steady-state may be achieved, similar to plasmas sustained by continuous laser beams.

The RF linac free electron laser at LANL produces a burst of mode-locked micropulses having a duration of approximately 10 ps at a wavelength of 10.6 micrometers and a peak power of approximately 50 MW. These micropulses are spaced 46 ns apart in a burst (macropulse) lasting for 100 to 300 microseconds. The macropulses occur at rate of 1 Hz, and the average power during the duration of the macropulse is approximately 10 kW.

Self initiation of plasmas (breakdown) at the focus of a pulsed laser beam has been observed since the advent of Q-switched ruby lasers nearly thirty years ago. In general, the threshold intensity required for breakdown is inversely related to the pulse length for pulses shorter than a microsecond. At the intensities characteristic of our FEL experiments it is likely that breakdown did not occur at the first 10 ps pulse, but cascaded through absorption of subsequent pulses in the plasma electrons remaining from previous pulses.

We are developing a theoretical model to investigate the question of breakdown threshold for the long wavelength, short pulse regime of our experiments. During the 10 ps duration of the laser pulse, there are only approximately 250 optical cycles and only approximately 10 electron-atom collisions. To study this process, we have developed a model to calculate the evolution of the electron distribution function throughout a sequence of 10 picosecond pulses, following the electron cascade to breakdown. During the process leading up to breakdown, optical energy is absorbed by the electrons, and elastic collisions between the electrons and atoms are dominant. These elastic collisions are modeled assuming that the electrons do not lose any kinetic energy to the massive atom, and the average collision results in a 90 degree change in the electron direction. As the electrons gain energy, inelastic collisions produce excited atoms and molecules and produce additional electrons through impact ionization. In our model we include molecular vibration and dissociation for hydrogen, and ionization from metastable atoms for argon.

Between collisions, the electron oscillates in the optical electric field gaining "quiver" energy. On collision, the electron changes direction and begins to gain additional energy from the electric field. In this way the electron rapidly gains energy from the electric field and begins suffering inelastic collisions which leads to additional electrons being formed by impact ionization. During the time between pulses the high energy electrons continue to suffer inelastic collisions producing additional electrons and reducing the average energy of the electron distribution. The next pulse interacts with all the electrons created by the previous pulse and the number of electrons cascade over several pulses to breakdown. The calculation begins with a single electron in the focal volume and cascades until the focal volume is fully ionized. For the conditions of the LANL experiments the focal volume contains approximately 10^{12} electrons. An example of the model calculation is shown in Figure 1. The number of electrons in the focal volume increases in a stepwise fashion as each new micropulse is absorbed. For argon the excitated atom population is also shown. The argon reaches breakdown during the 7th pulse, and hydrogen reaches breakdown during the 9th pulse.

Obviously, the model predictions do not agree with the observed results. Recombination and attachment were included in the model, but their effect was negligible for both gases. Diffusion of the electrons out of the focal volume may occur during the last few pulses preceding breakdown, but these would be similar for both hydrogen and argon. Preliminary calculations based on the Taylor similarity solution for point explosions suggest that gasdynamic expansion during the last few pulses may reduce the electron gain per pulse to zero for hydrogen but not for argon. This could explain the observed difference in breakdown threshold in the FEL experiments. Additional experiments and more detailed theoretical calculations will be required to resolve this issue.

The combination of pulse length and wavelength used in the LANL experiments are unique to that FEL. However, we have undertaken an experimental study of picosecond pulse breakdown using single pulses produced by a neodymium-YAG laser at wavelengths of 530 nm and 1.06 μm to lend insight into the breakdown process and to develop diagnostic techniques.

The experimental technique used to measure the time to breakdown during a single 70 ps laser pulse is shown in Figure 2. The method uses the pump-probe technique, where a beam of one wavelength is used to create the breakdown, and a beam of a different wavelength is used to observe the plasma formation. In Figure 2 the green (530 nm) beam is used to cause plasma breakdown and the orange (590 nm) beam is used to detect it. The two beams are arranged collinearly to remove errors produced by beam refraction due to shock formation. It is difficult to resolve picosecond times electronically, and an optical delay line is used to vary the timing between the 1 ps probe pulse and the 70 ps pump pulse. A 150 μm movement of the prism will vary the delay by 1 ps, and by scanning the delay line the transmitted pulse energy will produce a curve as indicated in the figure. Variation of the power of the pump pulse or the pressure within the test cell will shift the time at which the amplitude of the transmitted signal decreases.

The results of a preliminary experiment are shown in Figure 3. For this experiment the plasma was formed in ambient air by the 70 ps pulse at a wavelength of 532 nm and focused by a 76 mm focal length lens. The upper curve corresponds to pulse energy of approximately 1.5 mJ which is near threshold. The lower curve corresponds to plasmas formed with a pulse energy of approximately 5 mJ. The plasma formed by the 5 mJ pulse initiates approximately 37 ps earlier than that formed by the 1.5 mJ pulse, indicating a faster rate of electron production. Note, also that the plasma formed by the larger pulse absorbs a larger fraction of the probe pulse energy.

This diagnostic technique should permit us to determine the relative roles of multiphoton and electron impact ionization in the processes leading to plasma breakdown in picosecond optical fields. It can also be used to evaluate the predictions of the theoretical models and, if further FEL experiments at 10.6 μm are possible, provide a means to diagnose the cascade breakdown process.

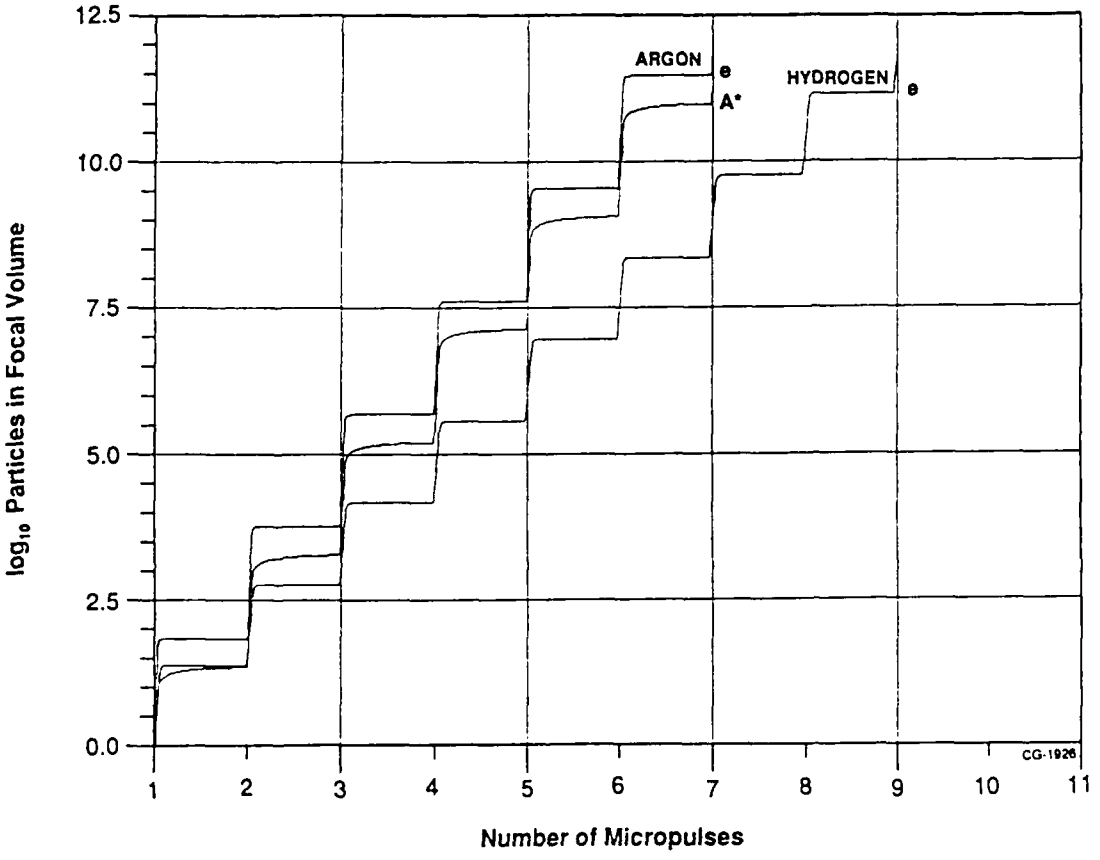

Figure 1

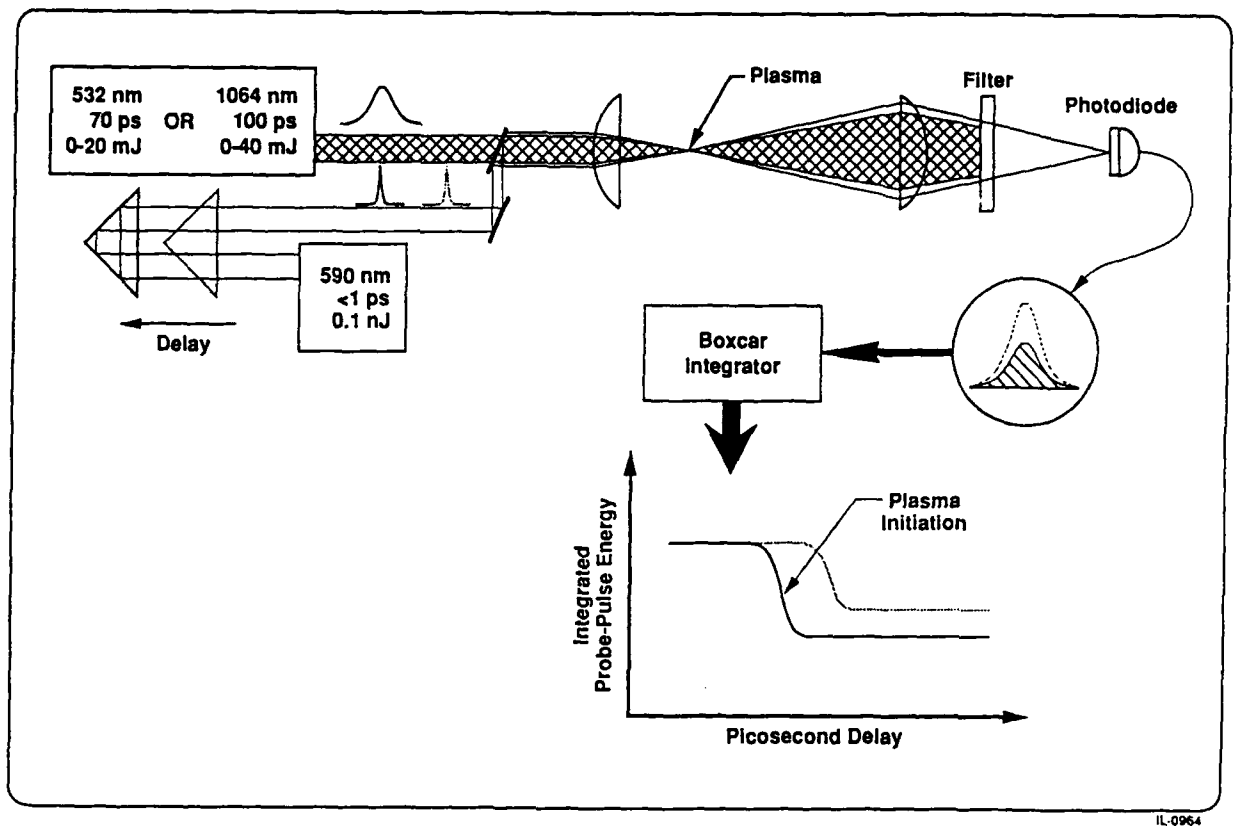

Figure 2

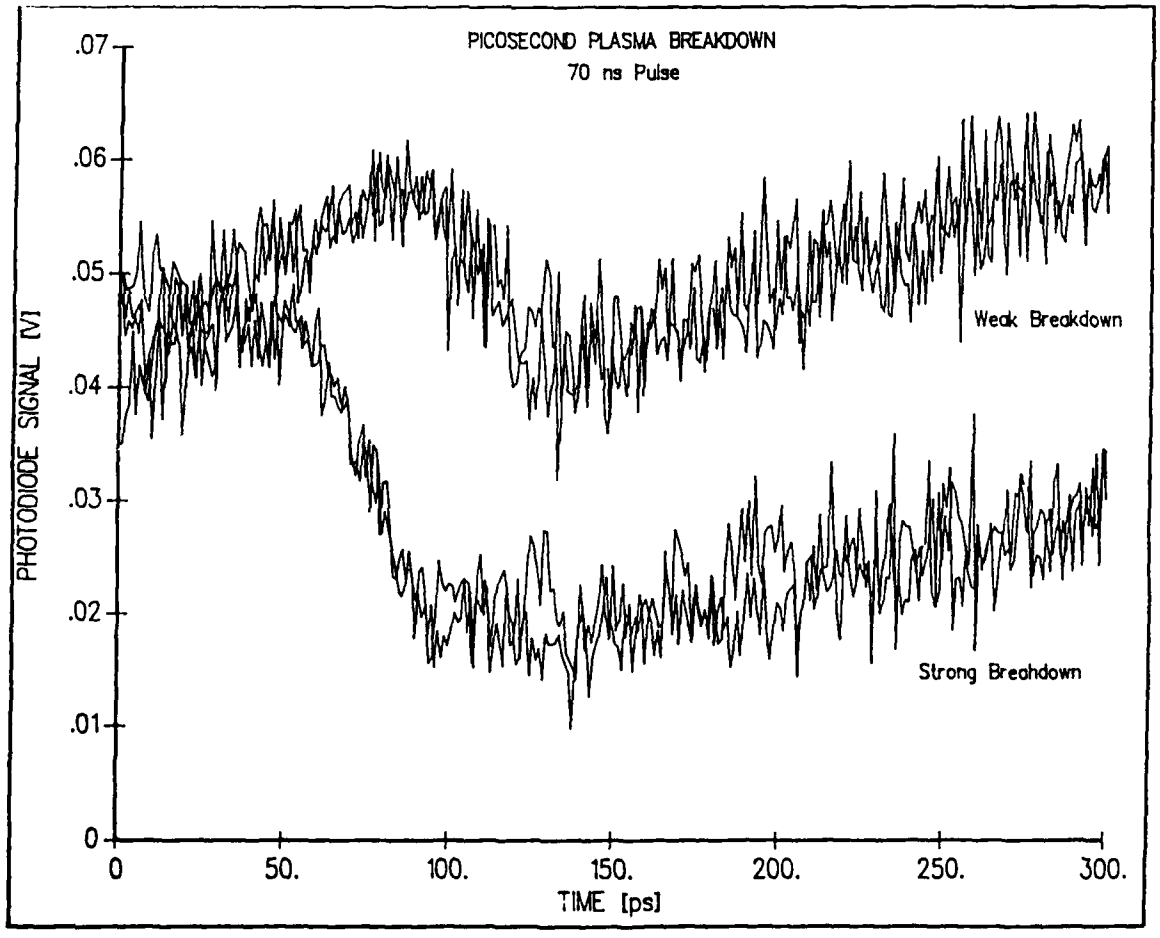

Figure 3

PLASMA SCALING MECHANISMS FOR CW LASER PROPULSION

AFOSR Grant No. 89-0274

Principal Investigators: Herman Krier and Jyoti Mazumder

Department of Mechanical and Industrial Engineering
University of Illinois at Urbana-Champaign

SUMMARY/OVERVIEW:

This investigation is aimed at understanding the fundamental energy transfer mechanisms in and characterizing the performance of laser sustained plasmas (LSP's). The fraction of incident laser power absorbed by the argon and/or hydrogen plasma and the fraction converted to useful gas enthalpy are measured with a water cooled calorimeter and exhaust gas thermocouples, respectively. Numerical modelling of the two dimensional plasma flow is used to predict plasma properties at conditions not available in the laboratory. Emission spectroscopy is used to map plasma temperatures and densities in the plasma core and to evaluate the usual assumption of plasma local thermodynamic equilibrium (LTE). The spectroscopic approach can provide an independent measure of plasma absorption and thermal conversion efficiency in order to evaluate the relationship between experimental and numerical results. Laser induced fluorescence (LIF) of the hot gas surrounding the plasma core may be used for a similar purpose. This investigation has confirmed the proposed idea that LSP's are a feasible means of heating rocket propellant gas, with more than 80% of the incident laser power absorbed in a 2.5 atmosphere hydrogen plasma and 72% converted to gas enthalpy. This investigation will determine the validity of the LTE assumption in numerical modelling so that the code (or modified version) can be utilized with full confidence at high laser power (10 MW), and it will continue to pursue optimum operating conditions and environment for laboratory LSP's.

TECHNICAL DISCUSSION:

Introduction

The central issue in the study of laser sustained plasmas for thermal rocket propulsion is the accurate prediction of plasma performance at operating conditions likely to be required in practice. That is, laser power of one to ten megawatts or higher, chamber pressures of two to five atmospheres or higher, and propellant mass flux to achieve optimum performance. High laser power will be required to produce a practical thrust level, and the performance advantages of elevated pressure (above one atm.) and mass flux are well documented [1-4]. Predictions can be made by the application of an appropriate numerical model, and through the measurement of plasma properties at conditions available in the laboratory from which trends are identified.

Before reliable extrapolations and numerical predictions can be made, the fundamental energy transfer mechanisms within the laser sustained plasma must be clearly understood. The absorption of laser power by the electrons via inverse bremsstrahlung (and other minor absorption mechanisms), the subsequent transfer of energy to the surrounding heavy particles, the convection and conduction of energy out of the plasma,the diffusion of particles within and out of the plasma, and the radiation of energy within and out of the plasma must all be included in this understanding. The performance of an LSP as defined by its global absorption (percentage of incident laser power absorbed on the whole) and thermal conversion efficiency (percentage ending up as thermal energy in the plasma exhaust gas) must be related to the internal plasma processes and understood on those terms.

As outlined in the above summary, this investigation relies on several independent diagnostic techniques in order to characterize the LSP. The primary tools have been calorimeter

measurements of transmitted laser power and thermocouple temperature measurements of plasma exhaust gas. The transmitted power is related to the absorbed power and the bulk gas temperature increase through the plasma is related to the thermal conversion efficiency. These techniques have been used to experimentally map the performance of argon LSP's as functions of laser power, gas pressure and mass flux, beam focusing geometry, and multiple plasma separation [1-3]. In recent experiments hydrogen plasmas have exhibited similar performance trends, but with much improved thermal conversion efficiency [4,5]. This is a very encouraging finding and will be detailed in the experimental results section of this abstract.

A two dimensional numerical model has been developed for argon and hydrogen plasmas at one atmosphere gas pressure [2,3]. The prediction of experimental argon LSP performance trends has been successful with the major difficulties being in the energy balance determining thermal conversion efficiency, and in the prediction of plasma blowout. The model always overpredicts both thermal efficiency and blowout mass flux. The model does not predict the existence of one atm. hydrogen plasmas, which agrees with the experimental inability to sustain a hydrogen plasma at one atmosphere. As encouraging as these numerical results are, there is an obvious need for an extension to higher pressure, and to explain and resolve the differences from experiments.

Detailed non local thermodynamic equilibrium emission spectroscopy will result in a fundamental understanding of the energy transfer processes in the LSP [4]. This knowledge will guide future development of the numerical model and provide a more physical foundation for explaining the well known trends in the primary experimental data. This technique involves the measurement of electron number density in the plasma and atomic excitation temperature directly. Quantities such as heavy particle temperature and density and electron temperature will be determined through an analytical procedure using the experimental data as input.

A laser induced fluorescence study is also planned to provide a measure of the plasma gas temperature in the regions outside of the plasma core and unreachable by emission spectroscopy or thermocouple thermometry. This will provide another alternative means of determining thermal conversion efficiency and will be a source for temperature contour comparison to the numerical model.

Experimental Results

The position and geometry of the LSP are the keys to overall energy transfer. The plasma will stabilize at a point in the incident beam where energy absorption just balances losses due to radiation, conduction, and convection. LSP performance can be characterized as a function of mass flux, beam focusing geometry, gas pressure, and laser power. Thermal efficiency is maximized when beam absorption is maximized and radiation loss is minimized. The best previously achieved thermal efficiencies and global absorptions are summarized here for comparison with the results of current work. The maximum thermal efficiency achieved using an argon plasma was 46% with a global absorption of 97% [1], and the maximum thermal efficiency achieved using a single argon-helium mixture plasma was 56% with a global absorption of 86% [3].

Actual laser thrusters would use hydrogen as the propellant because its low molecular weight allows high specific impulse. Until this year all work has been done in inert gases because the proper facilities for handling hydrogen safely were not available. A new hydrogen handling and safety system has been designed and installed. A description of this system can be found in Ref. 4.

A series of hydrogen plasma experiments was performed for each of three chamber pressures, 1.80 atm., 2.14 atm., and 2.5 atm. These experiments although not complete have provided some interesting results. Figure 1 is a plot of the results of those experiments, showing global absorption and thermal efficiency as a function of hydrogen flux. Global absorption is a strong function of gas pressure, but a relatively weak function of mass flux. For a 7 kW laser input, it was impossible to maintain a hydrogen plasma at chamber pressures lower than approximately 1.5 atm. This is due to the low value for absorption coefficient at this pressure (related to electron number density) and the high thermal conductivity of hydrogen. The plasma cools (radiates, conducts and convects heat) faster than it absorbs energy from the laser which results in an instability, or blowout, at too low pressure.

Note that the trends for absorption and efficiency are similar for those of past 1 atm argon runs. The absorption decreases with increasing mole flux while the efficiency increases with mole

flux until reaching a peak, then decreases to blowout. The highest efficiency at 1.80 atm. was 61.2% with a corresponding global absorption of 64.4% at 828 moles/m^2s. The highest efficiency at 2.14 atm. was 69.2% with a corresponding absorption of 72.4 % at 1198 moles/m^2s. The highest efficiency at 2.50 atm. was 72.3% with a corresponding absorption of 80.8% at 1071.8 moles/m^2s.

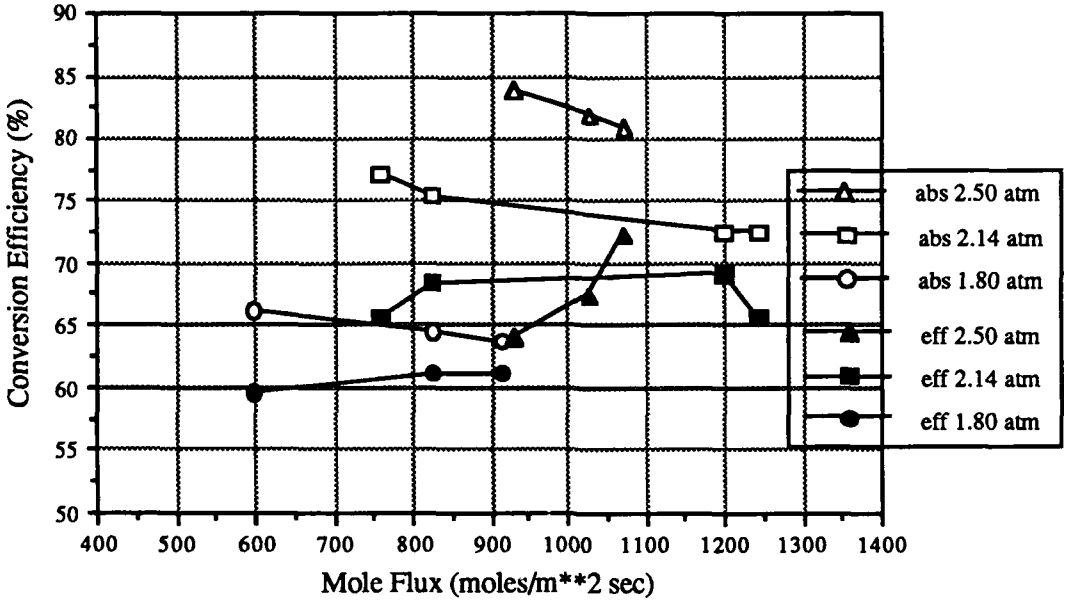

Figure 1 Global absorption and thermal efficiency as a function of H2 mole flux at three different chamber pressures.Laser power is 7 kW, beam geometry is f/4.

Based on the results for pure hydrogen several key points can be made. The global absorption of the pure hydrogen plasmas is a strong function of gas pressure. Absorptions are in the 65% range for 1.8 atm. but increase to over 80 % for 2.5 atm. This strong dependence of absorption on pressure is a major reason why pure hydrogen LSP's could not be sustained below ~1.5 atm. It also implies that future experiments at even higher pressure might produce plasmas exhibiting near complete absorption.

The notion that pure hydrogen plasmas would be cooler than argon plasmas with a more even spread of heating due to the high thermal conductivity of hydrogen appears to be supported by the data. The evidence for this is that the radiation loss (the difference between absorbed and retained laser power) for all the pure hydrogen plasmas is very low when compared with previous pure argon LSP's. So even though the global absorption of the pure hydrogen LSP's is lower than that for the pure argon LSP's, the thermal efficiency is greater.

If a 10 MW hydrogen LSP could be sustained with an efficiency of 72% , a rocket powered by such a plasma could produce almost 15 kN of thrust with a specific impulse of 1000 seconds. The problem now is to provide an accurate numerical model which could verify the way in which plasma performance scales at very high input power.

Non-LTE Emission Spectroscopy

Defining the thermodynamic state, be it an equilibrium state or otherwise, is a key issue for the basic physical understanding and performance evaluation of plasmas in regard to rocket propulsion. This research aims to provide more accurate LSP diagnostics and to better evaluate their performance based on these diagnostics. LSP operating conditions will be defined for which local thermodynamic equilibrium can be guaranteed so that equilibrium numerical modeling can be undertaken with full confidence.

In determining the thermodynamic state of the plasma, it is important to understand the concept of plasma temperature and the partitioning of energy. The energy content of the plasma gas is taken up by various modes. These include the kinetic energy of the free electrons and the heavy particles (neutral atoms and ions), the ionization energy of the ions, and the electronic excitation of the heavy particles. To a good approximation, the distribution of the energy in each of these modes can be characterized by a temperature parameter associated with Maxwell-Boltzmann statistics. The degree of ionization in the plasma can be similarly characterized by temperature (through the Saha equation). If the plasma is in thermodynamic equilibrium then the thermodynamic state is completely determined by the values of any two properties such as pressure and temperature. In thermodynamic equilibrium Boltzmann's formula for the distribution of excited electronic states, Maxwell's law for the distribution of particles velocities (energies), and Saha's equation describing the plasma composition are all associated with the same temperature parameter.

As mentioned previously the past LSP research has been directed toward measuring their performance in terms of global laser absorption and thermal conversion efficiency. In order to better understand these results on a physical level it is important to be able to measure temperature and densities inside the plasma. Absorption of laser energy and radiation from the plasma at each point in the plasma will depend on these plasma conditions, thus enabling an understanding of the global results on a local level.

In this research, diagnostic techniques will be applied which are independent of the LTE assumption. These techniques follow those of Eddy and incorporate both direct spectroscopic measurements and analytic solution techniques [6]. Electron number density can be determined through either a spectral line broadening measurement or a measurement of continuum emission. The upper level excited state distribution temperature and state populations can be determined from a measurement of spectral line intensities. Other relevant parameters such as electron and heavy particle kinetic temperatures, atomic number density, and the total excitation temperature (relating the ground state to the highest excited state), can be calculated through an iterative simultaneous solution of the appropriate analytical expressions.

It is a goal of this research to arrive at better values for absorption and emission coefficient based on the measured or calculated value of number densities and temperatures. It is expected that this will lead to a more fundamental understanding of the laser energy conversion process and to more accurate determinations of global absorption and thermal conversion efficiency.

All the computer simulations of LSP's reported assume a single temperature in the energy equation and use LTE property values. In order to have confidence in using a computer model for operating conditions not attainable in the laboratory, it must be known for certain whether the observed differences from the experimental data are due to non-LTE
effects. In the event that non-LTE is shown to be a dominant factor for certain LSP experimental conditions, either a model must be developed which takes these effects into account, or care must be taken to rely upon the current models only when LTE can be assured. The results of this research will provide guidance in this regard.

References

1. Zerkle, D.K., Schwartz, S., Mertogul, A., Chen, X., Krier, H., Mazumder, J., "Laser-Sustained Argon Plasmas for Thermal Rocket Propulsion," *J. Propulsion and Power*, Vol. 6, No. 1, pp. 38-45, Jan.-Feb. 1990.
2. Mazumder, J., Krier, H., "Experimental and Numerical Studies of Laser Sustained Gas Plasmas," Final Technical Report under Grant No. AFOSR-88-0129, April 1989.
3. Schwartz, S., Mertogul, A., Eguiguren, J., Zerkle, D., Chen, X., Krier, H., Mazumder, J., "Laser-Sustained Gas Plasmas for Application to Rocket Propulsion," AIAA paper 89-2631 presented at the 25th Joint Propulsion Conference, Monterey, CA, July 10-12, 1989.
4. Krier, H., Mazumder, J., "Experimental Studies of Laser-Sustained Argon and Hydrogen Plasmas," Annual Technical Report under Grant No. AFOSR-89-0274, March 1990.
5. Mertogul, A., Zerkle, D.K., Krier, H., Mazumder, J., "CW Laser Sustained Hydrogen Plasmas for Thermal Rocket Propulsion," AIAA paper 90-2637 to be presented at the 21st International Electric Propulsion Conference, Orlando, FL, July 18-20, 1990.
6. Eddy, T.L., "Low Pressure Plasma Diagnostics Methods," AIAA paper 89-2830, presented at the 25th Joint Propulsion Conference, Monterey, CA, July 10-12, 1989.

COUPLING BETWEEN GAS DYNAMICS AND MICROWAVE ENERGY ABSORPTION

AFOSR Grant No. AFOSR-89-0312

Principal Investigator: Dr. Michael M. Micci

The Pennsylvania State University
Department of Aerospace Engineering
University Park, PA

SUMMARY/OVERVIEW:

There is an understanding of the process of microwave energy addition to a high pressure gas for propulsive purposes for some of the available absorption modes but no unified comparison of all the modes in terms of absorption efficiency, maximum temperature, plasma stability, etc. Also there is little knowledge of the coupling of the absorbed energy to the gas dynamics required to obtain propulsive thrust. This research is the first experimental effort to examine and compare free-floating resonant cavity microwave absorbing plasmas and planar propagating plasmas in various gases as well as the first examination of the coupling of the energy absorption to the gas dynamics in order to convert internal thermal energy of the gas to directed kinetic energy by means of a nozzle expansion. The research will provide insight to the entire field of high temperature gas flows driven by radiation absorption.

TECHNICAL DISCUSSION:

Experiments with high pressure free-floating helium and nitrogen discharges generated in a microwave resonant cavity for use in an electrothermal thruster were conducted. The cavity, operating in the TM_{012} mode, generated the discharges within a quartz sphere which allowed the discharge to be both free-floating and away from solid surfaces. Input powers of up to 400 W were used with gas pressures up to 300 kPa (absolute) and mass flow rates up to 4.63×10^{-4} kg/s.

For a given plasma in the resonant cavity, there is a maximum operating pressure, above which the plasma is extinguished. The maximum operating pressure for a given input power is significantly greater for helium discharges than for nitrogen discharges. It was possible to sustain a nitrogen discharge up to a pressure of only -60 kPa (gauge) with an input power of 450 W, whereas helium discharges displayed much higher maximum pressures for cases both with and without flow present. The higher maximum pressures exhibited by helium discharges are believed to be due to the absence of rotational and vibrational modes of excitation which results in a lower fractional electron energy loss per collision.

The introduction of a gas flow did raise the maximum operating pressure of the discharge. For the no-flow case, the maximum pressure is 184 kPa (gauge) at an input power of 400 W. For a flow velocity of 28.9 cm/s in the straight quartz sections of the system, the maximum operating pressure was 218 kPa (gauge), at an input power of 433 W. The tests were discontinued at an input power of 505 W, as higher input powers resulted in the plasma positioned very close to (but not touching) the quartz surface, with resulting rapid heating of the sphere indicated by the red glowing of the quartz in this region. For an increased flow velocity of 200 cm/s, the maximum operating pressure was 230 kPa (gauge) at an input power of 400 W.

A digital thermometer with chromel/alumel thermocouples was used to determine the temperature of the flowing gas both upstream and downstream of the plasma. The downstream thermocouple was approximately 20 cm from the plasma. In these tests, the cavity was again tuned for minimum reflected power, while keeping the plasma away from the quartz sphere. The thermal efficiency of the energy transfer from the plasma to the flowing gas may be calculated from the temperature rise measurements:

The total efficiency of the system, η, defined as the ratio of the power in the flowing gas to the incident microwave power, is shown in Figure 1 as a function of mass flow rate. The total efficiency increases nearly linearly with mass flow rate and is relatively independent of input power, with a maximum of 25% measured with the current experimental system. The maximum mass flow rate is currently limited by the experimental system, which is being upgraded to allow higher flow rates. It should be borne in mind that the downstream thermocouple was located 20 cm downstream of the discharge, leading to significant heat losses in the downstream pipework. Moving the thermocouple nearer to the discharge would yield higher measured thermal and total efficiencies.

The technique of using measurements of the continuum radiation to determine electron temperature and electron number density has been used in previous investigations because of its accuracy and insensitivity to deviations from local thermodynamic equilibrium (LTE). Absolute measurements of the continuum radiation were made at a wavelength of 4250 A as there are no neighboring lines to interfere with the continuum signal at this wavelength. The spectroscopic system was calibrated with a calibrated lamp. The measured electron temperatures, T_e, versus pressure for several input powers and mass flow rates are shown in Figure 2. It can be seen that T_e is insensitive to changes in input power, pressure or mass flow rate and varies from 10,200-10,900 K. Also observed is that at low pressure, the introduction of a mass flow slightly decreases T_e from the no flow case value, but further increase of the mass flow rate has little effect. The electron number densities may be evaluated by using the Saha equation and the calculated values of T_e. Using this method, n_e was found to vary between 5.8×10^{19} m^{-3} and 1.32×10^{20} m^{-3}.

The stabilization of propagating plasmas generated in a waveguide was achieved this past year. Although a stabilization of the plasma is possible in principle by establishing a counter flow with a flow speed exactly equal to the propagation velocity of the plasma, this method is rather impractical, since the required match between the velocities has to be absolutely accurate during the entire period of operation. Pressure and power fluctuations, however, will continuously change the plasma velocity, making this exact match with the flow velocity virtually impossible.

A very simple and highly efficient way of stabilizing the plasma is inserting a bluff body made out of dielectric material such as boron nitride into the flow. Bluff bodies have been used extensively as "flameholders" in such combustion devices as afterburners in jet engines and ramjets. The bluff body constricts the flow cross section thus causing the flow speed to increase if the flow is subsonic. If the dimensions are properly chosen this increased flow speed is bigger than the contrary plasma propagation velocity, so that the plasma cannot travel upstream across the bluff body. Right behind the bluff body, however, there exists a recirculation zone with high randomly oriented velocities but no particular flow direction. The plasma can therefore move easily upstream into the recirculation zone and stays trapped here since further propagation across the bluff body is not possible. The conical bluff body was kept in place by three fins which pressed against the quartz tube walls. Boron nitride was used as the bluff body material since it shows negligible microwave absorption and high thermal conductivity thus avoiding thermal stresses within the body. The plasma itself has a hot, white-glowing cylindrical core aligned along the E-field of the TE_{10} mode present in the waveguide. The core is surrounded by a bluish, ellipsoidal shaped cooler plasma.

Fig. 3 shows the coupling efficiencies as a function of helium mass flow for three incident power levels. As can be seen, the coupling efficiencies increase with mass flow. The reason for this is believed to be due to the skin-effect: the cooler the plasma because of increased forced convective cooling due to higher mass flows, the lower is its electrical conductivity. This increases the skin-depth, which is the distance up to which the electromagnetic fields can penetrate before having been attenuated to 1/e of its initial strength, e being the Euler number. The larger the skin-depth, however, the more energy can actually be dumped into the plasma. It can also be seen that the coupling efficiency decreases with increased input microwave power. This is because for a fixed plasma size (determined by the bluff body) the amount of absorbed microwave power remains fairly constant. Thus as the input power is increased the coupling efficiency, which is the ratio of absorbed power to incident power, decreases. It was found that pressure has only a slight effect on the coupling efficiency.

Figure 4 shows the measured electron temperatures which are all in the range between 12,100 K and 12,700 K and are fairly constant with respect to incident power and mass flow. However, the electron temperatures seem to increase with lower pressures.

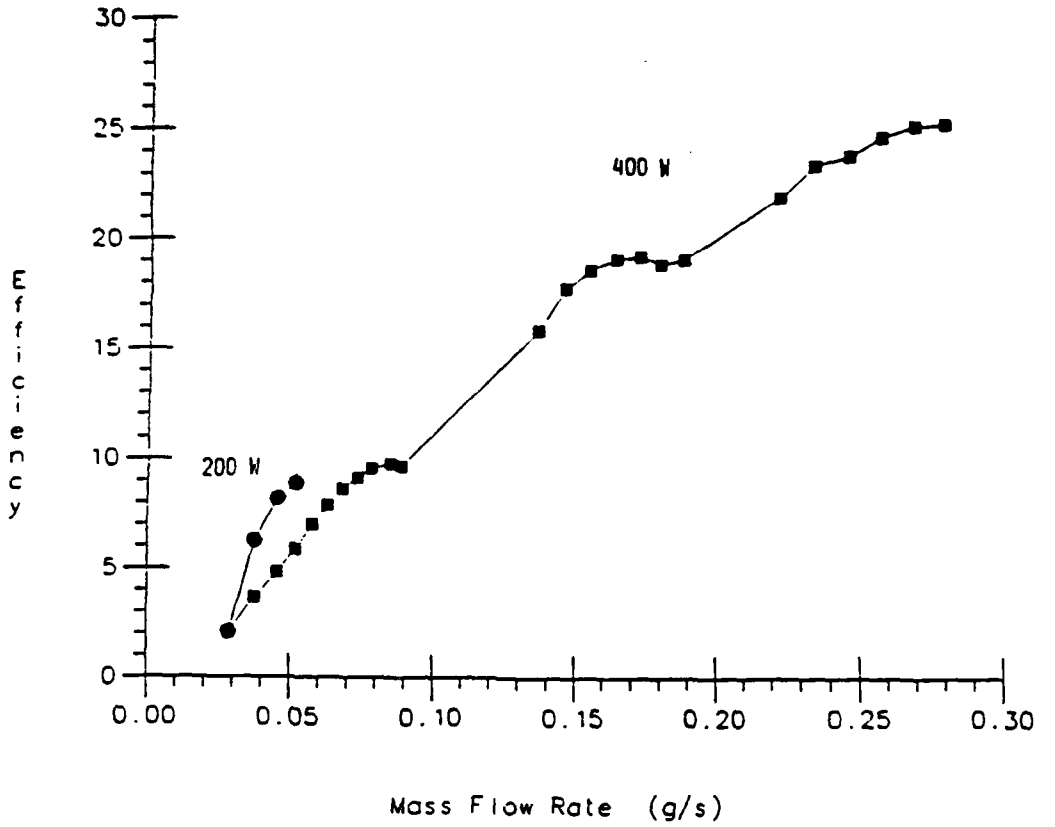

Figure 1. Total efficiency versus mass flow rate for resonant cavity helium plasmas showing efficiency increasing with mass flow.

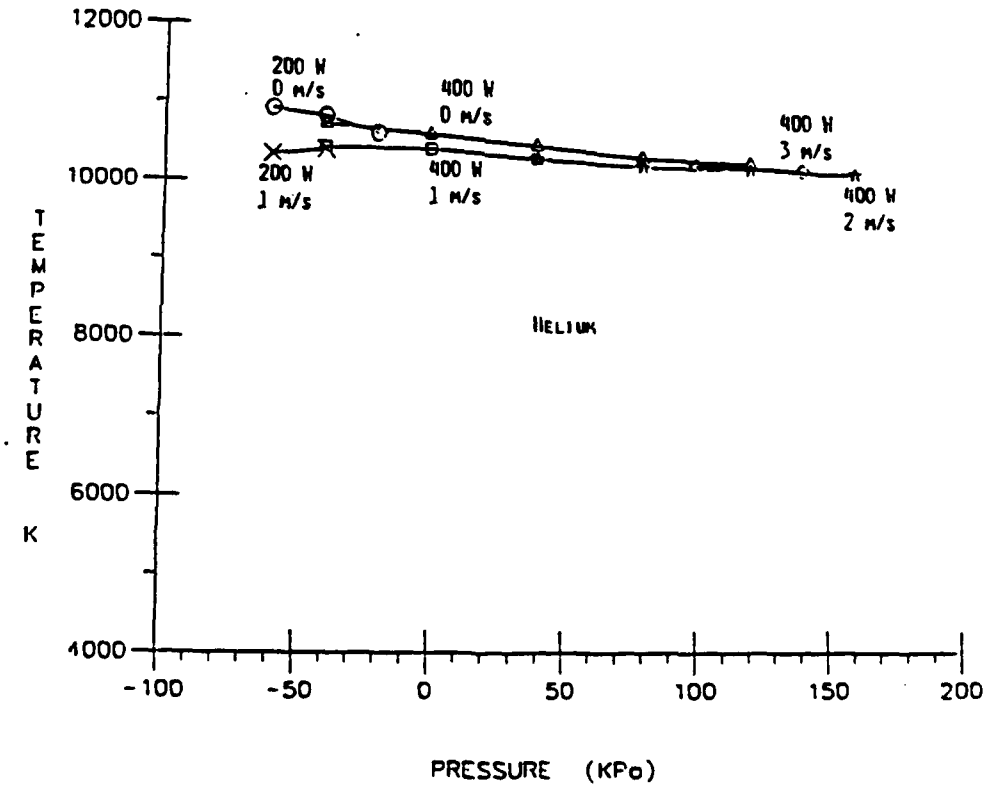

Figure 2. Electron temperature versus pressure for resonant cavity helium discharges showing little power or pressure dependence.

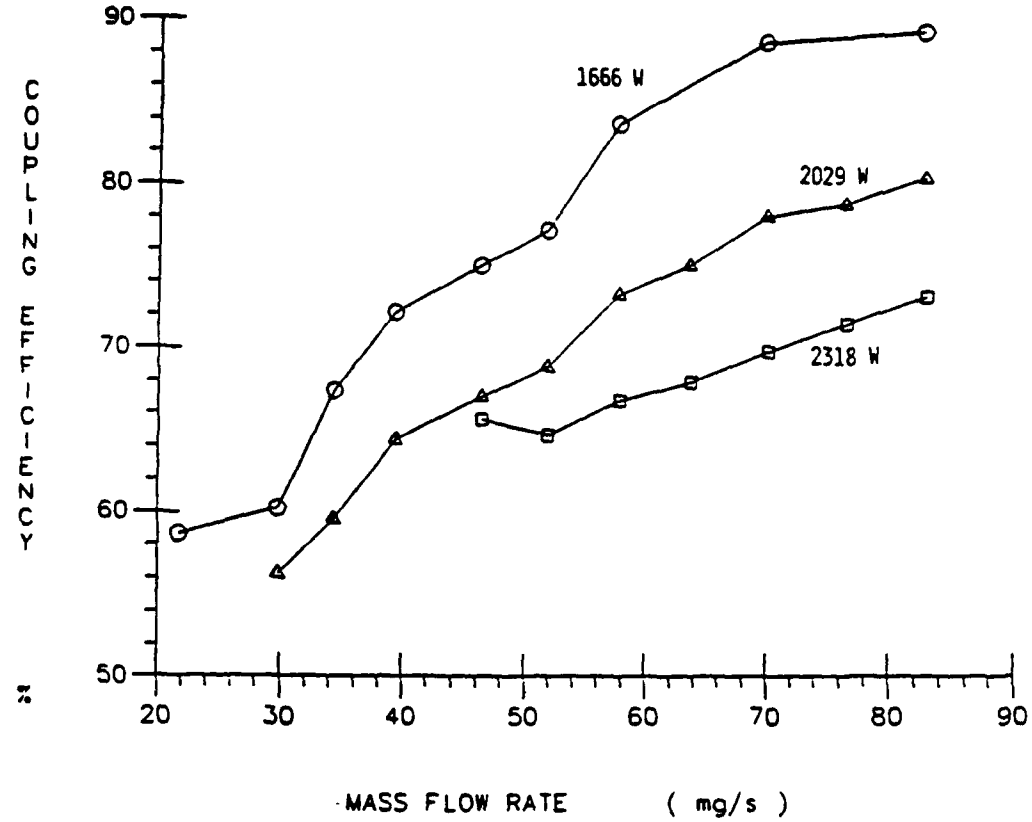

Figure 3. Coupling efficiency versus mass flow rate for a propagating helium plasma at one atmosphere and three incident power levels showing efficiency increasing with mass flow.

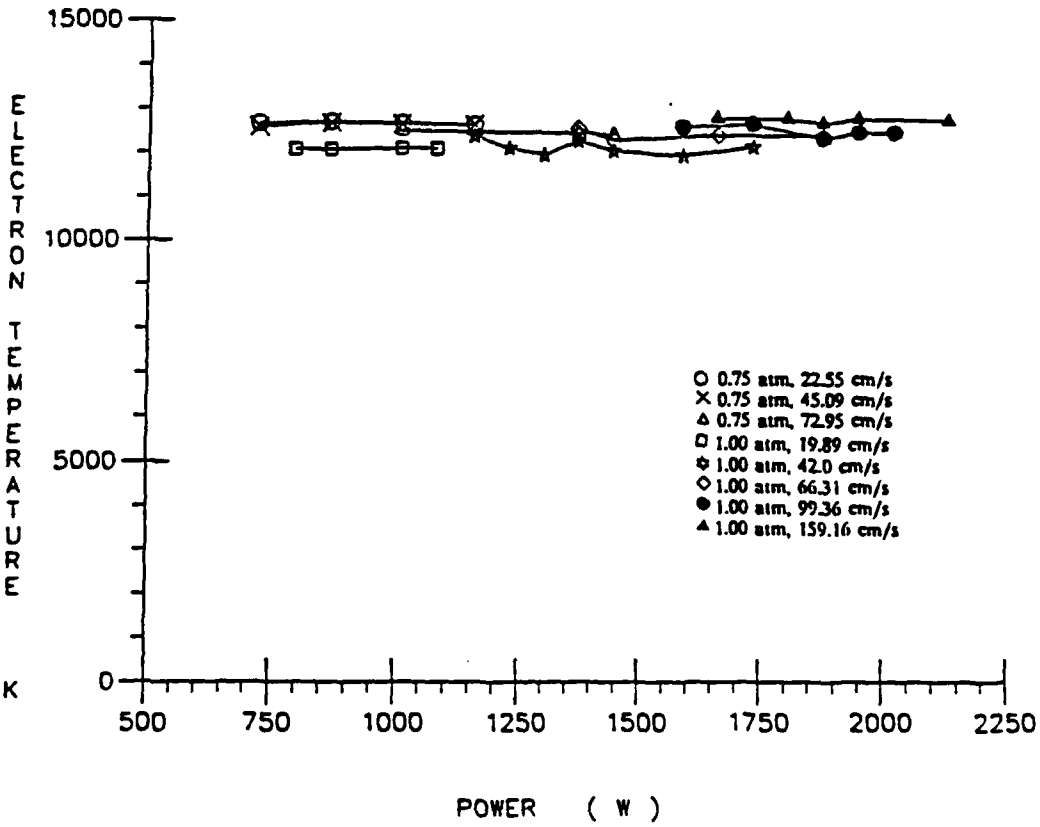

Figure 4. Electron temperature versus incident power for propagating helium plasmas showing little pressure or flow rate dependence.

COUPLING BETWEEN GAS DYNAMICS AND MICROWAVE ENERGY ABSORPTION

(AFOSR Grant No. 89-0312)

Principal Investigator: Charles L. Merkle

Department of Mechanical Engineering
104 Research Bldg. E
University Park, PA 16802

SUMMARY/OVERVIEW

The detailed characteristics of microwave-gasdynamic interactions are being studied on the basis of a detailed numerical procedure. The analysis utilizes a coupled solution of Maxwell's equations and the Navier-Stokes equations to determine the characteristics of the resulting plasma, its controllability, absorption efficiency, and potential for propulsion applications. This complete two-dimensional model is being used in conjunction with companion experiments to ascertain the scientific feasibility of microwave propulsion.

TECHNICAL DISCUSSION

Microwave energy promises to provide attractive propulsion performance, but detailed questions concerning its scientific feasibility must first be addressed. The present effort, in connection with the companion experimental effort by Micci, represents a program to provide information upon which these feasibility assessments can be made. Major issues concern the dynamic and thermodynamic characteristics of microwave plasmas, how effectively their size and location can be controlled to prevent arcing to the walls and to ensure uniform heating of the gas, and the fractio of total input power that can be absorbed in the gas and used for propulsive purposes.

The experimental setup being simulated is shown schematically in Fig. 1a. Helium gas flows from top to bottom through a quartz sphere-cylinder tube that passes through a cylindrical microwave cavity. The microwave energy is fed into the cavity by means of a coupling probe which is here represented by an axisymmetric waveguide as shown in Fig. 1b, so as to set up a particular standing wave mode (TM 012 has been used so far). The analytical model consists of Maxwell's equations for the electro-magnetic field, and the Navier-Stokes equations for the fluid dynamic field. Because of the finite conductivity of the plasma, the solutions of the two field equations are strongly coupled. The Navier-Stokes equations are solved by a second order accurate implicit time-marching procedure, while the Maxwell equations are solved by an explicit time marching method and averaged over a period to get the power deposited in the gas.

Parametric studies with the computational model indicate that it predicts trends that are similar to those observed experimentally. For example, predictions of the

peak temperature in the plasma closely match the experimentally measured electron temperatures (see Fig. 2a) and the size, shape and location of the plasma are also in general agreement with the experimental findings. Increasing the Reynold's number (flow velocity) causes the plasma to move toward the central node of the cavity, but has little effect on the peak temperature, again in agreement with experiments. The calculations also show that at the lowest Reynold's numbers considered, buoyancy introduces a recirculating region just above the center of the plasma, but this causes little difference in the overall plasma shape. Estimates of the ratio of the absorbed power to the reflected power are also in good agreement with experiment (Fig. 2b).

Calculations for various tube-to-sphere diameter ratios show that the location at which the plasma forms depends upon the geometrical configuration. When the tube is one-fourth the size of the sphere as in the experiments (Fig. 1), the plasma forms near the middle of the sphere in agreement with the experimental findings. When the tube diameter is increased so the tube has constant area, the plasma forms near the end of the cavity through which the microwaves enter. The flow perturbations created by the spherical enlargement apparently provide a preferred location for the plasma.

Companion parametric studies indicate the plasma grows slowly in size and its peak temperature decreases slightly as the input power is increased. At the highest power levels, the central, high temperature portion of the plasma splits into two centers encompassing the middle and the upper node of the standing microwave field. The one area in which the computations deviate from the experiments is in the predicted threshold powers which are higher than those observed experimentally. Improved physical models are being considered to explain this short-coming.

Representative temperature and velocity contours and flow streamlines for a representative case are shown in Fig. 3, along with the corresponding electric fields. The velocity profiles in this case show the flow nearly reverses, while the streamlines show the flow deviates around the plasma in much the same manner as observed in laser plasmas. The electric fields are strongly distorted over their non-conducting shapes. Clearly absorption losses must be included in the solution of Maxwell's equations.

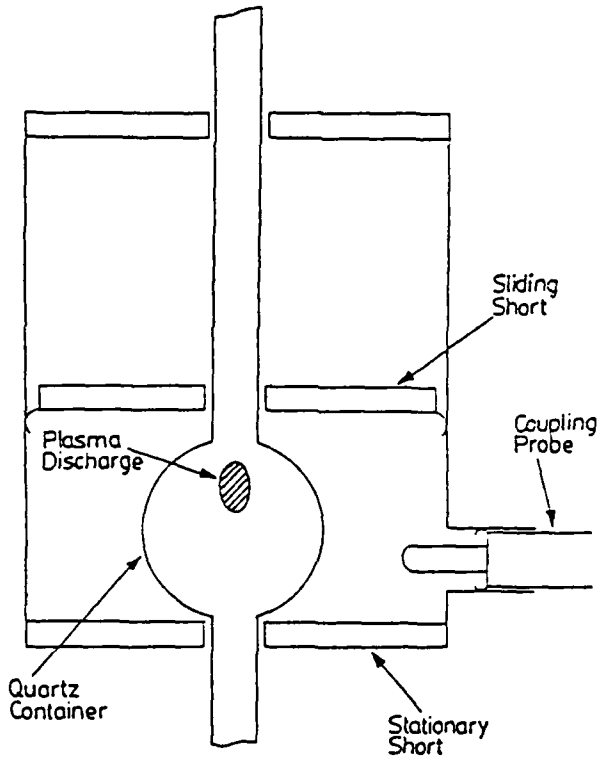

Fig. 1a An illustration of the discharge location inside the resonant cavity.

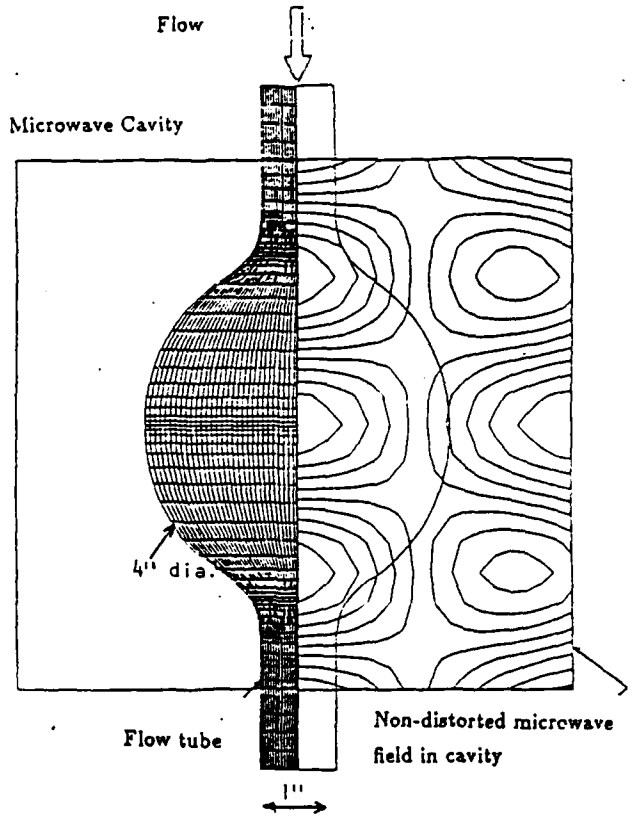

Fig. 1b Representative geometry for microwave-gasdynamic interaction showing generalized nonorthogonal grid in flow domain and superimposed microwave cavity with electric field lines.

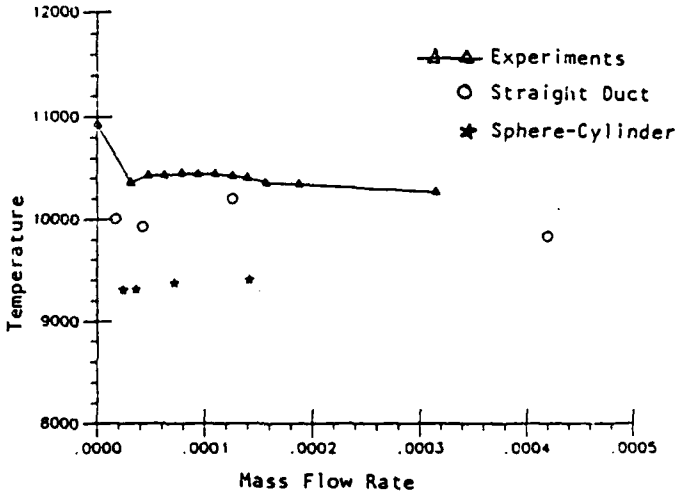

Fig. 2a Comparison of computed peak temperatures with experiments. Solid line is from experiments. The circles are straight duct calculations and the stars are the sphere-cylinder calculations.

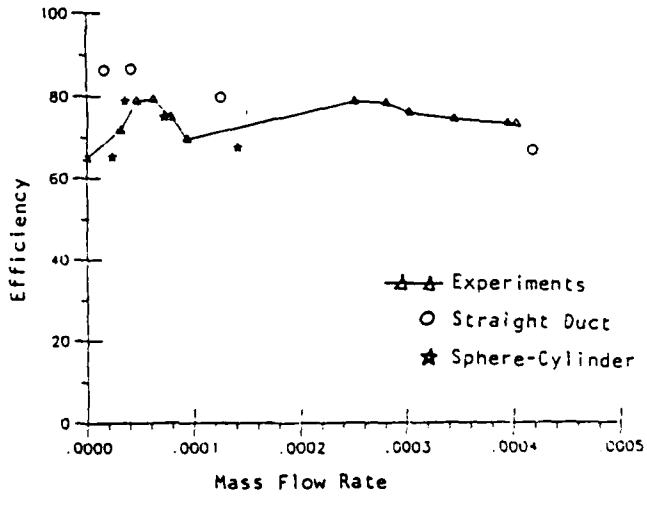

Fig. 2b Comparison of coupling efficiencies from computations and experiments.

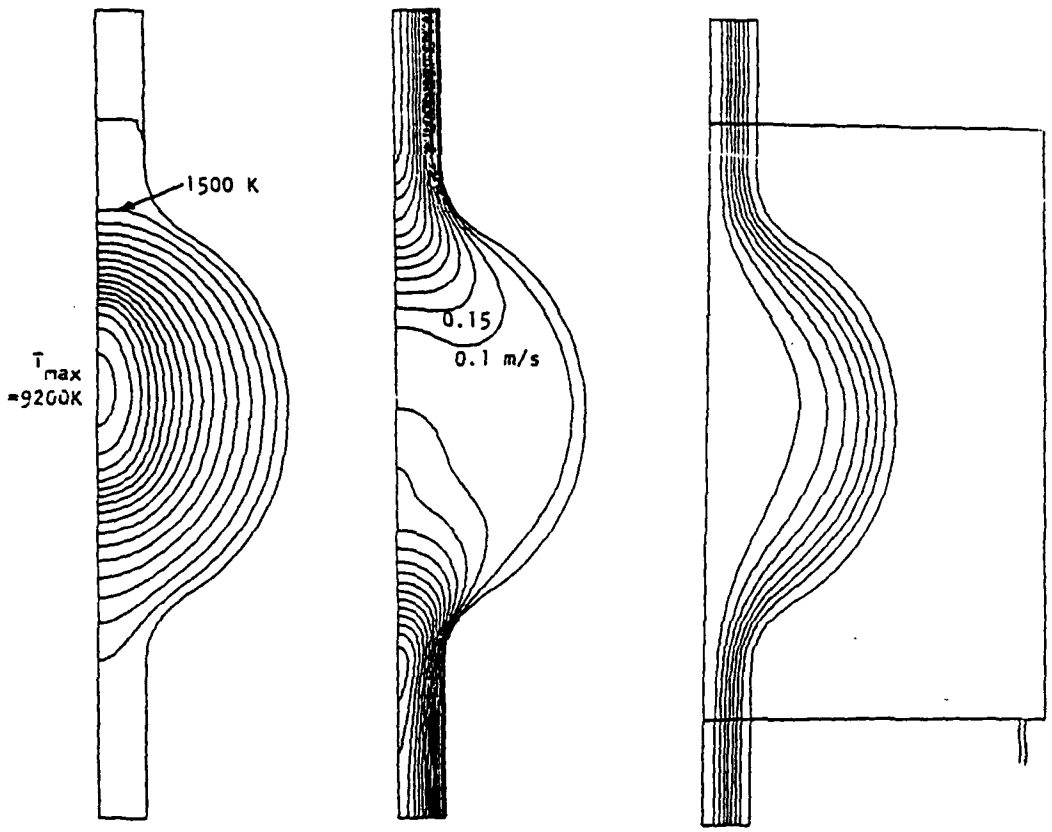

Fig. 3a Representative solution of sphere-cylinder configuration. P = atm, T = 1000 K, u = 0.336 m/s, m = 1 x 10^{-5} kg/s, Re = 10, T_{inc} = 3 KW, P_{ref} = 0.8 KW.

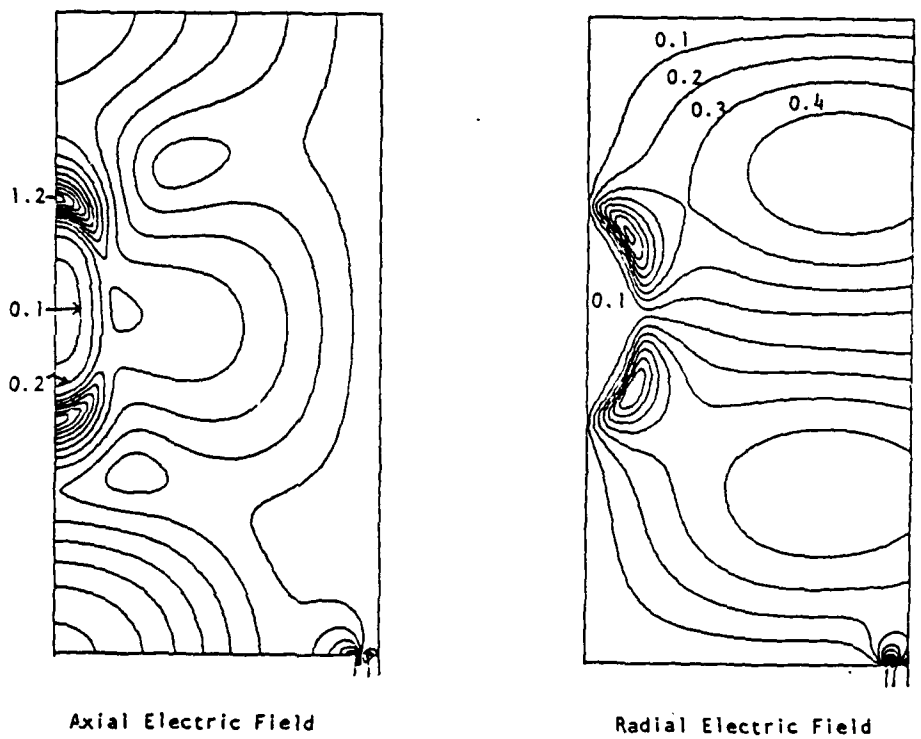

Fig. 3b Distorted electric field solutions corresponding to the case on Fig.3a . The field lines are normalized with respect to E_{ref} = 25000.

RF Wave Propagation in the Plasma of a Tandem Mirror Rocket

Grant No. AFOSR-90-NA-001

Principal Investigators: F. R. Chang-Díaz*, T. F. Yang

MIT Plasma Fusion Center
Cambridge, Massachusetts 02139

Summary

The propagation of rf waves launched in the end cell and central cell of the tandem mirror propulsion device has been investigated both theoretically and experimentally. Theoretically, a computer code has been developed to study the wave propagation in a nonhomogeneous magnetic field. It was found that the amplitude of the wave excited in the plasma peaked while approaching the resonance, but then damped out, indicating strong absorption of the wave by the plasma. The absorption took place near the axis. The experimental results confirmed the theoretical prediction of the phenomena of the resonance effect. A very important discovery of this experiment was the broadening of the ICRF Fourier spectrum in the presence of the plasma. This broadening can be viewed as the detuning of the Q value of the resonance circuit due to plasma loading.

Technical Discussion

(1) Introduction

A tandem mirror plasma experimental facility was established for space propulsion developmental studies. The experimental program encompasses three areas of study. First, to establish the fundamental plasma properties for the range of propulsion application. Second, to seek ways to maximize plasma heating, thus the improvement of power conversion efficiency and third, to study the plasma properties at the exhaust. The power conversion method will be to inject the rf power into the plasma to heat the ion species at the ion cyclotron resonance frequency (ICRF). Hence, understanding the physics of wave propagation in this device is fundamental to achieving the phases just mentioned. Wave propagation in a hot plasma contained in highly nonhomogeneous magnetic field is a very complicated problem which was briefly touched upon during the closing of the mirror fusion program. Nevertheless, in the theoretical area, extensive analytical work was done during early years of this program leading to the development of a computer code, BEACH, which will be described later.

(2) Experimental Setup

The schematic of the experiment is shown in Fig. 1. There are double half-loop antennae in the south end cell and in the north end of the central cell. Both antennae are located at fields higher than the corresponding ones for their resonant frequencies ($\omega < \omega_{ci}$). The frequency of the rf power is in resonance of the ion cyclotron frequency at the field of the midplane of each cell. When rf radiation was emitted at the antennae, the wave excited in the plasma travels both radially inward and axially toward the center of each cell. The diagnostics enclosed by the box in Fig. 1 are currently operational which were built, installed and tested in the past year. A scanning spectrometer and a retarding field grid energy analyzer will be installed later.

(3) Theoretical Results

A computer code, BEACH, solving the reduced Maxwell equations for the configurations shown in Fig. 1, has been developed. The excited wave in the plasma calculated by

* Astronaut Office, NASA Johnson Space Center, Houston, Texas

the code is shown by the perspective view in Fig. 2. It shows the R and Z axis on the horizontal plan and the vertical axis as $\tilde{B}_z$. The antenna is located at $R = 15$ cm. The B-dot probe is located 35 cm from the antenna. The rf is in resonance with ion cyclotron frequency for the field at $Z = 35$ cm. The figure shows that wave amplitude is growing when it travels away from the antenna and becomes peaked near the resonance point, $R = 0$ cm and $Z = 35$ cm, then damps quickly from 35 to 50 cm. This indicates that the wave energy is being absorbed by the ions. Figure 2a is $n = 0$ mode generated by a single turn antenna, whereas Fig. 2b shows the $n = 1$ mode generated by a double half-turn loop antenna. The experiment was done for the later case.

(4) Experimental Results

The B-dot probe allows the measurement of $\tilde{B}_r$, $\tilde{B}_\theta$ and $\tilde{B}_z$. $\tilde{B}_r$ and $\tilde{B}_\theta$ were very small. The Fourier spectrum of B_z is shown in Fig. 3. Figure 3a is the wave in the vacuum. The fundamental frequency is 3 MHz marked by 0. The harmonics are marked by 1,2,3 and 4. The peaks in between may be due to the imperfection of the rf transmitter.

A comparison of Figs. 3a and 3b shows that the amplitude of fundamental frequency peak 0 is one unit in the vacuum and 50 units in the plasma. The half-width is about 0.1 MHz for the vacuum and 1 MHz for the plasma. Therefore the amplitude of the wave is 50 times higher in the plasma than in the vacuum at the resonance which confirms the theoretical prediction. The width of the wave is 10 times broader. The reason that the plasma signals are much larger than the vacuum signals is that the ICRF $\tilde{B}_z$ is evanescent in the vacuum, while the presence of the plasma allows it to propagate. This large broadening indicates increasing resistance due to the loading of plasma. There is little evidence that the wave injected in the end cell will propagate into the central cell or vice versa because of the fact that the wave energy is damped and absorbed near the resonance in the respective cells. There is also little evidence of heating electrons at the edge [1], an indication of less loss and higher efficiency.

(5) Plasma Broadening of ICRF Spectrum

One of the discoveries made on this plasma propulsion experiment is the broadening of the ICRF Fourier spectrum in the presence of a plasma. Comparison of a vacuum ICRF shot to a plasma ICRF shot clearly shows this effect. We propose an explanation for this effect. The broadening is thought to be caused by the detuning of the plasma Q as defined by

$$Q = \frac{f}{\Delta f} = \frac{\omega L}{R} .$$

Since the antenna was originally tuned for vacuum, the Q is very large for a vacuum shot (hence a narrow peak). However, the presence of a plasma increases the serial resistance of the equivalent RLC resonance circuit, therefore $Q = \frac{\omega L}{R}$ decreases, causing $\Delta f (= \frac{f}{Q})$ to increase. This increase in the width of the fundamental mode is then observable during the discharge.

References

[1] F. R. Chang Díaz, T. F. Yang, PFC/RR-89-15 (1989).

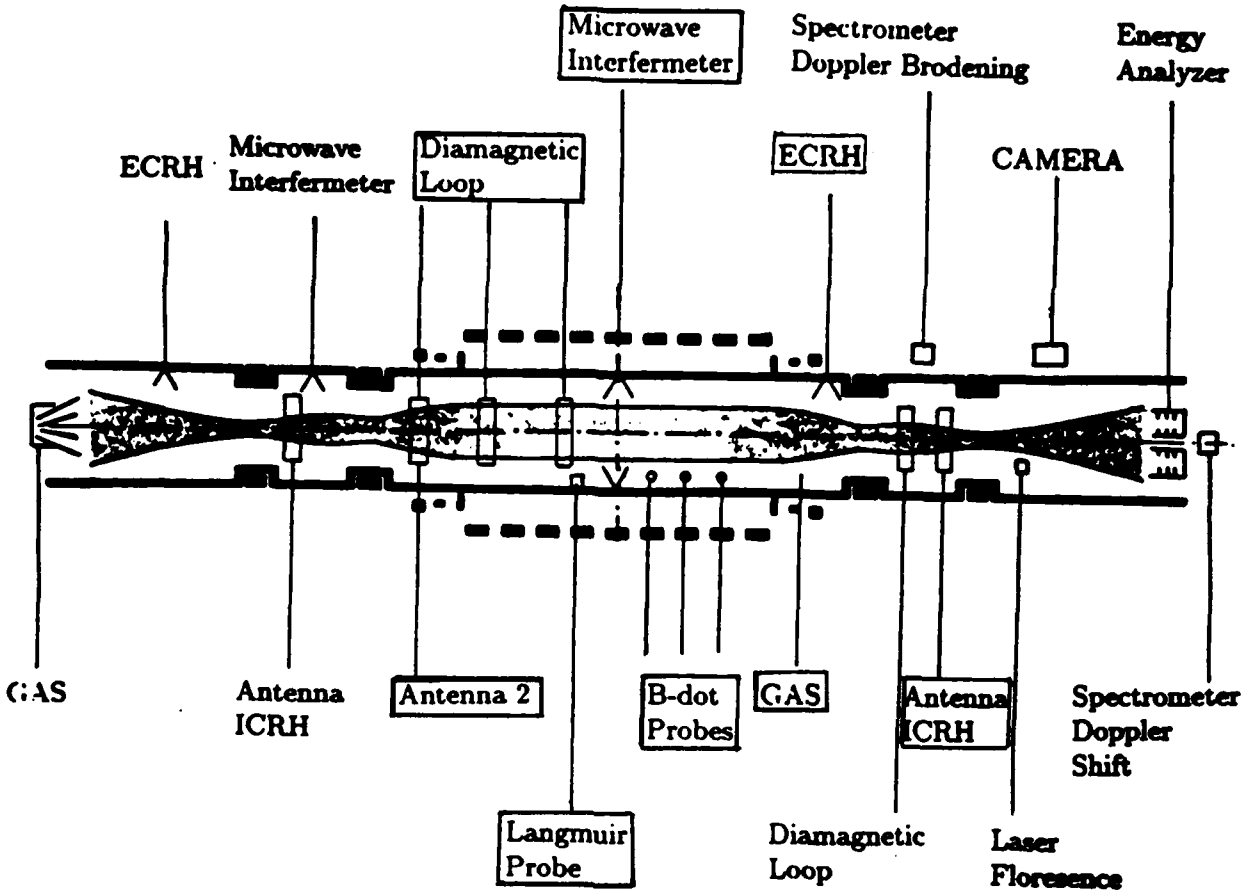

Figure 1. Schematics of Tandem Mirror configuration and diagnostics lay out. The diagnostics used presently are enclosed in the box.

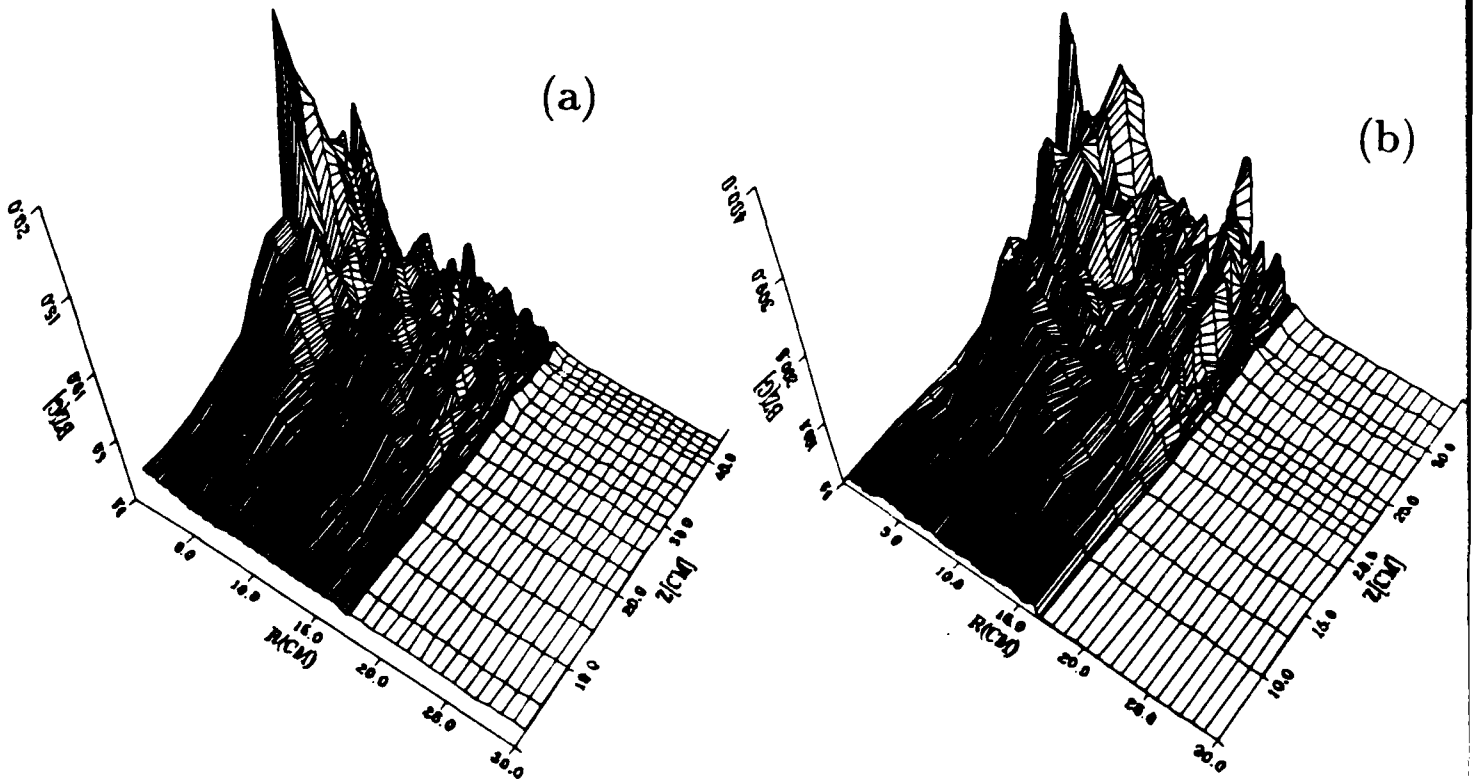

Figure 2. Theoretical wave propagation for (a) single loop antenna and (b) double half loop antenna.

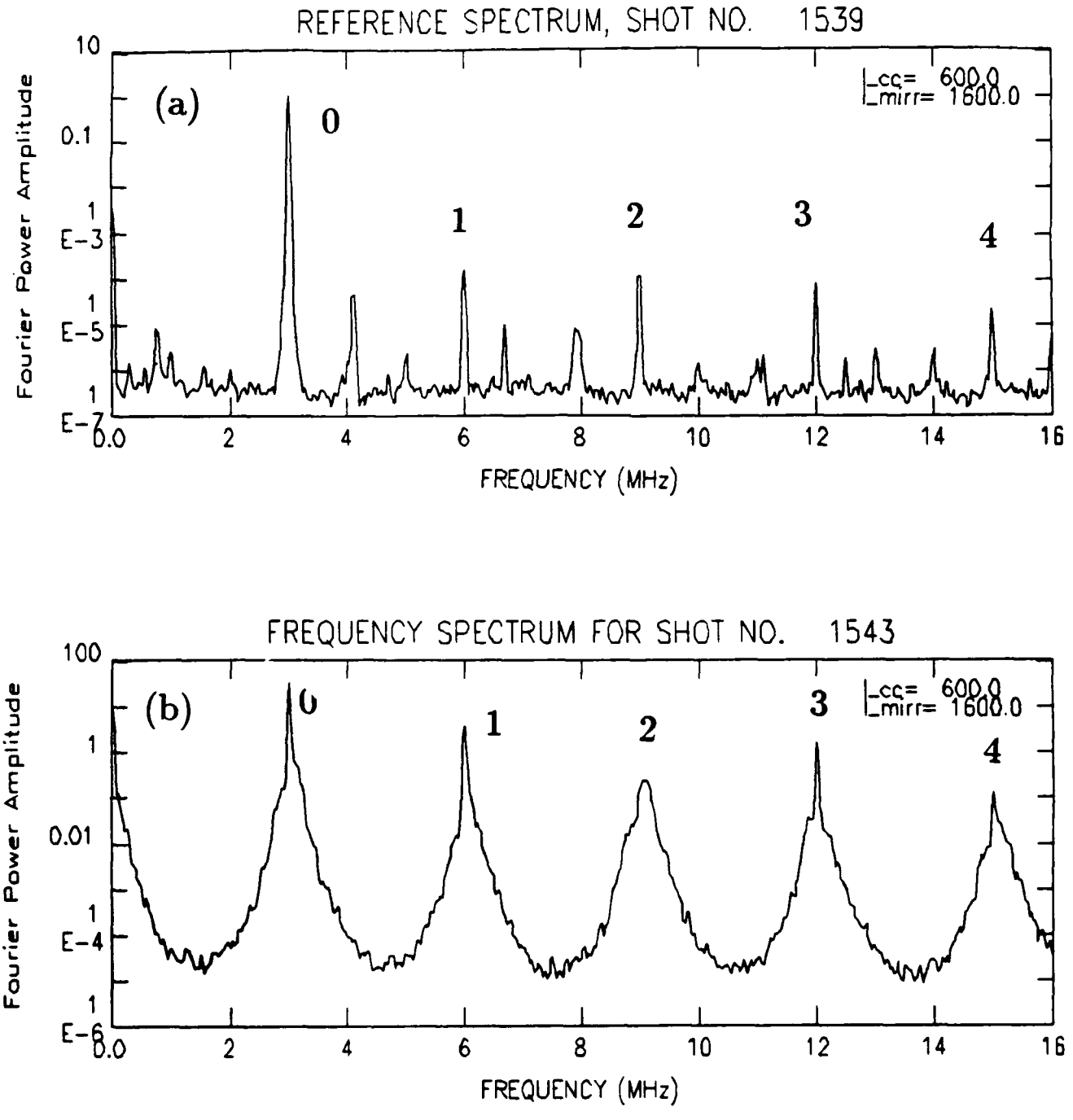

Figure 3. Fourier spectrum of the measured wave of frequecy of $3MH_z$: (a) in the vacuum and (b) in the plasma. The amplitude and width of the wave in the plasma are much larger then in the vacuum.

227-90R1.ABS

HEATING OF A LIQUID/VAPOR MIXTURE BY A PULSED ELECTRIC DISCHARGE

AFOSR Contract No. F49620-87-C-0061

R. L. Burton, B. Hilko, F. D. Witherspoon, G. Jaafari

GT-Devices, Inc., Alexandria, VA 22312

SUMMARY:

Arc discharge heaters in the 5-1000 MW class, used for pulsed electrothermal propulsion and for hypersonic combustion research, are required to ingest their working fluid in solid or liquid form to keep working temperatures within the desired 6000-20,000°K range. This research effort seeks to understand the two-phase heating process for liquid water injected into a 5 MW, 100 atm. capillary-confined pulsed arc. Water is injected as a straight jet (0.2 mm diameter) or as a uniform thin film covering the capillary wall. Power pulses of 15-60 μs duration at currents up to 5.5 kA have been used. Voltage, current, pressure, photographic, and arc spectral measurements were performed to give a large data base of information covering various discharge parameters, such as injection configuration, capillary size, power loading and pulse duration. A numerical 1-D plasma flow model has been developed and can accurately predict the highly transient response of the capillary over a broad range of discharge conditions.

TECHNICAL DISCUSSION:

In a liquid fuelled pulsed electric discharge [1, 2, 3] a variety of complex, interdependent phenomena can participate in the energy transfer and mixing processes occurring between the liquid vapor and plasma components (see Fig. 1). Plasma radiation, thermal conduction and convection all contribute heat flux for evaporation of the liquid. Vapor-plasma mixing can occur in the fast flow-field as a steady surface erosion, or via instabilities leading to a more-or-less explosive breakup of the injected liquid. The goal of this research is to identify the

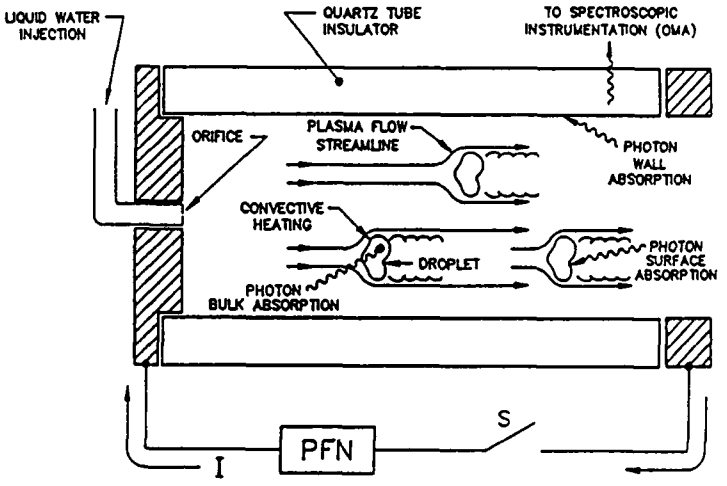

Figure 1

mechanisms dominating the liquid-vapor heating and mixing processes occurring in the high pressure, high enthalphy flow.

Over the first two years we have developed an understanding of these unsteady discharges by the application of various diagnostic techniques for obtaining detailed measurements of the time-dependent plasma conditions (i.e., density, temperature, pressure) and of the liquid/vapor interface. Over the past year emphasis has been placed on modeling and numerical simulation of the discharge dynamics for comparison with the available experimental data.

The numerical method used for this study is an algorithm developed specifically for the solution of time-dependent flow problems containing steep gradients and shocks. The algorithm, called Flux-Corrected Transport (FCT) [4, 5], incorporates methods of general applicability to calculate accurately the dynamics of the fluid equations. The FCT algorithm can provide a complete two-dimensional unsteady flow solution in the high density continuum regime, and potentially can also model the free-molecular regime.

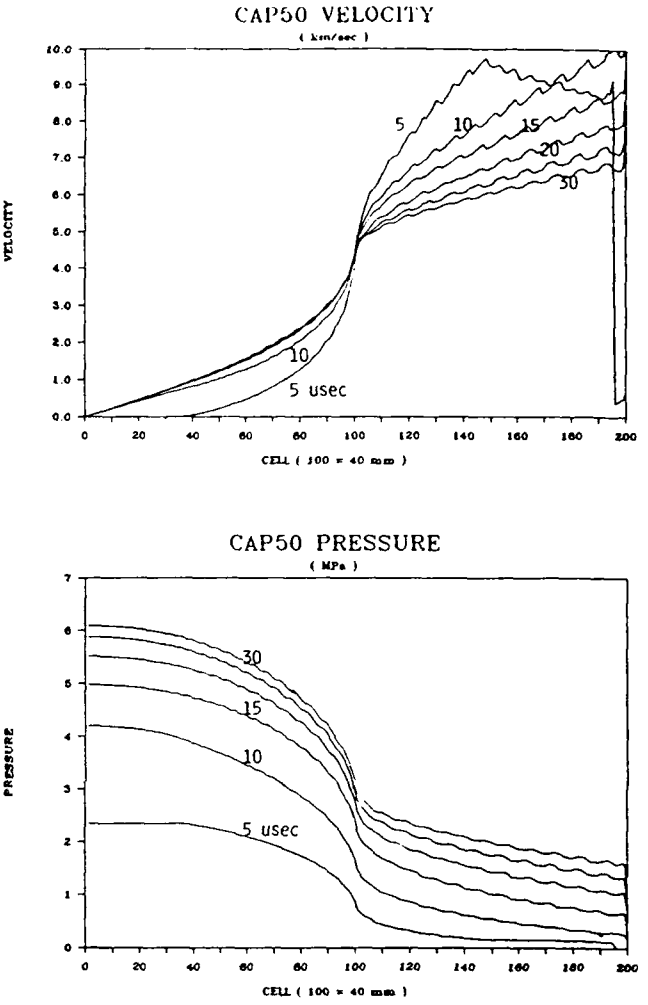

Figure 2

The discharge dynamics are being studied with a simplified 1-D description of this two-phase flow problem. Input to the model consists of the geometrical factors such as capillary and liquid jet dimensions and the experimentally measured current pulse. The model contains the following basic features.

Energy and mass exchange between the liquid and plasma is taken to be a purely surface localized phenomenon. Water is evaporated from the liquid, surface area S, due to the local plasma heat flux q to provide an ablated mass flux $dm/dt = Sq/H_p$ into the plasma volume, where H_p is the plasma enthalpy. In the 1-D description, radial dynamics are not considered so that the evaporated mass at each axial position is radially distributed instantaneously and uniformly. Heat flux to the liquid is dominated by radiative transfer. Though the plasma eventually

behaves as a blackbody source, the optically thin to thick transition can take a significant fraction of the pulse time. Such a transition is simulated by using $q = A(t)\sigma T^4$ $(0 \leq A(t) \leq 1)$ with the choice of amplitude function being guided by various optical and spectroscopic radiation measurements on the discharge. In order to obtain an accurate description of the electrical behavior, a modified Spitzer resistivity model is used where $\eta = C(z,n_e,T)T^{-3/2}(1 + 2\nu_{eo}/\nu_{ei})$. The resistivity coefficient incorporates the dependence on temperature, density and ionization level. Also, the contribution due to electron-neutral scattering is included via the collision frequency ν_{eo}.

Model output is plasma density, velocity, pressure and temperature, plotted versus axial distance for selected times during the pulse. The simple case of a step pulse in current is shown in Fig. 2, which shows profiles of the plasma flow velocity and pressure at 5 to 30 μsecs. The ohmically-heated capillary is a cylindrical, 40 mm long discharge chamber, occupying computational cells 1-100, and having a uniform coating of water on the 5 mm diameter inner wall. Boundary conditions at the capillary exit (cell 100) are simplified by venting the plasma into a second 5 mm diameter pipe, occupying cells 101-200, in which the flow is supersonic and does not influence the capillary dynamics.

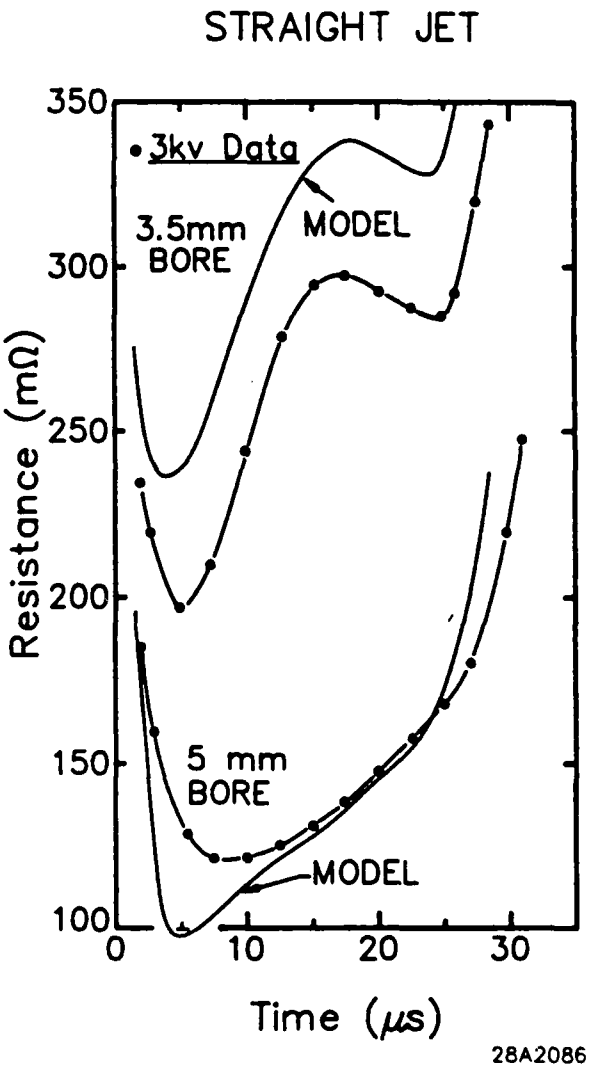

Figure 3

Experimental measurements and the model predictions of the total resistance of the capillary are compared in Figure 3. This data is obtained for straight jet injection in both 3.5 mm and 5.0 mm diameter capillaries. The present model can accurately reproduce the highly transient behavior of the measured discharge parameters, such as resistance vs time shown in the Figure 3. Good agreement with experimental data is obtained over a broad range of discharge conditions, from T = 3-4 eV, ρ = 0.01 kg/m^3 to T = 1 eV, ρ = 0.3 kg/m^3.

Although the present AFOSR basic research program is near completion, this work has advanced our knowledge and understanding of liquid fuelled capillary discharges. Other applications oriented programs based on this technology will benefit substantially from the experimental and theoretical studies that have been performed during this basic research effort. Considerable confidence has been gained in our ability to model the discharge, and therefore also in our design and predictive capabilities.

REFERENCES

[1] R. L. Burton, et. al., "Investigation of a Repetitive Electrothermal Thruster," GT-Devices, Inc., Report GTD 86-5, NASA CR-179464, NASA-Lewis Research Center, August 21, 1986.

[2] R. L. Burton and B. K. Hilko, "Heating of a Liquid/Vapor Mixture by a Pulsed Electric Discharge," GT-Devices, Inc., Report GTD 88-8, AFOSR Contract No. F49620-87-C-0061, Annual Technical Report, July 31, 1988.

[3] R. L. Burton, B. Hilko, and F. D. Witherspoon, "Heating of a Liquid/Vapor Mixture by a Pulsed Electric Discharge," GT-Devices, Inc., Report GTD 89-9, AFOSR Contract No. F49620-87-C-0061, Annual Technical Report, July 31, 1989.

[4] J. P. Boris and D. L. Book, "Flux-Corrected Transport I: SHASTA-A Fluid Transport Algorithm That Works," J. Comp. Phys. 11, 38, 1973.

[5] R. L. Burton, N. K. Winsor, and F. D. Witherspoon, "Numerical Modeling of Fully Viscous Rocket Plume Flows," GT-Devices, Inc., Report GTD 88-9, Contract NAS3-25497, NASA-Lewis Research Center, August 26, 1988.

DIELECTRIC CHARGING PROCESS IN HIGH VOLTAGE SOLAR CELL ARCING

(AFOSR-87-0340)

Principal Investigator: Daniel E. Hastings

Massachusetts Institute of Technology
Cambridge, MA 02139

Abstract

Serious interactions are known to occur between the high voltage solar arrays and the ionospheric plasma. The most serious problem is thought to be arcing. The charging process of the dielectric coverglass by charged particles is studied numerically. Three possible charging mechanisms are considered: ion charging, ion-induced secondary electron (IISE) charging and enhanced field emission electron (EFEE) charging. The IISE charging can lead to a steady state unless the EFEE charging becomes significant. If there is a field emission site with a high electric field enhancement factor β on the interconnector, then EFEE charging can be initiated. Once the EFEE charging is initiated, it leads to the Townsend breakdown in the neutral gas desorbed from the coverglass. For a given geometry, the threshold voltage is determined by the upper bound of the field enhancement factor and calculated to be -220 volt.

1. Introduction

In the future, increased activities in space will require large amounts of energy, of the order of 100 kW to 1 MW. Use of high voltage solar arrays minimizes the power loss and the mass of the transmission lines. When the voltage drop of the solar arrays is increased substantially, however, we can no longer neglect the interaction between the solar array and the surrounding space plasma. Arcing is known to be the most severe interaction problem. Arcing is typically defined as a sudden large current pulse in the plasma current collection to the negatively biased part of the solar array. Arcing gives rise to electromagnetic interference as well as possible surface damage.

Hastings *et.al.*[1], proposed that the breakdown occurs by ionization of the neutral gas desorbed from the dielectric coverglass due to electron stimulated desorption (ESD) by electrons emitted from the interconnector. In solar array arcing by this mechanism the dielectric coverglass acts as the anode. But the potential of the dielectric coverglass is determined by charging due to charged particles. The purpose of this paper is to study the charging process of the coverglass and consider the breakdown mechanism by ionization of the desorbed neutral.

The rate of change of the surface charge density σ on the dielectric surface is given by

$$\frac{d\sigma(x)}{dt} = j_{id}(x) - \int (\gamma_{ee}(x) - 1)P(x,y)j_{ec}(y)dy - \int (\gamma_{ee}(x,x') - 1)P(x,x')j_{ee}(x')dx', \qquad (1)$$

where j_{id}, j_{ec}, and j_{ee} are the current densities of ions to dielectric, electrons from conductor, secondary electrons from dielectric, respectively, and $\gamma_{ee}(x,x')$ is the secondary electron yield at

the point x due to the electrons emitted from the point x' and $P(x,y)dx$ is the probability that the electron emitted from y hits the dielectric surface in the range x to $x+dx$. The system we consider is shown in Fig. 1.

In this paper we solve Eq. (1) numerically. We consider three charging mechanism:(1) charging due to ambient ions, (2) charging due to ion-induced secondary electrons (IISE), (3) charging due to enhanced field emission electrons (EFEE). We show later that the time scales of these processes are different, and therefore we can consider the three charging processes separately.

2. Numerical schemes used for each charging process

The model system we consider here consists of two 0.11 mm thickness dielectric plates with $\epsilon_d = 2\epsilon_o$. The plates sit on an underlying conductive plate with a 1 mm gap. The ambient plasma environment is $n_e = 5\times 10^{11}(1/m^3)$ with $T_e = T_i = 0.1eV$. The conductor plate is biased to -500 volt unless noted otherwise. The system is a two dimensional real space and a three dimensional velocity space with periodic boundaries in the y direction and a Dirichlet boundary condition in the x direction.

For the charging of the system by collection of ions, the ion current to each point on the solar cell surface is calculated by integrating the equation of motion for test particles from the sheath edge to the solar cell. For the charging of the system by electrons from the conductor, we integrate test electron orbits from the conductor and calculate the secondary electron yield γ_{ee} and the impact probability P. The secondary electron yield was calculated by[2]

$$\gamma_{ee} = 7.4\times\gamma_{max}\frac{E_i}{E_{max}}\exp(-2\sqrt{\frac{E_i}{E_{max}}})\exp(2(1-cos\theta_i)), \qquad (2)$$

where E_i is the incident energy, θ_i is the incident angle, and typically $\gamma_{max} = 2.4$ and $E_{max} = 250eV$.

We considered two types of electron emission from the conductor. The first is ion-induced secondary electron (IISE) emission by the ambient ion current. A typical value for the yield γ_{ie} was used. The second mechanism is enhanced field emission (EFE) given by

$$j_{ec}(y) = A(\beta E)^2\exp(-\frac{B}{\beta E}), \qquad (3)$$

where $A = 1.54\times 10^{-6}\times 10^{4.52\phi_W^{-1/2}}$, $B = 6.53\times 10^9\phi_W^{1.5}$ and ϕ_W is the surface work function. This is the Fowler-Nordheim formula for field emission with field enhancement factor β[3]. We assume that the electric field is enhanced by some mechanisms such as dielectric impurity or microscopic structure on the conductor surface. A reasonable value for ϕ_W is 4 eV.

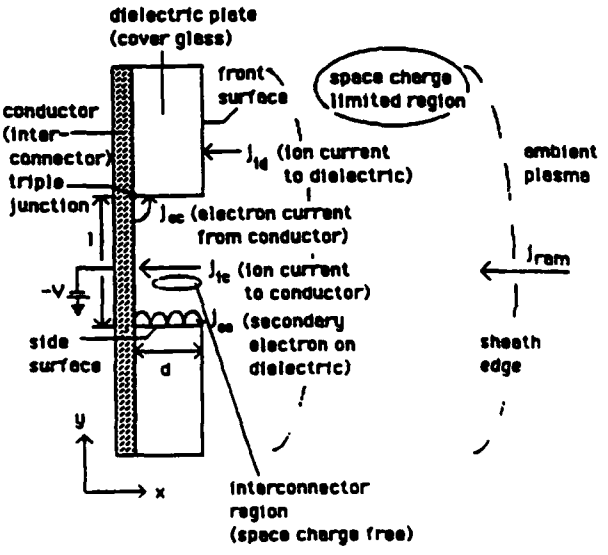

Fig. 1 Schematic view of system

These two numerical schemes allow us to go to very long times for reasonable computational cost. A particle in cell code (PIC) code was also used for the EFEE charging after the space charging effect became substantial.

3. Numerical results

(3-1) Ion charging

As the initial conditions we chose $\phi_s = 0$ for the dielectric front surface and $\phi_s(x) = (V)(1 - x/d)$ for the side surface. After $2000\omega_{pi}^{-1}$ the current to the dielectric front surface becomes nearly zero. The front surface attains its steady state by gaining potential ≈ 5 volt just positive enough to repel the incoming $5eV$ ion flow. The ions which enter the interconnector region can not hit the dielectric side surface. The ions never strike the vicinity of the triple junction.

(3-2) Electron charging

As the initial condition for both types of electron charging we used the steady state obtained by the ion charging.

(3-2-a) IISE charging

The electrons emitted from the conductor mainly strike the dielectric side surface near the corner $x \simeq d$. They mostly give more than one secondary electron per incident electron and the side surface potential goes up due to the positive charging. The time scale of this charging process is one order of magnitude longer than that of ion charging. The incresed side surface potential deflect the incoming ions away from the triple junction and decrease the number of electrons which impact the side surface. Eventually no electrons from the conductor impact the dielectric before they escape outside the sheath and the steady state is attained. This occurs at $t = 1.5 \times 10^5 \omega_{pi}$ for our case.

(3-2-b) EFEE charging

If β is large enough, once the emission current becomes substantial, the EFEE charging develops very rapidly because of its exponential dependence on the field E and we no longer have the steady state by the IISE. Since the details of the emission site are beyond the purpose of this paper, we arbitrarily choose β so that the emission current j_{ec} can be comparable to the ambient ion ram current j_{ram}. For our geometry we assume $\beta = 282$ uniformly over the conductor surface. This $\beta = 282$ is a reasonable value according to Ref. [3]. The electric field at the triple junction keeps increasing very rapidly. At $t = 8 \times 10^4 \omega_{pe}^{-1}$ we can no longer neglect the space charge effect produced by the emission current itself and we used the PIC code.

4. Discussion

On the basis of these numerical calculations, we can draw a picture of how the solar cell dielectric is charged after the conductor reaches the bias potential. The time history of the electric field at the triple junction is shown schematically in Fig. 7.

The phases (1) and (2) occur for every solar cell on the solar array. Among the solar cells, some might have a whisker or dielectric impurity on the conductor surface, which enhances the electric field. If the enhancement is high enough, the EFEE charging is initiated and phase (3) in Fig. 7 develops rapidly. The emission current from the conductor becomes substantial so that we can no longer neglect desorption of neutral gas from the dielectric surface.

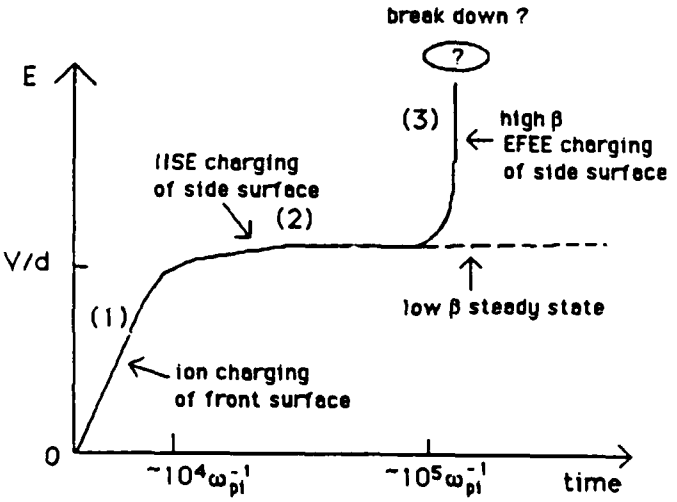

Fig. 2 Electric field at the triple junction vs. time

We now examine the possibility of the Townsend breakdown of the desorbed neutral gas. The Townsend breakdown criteria is given by[4],

$$\gamma(\exp(\int \alpha dx) - 1) \geq 1. \qquad (4)$$

For simplicity, we now assume that α is constant over the surface and give it by $\alpha = n_n \sigma_{ion}$. The density to satisfy Eq. (4) is given by $n_n \geq 2.2 \times 10^{23}(1/m^3)$ for $\gamma = 0.1, \sigma_{ion} = 10^{-19} m^2$ and

$d = 0.11mm$, where $\gamma = 0.1$ is a typical value for ion-induced secondary electron yield.

We assume that the neutral gas is desorbed due to heating of the dielectric surface by the electron current. We consider the desorbed neutral flux simply by energy consumption. We define desorption energy efficiency η_{dsp} by the fraction of incoming energy to be spent in desorption. Then the neutral density is given by

$$n_n = \frac{\eta_{dsp}}{E_{dsp}} \frac{\text{electron energy flux}}{v_n} = \frac{\eta_{dsp}}{E_{dsp}} \frac{j_e(E_i - \gamma_{ee}E_e)}{ev_n}, \tag{5}$$

where E_e is the secondary electron emission energy. From the numerical results, the electron energy flux is estimated to be $10^8(W/m^2)$. Then the neutral density satisfies the breakdown criteria $n_n \geq 2.2 \times 10^{23}(1/m^3)$ at $\eta_{dsp} = 0.1$ for $E_{dsp} = 0.5eV$ and $v_n = 550(m/s)$ where a typical value for physisorption is used for E_{dsp} and $v_n = \sqrt{2\kappa T_s/m_n}$ for $T_s = 300K$ is assumed.

We now estimate the threshold voltage. If the desorption energy efficiency η_{dsp} is given, the minimum energy flux to satisfy the breakdown condition is calculated using Eq. 5. For an example, we consider a case of $\eta_{dsp} = 0.1$. Then the energy flux is $10^8(W/m^2)$. A practical upper bound of β observed so far is $\beta \simeq 500$ [3]. The energy flux is approximated by $j_{ec}E_{\|}(d/2)$ and the minimum electric field to give the energy flux $10^8(W/m^2)$ is calculated to be $E_{\|} = 4.7 \times 10^6(V/m)$ using Eq. 3 with $\beta = 500$. If the electric field can reach $E_{\|} = 4.7 \times 10^6(V/m)$ started from $E_{\|} = V/d$ due to the EFEE charging in a certain time, the breakdown is possible.

We consider the possibility of breakdown within 5400 sec which is one circulation time in LEO. We use Eq. 1 to calculate the rate of change of electric field at the triple junction. The electric field at the triple junction is given by $E_{\|} = \phi_s/(d/2) = \sigma/C_{diele}/(d/2)$. Keeping only the second term in Eq. 1 and assuming $\gamma(x,y) \simeq \gamma_{ee}$ and $j_{ec}(y) = j_{ec}(y = \text{triple junction})$, we have

$$\frac{dE_{\|}}{dt} = \frac{(\gamma_{ee} - 1)j_{ec} \int P(d/2, y)dy}{Cd/2}, \tag{6}$$

where we estimate $\int P(d/2, y)dy \simeq 0.1$ from the result of the orbit integration and $C \simeq 3.5 \times 10^{-6}(F/m^2)$. For simplicity we assume the normal incidence $\theta_i = 0$ for γ_{ee} in Eq. 2 and set $E_i = eE_{\|}(d/2)$. We now integrate Eqs. 2, 3, and 6 numerically with $E_{\|}(t = 0) = V/d$ and $\beta = 500$. The result is that we need $V < -220$ volt to reach $E = 4.7 \times 10^6(V/m)$ within 5400 sec with $\beta = 500$. Since the highest β gives the fastest rate of change of $E_{\|}$, we can conclude that $V = -220$ volt is the threshold bias voltage for the case we considered.

5. Conclusion

The results we have obtained are summarized as follows:

·Ambient ions charge the dielectric front surface leaving the side surface relatively uncharged.

·Ion-induced secondary electrons from the conductor can charge the side surface and a steady state is obtained unless enhanced field emission becomes significant.

·Enhanced field emission electron (EFEE) can charge the side surface if the field enhancement factor is high. Once the EFEE charging is initiated it can lead to the Townsend breakdown.

·For a given geometry, the threshold voltage is determined by the upper bound of β. This is estimated to be -220 volt for our case.

References

1. Hastings D. E., Weyl G., and Kaufman D.,"A simple model for the threshold voltage for arcing on negatively biased high voltage solar array," *to be published in J. Spacecraft & Rocket.*
2. R. C. Chaky, J. H. Nonnast, and J. Enoch., *J. Appl. Phys.*, Vol. 52(12), 1981, pp. 7092-7098.
3. Latham R. V.,*High voltage vacuum insulation,* Academic Press, New York, 1981.
4. Howatson A. M, *An introduction to gas discharge,* Pergamon Press, Oxford, 1965, pp61.

SPACECRAFT INTERACTION WITH AMBIENT AND SELF-GENERATED PLASMA/NEUTRAL ENVIRONMENT

Contract starting date: June 1, 1990

Principal Investigator: Torkil S. Mogstad

McDonnell Douglas Space Systems Co.
Huntington Beach, CA 92647

Summary

Plasma clouds can be generated by many types of interaction between a spacecraft and its environment. These plasma clouds can interact with the body from which they came by providing an artificial environment for high voltage surfaces (solar arrays, transmission lines, etc.). Enhanced sputtering and arcing, leading to reduced performance of the solar arrays, may be the end result. In order to better understand and hopefully predict the occurrence of such phenomena, a microscopic model of the arcing process and a macroscopic model of the plasma/neutral environment will be developed. The macroscopic model will serve as input to the microscopic model.

Introduction

Large plasma clouds around a spacecraft can be generated by outgassing, power system effluents, propulsion plumes, thruster firings, and dumps of neutrals, which subsequently become ionized via various mechanisms. Plasma clouds may also be generated by operation of plasma contactors.. The interaction of these plasma clouds with the body from which they originated is of interest for many reasons. One major reason is that they provide an artificial environment for any high voltage surfaces (solar arrays, transmission lines, etc.) on a space platform/vehicle. These surfaces may be exposed to the space environment either through design, or by erosion of the insulation. In this artificial plasma environment enhanced sputtering and arcing may occur. Both of these processes are life limiting and must be understood to lead to

effective design and location of propulsion systems on board the space platform/vehicle.

A two fold macroscopic and microscopic program has been proposed. The macroscopic program will develop plasma simulation models for the ionization and motion of plasma clouds near large space platforms/vehicles. This will provide the neutral and plasma environment which will be used in the microscopic model of the high voltage surface. The microscopic effort consists of development of models of the arcing and sputtering as a function of among other things the plasma and neutral environment. The goal is to provide a predictive capability for the occurrence and prevention of arcing on high voltage surfaces.

The research will be conducted on a jointly basis between McDonnell Douglas Space Systems Co. (MDSSC) and MIT, but for practical reasons the task has been divided into two parts. Professor D. E. Hastings at MIT is responsible for the microscopic arcing model, whereas the development of a macroscopic simulation model for the ionization of the neutral effluent and the subsequent motion of the plasma cloud will be undertaken by MDSSC.

The objective is to develop a model of the neutral and charged particle self-induced environment around a space platform/vehicle. Current models have treated outgassing rates up to a maximum of kg/hr, only. We want to extend this to rates of kg/s, which corresponds to the effluent mass flow out of a megawatt type chemical or nuclear power system. The model should include altitudes up to 1000 km and all inclinations. Current models are mainly concerned with low inclination LEO conditions.

Neutral Expansion

The initial expansion of the neutral effluents will be modeled by a combination of the Method of Characteristics (MOC) and Direct Simulation Monte Carlo (DSMC) in the continuum and rarefied regimes, respectively. There are several potentially important interactions between the platform surfaces and the effluents. The model will consider chemical reactions, hopefully including reaction rates and their dependence on temperature and catalytic effects. In addition to the high mass flow effluents, the platform will exhibit outgassing, desorption, etc. The degree of surface accommodation has to be estimated; this will depend on particle energies and their

impact angles (ram/wake effects). Secondary and backscattered electrons should be considered.

Geometry

A more or less generic platform geometry will b defined, based on the geometry in the POLAR (Potentials Of Large objects in the Auroral Region) code, developed by AFGL/S-Cubed. This code has been acquired from AFGL, and is currently being tested at MDSSC. Once the neutral flow-field has been characterized, a functional fit to the simulation data can be generated; this will define the initial conditions for the plasma model.

Ionization

Part of the initial neutral distribution will become ionized and create a platform induced plasma. Several charging/ionization mechanisms are possible; some of them are

- Charge Exchange
- Photo-ionization
- Chemical Reactions
- Critical Velocity Ionization
- Auroral Charging
- Galactic/Solar Cosmic Rays
- Solar Wind
- Recombination

For the charge exchange we need to define the ambient ion environment and the appropriate cross-sections. Optical thickness of the platform effluent cloud must also be taken into consideration. To compute the photo-ionization we will need solar flux and cross-section for various photon energies. Optical thickness of the cloud will be important. We need to estimate all chemical reactions of importance and their dependence on surface materials, temperature, energies, etc. Critical ionization is still a poorly understood phenomenon, however, it might be possible to include it as some sort of artificial term. Charged particles in the auroral regions and in the form of cosmic rays and solar wind can ionize the neutrals. Particle fluxes and energies, as well as cross-sections are needed. The various recombination mechanisms should be included.

Dynamics

After an initial neutral and plasma distribution has been estimated, we can investigate the dynamics. A set of fluid equations, including continuity equations, momentum equations, energy equations, and charge conservation, will be derived. For simplicity reasons these will be 2-D equations. The equations will be expanded and simplified in accordance with the appropriate collisional regime. The momentum equations should include all collisions that might effect the dynamics. All relevant collision frequencies have to be estimated. We have to decide what length scales the equations shall be valid for and integrated over. Diamagnetic plasma effects might have to be considered. Kinetic coefficients in the energy equations, such as viscosity and heat transfer, will be characterized using model forms. A numerical solution of the set of fluid equations for the neutrals and the plasma will be attempted. We will start development of a finite element code for this purpose.

ECR PLASMA ENGINE RESEARCH

Grant No. AFOSR-87-0205

F. E. C. Culick and J. C. Sercel

California Institute of Technology
Pasadena, California 91125

SUMMARY/OVERVIEW:

The Electron-Cyclotron-Resonance (ECR) plasma engine is an electrodeless electromagnetic plasma accelerator which is being investigated for its potential use in electric propulsion, beamed energy propulsion, and advanced nuclear propulsion (Ref. 1). Motivation for study of this device vis-á-vis other plasma acceleration schemes stems from calculations which suggest its potential to deliver high specific impulse, long life, and high unit power handling capability while processing any of several propellant species, some of which are not useable in alternative electric thruster concepts.

This research is directed at developing the first quantitative theoretical model of the operation of the ECR plasma engine. To accomplish this objective, both analytical and experimental research is being conducted. In the analytical aspect of this program a quasi-one-dimensional, steady-state model of the acceleration process has been developed. Numerical calculations based on this model have been conducted to provide quantitative predictions of physical parameters which are tested experimentally. In addition, a simple formulation has been developed which allows calculation of the trajectory of an accelerating plasma in the presence of an applied, diverging magnetic field. Tests on a laboratory ECR plasma accelerator have been conducted. Several diagnostic tools, including a gridded energy analyzer, a Faraday cup current density analyzer, Langmuir probes, emissive probes, and a diamagnetic loop have been used to measure physical parameters of interest.

TECHNICAL DISCUSSION

The theoretical aspect of this research consists of two separate modeling efforts. The first is a three dimensional calculation to predict the plasma trajectory of an ECR accelerator. The second, more extensive modeling effort, is the development of a quasi-one-dimensional three-component model which is used to understand non-equilibrium and radiation effects.

Calculation of Plasma Trajectory in a Diverging Magnetic Field: We have used a collisionless, steady-state, cold, two-fluid model to predict the trajectory of the ECR plasma as it is accelerated through a diverging magnetic field. Our model, which is an extension of Kosmahl's model (Ref. 2), allows the calculation of the angle by which the plasma trajectory diverges during separation from the magnetic field. The divergence angle is important because the fraction of the momentum of the flowing plasma which is useful for thrust varies as the cosine of the divergence angle.

Our analysis addresses the acceleration of a plasma which is initially at a specified velocity and position in a cylindrically symmetrical system. An applied, strictly

longitudinal magnetic field is assumed. Although random thermal energy effects are neglected in the cold plasma approximation, an important effect of the plasma enthalpy is included as the energy and magnetic dipole moment associated with electron Larmor motion perpendicular to magnetic field lines.

We use a Lagrangian formulation to describe an electron fluid and an ion fluid which mutually interact via an induced ambipolar electric field. The condition of quasi-neutrality is valid throughout the region of interest in this device, so the ion plasma density is assumed equal to the electron plasma density. As the plasma is accelerated under the influence of the diamagnetic body force, the kinetic energy of the electron Larmor motion is converted to directed kinetic energy of both ions and electrons.

We have used this model to predict the plasma trajectory for the magnetic field configuration which we are testing in the experimental aspect of this research. Plasma trajectories are calculated for eleven initial positions, all 5 cm downstream of the center of the solenoid, for eleven radial positions with radii ranging from zero to 5.5 cm. The Lagrangian two-fluid equations of motion are integrated using the LSODE ordinary differential equations package.

Figure 1 shows the plasma trajectories predicted by these calculations. The magnetic field lines are superimposed on the graph as dotted lines to show where the plasma crosses the field lines. Calculations of plasma trajectories in other field configurations confirm Kosmahl's assertion that beam divergence losses can be made small in ECR plasma accelerators.

Nonequilibrium and Radiation Effects Model: Nonequilibrium and radiation effects are treated using a steady-state, quasi-one-dimensional, three-component model. The three components included are the electron fluid, the ion fluid, and the neutral gas, which is addressed under the assumption of rarified flow. Using this model we can solve for plasma density, gas atom density, axial velocity, and each of two components of the electron temperature (perpendicular and parallel to magnetic field lines). Source terms are present in the model to account for phenomena such as coupling microwave power into the plasma at ECR, collisional energy transfer between the perpendicular and parallel components of the electron temperature, cross-field (Bohm) diffusion, ionization, radiation, and ambipolar diffusion.

The set of equations which embody the model have been presented in previous publications (Refs. 3,4). The LSODE ordinary differential equations package has been used to calculate numerical solutions to the equations. The results of one such calculation are presented in Figures 2, 3, and 4. The boundary conditions used in Figure 2 include an initial gas velocity equal to the initial plasma velocity of 100 m/s, an initial electron temperature of 2.5 eV, an initial neutral gas density of 6×10^{18} m^{-3}, and an inlet ionization fraction of 0.1. Coupled ECR power in this case was taken to be 20 kW/m^2. The ECR heating region was assumed to be centered at z=0.1 m falling off up-stream and down-stream as a Gaussian function over a characteristic length of 1 cm.

Figure 2 shows the variation of plasma velocity as a function of 'z', the distance down-stream from the window. Figure 3 shows the variation of neutral atom and plasma density with z. Figure 4 shows the variation of the perpendicular and parallel components of the mean electron thermal energy with z. Predicted losses due to ionization, radiation, diffusion, propellant utilization, and particle collision phenomena amount to approximately 25 percent of coupled microwave power in this calculation.

Experimental Studies An experimental test bed has been developed as part of this activity (Refs. 4,5). Several diagnostic tools have been used to measure physical parameters of interest in further developing a basic scientific understanding of this device. Our diagnostics include a gridded energy analyzer, a Faraday cup current density analyzer, Langmuir probes, emissive probes, and a diamagnetic loop. We have measured the accelerated ion energy distribution, the accelerated plasma density (and hence the propellant utilization), perpendicular and parallel components of the electron temperature, the magnitude and spatial variation of the plasma potential, and plasma beta in the ECR heating region.

Our measurements have shown that the propellant utilization, ion energy, plasma potential, and plasma beta are consistent with theoretical predictions based on the measured electron temperature. However, electron temperatures have been lower than predicted by theory. The most likely explanation for this observation is that axial conduction of electron thermal energy is carrying a significant fraction of the coupled power down-stream where it is dissipated via inelastic collisions of electrons with neutral atoms in the vacuum tank.

Preliminary Conclusions, Continuing Work, and Plans If axial conduction of thermal energy via electron transport is responsible for the observed lower-than-expected electron temperatures, the theoretical performance of the ECR plasma engine is probably not significantly reduced. We believe the effect of such a process would be to extend the acceleration region out farther beyond the heating region than is predicted by the present model. Such an extension of the acceleration region would have the negative effect of dramatically reducing the maximum allowable vacuum system background pressure for verification of thruster performance.

For the present research effort, it is necessary to incorporate the effects of axial heat transport and vacuum system back pressure into the existing model. Once verified by comparison with our experimental measurements, the present theory can then be used to predict the theoretical performance of the ECR plasma engine. To this end, the nonequilibrium and radiation effects model has been modified to include the Spitzer-Harm heat conduction formula for axial heat transport along magnetic field lines. We plan to perform numerical calculations based on this modified model and to compare the results of these calculation with our experimental measurements before publishing the final report for this research effort.

References:

1. Kosmahl, H. G., "Three-Dimensional Plasma Acceleration Through Axisymetric Diverging Magnetic Fields Based on Dipole Moment Approximation" NASA Technical Note, NASA TN D-3782, Lewis Research Center, January 1967.

2. Sercel, J. C.,"Electron-Cyclotron-Resonance (ECR) Plasma Acceleration," AIAA-87-1407, presented at the AIAA 19th fluid Dynamics, Plasma Dynamics, and Lasers Conference, June 8-10, 1987/ Honolulu, Hawaii.

3. Sercel, J. C.,"Electron-Cyclotron-Resonance (ECR) Plasma Thruster Research," AIAA-88-2916, presented at the AIAA/ASME/SAE/ASEE 24th Joint Propulsion Conference, July 11-13, 1988/Boston, Massachusetts.

4. Sercel, J. C.,"ECR Plasma Thruster Research," AIAA-89-2379, presented at the AIAA/ASME/SAE/ASEE 25th Joint Propulsion Conference, July 10-12, 1989/Monterey, CA.

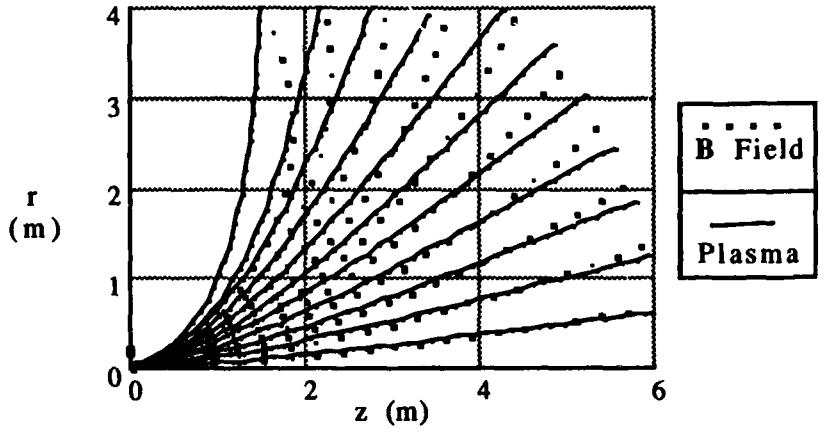

Figure 1 - Calculated Plasma Trajectory for Existing ECR Plasma Thruster Research Apparatus

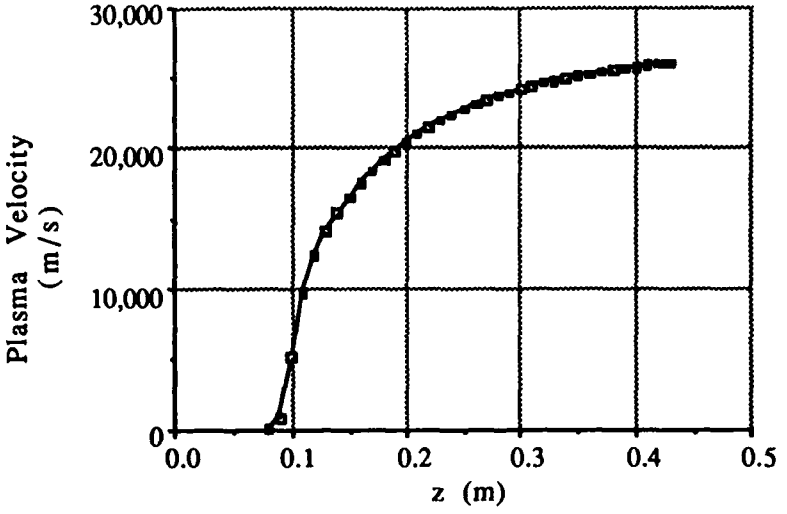

Figure 2 - Calculated Plasma Velocity as a Function of Distance from Dielectric Window

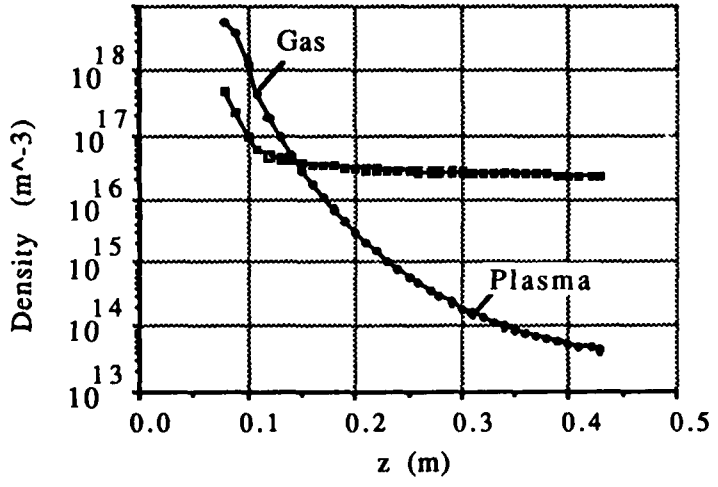

Figure 3 - Calculated Plasma Density as a Function of Distance from Dielectric Window

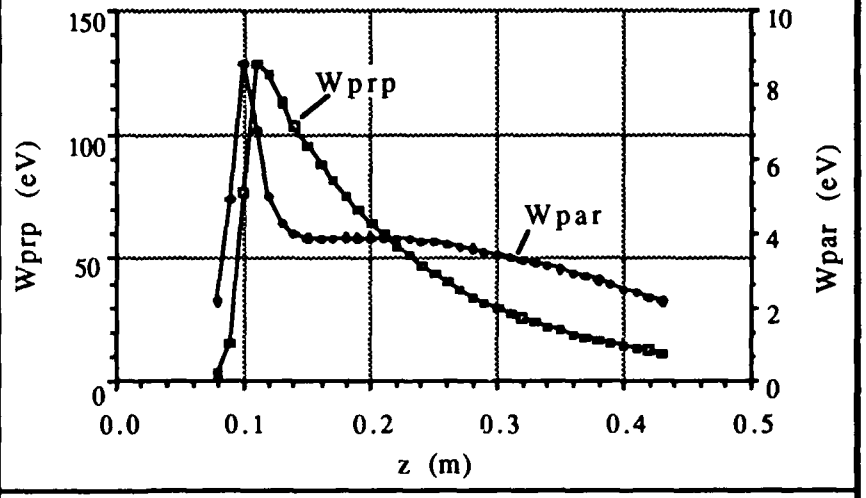

Figure 4 - Calculated Mean Electron Energy as a Function of Distance From Window

OSCILLATORY INTERNAL FLOWS IN SOLID PROPELLANT ROCKETS

(AFOSR Grant No. TBD and Contract No. TBD)

Principal Investigators: G. A. Flandro and R. S. Brown

School of Aerospace Engineering
Georgia Institute of Technology
Atlanta GA. 30332

and

United Technologies/ Chemical Systems Division
P. O. Box 49028
San Jose, CA. 95161-9028

SUMMARY/OVERVIEW: This collaborative research program is investigating the basic and unique mechanisms by which oscillatory motions produced by acoustic fluctuations interact with the mean gas motion in the combustion chamber of solid propellant rockets. Current predictive models, which form the basis for combustion stability predictions, do not correctly account for the boundary conditions and acoustic energy effects resulting from the vorticity produced and transported by both the mean and oscillatory flows. Correcting these deficiencies will significantly increase the accuracy and reliability of stability predictions and methods for correcting motor problems.

TECHNICAL DISCUSSION: Recent measurements and analyses of the mean and oscillatory flow fields in solid propellant rocket motors have demonstrated the unique behavior of the basic fluid mechanics. Radial profiles of the mean velocity vector and turbulence show the evolution of gas from the propellant surface causes the flow to be dominated by pressure and inertial forces, and not by viscous forces. Thus, the flow is rotational because of inertial effects and the time average vorticity results from the forces required to turn and accelerate the flow from the side wall to the axial direction. Interpreting these flows by analogy to growing and/or fully developed turbulent boundary layers is, therefore, not only invalid but is also very misleading. In fact, the concept of a boundary layer is not valid for these flows because the velocity gradients extend a substantial distance across the flow channel. Furthermore, turbulence is important only towards the aft-end of the motor, not all along the motor, as is usually assumed.

When acoustic waves are imposed on this steady rotational flow, two phenomena are observed which differ significantly from the classical irrotational behavior which has been assumed to characterize these waves (1,2). First, the measured magnitudes of the waves differ significantly from the expected plane wave

behavior. As shown in figures 1 and 2, the radial variation of the axial component of the oscillatory velocity extends well into the core of the flow channel and the classical irrotational behavior is limited to approximately 1/3 of the flow area near the core region. In addition, the limited measurements which resolved the vector direction of these waves indicate that the oscillatory vorticity is substantial and thereby essential to understanding the wave behavior. Thus, not only is the wave motion rotational, but the gradients have characteristic distances which significantly exceed the thickness of the acoustic boundary layer. Therefore, an acoustic boundary layer approach is not valid for interpreting the effect of wall blowing on the wave motion.

Preliminary analyses of these flows by Flandro (3,4,5) have determined that including the production and transport of vorticity can account for these observed effects. The velocity overshoot is caused by a travelling shear wave that is generated at the surface and propagates radially with the mean radial speed of the gas. The amplitude decreases because of viscous damping and because the radial mean velocity approached zero and the chamber centerline. The shear wave results from vorticity introduced because the flow must enter the chamber normal to the surface. It is not necessary to invoke the effects of viscosity directly to account for these main features of the flow.

The theoretical maximum velocity overshoot is twice the amplitude of the acoustic motion. The unsteady velocity is nearly in phase with the local acoustic pressure, instead of lagging the pressure by 90 degrees as assumed in the conventional combustion stability models. The depth of the shear wave penetration into the chamber, it's wavelength, and the overshoot amplitude are controlled by two Reynolds numbers controlled respectively by the injection speed of the mean speed and the acoustic wave number. For the low-order axial modes, the rotational perturbations dominate the flow. They also show a strong axial dependence which modifies the apparent combustion response in a manner similar to that usually attributed to the classical form of velocity coupling.

The analytical studies to be conducted under the collaborative program will remove these limitations from the mathematical stability models and thereby significantly enhance both the physical understanding of the phenomena as well as improve the ability to anticipate and correct motor designs. First, careful modelling will establish the best method for incorporating the effects of vorticity transport and the associated boundary conditions into the internal flow problem. Next, the time dependent flows will be separated into two separate modules. The first module is directed towards producing an accurate analytical representation of the time-dependent flow in a form which is suitable for practical motor design studies. The module will this first module by comparison to a detailed finite difference computational solution to the full viscous internal

flow problem. This second module will utilize a new fully vectorized three-dimensional Navier-Stokes code being written to support this program.

Additional measurements of the oscillatory velocity vector profile will also obtained to characterize the acoustic environment in detail. High resolution oscillatory velocity profiles will be measured upstream of the turbulent transition in the mean flow for three purposes. First, analytical studies, such as the recent preliminary analytical predictions by Flandro presented in figures 1 and 2, show that high axial and radial spatial resolution of the acoustic velocity vector profiles are needed to adequately test analytical predictions of velocity vector profile. Second, the range of flow and acoustic conditions tested must be extended to adequately encompass the typical range of motor conditions. These additional conditions include evaluating the effects of surface Mach No., acoustic frequency, and surface admittance. Third, the effect of kinematic viscosity requires definition to assess the relative contributions of viscous and inertial forces in the acoustic flow field. This contribution can be investigated by measuring the effect of mean pressure on the acoustic velocity vector profiles.

The analytical and experimental results will be compared to establish the validity of the flow field representation and to provide a basis for significantly improving the accuracy of stability predictions.

References

1. Brown, R.S., Blackner, A.C., Willoughby, P.W., and Dunlap, R., "Coupling Between Velocity Oscillations and Solid Propellant Combustion", Journal of Propulsion and Power, 2, pp. 428-437, 1986.

2. Brown, R.S., Blackner, A.C., Willoughby, P.W., and Dunlap, R., "Coupling Between Velocity Oscillations and Solid Propellant Combustion", Final Report on contracts F49620-81-C-0072 and F49620-84-C-0082, Chemical Systems Division, August 1986.

3. Flandro, G.A., "Analysis of Oscillatory Vorticity", CSD IR&D Report 86-6.4, December 1986.

4. Flandro, G.A., Finlayson, P.A., and Brown, R.S., "A Rational Model for Velocity Coupled Response", Paper presented at 26th JANNAF Combustion Meeting, Pasadena, CA., October 1989.

5. Flandro, G.A., :Effects of Vorticity on Axial Waves in a Porous Tube with Blowing", CSD IR&D Report 88-6.4, January 1989.

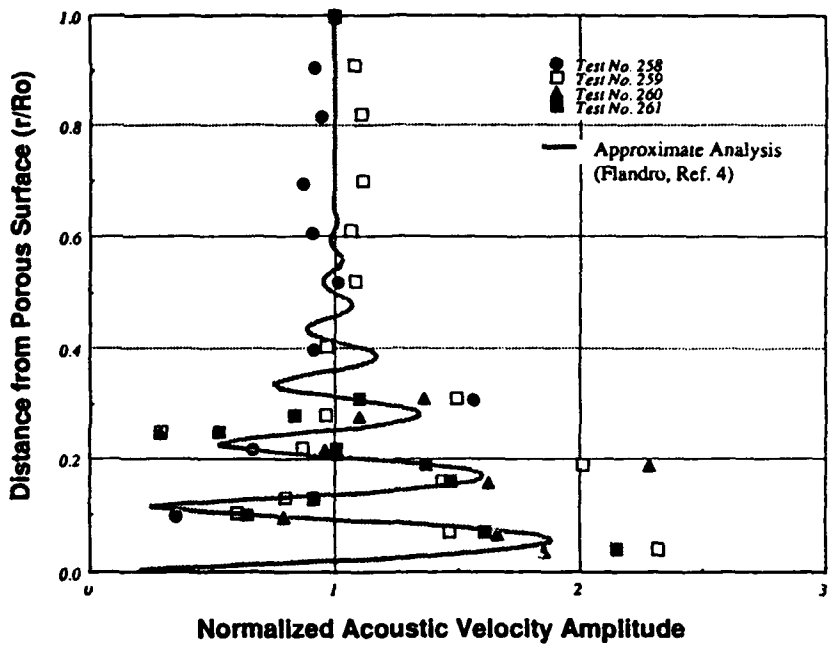

Figure 1. Comparison of Approximate Solution with Cold Flow Data

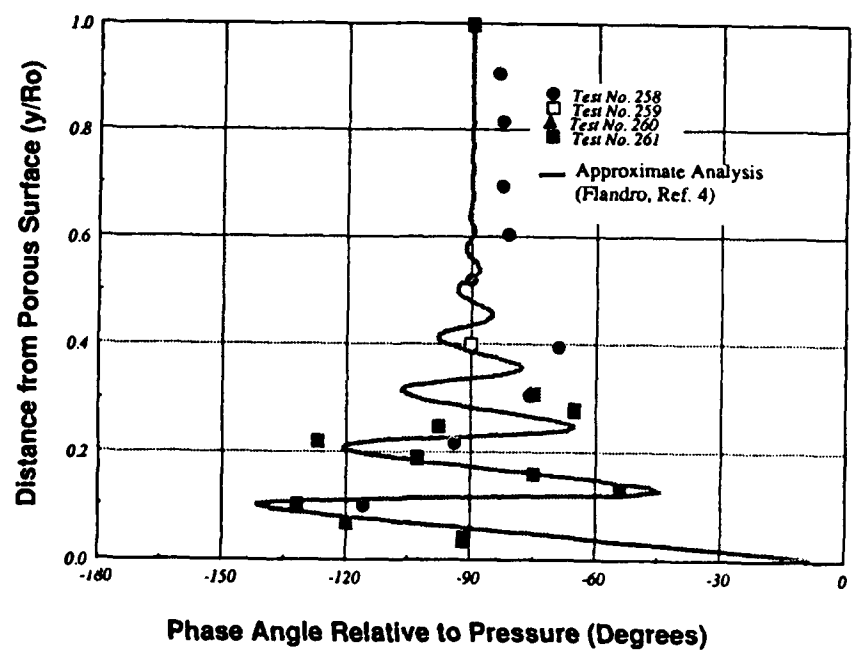

Figure 2. Comparison of Approximate Solution with Cold flow Data

ACOUSTIC WAVE INTERACTION WITH A LOW MACH NUMBER SHEAR FLOW

(AFOSR Grant No. 89-0023)

Principal Investigator: **David R. Kassoy**

Mechanical Engineering Department
Center for Combustion Research
University of Colorado
Boulder, CO 80309-0427

SUMMARY:

The objective of this study is to elucidate the acoustic-shear flow interactions in solid rocket engine chambers, where the characteristic Mach number M is small. The traveling wave study emphasizes acoustic refraction phenomena and viscous acoustic boundary layer structure. The results, obtained from a perturbation based-analysis, show the explicit effects of the key dimensionless parameters in the physical system. The standing wave study shows that transverse and oblique acoustic modes evolve from the interaction of longitudinal modes with the shear flow. It is found that, in the parameter ranges typical for solid rocket gasdynamics, the alteration of both traveling and standing acoustic waves by the mean shear flow is $\mathcal{O}(M)$, relative to the imposed acoustic disturbance.

AUTHORS: **Meng Wang** and **D.R. Kassoy**

TECHNICAL DISCUSSION

1. Traveling Wave Study

A study is made of acoustic wave propagation through a low Mach number shear flow in a long, narrow, planar duct with impermeable walls. Concern is focused on acoustic refraction, physical characteristics of the acoustic boundary layer and the relevance of nonlinear effects, issues of controversy between Baum and Levine's recent rocket-oriented numerical solutions [1] and those from classical linear analysis [2–4] for sound waves. The primary goals of the present work are to reformulate the acoustic-shear flow interaction problem, specifically for parameter ranges relevant to solid rocket engines, to assess the validity of classical linear solutions [2–4] as applied to rocket flow conditions, as well as to gain more physical insight about acoustic refraction effects by systematic mathematical modeling efforts.

The study is based on a laminar flow model for a viscous, heat conducting fluid. Perturbation methods, based on the small mean flow Mach number M and high Reynolds number $R_e \gg \mathcal{O}(1/M)$, are employed to find solutions for both the transport-free core region and the extremely thin acoustic boundary layer adjacent to the impermeable duct wall. As in the earlier studies [2–4], quasi-steady solutions of the form

$$[\hat{p}, \hat{u}, \hat{v}] = [F(\kappa, y), G(\kappa, y), H(\kappa, y)]\, e^{i(\kappa x - t)} \tag{1}$$

are constructed for the dimensionless acoustic pressure, the horizontal acoustic velocity and the transverse acoustic velocity, respectively. A boundary value problem is solved to obtain the amplitude functions F, G, H, and the wave propagation constant κ. The solution procedure is more elementary than that used in the classical linear analyses because the low Mach number expansion approach simplifies the basic mathematical model.

When acoustic waves pass through a fluid, nondimensional horizontal velocity disturbances of $\mathcal{O}(M^2)$, relative to the $\mathcal{O}(M)$ parallel shear flow velocity $U(y)$, always correspond to $\mathcal{O}(M^2)$ acoustic disturbances in pressure and other thermodynamic parameters, relative to their mean values. The refraction of acoustic waves by the mean flow velocity gradient results in a nonuniform distribution of the acoustic pressure across the duct. When Ω, the ratio of the transverse acoustic time in the duct to the wave period, is of $\mathcal{O}(1)$ or smaller, acoustic refraction is associated with $\mathcal{O}(M^3)$ changes in the static pressure, or $\mathcal{O}(M)$ change in the acoustic pressure. Solutions for this case, which is typical in solid rocket motors, are exemplified in Fig. 1. In the higher frequency case, $\Omega \geq \mathcal{O}(M^{-1/2})$, the refraction effect appears at $\mathcal{O}(M^2)$ and $\mathcal{O}(1)$ variations in the static pressure and acoustic pressure, respectively. The well-known results about acoustic refraction, e.g., its dependence on wave frequency, the mean flow Mach number and the flow profile, are obtained in terms of key dimensionless parameters.

Our acoustic solutions agree to $\mathcal{O}(M)$ with those from classical linear theory [2–4]. Example calculations show acoustic refraction effects of comparable size with Baum and Levine's fully numerical solutions [1], although the latter contain turbulent effects arising from a k–ϵ model. The two types of solutions are in qualitative agreement if comparisons are made in the same parameter range. The nonlinear convective terms, as obtained in our perturbation equations, are $\mathcal{O}(M)$ smaller than those responsible for acoustic refraction. They contribute very little to either the acoustic or the overall flow quantities, on the time scale of a few acoustic periods considered by Baum and Levine [1].

In the thin acoustic boundary layer, the acoustic pressure is basically uniform across the layer, equal to that at the outer edge of the layer. The horizontal velocity perturbation obeys the classical Stokes solution. The phase difference between the acoustic pressure and horizontal velocity varies only with the transverse boundary layer coordinate. In addition to the transverse velocity components caused by viscous and thermal diffusion across the boundary layer, an additional component due to the mean shear flow effect in the core is found to exist in the boundary layer. The latter causes the transverse velocity to grow with the boundary coordinate (see Fig. 2). The core and boundary layer solutions are matched in a region of common validity.

The nonlinear effects in the boundary layer are again found to be $\mathcal{O}(M^2)$ relative to the basic variations occuring there. Acoustic streaming associated with the nonlinear convective terms is insignificant relative to the amplitude of refraction effects. The velocity profiles show considerable resemblence to Baum and Levine's computational results. The effective boundary layer thickness also shows order of magnitude agreement with their numerical output.

More details of this work have been reported in [5].

2. Standing Wave Study

Standing waves provide a better representation of longer-time scale acoustic processes in solid rocket engine chambers, where reflections from solid boundaries and the nozzle flow are important. The interaction between standing acoustic waves and a parallel shear flow is investigated. The wave modes, of the same amplitude as in the traveling wave study, exist in a planar region bounded by special boundaries that act as perfect reflectors for acoustic waves but allow the passage of a fully-developed low Mach number shear flow $U(y)$. The two sidewalls are assumed

impermeable. This configuration permits us to study the impact of multiple wave reflections on the acoustic-shear flow interaction, on time scales large compared to the wave period.

The modeling effort is concentrated on the transport-free core region where the Euler equations are valid. Low Mach number asymptotics are again employed to derive the acoustic equations. Particular interest is focused on the transients evolving from an initial velocity distribution in the longitudinal (flow) direction x, defined by $\hat{u}_i = A\sin(k\pi x)$. When the two dimensions of the duct are of comparable size, and if the mode number k is an $\mathcal{O}(1)$ quantity, the shear flow causes only an $\mathcal{O}(M)$ correction to the acoustic pressure, as in the traveling wave case. The acoustic pressure and longitudinal velocity are given by

$$\hat{p} = -A\sin(k\pi t)\cos(k\pi x) + Mp_2(x,y,t), \qquad \hat{u} = A\cos(k\pi t)\sin(k\pi x) + Mu_2(x,y,t). \qquad (2)$$

The leading order wave field is independent of the transverse coordinate y.

A two-dimensional wave equation is derived for p_2, the $\mathcal{O}(M)$ correction to the acoustic pressure. The shear flow velocity $U(y)$, which appears in the forcing function in the equation and in the boundary conditions, initiates and drives y-dependent acoustic modes of $\mathcal{O}(M)$. An analytical solution is obtained by using the Laplace transformation technique and Fourier series expansions. The solution contains nonresonant spatial modes that are explicitly x-dependent (longitudinal), y-dependent (transverse), and x,y-dependent (oblique), as well as resonant modes when resonant conditions are satisfied by the flow field and the duct geometry.

The solution can be written as $p_2 = p_{2c} + p_{2r}$. Here p_{2c} is y-independent, and is proportional to the average shear flow velocity in the duct. It describes the deformation of the leading order x-dependent acoustic pressure in (2) caused by the bulk convection in that direction. The second part p_{2r} describes the evolution of transverse and oblique acoustic modes, generated as a result of interaction between the longitudinally distributed initial disturbance and the shear flow velocity gradient (refraction). The pressure response $\hat{p}$ in (2) at a fixed location becomes fairly complicated, as demonstrated in Figs. 3a and 3b. In Fig. 4 the refraction-induced acoustic pressure in the duct is depicted at a given time.

As in the traveling wave problem, the magnitude of the acoustic refraction is found to depend strongly upon the magnitude and the characteristics of the shear flow velocity. For given duct geometry, both the refraction and bulk convection effects increase with increasing mode number of the initial disturbance. Higher frequency modes are more strongly influenced by the shear flow.

REFERENCES

[1] J.D. Baum and J.N. Levine, "Numerical investigation of acoustic refraction", *AIAA Journal*, **25**(12), 1577–1586, (1987).

[2] D.C. Pridmore-Brown, "Sound propagation in a fluid flowing through an attenuating duct", *J. Fluid Mech.*, **4**, 393–406, (1958).

[3] P. Mungur and G.M.L. Gladwell, "Acoustic wave propagation in a sheared fluid", *J. Sound Vib.*, **9**(1), 28–48, (1969).

[4] A.S. Hersh and I. Catton, "Effect of shear flow on sound propagation in rectangular ducts", *J. Acoust. Soc. Am.*, **50**(3), 992–1003, (1971).

[5] M. Wang and D.R. Kassoy, "A perturbation study of acoustic wave propagation through a low Mach number shear flow", submitted to *J. Fluid Mech.*, (1990).

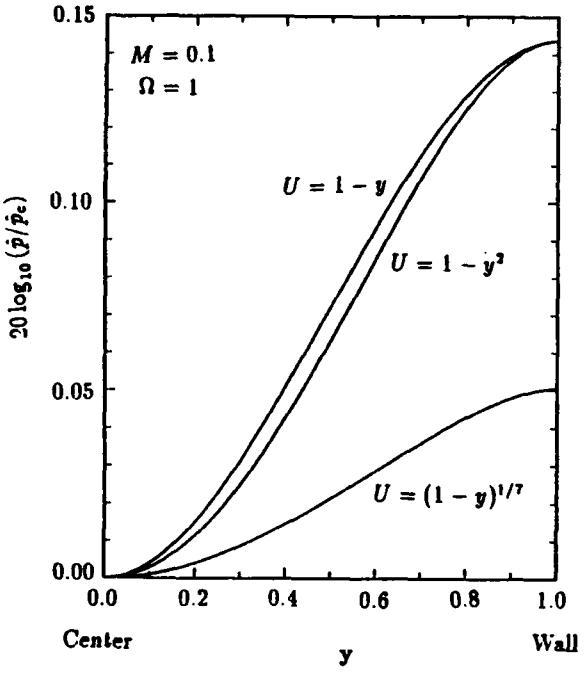

Figure 1: Acoustic pressure profile in decibels, for downstream wave propagation in three types of shear flows $U(y)$. The maximum shear flow Mach number $M = 0.1$, and the dimensionless frequency $\Omega = 1$.

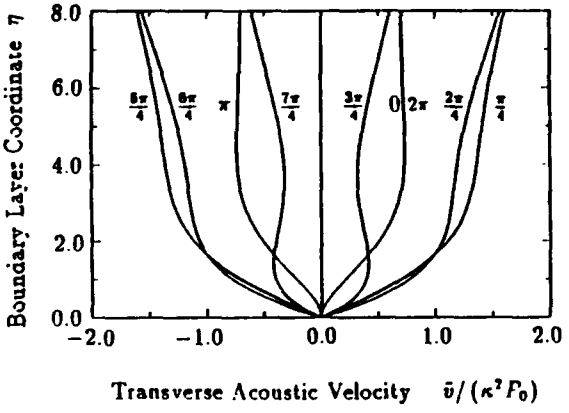

Figure 2: Profiles of the normalized transverse velocity across the acoustic boundary layer adjacent to an adiabatic wall, at a specified horizontal coordinate $x = 0$. The wave propagation constant $\kappa = 0.95$. Curves are shown for $\pi/4$ increments over one acoustic period.

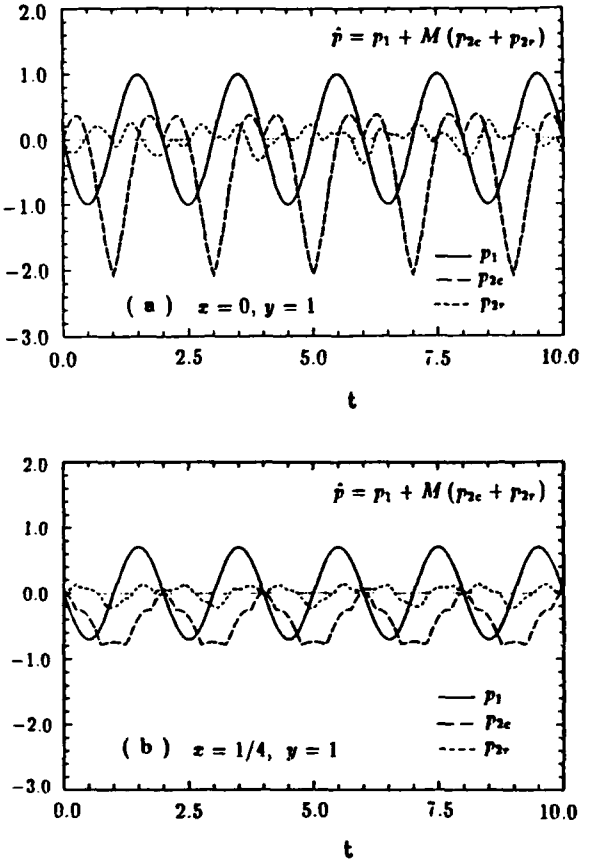

Figure 3: Time variations of p_1, p_{2c} and p_{2r} at locations (a) $x = 0$, $y = 1$; and (b) $x = 1/4$, $y = 1$, due to the evolution of an initial velocity disturbance $\hat{u}_i = \sin(\pi x)$ in the shear flow field $U = 1 - y^2$. The ratio of the transverse to longitudinal dimensions $h = 0.5$.

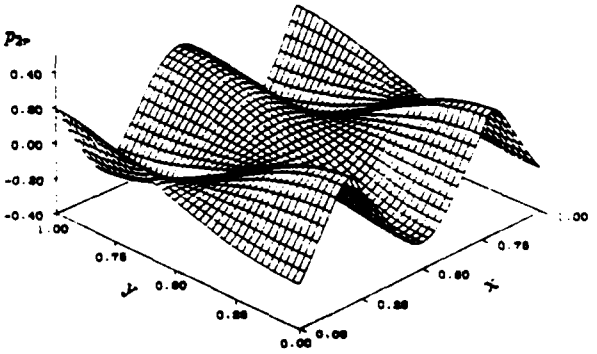

Figure 4: Distribution of p_{2r} at $t = 1/4$, generated by an initial velocity disturbance $\hat{u}_i = \sin(3\pi x)$ in the shear flow field $U = 1 - y^2$. The ratio of the transverse to longitudinal dimensions $h = 1/6$.

NUMERICAL INVESTIGATION OF ENERGY EXCHANGE MECHANISMS BETWEEN THE MEAN AND ACOUSTIC FLOW FIELDS IN SOLID ROCKET COMBUSTION CHAMBERS

AFOSR Contract F49620-89-C-0124

Principal Investigator: Dr. Joseph D. Baum

Science Applications International Corporation
1710 Goodridge Dr, MS 2-3-1
McLean, VA 22102

Summary/Overview:

This research effort is directed at understanding the energy exchange mechanisms between the mean and the acoustic flow fields in a solid propellant combustion chamber. The numerical approach to the simulation and understanding of these mechanisms was based on the investigation of the interaction between the turning mean flow and the standing and traveling acoustic waves in a simulated solid propellant rocket combustor. The time-dependent compressible Reynolds-averaged Navier-Stokes equations were solved using a non-iterative Linearized Block Implicit scheme. While past investigations examined energy exchange between the mean flow field and acoustic *traveling* waves (both upstream and downstream), the present effort investigated energy exchange between the mean flow and the *standing* acoustic waves in the cold flow simulator.

Technical Discussion:

Energy exchange between the mean flow field and acoustic *traveling* waves (both in the upstream and downstream directions) was investigated in past years [1]. To address some of the concerns raised in the community about possible differences in energy exchange mechanisms between **traveling** and **standing** acoustic waves, the present effort investigated energy exchange mechanisms between the mean flow field and standing acoustic waves. A typical tactical solid rocket combustor with a large length to diameter ratio and a short nozzle was modeled in this study. Figures 1a through 1c show the computational mesh for the complete motor and for expanded views of the nozzle and the near-wall mesh. Constant injection velocity (M=0.0022) was prescribed at the outer wall. Symmetric conditions were applied at the centerline. A hard-wall boundary condition was applied at the head-end (left boundary) during the steady state computation. The flow through the throat was choked; the Mach number at the exit plane was 4.92. Hence, the solution can be integrated through the sonic throat to the supersonic portion of the nozzle. This configuration finally alleviates the problem of modeling non-reflecting boundary conditions; a problem which in the past prevented the modeling of traveling wave propagation for many wave cycles [1].

Very fine mesh was used near the injection surface to properly resolve the acoustic boundary layer and the acoustic-mean flow processes which where shown to occur there [2]. The closest grid point was located 2.1 μm from the injection surface. One hundred sixty four grid points were used in the axial direction. Approximately 120 points were placed in the axial direction inside the combustor. The length of the simulated combustor was approximately 0.356 m, a distance chosen to yield a standing wave frequency of 500 Hz. Since the largest expense in these calculations is the computation of the steady state flow, which may take many more time steps than the calculation of the quasi-steady solution, a combustor length which will yield a standing-wave frequency of 500 Hz was chosen. Thus,

a driven acoustic wave with a frequency of 1000 Hz may utilize the same steady solution and should yield a standing wave with two nodes in the combustor, each wave spanned by 60 axial points, a sufficiently accurate description.

After convergence to a steady solution, acoustic waves were initiated at the head-end as downstream traveling compression waves. Energy exchange mechanisms were examined after convergence to an almost perfectly periodic solution. Since the natural standing wave frequency of the chamber was 500 Hz and the perturbation frequency was 1000 Hz, a standing wave containing two nodes was established in the chamber.

Complex wave evolution phenomena were demonstrated near the injection surface. Acoustic velocity transition was observed to initiate at the acoustic velocity nodes (of the standing wave) and then propagate diagonally away from the injection surface toward the pressure node location (Fig 2), thus resulting in a continuously varying phase difference between the axial acoustic velocity inside and outside the acoustic boundary layer (Fig 3). To complicate matters, while for traveling waves the phase angle between the acoustic velocity and acoustic pressure outside the acoustic boundary layer is constant, it is shown that for standing waves, this phase angle varied temporally (during the wavecycle) and spatially, as a function of location with respect to the standing wave (Table 1). It is thus suggested that a proper simulation of the interaction between the flow in a combustor and the combustion of the solid propellant requires the coupling of the instantaneous local flow field with the propellant combustion model. The temporal and spatial evolutions of both the mean and the acoustic flow fields must be acounted for.

The rms acoustic pressure results demonstrated excitation of acoustic energy in the chamber, a phenomenon that will be investigated in the future. The rms results also demonstrate the strong dependence of acoustic streaming processes (such as Richardson's annular effect) on the amplitude of the acoustic velocity oscillations and viscous dissipation. In addition, the rms acoustic boundary layer thickness was shown to vary within the standing wave: boundary layer thickness near the nodes of the axial acoustic velocity varied betwen 440-520 μm, while near the axial acoustic velocity anti-nodes boundary layer thickness increased to 650-700 μm, with an almost continuous transition between these values. In comparison, acoustic boundary layer thickness for traveling waves was only 105 μm. Since the mean flow conditions are not drastically different, it is postulated that repetitive processing of the acoustic boundary layer by upstream and downstream waves resulted in boundary layer thickening.

Finally, examination of the time averaged solution demonstrated large vorticity production and acoustic streaming phenomena. It was shown that the instantaneous vorticity produced eddies and the mechanical dissipation near the wall followed the local radial derivative of the axial acoustic velocity. Correspondingly, the time-averaged vorticity and dissipation function contours were confined to a region near the wall, with maximum values at the acoustic velocity anti-node locations. Very little dissipation and vorticity production were observed near the acoustic velocity nodes, indicating that significant dissipation and vorticity production can occur only through the interaction between the acoustic velocity flow field with the mean flow injected through the periphery. The time-averged axial energy flux results demonstrated large positive acoustic energy fluxes at the first and third quadrants of the chamber, and damping at the second and fourth quadrants, in agreement with Rayleigh's criterion.

So far we have investigated energy exchange mechanisms in viscous-dominated flow fields. Since the ultimate objective is to understand these energy exchange mechanisms in solid propellant combustors in which both thermal and viscosity-controlled mechanisms play an important role, research in the upcoming year will focus on energy exchange mechanisms between the mean and acoustic flow fields in the presence of a thermal boundary layer near the wall. Finally, the thermal boundary layer will be replaced by a burning solid propellant.

REFERENCES

1. Baum, J.D., "Numerical Study of Acoustic Refraction Phenomenon; Effect of Upstream and Downstream Propagation," AIAA Preprint 87-0544 presented at the AIAA 26th Aerospace Sciences Meeting, Jan 11-14, 1988, Reno NV.

2. Baum, J.D., "Numerical Investigation of Acoustic Wave Propagation in a Sheared Mean Flow," AIAA Preprint 87-2739, presented at the AIAA 11th Aeroacoustics Conference, Sunnyvale CA, Oct 19-21, 1987.

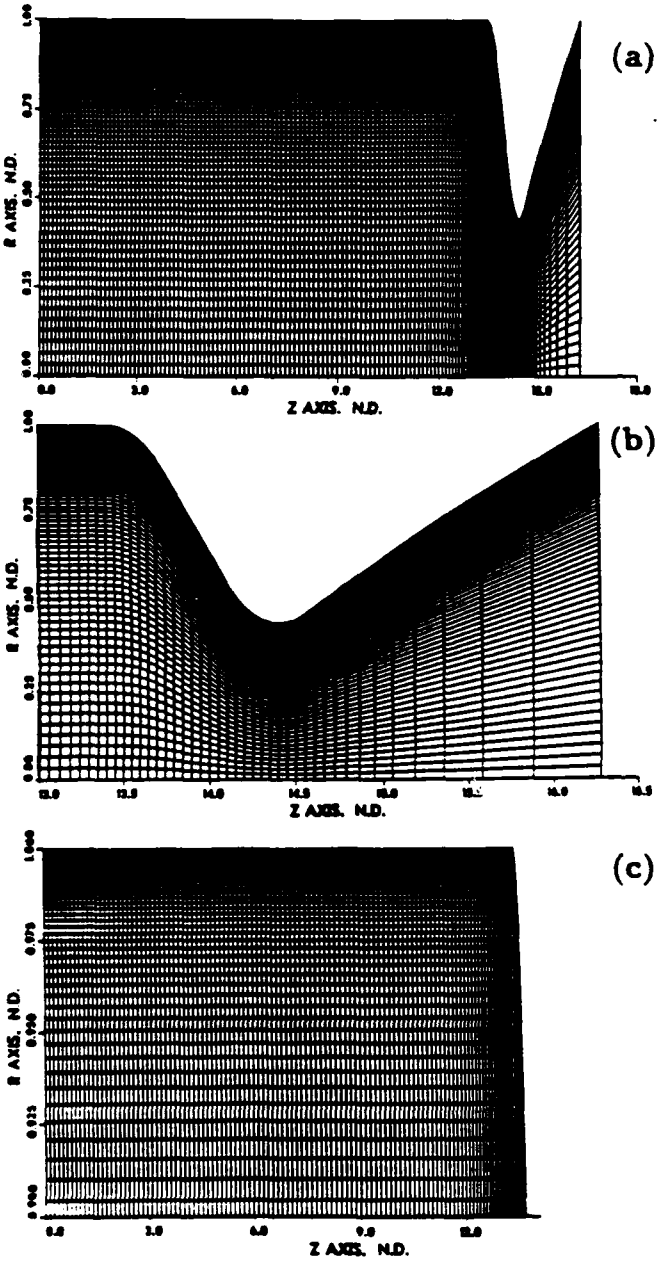

Fig 1. Computational Grid for: a) the Complete Motor Configuration; b) Expanded View of the Nozzle; and c) Near Injection Surface.

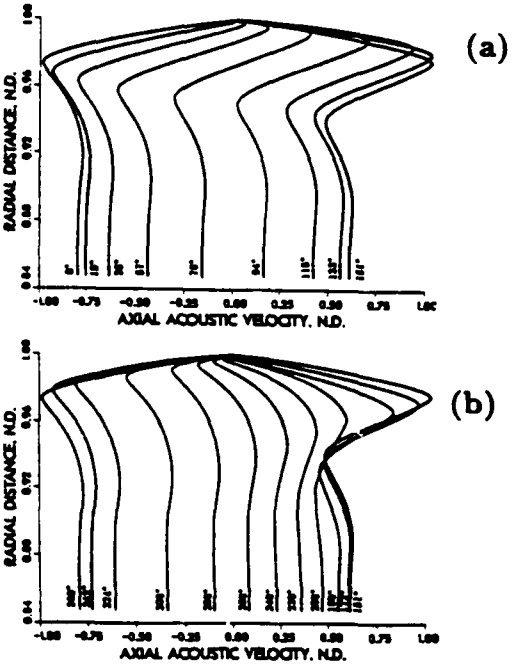

Fig 2. Time Evolution of Axial Acoustic Velocity Profiles Near the Injection Surface, Z=0.064m: a) Minimum to Maximum; b) Maximum to Minimum.

Distance from Head End in Wavelengths	Axial Acoustic Velocity Transition Phase Lag: Wall to Centerline		Acoustic Pressure and A Acoustic Velocity Transi Phase Lag	
	+ to -	- to +	+ to -	- to
0.36λ	108	93	61	65
0.76λ	54	87	-94	-2
1.13λ	104	36	47	61
1.52λ	61	79	-104	7
1.88λ	43	69	173	-5

Table 1. Transition Phase Differences.

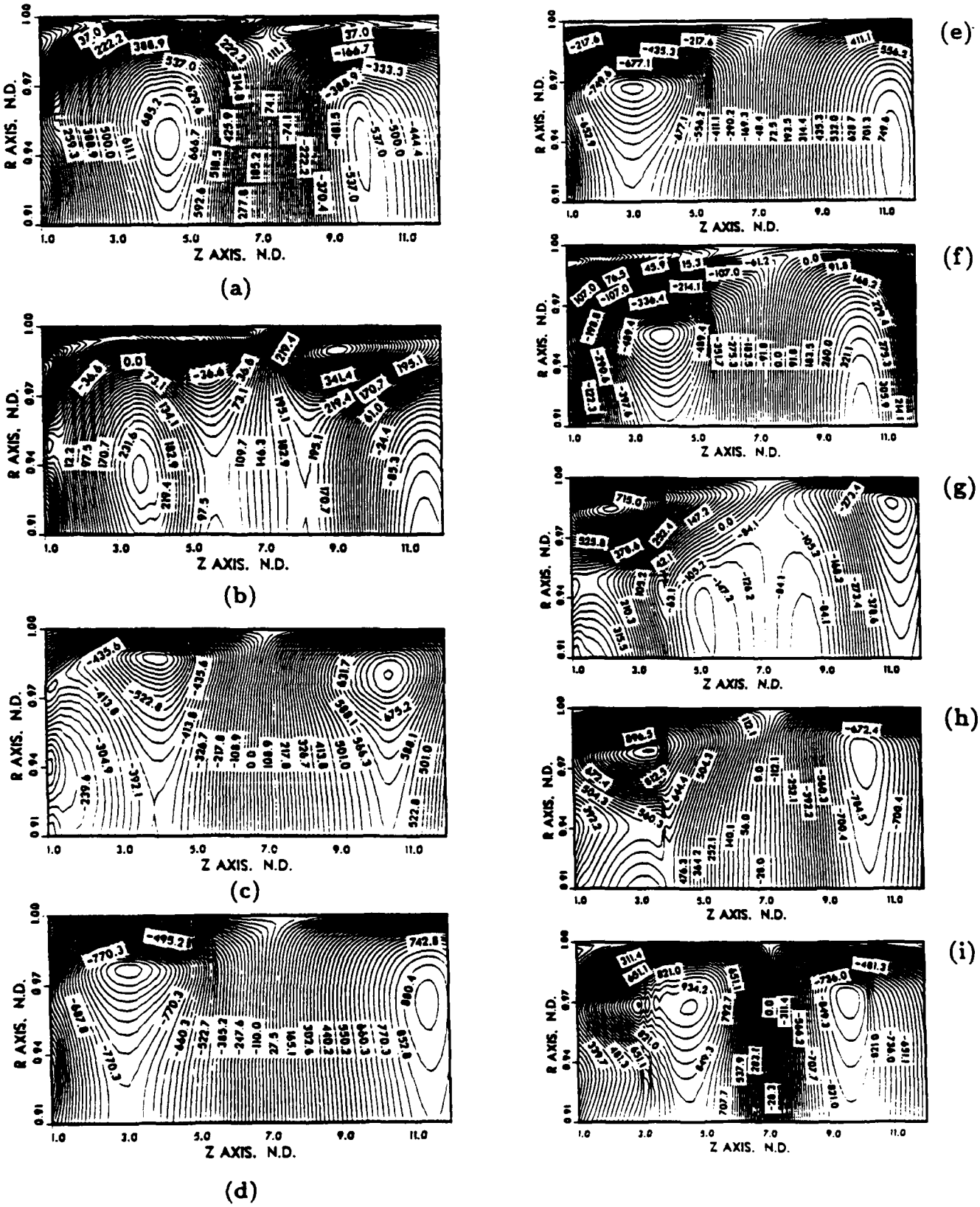

Fig 3. Axial Acoustic Velocity Contours at: a) time=14.666 ms; b) time=14.777 ms; c) time=14.888 ms; d) time=15.0 ms; e) time=15.111 ms; f) time=15.222 ms; g) time=15.333 ms; h) time=15.444 ms; and h) time=15.555 ms.

FLAME-ACOUSTIC WAVE INTERACTION DURING AXIAL SOLID ROCKET INSTABILITIES

(AFOSR Grant/Contract No. AFOSR-84-0082)

Principle Investigators: B. T. Zinn, B. R. Daniel and U. G. Hegde

School of Aerospace Engineering
Georgia Institute of Technology
Atlanta, GA 30332

Summary/Overview:

This research program investigates the driving and damping of axial instabilities in solid propellant rocket motors by gas phase solid propellant flames and "flow turning", respectively. The response of diffusion flames, stabilized on the side wall of a duct, to imposed axial acoustic waves has been investigated by using flame radiation measurements and laser Doppler velocimetry (LDV). These measurements reveal the presence of oscillatory flame heat release rate, flame regions which either drive or damp the waves, and a highly complex flow field in the flame region. The net effect of the driving/damping regions determines whether the flame drives or damps the waves. This research aims to identify flame and "near wall" flow processes which contribute significantly to the driving and damping of solid propellant rocket motor instabilities.

Technical Discussion:

The onset of combustion instabilities depends upon the relative magnitudes of the driving and damping processes within the combustor which add and remove energy from the waves. Consequently, the elimination or reduction in the occurrences of combustion instabilities in solid propellant rocket motors requires identification of the processes which add or remove energy from the waves, and the development of an understanding of the mechanisms which control these processes. It is generally accepted that energy supplied by solid propellant combustion processes is responsible for the initiation and maintenance of instabilities inside rocket motors. It is also accepted that nozzle damping, viscous dissipation, heat transfer and "flow turning" are processes which contribute to the damping of combustion instabilities in solid rockets. This research program is

investigating gas phase flame processes which drive combustion instabilities and the damping provided by "flow turning".

Since actual solid propellant flames cannot be used in these studies, because of their extremely small dimensions, smokey nature, and rapid burnout, other flames which simulate, in some respects, actual solid propellant flames have been used in the present and related studies. In the present investigation, the response of diffusion flames, stabilized on the bottom wall of a rectangular duct (see Fig. 1), to the excitation of axial acoustic fields has been studied. This investigation focused on determining (1) the driving/damping of acoustic waves by the diffusion flames, and (2) the damping of the waves by "flow turning" in the flame region.

The experimental setup consists of a 2.5 meter long, 3.75x7.5 cm^2 duct with a diffusion flame burner installed on its bottom wall. The diffusion flame burner consists of parallel, alternating, oxidizer and fuel slots which produce three diffusion flames. Two acoustic drivers attached to the duct wall just upstream of the exit plane are used to excite a standing longitudinal acoustic wave inside the duct, which simulates an axial instability in an unstable rocket motor. The location of the flame relative to the acoustic field can be changed by axial translation of the "hard" termination at the upstream end of the duct. This "hard" termination is made of porous material and it is used to inject a mean flow into the duct in "flow turning" studies. Three pressure transducers on the wall above the burner are used to characterize the excited acoustic field and the flame location with respect to the standing wave.

The driving/damping of the acoustic field by the diffusion flame was studied by measuring acoustic pressures, flame radiation and velocity distributions in the flame region. The flame radiation was measured with a system consisting of a C-H optical filter, a Hamamatsu R-268 photomultiplier and a Neff 122 amplifier. The velocity field in the flame region was measured with a 5 watt Coherence argon-ion laser and a TSI 9100-7 dual beam forward scatter LDV system. The acoustic pressures were measured with piezoelectric pressure transducers mounted on the upper and attached to a probe.

The flame C-H radiation describes the time dependence of the flame chemiluminescence which is proportional to the flame reaction and heat release rates. Since Rayleigh's criterion indicates that the phase difference between the heat release and pressure oscillations determines whether the flame adds or removes energy from the oscillations, the measured flame radiation and pressure data were used to determine the operating conditions under which the flame drove or damped the acoustic field, and the driving/damping provided by different regions of the flame.

To determine the driving/damping of a given flame region surrounded by a control surface S, the integral $\int_S Ids = \int_S p'v'\cos\phi ds$ where I, p', v', and ϕ are the acoustic intensity, pressure amplitude, normal velocity amplitude, and the phase difference between p' and v', respectively, was evaluated using measured p', v' and ϕ data. This integral determined whether a net amount of acoustic energy was "generated" or "absorbed" within the investigated region, which corresponds to "driving" and "damping" by the region, respectively. For example, the driving within the flame region (see Fig. 2) bounded by the horizontal lines $y=y_1$ and $y=y_2$ was determined by determining the acoustic intensity integrals (denoted by P_1 and P_2) along the lines $y=y_1$ and $y=y_2$. This region drove the waves when $\Delta P=P_2-P_1$ was positive, and vice versa.

The flame radiation measurements showed that the interaction of the investigated flame with the acoustic field produced space dependent, oscillatory, reaction and heat release rates having the same frequency as the excited acoustic field. Driving occurs in some flame regions where the heat release occurs in phase with the pressure oscillations while damping occurs in the remaining flame regions. The overall effect of the flame upon the acoustic wave depends upon the relative magnitudes of these "driving" and "damping" regions. The flame radiation and velocity data were consistent and they identified the same flame regions as being "drivers" or "dampers" of acoustic waves. The measured data suggest that the pressure and velocity oscillations affect the processes which control the response of the diffusion flame to acoustic oscillations. Finally, the response of the investigated diffusion flames is frequency dependent and it shows that these flames generally drive the acoustic waves at frequencies below 700 Hz.

Finally, a new diffusion flame burner, see Fig. 3, which better simulates the behavior of gas phase solid propellant flames was developed. It consists of 1537 hypodermic tubes arranged in a 29x53 matrix. Oxidizer flow supplied through the hypodermic needles simulates the combustion products produced by the burning oxidizer particles (e.g., ammonium perchlorate) in a composite solid propellant, and the fuel flow through the spaces which surround the hypodermic needles simulates the flow of the pyrolysis products of the propellant binder. This burner is currently bein used to investigate the effects of frequency, flame position relative to the acoustic field, mean flow velocity and the amplitude of the acoustic waves upon the damping provided by "flow turning".

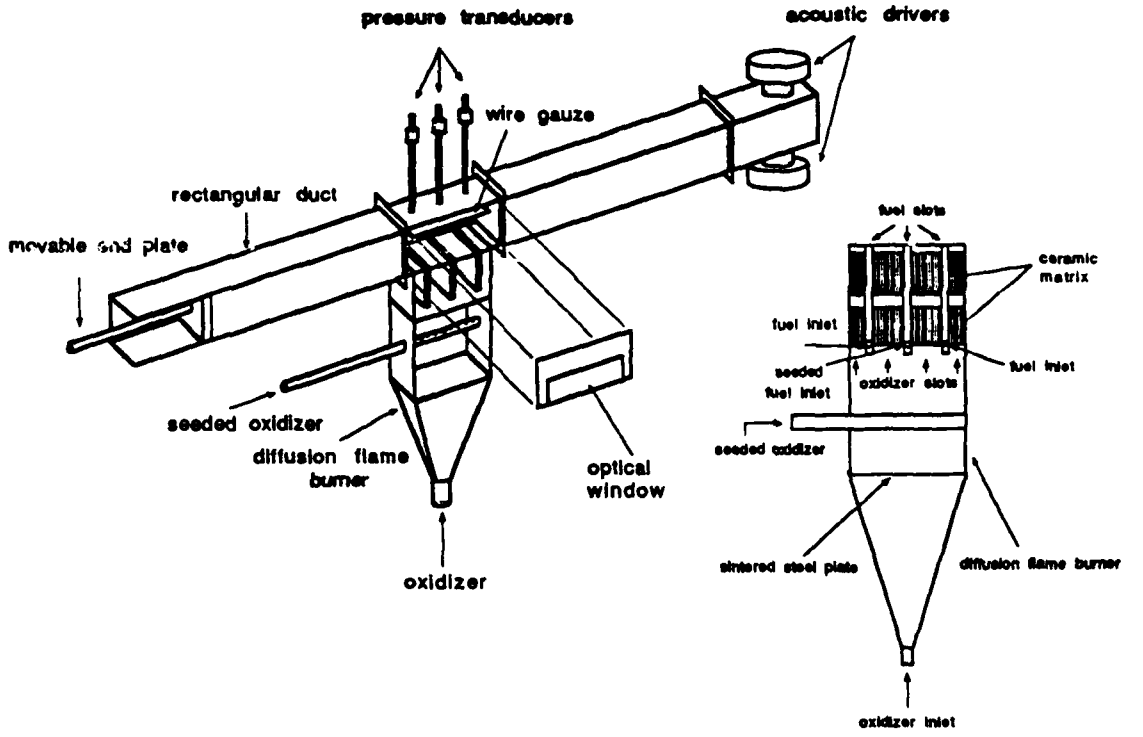

Figure 1. A Schematic of the Experimental Setup

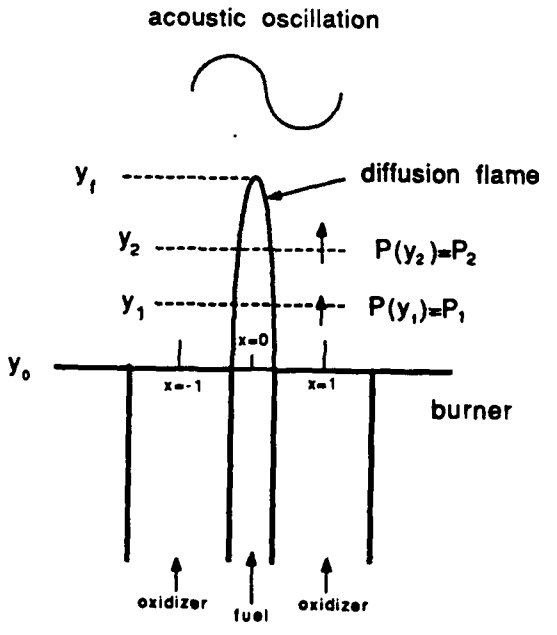

$$P=\int_{-1}^{1} p' \, Re[v'(x,y)]dx$$

Driving occurs in a given region $\Delta y=y_2-y_1$ bounded by $x=-1$ and $x=1$ when $\Delta P=P_2-P_1>0$

Figure 2. Driving Criterion of the Diffusion Flame

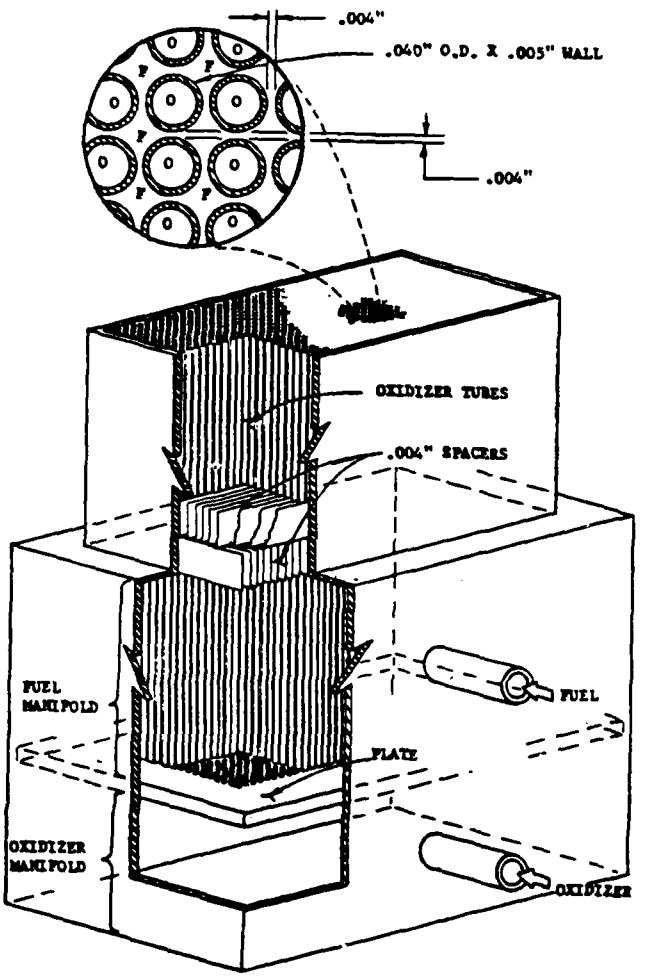

Figure 3. A Schematic of the Newly Developed Diffusion Flame Burner.

FRACTAL IMAGE COMPRESSION OF RAYLEIGH, RAMAN, LIF AND LV DATA IN TURBULENT REACTING FLOWS

(AFOSR Contract no. 88-0001)

Principal Investigators: W.C. Strahle and J.I. Jagoda

School of Aerospace Engineering
Georgia Institute of Technology
Atlanta, GA 30332

SUMMARY / OVERVIEW

This study deals with the use of fractals to improve the quality of data acquired during the investigation of turbulent reacting flows. Particular emphasis has been placed upon the development of novel techniques to filter the results of noisy measurements and interpolate between temporally widely spaced data points. The flow field selected to develop these techniques is the flame anchoring region of a solid fuel ramjet which is of practical interest in its own right. This flow field is represented by flow over a backward facing step in which the solid fuel is simulated by injecting a hydrogen and a diluent through a porous plate behind the step (see Fig.1). The velocity and shear stress distributions are determined using laser Doppler velocimetry while mixing and temperature profiles are measured using Rayleigh and Raman scattering.The flow is also being modeled using a modified k-ε model.

TECHNICAL DISCUSSION

Earlier measurements and predictions were carried out for the cold (i.e. non-reacting) flow. Here the fuel was replaced by a bleed flow of carbon dioxide resulting in excellent agreement between the predicted and measured results of the velocity field and the mixing distributions.

During the past year the main thrust of this investigation concentrated upon mapping the mixing and temperature distributions in the flow field. The performance of the Raman system was checked by comparing the Raman scattering intensity in a stream of air with that in a stream of pure nitrogen. This check was repeated before each series of measurements. In addition, the performance of the Raman system was tested at elevated temperature. Under these conditions the number density of nitrogen molecules in the test volume is considerably lower resulting in a much weaker Raman signal. The nitrogen concentration in the hot combustion products of a lean, turbulent diffusion flame (i.e. under conditions for which air predominated) was compared with that in air at room temperature. The perfect gas relations were used to calculate the approximate local mean exhaust gas temperature. This temperature was then confirmed to within 50 degrees Kelvin using a fine thermocouple.

Inside the tunnel it proved impossible obtain the correct ratio between the Stokes line intensities in air and pure nitrogen since small amounts of light leaked past the notch filter and spectrograph. This noise was removed by filling the tunnel with argon and determining the intensity of the stray light at each location which was then subtracted from the local Raman signals. The corrected Raman signals calibrated perfectly.

The numerical code used to simulate the flow under investigation is a heavily modifyed version of a two dimensional elliptical solver. The model is based upon the two equation k-ε turbulence model and a hybridized upwind scheme to calculate the steady state fluid properties in an incompressible, but variable density flow behind the step. Favre

averaging of the conservation equations accounts for the variable density effects. Allowance is made for the low speed fuel flow injected behind the step. The resulting mixture fractions and temperature profiles are calculated from the chemical reactions. Species fluctuations due to turbulence were omitted and local thermodynamic equilibrium was assumed. The wall proximity effects on the k-ε equations were simulated using a low Reynolds number law of the wall model.

The porous floor behind the step in the tunnel is divided into three sections. The first part is blocked off. Hydrogen mixed with a diluent is injected through the next section while an inert is injected downstream to keep the porous floor cool.

Laser velocimeter data obtained in the tunnel with combustion have previously been reported. The presence of combustion was found to lengthen the recirculation region. At first the model predicted a shortening of the recirculation with combustion. However, with more careful modeling of the heavy, injected argon and by tightening the grid points in the vicinity of reattachment the lengthening of the recirculation region could be predicted.

Local nitrogen concentrations in the test region were determined by measuring the intensities of the nitrogen Stokes line. Local concentrations of the bleed flow were estimated by mapping the nitrogen concentrations above the porous plate using first argon then nitrogen as a diluent (Fig. 2). No appreciable increase in nitrogen was observed when nitrogen was used as the diluent indicating that the bleed gas concentration in the recirculation region is very small. Figure 3 shows the nitrogen concentration profiles at five axial locations behind the step. At all locations, the levels of nitrogen are lower in the shear layer and recirculation zone than in the free stream. Since the concentration of bleed gas has been shown to be small, the the variation in nitrogen concentration is predominantly an effect of temperature.

In light of the above, an estimate of the temperature distribution can be obtained from the nitrogen concentration measurements using the perfect gas laws. Figure 4 shows vertical temperature distributions calculated from the data in Fig. 3. The flame is clearly confined to the shear layer with the maximum temperature coinciding with the location at which the visible flame was observed. The temperature drops somewhat in the lower half of the recirculation region which is fuel rich and where heat is transfered to the tunnel floor. Since these temperatures are only approximate as the presence of combustion products has been neglected, the Raman results have been confirmed by Rayleigh scattering.

The RMS values of the temperatures are shown in Fig. 5. The largest temperature fluctuations were observed in the region of greatest temperature gradient where the cold freestream mixes with the top of the hot shear layer.

The measured temperature profile at a representative location is compared with profile calculated using the model in Fig. 6. Clearly, the predicted flame is positioned too close to the floor. Thus, the model predicts too rapid a rate of mixing between the air and fuel in the shear layer.

The theoretical work on the hidden variable fractal interpolation technique has been completed. This technique will be used to interpolate between the temporally widely spaced temperature data using the simultaneously measured velocity data which can be acquired at a much higher data rate. Its application must await the availability of joint velocity - temperature data.

The main emphasis during the remainder of this contract year will be on the acquisition of the joint velocity - temperature data. Laser induced fluorescence and hidden variable fractal interpolation will be applied during the follow up year.

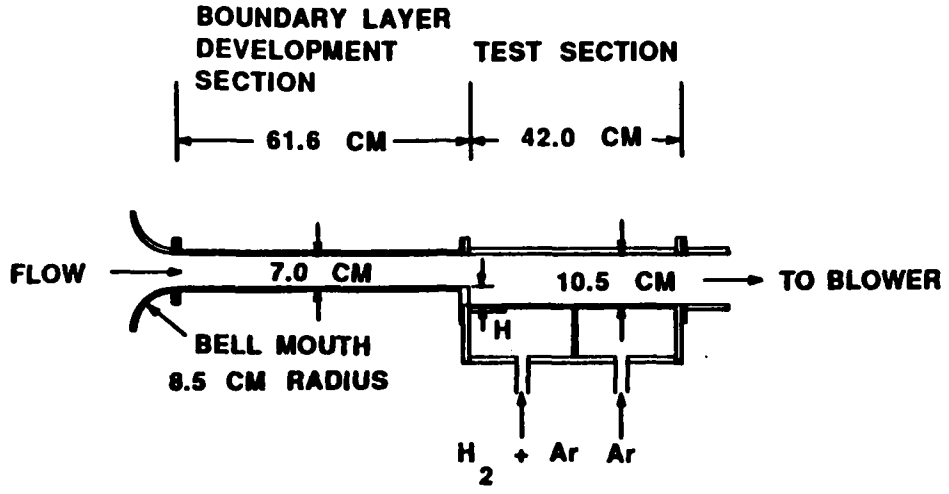

FIG. 1) SCHEMATIC OF TUNNEL

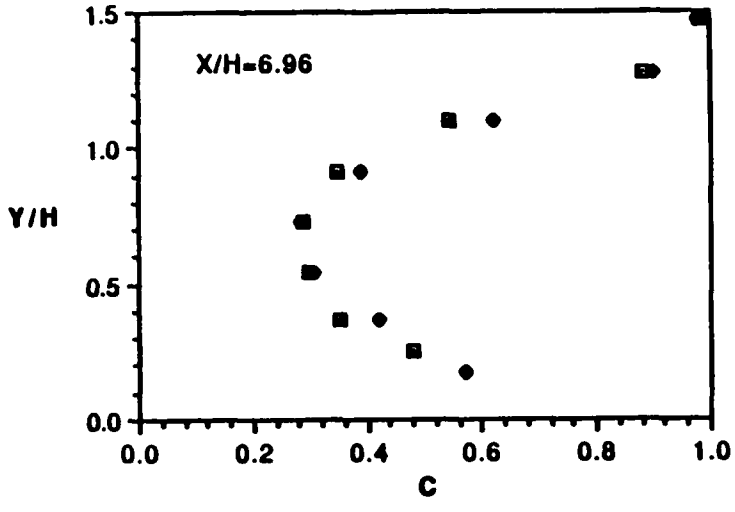

FIG. 2) COMPARISON OF NORMALIZED NITROGEN CONCENTRATIONS WITH ARGON (⊡) AND NITROGEN (◆) AS DILUENT, 7 STEPHEIGHTS DOWNSTREAM OF THE STEP

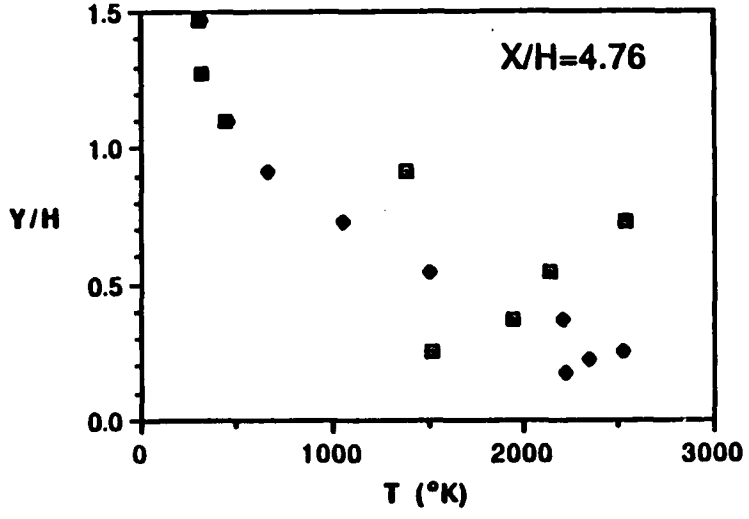

FIG. 6) COMPARISON OF MEASURED (⊡) AND CALCULATED (◆) TEMPERATURE DISTRIBUTION AT 4.76 STEPHEIGHTS BEHIND THE STEP

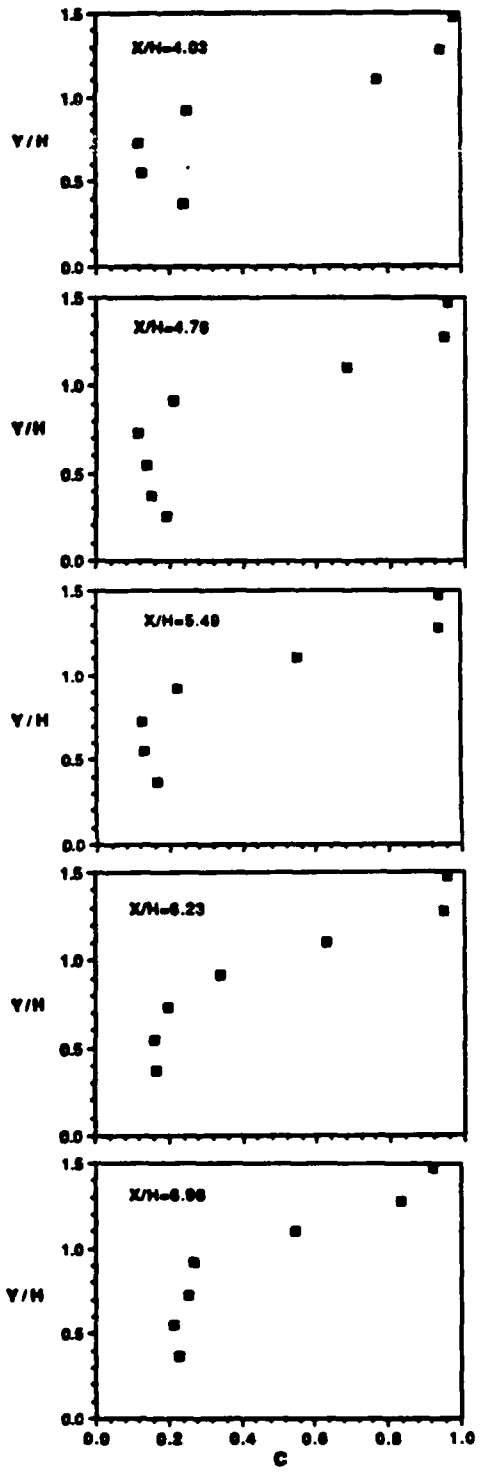

FIG. 3) NORMALIZED NITROGEN CONCENTRATIONS VS HEIGHT ABOVE TUNNEL FLOOR

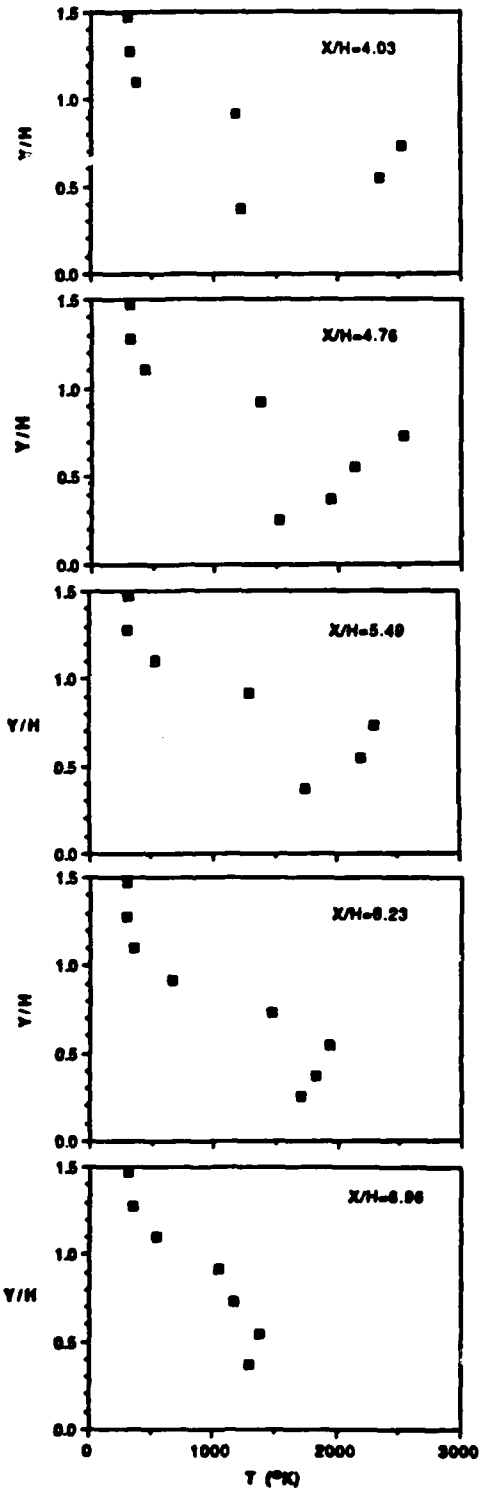

FIG. 4) TEMPERATURE DISTRIBUTION

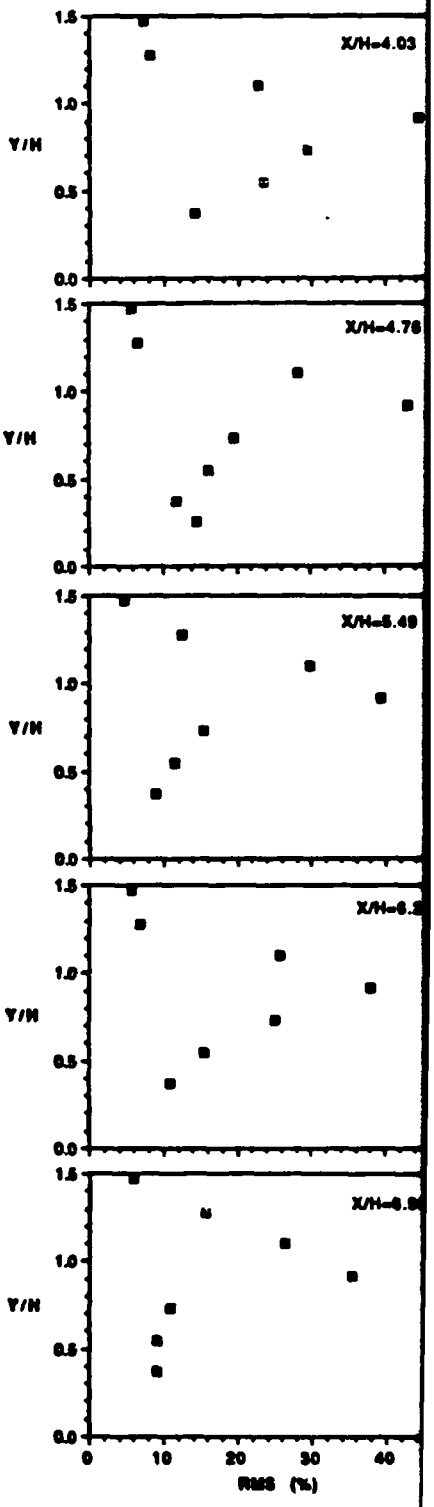

FIG. 5) TEMPERATURE FLUCTUATIONS AS %AGE OF LOCAL MEAN

PLUME TECHNOLOGY

AFOSR Contract 2308/M2

Principal Investigators: D. P. Weaver and D. H. Campbell*

Astronautics Laboratory (AFSC)
Edwards Air Force Base, California 93523-5000

SUMMARY/OVERVIEW:

Investigations of the flowfield structure inside a rocket nozzle and in plume flow exhausting into a low density background, and the process of vibrational state relaxation of rocket exhaust plume effluents is being investigated using a variety of experimental and theoretical techniques. A high energy atmospheric simulator is also being developed to be used to investigate the interaction of high speed oxygen atoms with plume gases and spacecraft materials. A detailed understanding of the important physical processes responsible for the production of ultraviolet and infrared emission from high altitude liquid rocket motors is the primary goal of these studies. At present, the prediction of plume signatures relies on empirical assumptions about the flowfield structure and molecular excitation and relaxation processes. This research is aimed at delineating some of the most important basic flowfield and collisional processes in rarefied expansion flows.

TECHNICAL DISCUSSION:

In order to accomplish these stated goals, a series of investigation is being carried out to obtain information on the process of boundary layer expansion from nozzles into a low density background. The expansion of the boundary layer as the flow approaches the nozzle lip is a complex gas dynamic problem which can be complicated by the rarefaction of the flow to densities and temperatures at which the translational mode of the gas can become non-equilibrium. The gas that originates in the boundary layer is the primary source of flux into the higher angles (>60°) which can (1) interfere with optical detectors on a spacecraft via radiation in the visible, UV, or IR, (2) contaminate spacecraft surfaces, or (3) collide with the high velocity freestream species to produce excitation of electronic, vibrational or rotational molecular energy levels which can then radiate. The chemical state of this boundary layer gas will depend critically on the structure of the flowfield inside and outside of the nozzle.

An experimental study is being conducted using a 0° halfangle nozzle (tube) inside a vacuum chamber. Optical diagnostics of the flowfield is being accomplished using the electron beam fluorescence technique. The boundary layer is being mapped at various positions inside the tube and immediately outside the tube exit plane. These results will be compared to theoretical predictions of the flow, using both continuum Navier-Stokes techniques and the direct simulation Monte Carlo technique, which can predict flowfields when non-continuum conditions apply.

The other primary thrust of this work is an investigation of the process of vibrational relaxation of plume species in vacuum expansion flows. The basic phenomena of vibrational relaxation in expansion flows is being investigated via modeling and

---

* University of Dayton Research Institute On-Site Contractor

experimental work using free jets. To date, the flowfield and vibrational relaxation process have been investigated separately. Due to the effects of translational non-equilibrium in vacuum expansion flows, the angular variation of the flowfield properties is not predictable in any simple way. Calculations using the Direct Simulation Monte Carlo Technique for argon expansion from a sonic orifice and from a small tube have illustrated the basic angular characteristics of nozzle boundary layer flow to vacuum over a stagnation Knudsen number range of 0.05 - 0.005. Deviation of the angular number density distribution in the far field from the ideal cosine law occurs at angles greater than 60° (Figure 1). The detailed structure of the "boundary layer" found at the exit plane of an orifice or tube has little effect on the subsequent angular flow in the far field. Any significant change in the number density, on the other hand, does have a measurable effect on the angular distribution of flow parameters in the far field for the range of parameters investigated (Figure 2). Consequently, it is important to have an accurate measure of this parameter at the computational startline, which for a nozzle at high altitude means an accurate prediction of the boundary layer density near and at the exit plane. For the portion of the flow originating near the wall and expanding to higher angles, a much accelerated expansion will occur compared to the flow near the centerline. Kinetic collisional processes such as condensation and internal energy relaxation will consequently have an angular dependence as well.

The vibrational relaxation work has used a rate equation modeling technique to track the vibrational levels of various gases with various starting population distributions expanding in a free jet. It has been demonstrated that the final "frozen" vibrational population distribution of plume gases can be highly non-equilibrium with a large amount of population in higher vibrational levels. Experimental measurements of vibrational level populations of electric discharge heated gases in free jets are presently being conducted.

The oxygen ion beam source has been successfully neutralized using an inertially tethered gas cloud device and the resulting neutralized oxygen atom beam is presently being characterized.

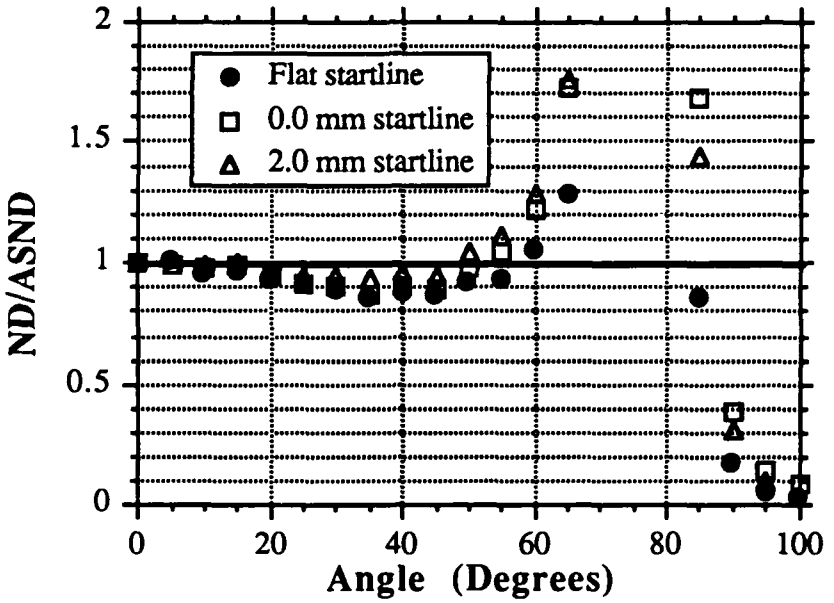

Figure 1. Angular distribution (at x/D=5.0) of the ratio between calculated number density and Askenas-Sherman cosine law prediction for three different startline profiles (measurements in key refer to thickness of orifice). Argon gas expansion to vacuum.

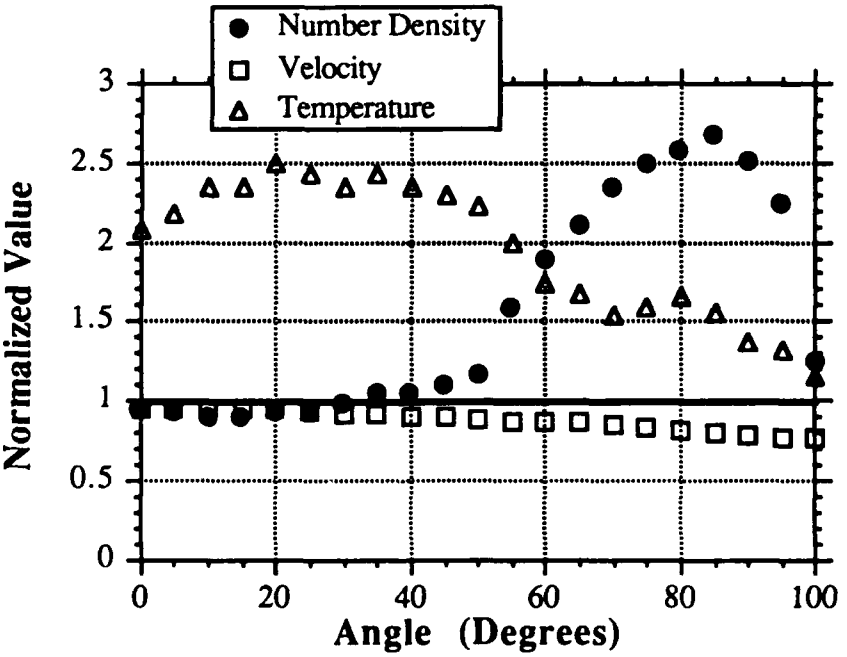

Figure 2. Angular distribution (at x/D=5.0) of the ratio of flow parameters between results for baseline startline number density and a factor of 10 higher startline number density. Argon gas expansion to vacuum from 2.0mm, 2.0mm thick orifice diameter orifice.

KINETIC STUDIES OF METAL COMBUSTION IN PROPULSION

AFOSR Grant No. 89-0086

Principal Investigator: Arthur Fontijn
Research Collaborators: Peter M. Futerko, Aleksandar G. Slavejkov

High-Temperature Reaction Kinetics Laboratory
Department of Chemical Engineering
Rensselaer Polytechnic Institute
Troy, NY 12180-3590

SUMMARY

The transfer of engineering data, on rocket chamber and plume combustion, from present to advanced propulsion systems, is hampered by a lack of understanding and knowledge of individual B and Al species reactions. Experiments with our unique HTFFR (high-temperature fast-flow reactor) technique have shown a wide variety of ways by which temperature affects the rate coefficients. This emphasizes the need for accurate measurements on further B and Al reactions, which need to be included in rocket combustion models. Moreover, a framework needs to be established to allow estimates on yet other reactions. Here we report both new measurements and a correlation which unifies activation energies for a series of BCl and AlCl reactions.

TECHNICAL DISCUSSION

A variety of measurements have been made this past year. These include an extension of the series of rate coefficient measurements of B and Al radical oxidation reactions and establishment of dominant reaction mechanisms (product paths).

Rate Coefficient Measurements

The following k(T) measurements, expressed in $cm^3 molecule^{-1} s^{-1}$, have been completed:

(1) $BCl + HCl \rightarrow BCl_2 + H$ T = 1250 to 1620 K
$k(T) = 1.2 \times 10^{-10} \exp(-12100\ K/T)$

(2) $BCl + SO_2 \rightarrow OBCl + SO$ T = 460 to 1700 K
$k(T) = 3.5 \times 10^{-22}\ T^{3.1} \exp(-1595\ K/T)$

(3) $BCl + N_2O \rightarrow OBCl + N_2$ T = 690 to 1000 K
$k(T) = 3.0 \times 10^{-22}\ T^{3.0} \exp(-3626\ K/T)$

The significance of the work on reactions (2) and (3) is discussed in the next section. Reaction (1) was studied to provide a comparison to the AlCl + HCl

reaction. Over the whole temperature range observed the BCl reaction may be seen, Fig. 1, to be an order of magnitude faster. This observation on an endothermic pair of reactions[1] parallels our finding, on the exothermic pairs BCl, AlCl + O_2 and BCl, AlCl + CO_2, that the BCl reactions are faster (have a larger cross-section), Fig. 2. This can be understood in terms of the larger orbital of the outer electrons (involved in the formation of the new bond) in the BCl case, which is equivalent to a larger reactive cross-section.[2]

Correlation of Activation Energies

Figure 2 shows that the O_2 reactions have smaller temperature dependences (activation energies) than the corresponding CO_2 reactions, as can be approximated from the average slopes. It is tempting to try to correlate this with physical properties of the reactants. Such has sometimes been done successfully for reactions observed over narrow temperature ranges where there is no deviation from $\ln k(T) = A \exp(-E/RT)$ Arrhenius behavior. It has apparently not previously been attempted for observations covering wide temperature ranges, where the Arrhenius plots are curved. Merely considering the small number of reactions of Fig. 2 would be insufficient to obtain meaningful correlations. We therefore have extended our measurements to reactions (2) and (3). We now find that by expressing all these rate coefficients in terms of $k(T) = AT^n \exp(-E/RT)$, and fixing n anywhere between 2 and 4, that E correlates closely with $IP_{MCl} - EA_{OX}$. Here the first term is the ionization potential of BCl or AlCl and the second term represents the electron affinity of the oxidant. This is illustrated in Fig. 3 for n = 3. A physical explanation for these findings will be offered at the meeting. No correlation between E and reaction exothermicities or *O-X (O-O, O-SO, etc.) bond dissociation energies* is evident. We plan to further test this unified presentation of BCl and AlCl reaction activation energies by studying the AlCl equivalents of reactions (2) and (3) and repeat the AlCl + CO_2 measurements with the present, improved, HTFFR configuration.[2] The scatter in the original measurements of that reaction is such that a comparison to the other reactions of Fig. 3 is not convincing.

Identification of Product Paths

The existence of the E versus IP_{MCl}-EA_{OX} relation of Fig. 3 suggests that all these MCl reactions proceed via a similar dominant mechanism. As formation of an oxychloride is from thermochemical considerations the only accessible channel for the CO_2, SO_2, and N_2O reactions, this mechanism then would have to be oxychloride OMCl formation. Thus, while the original studies of the BCl and AlCl reactions with O_2 could not distinguish between the various channels which would be accessible based on thermochemical considerations,[3,4] it now appears that OMCl formation dominates.

The reactions of AlO with HCl and Cl_2 (the interpretation of the HTFFR results of which we completed this year)[5] similarly have a number of thermochemically accessible product paths. We therefore extended our laser-induced fluorescence measurements to look for the potential product AlCl and established that less than 5% of AlO reacted could have formed this species. This indicates that abstraction reactions dominate. This may be contrasted with

observations on NaO + HCl where a four-center channel, NaCl + OH formation, dominates.[6] The amphoteric element Al in this respect thus resembles a metalloid more than an alkali metal.

References

1. A.G. Slavejkov and A. Fontijn, "HTFFR Kinetics Studies of the Reactions of AlCl and BCl with HCl at High Temperatures", Chem. Phys. Lett., 165, 375 (1990).

2. A.G. Slavejkov, P.M. Futerko and A. Fontijn, "High-Temperature Fast-Flow Reactor Kinetics Study of the Reaction Between BCl and CO_2 From 770 to 1830 K", Twenty-third Symposium (International) on Combustion, in press.

3. A.G. Slavejkov, D.F. Rogowski and A. Fontijn, "An HTFFR Kinetics Study of the Research Between BCl and O_2 from 540 to 1670 K", Chem. Phys. Lett., 143, 26 (1988).

4. D.F. Rogowski and A. Fontijn, "An HTFFR Kinetics Study of the Reaction Between AlCl and O_2 from 490 to 1750 K", Twenty-first Symposium (International on Combustion (The Combustion Institute, Pittsburgh, 1988), p. 943.

5. A.G. Slavejkov, C.T. Stanton and A. Fontijn, "High-Temperature Fast-Flow Reactor Kinetics Studies of the Reactions of AlO with Cl_2 and HCl Over Wide Temperature Ranges", J. Phys. Chem., in press.

6. J.A. Silver, A.C. Stanton, M.S. Zahniser and C.E. Kolb, "Gas-Phase Reaction Rate of Sodium Hydroxide with Hydrochloric Acid", J. Phys. Chem., 88, 3123 (1984).

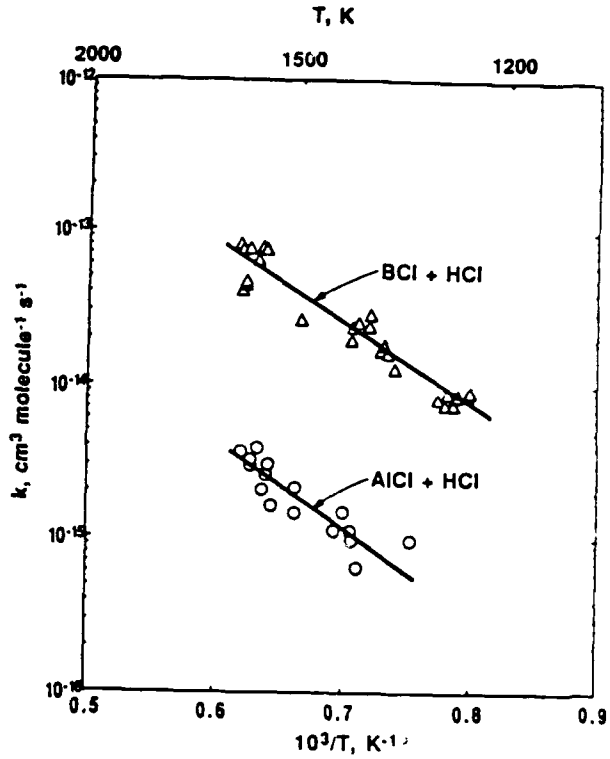

Figure 1. Arrhenius Plots of the BCl + HCl and AlCl + HCl Rate Coefficients.

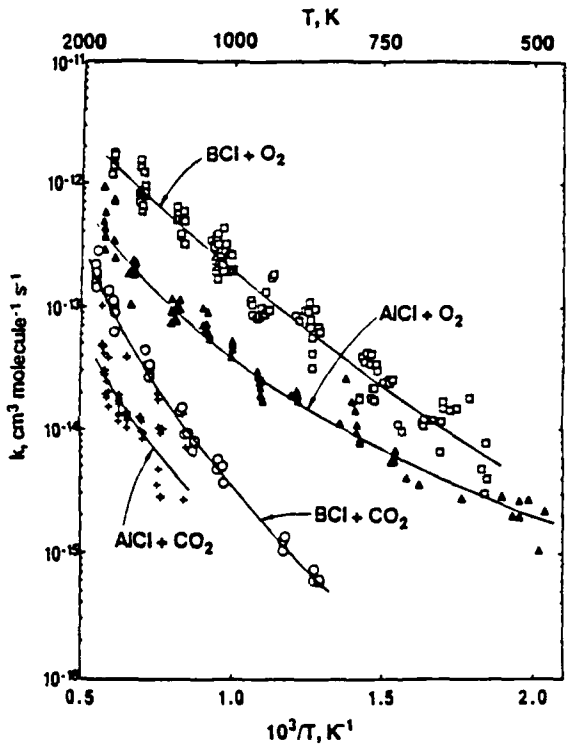

Figure 2. Arrhenius Plots of the Rate Coefficients of the BCl and AlCl Reactions with O_2 and CO_2

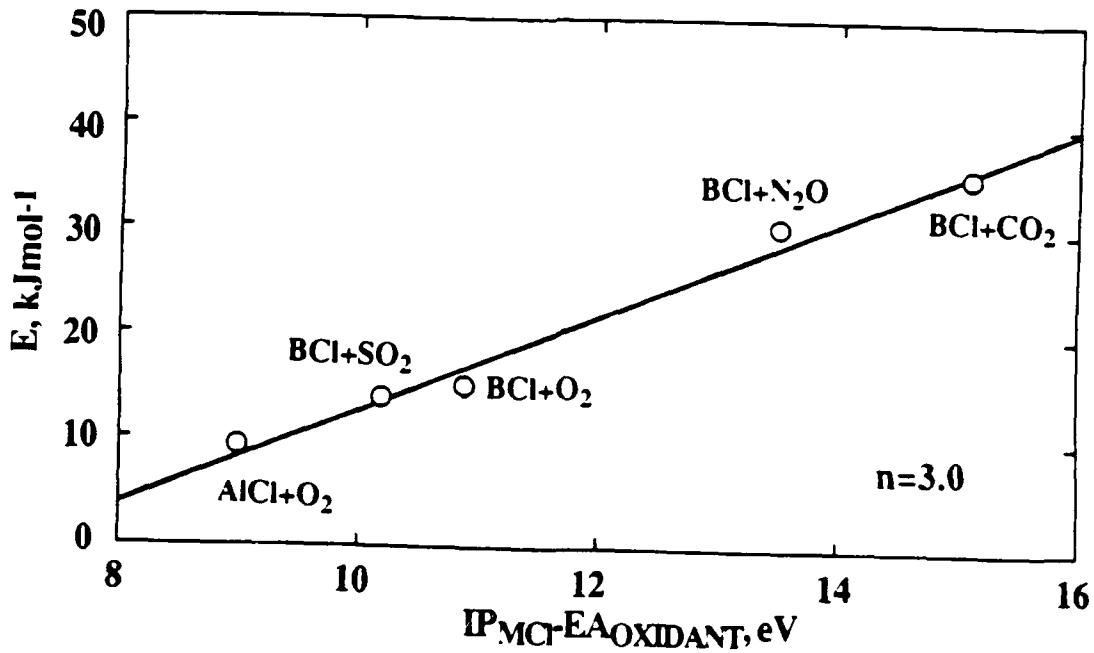

Figure 3. Correlation of the Activation Energies of the Reactions of BCl and AlCl Reactions with Various Oxidants.

MEASUREMENTS AND CHEMICAL KINETIC SIMULATION OF THE STRUCTURE OF MODEL PROPELLANT FLAMES

AFOSR Grant Number AFOSR-90-0121

Melvyn C. Branch and Hasan Dindi
Center for Combustion Research
University of Colorado
Boulder, Colorado 80309-0427

SUMMARY/OVERVIEW:

In order to provide direction in the testing of propellant formulations derived from newly developed energetic compounds, complex integrated models of multidimensional and multicomponent decomposition, vaporization and combustion are needed. The research reported here addresses the very important but unresolved question of the structure of gas reaction zones associated with these materials. Gas phase flames of hydrocarbon species with nitrogen oxides are known to be important in the combustion of new nitramine derived rocket propellants and similar energetic materials. These flame reaction zones are so thin during the high pressure combustion characteristic of real propellants, however, that it has only been possible to study the detailed chemical kinetic mechanism of these gas reactions in model flames. The research presented here will summarize our experience in measuring the composition profiles and temperature in selected model flames and in modeling the structure of the flames.

TECHNICAL DISCUSSION:

CH_4-N_2O Flames: Laminar, premixed flat flames of CH_4 with N_2O have been stabilized and studied at 50 torr. This study represents the first nearly complete study of the structure and kinetics of CH_4/N_2O flames including stable and unstable species measurements and detailed chemical kinetic modeling. Three flames were investigated with slightly fuel rich, near stoichiometric and lean mixtures. Stable species concentration profiles were measured using probe sampling with gas chromatographic sample analysis. Laser-induced fluorescence was used to measure the composition of the intermediate species CH, CN, NH, NH_2 and OH. Temperature was measured by coated, radiation corrected thermocouples and by the LIF rotational temperature of CN. The CH_4/N_2O flames have high N_2 and H_2O and low NO concentration in the products. The CO is oxidized to CO_2 through its reaction with OH. These flames are characterized by strong radical emission spectra, but no NH_2 fluorescence signal was observed. A reaction mechanism was developed for the CH_4/N_2O flames and results are presented comparing the calculated and experimental profiles of species concentration for the flame with equivalence ratio 1.13. Comparison of the stable species profiles is very good; comparison of the unstable species profiles is qualitatively correct with some displacement of the location of the concentration maxima calculated compared to the data. Sensitivity analysis was used to evaluate the effects of changing rate constants in the mechanism on the species concentration profiles. The flame modeling and sensitivity analysis suggests the major reaction paths responsible for the conversion of reactants to products and the formation and

consumption of the intermediates.

In a related study, we have measured the composition of stable and unstable species and temperature of a CH_4-N_2O-Ar flame using a molecular beam sampling system and mass spectrometric (MBMS) analysis at the Catholic University of Louvain, Belgium. This study provided a unique opportunity to study the same flame chemistry using a significantly different apparatus. The overall structure of the flame measured by molecular beam sampling was essentially the same as that reported above. The major new results obtained resulted from the large range of intermediate species which could be identified with the MBMS system. We were able to measure quantitative profiles of H and OH and qualitative profiles of HCN, NCO, CH_3, and HCO and we were able to measure profiles of HNCO and C_2H_2 for the first time in such flame systems. The flame modeling is in progress making use of these new data.

CO-N_2O Flames: In our previous studies of flames supported by nitrogen oxides, we have found that reactions of CO with N_2O and NO_2 can form an important reaction path for transformation of CO to CO_2. Since little high temperature kinetic data and no flame data on these reactions are available, we have initiated a study of laminar premixed flames of CO and N_2O or NO_2. Laminar premixed flames of CO and N_2O have been studied first using the apparatus and techniques described above. Composition profiles of all the stable species have been measured (CO, CO_2, O_2, N_2O, NO, N_2) in flames at three different equivalence ratios. The LIF measurements showed no CN or HCN so that for these flames the only significant intermediate is O. The flames can be described completely by a reaction mechanism containing 15 reactions and our flame modeling has shown that most of the flame structure can be described with four elementary reactions, giving it perhaps the simplest flame chemistry available. It was also found that with the addition of trace amounts (¡1completely and the burning velocity increases significantly due to the addition of new radical species. LIF measurements in these CH_4 added flames show distinct peaks of CH, CN and NH.

PUBLICATIONS:

1. M.C. Branch, F.N. Alasfour and M.A. Habeebullah,"Structure of Laminar Premixed CH_4/N_2O and CH_2O/N_2O Flames," Proceedings of the Joint Meeting of the British and French Sections of the Combustion Institute, the Combustion Institute, Ro:.en, pp. 167-170, 1989.

2. M.C. Branch, A. Alfarayedhi, M. Sadeqi and P.J. Van Tiggelen, "Measurements of the Structure of Laminar Premixed Flames of $CH_4/NO_2/O_2$ and $CH_2O/NO_2/O_2$ Mixtures," Combustion and Flame, in press.

3. M.C. Branch, M.A. Habeebullah, F.N. Alasfour, A. Daghouche and H. Dindi," Structure of Model Gas Phase Flames Associated with Nitramine Propellants: CH_4, CH_2O and CO with NO, N_2O, NO_2 and O_2," Proceedings of the 26th JANNAF Combustion Meeting, in press.

4. M.A. Habeebullah, F.N. Alasfour and M.C. Branch, "Structure and Kinetics of CH_4/N_2O Flames," 23rd Symposium (International) on Combustion, Orleans, France, July 22-27, 1990.

MEASUREMENTS OF CH_4-N_2O FLAME STRUCTURE BY MOLECULAR BEAM SAMPLING-MASS SPECTROMETRIC ANALYSIS

- MAJOR SPECIES CONCENTRATION PROFILES FOUND TO BE SIMILAR TO THOSE MEASURED BY PROBE SAMPLING AND GAS CHROMATOGRAPHIC SAMPLE ANALYSIS.
- SEVERAL SPECIES IDENTIFIED FOR THE FIRST TIME IN THESE FLAMES: HNCO, C_2H_2, HCO, NCO, HCN.
- FLAME MODELING IS IN PROGRESS.

CH4/N2O/Ar FLAME STRUCTURE

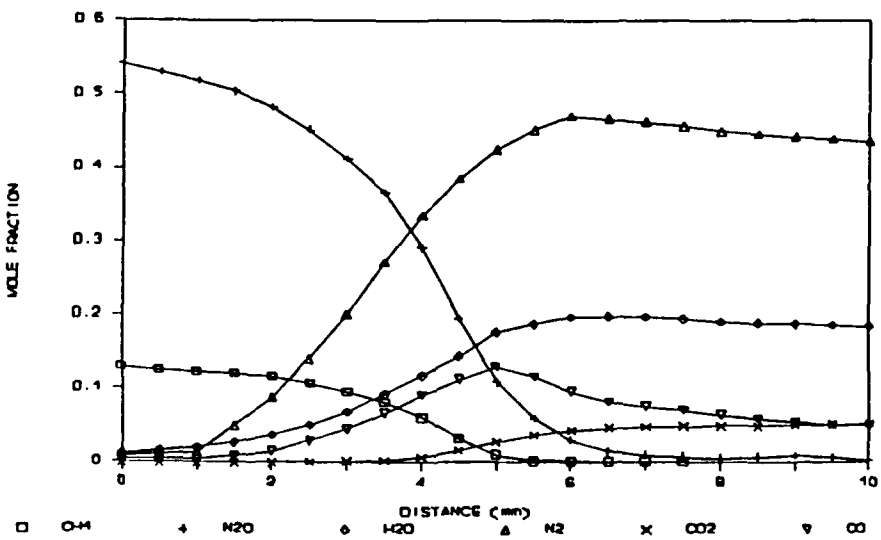

CH4/N2O/Ar FLAME STRUCTURE

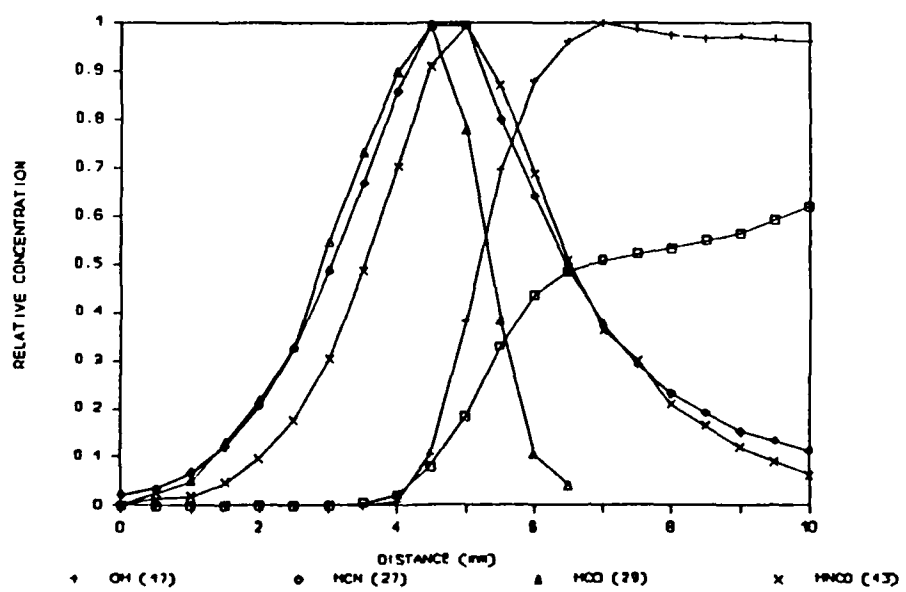

MEASUREMENTS AND MODELING OF CO-N_2O FLAME STRUCTURE

- LIKELY REACTION MECHANISM IDENTIFIED:

  $CO + N_2O = CO_2 + N_2$

  $N_2O + M = N_2 + O + M$

  $N_2O + O = N_2 + O_2$

  $N_2O + O = NO + NO$

- THE ONLY REACTIVE INTERMEDIATE IN THE MECHANISM IS OXYGEN ATOM.
- TRACE ADDITIVES SHOWN TO HAVE MAJOR EFFECT ON FLAME STRUCTURE.

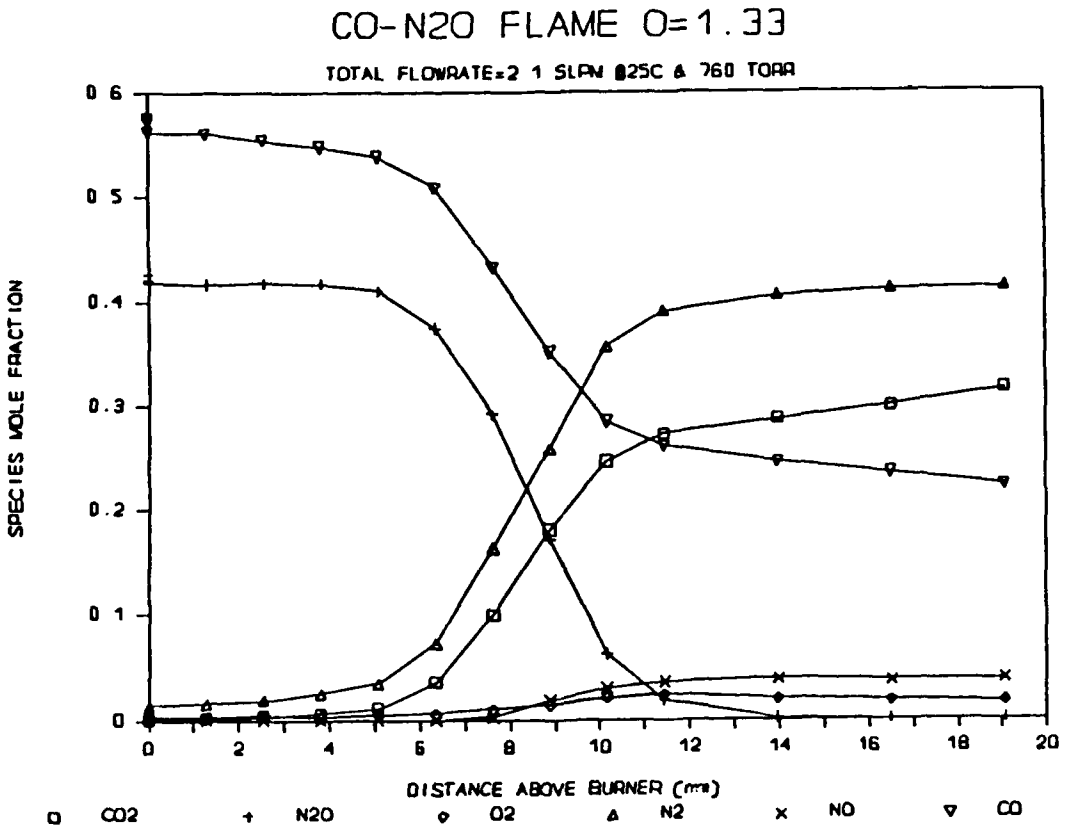

HIGH-RATE THERMAL DECOMPOSITION OF NEW POLYCYCLIC NITRAMINES

AFOSR-89-0521

Thomas B. Brill

Department of Chemistry
University of Delaware
Newark, DE 19716

SUMMARY/OVERVIEW:

The kinetics and mechanisms of thermal decomposition of new polycyclic nitramines and energetic binders to be used in advanced propellants are being investigated at high heating rates. The Simultaneous MAss and Temperature CHange (SMATCH)/FTIR technique perfected in our programs is being used in conjunction with a non-isothermal kinetic model to simulate the microscopic chemical detail of a burning surface. Kinetic constants and mechanisms are being extracted. This detail is new and is needed to model the combustion and possible instabilities of advanced propellant formulations.

TECHNICAL DISCUSSION

New generation propellants composed to polycyclic nitramines (eg. hexanitro hexaza isowurtzitane, PCN) and energetic binders (eg. NC, AMMO, BAMO, GAP, polyvinylnitrate, polyglycidylnitrate) have different combustion characteristics from conventional propellants. Modeling of the combustion process is needed as part of a national effort to develop new high-energy propellants. The approach in our laboratory is to simulate the microscopic chemical and physical detail that exists at the surface of a burning material. Thus, high heating rates and elevated pressure conditions are sought. Real-time temperature change, mass change and chemical species measurements are needed. Over the past 2.5 years we have developed and perfected a new technique that permits simultaneous measurement of the mass change, temperature change and concentrations of the IR active gas products near the surface of a material heated at a rate up to 300°C/sec. This technique is called SMATCH/FTIR spectroscopy. By using non-isothermal kinetics, the rate of mass loss can be used to determine the global kinetic constants (Ea and log A) for regression of the sample at a high heating rate. The near-surface gas products can help establish the mechanisms of the rapid thermolysis process. Experiments conducted at rapid heating rates are considerably more representative of combustion than those at slow heating rates. However, high rate experiments cause the chemical processes to couple with heat and mass transfer. Thus, we are attempting to design our experiments so that the transport properties can be tested and modeled, if necessary.

APPROACH

SMATCH/FTIR Spectroscopy is a new technique that permits the rate of mass and temperature change and the near surface gas products to be measured simultaneously on a sample heated at dT/dt up to 300 K/sec.

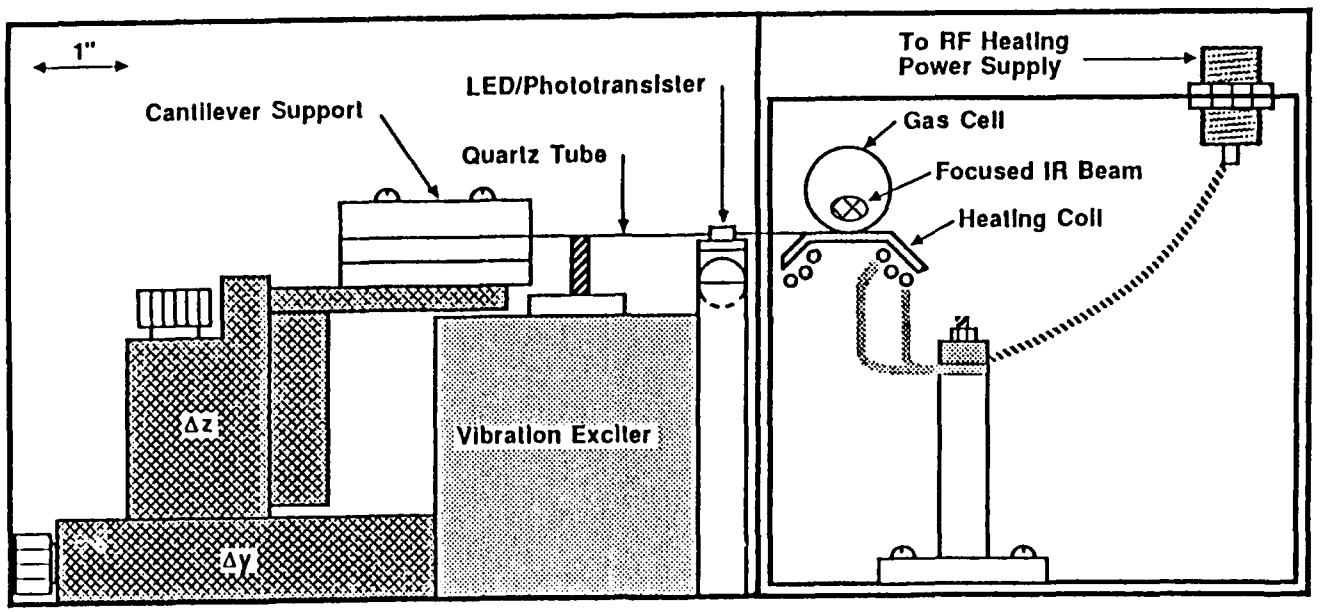

A RESULT

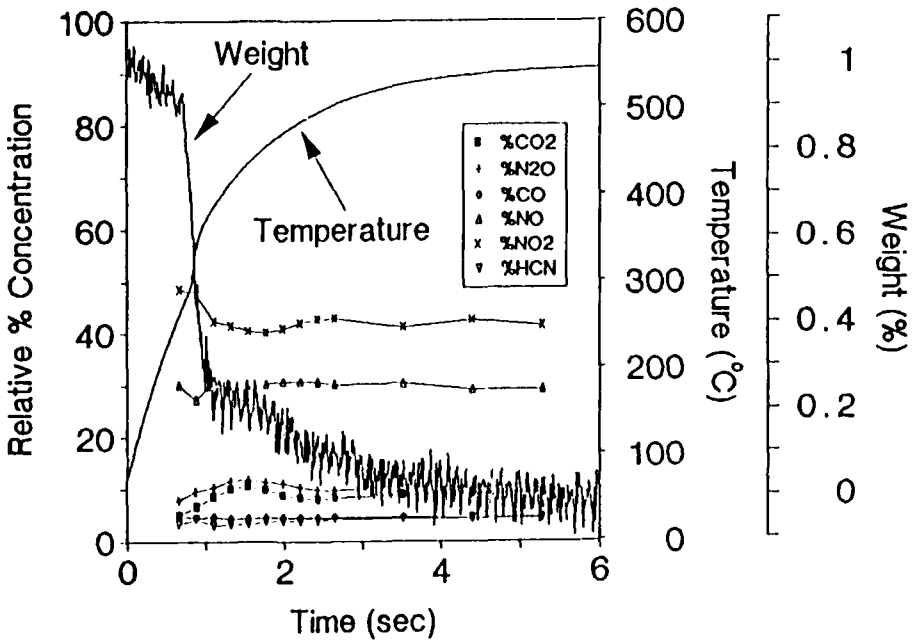

SMATCH/FTIR STUDY OF PCN

Conclusions:

1. E_a and log A are much lower at high heating rates than low heating rates
2. NO_2 and NO dominate the thermal decomposition of PCN

The rate of mass change and temperature change was used to calculate Ea and log A for hexanitro hexaza wurtzitane (PCN) and nitrocellulose (NC). The linearized rate expression is

$$\frac{d\alpha}{dt} = Ae^{-Ea/RT}(1-\alpha)^2$$

	E_a (kcal/mol)	log A(sec^{-1})
PCN	20 ± 2	8.5 ± 1
13%NC	32 ± 2	16.1 ± 1

FUTURE PLANS

Minaturize SMATCH/FTIR technique to permit high-rate thermal decomposition kinetics to be studied under conditions closest to those of combustion, eg.,

(1) high pressure

(2) sample heating from the surface inward.

Continue the study of the thermolysis of PCN and model PCN residues in NO and NO2 atmospheres to develop a fast thermolysis model.

Continue to develop fast thermolysis models for energetic binders.

HIGH PRESSURE COMBUSTION KINETICS OF PROPELLANTS

AFOSR PROGRAM ELEMENT 2308M1

Principal Investigators: Tim Edwards, Steve Zabarnick

Air Force Astronautics Laboratory (AFSC)
AL/LSCC, Edwards AFB, CA 93523-5000

SUMMARY/OVERVIEW:

This research is designed to examine the structure and reaction mechanisms of solid propellant flames. The understanding of these mechanisms is limited at present. It is believed that a better knowledge of propellant flame chemistry is needed for improvements in current propellant performance and instability models. This research involves experimental studies of both solid propellant flames and propellant-related flames, such as gas flames with NO_2 and N_2O as oxidizers. The major experimental tools used in this research are laser-based combustion diagnostics such as laser-induced fluorescence. Chemical kinetic models of the flame chemistry are compared to the experimental measurements.

TECHNICAL DISCUSSION

In comparisons of experimental results in a low pressure premixed $CH_4/NO_2/O_2$ flame with modeling results (Sandia premixed flame code) [1], it was found that species profiles were often not well predicted by an extended version of the Miller/Bowman mechanism for nitrogen chemistry in flames [2]. For example, the comparison of experimental and theoretical results for NO_2 are shown in Figure 1. This indicates that more research in nitrogen chemistry in flames needs to be done before mechanisms can be reliably applied to more complex systems, such as solid propellant flames. Similar differences between model and experiment have been observed in a study of a series of NO_x-oxidized flames at low pressure at the University of Colorado [3]. One of the most interesting results of this work is the finding of much greater amounts of CN in CH_2O/NO_2 flames than predicted, possibly because of reactions of HCO with NO and N_2O. At AL, some difficulties with CH LIF measurements were resolved, showing that the apparent double-peaked behavior was due to a complex combination of photolytic effects and non-target NO_2 LIF [1]. As shown in Figure 2, the first peak in the CH profile was a combination of laser-generated CH and NO_2 LIF, while the second peak was CH with a small contribution from another molecule, perhaps NCO.

Chemical modeling of the flame above an HMX-based solid propellant (73% HMX, 17 % TMETN, 10% polyester binder) at 15 atm has also been recently performed at AL [4], and compared with experimental species profiles from LIF [5] and absorption [6]. Two chemical kinetic mechanisms have been used, one by Hatch with 78 reactions involving 27 species [7] and the extended Miller/Bowman mechanism with 252 reactions involving 54 species [1,2]. The Sandia premixed flame code was used in the burner stabilized flame mode, with the input temperature profile from the data of Vanderhoff [8]. Two schemes for the breakup of the HMX were tested, one suggested by Kubota [9] (R1) and the other estimated [4] from the thermolysis data of Brill [10] (R2):

$$HMX\ (C_4H_8N_8O_8) \rightarrow 4/3\ NO_2 + 4/3\ N_2O + 2\ N_2 + 4\ CH_2O \qquad R1$$

$$HMX \rightarrow 2\ H_2CN + 2\ CH_2O + 2\ N_2O + 2\ NO_2 \qquad R2$$

The testing of other mechanisms, such as that of Melius, is planned. The TMETN was assumed to break up into C_2H_4, CH_2O and NO_2 [4], based on data from Brill [11], while the polyester binder was assumed to break up into C_2H_4 and CO_2:

$$-[(-CH_2-CH_2-O-(C=O)-(CH_2)_4-(C=O)-O-]_n \rightarrow 3\ C_2H_4 + 2\ CO_2. \qquad R3$$

The Hatch mechanism does not include hydrocarbons, so the binder was assumed to form CH_2O [4]. The comparison of the experimental CN profile data and modeling predictions is shown in Figure 2 (Hatch mechanism) and Figure 3 (Miller/Bowman mechanism). With the Hatch mechanism, R2 gives a much better approximation to the experimental data than R1. With the Miller/Bowman mechanism, this is reversed. This is apparently due to the C2H4 from the binder forming CN. Thus, although earlier studies indicated that R1 was incompatible with the experimental data [4], it now appears possible that the CN data does not contradict R1. A possible solution to this question may be supplied by CARS measurements in this propellant flame [12], which have shown significant amounts of HCN under ignition conditions. If HCN is seen near the surface, this would confirm the importance of the H_2CN/NO_2 pathway in HMX combustion chemistry.

1. Zabarnick, S., "Laser-Induced Fluorescence Diagnostics and Chemical Kinetic Modeling of a $CH_4/NO_2/O_2$ Flame at 55 Torr," submitted to Combustion and Flame.

2. Miller, J. A., and Bowman, C. T., "Mechanism and Modeling of Nitrogen Chemistry in Combustion," Progress in Energy and Combustion Science, Vol. 15, pp. 287-338, 1989.

3. Branch, M. C., et al, "Structure of Model Gas Phase Flames Associated with Nitramine Propellants: CH_4, CH_2O and CO with NO_2, N_2O and O_2," paper presented at 26th JANNAF Combustion Meeting, Oct 1989.

4. Edwards, T., "Investigation of Solid Propellant Combustion Chemistry," AIAA Paper 90-0547, Jan. 1990.

5. Edwards, T., "Laser-Induced Fluorescence in High Pressure Solid Propellant Flames," Applied Optics, Vol 26, No. 17, pp. 3496-3509, 1987; "Solid Propellant Flame Spectroscopy," AFAL-TR-88-076, 1988.

6. Vanderhoff, J. A., "Spectral Studies of Solid Propellant Combustion: II. Emission and Absorption Results for M-30 and HMX1 Propellants," Technical Report BRL-TR-3055, December, 1989. Also, "Spectral Emission and Absorption Studies of Solid Propellant Combustion," 25th JANNAF Combustion Mtg,Vol. IV, CPIA Pub. 498, pp. 537-547, 1988.

7. Hatch, R. L., "Chemical Kinetics Modeling of HMX Combustion," 24th JANNAF Combustion Meeting, CPIA Publication 476, Volume I, pp. 383-391, 1987; also 23rd JANNAF Combustion Meeting, CPIA Publication 457, Volume I, pp. 157-165, 1986.

8. Vanderhoff, J. A., and Kotlar, A. J., "Simultaneous Determination of Temperatures and OH Concentrations in a Solid Propellant Flame," paper to be presented at 23rd Symposium (International) on Combustion, July, 1990. In this paper, a temperature of 2740±280 K is measured from data collected (averaged) between 0 and 0.4 mm above the propellant surface. For the model, the temperature was assumed to rise from a surface temperature of 700 K to the adiabatic temperature of 2600 at 0.2 mm above the surface.

9. Kubota, N., and Sakamoto, S., "Combustion Mechanism of HMX," Propellants, Explosives, Pyrotechnics, Vol. 14, pp. 6-11, 1989.

10. Oyumi, Y., and Brill, T. B., "Thermal Decomposition of Energetic Materials 3. A High-Rate, In Situ, FTIR Study of the Thermolysis of RDX and HMX with Pressure and Heating Rate as Variables," Combustion and Flame, Vol. 62, pp. 213-224, 1985.

11. Oyumi, Y., and Brill, T. B., "Thermal Decomposition of Energetic Materials 14. Selective Product Distributions Evidenced in Rapid, Real-Time Thermolysis of Nitrate Esters at Various Pressures," Combustion and Flame, Vol. 66, pp.9-16, 1986.

12. Stufflebeam, J. H., and Eckbreth, A. C., CARS Diagnostics of Solid Propellant Combustion at Elevated Pressure," to be published in Combustion Science and Technology.

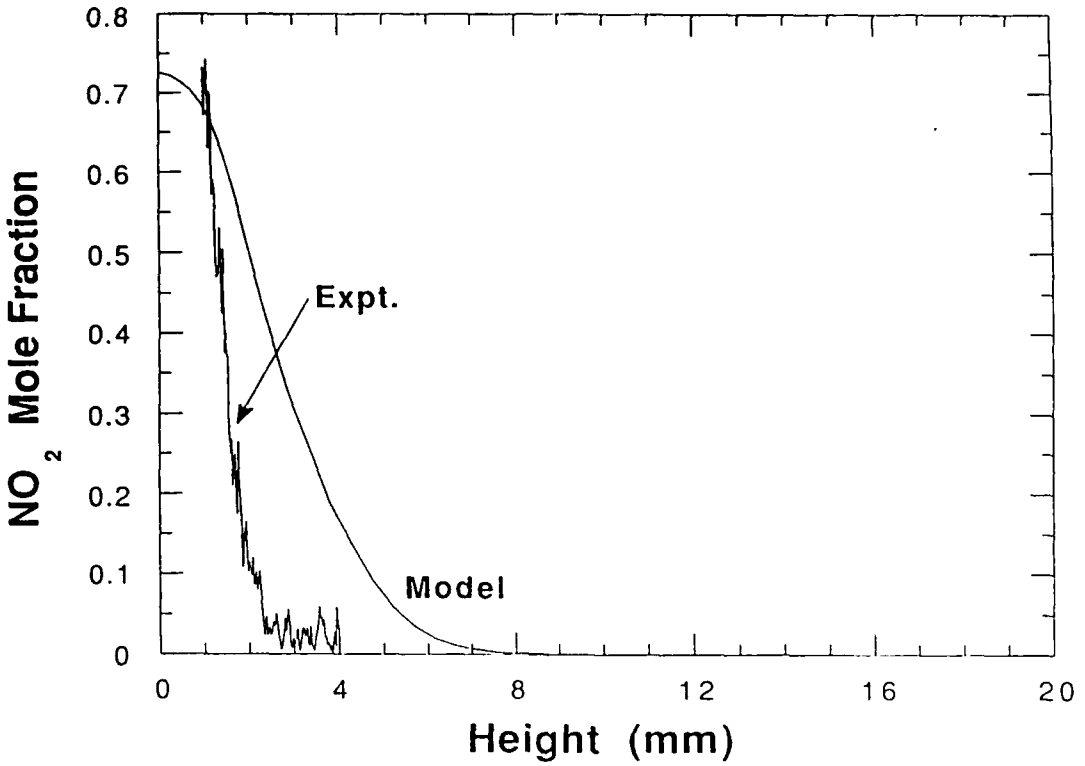

Figure 1. Comparison of experimental NO_2 LIF relative concentration profile with chemical kinetic modeling (252 reactions) results [1]. Peak of experimental profile set equal to peak of model; $CH_4/NO_2/O_2$ flame, 55 torr.

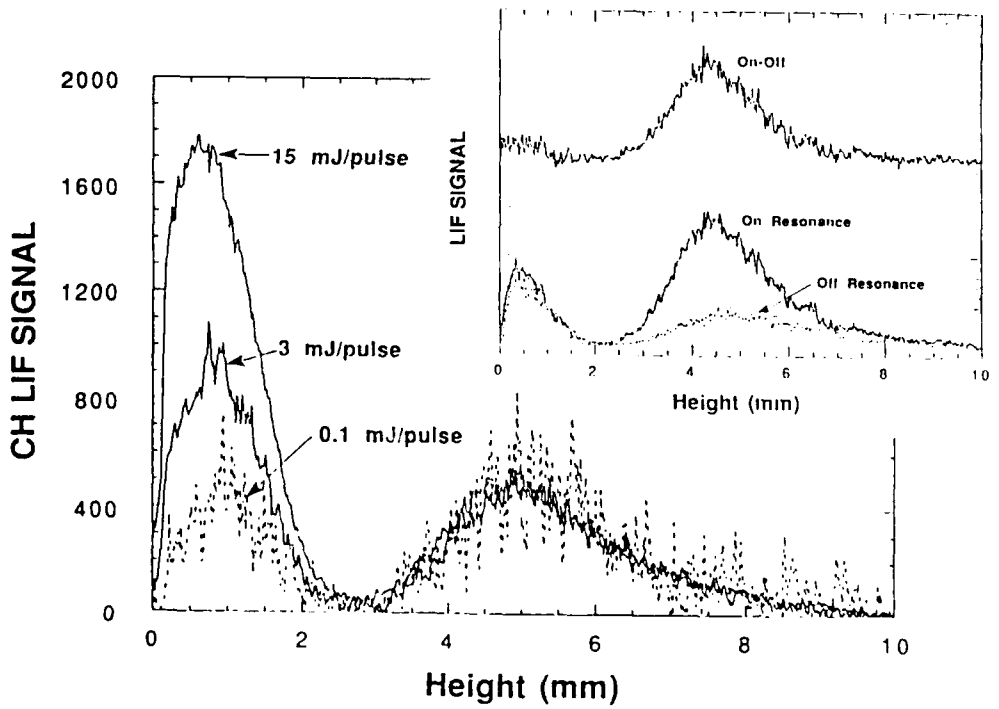

Figure 2. Changes in CH LIF profiles in $CH_4/NO_2/O_2$ flame at 55 torr due to changes in laser power. Excitation wavelength for CH is 434.4 nm (0,0 $P_1(6)_{c,d}$), detection is 430±0.75 nm (Q branch of 0,0).

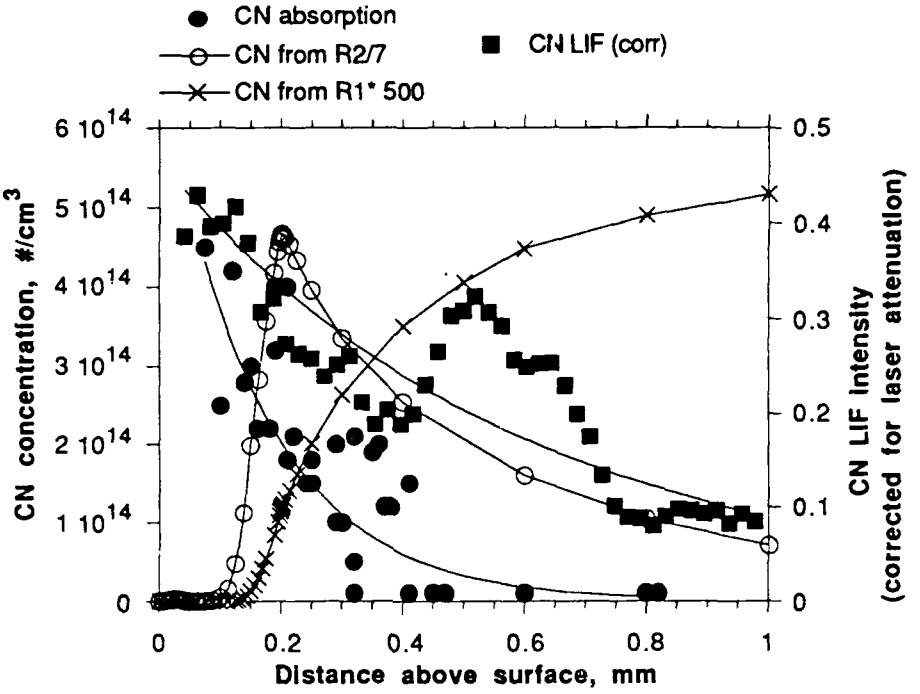

Figure 3. Comparison of experimental CN concentration profile with chemical kinetic modeling for HMX propellant, 15 atm. Model used 78 reactions involving 27 species [4].

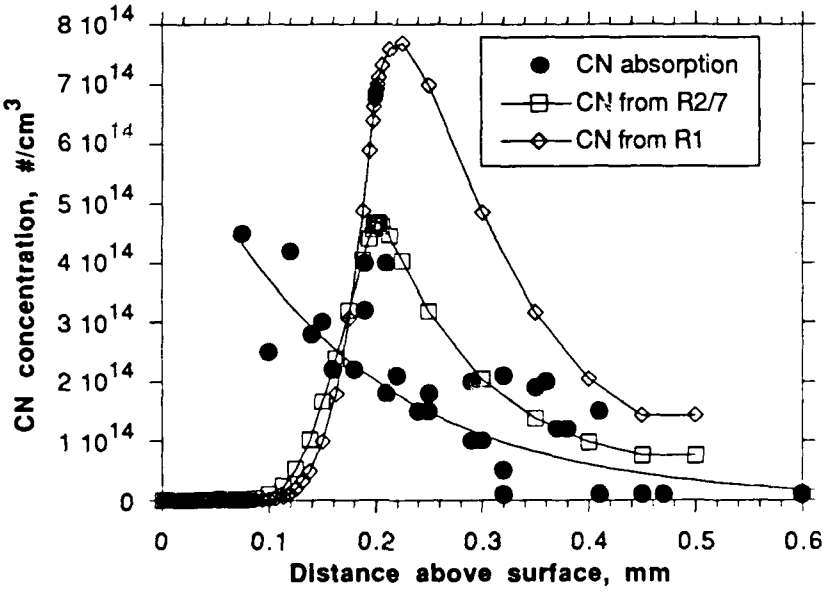

Figure 4. Comparison of experimental CN concentration profile with chemical kinetic modeling for HMX propellant, 15 atm. Model used 252 reactions involving 54 species [1,2].

CHEMICAL KINETIC DATA BASE FOR PROPELLANT COMBUSTION

(AFOSR CONTRACT-ISSA-90-0033)

Principal Investigator: Wing Tsang

Chemical Kinetics Division
National Institute of Standards and Technology
Gaithersburg, Maryland 20899

Summary:

We describe the status of a program aimed at the development of an evaluated chemical kinetic data base of single step reactions for use in the computer simulation of propellant combustion. Current efforts are aimed at the gas phase reactions involved in RDX decomposition. All of the possible reactions involving 28 of the most likely compounds that are present in such decomposition systems are to be considered. The conditions covered range from 500-2500 K and 10^{17}-10^{22} particles cm^{-3}. The results of the first years effort have lead to recommended rate expressions for of all pertinent reactions of the following species H, H_2, H_2O, O, H, OH, HCHO, CHO, CO, NO, NO_2, HNO, HNO_2, HCN, and N_2O with each other.

Technical Discussion:

Quantitative understanding of the detailed chemical kinetics of propellant combustion can have important impacts on the formulation of such mixtures, the optimization of current systems and the design of new combustors. A complicating factor has been the scores of rate expressions of elementary reactions that are needed to give a complete description of the chemical processes. For many years the necessary experimental tools and theoretical understanding were not available for the development of such a chemical kinetic information base. In addition there is also a need to identify key reactions and develop simple mechanisms. This is not an easy task. With these two major impediments, it is not surprising that as far as the chemistry is concerned much work in this area has been empirical. This implies the necessity of a great deal of physical testing. The expense of such efforts is a severe limitation on innovative efforts in this area.

In recent years a number of exciting technological developments have made it worthwhile to look anew into the possibility of developing a more basic understanding of propellant chemistry. These include; a) Rapid progress in computational capabilities, so that the simulation of increasingly realistic physico-chemical systems are or will be well within our capabilities. Thus, a chemical kinetic data base can be used immediately. b) Development of experimental and theoretical capabilities in chemical kinetics, so that the needed rate constants can be measured or estimated. c) Extensive applications of powerful modern diagnostic techniques to laboratory systems, so that we are developing much better pictures of the micro-structure of combustion processes. However, the interpretation and the projection of such results to real systems is crucially dependent on the existence of a correct detailed model. Given the large number of parameters one can always "fit" a particular experimental observation. Only the model with the

correct inputs can be expected to project results to real systems.

The compounds that will be considered are listed in the reaction grid in Figure 1. There can be little question regarding the inclusion of the small species(4 atoms or less). They include practically all the possibilities. Many of these species have been detected in experiments involving RDX. Other are natural precursors or products of these compounds. The selection of the larger fragments is more speculative. Most of these have not been detected and the possibilities are considerably larger than the number of species that we have chosen. Mechanistic considerations enter into the selection. We postulate that detrimerization occurs at a very early stage in the decomposition and that all linear species larger than the monomeric methylene nitramine are so unstable that they need not be considered. No claim is made that we have the correct mechanism. As new data are accumulated species can be added or removed.

The essence of the work is the evaluation of existing data and the estimation of rate expressions where data do not exist. Our experience in these matters has led to the following procedure. First preference is given to experimental determinations where the mechanism is clear-cut. Frequently, this is from direct determinations of the rate of disappearance or appearance of reactants or intermediate products in real time. We have also found that in complex situations, careful modeling of the temporal history of products and intermediates can lead to accurate results. In many cases these may not be individual rate constants, but very accurate ratios of rate constants. We are thus able to generate very accurate networks of reactions. In the absence of kinetic data, thermodynamic considerations in

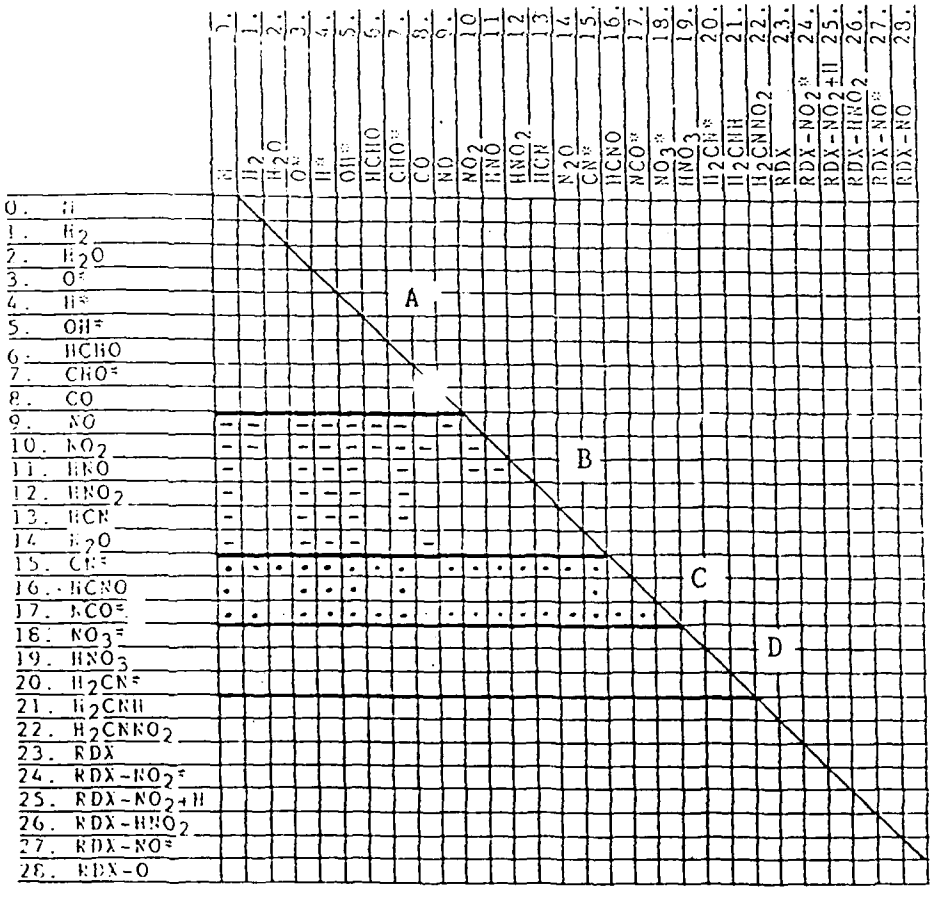

Fig. 1
Reaction grid
(-) past year's
work, (·)
current work

the form of detailed balance are used. For the substances under consideration in the current review the thermodynamics are all well established. In other cases, rate constants are assigned on the basis of analogy or thermokinetic information. Rate theory is used in a semi-empirical manner. Initial applications are for extrapolation and interpolation. Most encouragingly, the important parameters that have been derived from experiments are not unreasonable and we feel increasing confidence in transferring such numbers to related systems where there are no data. In all cases we assign an uncertainty value to our recommendations. This is a subjective number. It is based on the intercomparison of data sets, considerations imposed by related reaction mechanisms and the constraints imposed by thermodynamics and theory. Quantitatively, it means that the user of the data should feel free to adjust the rate constant in his models within these limits.

The reaction grid in Figure 1 is divided into a number of blocks. Block A consists of the reactions involved with formaldehyde oxidation. We have already prepared data sheets for these reactions in the context of hydrocarbon combustion. Block B contains reactions involving the smaller nitrogenated species. This has now been completed. 39 specific interactions leading to recommendations for the rate expressions for 50 individual reaction have been considered. With its completion it should be possible to model HCHO-NO_2 combustion systems. The current work is in Block C. Its completion will permit the modeling of the HCN-NO_2 system. An even more crucial test will be the simulation of HCHO-HCN-NO_2 flames. It is expected that the overall process will involve continuous iteration between data evaluators, modelers and experimentalists.

The basic product from this work is the data sheet. It begins with a statement of the reaction. This is followed by summaries of previous investigations. Included are descriptions of the experimental conditions and methods, the results of the experiments in the form of the rate expressions and estimated errors. The latter is usually based on the author's estimates. Also included in this data block are the recommendations from earlier reviews. In many cases we use these as the starting point for our work. The final entry gives our recommendations and the estimated uncertainties. The next section contains the justification for the recommended expression. The final section contains the references, the person who carried out the analysis and the date.

The work described here has benefited from the intensive research effort aimed at understanding NO_x formation and destruction at high temperatures and stratospheric ozone depletion at low temperatures. Pressures are either near atmospheric or below. What has been done in this work is to apply the best existing theory in a semi-empirical manner to cover the intermediate region between the high and low temperatures and to extend the pressures to ranges and collision partners more in tune with propellant applications. Some of the extrapolations are very long and the estimates are usually analogies. There is thus a great need for high quality experimental work. The excellent reproducibility of all the data particularly the shock tube results, demonstrate that such efforts are well within the state of the art.

In Figure 2 we show the results of our RRKM fit of the measured rate constant for the reaction $O+NO+N_2 \rightarrow NO_2+N_2$ in the lower pressure regime. The

high temperature point was derived from the rate constant of the reverse decomposition reaction and the equilibrium constnat. Note the characteristic curved Arrhenius plot and the error that would have been introduced had one simply extrapolated in a linear fashion the lower temperature results. In combination with the measured high pressure rate constant (2nd order limit) the RRKM methodology permits the deduction of an expression that yields a rate expression over all pressures and temperatures. The specific expression is $k=[k_0k_{inf}/(k_0+k_{inf}/N_2]*.95-10^{-4}T$ where $k_o = 1.3x10^{-23}(1/T)^{2.87}exp(-781/T)cm^6molecule^{-2}s^{-1}$ and $k_{inf}=2.2x10^{-9}(1/T)^{0.75}$ $cm^3molecule^{-1}s^{-1}$. Figure 3 summarizes our recommendations and experimental results for $OH+NO_2$ combination. They demonstrate the problems in determining accurate high temperature rate expressions.

Plans for the next year involve expansion of the data base to cover the reactions listed in Block D (Figure 1). This will involve the reactions of NO_3, HNO_3 and H_2CN radicals with the secies that have been covered so far and with each other. Completion of the work on the first two radicals will complete coverage of the nitrogen oxides and should permit us to model formaldehyde and HCN decomposition systems with nitric acid and thus provide another test of the correctness of the data base. Due to the fact that these species are important in atmospheric chemistry there exists considerable information on their kinetic behavior. Nevertheless, some of the problems that we have mentioned before will become increasingly important as we evaluate the data and attempt to make estimates. This is even more the case for H_2CN, the first distinctly "nitramine based" species that we will be treating.

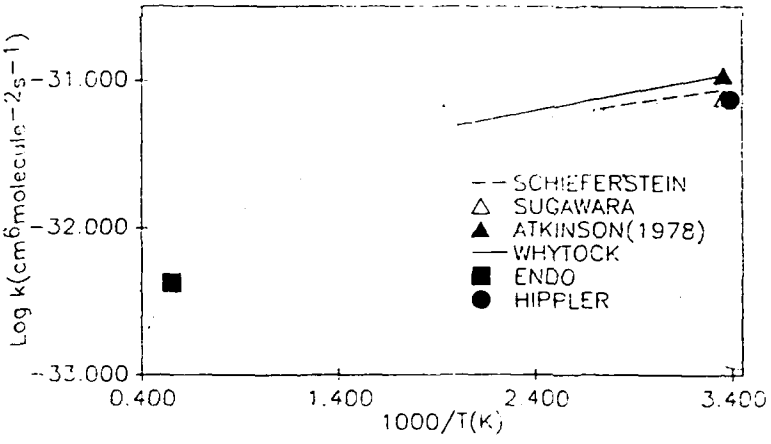

Figure 2. Summary of experimental work and recommendations (dotted line) on $O+NO+N_2=NO_2+N_2$.

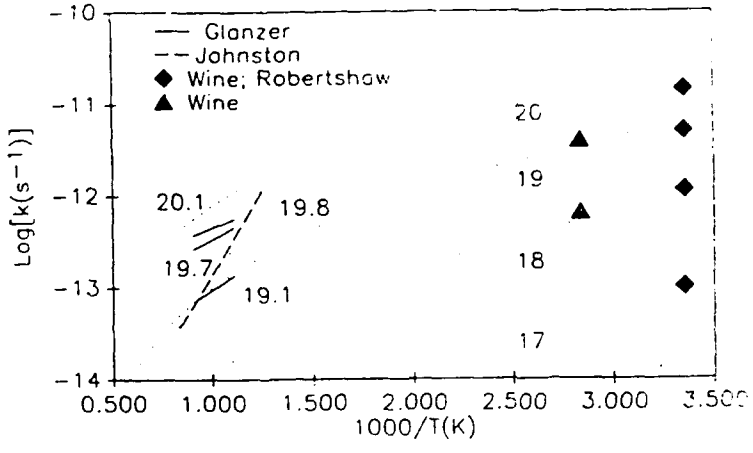

Figure 3. Summary of experimental work and recommendations (dotted line) on $OH+NO_2=HNO_3$. Symbols are low temp. studies at log(densities). Lines are measurements from HNO_3 decomposition

LIQUID ROCKET ENGINE COMBUSTION INSTABILITY

AFOSR Grant Number AFOSR 90-0121

John W. Daily
Center for Combustion Research
Department of Mechanical Engineering, University of Colorado
Boulder, Colorado 80309-0427

I. OVERVIEW

Our long term objective is to understand the mechanism of combustion instability in liquid rocket engines. It is characterized by large amplitude combustion chamber pressure oscillations which causes enhanced heat transfer to the chamber walls, ultimately resulting in extensive engine damage. In the past, a number of important processes have been identified as potentially responsible for combustion instabilities. These include atomization, vaporization, mixing of fuel and oxidizer, combustion chemistry and chamber acoustics. Analytical and numerical approaches have been proposed to predict stability characteristics for engine design based upon simplified models of the oscillatory behavior of the various processes. Despite past work in the field, predictive ability still remains elusive. Our approach involves experimental, analytical and computational methods. This work is in collaboration with Aerojet TechSystem of Sacramento, California.

II. TECHNICAL DISCUSSION

Under certain operating conditions, atomization is the rate controlling process for instability growth in many rocket motors. However, since the details of the injection fluid mechanics are not well known, it is difficult to make quantitative predictions even with advanced numerical codes. The objective of our present work is to provide a comprehensive picture of atomization mechanism and droplet distribution for coaxial and impinging jet type atomizers and to understand how this couples with the chain of events leading to large amplitude pressure oscillations.

A. Background

In liquid rocket motors using coaxial injectors, the velocity difference between the liquid fuel jet and the surrounding oxidizer stream is of the order of 100 meters per second. Some of the important characteristics of atomization are the ligament length or distance from the jet exit to the break-up point of the liquid sheet, size and velocity distribution of the resulting droplets and the resulting spray angle. In liquid rocket motors, due to large velocity differences, the ligament is almost non-existent and thus the spray begins to spread almost at the point of injection. A number of theories have been proposed to explain atomization in high speed flows and several have been verified to be incorrect by the experiments of Reitz and Bracco (1982). In Table 1, we summarize past experimental results designed to

understand the effect of variation in physical properties of the liquid jet on the atomization charcateristics.

Increasing	Liquid viscosity	Surface tension	Gas density
Breakup length	increases[13,6]	decreases[6]	decreases[13]
Droplet size	increases[7]	increases[7]	decreases[7]
Divergence angle	decreases[13], little effect	no effect[7]	decreases[13], small effect of gas pressure

TABLE 1. Effect of fluid properties

From their numerical simulations, Childs and Mansour (1989) reported that in addition to liquid surface tension, the boundary layer thickness of both phases are important parameters that determine the growth of symmetrical disturbances in planar jets. It would be useful to understand the significance of these parameters under specified atomization conditions. Rangel and Sirignano's (1988) vortex-method nonlinear simulations predicted a critical wavenumber (for density ratio larger than 0.2) below which the interface sheet rolls up into a vortex singularity and above which only partial rollup occurred. In Table 2, we summarize literature results on the effect of flow and geometrical parameters that influence the atomization process.

Increasing	Relative jet velocity	Liquid flow rate	Injector length to diameter ratio
Breakup length	increases[9], not true at trans.	?	not clear[7]
Droplet size	decreases[7]	increases[7]	increases[7]
Spray angle	increases[13], little effect	?	decreases[7],

TABLE 2. Effect of flow velocities and geometrical parameters

Although extensive data on atomization are available (Putnam et. al (1957) and Lefebvre (1989)) they are generally empirical in nature. Thus, there is an imperative need to understand the underlying physical processes through carefully designed experiments, analysis and numerical computations.

Atomization by the impingement of two liquid jets is an economical alternative. This method of atomization was originally studied by Spanogle and Hemmeter (1931) for use in a two-stroke cycle engine. Heidmann, Priem and Humphrey (1957) studied impinging jets open to the atmosphere. They observed that upon impingement of two jets, a ruffled sheet of

liquid was formed perpendicular to the plane of the jets. This sheet disintegrated to produce groups of droplets. Waves propagated from the point of impingement resulting in formation of ligaments, which in turn disintegrated to form groups of droplets. The frequency of these waves increased with increased injection velocity and decreasing impingement angle. Jet diameter and length before impingement had a negligible effect on wave frequency. Lourme (1986) has conducted experiments in pressurized chamber and measured the droplet size under different experimental conditions. Several attempts have been made to develop an analytical model for impinging jets atomization. Taylor (1961) used the sheet thickness measurements to calculate its shape. Hasson and Peck (1964) developed an elegant model based on mass conservation and geometrical considerations for the thickness distribution in the sheet. Their model is in close agreement with previous experimental results. Lefebvre (1989) mentions that, under typical operating condition of rocket engine, the spray is produced both by a process resembling jet breakup and by a rather ill-defined sheet formation at the impingement point. This complete process needs to be studied in more detail.

B. Scientific Approach

A ramjet combustor facility, at the Center for Combustion Research, is presently being modified to study atomization. By appropriate experimental scaling, this facility allows for both cold and hot flow experiments in a combustion chamber designed to modulate pressure and velocity fields. Both coaxial and impinging jet atomizers will be studied. The chamber's exhaust nozzle area is varied by a mechanical chopper, thus simulating the feedback loop in a rocket engine by imposing controlled oscillations. The chopper can generate oscillations of up to 6000 Hz. Non-intrusive optical methods will be used in determining drop size distribution, drop velocity and number density. In hot flow experiments, light emitted by the flame will be image processed to determine the heat release pattern during imposed pressure oscillations.

Jet instability and aerodynamic effects are being studied analytically. Recent linear inviscid and viscous stability theories, developed for gas phase combustion in coaxial jets, are being extended to include non-linear effects and two-phase flows by use of proper interface matching conditions. The eigenfunctions from these analyses provide considerable insight into the mechanisms responsible for the growth of instabilities. The non-linear theory will allow calculation of the growth rate of disturbances at the liquid-oxidizer interface as a function of the flow parameters and perturbation amplitude. The ultimate stability characteristics of a given engine will be determined by the coupling of the unsteady combustion dynamics with the chamber geometry. In the past, the fluid mechanics has not been treated dynamically. In our approach, we will incorporate the fluid dynamics using the method of multiple time scales as was applied successfully by our group for ramjets.

A direct numerical simulation technique has been developed to study forced transitional flow in coflowing, gaseous chemically reacting jets. This is being extended to handle two-phase flows. Higher order accurate finite difference and spectral methods are currently under investigation. Model problems in which the geometry, atomization and chemical reaction process are simplified will be simulated. Results from these simulations will help to further understand the physical mechanisms involved in atomization.

C. References

1. Castleman, R. A., "The Mechanism of the Atomization of Liquids," J. Res. Natl. Bur. Stand., Vol. 6, No. 281, pp. 369-376 (1931).

2. Childs, R. E. and N. N. Mansour, "Simulation of Fundamental Atomization Mechanisms in Fuel Sprays," J. of Propulsion, Vol. 5, No. 6, pp. 641-649, (1989).

3. Fraser, R. P.,"Liquid Fuel Atomization," Sixth Symposium (International) on Combustion, Reinhold, New York, pp. 687-701, (1957).

4. Harrje, D. J., and F. H. Reardon, (Ed.), *Liquid Propellant Rocket Instability*, NASA SP-194, (1972).

5. Hasson, D. and P. Peck, "Thickness Distribution in a Sheet Formed by Impinging Jets," A.I.CH.E. J., Vol. 10, No. 5, pp. 752-754, Sep. (1964).

6. Heidmann, M. F., R. J. Priem, and J. C. Humphrey, "A Study of Sprays Formed by Two Impinging Jets," NACA TN 3835 (1957).

7. Lefebvre, A. H., *Atomization and Sprays*, Hemisphere Pub. Co., New York (1989).

8. Lourme, D., "Like-on-Like Injector Spray Characterization For the Ariane Viking Engine," AIAA/SAE/ASME 22nd Joint Propulsion Conference, Huntsville, 16-18 June (1986).

9. Phinney, R. E.," The Breakup of a Turbulent Liquid Jet in a Gaseous Atmosphere," J. Fluid Mech., Vol. 60, pp. 689-701 (1973).

10. Putnam, A. A., et. al., *Injection and Combustion of Liquid Fuels*, WADC Technical Report 56-344, Battelle Memorial Institute, March (1957).

11. Rangel, R. H., and W. A. Sirignano, "Nonlinear growth of Kelvin-Helmholtz instability: Effect of surface tension and density ratio," Phys. Fluids, Vol. 31 (7), pp. 1845-1855, (1988).

12. Rayleigh, Lord, "On the Instability of Jets," Proc. London Math. Soc., Vol. 10, pp. 4-13 (1878).

13. Reitz, R. D. and F. V. Bracco, "Mechanism of atomization of a liquid jet," Phys. Fluids 25 (10), pp. 1730-1742, October (1982).

14. Spanogle, J. A., and G. T. Hemmeter, "Development of an Impinging-Jet Fuel-Injection Valve Nozzle," NACA TN 372 (1931).

15. Taylor, G. I., "Formation of Thin Flat Sheet of Water," Proc. Roy. Soc. (London), A259, 1 (1961).

AFOSR SPONSORED RESEARCH IN DIAGNOSTICS OF REACTING FLOW

PROGRAM MANAGER: JULIAN M. TISHKOFF

AFOSR/NA
BOLLING AFB DC 20332-6448

SUMMARY/OVERVIEW: The Air Force Office of Scientific Research (AFOSR) program in diagnostics of reacting flow currently is focused on three areas of study: gas-phase measurements, plasmas, and particle/droplet measurements. An assessment of major research needs in each of these areas is presented.

TECHNICAL DISCUSSION

AFOSR is the single manager for Air Force basic research, including efforts based on external proposals and in-house work at Air Force laboratories. The diagnostics of reacting flows task is assigned to the AFOSR Directorate of Aerospace Sciences along with programs in rocket propulsion, airbreathing combustion, fluid and solid mechanics, and civil engineering.

Interests of the AFOSR diagnostics of reacting flow task are given in the SUMMARY section above. This program, now in its ninth year, has produced many "first-ever" laser-based measurements. The instrumentation with which these measurements were made is becoming commonly available for laboratory and bench test utilization. Measurements range from microscopic to macroscopic scales with relevance to: plasma acceleration; combustion aerothermochemistry; the behavior and synthesis of advanced energetic materials; characterization of exhaust plume formation and radiation; and dynamic control of propulsion, weapon and power generation systems.

Decisions on support for research proposals are based on scientific opportunities and technology needs. Current AFOSR perceptions of scientific opportunities appear in Figure 1. As indicated by the orientation of the arrows in Figure 1, the task area with the greatest growth potential is plasmas.

The purpose of this abstract has been to communicate AFOSR perceptions of research trends to the university and industrial research communities. However, communication from those communities back to AFOSR also is desirable and essential for creating new research opportunities. Therefore, all proposals and inquiries for fundamental research are encouraged even if the content does not fall within the areas of emphasis described herein. Comments and criticisms of current AFOSR programs also are welcome.

Air Force Basic Research
Aerospace Sciences
Diagnostics of Reacting Flow

Science Area	Trend	Decrease	Increase
Gas-Phase Measurements		Possible Shift To Fluid Mechnaics	
Plasmas			Two New Efforts Initiated
Particle/Droplet Measurements		Transition To Applied Use	

DETECTING MICROWAVE EMISSION FROM TERRESTRIAL SOURCES: A FEASIBILITY STUDY

AFOSR-88-0257

T. C. Ehlert and T. K. Ishii

Marquette University, Milwaukee, WI 53233

SUMMARY:

The detection of discrete, spontaneous microwave emission from terrestrial sources has been studied and appears to be feasible. A Dicke receiving system has been designed for this purpose. Possible applications include remote detection of processes which produce high temperature gases, e.g. jet engines and explosions, determining the rotational properties of molecules which are difficult to study by absorption spectroscopy, studies of intermolecular energy transfer processes, and studies of the role of rotation in energy transfer to and from surfaces.

TECHNICAL DISCUSSION:

Introduction

The objective of this research is to observe discrete, spontaneous microwave emission from a terrestrial source. We have chosen H_2O vapor's 22 GHz transition because it has been thoroughly studied in absorption and microwave components for this frequency are not exceedingly expensive. The block diagram of the system, shown in Fig. 1., is an application of a Dicke receiving system. The receiver compares signals from two waveguides, each approximately eight meters long, one containing water vapor as the emission source, another containing dry air as the reference. Each waveguide is terminated by a brass plate. Since it is known that the microwave reflectivity of brass is close to one, the microwave emissivity of brass is low so the brass plate will act as a cold background source. As stated in the radiative transfer equation[1], if the water vapor is in front of a background colder than the vapor itself, it will be observed as an emitter, and the signal from the waveg-

uide containing water vapor will be greater than that from the reference waveguide due to the emission by water vapor. For our source design (waveguide temperature = 298 kelvins and steam pressure = 10 mb), the brightness temperature from the H_2O source will exceed that from the reference source by 1.8 kelvins. The Dicke receiver, including a waveguide chopper switch, front end 22 GHz low noise amplifier (LNA), 30 MHz IF amplifier, and lock-in amplifier, allowed us to detect this radiation difference. For our system (LNA noise figure $\leq$ 5dB, the IF amplifier's bandwidth = 100 MHz, and the lock-in amplifier's time constant = 30 seconds), the minimum detectable difference is 0.35 kelvins.

Progress Report

1. Publication and filing: We have submitted and filed the annual report for 1988-1989. In this report, we used a heterodyne receiving system to detect the emission from water vapor. Because the signal to noise ratio is less than one, a digital video integration technique was developed and used. We also submitted a paper, titled "Digital Video Integration Techniques for Faint Signal Measurement", to both IEEE Transaction on Instrumentations and Measurements and the 34^{th} Midwest Symposium on Circuits and Systems.

2. Emission sources preparation: We have cleaned all the waveguides in order to reduce the loss caused by the waveguides themselves. A vacuum system has been designed so that pressure and gas content in the waveguides can be controlled. Also, a vacuum aperture which minimumizes microwave leakage was designed. Two linearly tapered waveguide adapters from K-band to X-band, for the connection between waveguide chopper switch and both the emission and the reference sources, were designed and fabricated. The insertion loss of these adapters was tested and found to be less than 1.5 dB.

3. Receiver system preparation: For driving the waveguide chopper switch and sending the reference signal to a lock-in amplifier, a 2.9 Hz square wave generator was designed, fabricated and tested. The required local oscillator signal is generated by a klystron operated at 7.4 GHz frequency passing through a waveguide frequency multiplier and using the third harmonic at 22.205 GHz. A frequency multiplier using a detector was not satisfactory. An improved design, using a step recovery diode, is progressing. A high pass filter which cuts off the signal below 17 GHz with

insertion loss more than 60dB at stopband and less than 1.5 dB at passband has been designed, fabricated and tested. This filter is used to remove the unwanted first and second harmonics produced by the frequency multiplier.

4. Extension of concept and development of backup procedure: The Dicke receiver is capable of detecting the expected power difference between the emission and the reference sources. However, it can not tell which one has higher power. By extending and improving the technique of digital video integration, it is possible to determine not only the power difference but also polarity. To use this technique in the receiving system , the locked-in amplifier is replaced by an A/D converter and the sampled output of the converter is connected to an add/subtract device. At one interval the amplifiers is receiving the radiation from the emission source and the sampled output is added. At the next interval the amplifiers is receiving the radiation from the reference source and the sampled output is subtracted. If the process is continued for a long period time, then the net counted score will show both power difference and polarity. A computer simulation of this process supported this technique. For a 256 discretized voltage levels and a 200 Hz sampling rate has shown a signal to noise ratio of -50dB discernibility.

Conclusion

Detailed analysis shows that the signal (as brightness temperature) from the emission source containing water vapor will be 1.8 kelvins greater than that from the reference containing dry air. Our Dicke receiver is capable of detectecting 0.35 kelvins difference. The preparation of the experimental apparatus is progressing well. At present, no major difficulty in achieving this study has emerged.

References

1. M.L. Meeks, "Methods of Experimental Physics: Volume 12 Astrophysics Part B: Radio Telescopes", Academic Press, NY, 1976.

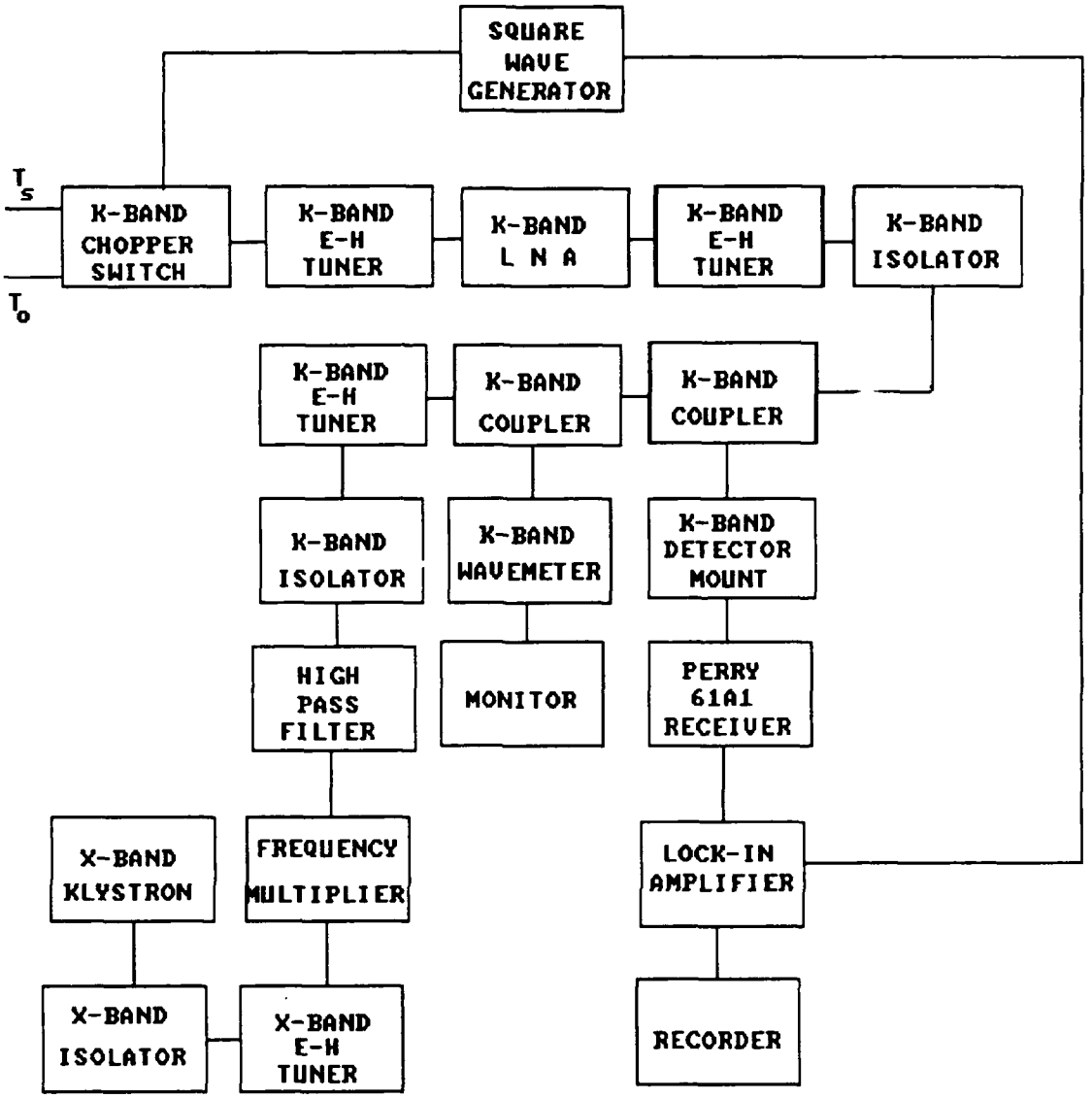

Fig. 1 Block Diagram of Dicke Receiving System Apparatus. To and Ts Repersent Equivalent Noise Temperatures of Dry Air and Steam Filled Waveguides, Respectively.

TWO- AND THREE-DIMENSIONAL MEASUREMENTS IN FLAMES

AFOSR Grant No. 88-0100

Marshall B. Long (Co-Principal Investigator)

Yale University
Department of Mechanical Engineering and Center for Laser Diagnostics
New Haven, Connecticut 06520-2157

SUMMARY/OVERVIEW

Laser diagnostic techniques are being developed that are capable of two- and three-dimensional mapping of scalars in turbulent flames. In addition, we wish to extend our imaging methods to allow the measurement of the temporal evolution of flow structures in two and three dimensions. Whenever possible, the techniques are tailored to measure quantities and flow configurations of current interest to combustion modelers. The availability of quantitative data on the spatial and temporal characteristics of structures in turbulent reacting flows will aid in understanding the interaction of chemical reactions with the turbulent motion. A better understanding of this key interaction is important for testing existing models of turbulent combustion as well as for suggesting new models.

TECHNICAL DISCUSSION

During the past year, progress has been made in several areas of our work on two- and three-dimensional diagnostics. Some specific achievements include the following:

1. Investigation of Differential Diffusion Effect

One of the aspects of reacting flows that makes their complete characterization so difficult is the large number of species present. Even a simple flame contains fuel, oxidizer, intermediates, combustion products, and relatively inert components. In general, each of these components will possess a unique diffusion coefficient. In most of the work in turbulent combustion, however, the simplifying assumption is made that a single diffusion coefficient can be used to characterize all of the species present and that differential diffusion effects can be neglected at reasonably high Reynolds numbers.

A Rayleigh scattering experiment was performed that allowed some of the simplifying assumptions to be checked by providing a direct measurement of differential diffusion effects. In the experiment, hydrogen (which has a Rayleigh cross section lower than that of air) and Freon (which has a higher Rayleigh cross section) were mixed in a ratio so that the effective Rayleigh cross section of the mixture was precisely the same as that of air. The mixture exited into a slowly coflowing stream of air through a cylindrical nozzle, and the resulting turbulent jet was investigated using planar Rayleigh scattering. Because the Rayleigh cross section of the mixture is the same as that of the air, the Rayleigh signal is independent of the mixing of the H_2/Freon jet with the air. However, if the ratio of H_2 to Freon changes due to the different diffusivities of the components, the Rayleigh signal will vary, with Freon rich regions providing more Rayleigh scattering and H_2 rich regions scattering less than the air or regions of the correct ratio.

The experiment showed that the effect is readily observable and that the magnitude of the effect is larger than that predicted by previous modeling efforts. Measurable differential diffusion is found at Reynolds numbers as high as 20,000 and as far downstream as 30 nozzle diameters. In addition to H_2/Freon/air experiments, differential diffusion is also observed when a mixture of H_2 and CH_4 is issued from the nozzle. (H_2 and CH_4 have less disparate diffusion coefficients than H_2 and Freon and may have more implications for combustion work.)

Although the experiment to measure these effects was proposed nearly ten years ago, previous attempts to make the measurement using single-point techniques were not successful. Two critical aspects in the success of the current experiment were (1) the high sensitivity imaging capability of the CCD detector and (2) the use of a second CCD detector to ensure that the Rayleigh cross section of the H_2/Freon mixture was precisely the same as that of air. The results of the experiments have implications for both theorists and experimentalists.

Further information on differential diffusion was obtained in a recent set of experiments done in collaboration with researchers at the University of Sydney in Australia. In the experiments, a direct measurement of the differential diffusion of gas and particles was obtained. A turbulent jet was seeded with both aerosol particles and a fluorescing molecular species, and the nozzle gas concentration was simultaneously inferred in different ways using two separate CCD detectors. One detector recorded the fluorescence intensity from biacetyl molecules seeded in the nozzle gas. During the same laser shot the other detector inferred the nozzle gas concentration from the Lorenz-Mie scattering from the submicron-sized aerosols. The only difference in the concentration distribution measured by the two techniques was due to the difference in diffusivities of the aerosol and molecular tags. Since the aerosols do not diffuse as rapidly as the molecules, the concentration distribution inferred from aerosol scattering contained more fine-scale structure and more steep gradients than that recorded by fluorescence.

2. Time Evolution of Turbulent Premixed Flames

One of the goals of our research is to measure the temporal evolution of large-scale structures in turbulent reacting flows. One of the main difficulties in realizing this goal is the high speed operation required of both the laser source and the detector. In our previous AFOSR work, we were able to use a high speed framing camera and a CW argon-ion laser to record the Lorenz-Mie scattering from an aerosol-seeded premixed flame at an image repetition rate of 48 kHz. The series of images provides useful information on convection velocities and burning velocities[2]. The main drawbacks of this approach, however, are the dependence on marker particles to infer the behavior of the flames and the relatively limited image quality available from the framing camera.

In a current experiment, we are trying to obtain the same information without the limitations imposed by our previous experimental configuration. A double-pulsed Nd:YAG laser (pulse separation of 100 μs) is used to illuminate the flow, and Rayleigh scattered light from molecules in the flow is collected by the imaging optics. A high-speed rotating mirror displaces subsequent images onto different portions of an intensified CCD detector. Although only a single pair of images is produced, burning and convection velocities can still be obtained, and the quality of the data is considerably improved.

3. Development of a Technique for Measuring the Three-Dimensional Time Evolution of Turbulent Flames

As turbulence is inherently three-dimensional, ambiguities remain with measurements in only two dimensions, and quantities such as the scalar gradient and flame curvature cannot be completely determined. The lack of three-dimensional information also leads to uncertainties in the velocities determined in our time sequence data. We are, therefore, developing a technique for recording a pair of three-dimensional data sets separated in time by a short (100 μs) interval.

The technique is based on the use of a series of closely spaced parallel laser illumination sheets of different wavelengths. A single CCD detector is used with color filters and image displacing wedges which cause the elastic scattering from each illumination sheet to be imaged onto a separate region of the detector. To obtain temporal information, a high-speed rotating mirror is again used to displace the images onto different regions of the detector.

In our initial experiment, four laser sheets are formed from the second-harmonic output of a Nd:YAG laser and from the first-, second-, and third-order stimulated Raman scattering from a liquid filled cell pumped by a portion of the 532 nm beam. The laser is double pulsed, and the Lorenz-Mie scattering from an aerosol-seeded premixed flame is recorded at two times separated by an interval of 100 μs.(i.e., a total of eight images is recorded on the CCD detector). This data should allow unambiguous determination of the burning velocity in premixed flames as well as investigation of the effect of curvature on the burning velocity.

REFERENCES

1. A.R. Kerstein, R.W. Dibble, M.B. Long, B.Yip, and K. Lyons, "Measurement and Computation of Differential Molecular Diffusion in a Turbulent Jet," Proceedings of the Turbulent Shear Flows Conference, Stanford, CA, August 1989.

2. M. Winter and M.B. Long, "Two-Dimensional Measurements of the Time Development of a Turbulent Premixed Flame," Combust. Sci. Tech. 66, 181 (1989).

NONLINEAR SPECTROSCOPY OF MULTICOMPONENT DROPLETS

AFOSR Grant No. 88-0100

Richard K. Chang (Co-Principal Investigator)

Yale University
Department of Applied Physics and Center for Laser Diagnostics
New Haven, Connecticut 06520-2157

SUMMARY/OVERVIEW

Noninstrusive in-situ optical diagnostic techniques have the potential of determining the chemical species and physical properties of multicomponent liquid droplets in a spray combustor. Our research is directed toward the understanding of nonlinear optical processes occurring within individual droplets which may or may not retain their spherical shape after irradiation by a high-intensity laser beam.[1] The two main research results during the past year are : (1) the observation that stimulated Raman scattering (SRS) in droplets is not directly pumped by the input laser beam but is pumped by the stimulated Brillouin scattering (SBS) internal to the droplet; and (2) the realization that the phase velocity of the internally trapped radiation is dependent on the mode number and mode order of the morphology-dependent resonances (MDR's) of a sphere.

TECHNICAL DISCUSSION

The spherical liquid-air interface of a droplet (with radius a much greater than the wavelength) acts as an optical cavity for the internally generated wavelength-shifted radiation, such as fluorescence, spontaneous Raman scattering, and spontaneous Brillouin scattering. Stimulated radiation at specific wavelengths within the spontaneous emission profile will occur when the internally generated waves propagate around the droplet rim with a round-trip gain greater than the round-trip loss. During the input pump pulse, the fluorescence will turn into laser emission, the spontaneous Raman scattering will turn into intense SRS, and the spontaneous Brillouin scattering will turn into SBS. For organic and aqueous liquid droplets without any fluorescent dyes, only SRS and SBS will take place at specific wavelengths corresponding to the droplet MDR's.

The frequency shift of the first-order Stokes SRS from the input pump laser frequency is equal to the molecular vibrational frequency and can, therefore, provide chemical species indentification of the multicomponent liquid droplet. In principle, the relative intensities among the various SRS peaks also contain quantitative information about the relative concentration of the multicomponent species. In order to improve the accuracy of the relative concentration, which is deduced from the relative SRS intensities, our original research goal is to determine the reduction of SRS intensity fluctuations when the input radiation from a Q-switched Nd:YAG laser is changed from operating in a multimode to a single-mode. When the laser is switched from multimode to single-mode,[2] a reduction is noted in the fluctuation of the SRS intensity as well as in the SRS threshold.

When the input laser is operating in a single-mode, we have experimentally determined that the threshold for SBS in droplets is reached before the threshold for SRS. In multimode operation, the SRS threshold is reached first. Once the SBS within the droplet is fully established,

the SRS is more efficiently pumped by the SBS than by the laser. Contrary to the optical cell results, we noted that the SRS threshold of droplets irradiated by a single-mode laser beam is ≈3 times lower than that irradiated by a multimode laser beam. In addition, by simultaneously measuring the time profiles of the SRS, SBS, and the single-mode input laser pulse, we noted that the growth of SRS is correlated with the decay of SBS, because the internal Brillouin wave is depleted in pumping the Raman wave.

Another nonlinear optical diagnostic technique for concentration determination within the droplet is coherent anti-Stokes Raman scattering (CARS). Unlike SRS, which does not have any phase-matching requirement, CARS requires phase matching of the input pump, input Stokes, and output anti-Stokes waves. The phase-matching concepts originally developed for plane-wave propagation in an infinite medium have been extended for guided-wave propagation in optical fibers. To date, the ability to improve the phase-matching velocity of the generating and generated waves circulating within a droplet has not been considered.

The Lorenz-Mie theory is developed for a plane wave incident on a sphere with radius **a** and index of refraction $n(\omega)$. Much of our understanding of MDR's is reached by examining the internal electric field distribution. When the input wavelength of the plane wave is not on a MDR, the internal waves are not guided at all. When the input wavelength is on a MDR with mode number **n** and mode order ℓ, the internal waves are guided and the internal field distribution is a standing wave with **n** peaks as the zenith angle θ is varied from 0° to 180° and with ℓ peaks as the radial distance is varied from 0 to **a**. The standing wave of a MDR can be decomposed into two counterpropagating traveling waves around the droplet circumference. The phase velocity $[\pm v_{\ell}^{MDR}(\omega)]$ of the two counterpropagating waves (forming the standing wave at a MDR with **n**, ℓ) can be calculated. Depending on the ℓ's of the MDR's, $\pm v_{\ell}^{MDR}(\omega)$ varies from c to $c/n(\omega)$, where c is the speed of light in air and $c/n(\omega)$ is the speed of light in liquid. Physical insight about the dependence of $\pm v_{\ell}^{MDR}(\omega)$ on ℓ can be reached by noting the internal field distribution of the MDR's. The low ℓ MDR's are very confined within the droplet and, hence, their phase velocity approaches the phase velocity of a plane wave in liquid $[c/n(\omega)]$. The internal field distribution of the larger ℓ MDR's is more extended outside the droplet and, hence, their phase velocity approaches that of a plane wave in air (c).

Figure 1 shows the schematic of the effective index of refraction $n_{eff}(\omega) = c[v_{\ell}^{MDR}(\omega)]^{-1}$ as the MDR mode order is increased from $\ell = 1$. Figure 2 shows the calculated phase velocity (normalized to c) versus wavelength (in wavenumbers cm^{-1}) for MDR's with different **n**, ℓ. Because phase-velocity matching is more difficult to calculate for the CARS process than for the third-order sum-frequency generation (TSFG) process, we have been concentrating our attention on the latter. For $\mathbf{a} = 30\ \mu m$, Fig. 2 shows the dependence of the calculated phase velocity on the droplet size parameter $x = 2\pi a/\lambda$. We have experimentally investigated the dependence of TSFG as the droplet **a** is changed.[3] In droplets, the TSFG spectra consist of peaks associated with various triple combinations of the input laser wave (ω_L) and the first-order Stokes SRS wave (ω_{1s}).

REFERENCES

1. R.K. Chang and A.S. Kwok, "High Intensity Laser Beam Interactions with Single Droplets," in AGARD Conference Proceedings No. 454 on Atmospheric Propagation in the UV, Visible, IR and MM-Wave Region and Related Systems Aspects (NATO, Specialised Printing Services, Essex, England, 1990), p. 20-1.

2. J.-Z. Zhang, G. Chen, and R.K. Chang, "Pumping of Stimulated Raman Scattering by Stimulated Brillouin Scattering within a Single Droplet: Input Laser Linewidth Effects," J. Opt. Soc. Am. B 7, 108 (1990).

3. D.H. Leach, W.P. Acker, and R.K. Chang, "The Effect of the Phase Velocity and Spatial Overlap of Spherical Resonances on Sum-Frequency Generation in Droplets," submitted to Opt. Lett.

FIG. 1:

Schematic of the range of values for the effective index of refraction $n_{eff}(\omega) = c[v_{\ell}^{MDR}(\omega)]^{-1}$ [where $v_{\ell}^{MDR}(\omega)$ is the phase velocity of a MDR with mode order ℓ at frequency ω] for the fundamental frequency ω_{1s} and its third harmonic at frequency $3\omega_{1s}$. MDR's with $\ell = 1$ have $n_{eff}(\omega)$ nearly equal to the bulk refractive index $n(\omega)$, and MDR's with highest ℓ have $n_{eff}(\omega)$ nearly equal to the air refractive index $n(\omega) \approx 1$.

FIG. 2:

The dependence of the normalized phase velocity $[v_{\ell}^{MDR}(\omega)/c]$ as a function of wavelength (in wavenumbers cm^{-1}) or droplet size parameter. The phase velocity is defined only at discrete values of the droplet size parameters which correspond to MDR's with mode number **n** and mode order ℓ.

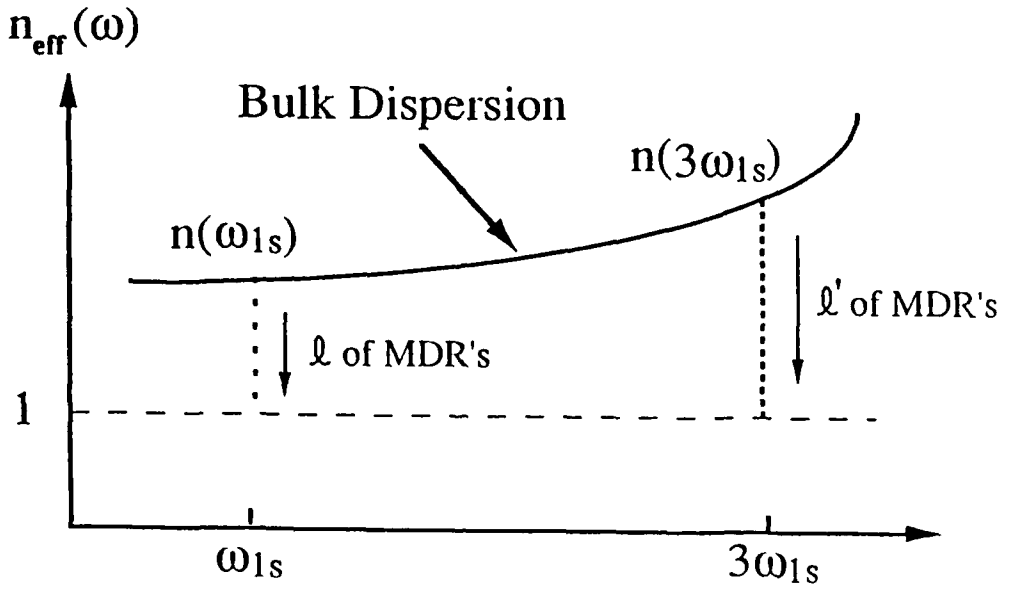

FIGURE 1

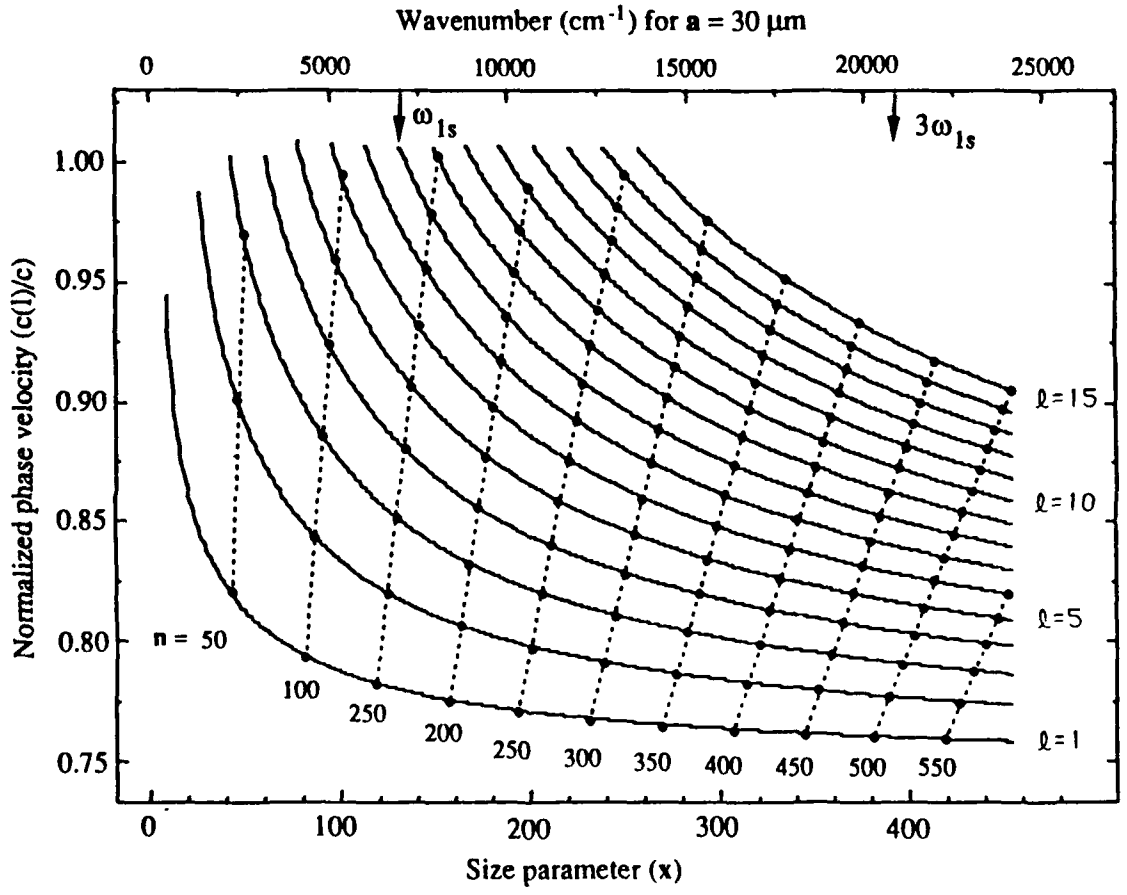

FIGURE 2

ADVANCED DIAGNOSTICS FOR REACTING FLOWS

AFOSR-89-0067

Ronald K. Hanson
High Temperature Gasdynamics Laboratory
Mechanical Engineering Department
Stanford University, Stanford, CA

SUMMARY/OVERVIEW

This research is directed toward innovation of advanced diagnostic techniques applicable to combustion gases and plasmas, with some emphasis on high speed flows. The primary flowfield parameters of interest are species concentrations, temperature, pressure, density and velocity, and quantities derivable from these parameters such as heat flux (from temperature gradient) and mass flow rate (from density and velocity). Techniques under study utilize laser absorption and laser-induced fluorescence, with the latter capable of providing both single-point and multi-point (2-d and 3-d) measurements. Laser sources include tunable cw lasers (ring dye and solid-state) and tunable pulsed lasers (excimer-pumped dye and narrow-linewidth excimer). Wavelength modulation and high-speed frequency modulation (FM) spectroscopy techniques are under study to provide increased data recording rates.

TECHNICAL DISCUSSION

In the following paragraphs we highlight primary activities of the past year.

Plasma Diagnostics

Recent research has focussed on single-point laser-induced fluorescence (LIF) techniques for temperature measurements in atmospheric pressure plasmas. An RF-powered plasma torch (1 kW), operating on argon with trace levels of additives, has been developed and used for this work. Two methods are being studied, one based on single laser line excitation and the other based on two-line excitation. In the former case, a single transition of Si atoms is excited, and fluorescence is collected from two upper states, both populated through collisional transfer from the laser-coupled upper state. The ratio of these two LIF signals reflects the temperature in the upper states of the atom. The second method involves laser-pumping two lower levels of Si to a common upper level. The ratio of LIF signals in this case reflects the temperature in the lower levels of the atom. Initial results are shown in Fig. 1; note the good agreement found at high temperatures. The discrepancy at lower temperatures reflects the fact that the plasma temperature is different in the lower and upper levels of the atom.

Laser-Wavelength Modulation Spectroscopy

A significant accomplishment during the past year has been the development of wavelength modulation techniques to perform single-point LIF of OH in supersonic combustion flows. These measurements entail rapid scanning of a cw ring dye laser across a spectral region encompassing two OH absorption lines, thereby producing a time-dependent LIF signal which contains the complete absorption line profiles of both transitions. We can infer temperature from the ratio of line intensities, pressure from the linewidths, and velocity from the Doppler shift of these lines relative to those of a static sample. Such measurements are made at a repetition rate of 3.5 kHz, with the result that all three flow parameters (temperature, pressure and velocity) are determined simultaneously at time intervals of about 300 microseconds. Sample results are

shown in Fig. 2 for a single laser scan at a small point (0.2mm x 0.2mm x 0.2mm in extent) on the axis of an atmospheric pressure, supersonic combustion (CH_4-air) stream. The mole fraction of OH was less than 1000 ppm. Recently, we have extended this work to shock tube flows using absorption detection, and have shown that the approach can be used to measure temperature, pressure, density, velocity and mass flux (the product of density and velocity) in both OH and NO. In some cases the laser frequency is fixed and multiple laser beams are used, at different angles to the shock tube flow, and this approach allows continuous recording of the flow velocity. Extension to multiple wavelengths will allow simultaneous, continuous recording of velocity and temperature.

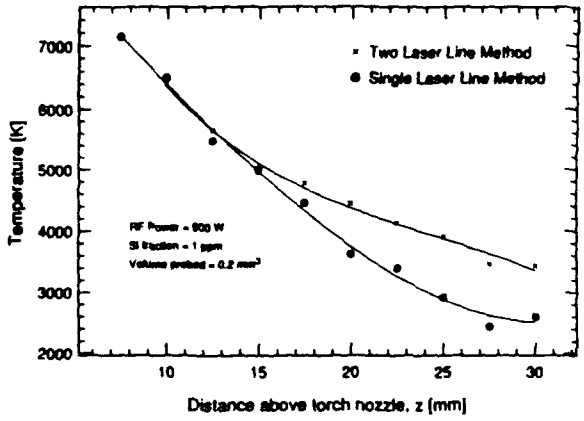

Fig. 1. Measurements of temperature in a plasma using LIF of Si.

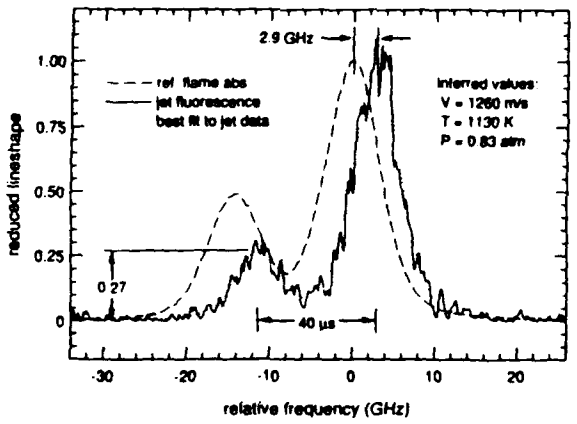

Fig. 2. Measurements of temperature, pressure and velocity in supersonic combustion using wavelength-modulation LIF of OH.

PLIF Imaging in Shock Tube Flows

Shock tubes and tunnels provide a convenient means of studying nonequilibrium gasdynamic phenomena and of simulating conditions relevant to advanced air-breathing propulsion systems. Our objective in this project is to establish capabilities for PLIF imaging in such flows. During the past year we have investigated several aspects of imaging OH and NO, including the development of techniques for probing flows with vibrational and chemical nonequilibrium. As an example, we investigated shock-induced ignition of H_2-O_2-Ar mixtures using a nonplanar end wall to generate flow nonuniformities. Two single-shot PLIF images of OH are shown in Fig. 3. (Note that the end wall has a triangular groove, about 2 mm deep, at the boundary of the imaged region.) The strong 3-d character of the flowfield, and the capability of the PLIF system to capture such details, are apparent. Other work in progress involves vibrational nonequilibrium supersonic flow of NO over a wedge and transverse injection of H_2 into a supersonic, high temperature air flow.

Velocity Imaging

Work has continued on our concept for imaging velocity through PLIF monitoring of Doppler-shifted absorption. The approach utilizes a pulsed tunable dye laser with a spectral width greater than both the absorption linewidth and the Doppler shift. Use of multiple sheets allows inference of two velocity components. Recent work has involved assembly of a small gas-fired rocket motor to provide a controlled source of supersonic combustion gases. Following check-out of this flow facility, we plan to attempt single-shot velocity imaging using two fast-gated PLIF cameras. One camera will record the PLIF image associated with forward propagation of the laser sheet through the flow, while the second camera will record the PLIF image from the retroreflected beam. Eventually, we hope to implement two laser sources and two additional cameras, which should enable simultaneous, single-shot imaging of both temperature and velocity.

Laser-Photolysis Shock Tube

During the past year we have continued development of a shock tube which combines gasdynamic heating with excimer laser photolysis as a means of generating controlled levels of radical species at elevated temperatures. This device provides new capability for fundamental studies of reaction kinetics and spectroscopy relevant to combustion. A critical aspect of the research is the continued development of sensitive species detection schemes using laser and atomic resonance lamp sources. To verify this new shock tube strategy, we have performed experiments in $NO-H_2-N_2O-Ar$ mixtures at high temperatures. At these conditions (see Fig. 4), the N_2O rapidly decomposes to form O atoms, which then react via $O + H_2 \rightarrow H + OH$. Subsequent photolysis of NO to form a comparable level of O causes further reaction with the excess H_2 by the same mechanism. By monitoring the O-atom decay rate in such experiments, we are able to extract the rate coefficient for both the pyrolysis- and photolysis-driven reactions. The rate coefficients (see Fig. 5) are in excellent agreement, thereby confirming the validity of the photolysis approach. Other work with this shock tube has led to several publications in recent months.

FM Spectroscopy With Tunable Solid-State Lasers

During the past year we have begun to explore the use of solid-state laser sources to perform absorption spectroscopy. These sources, like ring dye lasers, may be viewed as tunable, narrow-linewidth sources, but they have several distinct advantages. In particular, they are economical, rugged and compact, with the potential to be used in process control and flight instrumentation. The research issues at present involve learning how to modulate the lasers and investigating the spectroscopy of species which absorb at the near-ir wavelengths presently available from these sources. We have focussed our initial work on O_2, which is both a critically important species and has a fortuitous (but weak) absorption band near 760 nm. A computed absorption spectrum of oxygen illustrating the magnitude of the absorption (path length of 5 m) and the spectral location of the specific laser we are utilizing is given in Fig. 6. Because of the low absorption coefficient, we are pursuing various frequency modulation (FM) schemes which enable detection of weak absorption at relatively rapid rates. An example result, based on detection at the 2f frequency, is shown in Fig. 7. Here the laser was modulated at f = 50 kHz while the laser current was swept at 300 Hz. Thus the 2f spectrum, closely related to the second derivative of the absorption spectrum, can be recorded in a few ms; faster rates will be possible with improved electronics. The potential to detect O_2 concentration, temperature through line (peak) ratios, and velocity through Doppler shift of line positions, is apparent even in these initial results. Work is in progress to extend the modulation to higher frequencies and to apply the method in high-speed and high temperature flows.

Other Projects

Other projects currently underway include: (1) extension of PLIF to 3-d imaging and to fast 2-d imaging; (2) simultaneous imaging of droplet, OH and temperature fields in spray flames using a combination of PLIF and planar Mie scattering; (3) development of advanced solid-state camera systems with improved performance characteristics; (4) development of single-shot temperature imaging strategies based on PLIF; and (5) addition of a shock tunnel to the existing shock tube to enable PLIF studies in hypersonic flows.

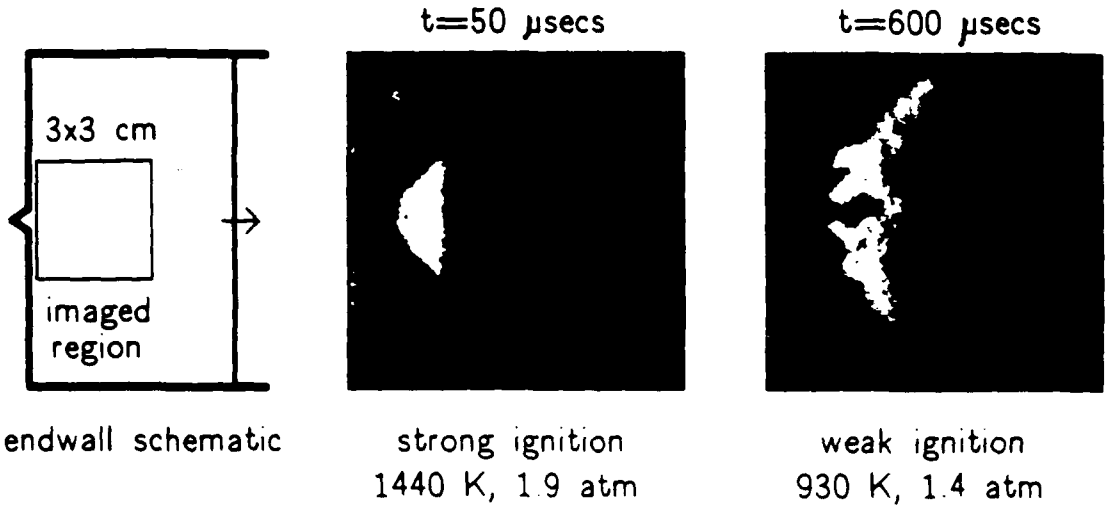

Figure 3. PLIF imaging in a shock tube.

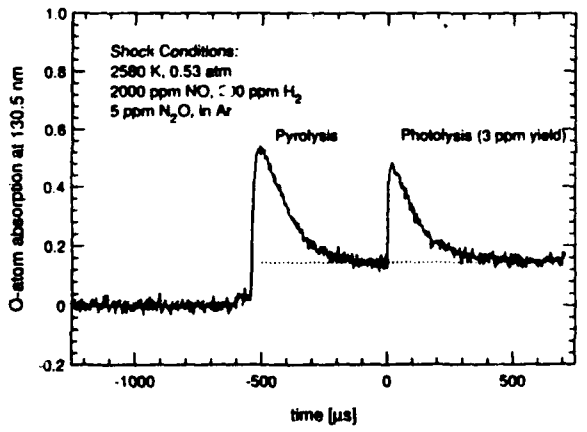

Figure 4. Photolysis shock tube data.

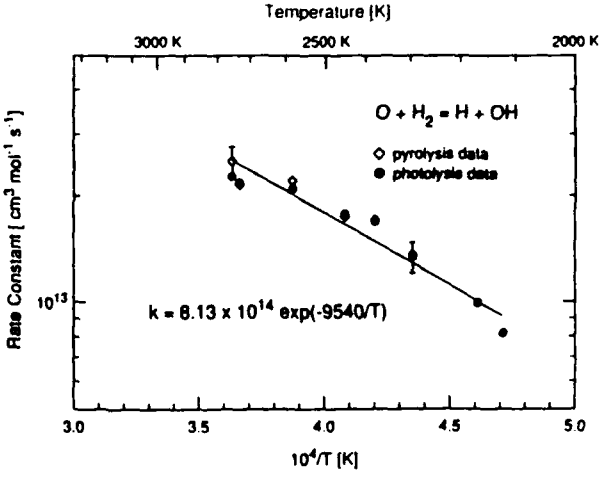

Fig. 5. Rate coefficient results.

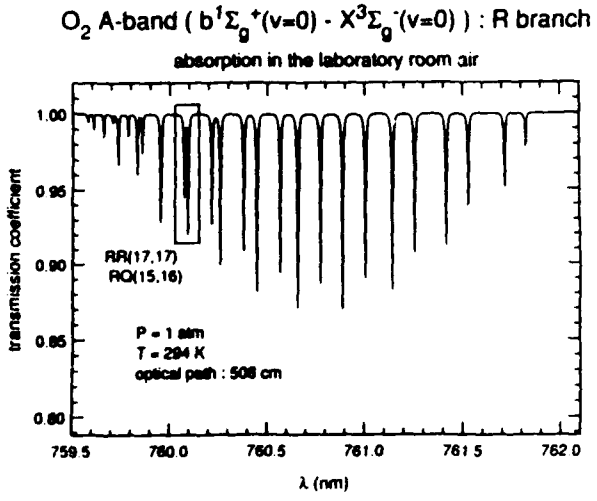

Figure 6. Computed O_2 absorption spectrum.

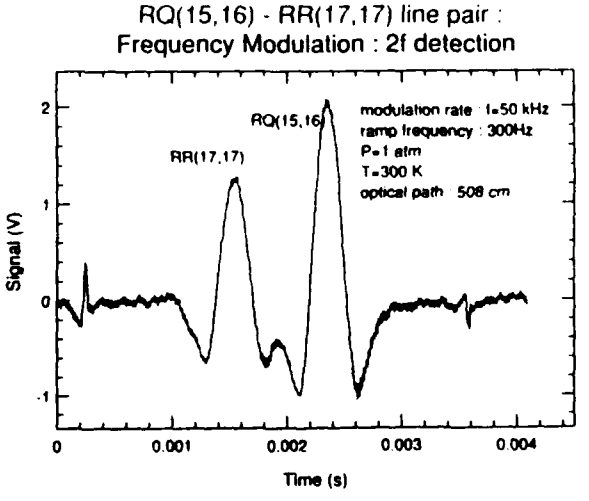

Fig. 7. FM data for O_2 absorption.

TWO DIMENSIONAL COHERENT ANTI-STOKES RAMAN SCATTERING WITH APPLICATION TO THE HYDROGEN ARCJET

EDWARD J. BEITING (PRINCIPAL INVESTIGATOR)

The Aerospace Corporation
P. O. Box 92957
Los Angeles , CA 90009

SUMMARY/OVERVIEW

This is an experimental program to extend the utility of coherent anti-Stokes Raman spectroscopy (CARS) as a diagnostic of flows and plasmas. Pump and Stokes radiation focused into a sheet produces a line of anti-Stokes radiation in the cross section of a flow. The anti-Stokes radiation detected with a multichannel array provides one angle of projection data. A cross section of an asymmetrical region is calculated from projection data taken at several angles using tomographic algorithms. Only one projection is required to reconstruct the cross section of a cylindrically symmetric flow. This technique allows the measurement of field maps of internal state distributions (temperatures) and number densities. Currently, CARS is restricted to collecting data sequentially at single points in space. This first year of work was devoted to equipment acquisition, apparatus design and construction, computer algorithm development, and collection of initial data.

TECHNICAL DISCUSSION

METHOD

In the CARS process, three fields $E_1(\omega_1)$, $E_2(\omega_2)$, and $E_3(\omega_3)$ impinge on a medium and mix through the third order nonlinear susceptibility χ_{ijkl} to generate a fourth wave $E_4(\omega_4)$ at a frequency ω_4. If we assume the input fields are plane monochromatic waves propagating in the z direction with aligned polarizations, and the medium has no spatial symmetry, then χ_{ikjl} can be written as a scalar and the solution of Maxwell's equations with a nonlinear polarization source term yields

$$\frac{\partial^2 E_4}{\partial z^2} + 2ik_3 \frac{\partial E_4}{\partial z} = -4\pi \left(\frac{\omega_4}{c}\right)^2 \chi(\omega_1,\omega_2,\omega_3) E_1 E_2^* E_3 \exp(i\Delta k z) \qquad (1)$$

where $\Delta k = 2k_1 - k_2 - k_3$ and $k \equiv n\omega/c$. Assuming a solution of the form $E_4(z) = E_4^0(z)\exp(ik_4 z)$ and noting $\Delta k << 2k_3$ for phasematched geometries, the spatial variation of E_4^0 is small and the second derivative can be ignored. Accordingly, the spatial variation of the amplitude of the CARS field can be written

$$\frac{dE_4^0}{dz} = K(\omega_4)\chi(\omega_1,\omega_2,\omega_3) E_1 E_2^* E_3 \exp(i\Delta k z) \qquad (2)$$

where $K(\omega_4)$ is a known function of ω_4. This expression can be simplified further using the following assumptions which are valid for most experimental implementations of CARS: $\Delta k = 0$ (phasematched waves); the amplitudes of E_1, E_2, and E_3 are independent of z over the region they coherently interact; $E_1(\omega_1) = E_3(\omega_3)$; and $\omega_1 = \omega_3$. Then Eq. (2) becomes

$$E_4^0(\omega_4) = K(\omega_4)E_1^2E_2^* \int \chi(\omega_1,\omega_2)dz. \tag{3}$$

Noting $I_4(\omega_4) = \frac{n_4 c}{8\pi}|E_4^0(\omega_4)|^2$, the CARS intensity can be written

$$\tilde{I}_4(\omega_4) = A(\omega_4)\left(\left[\int \chi_{nr}(z)dz + \int \sum_j \frac{\delta_j}{\gamma_j}\chi_j^i(z)dz\right]^2 + \left[\int \sum_j \chi_j^i(z)dz\right]^2\right) \tag{4}$$

where $\chi_j^i(z) = a_j(z)\gamma_j/(\delta_j^2 + \gamma_j^2)$, $\delta_j = \Omega_j - (\omega_1 - \omega_2)$, Ω_j is a Raman resonance frequency, χ_{nr} is the bulk nonresonant susceptibility, γ_j is the halfwidth of the resonance, a_j is the line strength parameter, $A(\omega_4)$ is the amplitude, and the sums are taken over all Raman resonances.

If the lasers are focussed into a thin sheet with a transverse coordinate x and ω_2 is tuned such that δ_j is large for all resonances then the signal that results is due primarily to the interaction of the waves with the nonresonant susceptibility. Then a projection in terms of the molecular density is obtained:

$$P(x) \equiv [\tilde{I}_4(\omega_4)]^{\frac{1}{2}} = \int \chi_{nr}(x,z)dz = \tilde{\chi}_{nr}\int \tilde{n}(x,z)dz \tag{5}$$

where $\tilde{\chi}_{nr}$ is a known constant and $n(z)$ is the number density of the gas. A reconstruction from this projection yields a map of the density directly.

Now if ω_4 is chosen such that $\delta_j = 0$ for a strong resonance that is isolated from neighboring resonances ($\Omega_j - \Omega_{j\pm1} >> \gamma_j$) then $\chi_j^i >> \chi_{nr}$ and only the last term in Eq. (4) contributes:

$$P(x) \equiv [\tilde{I}_4(\omega_4)]^{\frac{1}{2}} = \int \chi_j^i(x,z)dz. \tag{6}$$

Noting that $\chi_j^i \propto n(x,z)\Delta_j(x,z)$ one can obtain a spatial map of Δ_j, the population difference between the two states in the Raman resonance j. In thermal equilibrum this defines a temperature. Under nonequilibrium conditions, measuring $\Delta v = 1$ transitions for a line from each vibrational level starting with v = 0 allows spatial maps of the population of the vibrational energy levels to be constructed.

PROGRESS

Work was begun this fiscal year and was partitioned into two tasks: the construction of an experimental apparatus to test the feasibility of the concept and software development to acquire and analyze the data. The experimental development was divided into three subtasks: 1) Stokes laser development; 2) hydrogen source and vacuum chamber design and construction; 3) detection system selection, integration and installation. These three subsystems are being assembled in the space of a single 4' × 8' optics table. Component layout is shown in Figure 1.

Initial tests are being made using a grazing incidence dye laser oscillator. This configuration lends itself to multiple wavelength operation by splitting the tuning mirror into several sections. Currently, the laser output is the zeroth order reflection off the diffraction grating. This output coupling scheme is not efficient in surpressing amplified spontaneous emission (ASE) but ASE is desirable in this application to excite multiple Q-branch Raman transitions. Using LDS 698 dye in methanol and operating the laser at 683 nm, the amplifier has an efficiency near 15 percent. The second harmonic from a Nd:YAG laser with an unstable resonator longitudinally pumps the dye amplifier producing a Stokes beam with an annular cross section. This output is expanded to an outer diameter of 8 mm using a telescope. The expansion telescope between the dye oscillator and amplifier defines the Stokes beam divergence.

Choosing pump and Stokes beams with an annular cross section rather than beams with Gaussian profiles serves to increase the dynamic range of the detection system when probing a flow with a circular cross section. The CARS signal scales quadratically with interaction length and this interaction length varies from the full diameter of the flow at the center to zero at the edge. Therefore, an ideal profile of a beam focussed into a flat sheet will have its maximum intensity on the edges rather than at the center. An annular beam focussed by a cylindrical lens approximates this ideal better than a Gaussian beam.

A small (12" × 12" × 30") rectangular vacuum chamber was built to house the hydrogen flow. For collinear phasematching, the Stokes and pump beams must be overlapped in vacuum to avoid the creation of CARS signals through the nonresonant susceptibility of the ambient. This chamber is fitted with enough electrical feedthroughs to operate a rotation stage, a fast pulse value, and an electric discharge. Additional ports are used for rotary feedthroughs, gas inlets, vacuum gauging, and optical access. To minimize the required pumping speed, a pulsed solenoid valve will be used as a source of hydrogen. A suitable valve has been acquired and driver circuitry for this valve was built inhouse.

The detection system consists of a 2D intensified CCD camera attached to a half meter spectrograph. A Photometric CCD system was purchased with a PM512 detector. This system has a very low dark count rate but is not capable of single photon detection. Accordingly, a GEN2 microchannel plate intensifier will be mated to the CCD camera. The intensifier uses a P46 phosphor rather than the standard P20 phosphor to avoid possible saturation effects.† The P46 phosphor is 3× to 5× less efficient than the P20 phosphor. However, a luminous gain of less than 100 is required to acheive single photon detection whereas GEN2 intensifiers typically have luminous gains of 10^4. The intensifier reduces the linear spatial resolution of the CCD system by a factor of about two. This is not important for this application. However, the intensifier also decreases the dynamic range which may be troublesome for some experiments.

The first spectrum from this apparatus is shown in Figure 2. The chamber was evacuated and filled with hydrogen. Stokes and pump beams with annular profiles were combined using a dichroic mirror inside the chamber and focussed into a flat sheet with a width of 8 mm using a 300 mm focal length cylindrical lens. The beams were recollimated using another cylindrical lens and relayed to the spectrograph. As the data acquisition software for the CCD system was not completed, this spectrum was recorded using a PAR OMA system with a SIT vidicon detector. The Raman transitions shown in the figure were excited only by the residual ASE from the dye laser. The line marked "nonresonant susceptibility" is the signal created by the narrowband laser output through χ_{nr} of hydrogen. This line can be placed anywhere in the spectrum by tuning the dye laser. At room temperature, the Q(1) resonant susceptibiltiy is $\approx 10^3$ that of the nonresonant susceptibility. The Q(1) line shown in Figure 2 is saturating the OMA detector.

As the Photometrics system was only recently delivered, effort on software development centered on writing a versatile data analysis and display program. Approximately 60 percent of this program is now operating on our VAX computer. It is an interactive program containing sections for: data import; creation, calibration, and filtering of projections and their display; reconstruction of both data and phantom projections; statistical study of both the projections and reconstructions; 3D surface and contour displays of reconstructions.

Plans for the remainder of the fiscal year include the construction of the reference channel, the writing of the data acquisition and pixel manipulation software, and the acquisition of calibration and single projection data from a pulsed supersonic cylindrically symmetric flow of hydrogen.

---

†D.R. Snelling, G.J. Smallwood, R.A. Sawchuck, *Appl. Opt.* **28**, 3226 (1989).

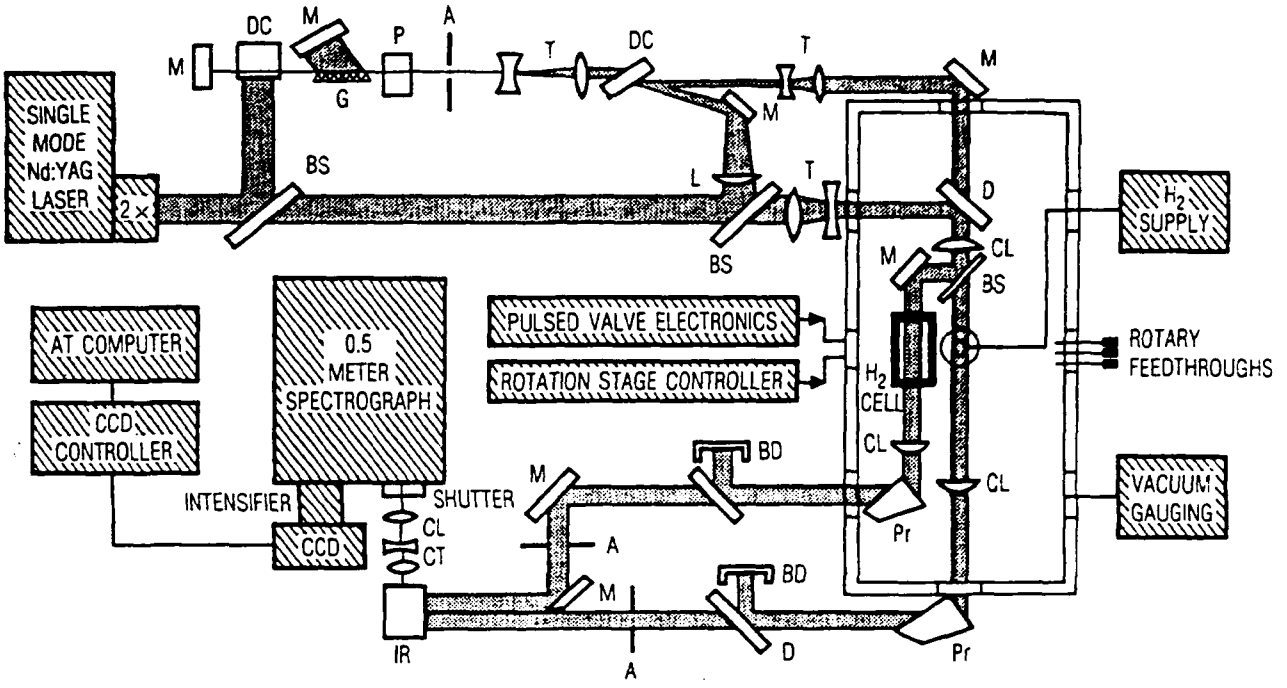

Figure 1. Experimental configuration used to study CATCARS concept. CODE: A, aperture; BD, beam dump; BS, beam splitter; CL, cylindrical lens; CT, cylindrical telescope; D, dichroic mirror; DC, dye cell; IR, image rotator; G, diffraction grating; L, spherical lens; M, mirror; P, polarizer; Pr, prism; T, spherical telescope; 2X, doubler.

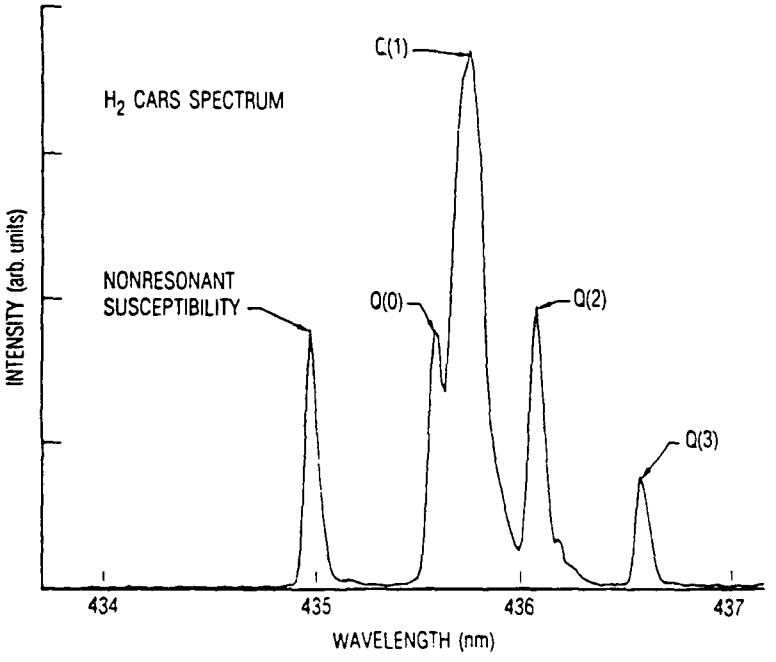

Figure 2. CARS spectrum of room temperature H_2. Collinearly phasematched Stokes and pump beams where focussed into an 8 mm wide flat sheet. All H_2 transitions were excited by ASE from the dye laser. The dye laser was tuned off resonance to generate the CARS signal to the left of the Q-branch transitions through the nonresonance susceptibility.

TITLE: ENERGY CONVERSION DEVICE DIAGNOSTICS

Principal Investigator: B.N. Ganguly

WRDC/POOC-3
WPAFB OH 45433-6563

SUMMARY/OVERVIEW: The two most important parameters of interest for the characterization of the transport properties of near equilibrium plasmas are the reduced electric field E/n, where E in the electric field and n is the gas density, and Te, the electron temperature. Due to the dependence of the transport properties on E/n and Te, the knowledge of these two parameters permits development of a discharge model that can quantify the interelectrode loss processes. The current emphasis of the task is to investigate the range of applicability of plasma emission spectroscopy and Rydberg State Stark spectroscopy to permit measurement of electron temperature (or excitation temperature) and electric field, respectively, in quasi-equilibrium and equilibrium alkali plasmas. These measurements are made with high spatial resolution and deviations from near equilibrium caused by boundary effects can also be observed.

AUTHORS: B.N. Ganguly and S.D. Marcum

TECHNICAL DISCUSSION:

A. Effect of Radiative Cascade on Electron Excitation Temperature Measurement-The electron temperature (excitation temperature) measurement in equilibrium (quasi-equilibrium) plasmas are usually obtained from the emission line intensity ratios or Boltzmann plot method[1]. These procedures strictly are valid only for measurements based on high principal quantum number states, since the population densities of these high n states are in Saha equilibrium. The emission intensities from high n states are weak, because the excitation cross-section as well as the A coefficient decrease rapidly with increasing n. Accurate intensity measurements are usually feasible only for lower n states whose population distribution may deviate significantly from the equilibrium distribution.

In this work, the measured emission intensities from a hot cathode (1100 k), low current density, low pressure argon-cesium discharge has been compared with the calculated intensities obtained from a detailed balance rate equation of the form

$$\frac{dn(j)}{dt} = Ke\ ne\ ng + \sum_{i>j} n(i)Aij - n(j) \sum_{j>k} Ajk \quad -(1)$$

and

$$Ijk = Ajk\ n(j)\ (E_j - E_k)\ \text{watts/cm}^3$$

The population density of the upper state is obtained from the steady state solution of equation (1). The right hand side terms represent election impact excitation, radiative cascade and loss due to spontaneous emission. The infinite set of equations (1) was reduced to a finite set that included excited states up to n=10 (all L and J) for a total of 53 cesium levels. The electron impact excitation cross-sections used in this calculation was obtained by first order many body theory[2]. The electron impact excitation rates are calculated by numerically integrating cross-sections over assumed Maxwellian distributions for a range of temperatures.

The radiative cascade contribution to the intensity is found to be as high as 30 percent for low n,l states. This effect can introduce large errors for temperature measurement based on the intensity ratio of two lines. The temperature measurement using Boltzmann plot method will also show departure from a single valued temperature even for a thermal equilibrium plasma. The radiative cascade contributions to the intensity for nD to 6P, nP to 6S and nS to 6P emission lines are shown in Figure 1.

The visible and near uv emission spectrum obtained from the hot cathode argon-cesium discharge is shown in Figure 2. The calculated best fit normalized intensities are also shown in the figure. The calculated intensity ignores radiation trapping and, therefore, the predicted intensities for low n transitions to the ground state are expected to be greater than the measured intensities. The electron excitation temperature corresponding to the best fit is found to be 4900±500K.

B. Rydberg State Stark Spectra of Cesium-The electric field values in thermionic cathode discharges are expected to be low (≤100v/cm). The hydrogenic Stark broadening approximation, which permits low plasma electric field measurements for near degenerate atomic species[3], cannot be applied to high Z alkali atoms. In order to test the sensitivity of the Rydberg state spectrum of cesium to applied electric field, the high n spectra have been measured in different discharge environments (1 torr argon + 0.03 torr cesium) with applied electric fields from 5v/cm up to 40v/cm. The Stark spectra, obtained by 6S to nP laser excitation, from n=25 up to 29 are shown in figure 3 and figure 4 with applied electric field 5 v/cm and 10 v/cm, respectively. The measured spectra show the field dependent sensitivity of the Stark energy shift and intensity redistribution from $nP^{1/2}$ to $nD^{3/2}$ and $nS^{1/2}$ states.

The Rydberg State Stark structure has been calculated by the procedure developed by Zimmerman et al[4]. The calculated energy levels agree with the experimental data within the accuracy of the measurement (±0.15cm^{-1}), whereas, the Stark intensity redistribution shows the general trend but does not fit the measured data very well. This could be a consequence of the electric field dependant nodal location shift of the Stark eigenstates, the intensity is

very sensitive to the relative phase shift of the nodes. The high n Stark energy levels, on the other hand, do not depend significantly on the details of the nodal structures of the wavefunction. The radial matrix integration procedure may have to be revised to obtain good agreement between the experimental and the calculated intensities.

The measured cesium Rydberg State Stark spectra show that it is possible to obtain plasma electric field values with ± 5v/cm resolution.

REFERENCES

1. H. Griem, Plasma Spectroscopy, pp 267-278, McGraw-Hill (1964)

2. R.E.H. Clark, J. Abdallah Hr., G. Csanak, J.B. Mann and R.D. Cowlan, Los Alamos Manual LA-111436-M, Vol 1 and 2 (1988).

3. B.N. Ganguly and A. Garscadden, Applied Physics Letter, 46, 540, (1985).

4. M.L. Zimmerman, M.G. Littman, M.H. Kash and D. Kleppner, Phys. Rev: A20, 225 (1979).

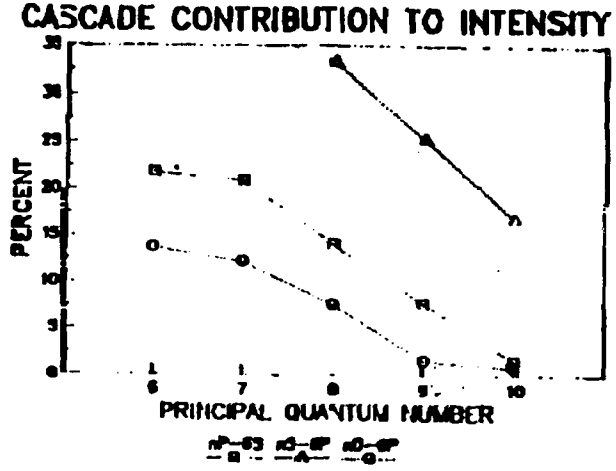

FIGURE 1

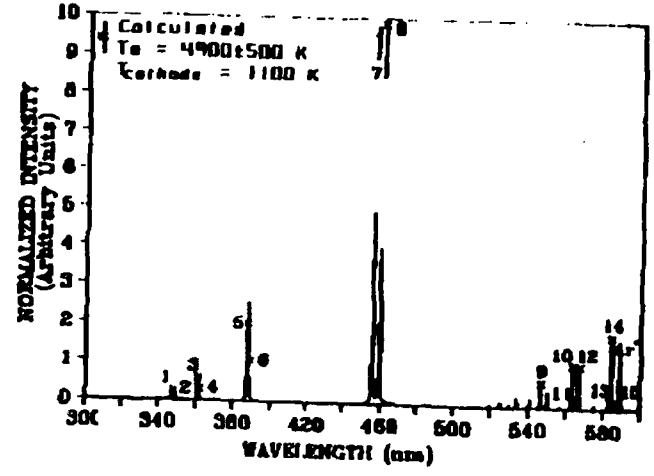

FIGURE 2

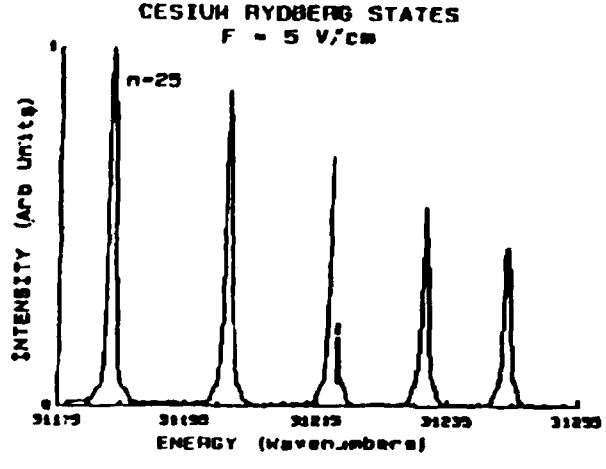

FIGURE 3

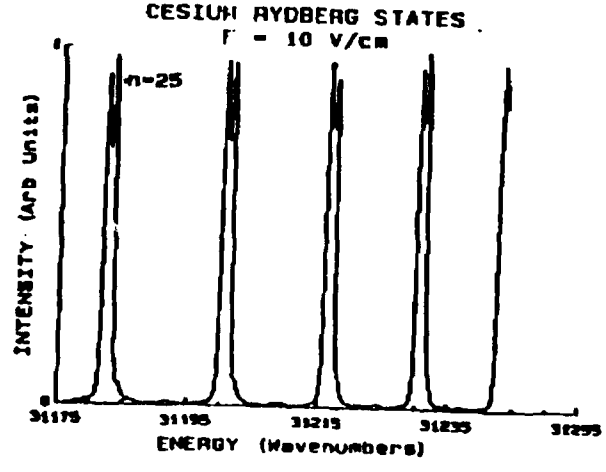

FIGURE 4

NOVEL NONLINEAR LASER DIAGNOSTIC TECHNIQUES

(AFOSR Contract No. F49620-88-K-0003)

Principal Investigators: David L. Huestis, Gregory W. Faris, and Jay B. Jeffries
Collaborating Staff: Mark J. Dyer

SRI International
Molecular Physics Laboratory
333 Ravenswood Ave.
Menlo Park, CA 94025

SUMMARY/OVERVIEW:

At SRI we have been developing the approach called two-photon-excited fluorescence (TPEF) or two-photon LIF for quantitative detection of "difficult" atoms, molecules, and free radicals, such as N, O, F, and Cl atoms, and F_2 molecules. By "difficult" we mean that the usual one-photon LIF technique is not possible using visible or near-uv lasers. Under the current AFOSR contract we have been developing multiphoton techniques for the quantitative detection of F and F_2. We describe in detail our recent work on detection of F atoms and F_2 molecules using vuv radiation generated by Raman shifting an ArF laser.

During the the next AFOSR contract our research will concentrate on enhancing and improving the TPEF technique by (1) extending the range of species that can be detected, to include atomic ions, through improvements in vuv laser sources and excitation schemes and (2) increasing the utility, and the amount of information that can be obtained from TPEF detection by utilizing the newly developed approach of amplified spontaneous emission from two-photon excited atoms.

TECHNICAL DISCUSSION

Multiphoton Detection Techniques for F and F_2

Previous work under AFOSR contract has led to the demonstration of sensitive two-photon-excited fluorescence-detection schemes for atomic fluorine [1,2] and molecular fluorine [3,4]. Both demonstration experiments were performed with relatively low laser energies (~10 μJ at 170 nm for F and ~50-200 μJ at 207 nm for F_2) generated by doubling and/or Raman-shifting the output of a tunable Nd:YAG-pumped dye laser. Because the sensitivity of the two-photon-excited fluorescence detection depends on the square of the laser power, it is advantageous to have larger laser powers.

We are working on a new approach for the production of higher powers for F and F_2 detection. There is a coincidental overlap of the tuning range of the ArF excimer laser when twice anti-Stokes Raman-shifted in HD gas and the energy for two-photon excitation of the $^2D^o_{3/2} \leftarrow {}^2P^o_{3/2}$ fine structure line of atomic fluorine. Additionally, there are two-photon coincidences for the $F^1\Pi_g \leftarrow X^1\Sigma^+_g$ v' = 3 and v' = 2 transitions in molecular fluorine with the first Stokes Raman-shifted lines of ArF in D_2 and HD, respectively. The apparatus used for this

scheme is shown in Figure 1. The laser used is a Lambda-Physik (150 MSC) laser with oscillator and amplifier discharge chambers. The oscillator provides ~1.3 mJ energy in ~1 cm^{-1}. When operated as a standard oscillator injection-locked amplifier pair, the spatial mode was of inadequate quality for multiple-order anti-Stokes Raman shifting. For this reason, the laser was modified to allow for spatial filtering between the oscillator and amplifier, the amplifier unstable-resonator cavity was removed, and the filtered oscillator pulse was triple-passed vertically through the amplifier discharge chamber, taking advantage of the longer vertical aperture. This resulted in somewhat lower output power (~60 mJ), but a large enhancement for the final Raman-shifted powers. Careful adjustment of the MgF_2 windows allowed good amplitude stability and a 200:1 polarization of the output. Because the gain coefficient in HD is quite low, a liquid nitrogen temperature Raman cell, shown in Figure 2, was constructed. This increases the gain coefficient due to redistribution of the HD ground state population and reduces the losses as impurities are frozen out. The HD cell and the liquid nitrogen jacket are enclosed in an outer, evacuated cell which provides temperature insulation, prevents condensation on the inner cell windows, and provides an evacuated path for the vacuum ultraviolet light that is produced.

We have examined the capabilities of this system for Stokes and anti-Stokes production for both HD and D_2. Using a vuv spectrometer to resolve the anti-Stokes orders at least 8 anti-Stokes orders were observed when shifting in D_2 (132 nm) and 4 anti-Stokes orders in HD. Some measured Stokes and anti-Stokes orders are shown in Figure 3. For both HD and D_2, stimulated rotational Raman scattering limits the main vibrational lines at lower pressures. The measured power at 170 nm for F atom detection is 1 mJ, while >6 mJ is generated at 205 nm for F_2 detection. Demonstration measurements of F atom and F_2 detection using this source are in progress.

UV and VUV Generation and Detection Techniques

During the next contract period we will develop two photon resonant difference frequency generation and two-color two-photon excitation as techniques for short wavelength detection and apply these to detection of a number of interesting species, including C^+, Si^+ and F. The well developed approaches for short wavelength generation (Raman shifting, doubling, and nonresonant mixing) have important limitations that confine their use to specific wavelength ranges. Perhaps the most important recent development has been the introduction of the β-BaB_2O_4 (BBO) and LiB_3O_5 (LBO) crystals which provide convenient doubling from 205 to 250 nm and nonresonant mixing to about 180 nm. To obtain broadly tunable wavelengths below about 180 nm, we plan to investigate two-photon resonant difference frequency generation in gases (Xe, Kr, and H_2) using an excimer laser and a tunable dye laser. This four wave mixing process uses the high energies in the excimer and dye lasers to give relatively high (microjoule) energies in the vuv (105-175 nm) sufficient for subsequent two-photon excitation. It will also take advantage of the good spatial mode quality of the ArF laser source describe above.

Laser-Excited Amplified Spontaneous Emission

The use of laser-excited amplified spontaneous emission (ASE) to measure velocity and species concentrations in reacting flows will be a new task during the next contract period. These ASE measurements can be made on gas flows having only single-port access;[5] the signal is collected along the same beam path as the excitation laser uses. The large collimated signal makes this method attractive for reactive environments with substantial background optical emission. The ASE gain, divergence, and signal loss mechanisms all must be understood for quantitative concentration measurements. Velocity determination is possible from the wavelength or

wavelength distribution of the signal; assessment of the feasibility of this approach requires research on the gain narrowing of the Doppler lineshape. The ASE process is also a loss mechanism for multiphoton laser-induced fluorescence and resonance-enhanced multiphoton ionization so that quantitative measurements on atoms using these techniques must account for ASE losses.

REFERENCES:

1. W. K. Bischel and L. E. Jusinski, Chem. Phys. Lett. **120**, 337 (1985).

2. G. C. Herring, M. J. Dyer, L. E. Jusinski, and W. K. Bischel, Opt. Lett. **13**, 360 (1988).

3. G. W. Faris, M. J. Dyer, W. K. Bischel, and D. L. Huestis, Annual Report AFOSR Contract No. F49620-88-K-0003, SRI International Menlo Park, CA (April 1988).

4. G. W. Faris, M. J. Dyer, D. L. Huestis, and W. K. Bischel, in preparation.

5. A. D. Sappey and J. B. Jefferies, Appl. Phys. Lett. **55**, 1182 (1989).

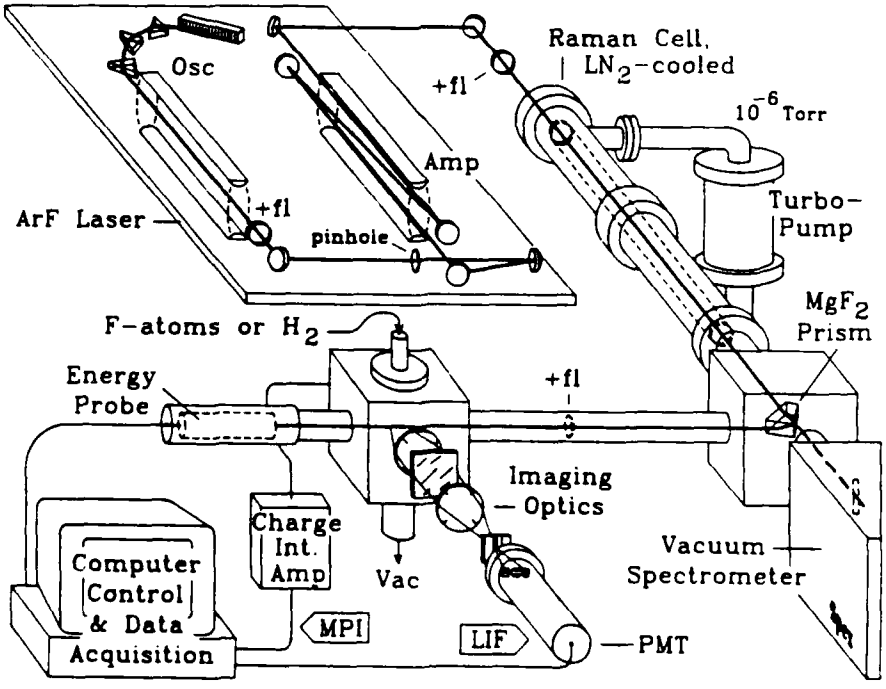

Fiugre 1. Experimental apparatus for VUV multiphoton LIF and MPI detection.

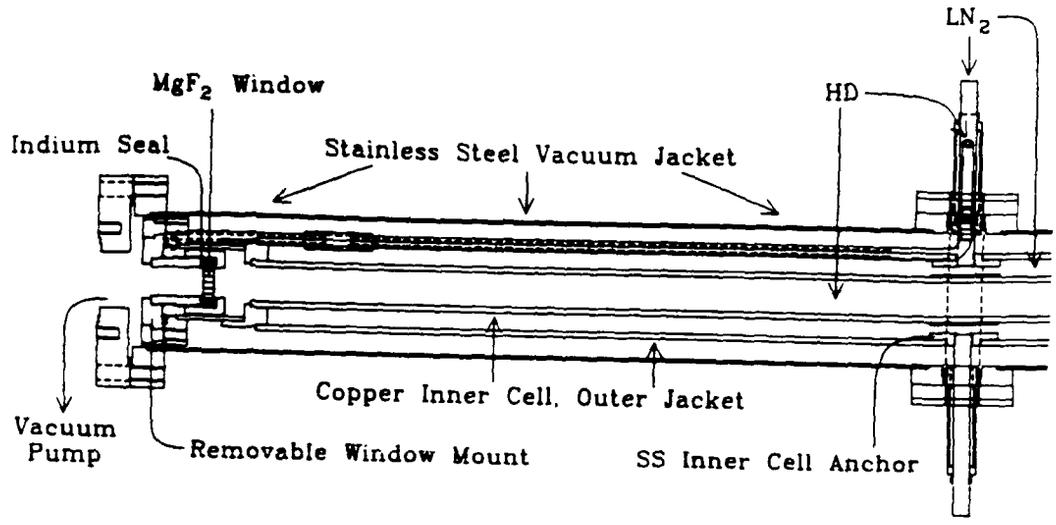

Figure 2. Cut-away view of liquid nitrogen cooled Raman cell.

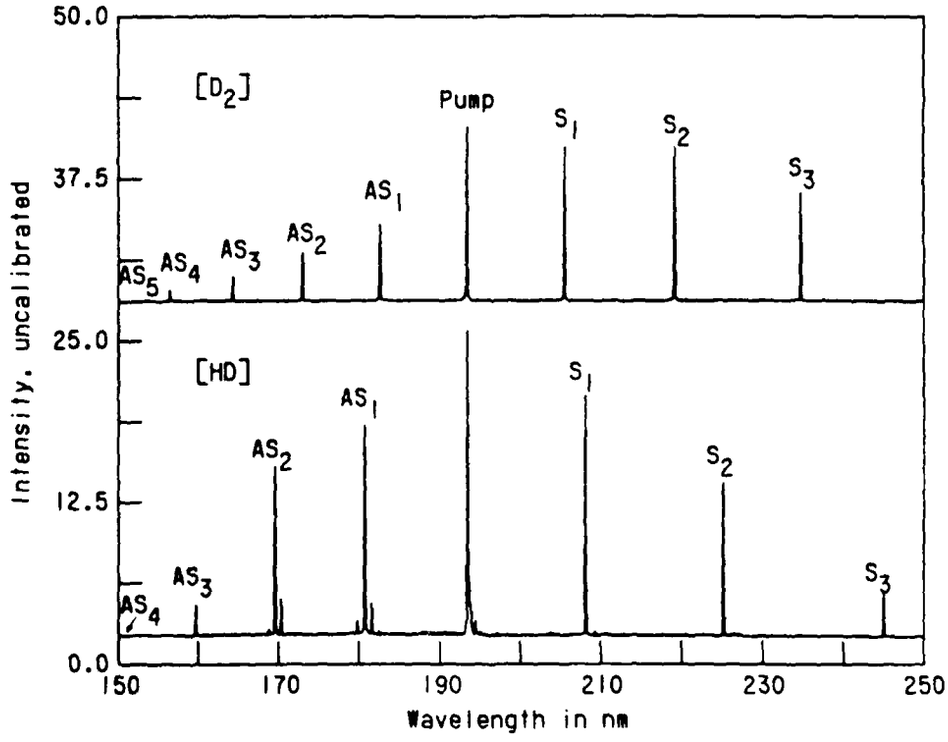

Figure 3. Stimulated Raman frequency conversion in D_2 (298° K) and HD (77° K) for a density of 6 amagat. Relative intensities have not been corrected for the spectral response of the photomultiplier, filter, and spectrometer.

ASYNCHRONOUS OPTICAL SAMPLING FOR LASER-BASED COMBUSTION DIAGNOSTICS IN HIGH-PRESSURE FLAMES

AFOSR Grant No. AFOSR-84-0323

Galen B. King
Normand M. Laurendeau
Fred E. Lytle

Flame Diagnostics Laboratory
School of Mechanical Engineering
Purdue University
West Lafayette, IN 47907

SUMMARY/OVERVIEW:

This research is concerned with the development and subsequent testing of a new laser-based combustion diagnostic for the quantitative measurement of both major and minor species concentrations in high-pressure flames. The technique, called Asynchronous Optical Sampling (ASOPS), is a state-of-the-art improvement in picosecond laser spectroscopy. ASOPS is a pump/probe method which will allow determination of both electronic quenching and state-to-state relaxation rates. Such information is necessary for quantitative application of both laser-induced and laser-saturated fluorescence at high pressures. The specific goal of the project is to develop and prove the viability of the ASOPS technique as a practical, quenching independent diagnostic. This will be achieved through measurements of atomic sodium, indium and the hydroxyl radical in simple flames.

TECHNICAL DISCUSSION

The ASOPS process is illustrated in Fig. 1a, which shows the excited state population produced by several pump pulses over which the temporal positions of several probe pulses have been superimposed. Each successive probe pulse is delayed in time relative to the pump pulse train by a constantly increasing duration which is determined by the beat frequency of the system. Thus each probe pulse samples the excited-state population at a slightly later time than the immediately preceding pump pulse. This is equivalent to varying the optical delay line in a conventional pump/probe instrument. The entire process of Fig. 1a repeats itself when the cumulative delay equals the period of the pump laser. Hence any modulation of the probe beam, resulting from the creation and subsequent decay of the excited state, repeats at the beat frequency of the system. Therefore, in contrast to a conventional pump/probe instrument, there is no need to amplitude modulate either beam to employ synchronous detection.

Figure 1b illustrates the change in intensity which occurs owing to stimulated emission from the excited state population shown in Fig. 1a. The net effect of the ASOPS technique is that a small amplitude waveform, which is directly related to the fluorescence decay of the species under study, is impressed onto the probe laser intensity. In essence, a temporal transformation of the excited-state decay is performed with the time scaled by the factor $[f_{pump}/(f_{pump}-f_{probe})]$, where f is the repetition rate of the two lasers. The ASOPS technique is thus the optical analog of a sampling oscilloscope.

A block diagram of the current ASOPS instrument is shown in Fig. 2. The pump and the probe beams are derived from frequency-doubled dye lasers, which are synchronously-pumped by frequency-doubled, mode-locked Nd:YAG lasers. The mode-locking frequencies are generated by two frequency synthesizers operated in a master-slave (i.e. phase-locked) configuration to minimize drift in the beat frequency of the system. The probe intensity is monitored by a photodiode subtraction circuit the output of which is amplified and directed to the signal processing system. Triggering the signal processing system is accomplished by frequency doubling and electronically mixing the synchronous voltage output from each synthesizer.

Although the ultimate goal of the ASOPS project is to measure the hydroxyl radical in high-pressure flames, studies of other species have been needed to lay a groundwork for this difficult task. In previous papers,[1,2] we reported initial ASOPS measurements of Rhodamine B in methanol. Flame studies began with measurements of the relative number density of atomic sodium in an atmospheric $CH_4/O_2/N_2$ flame.[3,4] Figure 3 shows a more recent ASOPS signal for sodium. The pump beam (20 mW) is tuned to the $3S_{1/2} \rightarrow 3P_{3/2}$ transition (589.0 nm) and the probe beam (5 mW) is tuned to the $3P_{1/2} \rightarrow 5S_{1/2}$ transition (615.4 nm). A peak SNR of 39:1 was obtained after 256 averages on the digitizing oscilloscope.

Temporal studies of the sodium results have also been completed. A rate equation analysis was applied and the resulting curve fit to the data of Fig. 3 yields an electronic quenching rate $Q_e=1.72\times10^9$ sec^{-1}. This value corresponds favorably with literature values ranging from 1.4×10^9 sec^{-1} reported by Takubo et al[5] in a propane/air flame to 2.1×10^9 sec^{-1} reported by Russo and Hieftje in a natural-gas/air flame.[6]

We have now extended the ASOPS technique to the ultra-violet with the measurement of atomic indium in an atmospheric C_2H_2/air flame. Both the pump and the probe beams were set to the same wavelength of 303.94 nm. The ASOPS signal for atomic indium is shown in Fig. 4. This result represents the

---

[1] P. A. Elzinga, F. E. Lytle, Y. Jiang, G. B. King, and N. M. Laurendeau, *Appl. Spectrosc.* **41**, 2 (1987).

[2] P. A. Elzinga, R. J. Kneisler, F. E. Lytle, Y. Jiang, G. B. King, and N. M. Laurendeau, *Appl. Opt.* **26**, 4303 (1987).

[3] G. J. Fiechtner, Y. Jiang G. B. King, N. M. Laurendeau, R. J. Kneisler, and F. E. Lytle, *Twenty-Second Symposium (International) on Combustion*, The Combustion Institute, Pittsburgh, PA, p. 1915 (1988).

[4] R. J. Kneisler, F. E. Lytle, G. J. Fiechtner, Y. Jiang, G. B. King, and N. M. Laurendeau, *Opt. Lett.* **14**, 260 (1989).

[5] Y. Takubo, T. Okamoto and M. Yamamoto, *Appl. Opt.*, **25**, 740 (1986).

[6] R. E. Russo and G. M. Hieftje, *Appl. Spectrosc.* **36**, 92 (1982).

first UV pump/UV probe signal with the ASOPS methodology. The UV ASOPS measurement was unattainable prior to our work on enhanced efficiency of second-harmonic-generation (SHG).[7] The pump power is ~20 mW while the probe power is ~ 1 mW. The high UV powers are difficult to maintain and with the Einstein coefficient for indium approximately 1000 times that for OH, more work needs to be done to reduce the noise in the measurement before routine measurements of OH can be made.

The continuation of the UV measurements to include OH requires a large effort to improve the ASOPS SNR. The detection system is currently being redesigned to increase its bandwidth and reduce its background. Electronic and optical improvements need to be made to both the Nd:YAG lasers as well as the synchronously pumped dye lasers to reduce both amplitude and phase noise. The data collection system also needs to be upgraded to take full advantage of the speed of the ASOPS measurement.

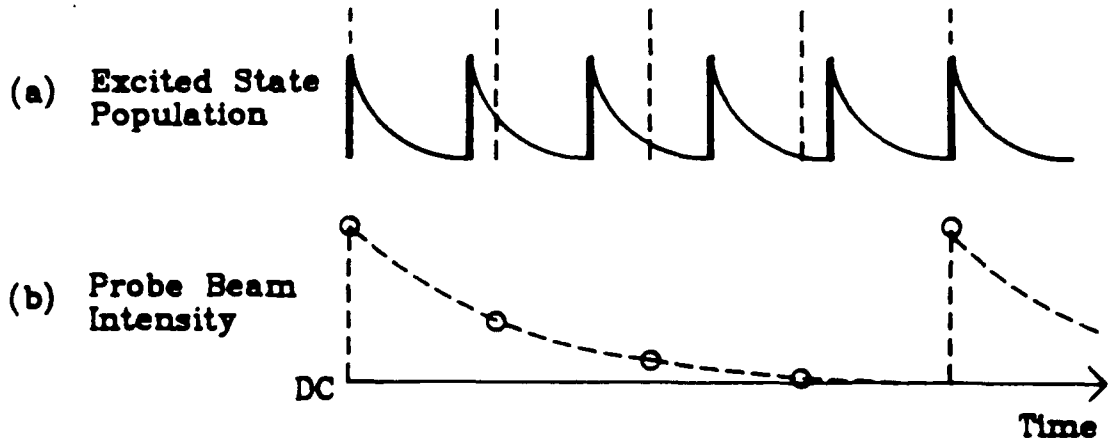

Figure 1. ASOPS timing diagram showing (a) excited state population and (b) probe beam intensity. The probe pulses in (a) are indicated by the vertical dashed lines.

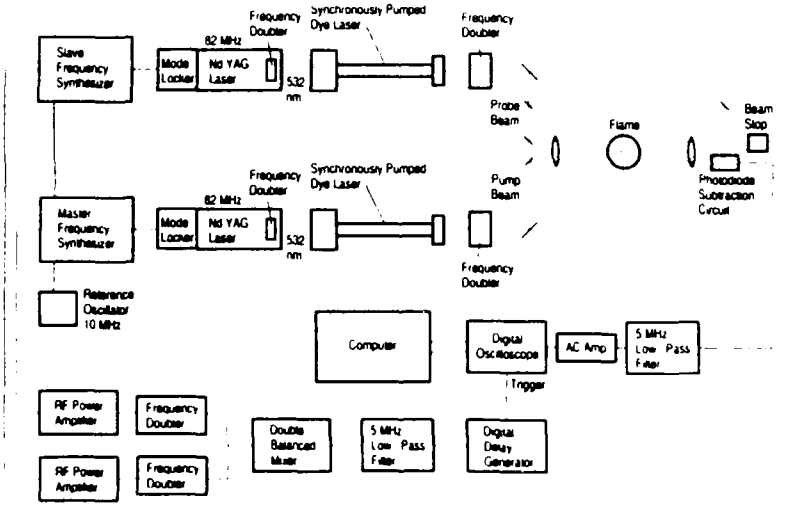

Figure 2. Block diagram of the current ASOPS instrument.

[7] G. J. Fiechtner, G. B. King, N. M. Laurendeau, R. J. Kneisler, and F. E. Lytle, *Appl. Spectrosc.* **43**, 1286 (1989).

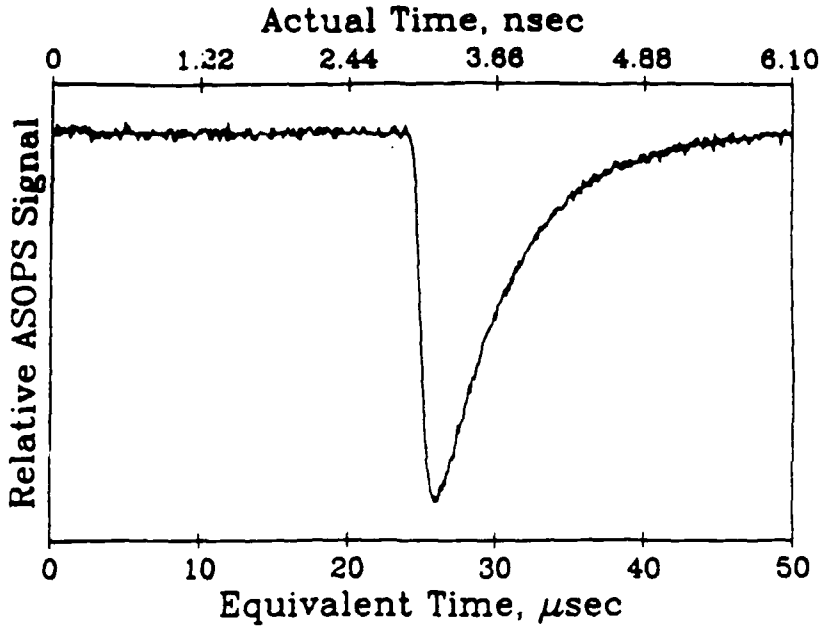

Figure 3. ASOPS signal for atomic sodium.

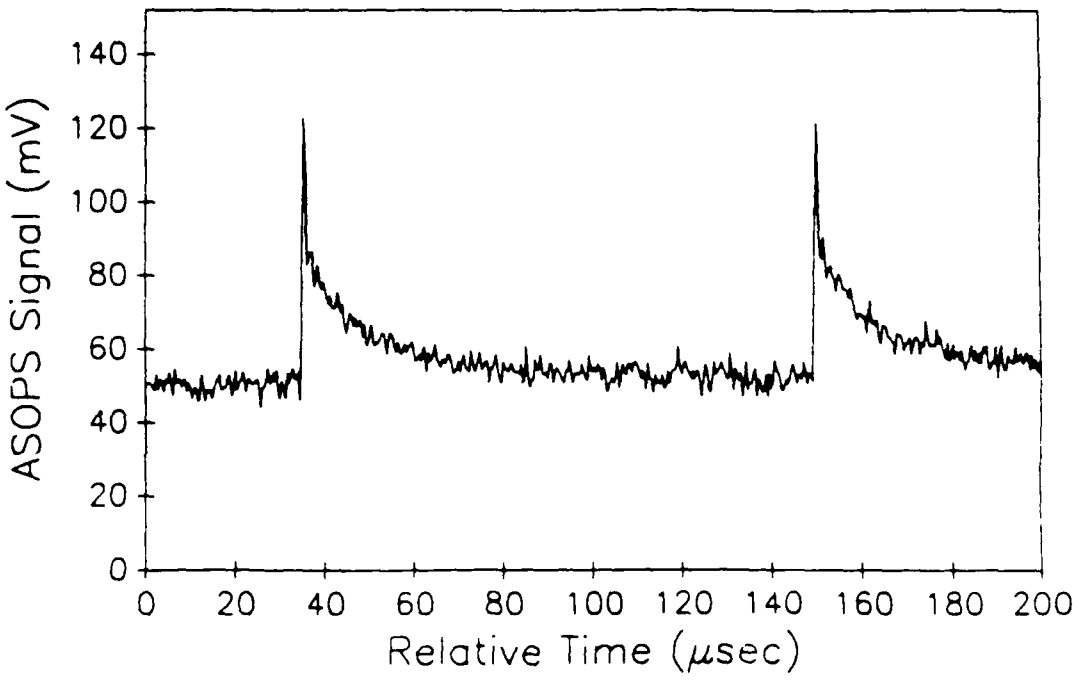

Figure 4. ASOPS signal for atomic indium.

AFOSR SPONSORED RESEARCH IN AIRBREATHING COMBUSTION

PROGRAM MANAGER: JULIAN M. TISHKOFF

AFOSR/NA
BOLLING AFB DC 20332-6448

SUMMARY/OVERVIEW: The Air Force Office of Scientific Research (AFOSR) program in airbreathing combustion currently is focused on six areas of study: supersonic combustion, reacting flow, soot, sprays, kinetics, and boron slurries. An assessment of major research needs in each of these areas is presented.

TECHNICAL DISCUSSION

AFOSR is the single manager for Air Force basic research, including programs based on external proposals and in-house work at Air Force laboratories. Airbreathing combustion is assigned to the AFOSR Directorate of Aerospace Sciences along with programs in rocket propulsion, diagnostics of reacting flow, fluid and solid mechanics, and civil engineering.

Interests of the AFOSR airbreathing combustion task are given in the SUMMARY section above. Many achievements can be cited for these interests, yet imposing fundamental research challenges remain. The objective of the program is publications in the refereed scientific literature describing significant new understanding of multiphase turbulent reacting flow. Incremental improvements to existing scientific approaches, hardware development and computer codes fall outside the scope of this objective.

Decisions on support for research proposals are based on scientific opportunities and technology needs. Current AFOSR perceptions of scientific opportunities appear in Figure 1, and areas of emphasis are indicated by arrows with positive slopes.

Major emphasis has been given to research on supersonic combustion to support hypersonic airbreathing propulsion technology. In FY87 new research efforts were directed at novel means for achieving ignition, combustion enhancement, and low-loss flameholding in supersonic combustion. FY89 saw new research in interactive control of fluid transport processes. These opportunities reflect a generic interest in interdisciplinary efforts between researchers in control theory and fluid transport behavior. For hypersonic propulsion a particular focus of interactive flow control is the investigation of means to overcome the suppression of mixing which high Mach number flows experience in relation to subsonic flows.

The behavior of single fuel droplets has been the subject of renewed research activity. Both computational and experimental capabilities appear to be poised to expand studies of spray combustion to spatial dimensions smaller than those of the droplets themselves. This research activity will be directed toward the interactions between droplets and gas-phase turbulent transport processes.

The purpose of this abstract has been to communicate AFOSR perceptions of research trends to the university and industrial research communities. However, communication from those communities back to AFOSR also is desirable and essential for creating new research opportunities. Therefore, all proposals and inquiries for fundamental research are encouraged even if the content does not fall within the areas of emphasis described herein. Comments and criticisms of current AFOSR programs also are welcome.

Air Force Basic Research
Aerospace Sciences
Airbreathing Combustion

Science Area	Trend	Decrease	Increase
Supersonic Combustion	→		Flow Control
Reacting Flow	→		Flow Control
Soot	→		
Sprays	↗		Drop-Turbulence Interactions, Nondilute Sprays Atomization
Kinetics	→		
Boron Slurries	↘		

IGNITION AND MODIFICATION OF REACTION BY ENERGY ADDITION: KINETIC AND TRANSPORT PHENOMENA

AFOSR Contract No. F49620-87-C-0081

Principal Investigators: Francis E. Fendell and Mau-Song Chou

Center for Propulsion Technology and Fluid Mechanics
TRW Space and Technology Group, One Space Park, Redondo Beach, California

SUMMARY/OVERVIEW

High-speed air breathing combustion systems necessitate the complete release of chemical energy during the relatively brief residence time of reactants within combustors of practical length: mixing, ignition, and chemical reaction must be achieved in a relatively short time. We address, from a fundamental chemical-dynamics and fluid-transport point of view, the use of both alternative, photochemical ignition (by laser irradiation) and ignition-promoting additives, in order to alter chemical-reaction pathways to achieve rapid ignition and enhanced combustion rate. We also address the influence of mixture inhomogeneity, and of departure from stoichiometric proportion in fuel/air mixtures, on the processes of ignition, flame development, and flame propagation. Chemical systems of particular interest include hydrogen/air and methane/air, often with trace amounts of carefully selected sensitizers. We seek to identify optimal circumstances [minimal input energy, minimal amount of sensitizer(s), etc.] for achieving ignition and burnup with currently available optical sources by irradiating premixtures flowing faster than the adiabatic flame speed, and by carrying out supporting approximate analyses of these experiments.

TECHNICAL DISCUSSION

Experiment - We have achieved volumetric homogeneous ignition of H_2/O_2, H_2/air, and CH_4/O_2 premixed flows in an open system at 1 atm and room temperature via ArF-excimer-laser (193-nm) photolysis of a small initial amount (0.5-2.0%) of NH_3 doping in the flow mixtures. Under the adopted procedure of mild laser focusing, optical multichannel-analyzer measurements show no discernible plasma ionic emission; hence, gaseous breakdown is precluded as a cause of ignition. At three locations, the ignition-delay times, based on the 308-nm OH-emission band, appear to be close in value; this suggests the presence of well-distributed ignition sites within the irradiated volume (~1.7x5.2x60 mm). Figure 1 shows the ignition-delay time as a function of initial NH_3 mole fraction in $H_2/O_2/NH_3$ flows for several fuel equivalence ratios. The ignition-delay time appears to be very sensitive to the initial NH_3 concentration, hence to the initial laser-energy-deposition density, and is insensitive to the fuel equivalence ratio between 0.35 and 3.0. Figure 2 shows that the minimum laser-energy-deposition density needed for ignition, ranging from 130 to 160 mJ/cm^3, is also relatively insensitive to the fuel equivalence ratio. The minimum laser-energy-deposition density increases to ~178 mJ/cm^3 for H_2/air/NH_3 flows and ~300 mJ/cm^3 for $CH_4/O_2/NH_3$ flows at the stoichiometric ratio, with corresponding minimum required NH_3 mole fraction of ~0.75% and 1.2%, respectively. The corresponding minimum radical pair (H + NH_2) density needed for ignition at the stoichiometric ratio is estimated

to be ~1.3×10^{17}, 1.9×10^{17} and 2.9×10^{17} cm^{-3}, respectively, for the three flow mixtures. The results from preliminary kinetic-modeling calculations suggest that the hot H atoms produced from the NH_3 photolysis may play an important role by enhancing the reaction $H(fast) + O_2 \rightarrow OH + O$. This leads to the observed short ignition-delay time and low minimum-energy-deposition density, relative to the values which hold for conventional thermal-ignition methods.

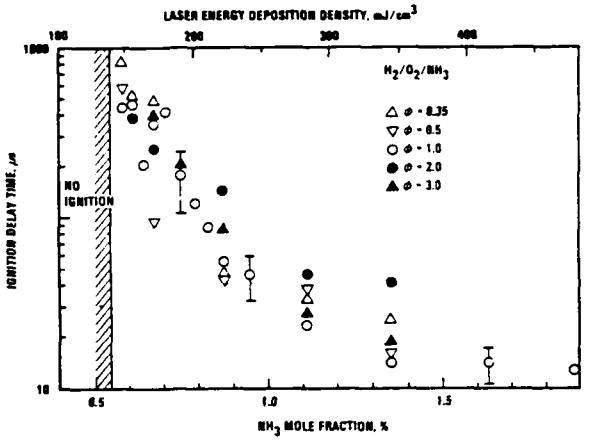

Figure 1. Ignition Delay Time in $H_2/O_2/NH_3$ Mixtures as a Function of Initial NH_3 Mole Fraction and Laser Energy Deposition Density. The Fuel Equivalence Ratios are (△) 0.35, (▽) 0.5, (○) 1.0, (●) 2.0, (▲) 3.0. The Shaded Area Indicates the Region of No Ignition.

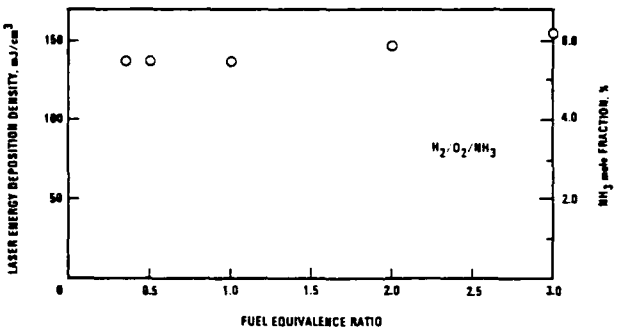

Figure 2. Minimum Laser Energy Deposition Density Needed for Ignition of H_2/O_2NH_3 Flow Mixtures at Several Fuel Equivalence Ratios

Analysis - We have discussed the deflagration-wave stabilization via postulated, temporally continuous sources (plane, line, and point) of nonintrusive energy deposition into the burned gas of a mixture flowing faster than its adiabatic flame speed (Carrier et al. 1990). Recently, we have examined the spherical flame propagation evolving from a transient, point-like, minimal-energy-deposition ignition in unburned mixture. The interplay of equivalence ratio, differing diffusivities for reactant species and heat, and flame curvature may introduce phenomena absent when the same equivalent-ratio/differing-diffusivity parameters hold for planar flames. Speculation exists (Strehlow 1984, pp. 390-392) that if the lighter reactant in a binary mixture is also stoichiometrically deficient, then the spherical-firefront speed approaches its large-flame-radius, planar-flame asymptote from higher values. However, the purportedly supportive data pertain to hydrocarbon-air flames of one-or-more-centimeter radius, which is twenty-five-or-more multiples of the 0.04-mm flamefront thickness, D/u, where D is the diffusion coefficient and u is the adiabatic flame speed. Thus, existing data, though possibly pertinent to radiative-heat-loss effects on firefront-propagation speed, seem of little relevance for flame-curvature phenomena. A need remains for spherical-flame-speed data taken at small, diffusive-scale values for the flamefront radius.

However, while some fundamental aspects of the spherical flame propagation (following the successful irradiation of a blob of premixture) remain to be resolved, we do know that the rate of flamefront propagation is characterized by the magnitude of the laminar flame speed. This highly subsonic speed is typically much less than the speed of the oncoming stream in many practical aerodynamic contexts. A very large number of energy-deposition sources, situated transverse to a stream of fast-flowing premixture, would be required to span that stream with flame, within a modest distance downwind of the plane containing the sources. Therefore, for practical purposes, attention is turned to the use of nonintrusive energy deposition in a

supersonically flowing mixture, not to initiate a flame propagation, but rather to initiate a detonation.

As background, we know that a Chapman-Jouguet (CJ) detonation can be initiated by a laser pulse in a combustible mixture of gases at an appropriate stoichiometry (Lee et al. 1978; Strehlow 1984, pp. 408-409). For some fuel-air mixtures, we know reasonably well the minimum-energy requirement, the pulse-duration requirements, and the deposition-volume requirements (Lee et al. 1978). We think that there is a broad range of pulse parameters (energy, volume, duration) over which the CJ detonation will be initiated and will propagate without transition to either a strong detonation or a weak detonation.

As further background, we know that, in a uniform channel flow at a speed that is several times the CJ detonation speed, the weak detonation (for which the downstream flow is uniform and supersonic) implies an entropy rise across the detonation that is greatly in excess of the entropy rise across a CJ detonation in the same mixture; the strong normal detonation (for which the downstream flow is uniform and subsonic) implies an entropy rise that is huge compared with that of the weak detonation. We have no reason to expect that, when successive pulses initiate successive CJ detonations (as in Figure 3), interaction of the spherical detonations with each other and with the channel walls would lead to the formation of a strong detonation across the channel. We know that, if, in a uniform channel, a periodic succession of CJ detonations leads to a reasonably uniform downstream flow, that flow can be only the uniform flow that would have emerged from either a one-dimensional weak detonation or a one-dimensional strong detonation. We see no reason to doubt that we can select a channel of cross-section A(x) [with $A'(x)>0$] so that the downstream flow has the smallest one-dimensional entropy rise, i.e., the entropy rise associated with the weak detonation. We are confident that a channel with $A'(x)>0$ can be selected such that the nonuniform flow has an average entropy (across the cross-section) that is smaller than that discussed in the previous sentence.

Several tasks, now listed, must be executed before the feasibility, reliability, and potential performance of such a configuration can be obtained.

1. One must establish, experimentally, the ranges of pulsed-energy deposition, volume of deposition, duration of deposition, and seeding (if needed) within which individual pulses will lead reliably to the initiation and propagation of CJ detonations.
2. One must establish, experimentally, that the very intricate configuration that results when two CJ detonations intersect and interact does not include phenomena that could lead to a strong detonation.
3. One must establish, experimentally, that when a CJ detonation interacts with a reasonably rigid wall, there are no artifacts of that interaction that can lead to a stronger detonation.
4. Upon the successful completion of tasks (1), (2), (3), together with a supportive estimate of performance, one should construct a primitive apparatus such as shown schematically in Figure 4, and one should then "pulse initiate" two successive CJ detonations in the presence of the solid wall to verify that no combination of (3) and (4) "sounds ominous".
5. The entropy rise across the reflected shocks that are part of the interacting-detonation problem is a major source of losses in a pulsed-detonation configuration. However, those losses decrease as the pulse spacing is shortened. In the limit of very short pulse spacing, the detonation front would be conical, and the flow configuration, upstream of the cross-section at which the detonation front intersects the channel wall, will be selfsimilar. One must carry out the theory for this

configuration (a very straightforward task) and continue the supersonic-flow analysis downstream of that intersection (not a particularly difficult task). When this step is done for a modest number of channel shapes, one will have a rather good fix on the performance (thrust) to be expected from such a configuration (Figure 5).

6. Nowhere in the foregoing is there any assessment of the means by which fuel is mixed into the incoming-air steam, nor is there an assessment of the structural integrity (or noise-generation level) of any realization of the schematically defined channels. These subjects need addressing.
7. Item (1) should be extended to include gas mixtures that are not quite perfectly mixed. In particular, if one should use a mixture (Figure 6) in which N% of the stoichiometrically proportioned constituents are molecularly mixed and (1-N)% are paired up in blobs of dimension a, so that the diffusion flame that would ensue after the molecularly mixed gases have completed their reaction would require a time a^2/D, where D is the Fickian diffusivity of the lighter ingredient. This extension has two purposes: (1) to ascertain the reliability of the configuration in the event of imperfect mixing, and (2) to ascertain whether, with deliberately contrived "two-stage" burning, one could design the system so that the CJ detonation is weaker (therefore, less entropy-producing) than its well-mixed counterpart would have been, and, thereby, whether one could deliberately use a "two-stage" mix to improve performance. We believe that this nascent idea merits further consideration.

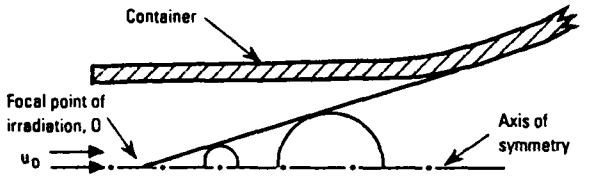

Figure 3. Each of the periodic pulses nonintrusively deposits sufficient energy [in a uniform supersonic stream (speed u_o) of combustible mixture, flowing in an axisymmetric container] to initiate directly a CJ detonation, which expands radially as it is convected downwind. The envelope of detonation - front positions is indicated.

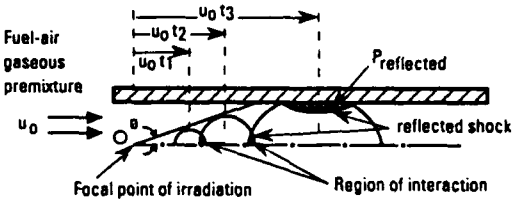

Figure 4. A simplified schematic showing three detonation fronts initiated in a premixed supersonic stream which is traveling faster than the detonation fronts (which travel at speed $u_o \sin a$). The downwindmost front has interacted with the wall, and a resulting shock travels through already-reacted gas.

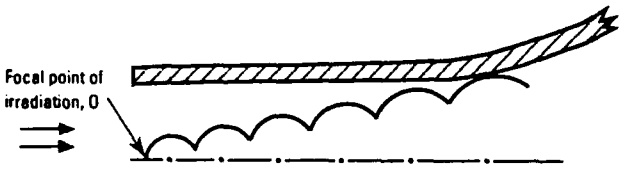

Figure 5. The "scalloped" front constituted by portions (actually, zonal strips) of the interacting spherical CJ detonation waves initiated by pulsing at a fixed finite frequency.

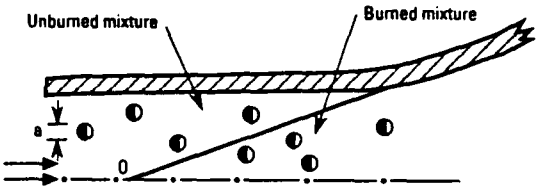

Figure 6. The half-shaded spheroids of scale a denote the (1-N) % of the mixture constituted by blobs consisting of fuel (shaded) and oxidizer (unshaded) in stoichiometric proportion. The well-mixed N% is converted to product gas in the oblique detonation.

REFERENCES

Carrier, G. F., Fendell, F. E., and Sheffield, M. W. (1990). Stabilization of a premixed planar flame by localized energy addition. AIAA Journal 28, 625-630.

Chou, M.-S., Zukowski, T. J., and Wong, E. Y. (1989). Ignition of $H_2/O_2/NH_3$, H_2/air and $CH_4/O_2/NH_3$ premixed flows by excimer laser photolysis of NH_3. Paper 89-94, Western States Section Fall Meeting. Pittsburgh, PA: Combustion Institute.

Lee, J. H., Knystautas, R., and Yoshikawa, N. (1978). Photochemical initiation of gaseous detonations. Acta Astronautica 5, 971-982.

Strehlow, R. A. (1984). Combustion Fundamentals. New York, NY: McGraw-Hill.

FUNDAMENTAL STUDIES OF LASER IGNITION AND KINETICS IN REACTIVE GASES

(AFOSR Contract No. 90-0025)

Principal Investigators: Andrzej W. Miziolek
Brad E. Forch
Associate Investigators: Norman M. Witriol*
Randy J. Locke*

U. S. Army Ballistic Research Laboratory
Aberdeen Proving Ground, MD 21005-5066

SUMMARY/OVERVIEW:

This year our efforts are concentrated on expanded studies of ultraviolet laser ignition of premixed reactive gases. New experimental tools, such as a tunable narrow-band excimer laser, streak camera, and variable pressure bomb, are being used for more comprehensive studies of laser-produced microplasmas and subsequent reactive gas ignition. In addition, a laser ignition modeling effort has been initiated and is underway. This modeling program is aimed at developing a capability to accurately predict the time and spatial chemistry and fluid dynamics of the laser-produced microplasma which transitions into a full flame. Spatially and time-resolved temperature and species concentrations from the simulations will be compared with experimental measurements of laser ignition of H_2/O_2 and H_2/air reactive gases using time-resolved pump-probe techniques.

TECHNICAL DISCUSSION

A. Laser Ignition Studies (Experimental)

Last year we reported on the effect of laser beam attenuation by atmospheric gases on the ignition curves for H_2/O_2 premixed gases using the ArF laser at 193 nm. We found that the minimum points in the incident laser energy (ILE) curve went up dramatically as the propagation pathlength was varied from 1 foot (ignition ILE = 0.8 mJ) to 20 feet (ignition ILE = 5.8 mJ). These results not only indicate caution in the reporting of the ILE curves as well as in considering the ArF laser as a practical igniter, but also strongly suggest that radiation at the O_2 absorption wavelengths is particularly important for efficient laser ignition. Studies are now underway using a recently acquired tunable excimer laser (Lambda Physik 150T) to understand better the relative roles of O_2 and H_2 laser excitation in the ignition process.

Laser ignition experiments involving the hydrogen atom 2-photon resonance at 243 nm[1] have been conducted and show an interesting isotope wavelength dependence.[2] Figure 1 shows the ILE dependence for the ignition of H_2/O_2 (curve a) and D_2/O_2 (curve b) using a tunable laser near 243 nm. The plots clearly show a wavelength shift which corresponds to 22 cm^{-1} at the two-photon level. This is exactly the energy difference in the n=2 excited state for the two different isotopes. Previously we observed a similar wavelength dependence for the formation of microplasmas in flows of pure H_2 and D_2 gases. Figure 2 shows the ignition ILE dependence on equivalence ratio for H_2/O_2 (Figure 2a) and D_2/O_2 (Figure 2b) with the laser set at the corresponding minimum

wavelength points (Figure 1) which are the wavelengths for maximum two-photon excitation. As can be seen, the two curves are basically alike as would be expected for these two fuel gases whose flame chemistry is quite similar.

An important question which thus far has remained unanswered pertains to the degree to which the species-specific microplasma chemistry influences the growth and behavior of the ignition kernel. We are attempting to address this question by studying the microplasmas in more detail, i.e. specifically by trying to determine their chemical composition. Figure 3 shows the microplasma emission spectra from two different fuel target molecules, i.e. propane (Figure 3a) and benzene (Figure 3b), using the ArF excimer laser.[3] Clearly, there are major differences in the formation of excited fragments in the microplasmas for these two molecules and, therefore, we expect that the subsequent ignition chemistry should be different as well. A particularly important, but difficult, goal to reach would be to fully characterize the laser-produced microplasmas with respect to the size, temperature, as well as major and minor reactive species which constitute a viable ignition kernel. Figure 4 shows preliminary results taken from a recently acquired streak camera (Hamamatsu Model C1587) of a laser-produced microplasma in a H_2/O_2 flow. This apparatus will be particularly useful for time-resolved spatial and spectroscopic studies of microplasma production and evolution.

B. Laser Ignition Studies (Modeling)

Previous modeling efforts of laser ignition have involved a fluid dynamic description of blast wave evolution and heating,[4] as well as a more complete model which includes some level of detailed chemistry.[5] However, to the best of our knowledge, a robust and well-tested model of laser ignition that can be used as a predictive tool currently does not exist. Our approach is to write a one-dimensional time-dependent code which describes the creation of the laser-induced kernel, as well as the time and spatial development of the system from laser-irradiation, to ignition, and finally to extinction.

Specifically, the new code that is being written includes the basic equations, those of continuity, continuity of the individual species, diffusion, motion, and energy balance, in one spatial dimension and time. The code utilizes the Chemkin II package, i.e. the thermodata and transport data sets (with our additions and alterations) and several of the thermodynamic and math algorithms. The set of time-dependent partial differential equations is solved using IMSL's DMOLCH, a finite element code which uses the method of lines with cubic Hermite polynomials. Physically, we assume the laser heats a spherical (cylindrical) kernel. The laser-induced heating is modeled by including a time and spatial dependent source term in the energy equation. The form of this term will be chosen to fit the time-dependent luminescent data obtained from the streak camera (as in Figure 4). From this input the code will model the time and radial dependencies of the temperature, density, pressure and species concentrations in the system. The results will be compared with temperature and species data obtained from time-resolved pump-probe experiments.

---

* NAS/NRC Postdoctoral Research Associates

1. B.E. Forch, J.B. Morris, and A.W. Miziolek, Book Chapter in "Laser Techniques in Luminescence Spectroscopy", **ASTM STP 1066**, 50-68, 1990.
2. B.E. Forch and A.W. Miziolek, **Combustion and Flame** (submitted).
3. R.J. Locke, J.B. Morris, B.E. Forch, A.W. Miziolek, **Appl. Opt.** (submitted).
4. J. Syage, E. Fournier, R. Rianda, R. Cohen, **J. Appl. Phys.**, 64, 1499, 1988.
5. U. Maas and J. Warnatz, **Combustion and Flame**, 74, 53, 1988.

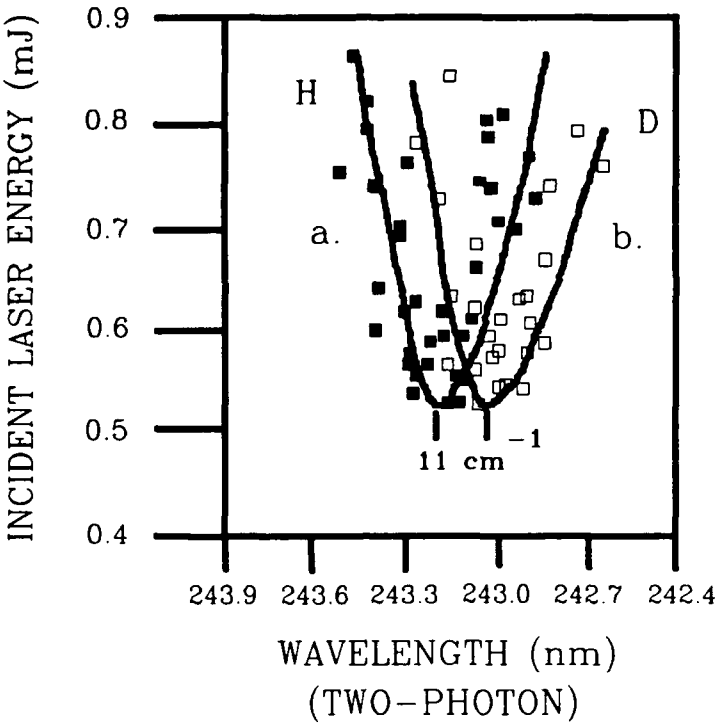

FIGURE 1. ILE NECESSARY TO IGNITE PREMIXED FLOWS OF: a. H_2/O_2 AND b. D_2/O_2, AS A FUNCTION OF EXCITATION WAVELENGTH NEAR 243 nm. A SHIFT OF +11 cm^{-1} OF IGNITION CURVE b. RELATIVE TO IGNITION CURVE a. IS EVIDENT.

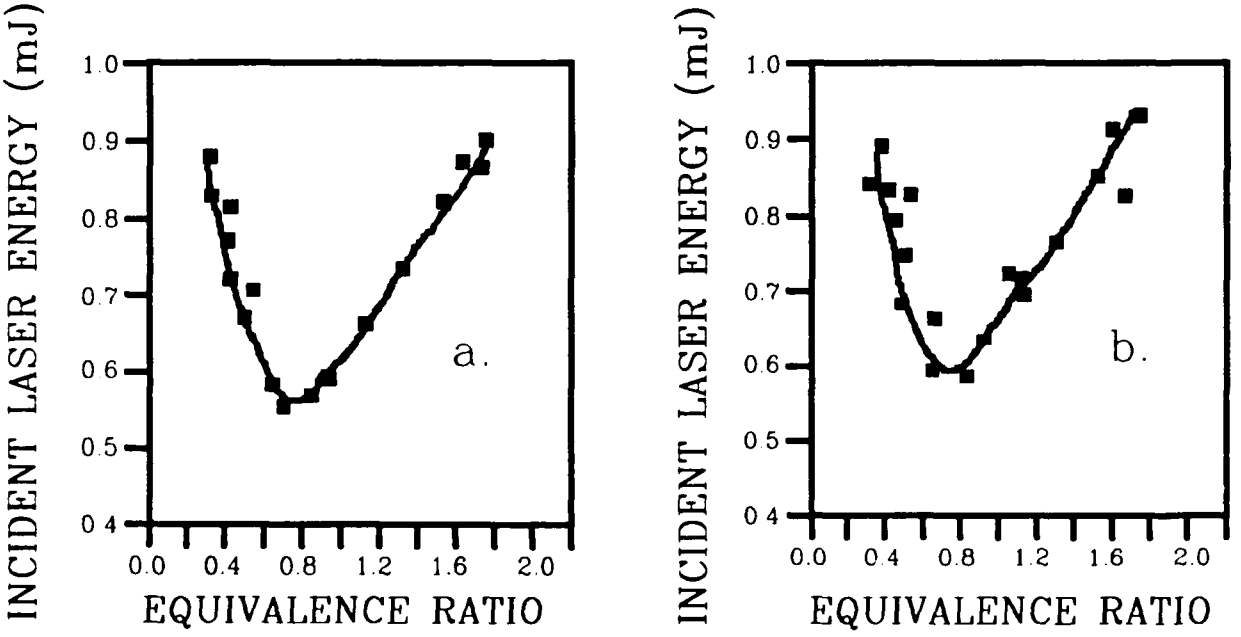

FIGURE 2. DEPENDENCE OF THE ILE REQUIRED TO IGNITE PREMIXED FLOWS OF: a. H_2/O_2 AND b. D_2/O_2, AS A FUNCTION OF EQUIVALENCE RATIO. THE LASER WAS SET AT THE PEAK OF THE TWO-PHOTON EXCITATION WAVELENGTH OF: a. H-ATOMS AT 243.07 AND b. D-ATOMS AT 243.00 nm.

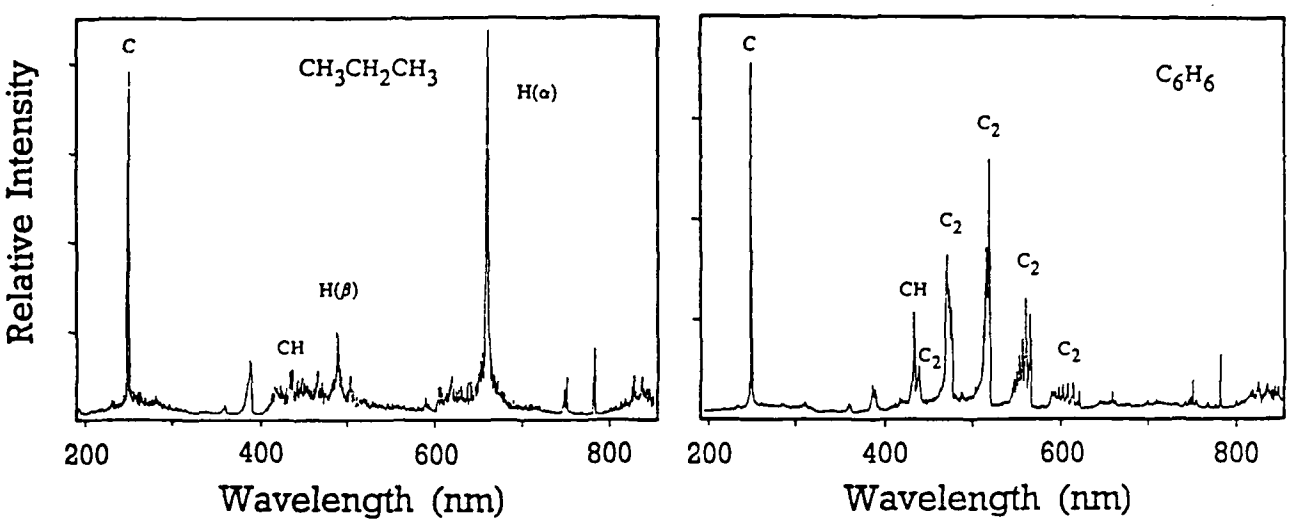

FIGURE 3. ArF LASER PRODUCED MICROPLASMA EMISSION SPECTRA FOR PROPANE (LEFT) AND BENZENE (RIGHT).

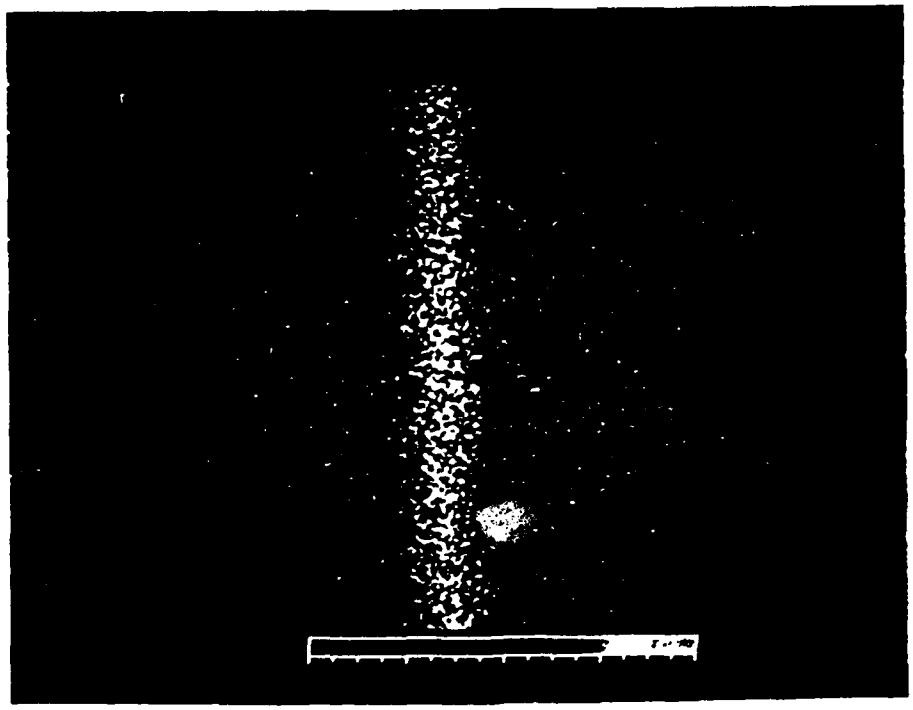

FIGURE 4. STREAK CAMERA TRACE FROM AN ArF LASER PRODUCED MICROPLASMA FORMED IN A PREMIXED H_2/O_2 FLOW; FULL SWEEP EQUALS 3 ns.

PRODUCTION OF COATED BORON POWDER BY A CHEMICAL VAPOR DEPOSITION PROCESS

(ONR Contract No. N00014-89-C-0247)

Principal Investigator(s):

J.J. Helble and C.L. Senior
PSI Technology Company
20 New England Business Center
Andover, MA 01810

H. Desai
CVD, Inc.
185 New Boston Road
Woburn, MA 01801

SUMMARY/OVERVIEW

In this program, boron particles were produced via a two-step chemical vapor deposition process which allows control over the size and concentration of boron particles. Particles were formed via decomposition of BCl_3 using a pulsed CO_2 laser in the first step and grown by condensation of BCl_3 in a thermal reactor in the second step. Control of the size of the particles was demonstrated by varying the composition of the gas mixture. As part of this program, evaluation criteria were developed for potential metal coatings for boron powder.

AUTHORS

J.J. Helble, C.L. Senior, and H. Desai

TECHNICAL DISCUSSION

Production of boron seed particles by decomposition of BCl_3 with a pulsed CO_2 laser was successfully demonstrated in Phase I of this program. As anticipated, the seed particles were not agglomerated under most experimental conditions. Particle size was a function of BCl_3 concentration. Growth of the seed particles via thermal decomposition of BCl_3 in a furnace was also successfully demonstrated in Phase I. Seed particles were grown from approximately 40 to 100 nm with particles observed as large as 200 nm. BCl_3 concentration in the growth furnace was shown to affect the final particle size and morphology.

Particle formation was accomplished in a stainless steel chamber with salt windows to allow passage of 10.6 μm radiation from a CO_2 laser. A mixture of BCl_3 and H_2 in He was flowed through the seed formation chamber. Particle growth occurred in an externally heated quartz tube located downstream of the seed formation chamber. Additional boron-containing gases (BCl_3/H_2/He) were added to the gas stream containing the seed particles before the growth

furnace. Particles were collected on cooled grids for transmission electron microscope (TEM) analysis.

In the seed formation experiments, the laser fluence was held constant at 3.5 J/cm^2 and the concentration of BCl_3 was varied. The concentration of BCl_3 in the seed formation chamber had a pronounced effect on the particle size and morphology. The effect on particle size is summarized in Figure 1. Below 0.5 percent BCl_3, the particle size is not a strong function of BCl_3 concentration. This indicates that there may be a lower threshold condition (temperature and BCl_3 concentration) needed to promote seed particle formation. At extremely high concentrations of BCl_3, coagulation may occur; clearly 1 percent BCl_3 is well below this upper threshold concentration.

The objective of the particle growth experiments was to demonstrate the capability to increase the size of the seed particles using thermal decomposition of a gaseous boron compound (BCl_3) in a furnace. In the particle growth experiments, the laser fluence was held constant at 3.5 J/cm^2 and the pulse repetition rate was 5 Hz. The concentration of BCl_3 in the seed formation chamber was maintained at 1 percent and the concentration of BCl_3 added to the gas downstream of the seed formation chamber was varied from 0 to 1 percent BCl_3. Temperature was held at a furnace set point of 1273 K, corresponding to a gas temperature in the hot zone of 1160 K.

Addition of BCl_3 to the furnace produced a dramatic change in particle size and morphology. When the BCl_3 concentration added to the growth furnace was increased to 0.51 percent, the sample collected contained a mixture of compact, spherical particles and larger agglomerates with an open structure. The non-spherical agglomerates ranged in size from 50 to 150 nm. The particles appeared to have some internal structure, suggestive of collision and partial solid state coalescence. Increasing the BCl_3 concentration in the furnace to 1 percent increased the particle size further and resulted in spherical

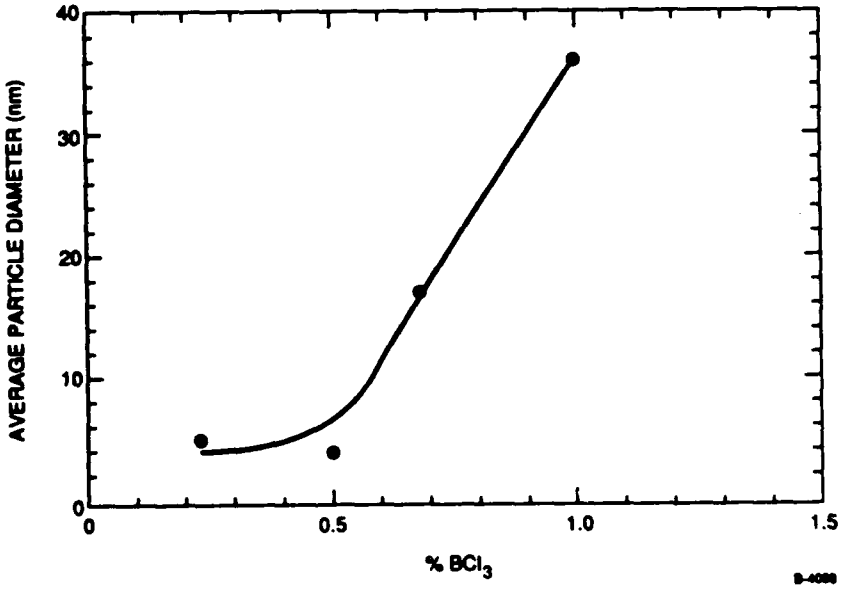

Figure 1. Average Particle Diameter as a Function of BCl_3 Concentration for Seed Particle Formation Experiments

particles. No large agglomerates were observed. A significant number of 20 nm particles are visible. Most of the larger particles fall in the range of 40 to 100 nm, although particles as large as 185 nm are visible.

The results of the particle growth experiments indicate that substantial particle growth was obtained at 1160 K from 40 nm to about 100 nm when BCl_3 was added in a concentration of 1 percent. Both coagulation and condensation appear to be important mechanisms for particle growth. One set of experimental conditions (0.51 percent BCl_3) produced chain-like agglomerates, while another (1 percent BCl_3) produced predominately spherical particles.

During Phase I a number of metals suitable for coating boron powders by chemical vapor deposition (CVD) were identified. These candidate materials and their physical properties are listed in Table 1. Although no attempt has been made yet to coat boron powders, there are data concerning coatings for boron fibers. Boron fibers have been coated with TiB_2 deposited by reducing gaseous $TiCl_4$ in the presence of hydrogen.[1] The deposition temperatures were in the range of 700 to 1000°C with deposition times of 20 to 120s. In these experiments there was an absence of a Ti metal layer on the surface. It is speculated that TiB_2 is formed by diffusion of boron through the coating to react with Ti on the surface. The coating of boron fibers with Zr[2] results in the formation of ZrB_2, which ignites in the presence of oxygen at 600°C. Unfortunately, liquid B_2O_3 remains as a product of this reaction. Similar reaction mechanisms exist for other borides, making them undesirable as coating materials for boron fuel powder.

For the metals suggested in the literature - magnesium, zirconium, and titanium - thermodynamic calculations clearly indicate that the refractory boride is the preferred phase, to the exclusion of pure metallic coating even at room temperature. Thermodynamic calculations are in agreement with experimental observations for the coating of boron with Ti or Zr. For these metals, formation of the boride may prove a hindrance to combustion. Magnesium boride on the other hand, may not be an impediment to combustion since it decomposes at 1473 K.

Other materials such as aluminum and zinc do not form borides, but easily form an oxide layer at room temperature which is very difficult to remove as seen from Table 1. One potentially attractive coating material is indium which forms an oxide that does not act as an oxidation barrier because it volatilizes at a low temperature (1123 K). Indium is a low melting point (430 K) metal with a vapor pressure of 1 Torr at 700°C making it relatively easy to deposit a thin film of the metal by CVD. Boron particles formed by the aerosol process along with indium vapors from an effusion cell can be introduced into a deposition zone where indium vapors will condense on the boron particle. Although

---

[1]Bouix, J., Vincent, H., Boubehira, M., and Viala, J.C. (1986), "Titanium Diboride-Coated Boron Fiber for Aluminum Matrix Composites," J. Less Common Metals 117, 83.

[2]Hall, J.T. (1990), Hughes Aircraft Co., private communication.

Table 1. Physical Properties of Metals, Oxides, and Borides

Compound	Melting Point (K)	Boiling Point (K)
B	2573	2823
B_2O_3	723	2100
Ti	1933	3560
TiB_2	3173	--
TiO_2	2113	2800
Zr	2125	4650
ZrB_2	decomp. 623	--
ZrO_2	3000	5300
Al	933	2740
Al_2O_3	2345	3253
In	430	2353
In_2O_3	--	volat. 1123
Mg	922	1380
MgB_6	decomp. 1473	--
MgO	3125	3873

indium oxide forms on the metal surface at room temperature, it poses no threat to the combustion process since it volatilizes at 1123 K, well below the combustion temperatures in air-breathing systems.

Phase I experiments have demonstrated formation of non-agglomerated boron seed particles which were subsequently grown by condensation. Future work will be directed toward increasing the final particle size and integrating a coating step into the process. Metals such as Ti and Zr do not appear promising as coating materials since they form borides that are oxidation-resistant even at high temperatures and therefore, will hinder the combustion of boron fuel particles. Formation of MgB_6 is predicted to occur upon coating with Mg, but this may not be so detrimental to good ignition of boron particles. Other metals such as Al tend to form oxides which may prove difficult to remove and hinder the oxidation of boron particles at high temperature. Indium, on the other hand, appears to be the coating material of choice due to its volatile oxide and the relative ease of deposition.

PRODUCTION AND COATING OF PURE BORON POWDERS

SBIR Topic N-89-007

Principal Investigator: Charles B. Criner
MACH I, Inc.
346 E. Church Road
King of Prussia, PA 19406

Summary/Overview

The purpose of this study was to evaluate the feasibility of two technologies. The first involved the synthesis of pure boron powder from a thermally unstable caged borane compound. The second involved using a technique of physical vapor deposition developed by MACH I, Inc. to coat magnesium on boron powder.

Technical Discussion

The results of the work led to the overall conclusion that the scope and objectives of the prescribed Phase I work were successfully achieved.

The following points were demonstrated by the experiment.

* The dilithium dodecaborane spontaneously decomposed into a moderately pure boron powder with a violent evolution of hydrogen between 400-500°C.

* The acid precursor of this salt also spontaneously decomposed into a moderately pure boron powder with a violent evolution of hydrogen at about 150°C.

* Using equipment and technique planned in the SBIR proposal, the purity levels of boron produced from the thermal decomposition of all caged boranes studied was lower than anticipated. This was due to the unexpected contamination of carbon in the compounds studied and the probable formation of boron oxide.

* The purity of the boron produced from thermal decomposition of caged boranes must be substantially increased in order for the boron to be commercially useful. Significant additional work would be needed to resolve the contamination problems noted.

* The cost of the caged borane is high and will probably always be prohibitive to the use of this material as a feedstock for the production of boron metal. The expected performance benefits from the synthesis of an ultra-pure boron metal was not achieved. The synthesis of boron without an oxide layer was not demonstrated.

* A successful method to coat boron powder with magnesium was developed and tested.

* The magnesium coated boron powder produced in this SBIR evaluation appeared to be more thermally active than the neat boron.

* The reactive ball mill method of coating appears to be cost effective and possibly useful for unstable organo-metallic compounds as well as low melting metals.

* The reactive ball mill coating technique appears to offer good potential for additional test evaluations. The low cost of this process would also lend itself to a commercial utility for coating a variety of metals other than boron. The concept also is safe, simple and scalable.

FUNDAMENTAL COMBUSTION PROCESSES OF PARTICLE-LADEN SHEAR FLOWS IN SOLID FUEL RAMJETS

(ONR CONTRACT No. N00014-86-K-0468)

Co-Principal Investigators: K. K. Kuo, V. Yang, T. A. Litzinger
S. T. Thynell, and W. H. Hsieh

Department of Mechanical Engineering
The Pennsylvania State University
University Park, PA 16802

The objectives of this research project are:

1) to acquire a basic understanding of physical and chemical mechanisms involved in the combustion of solid fuels under strong cross-flow conditions;
2) to advance the understanding of radiative heat transfer during combustion of high-energy solid fuels by determining temperature and species profiles and radiative properties of particulate matter of combustion products, using a Fourier-Transform Infrared (FT-IR) Interferometer;
3) to characterize the thermal degradation, pyrolysis, and ignition phenomena of the specially formulated solid-fuel samples via CO_2 laser pyrolysis studies; and
4) to determine the effects of initial temperature and pressure on the combustion behavior and burning rates of fuel-rich propellants and pyrotechnic materials.

Significant results obtained in the past year are summarized below.

I. Combustion of Solid Fuels under Cross-flow Conditions

The pyrolysis and combustion of several solid fuels have been studied under both subsonic and supersonic cross-flow conditions. Most of the solid fuels studied contained HTPB binder with the addition of different percentages of metal powders and combustion aids. This type of fuel was either obtained from the Naval Weapons Center or United Technologies Chemical Systems Division, or processed at The Pennsylvania State University. To study the effect of different binders on the ignitability and combustion processes of solid fuels, an energetic copolymer (BAMO/NMMO) was used to replace HTPB. These solid fuel samples were obtained from Aerojet Propulsion Company.

Results indicate that under atmospheric conditions, the HTPB fuels reach a critical temperature after which they either melt or ignite depending upon the free-stream temperature and the diffusion of oxygen into the near surface region. The BAMO/NMMO based solid fuels were found to exhibit better ignition characteristics than the HTPB fuels under atmospheric conditions. The addition of boron particles to the solid fuels enhanced the ignitability by their active participation in chemical reactions inside the boundary layer region. The effect of boron was more pronounced when added to the energetic copolymer as compared to the case with HTPB. Figures 1 and 2 show the regression history for the pure BAMO/NMMO and the [BAMO/NMMO]/boron (82.4/17.6) fuel samples. The combustion of the pure BAMO/NMMO lasted for 40 seconds, whereas the combustion of the boron-loaded fuel was completed in 20 seconds. The fastest regression rate took place at a location 2-3 cm from the rearward facing step.

To overcome certain difficulties encountered in ignition of solid fuels at low pressures, a high-pressure windowed test chamber has been designed and constructed to

study the combustion processes under pressures ranging from 1 to 10 atm. The chamber is capable of varying the Mach number from 0 to 1.5 through the use of a double-throat flow channel design. The second throat can be controlled using an electric actuator to control the pressure and flow conditions. Results from the high-pressure chamber will be presented at the meeting.

The combustion of homogeneous HTPB solid fuels under supersonic cross flows has been studied using a comprehensive numerical analysis. The formulation is based on the time-dependent multi-dimensional compressible Navier-Stokes equations and species transport equations. Features of this approach are the consideration of finite-rate chemical kinetics and variable properties. Turbulence closure is achieved using the Baldwin-Lomax algebraic model. The governing equations are solved numerically using a flux-vector splitting Lower-Upper Symmetric Successive Overrelaxation technique that treats source terms implicitly. The effects of various operating conditions on the combustion behavior of the HTPB-based solid fuel samples are treated in detail. Results indicate that both the inlet temperature and pressure have strong influences on the burning rate of the fuel sample. For the operating range considered, an optimum pressure is required to maximize the burning rate (see Fig. 3). The sample burns increasingly faster with pressure from one to four atmospheres. However, at a higher pressure, the heat released by chemical reaction is not sufficient to further increase the temperature of the cross flow. Therefore, the heat feedback to the fuel sample decreases and the burning rate diminishes.

The formulation of a two-phase model with reacting boron particles has been completed. The particles are divided into representative samples whose motion and transport are traced using a Lagrangian formulation. Appropriate source terms are added to the gas-phase equations to account for finite interphase transport. This separated flow treatment includes submodels for the ignition and combustion stages of the boron particles.

II. FT-IR Measurements of Combustion Products from Solid Fuels

During the past year, a rapid-scanning Fourier-Transform infrared (FT-IR) spectrometer has been purchased, installed, and interfaced with a low-pressure transparent test chamber in which a small strand of solid fuel is burned. The FT-IR has been set up so that it performs either emission or transmission/absorption measurements of species concentration and temperature of combustion products from solid propellants or fuels. The sample surface location is controlled using a He-Ne laser, a photodiode, and a PC; these components are used in a closed-loop feedback system for the purpose of maintaining the burning strand in either a fixed or programmable position with respect to the IR line-of-sight measurement location.

To date, numerous tests have been conducted using the FT-IR and a PC-based positioning system. Figure 4 shows the result of ten co-added emission spectra obtained from the burning of a solid fuel, containing 5% B and 95% BAMO/NMMO. These spectra were measured at 4 cm^{-1} wave number resolution using a liquid nitrogen cooled mercury-cadmium-telluride detector and KBr beamsplitter in a rapid scan mode. Since most solid propellants and solid fuels combust poorly in low-pressure inert environments, air was used as the purge gas. Examination of Fig. 4 reveals several interesting features. First, emission from soot and boron particles, which would be revealed in terms of spectrally continuous emission, is nearly absent. That is, the energetic binder (BAMO/NMMO) essentially decomposes and burns in the excess oxidizer environment to form large amounts of CO_2 and noticeable amounts of H_2O and CO, but the presence of small amounts of hydrocarbon molecules may be masked by H_2O emission near the 1,600-1,400 cm^{-1}

wave number interval. Second, gaseous combustion products containing B appears to be absent since the temperatures are too low; otherwise, one would expect to readily identify HOBO in two bands in the ranges of 1,750-2,250 and 3,450-3,750 cm^{-1}. Higher pressure tests will be conducted in the future to identify gaseous chemical species containing boron.

III. CO_2 Laser Pyrolysis and Ignition of Solid Fuels and MPMS Measurement of Gaseous Species Profiles

The combustion characteristics and CO_2 laser ignition behavior of pressed strands of boron/magnesium/Polytetrafluoroethylene (B/Mg/PTFE) pyrotechnic materials of varying compositions have been investigated. The amount of PTFE was held constant at 50% by weight while various amounts of boron (from 0-50%) were introduced to replace the amount of magnesium in the formulation. All tests were conducted in air at one atmosphere.

Experimental results indicated that the ignition delay time decreased monotonically as both the heat flux and the weight percentage of boron were increased. This behavior was partly attributed to the fact that boron has a significantly higher absorptivity than magnesium at 10.6 μm wavelength. Only samples with a boron loading $\geq$ 10% achieved self-sustained combustion. Figure 5 shows that the burning rate was highest with a 10% boron loading and decreased monotonically at higher boron percentages. Above 10% boron loading, the burning rate decreases due to a reduction in the intensity of the near-surface flame, which is believed to be produced primarily by the fluorination of Mg, and also due to the number density increase of ejected boron particles acting as "heat sinks" and reducing the energy feedback to the sample surface. It was also observed that near-IR emission was significantly higher for compositions containing 10% and 20% boron.

An MPMS (microprobe mass spectrometry) system has been developed and tests of solid fuels and propellants are underway. The objective of the system is to measure gaseous species profiles above burning samples heated by the CO_2 laser. Gaseous species are drawn through a quartz microprobe with a 50-100 μm orifice into a pre-chamber evacuated by a mechanical pump and then into the mass spectrometer chamber which is evacuated by a turbopump to a pressure of 10^{-6} torr. The system is based on a quadrupole mass spectrometer with a mass range of 1-500 amu. An 80386 computer and a function generator have been integrated with the electronics of the MPMS to control the mass detection sequence and timing. Software has been developed that allows sampling rates as high as 3,000 amu/s.

IV. Effects of Initial Temperature and Pressure on Combustion Behavior and Burning Rate of Fuel-Rich Solid Propellants and Pyrotechnic Materials

To study the effects of initial temperature and pressure on the combustion behavior and burning rate of various combustible solids, their regression rates under no cross-flow conditions have to be measured. An existing windowed high-pressure test chamber has been modified to control the initial temperatures of both the solid fuel sample and the test chamber in a broad range of -40 to 70 C. In order to achieve this range, a FTS constant-temperature circulation bath was acquired, installed and tested. A gas-phase heat exchanger system was also designed, fabricated and installed for controlling the initial temperature of solid-fuel samples and that of the purging gases. In addition, the windowed test chamber has also been modified to extend its testing pressure ranges to 62 MPa. A typical result shows that the burning rate of [BAMO/NMMO]/B (60/40) solid fuel increases from 1.89 to 2.13 mm/s when sample initial temperature increases from 25 to 60 C at MPa. The temperature sensitives of various samples are being characterized using the newly developed facility.

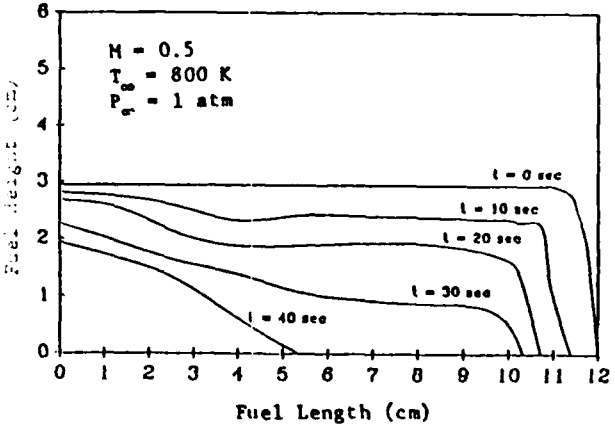

Fig. 1 Regression History for Pure BAMO/NMMO Solid Fuel Sample in Subsonic Mode of Combustion.

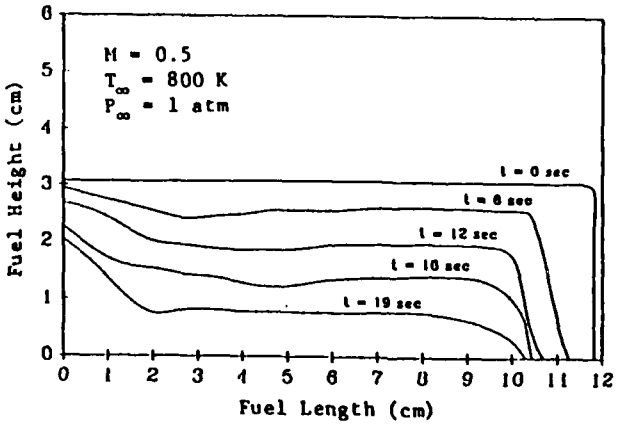

Fig. 2 Regression History for [BAMO/NMMO]/Boron (82.4/17.6) Solid Fuel Sample in Subsonic Mode of Combustion.

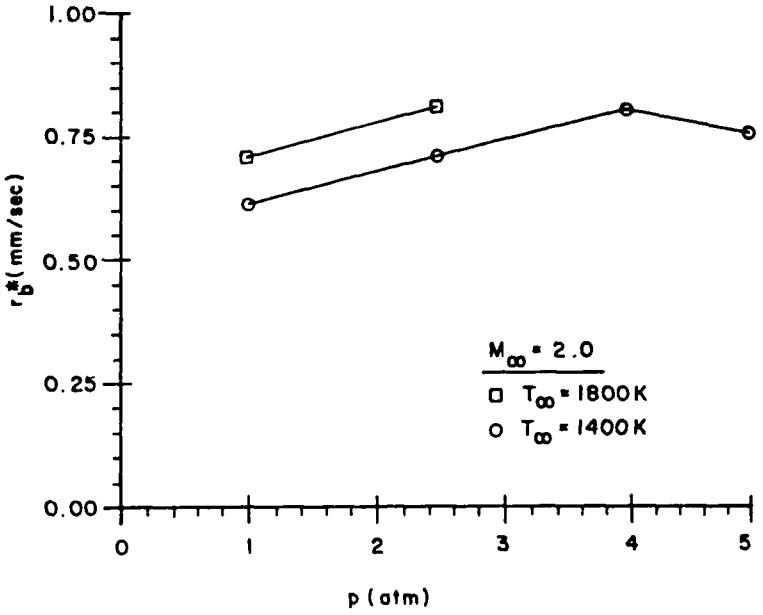

Fig. 3 Effect of Pressure and Free-Stream Temperature on Normalized Burning Rate of HTPB-Based Solid Fuel

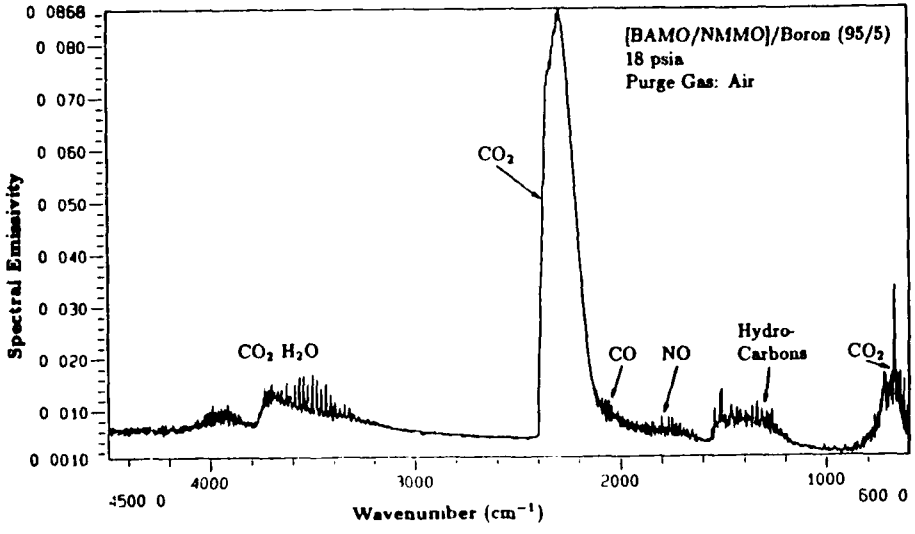

Fig. 4 Spectral Emissivity of Combustion Products of a [BAMO/NMMO]/Boron (95/5) Solid Fuel

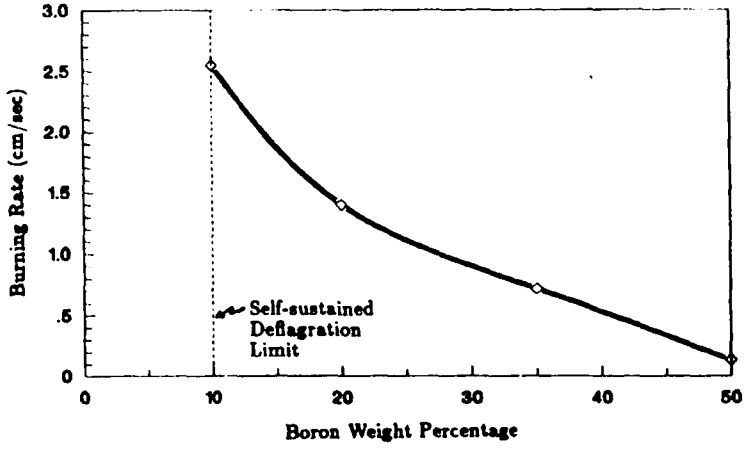

Fig. 5. Burning rate as a function of boron weight percentage for combustion of B/Mg/PTFE compositions in air at 1 atm

CHARACTERIZATION OF IR EMISSION FROM BORON COMBUSTION

(ONR Contract No. N00014-88-C-0492)

Principal Investigator: Kurt D. Annen

Aerodyne Research, Inc.
45 Manning Road
Billerica, MA 01821

SUMMARY/OVERVIEW:

The objective of this program is to analyze infrared (IR) emission from solid propellant combustion to obtain a better understanding of the chemical, physical, and radiative processes occurring in the combustion process. Our program interacts closely with the solid propellant combustion program of Penn State, using the spectral and radiometric IR measurements taken during their combustion tests. By comparing predictive models of IR emission with the measured data, chemical kinetic and radiative parameters used in modeling advanced propellants (such as those containing boron) can be checked, and a better understanding of the chemical and physical processes which control the rate of combustion can be obtained. Eventually, these techniques could yield new information on the boron oxidation mechanisms and rates occurring in boron propellant combustion and a verification of band strengths for the major boron combustion product species.

AUTHORS. K.D. Annen, J.C. Wormhoudt, and C.E. Kolb

TECHNIC' L DISCUSSION:

The infrared (IR) emission produced by the products of combustion of solid propellants has considerable military significance. Both the initial combustion products and the products of the secondary combustion or "afterburning", which occurs as the initial products mix with the surrounding atmosphere, are important contributors to the total IR emission. Measurements of the IR emission produced in combustion tests can allow better predictions of the IR emission produced by actual military systems, especially for advanced propellants containing boron, and can also provide a wealth of information about the chemical and fluid dynamic processes occurring in the solid propellant test.

The objective of our program is to complement the Penn State research on solid propellants. Our work will focus on analyzing the spectral and radiometric data obtained by Penn State to improve our understanding of the chemical, radiometric and fluid dynamic processes occurring in solid propellant combustion. Penn State is currently operating a Michelson FTIR spectrometer and a transparent strand burner chamber for solid propellant tests in

which the collection of spectral emission data is a major objective. During this period, we have worked on the development of IR radiation models to analyze emission spectra for several propellants obtained by Penn State. These radiation models and the preliminary fluid dynamics and chemical kinetics developed in the preceeding year will be used in the analysis of boron-containing spectral data when it is obtained.

An interesting propellant which has recently been tested by Penn State in their high pressure facilities with spectral measurements is a formulation consisting of boron and a BAMO/NMMO binder. Figure 1 shows a coadded spectrum, corrected for instrumental response. Last year, preliminary predictions were made for this propellant based on the following observations and assumptions. Penn State observed in their high pressure strand burner that the boron particles in the B/(BAMO/NMMO) propellant do not burn to completion at the propellant surface, but rather are ejected from the burning surface by the decomposition of the binder. Based on this information the concentration of gas phase boron species near the surface was assumed to be small. By analogy with nitramine decomposition processes, the BAMO/NMMO binder has been assumed to decompose to CH_2O, C_2H_2, N_2, NO_2, HCN, and H. Subsequent reactions to form CO, NO, and a variety of radical species occur rapidly. The peak temperature of the combustion products at a pressure of 35 psia, prior to reaction with the external atmosphere, was measured to be approximately 900 K. Higher temperatures were observed in the afterburning region of the strand combustion flowfield.

We expect to present comparisons between model predictions and the observed boron propellant emission spectra. Analysis to date, however, has been carried out on four other data sets. These are emission and absorption observations of two conventional propellants, NOSOL-363 and an AP/HTPB formulation. Understanding of these systems will serve as a basis for analysis of spectra of advanced propellants.

In all spectra, we see emission or absorption features due to CO, CO_2, H_2O and particles (with the exception of the AP/HTPB transmission spectrum which did not include water spectral regions). In addition, the AP-containing propellant gives well-resolved HCl line structure, while the NOSOL3 spectra show bands due to NO and H_2CO.

These spectral features can be used to estimate gas and particle temperatures and species column densities. Such observations can be used to produce a predictive model of the strand burner flame, which can then be modified to analyze data from the boron-containing propellant. Progress towards these goals, limitations in the present data, and opportunities for further observations will be discussed.

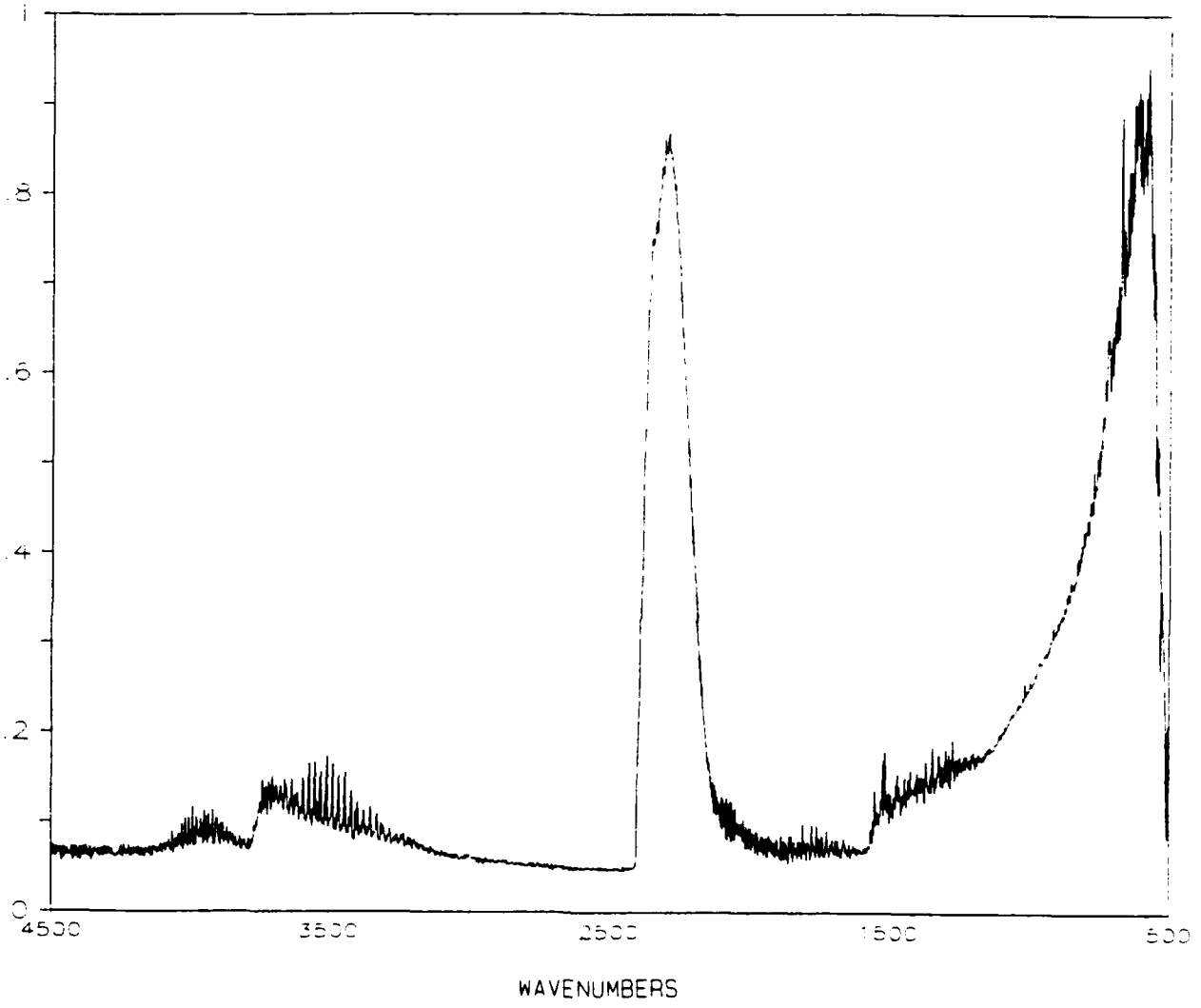

Figure 1. Observed B/(BAMO/NMMO) Emission Spectrum, Penn State High Pressure Combustion Laboratory, 4/27/90.

TRANSPORT PHENOMENA AND INTERFACIAL KINETICS IN MULTIPHASE COMBUSTION SYSTEMS†

AFOSR Grant No. 89-0223

Principal Investigator: Daniel E. Rosner‡
High Temperature Chemical Reaction Engineering Laboratory
Department of Chemical Engineering, Yale University
P.O. Box 2159 YS; New Haven, CT 06520,USA

SUMMARY/OVERVIEW

The performance of ramjets burning slurry fuels (leading to condensed oxide aerosols and liquid film deposits), gas turbine engines in dusty atmospheres, or when using fuels from non-traditional sources (*e.g.*, shale-, or coal-derived), depends upon the formation and transport of small particles across non-isothermal combustion gas boundary layers (BLs). Even airbreathing engines burning "clean" hydrocarbon fuels can experience *soot* formation/deposition problems (*e.g.*, combustor liner burnout, accelerated turbine blade erosion and "hot" corrosion). Moreover, particle formation and transport are important in many chemical reactors used to synthesize or process aerospace materials (turbine blade coatings, optical waveguides, ...). Accordingly, our research is directed toward providing chemical propulsion systems engineers and materials-oriented engineers with new techniques and quantitative information on important particle- and vapor-mass transport mechanisms and rates.

An interactive experimental/theoretical approach is being used to gain understanding of performance-limiting chemical-, and mass/energy transfer-phenomena at or near interfaces. This includes the development and exploitation of seeded laboratory flat flame burners (Section 1), flow-reactors (Section 3), and new optical diagnostic/spectroscopic techniques. Resulting experimental rate data, together with the predictions of asymptotic theories (Section 2), are then used as the basis for proposing and verifying simple viewpoints and effective engineering correlations for future design/optimization studies.

TECHNICAL DISCUSSION

1. SEEDED FLAME EXPERIMENTS ON SUBMICRON PARTICLE TRANSPORT

During this past year our emphasis has been on the further development of a $TiCl_4(g)$-seeded low strain-rate counterflow laminar diffusion flame technique for determining the *thermophoretic diffusivity*, $(\alpha_T D)_p$, and *Brownian diffusivity*, D_p, of flame-generated submicron $TiO_2(s)$ "soot" particles. As described earlier, our thermophoretic diffusivity inference is based on the existence of an easily measured particle-free ("dark") zone on either side of the diffusion flame sheet. Using LDV (radial) velocity measurements on N_2-diluted flames we have now confirmed that inferred $(\alpha_T D)_p$-values based on *observed* dark-zone thicknesses and observed (thermocouple) temperature gradients are well within 10% of values expected using a Waldmann's kinetic theory approach for dense spherical particles. We are now studying the dependence of the inferred $(\alpha_T D)_p$ on carrier gas momentum diffusivity (using helium substitution), and probing the structure of the "front" separating particle-free from particle-laden regions. Since this structure is due to the non-zero Brownian diffusivity of the particles, these latter measurements should allow the inference of α_T itself. The ability to reliably measure and ultimately predict (Section 2) the thermophoretic properties of isolated and aggregated flame-generated particles (carbonaceous soot, Al_2O_3, ...) and macromolecules (including PAH soot precursors) will be important to many technologies, including chemical propulsion and refractory materials fabrication.

---

† AFOSR/ONR Contractors Meeting on Propulsion, Atlanta, GA, 11-15 June, 1990

‡ For research collaborators consult **REFERENCES**

2. MULTIPHASE TRANSPORT THEORY

Not only can *thermophoresis* dominate the Brownian transport of small particles in combustion systems (see, eg., Eisner and Rosner, 1985, and Rosner and Kim, 1984) but we have recently shown that commonly encountered radiation fluxes can can cause the *photophoresis* of absorbing supermicron quasi-spherical particles, as illustrated in Fig.1(Rosner *et. al.* 1990).

Because of the need to accurately predict the Soret 'diffusion' of large, highly *nonspherical* molecules (*e.g.*, polycyclic aromatic soot precursors and large metal-organic vapors used to deposit thin films with useful optical properties) and the thermophoretic transport of *nonspherical* submicron particles (*e.g.*, long soot aggregates) we are continuing our research on predicting the *shape*- and orientation-dependence of their thermal diffusion velocities (Garcia-Ybarra & Rosner, 1989), and *photophoretic* velocities (Rosner,*et.al.*1989, Mackowski,1990), including the implications of these effects for agglomeration rates (Park & Rosner, 1989a) and combustion deposits formed from agglomerated particles (Tassopoulos, OBrien and Rosner, 1989). Our recent theoretical studies of the transport properties of asymmetric two-sphere aggregates (see Fig.2 and Mackowski,1990) reveal a strong tendency for them to align themselves with respect to **grad** T_g, despite the inevitable randomizing effects of Brownian rotation. Because particle size and shape also affect Brownian diffusivities, we are simultaneously developing useful engineering methods for predicting total mass deposition rates from 'coagulation-aged' *distributions* of suspended particles — including 'fractal' agglomerates and linear chains of uniform sized "primary" particles (see, *e.g.*, Rosner, 1989; and Rosner & Tassopoulos, 1989, and Rosner,1990)).

Another example of the interesting competition between particle *inertia* and particle thermophoresis (Park & Rosner, 1989b) has been clarified for the case of laminar boundary layers on surfaces with streamwise curvature , as in the case of combustion turbine blades)(Konstandopoulos and Rosner, 1990). In principle, thermophoresis "alone" can be used to "clean" a dusty gas well below the "inertial threshold", especially if heat addition to the gas is a simultaneous goal. For this reason we have calculated (Park and Rosner,1990) the (dimensionless, stretched) thickness of the "dust-free" layer adjacent to a hot wall toward which a heavily loaded submicron dusty gas is directed (see,eg. Fig.3). This is the same phenomenon we are exploiting in our counterflow flame measurements of $(\alpha_T D)_p$ (Section 1) except our calculations are for hot *solid* walls and include high (non-negligible) particle mass loadings.

3. GASIFICATION KINETICS OF SOLID BORON AND PYROLITIC GRAPHITE

Because of the energetic potential of boron as a solid fuel (or fuel additive) and the likely role of *surface* reactions involving the gaseous oxidant $B_2O_3(g)$ in the processes of fine boron-particle ignition, combustion and extinction, we have obtained and have submitted for publication flow reactor measurements of the intrinsic kinetics of the gasification of B(s) at surface temperatures between about 1300K and 2100K (Zvuloni *et al.*, 1989a, Zvuloni,1990). While the chemical propulsion implications of these measurements are emphasized in our AIAA publication (Zvuloni *et al.*, 1989a), the experimental techniques and the mechanistic implications of our results are emphasized in a full-length manuscript prepared for J. Phys. Chem (Zvuloni, Rosner and Gomez, 1990). We have also completed a preliminary set of measurement of the remarkably efficient gasification of *pyrolytic graphite* by OBOBO(g) (Zvuloni *et al.*, 1990c). Indeed, we find experimental (Fig. 4) and thermochemical evidence that at surface temperatures near 2000K, each arriving OBOBO(g) molecule is able to form 3 CO molecules which desorb from the surface (along with 2 "naked" B-atoms). These measurement will have interesting implications for boron-containing systems in which are present suspended organic soot particles and/or pyrolytic graphite containment walls.

CONCLUSIONS, FUTURE RESEARCH

In our OSR-sponsored Yale HTCRE Lab research during 1989-1990, only briefly described here, we have shown that new methods for rapidly measuring vapor- and particle-mass transfer rates and chemical gasification rates of boron and carbon surfaces, combined with recent advances in transport theory, provide useful means to identify and incorporate important, but previously neglected, mass transport phenomena in many propulsion engineering and materials engineering design/optimization calculations. We are now extending our work on the potentially important effects of new "phoretic" phenomena, 'polydispersed' particle populations, non-negligible particle inertia, and highly nonspherical particles (aggregates or molecules).

REFERENCES

Castillo, J.L., Mackowski, D.W., and Rosner, D.E., "Photophoretic Contribution to the Transport of Absorbing Particles Across Combustion Gas Boundary Layers", *Progress in Energy and Combustion Science* (in press,1990)

Garcia-Ybarra, P., and Rosner, D.E., "Thermophoretic Properties of Small Nonspherical Particles and Large Nonspherical Molecules," *AIChE J.*, **35**, [1], 139-147 (1989).

Eisner, A.E. and Rosner, D.E., Experimental Studies of Soot Particle Thermophoresis in Non-Isothermal Combustion Gases Using Thermocouple Response Techniques", *Combustion and Flame* **61**, 153-166(1985)

Gomez, A., and Rosner, D.E., "Thermophoretic Effects on Particles in Counterflow Laminar Diffusion Flames " (in preparation, 1990)

Mackowski,D.W., "Phoretic Behavior of Asymmetric Particles in Thermal Non-euilibrium with the Gas : Two-Sphere Aggregates", *J. Colloid and Interface Science* (in press, 1990)

Park, H.M., and Rosner, D.E., "Effect of Coagulation in the Boundary Layer on the Size Distribution of Thermophoretically Deposited Particles", *Chem. Engrg. Sci.* **44** (10) 2225-2231, (1989a)

Park, H.M.,and Rosner, D.E.,"Combined Inertial and Thermophoretic Effects on Particle Deposition Rates in Highly Loaded Dusty Gas Systems",*loc.cit.* **44**(10),2233 (1989b)

Park, H.M., and Rosner, D.E., "Thermophoretically Induced Phase Separation in Highly-Loaded 'Dusty' Gas Mixtures", *AIChE J.* (submitted, January 1990).

Rosner, D.E. and Kim,S.S., "Optical Experiments on Thermophoretically Augmented Submicron Particle Deposition From 'Dusty' High Temperature Gas Flows", *The Chemical Engrg. J.*(Elsevier) **29**,[3].147-157 (1984)

Rosner, D.E., Mackowski,D.W,. Tassopoulos,M., Castillo,J.L., and Garcia-Ybarra, P., "Effects of Heat Transfer on the Dynamics and Transport of Small Particles in Gases", Poster, **9th Int. Heat Transfer Conference**, August 1990,Jerusalem, Israel; AIChE Mtg.-(S.W.Churchill Birthday Symposium), November 1990, Chicago Il; *I/EC J.* (to be submitted)

Rosner,D.E.and Tassopoulos,M.," Deposition Rates from Streams Containing 'Polydispersed' Particle Populations of Arbitrary Spread",*AIChEJ* .**35**(9),1497-1508 (1989); see,also:"Total Mass Deposition Rates from 'Polydispersed' Aerosols"; *AIChE J.* **35**, (1), 164-167 (1989)

Tassopoulos, M., O'Brien, J. and Rosner, D.E, "Simulation of Microstructure/Mechanism Relationships in Particle Deposition", *AIChE J.*, **35**, (6),967-980,(1989)

Zvuloni, R., Gomez, A., and Rosner, D.E., "Direct Measurements of the High Temperature Kinetics of Solid Boron Gasification by its Higher Oxide $B_2O_3(g)$: Chemical Propulsion Implications", *A.I.A.A. J. Propulsion and Power* (in press 1990a)

Zvuloni, R., Rosner, D.E., and Gomez, A., "Role of Water Vapor on the Gasification Kinetics of Solid Boron by its Higher Oxide $B_2O_3(g)$", *A.I.A.A. J. Propuls. Power* (in press (1989b)

Zvuloni, R., Rosner, D.E., and Gomez, A., "OBOBO(g) as a Gasifier of Graphite: Measurements and Implications", (in preparation, 1990c)

Zvuloni, R., Rosner, D.E., and Gomez, A., "High Temperature Kinetics of Solid Boron Gasification By its Higher Oxide $B_2O_3(g)$: Flow Reactor Techniques, Rate Measurements and Their Chemical Implications", *J. Phys. Chem.* (to be submitted, 1990)

Zvuloni, R., **Flow Reactor Studies of the High Temperature Gasification Kinetics of Solid Boron and Carbon and Their Chemical Propulsion Implications**, PhD Dissertation, Dept. Chemical Engineering, Yale University, New Haven CT, May 1990

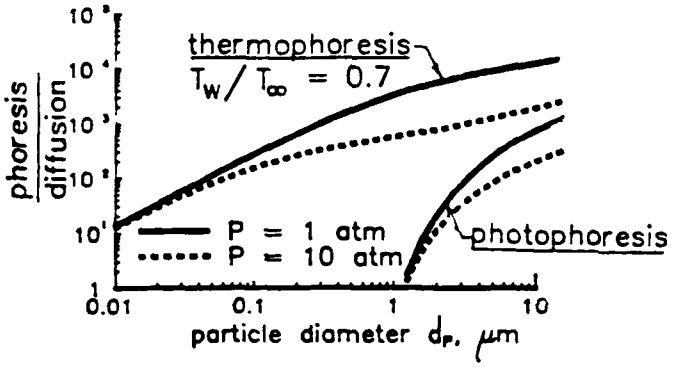

Fig.1 Relative importance of particle mass transport by the mechanisms of *Brownian diffusion* (reference case), *thermo*phoresis, and *photo*phoresis for equal radiative and Fourier energy flux across laminar boundary layers. (Size dependence for absorbing spherical particles) (after Rosner,*et.al.*,1990)

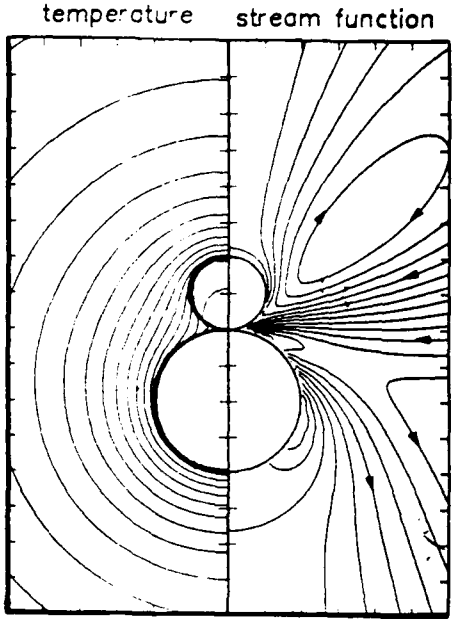

Fig.2 Predicted isotherms and streamlines in the vicinity of an asymmetric two-sphere aggregate with identical radiative properties but a size ratio of 2 (k_g/k_p=0.1,Kn_p<<1) (after Mackowski,1990)

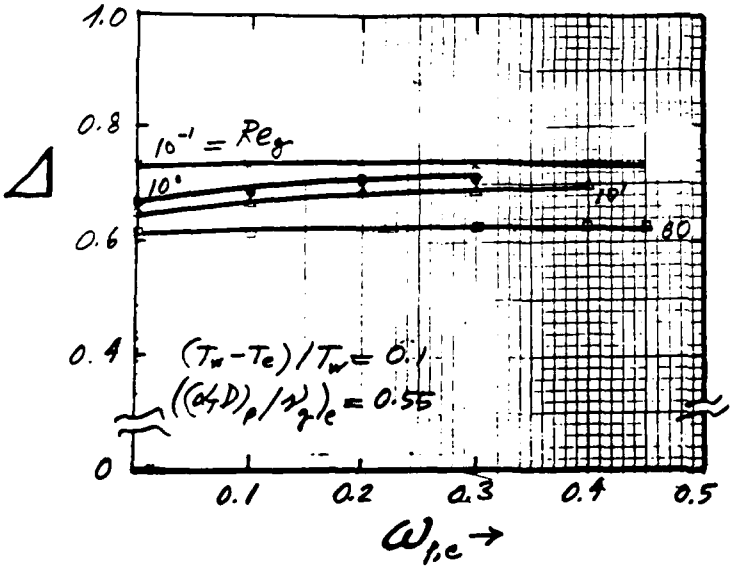

Fig.3 Predicted mass loading dependence of the 'rescaled' dust-free zone thickness at fixed values of the dimensionless temperature conrast- and thermophoretic diffusivity-parameters (after Park and Rosner, 1990)

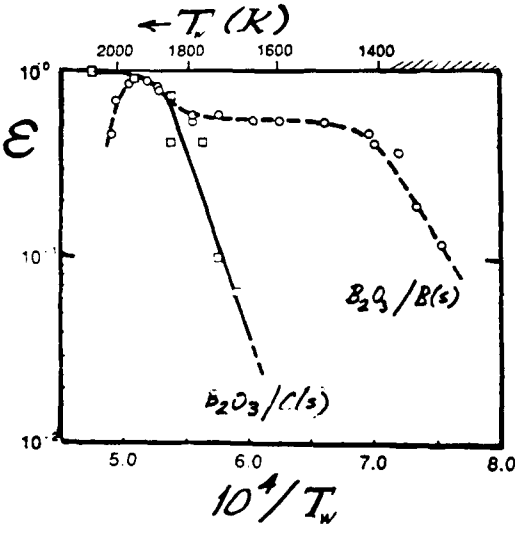

Fig.4 Experimentally inferred reaction probabilities for the attack of pyrolytic graphite and pyrolytic boron surfaces by OBOBO(g); reactant partial pressure *ca.* 0.55x10-1 Pa (after Zvuloni *et.al.*,1990)

KINETIC STUDIES OF METAL COMBUSTION IN PROPULSION

AFOSR Grant No. 89-0086

Principal Investigator: Arthur Fontijn
Research Collaborators: Peter M. Futerko, Aleksandar G. Slavejkov

High-Temperature Reaction Kinetics Laboratory
Department of Chemical Engineering
Rensselaer Polytechnic Institute
Troy, NY 12180-3590

SUMMARY

The transfer of engineering data, on rocket chamber and plume combustion, from present to advanced propulsion systems, is hampered by a lack of understanding and knowledge of individual B and Al species reactions. Experiments with our unique HTFFR (high-temperature fast-flow reactor) technique have shown a wide variety of ways by which temperature affects the rate coefficients. This emphasizes the need for accurate measurements on further B and Al reactions, which need to be included in rocket combustion models. Moreover, a framework needs to be established to allow estimates on yet other reactions. Here we report both new measurements and a correlation which unifies activation energies for a series of BCl and AlCl reactions.

TECHNICAL DISCUSSION

A variety of measurements have been made this past year. These include an extension of the series of rate coefficient measurements of B and Al radical oxidation reactions and establishment of dominant reaction mechanisms (product paths).

Rate Coefficient Measurements

The following k(T) measurements, expressed in $cm^3molecule^{-1}s^{-1}$, have been completed:

(1) $BCl + HCl \rightarrow BCl_2 + H$ T = 1250 to 1620 K
$k(T) = 1.2 \times 10^{-10} \exp(-12100\ K/T)$

(2) $BCl + SO_2 \rightarrow OBCl + SO$ T = 460 to 1700 K
$k(T) = 3.5 \times 10^{-22}\ T^{3.1} \exp(-1595\ K/T)$

(3) $BCl + N_2O \rightarrow OBCl + N_2$ T = 690 to 1000 K
$k(T) = 3.0 \times 10^{-22}\ T^{3.0} \exp(-3626\ K/T)$

The significance of the work on reactions (2) and (3) is discussed in the next section. Reaction (1) was studied to provide a comparison to the AlCl + HCl

reaction. Over the whole temperature range observed the BCl reaction may be seen, Fig. 1, to be an order of magnitude faster. This observation on an endothermic pair of reactions[1] parallels our finding, on the exothermic pairs BCl, AlCl + O_2 and BCl, AlCl + CO_2, that the BCl reactions are faster (have a larger cross-section), Fig. 2. This can be understood in terms of the larger orbital of the outer electrons (involved in the formation of the new bond) in the BCl case, which is equivalent to a larger reactive cross-section.[2]

Correlation of Activation Energies

Figure 2 shows that the O_2 reactions have smaller temperature dependences (activation energies) than the corresponding CO_2 reactions, as can be approximated from the average slopes. It is tempting to try to correlate this with physical properties of the reactants. Such has sometimes been done successfully for reactions observed over narrow temperature ranges where there is no deviation from ln k(T) = A exp(-E/RT) Arrhenius behavior. It has apparently not previously been attempted for observations covering wide temperature ranges, where the Arrhenius plots are curved. Merely considering the small number of reactions of Fig. 2 would be insufficient to obtain meaningful correlations. We therefore have extended our measurements to reactions (2) and (3). We now find that by expressing all these rate coefficients in terms of $k(T) = AT^n \exp(-E/RT)$, and fixing n anywhere between 2 and 4, that E correlates closely with $IP_{MCl} - EA_{OX}$. Here the first term is the ionization potential of BCl or AlCl and the second term represents the electron affinity of the oxidant. This is illustrated in Fig. 3 for n = 3. A physical explanation for these findings will be offered at the meeting. No correlation between E and reaction exothermicities or O-X (O-O, O-SO, etc.) bond dissociation energies is evident. We plan to further test this unified presentation of BCl and AlCl reaction activation energies by studying the AlCl equivalents of reactions (2) and (3) and repeat the AlCl + CO_2 measurements with the present, improved, HTFFR configuration.[2] The scatter in the original measurements of that reaction is such that a comparison to the other reactions of Fig. 3 is not convincing.

Identification of Product Paths

The existence of the E versus IP_{MCl}-EA_{OX} relation of Fig. 3 suggests that all these MCl reactions proceed via a similar dominant mechanism. As formation of an oxychloride is from thermochemical considerations the only accessible channel for the CO_2, SO_2, and N_2O reactions, this mechanism then would have to be oxychloride OMCl formation. Thus, while the original studies of the BCl and AlCl reactions with O_2 could not distinguish between the various channels which would be accessible based on thermochemical considerations,[3,4] it now appears that OMCl formation dominates.

The reactions of AlO with HCl and Cl_2 (the interpretation of the HTFFR results of which we completed this year)[5] similarly have a number of thermochemically accessible product paths. We therefore extended our laser-induced fluorescence measurements to look for the potential product AlCl and established that less than 5% of AlO reacted could have formed this species. This indicates that abstraction reactions dominate. This may be contrasted with

observations on NaO + HCl where a four-center channel, NaCl + OH formation, dominates.[6] The amphoteric element Al in this respect thus resembles a metalloid more than an alkali metal.

References

1. A.G. Slavejkov and A. Fontijn, "HTFFR Kinetics Studies of the Reactions of AlCl and BCl with HCl at High Temperatures", Chem. Phys. Lett., 165, 375 (1990).

2. A.G. Slavejkov, P.M. Futerko and A. Fontijn, "High-Temperature Fast-Flow Reactor Kinetics Study of the Reaction Between BCl and CO_2 From 770 to 1830 K", Twenty-third Symposium (International) on Combustion, in press.

3. A.G. Slavejkov, D.F. Rogowski and A. Fontijn, "An HTFFR Kinetics Study of the Research Between BCl and O_2 from 540 to 1670 K", Chem. Phys. Lett., 143, 26 (1988).

4. D.F. Rogowski and A. Fontijn, "An HTFFR Kinetics Study of the Reaction Between AlCl and O_2 from 490 to 1750 K", Twenty-first Symposium (International on Combustion (The Combustion Institute, Pittsburgh, 1988), p. 943.

5. A.G. Slavejkov, C.T. Stanton and A. Fontijn, "High-Temperature Fast-Flow Reactor Kinetics Studies of the Reactions of AlO with Cl_2 and HCl Over Wide Temperature Ranges", J. Phys. Chem., in press.

6. J.A. Silver, A.C. Stanton, M.S. Zahniser and C.E. Kolb, "Gas-Phase Reaction Rate of Sodium Hydroxide with Hydrochloric Acid", J. Phys. Chem., 88, 3123 (1984).

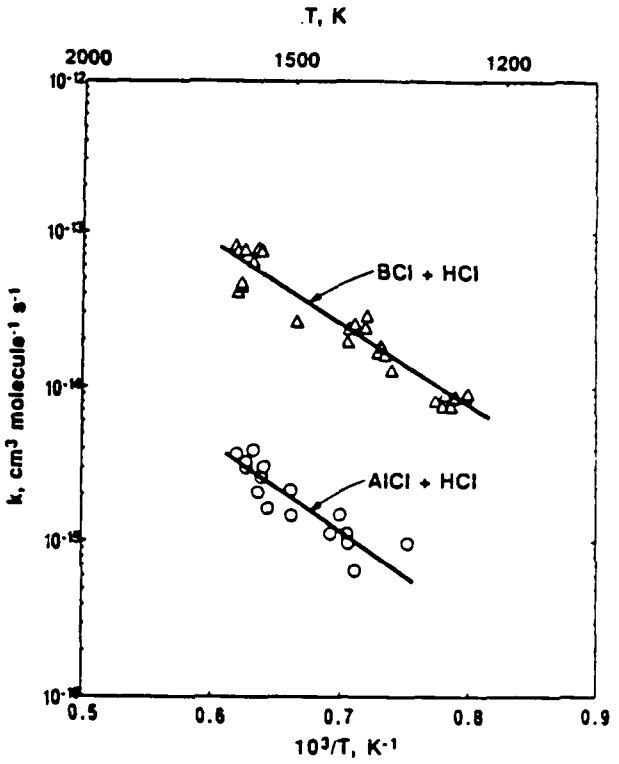

Figure 1. Arrhenius Plots of the BCl + HCl and AlCl + HCl Rate Coefficients.

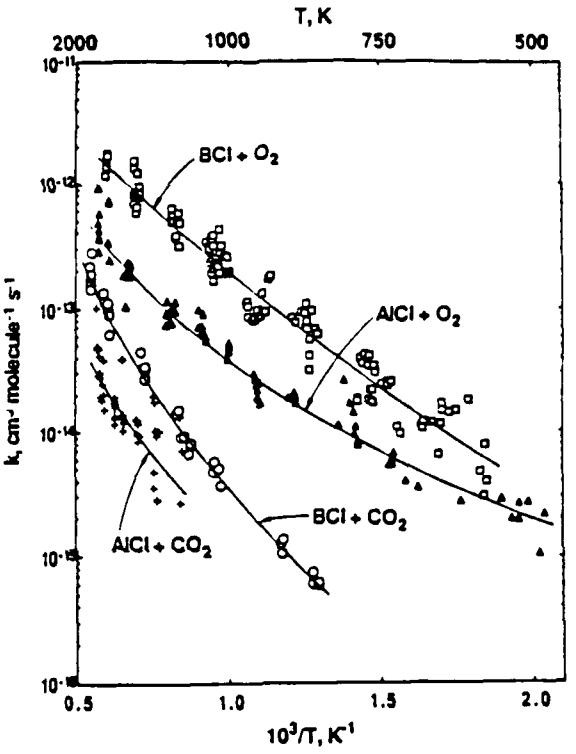

Figure 2. Arrhenius Plots of the Rate Coefficients of the BCl and AlCl Reactions with O_2 and CO_2

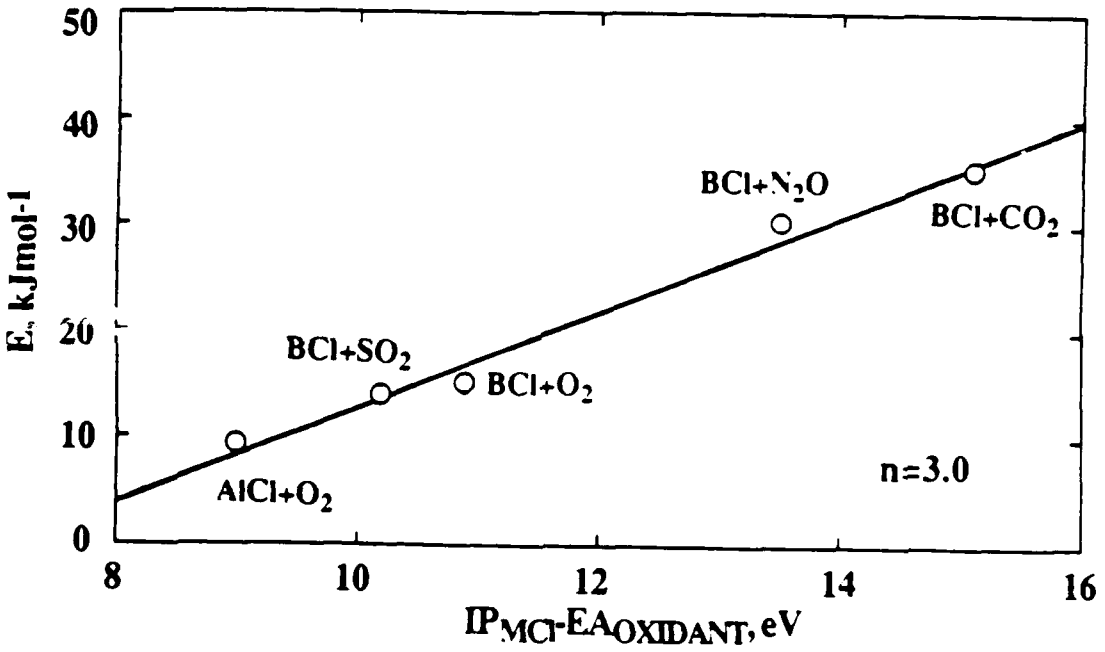

Figure 3. Correlation of the Activation Energies of the Reactions of BCl and AlCl Reactions with Various Oxidants.

FUNDAMENTAL STUDIES OF DROPLET INTERACTIONS IN DENSE SPRAYS

AFOSR Grant/Contract No. 90-0064

PRINCIPAL INVESTIGATOR:

W.A. Sirignano

Department of Mechanical Engineering
University of California
Irvine, CA 92717

SUMMARY/OVERVIEW:

The theoretical/computational study addresses the interactions amongst droplets in a non-dilute spray. Detailed flow fields in the gas surrounding droplets and between droplets and in the liquid droplet interiors are calculated via adaptive-grid, implicit finite-difference schemes. Transport in both phases, transient behavior, gas-phase mixing, and droplet drag and trajectory are determined. Special attention is given to the effects of the proximity of another droplet.

AUTHORS

W.A. Sirignano
S.E. Elghobashi
C.H. Chiang
I. Kim

TECHNICAL DISCUSSION

In a non-dilute spray, the transport rates and flow field in the droplet's surrounding gas film, the droplet drag coefficient, and the droplet vaporization rate are different from the values for an isolated droplet. Our theoretical/computational effort has concentrated on detailing the differences between droplets in a non-dilute spray and droplets in a dilute spray. Axisymmetric calculations of fuel droplets moving in tandem have been underway for several years. Those computations, with both constant properties and variable properties, are now completed. Axisymmetric calculations of liquid-oxygen (LOX) and fuel droplets in tandem have begun. New three-dimensional calculations of interacting droplets (with the relaxation of the tandem constraint) are now underway. A section of discussion is given to each of these three problems.

1. Description of the interacting fuel droplets research

The present research has concentrated on the interaction between two vaporizing fuel droplets which are moving in tandem. The single droplet model from our previous research[1] is modified with the addition of a grid generation routine and the readjustment of the velocity

of the downstream droplet as well as the variation of spacing. The results have significantly improved our basic understanding and our computational data base in the droplet-interaction research. A summary of the results is given as follow:

Figure 1 shows results for drag coefficients. Note that time increases as the droplet Reynolds number decreases. Due to the influence of recirculating flow from the lead droplet, the downstream droplet receives considerably less convection and hence less shear stress and less internal circulation. The drag coefficient of the lead droplet tends to be similar to that of an isolated droplet until the droplets are separated by less than 6 diameters. The drag coefficient of the downstream droplet is significantly lower than that of the lead droplet. A similar trend for the Nusselt and Sherwood numbers is also observed. See Figure 2. The dominant type of heating of the downstream droplet switches to conduction as the two droplets become sufficiently close that the downstream droplet reaches the near wake of the lead droplet.

Droplet trajectories are also analyzed for a wide range of initial Reynolds number, initial droplet spacing, initial droplet size ratio, and transfer number. Results of the type shown in Figure 3 indicate that droplet spacing could increase or decrease in time depending upon various factors. Separation becomes more likely as the downstream droplet becomes smaller relative to the lead droplet. For each initial droplet spacing, there exists a critical droplet-size ratio below which the droplet collision becomes unlikely. For decreasing initial spacing, the drag difference increases and the critical size ratio decreases. The critical size ratio increases as the initial Reynolds number decreases. An increase in initial Reynolds number serves to increase the approaching speed. The results from constant property computations overestimate the approaching (or separating) speed of the downstream droplet. For the cases with high transfer number, the rate of variation of droplet spacing is reduced. The correlations for the transfer coefficients of both droplets have been obtained and can be applied in the overall spray computations.

2. Description of the interacting LOX-fuel droplets research

The major effort of this research involves the detailed investigation of the tandem interactions between liquid oxygen (LOX) and fuel droplets. The forced convection of the gas phase, the transient deceleration of the flow due to the drag force, the surface regression as well as the relative motion between the droplets, the internal circulation and transient heating of the liquid phase and variable properties are considered. This analysis includes an unsteady, axisymmetric and laminar flow calculation. The entire computation will be performed for four basic configurations: (1) an isolated LOX droplet, (2) a LOX droplet following in the wake of another LOX droplet, (3) a LOX droplet following in the wake of a fuel droplet, and (4) a fuel droplet moving in the wake of a LOX droplet. Fuels are selected to be hydrocarbons and alcohols.

Our previous researches[1,2] have examined in detail the transport processes of isolated and interacting, vaporizing hydrocarbon-fuel-droplets, respectively. In the current study, the basic governing equations and interface conditions as well as the solution procedures remain the same. Therefore, the well developed codes will be utilized to facilitate the present research projects. The existing single droplet code will be employed after some modification to account for LOX properties. The available property information has been compiled and a

property table based on the ambient pressure and an extensive range of temperature has been constructed. Instead of computing the strongly coupled thermophysical correlations, the property routine will perform interpolation to retrieve values from the property table during the droplet computation. An experimental correlation between surface saturation pressure and temperature has been employed in the boundary-condition-solver[1]. The linearization treatment of this correlation is employed in the computations.

For the case of two droplets of different compositions moving in tandem, in addition to the property modification, one more species equation is required for the completeness of the problem. Also, note that the equation of state and pressure correction equation must be modified accordingly.

The results of vaporization rates, gas-phase composition, gas-phase mixing rates, drag coefficients, Nusselt numbers and Sherwood numbers are to be reported. The dependencies of the above quantities upon the droplet Reynolds numbers, droplet spacings, and transfer numbers are determined.

3. Description of the three-dimensional interactions of droplets

This project deals with the effects of the interaction amongst vaporizing droplets in a dense spray surrounded by high temperature gas. This study is an extension of recent and past research on axisymmetric configurations of isolated droplets and of interacting droplets in the wake of another droplet. The major new research thrust is the study of three-dimensional transient interactions. Figure 4 describes two droplets moving side by side with the initial velocity vectors lying in the same plane. This plane will be a plane of symmetry. Another plane of symmetry is perpendicular to the first plane and midway between the two droplets.

A generalized coordinate system has been developed to conform to the shapes of the boundaries to avoid errors due to interpolation. The governing equations are represented in the generalized coordinates. The ICE (Implicit Continuous-fluid Eulerian) method is being adapted to solve the fully coupled, nonlinear system of partial differential equations that govern the flow field. Calculations with this Navier-Stokes solver are expected by the summertime.

A three-dimensional grid-generation has been successfully achieved. The computational grid is generated from the solution of a system of Poisson equations in which the source terms are used to control the attraction between grid lines. This quasi-linear elliptic system of equations is solved by finite-difference discretization using the successive-over-relaxation (SOR) technique. Figure 5 and 6 represent cross-sections of the three-dimensional grid system at different times.

References

1. C.H. Chiang, M.S. Raju and W.A. Sirignano, Numerical Analysis of Convecting, Vaporizing Fuel Droplet with Variable Properties, to appear in *Int. J. Heat Mass Transfer*, also see *AIAA Aerospace Sciences Meeting*, Paper 89-0834 (1989).

2. C.H. Chiang and W.A. Sirignano, Numerical Analysis of Interacting, Convecting, Vaporizing Fuel Droplets with Variable Properties, submitted to *Int. J. Heat Mass Transfer*, also see *AIAA Aerospace Sciences Meeting*, Paper 90-0357 (1990).

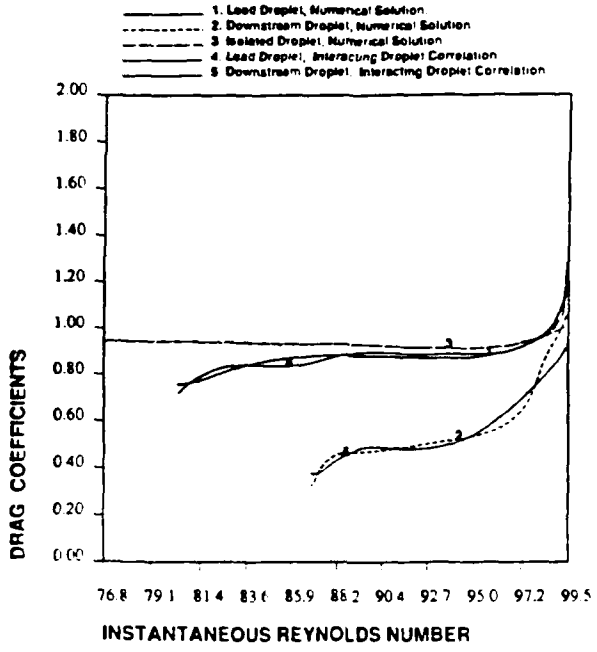

Fig. 1 Time variation of drag coefficients and correlations for the lead droplet and the downstream droplet.

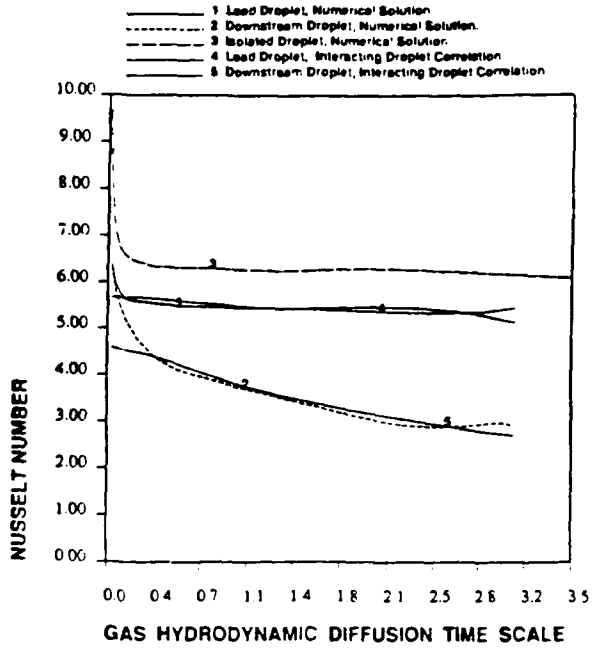

Fig. 2 Time variation of average Nusselt numbers and correlations for the lead droplet and the downstream droplet.

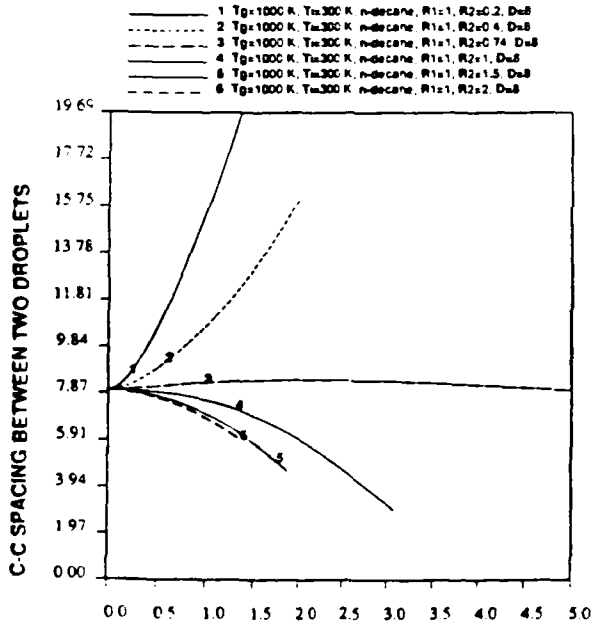

Fig. 3 Time variation of the average Sherwood numbers and correlations for the lead droplet and the downstream droplet.

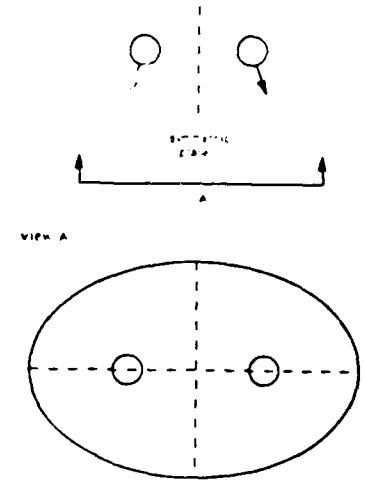

Fig. 4 Description of the physical domain

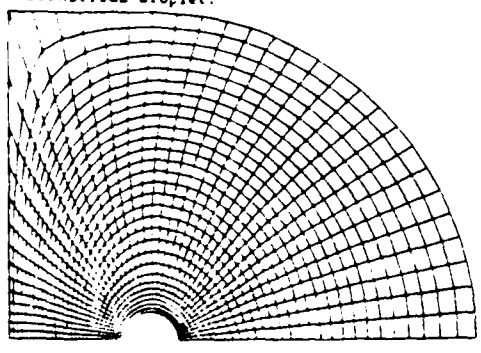

Fig. 5 Grid distribution

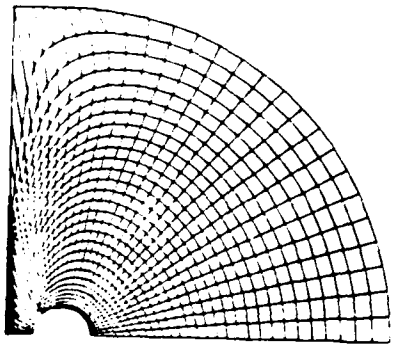

Fig. 6 Grid distribution

PARTICLE DISPERSION IN TURBULENT SHEAR FLOWS

AFOSR Grant No. 89-0392
Principal Investigators: Ian M. Kennedy and Wolfgang Kollmann

Dept. of Mechanical, Aeronautical and Materials Engineering,
University of California,
Davis,
Calif. 95616

SUMMARY

This project investigates the nature of particle dispersion in turbulent jets with an emphasis on the effect of the turbulence on current modelling of droplet drag and vaporization in sprays. A novel experimental facility has been built which provides Lagrangian statistics of single particle motion in a turbulent jet. Numerical simulations of the flow will serve to check the validity of the drag and vaporization correlations.

TECHNICAL DISCUSSION

(a) Experiments: The experimental apparatus is shown schematically in Fig.1. A turbulent jet of air is produced by the flow from a round nozzle. Typical Reynolds numbers of the jet are 20,000 in these experiments. The jet flow has been characterized in terms of length scales and spectra by hot wire anemometry. Single droplets of hexadecane or water are formed by a piezoceramic device at the top of the flow chamber. Droplet diameters range from about 50 μm to about 200 μm. They are injected onto the centerline of the jet with a spacing which is many times the droplet diameter so that these particles are non-interacting and the flow is unaffected by their presence.

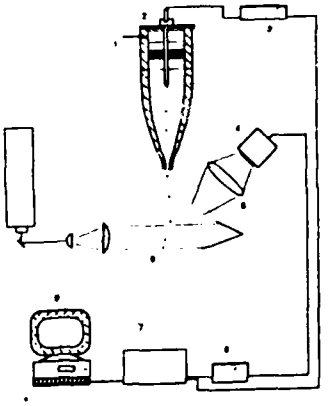

Fig. 1. Experimental Apparatus: 1) air supply; 2) droplet generator; 3) timing circuit; 4) photo-diode; 5) collection lens; 6) bandpass filter; 7) CAMAC data acquisition; 8) PS/2 computer; 9) Ar-ion laser sheet.

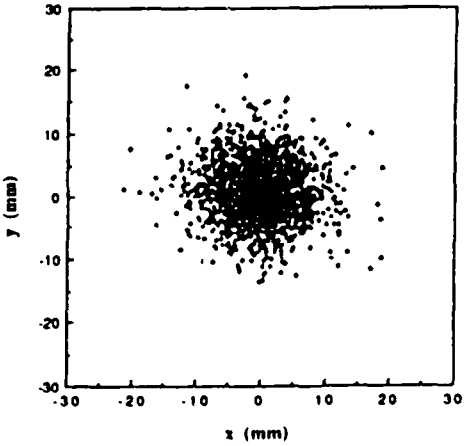

Fig. 2 Scatter plot of droplets at X/D=40

The positions of the particles at various downstream locations are determined by a laser scattering technique which is shown in Fig. 1. A sheet of light is formed from an Argon-ion laser. The sheet is directed across the jet. As a particle traverses the sheet of laser light it scatters light which is

collected by a lens. The droplet scattering is then imaged onto a position sensitive detector which can detect the X-Y coordinates of the droplet. The position sensing diode output is digitized by a CAMAC system for analysis on a computer. By this means statistically significant samples of particle positions are obtained. A scatter plot of 2,000 droplets is shown in Fig. 2. Droplet velocities are determined from the time of flight through the laser sheet which is of a known thickness.

A fundamental quantity which is of interest to us is the particle dispersion as a function of the time of flight from the point of injection in the turbulent jet. The dispersion is defined as the mean square displacement of the particles from their initial location at the origin of the jet. The dispersion of hexadecane and water droplets is shown as a function of the axial location in Fig. 3. By using measured times-of-flight of droplets from the nozzle to the measurement plane we can present the particle dispersion as a function of the time of flight from the nozzle in Fig. 4.

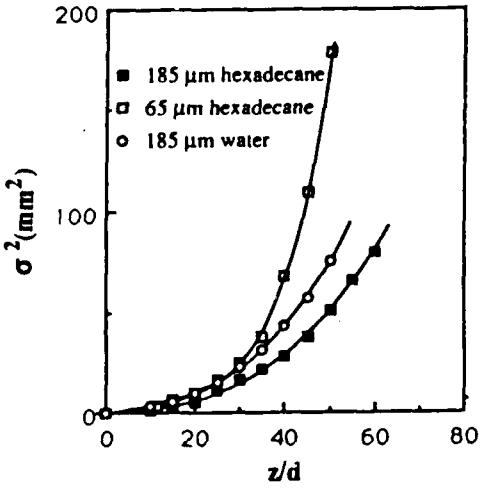

Fig. 3 Dispersion as function of X/D

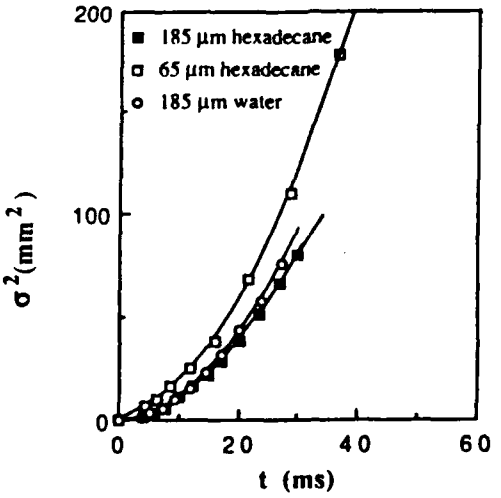

Fig. 4 Dispersion as function of time

(b) Stochastic Simulations: A stochastic simulation of the particle dispersion in the jet has been implemented. A Reynolds stress model has been used for the velocity field of the jet. The results from this code have served as the basis for the particle simulation which has been done in the same manner as Gosman and Ionniades and others. Using the statistics of the velocities a Gaussian pdf is sampled randomly at whatever point in the flow is occupied by the droplet. The random axial and radial velocity components are allowed to interact with the droplet for a time which depends on the lifetime of the turbulent eddy or on the transit time of the droplet through the eddy. The particle equation of motion is then integrated through the flow field with a fourth order Runge-Kutta scheme. Only the drag and gravity terms have been used in the particle equation of motion. The conditions of the experiment have been simulated.

One issue which we investigated with this simulation was the role of the Reynolds stresses on the dispersion of particles. It has been common practice to neglect this factor without adequate justification. The inclusion of the velocity covariance was achieved by performing a coordinate rotation at the

time of the velocity pdf sampling so as to impose a correlation on the radial and axial velocity components; the covariance that was predicted by the second order closure code was used. The calculations showed, in fact, that the velocity covariance played little role in determining the dispersion of the droplets in this flow. This result affirms the validity of the usual approach that has been adopted in modelling particle dispersion in shear flows.

The second aim of the simulation was to provide a comparison with the experimental dispersion results. One of the surprising outcomes of this comparison was the unexpectedly significant role for the initial conditions in affecting particle behavior and dispersion. Initially, we encountered great difficulty in matching the measured dispersion rates of the larger particles; the computed dispersion was much less. It was eventually discovered that the discrepancy was largely due to some initial velocity fluctuations in the radial direction as the droplets entered the flow field. The rms radial velocity fluctuations were estimated from the slope of the experimental curve of the dispersion as a function of the square of the time of flight at early times after droplet injection. Although the mean radial velocity was zero, the small fluctuations were shown numerically to account for the measured dispersion quite well. These results bear some potentially important implications for the modelling of sprays in which the initial or boundary conditions near the injector are rarely well-known.

(c) Vortex Dynamics Simulations: In order to compare simulations of droplet dispersion with measurements it is necessary to prescribe the forces which are acting on the particle. One of aims of the project is to evaluate correlations of the drag on vaporizing and non-vaporizing droplets. There are, however, a number of other forces which may be important in unsteady shear flows; these forces include the Basset force that accounts for history effects, virtual mass and pressure gradient forces. The common approach has been to ignore all forces but the drag and buoyancy terms if the ratio of droplet to gas densities is large. This assumption is very attractive because it yields considerable economies in calculating particle trajectories. The Basset term, for example, introduces an integral into the equation for droplet motion. The accuracy of this assumption in a turbulent shear flow at various pressures has not been examined in detail.

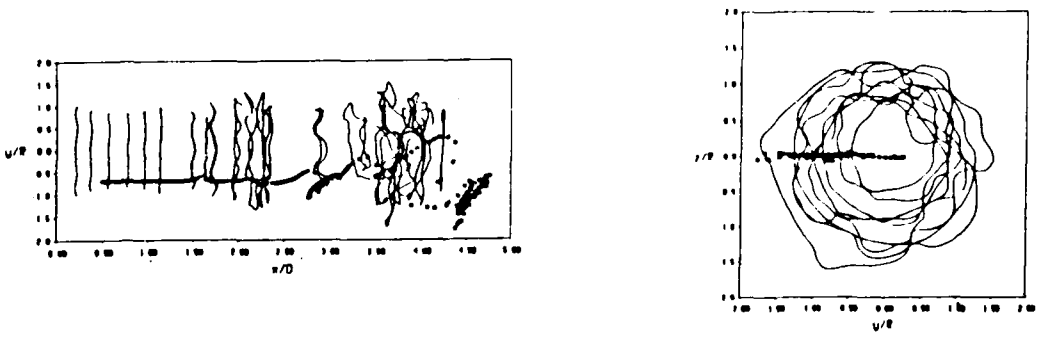

Fig. 5 (a) Side View of Vortices and Droplets (b) Head-on View

We have developed a fully three dimensional vortex dynamics calculation of the near field of a turbulent air jet. Particles are introduced into the flow field and their equations of motion are solved along with the vortex equations. Two types of particle equations were used viz., a general form with all terms and a so-called Type I approximation which includes only drag and gravity.

With the general droplet equation we show the position of 200 droplets of hexadecane in Fig. 5. The droplets were released at a radial position which was in the shear layer on the edge of the jet. The side view in Fig. 5 indicates that the droplets have been dispersed substantially across the jet and some have been flung beyond the jet boundaries. However, the head-on view reveals that very little azimuthal dispersion has been achieved. For this reason the 3D calculation was abandoned in favor of the much more efficient axisymmetric calculation. With this model of the near field of the jet we examined the effect of the the Type I approximation on the dispersion of droplets at 1 atmosphere and at 20 atmospheres (Fig. 6). Three particle diameters were considered viz., 25, 75 and 150 μm. At 1 atm the omission of the Basset, virtual mass and pressure gradient terms makes little difference to the dispersion for all sizes of particles that we considered. However, at 20 atm it is apparent that larger particles do exhibit some sensitivity to the Type I approximation; smaller particles show little influence from the Basset and other forces. The ratio of Basset and other forces to the drag force for 150 μm droplets was found to be as large as 30 to 40% at some times. Similar results have been obtained for vaporizing droplets. This indicates the need to be careful in the use of the Type I approximation for large particles at elevated pressures. The density ratio alone may not be a sufficient test for this accuracy of this approximation.

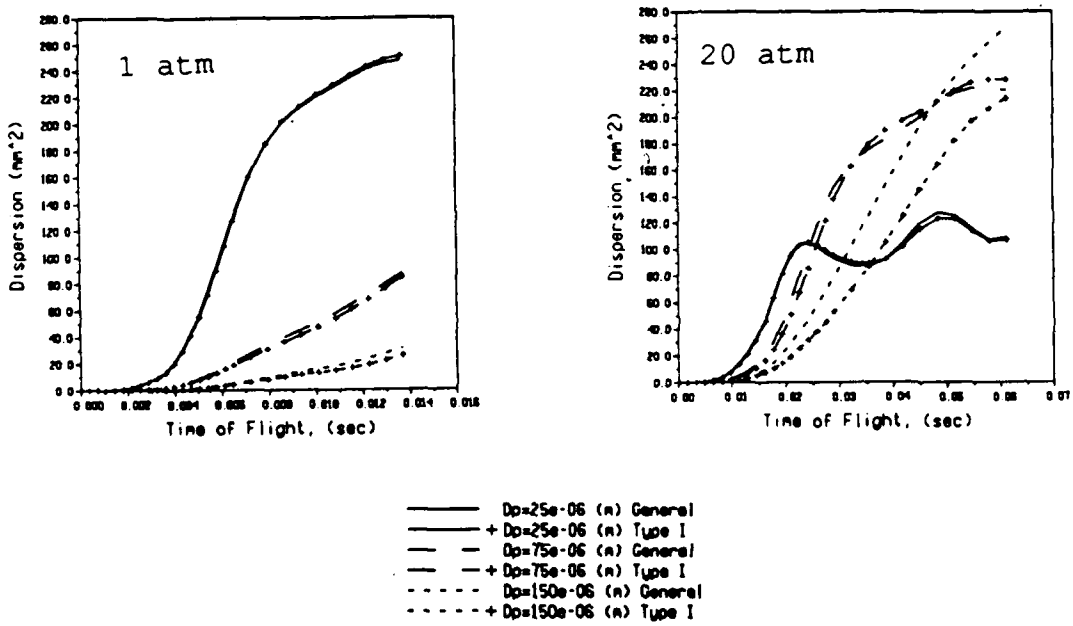

Fig.6 Droplet Dispersion for Type I Approximation and General Formulation

DROP/GAS INTERACTION IN DENSE SPRAYS

(AFOSR Grant No. 89-0516)

Principal Investigator: G. M. Faeth

218 Aerospace Engineering Building
The University of Michigan
Ann Arbor, Michigan 48109-2140

SUMMARY/OVERVIEW

Two aspects of drop/gas interactions in dense sprays are being studied: turbulence modulation and secondary drop breakup. Turbulence modulation is the direct production and dissipation of turbulence by the motion of a dispersed phase — it is the dominant mechanism controlling turbulence properties in dense sprays. Turbulence modulation is being studied experimentally, using homogeneous particle-laden flows; and theoretically, using statistical methods similar to those used to analyze electrical noise. Findings thus far have yielded generalized methods to estimate moments, probability density functions, and spatial and temporal correlations of continuous-phase velocity fluctuations; and have demonstrated the application of these results to estimate dense-spray mixing processes like turbulent dispersion. A better fundamental understanding of turbulence modulation, however, requires more information on particle-laden flows and particle wake properties in turbulent environments, which is the focus of current work.

An earlier study of dense pressure-atomized sprays showed that breakup intrinsically occurs by primary breakup at the liquid surface, followed by near-limit secondary breakup of most of the liquid. Motivated by this observation, near-limit secondary breakup is being studied within a shock tube, using holocinematography to provide three-dimensional time-dependent information, i.e., rates of drop formation, breakup times, and final drop size and velocity distributions. This information is vital for gaining a better understanding of separated-flow and mixing processes within dense sprays, since drop breakup tends to be rate-controlling in dense sprays, much like drop vaporization tends to be rate-controlling in dilute sprays.

TECHNICAL DISCUSSION

Introduction. Processes within the dense-spray region near the injector exit are not well known, which hampers understanding of sprays since the dense-spray region is the initial condition for the rest of the flow (Faeth, 1990). This motivated earlier study of the structure of the near-injector region of large-scale pressure-atomized sprays in this laboratory (Ruff et al., 1989, 1990a, b). The findings highlighted two aspects of dense sprays that are currently being studied: turbulence modulation, which is the direct effect of drops on gas-phase turbulence properties, and is the dominant turbulence mechanism of dense sprays; and secondary breakup, which is a rate-controlling step in dense sprays, much like drop vaporization is a rate-controlling step in dilute sprays. Progress in each area during the report period is discussed in the following.

Turbulence Modulation. Turbulence modulation is being studied in homogeneous particle-laden flows involving a uniform flux of particles falling in stagnant water or air environments. For these conditions, all continuous-phase turbulence properties are due to effects of turbulent modulation, allowing the phenomenon to be studied in dilute flows that are accessible for measurements. Measurements in air and water provide a means of varying particle spacing and the rate of dissipation in the flow over a wide range, so that trends can be identified. Measurements

involve two-point phase-discriminating laser velocimetry for continuous-phase properties, and motion-picture shadowgraphs and Mie scattering for particle properties.

Both turbulent dispersion and turbulence modulation have been considered theoretically. Analysis of turbulent dispersion involves particle trajectory calculations, using statistical time series methods due to Box and Jenkins (1976) to simulate the turbulent velocity field along the particle path. Experimental evaluation demonstrated that this approach was effective (Parthesarathy and Faeth, 1990a); therefore, current efforts are concentrating on predicting turbulence properties. The approach being studied involves extension of Campbell's theorem (Rice, 1954) from a linear to three-dimensional domain, so that the contributions of individual particle wakes can be summed to find the properties of the field. Individual wake properties were estimated from existing information, limited to mean and turbulent properties of wakes in nonturbulent environments.

Since the present flows are homogeneous and stationary, the rate of dissipation, ϵ, of turbulence kinetic energy can be estimated from the rate of production, i.e.,

$$\epsilon = \pi d_p^2 C_D \; U^2 \dot{n}''/8 \tag{1}$$

where dp, CD, U and $\dot{n}''$ are the particle diameter, drag coefficient, velocity and number flux, and ρ is the continuous-phase density. Equation (1) is based on the approximation that relative and absolute particle velocities are nearly the same, which is appropriate for present conditions. Then, given ϵ, the analysis yields the following expressions for velocity fluctuations in the streamwise and crosstream directions, $\tilde{u}'$ and $\tilde{v}'$:

$$\tilde{u}'/U = 3\tilde{v}'/(2U) = 6.8((\epsilon d_p/U^2)(\theta/d_p)^{2/3})^{1/2} \tag{2}$$

where $\theta = (C_D d_p^2/8)^{1/2}$. The coefficient in equation (2) has been fitted to some extent by only considering wake properties up to $175d_p$ from the particle, although wake velocities are small in comparison to present capabilities to measure them beyond this position (Parthesarathy and Faeth 1990b).

Figure 1 is an illustration of measured and predicted velocity fluctuations, plotted according to equation (2). Dark and open symbols designate air and water continuous phases. Aside from some scatter for $\overline{v}'$ in particle/air flows, where experimental uncertainties are high, equation (2) is in good agreement with the measurements. The range of the data involves particle Reynolds numbers of 40-600, $\overline{u}'/U$ of 0.001-0.1, and particle/continuous-phase density ratios of 2.5-2100, which spans conditions typical of sprays. An interesting feature of the results is the high degree of anisotropy evident from equation (1). This is caused by the intrinsic anisotropy of wake velocities and generally agrees with observations in dense sprays (Ruff et al., 1990b).

Other successes of predictions include Gaussian probability density functions of velocity fluctuations, in accord with measurements, and spatial correlations of streamwise velocity fluctuations in the crosstream direction illustrated in Fig. 2. The measured correlation is relatively independent of particle size and loading and approximates an exponential function, which agrees with predictions.

Measured spatial correlations of streamwise velocity fluctuations in the streamwise direction are illustrated in Fig. 3. Predictions correctly indicate the relative independence of the measured correlation on operating conditions, but not the exponential functional form illustrated in the figure. Additionally, predictions of integral scales were poor. These deficiencies are attributed to limited available information on the structure of wakes for the present Reynolds number range, in the presence of an ambient turbulence field (Parthesarathy and Faeth, 1990b).

Current work is emphasizing measurements of particle wake properties at modest Reynolds numbers in the presence of ambient turbulence in an effort to diagnose ineffective aspects of predictions. The next phase of the study will involve consideration of interactions between grid-generated turbulence and a dispersed particle phase, rather than just self-generated turbulence.

Secondary Breakup. Earlier measurements of the structure of large-scale (10-20 mm diameter) dense pressure-atomized sprays suggested two primary breakup mechanisms: aerodynamic breakup for nonturbulent liquids, and turbulent breakup for turbulent liquids (Ruff et al., 1990b). Additionally, it was found that the bulk of the liquid was unstable to secondary breakup for both primary breakup mechanisms. This behavior was supported by measurements of mean drop sizes that were significantly smaller over the bulk of the flow than near the liquid surface. Thus, this phase of the investigation is considering the mechanism and outcome of secondary breakup for conditions typical of dense sprays.

Scaling arguments suggest that aerodynamic primary breakup is most important for practical sprays (Faeth, 1990); therefore, these conditions are being used to define the secondary breakup regime of interest. Figure 4 is an illustration of this regime, using the low Ohnesorge number breakup regime map of Borisov et al. (1981). The regime map is plotted in terms of the drop Weber and Reynolds numbers based on gas density, We_{gp} and Re_p. The tests of Ruff et al. (1990a, b) follow a single trajectory on this plot for both nonturbulent and turbulent liquids. The full range available for aerodynamic primary breakup is somewhat broader, but still lies in the near-limit secondary breakup regime where deformation and weak stripping breakup are dominant. This assessment also agrees with the few secondary breakup events that were observed by Ruff et al. (1990b).

The dynamics and outcome of near-limit secondary breakup are poorly understood (Faeth 1990). Therefore, these properties are being studied using a shock tube with test drops injected in front of the shock wave with a piezo-electric generator. Measurements involve conventional flash shadowgraphs, to define breakup regime transitions; and holocinematography, to map out the evolution and outcome of the secondary breakup process.

Work during this report period involved assembling the shock tube, developing the drop generator, and developing the holocinematography system. The latter instrument was demonstrated successfully in the in-line (Gabor) configuration, providing a 35 mm diameter X 100 mm long field of view with hologram framing rates of 1kHz (Ruff et al., 1990c).

Current work involves developing the experiment. Subsequent measurements will continue throughout the next report period in order to define effects of Ohnesorge, Weber and Reynolds number variations. Future work also involves development of an off-axis holocinematography system, in order to improve the resolving power of this instrument.

REFERENCES

Borisov, A. A. , Gel'fand, B. E., Natazon, M. S. and Kossov, O. M. (1981) Droplet breakup regimes and criteria for their existence, *Inzh.-Fiz. Zh.*, Vol. 40, pp. 64-70.

Box, G.E.P. and Jenkins, G. M. (1987) *Time Series Analysis*, Revised Edition, Holden-Day, San Francisco, pp. 47-84.

Faeth, G. M. (1990) Structure and atomization properties of dense turbulent sprays, *Twenty-third Symposium (International) on Combustion*, The Combustion Institute, Pittsburgh, in press.

Parthesarathy, R. N. and Faeth, G. M. (1990a) Turbulent dispersion of particles in self-generated homogeneous turbulence, *J. Fluid Mech.*, submitted.

Parthesarathy, R. N. and Faeth, G. M. (1990b) Turbulence modulation in homogeneous dilute particle-laden flows, *J. Fluid Mech.*, submitted.

Rice, S. O. (1954) Mathematical analysis of random noise, *Noise and Stochastic Processes* (N. Wax, ed.) Dover Publications, Inc., New York, pp. 133-294.

Ruff, G. A. Sagar, A. D. and Faeth, G. M. (1989) Structure and mixing properties of pressure-atomized sprays, *AIAA J.*, Vol. 27, pp. 901-908.

Ruff, G. A. Bernal, L. P. and Faeth, G. M. (1990a) Structure of the near-injector region of non-evaporating pressure-atomized sprays, *J. Prop. Power*, in press.

Ruff, G. A., Wu, P.-K., Bernal, L. P. and Faeth, G. M. (1990b) Continuous- and dispersed-phase structure of dense non-evaporating pressure atomized sprays, *J. Prop. Power*, submitted.

Ruff, G. A., Bernal, L. P. and Faeth, G. M. (1990c) High-speed in-line holocinematography for dispersed-phase dynamics, *J. Appl. Optics*, submitted.

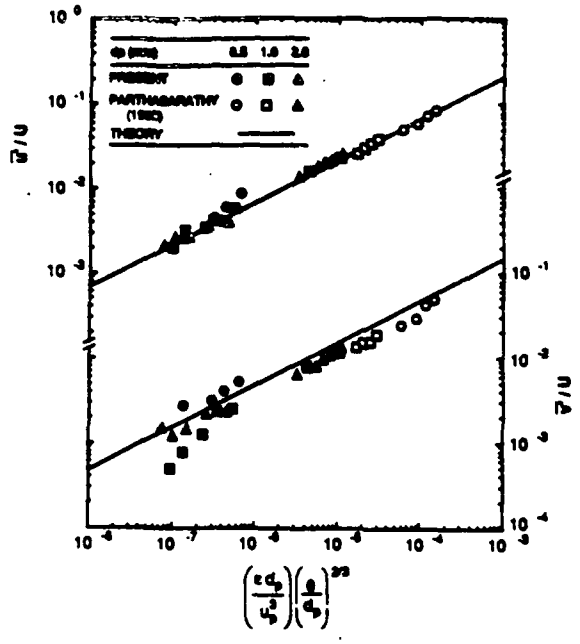

Fig. 1 Continuous-phase velocity fluctuations.

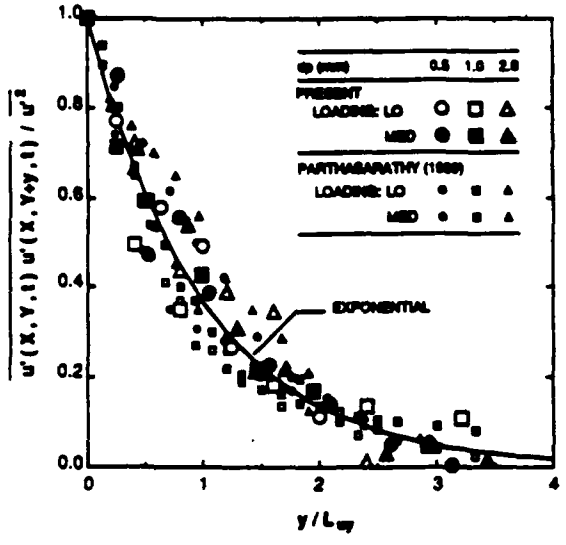

Fig. 2 Spatial correlation of streamwise velocity fluctuations in the crosstream direction.

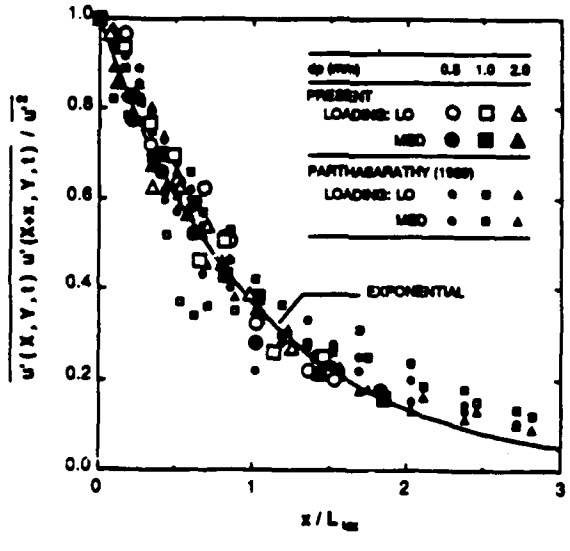

Fig. 3 Spatial correlation of streamwise velocity fluctuations in the streamwise direction.

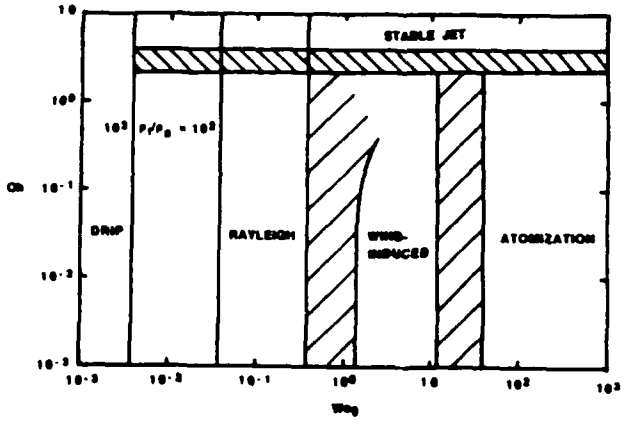

Fig. 4 Drop breakup regime transitions at low drop Ohnesorge numbers.

INVESTIGATION OF THE APPLICATIONS OF LASER-INDUCED FLUORESCENCE TO FUEL SPRAY AND SINGLE DROPLET VAPORIZATION

ARO Contract No. DAAL03-87-K-0120

Principal Investigator: Lynn A. Melton

Department of Chemistry
University of Texas at Dallas
Richardson, Tx 75083-0688

SUMMARY/OVERVIEW:

The development and application of laser induced fluorescence diagnostic methods for hydrocarbon fuels has continued. Exciplex fluorescence thermometry has been used to measure the (near surface) temperature of isolated droplets falling into a hot ambient. Direct calibration methods have been developed for exciplex-based vapor/liquid visualization; these methods should be simpler and more accurate than the previous photophysics-based methods. In addition, methods have been developed for correction for refraction effects by droplet surfaces, measurement of temperature fields within droplets, and production of monodisperse droplets at high pressures.

TECHNICAL DISCUSSION:

A. Temperature Measurements in Falling Droplets

Exciplex fluorescence thermometry has been used to measure the (near-surface) temperature of a 225 micron droplet, which had fallen 10 cm through a known heated ambient.[1] Decane was doped with 5×10^{-3} M pyrene. The optical density was sufficiently high that 90% of the incident light was absorbed within the outer 50-60 microns of the droplet, and thus, the temperatures inferred could be interpreted as "near-surface" temperatures. Spectra were taken on an optical multichannel analyzer, and droplet diameters were calculated from photomicrographs. These measurements are thought to be the first temperature measurements ever made of freely falling hydrocarbon droplets.

These temperature measurements required the development of protocols which must be respected if exciplex fluorescence thermometry of droplets is to yield accurate temperatures. Questions of optical depth, analysis of spectra, calibration, and interpretation were addressed. In particular, the effect of evaporation of a volatile solvent on the calibration of the (involatile) exciplex fluorescence thermometer was recognized, In

order to complete the analysis of that experiment, it was necessary to show that evaporation of the droplet was negligible (< 10% of the mass). However, the most interesting applications of exciplex fluorescence thermometry are in the determination of the temperatures of evaporating drops, and consequently, work has begun to develop improved exciplex fluorescence thermometers, which are concentration-independent.

An improved thermometry system, consisting of 10% 1-methylnaphthalene/10^{-4}% 1,3-di(1-pyrenyl)-propane (PYPYP), is under development. The PYPYP, which is at low concentration, functions as a concentration-independent intramolecular exciplex fluorescence thermometer. However, at the low concentrations at which it will do so, the optical density is not high enough to restrict the fluorescence to the droplet surface. The methylnaphthalene, at high concentration, acts as the primary optical absorber, and transfers its excitation to the PYPYP. Preliminary studies indicate that the temperatures determined with this new system will be "surface temperatures", since the solution will be extremely optically thick, and that they will be virtually independent of the degree of evaporation of the droplet since the thermometer calibration can be made virtually independent of the dopant concentration.

B. Quantitative Spray Visualization

Direct calibration methods for exciplex-based vapor/liquid visualization systems have been developed at United Technologies Research Center.[2] These direct calibration methods will complement the photophysics-based methods developed earlier. Vapor sources of known concentration were prepared by sealing small amounts of N,N,N'N'-tetramethyl-p-phenylenediamine (TMPD), the best monomer molecule, in quartz cuvets under vacuum. Since the vapor pressure of TMPD as a function of temperature is unknown, the absorbance of the cuvets as function of temperature was measured. The same cuvets could then be placed in the spray apparatus, at a known temperature, as a vapor source of known concentration. Droplets of known diameter were obtained by measuring the diameter of droplets at the edge of a non-evaporating spray. Correction must be made for non-uniform illumination of single droplets. Calibration factors were obtained as the ratio of the measured intensity to the known vapor or liquid mass.

Calibrated liquid and vapor images were obtained for a small air brush spray into hot nitrogen. Fig. 1 shows results obtained. The difference in information between averaged and instantaneous spray behavior is striking. As a result of this work, direct calibration methods will be available for other users of exciplex-based vapor/liquid visualization methods.

C. Single Droplet Physics

1. Optics of Droplets

Details of heat transfer to droplets can be obtained through "droplet slicing" diagnostics, in which a thin laser sheet illuminates an equatorial plane of the droplet. However, in such an experiment, the emitted rays pass through a hemisphere of hydrocarbon liquid before exiting the droplet, and they refract as they pass from the liquid to the surrounding atmosphere. The liquid hemisphere acts like a lens, which magnifies the center of the droplet and makes the collection of light originating near the surface difficult. A computer program was developed to correct for these effects and is being checked against measurements made on a glass hemisphere.

Methods have been developed which make it possible to determine unambiguously from an experimental image whether the laser sheet did indeed bisect the droplet.

2. Exciplex Fluorescence Thermometry Within Droplets

Using "droplet slicing" techniques and exciplex fluorescence thermometry, preliminary measurements of the temperature field within a falling droplet have been made. The fluorescence from a single droplet, which had fallen into heated nitrogen, was recorded on a color CCD camera. For droplet temperature measurements, the thermometry is carried out by separating the RGB outputs of the CCD camera and dividing the blue intensity by the green intensity pixel by pixel, to obtain a ratio which can be calibrated against the liquid temperature. In these experiments, signal processing takes the place of complex optical systems with multiple mirrors and separate blue and green filters.

3. Monodisperse Droplets at High Pressures

Monodisperse droplets have been produced routinely at pressures ranging up to 400 psi. The droplet-on-demand generator used in other experiments has been adapted for routine use in a pressure bomb -- with optical access -- which is rated to 60 atm.

REFERENCES

1. M.R. Wells and L. A. Melton, "Temperature Measurements of Falling Drops", J. Heat Transfer, accepted for publication (1990).

2. A. A. Rotunno, M. Winter, G. M. Dobbs, and L. A. Melton, "Direct Calibration Procedures for Exciplex-Based Vapor/Liquid Visualization of Fuel Sprays", Combustion Sci. and Technology, accepted for publication (1990).

QUANTITATIVE VISUALIZATION OF AN EVAPORATING FUEL SPRAY

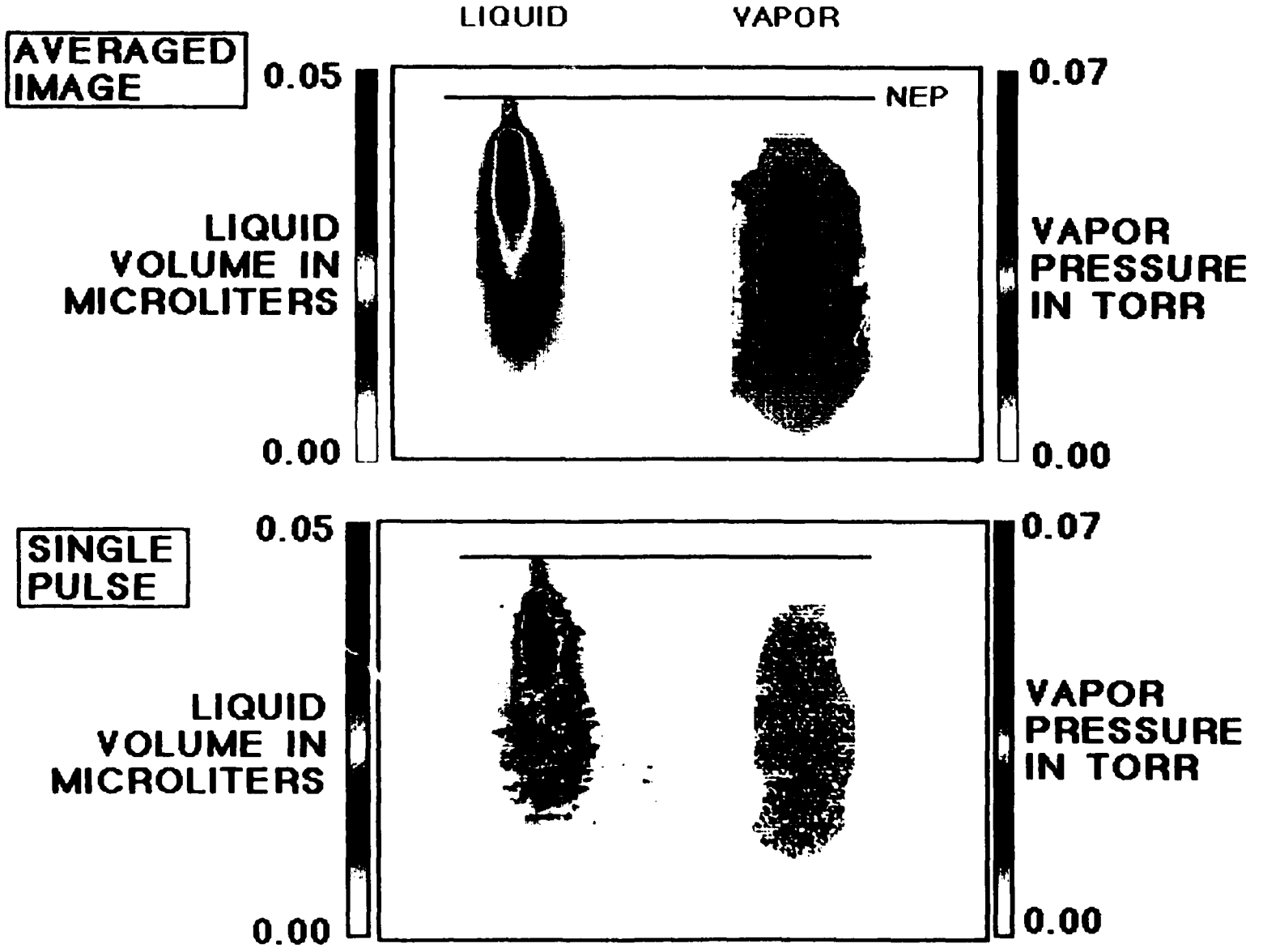

FUELS COMBUSTION RESEARCH

(AFOSR Grant-89-0034)

Principal Investigators: I. Glassman and K. Brezinsky

Department of Mechanical and Aerospace Engineering
Princeton University
Princeton, New Jersey 08544

SUMMARY/OVERVIEW

Progress in understanding soot formation in combustion systems and the effect of fuel type continues. Since results appear to reveal that soot nucleates at approximately the same temperature for all fuels and under all conditions, the present focus of this research is on the possibility that there is a fundamental high activation process controlling for all fuels and under all conditions. Corresponding studies of high temperature oxidation of hydrocarbons have concentrated on the aromatic components of jet propulsion fuels. Studies on benzene and singly alkylated benzenes have been completed. Data have been obtained on the dialkylated compounds, particularly the xylenes. Presented here are the results and suggested mechanisms for the oxidation of ortho-xylene.

TECHNICAL DISCUSSION

In earlier work on soot formation [1], it was observed that in co-flowing diffusion flames that soot nucleation occurred at ~1400°K irrespective of the fuels used or the extent to which these fuels were diluted with an inert. In light of the fact that recent work at Goettingen [2] on sooting pre-mixed flames could be interpreted [3] to have approximately the same nucleation temperature, more attention was devoted to studying the ramifications of this phenomenon. It could possibly reveal that there is a limiting high activation process that controls the soot formation under all conditions and for all fuels.

The earlier work [1] characterized the soot inception point as the first observation of soot on a thermocouple traversing the centerline of the flame apparatus. The procedure posed some difficulty in interpreting the proper temperature. Thus another technique was used in which a sooting flame of a particular height was diluted by nitrogen addition until all soot luminosity disappeared [4]. The temperature of the visible bluish flame front was then measured by a thermocouple at the apex and interpreted to be the Burke-Schumann flame front [5]. Due to blow-off conditions, heavily sooting fuels could not be evaluated because of the excessive dilution required. However, when the oxidizer stream was switched to pure oxygen, non-sooting flames could be obtained for all fuels tested to date [4].

The results have proved interesting. Ethylene isotherms obtained with both air and pure oxygen are shown in Fig. 1. In both cases the flame front corresponded approximately to where the 1320 C isotherm crosses the centerline. It is also interesting that the maximum temperature in the oxygen case is well above this temperature. Currently this effect is believed to be due to

non-infinite reaction rates. Figure 2 represents the centerline results obtained for methane, propane, iso-butane, n-butane, ethene, trans butene, 1-3 butadiene and allene. The flame front on the centerline exists at axial position (Z/H) = 1. As to be expected [5], methane, a single carbon atom species is anomalous. The temperature spread for all the other fuels evaluated is about 170 K (1340-1510 C). Since the fuels order according to their tendency to soot [3], that is, the most heavily sooting compounds require the greatest amount of dilution, it is currently believed that the method of observation of complete disappearance of luminosity results in the data spread. Currently the technique is being applied to aromatic fuels. Why these results appear about 300K higher than earlier measurements is currently under investigation.

In general, the oxidation mechanism of o-xylene was not observed to change significantly over the range of stoichiometries considered in the Princeton Flow reactor studies recently completed.

As the xylene fuel was consumed the major aromatic intermediates that appeared included benzene, toluene, o-tolualdehyde ($1,2\text{-}CH_3\phi CHO$), o-ethyltoluene ($1,2\text{-}CH_3\phi C_2H_5$), o methylstyrene ($1,2\text{-}CH_3\phi C_2H_3$), benzaldehyde ($\phi CHO$) and styrene ($\phi C_2H_3$). The major aliphatics detected were methane, acetylene, ethene, cyclopentadiene and vinylacetylene ($CH_2{=}CH\text{-}C{\equiv}CH$). Also found in significant amounts were CO and H_2. Other species found in relatively small concentrations included CO_2, ethane, allene, methylacetylene, butadiene, a linear C_6H_6, phenol, cresols ($CH_3\phi OH$), benzyl alcohol (ϕCH_2OH), ethylbenzene (ϕC_2H_5), o-methylbenzyl alcohol ($1,2\text{-}CH_3\phi CH_2OH$), indene ($CH_2\phi CH{=}CH$), naphthalene ($C_{10}H_8$), and benzofuran ($O\phi CH{=}CH$). Trace amounts of propene, 2-ethynyl-1-propene ($CH_2{=}C(CH_3)\text{-}C{\equiv}CH$), methyl cyclopentadiene, o-phthaldehyde ($1,2\text{-}CHO\phi CHO$), phthalan, and the other xylenes were also identified in each study. It was noted that except for the cresols and the xylenes all of the dialkylated species detected had the same isomeric structure as the parent fuel.

As in the case of the oxidation of meta and para xylene [6,7], very little evidence was found that suggested that ring destruction occurred before both of the side chains were consumed. The mechanism proposed in Fig. 3 and developed from the extensive data obtained and information in the literature suggests that o-xylene is consumed by both simultaneous and sequential oxidation of the methyl side chains. As depicted in Fig. 3, once the o-methylbenzyl radical is formed, the radical has two major paths through which it may decompose. The first path involves the abstraction of an H from the other methyl group, produces o-xylylene (o-quinodimethane or 5,6-bis (methylene)-1,3-cyclohexadiene) and is considered here to be the simultaneous oxidation route. The second path for the o-methylbenzyl radical is the oxidation of the radical site producing o-tolualdehyde and is considered to be the sequential oxidation path. Detailed support for the total mechanism described in Fig. 3 and the formation of many of the minor intermediates found in the flow reactor experiments is presented in Ref. 8.

Another interesting observation of the experimental studies was, as shown in Fig. 4, that o-xylene is more reactive than m- and p-xylene for a temperature of about 1155 K. The explanation of this effect is related to the proximity of the two methyl groups in o-xylene. Again, the detailed

explanation of the trend appears in Ref. 8.

REFERENCES

1. Gomez, A., Littman, M. and Glassman, I.: Comb. and Flame 70, 225 (1987).
2. Bohm, H., Hesse, D., Jander, H., Luers, B., Pritscher, I., Wagner, H. Gg., and Weiss, M.: 22nd Symp. (Int'l.) on Combustion, p. 403 (1989).
3. Glassman, .: 22nd Symp. (Int'l.) on Combustion, p. 298 (1989).
4. Smith, C.A.: "On Incipient Soot Particle Formation in Laminar Diffusion Flames", Princeton U. M.S.E. Thesis, 1990.
5. Glassman, I.: Combustion, 2nd Ed., Academic Press, Chaps. 4 and 8.
6. Emdee, J.L., Brezinsky, K. and Glassman, I.: Oxidation of y-xylene at 1160-1183K, Eastern States Meeting/The Combustion Institute, Paper No. 19, 1988.
7. Emdee, J.L., Brezinsky, K. and Glassman, I.: Oxidation of m-xylene, to be submitted for publication, 1990.
8. Emdee, J.L., Brezinsky, K. and Glassman, I.: Oxidation of o-xylene, accepted for publication in 23rd Symp. (Int'l.) on Combustion volume (1990).

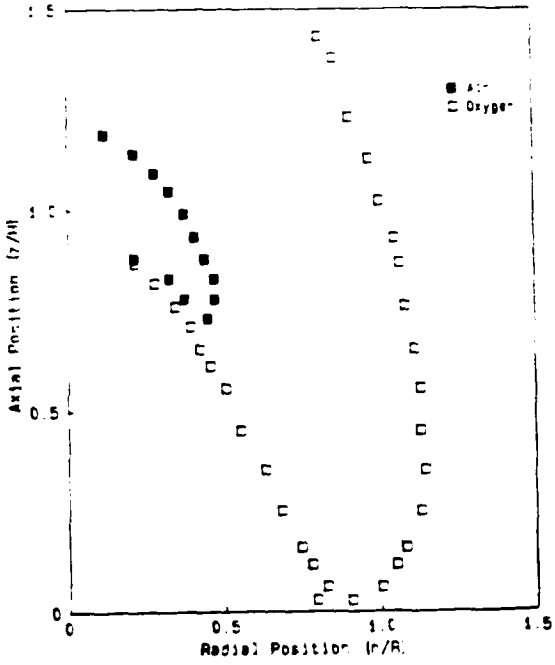

Figure 1. Direct Comparison of the 1227 °C Measured Isotherm from ~2 cm Inception Point Ethene Flame in Air and Oxygen

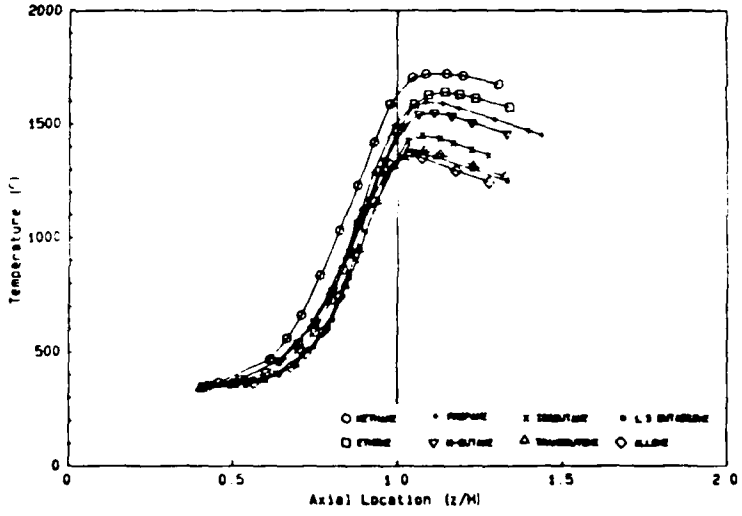

Figure 2. Center Line Thermocouple Measurements of ~2 cm Inception Point Flames in Oxygen for Various Fuels

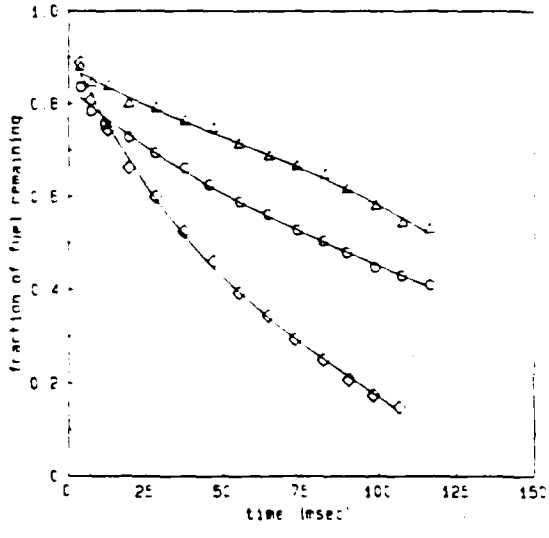

Figure 3. Fraction of fuel remaining for the oxidation of o-xylene (○), m-xylene (△), and p-xylene (◇), T = 1155K, φ = 1

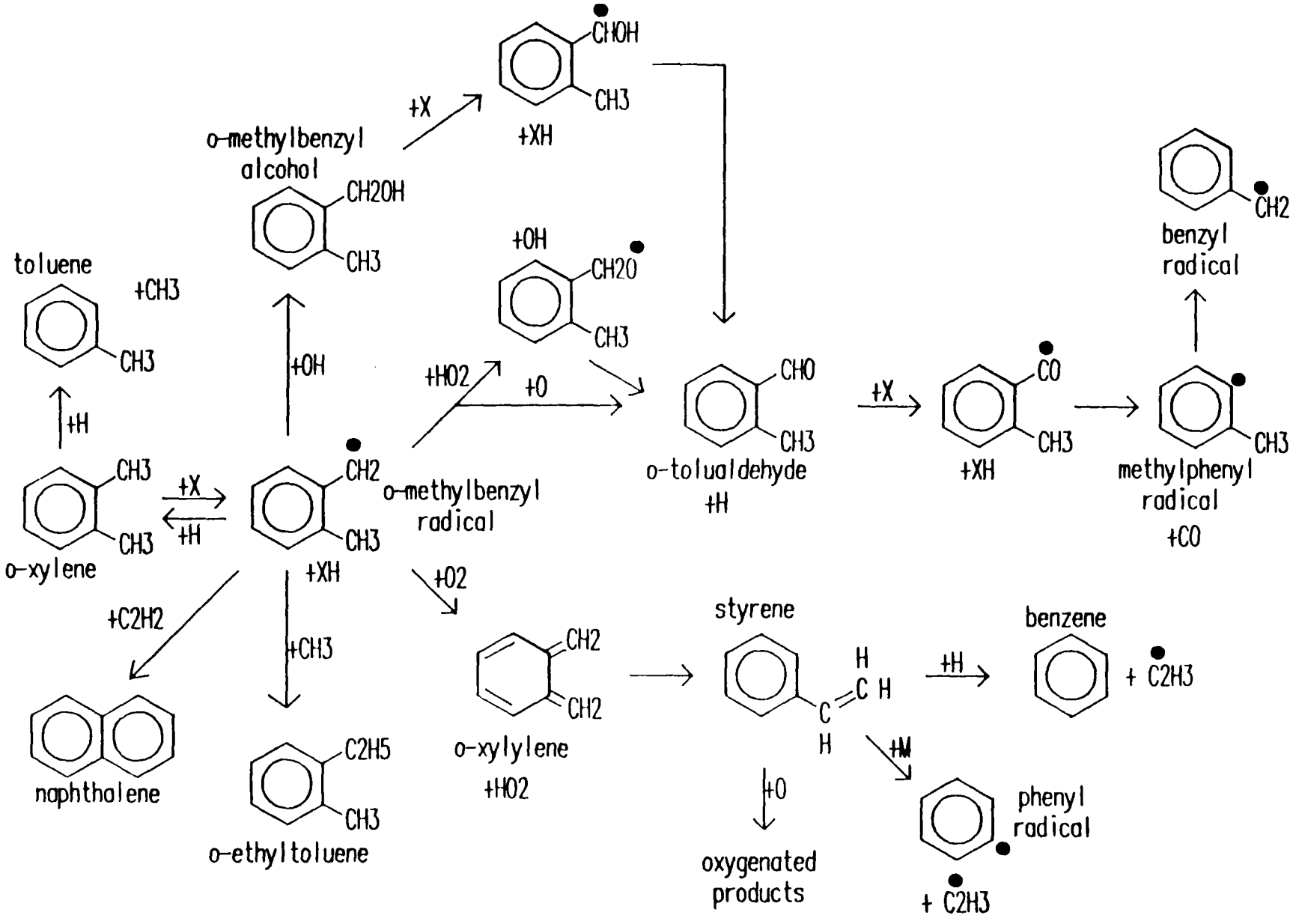

Figure 3. Reaction mechanisms for the oxidation of o-xylene.

DETERMINATION OF RATE-LIMITING STEPS DURING SOOT FORMATION

AFOSR Contract No. F49620-88-C-0051

Principal Investigator: Meredith B. Colket, III

United Technologies Research Center
E. Hartford, CT 06108

SUMMARY/OVERVIEW:

A variety of hydrocarbons are being pyrolyzed and oxidized in a single-pulse shock tube. Data will be used to identify rate-limiting steps during soot formation and to assist in the development or verification of chemical models describing formation of products and soot-precursors. In addition, simplified modeling concepts are being developed in order to describe soot production in flames. Both the experimental work and the modeling efforts indicate that benzene production is only one of several rate-limiting steps leading to soot formation. Furthermore modeling efforts support arguments that $C_3H_3 + C_3H_3$ reactions to form benzene are more important than previously assumed.

AUTHORS M. Colket, R. Hall, J. Sangiovanni, and D. Seery

TECHNICAL DISCUSSION

Eight separate series of single-pulse shock tube experiments have been completed. For each series, a hydrocarbon or a mixture of a hydrocarbon and oxygen were shock-heated in argon over an approximate temperature range of 1100K to 2000K. Total pressures were about five to ten atmospheres and dwell times were about 500 microseconds. Gas samples were collected automatically at the end wall of the shock tube and then were analyzed quantitatively using gas chromatography. Measured species include C1 to C14 hydrocarbons, carbon oxides, hydrogen, and oxygen. The existing capillary gas chromatograph is being converted to a gc/ms system to enhance identification of critical high molecular weight species. Hydrocarbons pyrolyzed (or oxidatively pyrolyzed) include toluene, benzene, dicyclopentadiene and cyclopentadiene. In addition, benzene has been copyrolyzed with hydrogen, and cyclopentadiene has been copyrolyzed with acetylene, biacetyl (as a source of methyl radicals) and benzene. The existing capillary gas chromatograph is being converted to a gc/ms system to enhance identification of critical high molecular weight species.

Preliminary comparisons of the data from the pyrolysis and oxidative pyrolysis of cyclopentadiene indicates that as the parent pyrolyzes, it principally decomposes into a C_3 and a C_2- hydrocarbon, and a portion of the C_3-hydrocarbon decomposes to methane and acetylene. However, cyclopentadiene oxidizes in a manner similar to that of benzene; i.e., extraction of carbon monoxide from the ring. Vinylacetylene and 1,3-butadiene are principle products of the oxidation.

Carbon balances (sum of all carbon in hydrocarbon species up to naphthalene) calculated from cyclopentadiene pyrolysis are very similar to that of benzene. Carbon balances have previously been shown to correlate well with the soot production from a particular hydrocarbon. The low carbon balance from cyclopentadiene (see Fig. 1) is not that surprising considering the aromatic character of cyclopentadiene, but the result is significant in that it demonstrates the potential importance of C5-rings to soot production. A further analysis of the species produced during the pyrolysis indicates that this is the first example in which benzene production does not correlate with the carbon balance. In Fig. 2 comparisons of benzene production are shown for several different fuels. Although, benzene production is low from cyclopentadiene, comparable to that formed from butadiene, its carbon deficit is larger, comparable to that of benzene and certainly greater than allene which forms a large amount of benzene. The implication of these results is that C5-compounds offer a route to formation of high molecular compounds which circumvents the formation of benzene. Previously, benzene had been considered to be a primary step to the formation (inception) of soot.

The high rates of production of benzene during allene pyrolysis are indicative of a fast benzene formation mechanism from recombination of C_3H_3 radicals. Most efforts of predicting benzene formation in flames have focused on reactions between C_2 and C_4-hydrocarbon species. Recent work by Miller and Melius argues against these mechanisms and in favor of the C_3 reactions. To test out the potential importance of reactions involving C_3-species, we have first duplicated the work of Harris and Wiener in their predictions of benzene production in a rich, premixed, laminar ethylene/air flame. Secondly, we have redone the calculations for benzene formation when the recombination reaction of C_3H_3 is included (with a rate constant of 1×10^{13} cc/mole/sec). With this added reaction, benzene production was increased by nearly a factor of two, thus supporting arguments that other routes to benzene production may have been underestimated in the past.

Soot Aerosol Dynamics Simulations

In the last annual report, we presented the results of a simplified aerosol dynamics model for soot growth. With the aim of modeling the growth of soot spheroids, we adapted the most recent version of a well-known aerosol dynamics code, MAEROS, which is a fixed- grid, sectional model including nucleation, surface growth, and coagulation. The lowest size class was assumed to approximate that of a benzene molecule, with an effective nucleation/inception rate given by the production rate of the smallest aromatic molecules, typically taken to be benzene. Surface growth was assumed to be due to acetylene deposition alone, at a rate given by the well-known Harris-Weiner growth rate expression. Provision for oxidative mass removal at a rate given by the Nagle and Strickland-Constable expression was also made in the model. This is admittedly a highly simplified picture of the soot growth that glosses over many details of the inception process; the only medium parameters except for temperature that need to be specified are the benzene formation rate and the concentration of the condensable acetylene vapor. The first comparison of the model with the experimental volume fraction data of Harris and co-workers, taken in a premixed, atmospheric pressure, ethylene-oxygen flame, was very good Both the magnitude and time dependence of the soot growth were modeled well, and

there was no need to allow for oxidation. Given the simplifications made, we recognized the obvious possibility that the agreement obtained was fortuitous. We therefore embarked on a project of trying to model other well-characterized flames. One set of calculations in progress is to see if the model reproduces the stoichiometric variation of soot production in the Harris flames; this work involves using CHEMKIN to calculate the acetylene concentration and the benzene source rate, and is in progress at this time.

The only other well-characterized data suitable for modeling purposes have been reported by Bockhorn, et.al. in low-pressure, premixed flames. Soot volume fraction profiles have been measured, and all the other input data needed to perform the modelling calculations are available. We have performed preliminary calculations for their 0.15 atmospheric propane/oxygen flame. Figure 3 shows the comparison of the calculated and experimental soot volume fractions, based on the experimental benzene concentration profile. With no oxidation, the calculated volume fractions are much too large, but there is considerable sensitivity to the oxygen concentration, as seen. For an oxygen concentration of about 1%, the agreement is good, at least for longer times. This flame is somewhat leaner than the Harris flame discussed earlier, so the need to incorporate oxidation is at least qualitatively reasonable. The foregoing calculation was based on the assumption that the benzene source rate is the effective inception rate. Naphthalene production rates are also available, and we have found that taking naphthalene as the inception source results in much better agreement at early times, and seems to require somewhat smaller oxygen concentrations at longer times. This is an aspect of the calculation that will be pursued further, together with other questions like the temperature sensitivity of the surface growth rate, and the overall sensitivity to reasonable uncertainties in temperature.

Fig. 1 Mass Recovery Following Pyrolysis in a Single-Pulse Shock Tube

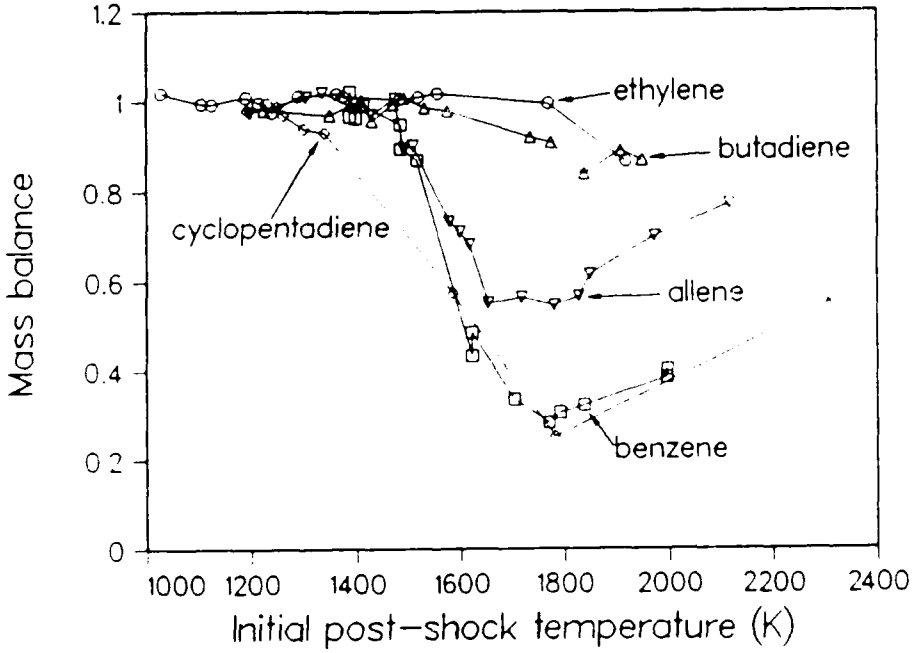

Fig. 2 Benzene Production During Pyrolysis in a Single-Pulse Shock Tube

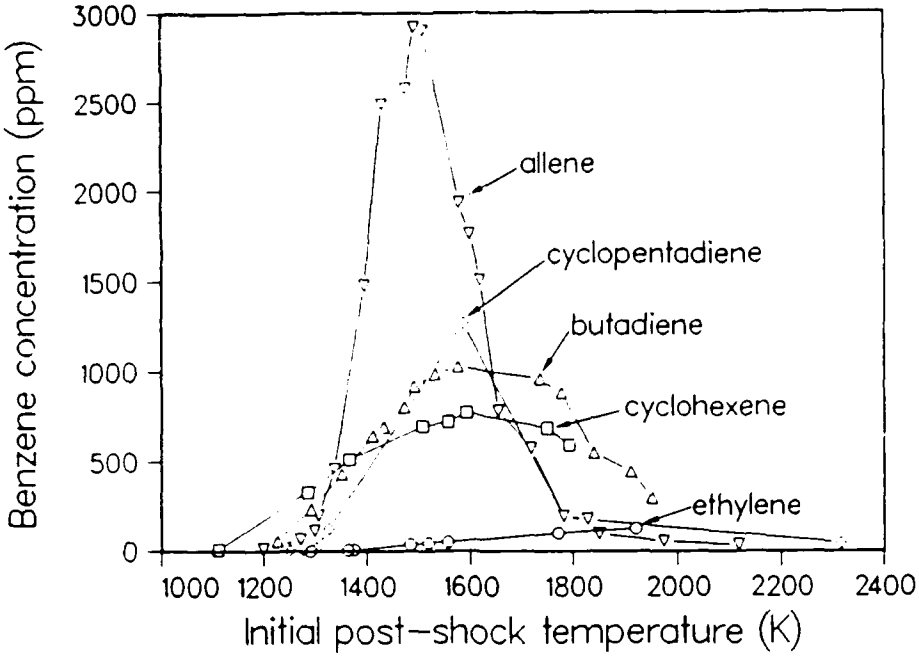

Fig. 3 Simulation of Bockhorn Flame Sensitivity to Oxygen Concentration

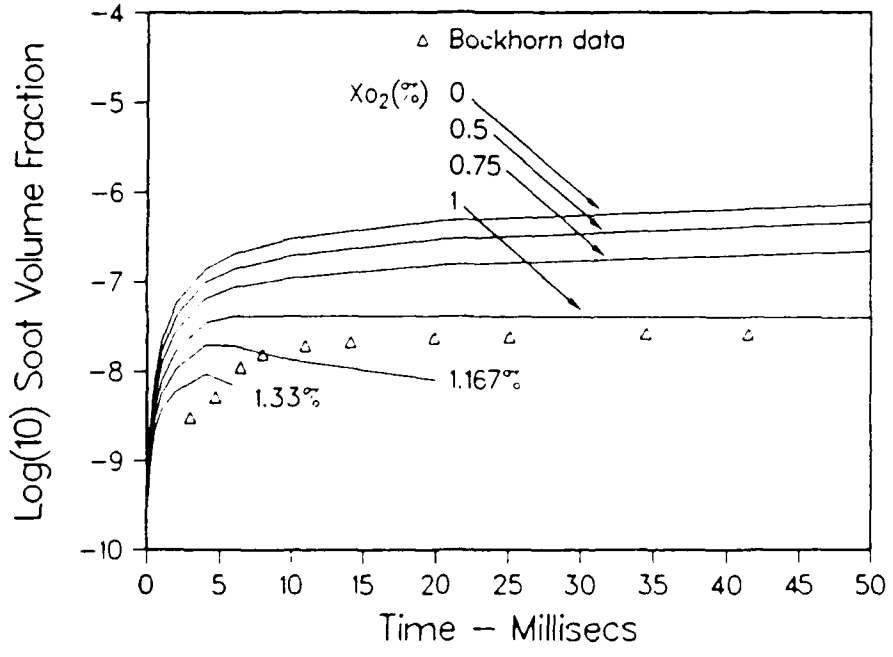

FUEL STRUCTURE AND PRESSURE EFFECTS ON THE FORMATION OF SOOT PARTICLES IN DIFFUSION FLAMES

(AFOSR Contract No. AFOSR-87-0145)

Principal Investigator: Robert J. Santoro

Department of Mechanical Engineering
The Pennsylvania State University
University Park, PA 16802

SUMMARY/OVERVIEW:

The present program addresses the need to provide a fundamental understanding of the processes which control soot particle formation under conditions applicable to future gas turbine engine operation. The approach taken emphasizes a detailed consideration of the basic phenomena involved in particle inception, surface growth and oxidation. In particular, the effects of fuel molecular structure and operating pressure are of interest. Because of the fundamental nature of the program goals, the present studies are conducted in well controlled laminar diffusion flames. Detailed measurements, involving laser-based techniques, are used to characterize the soot particle and velocity fields present in the flame. During the past year, investigations of the effects of fuel concentration and pressure have been emphasized. Recently, efforts have also been directed towards developing spectroscopic and mass spectrometric measurement techniques in order to obtain information on gas phase species. The present studies are expected to help in achieving a quantitative understanding of soot formation phenomena which will impact future gas turbine technology where operation will involve burning broad specification fuels at higher pressures.

TECHNICAL DISCUSSION

During the past year, studies have concentrated on the effects of fuel concentration and operating pressure on the soot formation process. In addition, collaborative efforts with workers at other institutions (Brown University and NIST) have been undertaken to examine the optical properties of soot aggregates formed in the flame [1] and the effects of buoyancy in jet diffusion flames [2]. In addition to these studies, efforts have been made to enhance the diagnostic capabilities available for future studies. In particular, a quadrapole mass spectrometer system has been acquired and is presently operative. This instrumentation will be utilized to obtain information on gas phase species present in the flame and is intended to better characterize the particle inception and surface growth regions. Additionally, a spectroscopic absorption system has also been assembled to provide wavelength extensive information on both soot particles and large precursor species present in the flame.

High Pressure Diffusion Flame Studies

A series of laminar diffusion flames have been studied over a range of pressures between 1 and 10 atm (.1 MPa to 1.0 MPa). The coannular diffusion flame burner and laser diagnostics for soot particle measurements are similar to those used for atmospheric flame studies previously reported [3,4]. The coannular burner has been mounted in a high pressure cell which is extensively described elsewhere [5]. The studies undertaken involved laminar diffusi ames burning ethene (C_2H_4), ethane (C_2H_6) and a mixture of ethane and propene (C_3H_6) in The measured soot volume fraction is obtained from laser extinction measurements and is rep esented by [6]:

$$-\int_o^D f_v\, dx = C(\lambda,m) \ln (I/I_o) \qquad (1)$$

where f_v is the local soot volume fraction, x lies along a laser path through the flame on a diameter D, $C(\lambda,m)$ is a constant which can be determined from Rayleigh light scattering theory to be 1.05×10^{-5} for m=1.57-0.56 i at λ=514.5nm [6], and finally I/I_o is the ratio of the transmitted to incident laser power. This quantity is proportional to the total soot present at a particular axial location in the flame. Figure 1 shows this quantity as a function of the non-dimensional axial location for the ethene/air flames at a series of operating pressures. If the increase in the maximum soot volume fraction at a particular operating pressure is related to that pressure through a power law dependence, that is

$$\left(\int f_v\, dx\right)_{max} \alpha\, P^n \qquad (2)$$

then a fit to the data can be used to yield a value for n. Figure 2 shows the maximum soot volume fractions as a function of the operating pressure along with the best fit value for n determined from a linear least square procedure. For the ethene flame, the fuel flow rate was 3.9 cm^3/s and n was found to be 1.05±.06 in good agreement with the results of Flower and Bowman who found n=1.2±0.1. It should be noted that results shown in Figures 1 and 2 have taken into account the slight burner diameter difference for the two studies. In the present study, the diameter was 1.1 cm where as Flower and Bowman employed a burner with a 1.27 cm diameter. Also shown on Figure 2 are the results for an ethene/air diffusion flame where a copper (Cu) rather than a stainless steel (SS) fuel tube was utilized. The results are very similar for both fuel tube materials.

Figure 2 also shows the results obtained for flames burning ethane or an ethane/propene mixture. For these flames, the pressure could only be varied over a range of 1 to 3 atm (.1 to .3 MPa) before a buoyancy driven flame instability was observed. These buoyancy effects at elevated pressure have recently been the subject of a collaborative investigation with workers at the National Institute of Standards and Technology (NIST) and are discussed elsewhere [2]. An analysis similar to that applied to the ethene flame studies yields pressure power dependences of n=1.88±0.13 and n=1.62±0.24 for ethane fuel flow rates of 2.80 and 3.85 cm^3/s, respectively. These higher values of the pressure power dependence appear to be related to fuel structure effects, the direct nature of which remains to be understood. These observations of a fuel structure dependence are consistent with previous studies [7].

As a further investigation of fuel molecular structure effects, a mixture of ethane (2.80 cm^3/s) and propene (0.7 cm^3/s) was studied and these results are also shown in Figure 2. In the ethane/propene study, the total carbon atom fuel flow rate was maintained constant with respect to the 3.85 cm^3/s ethane flame. For these conditions, the value of n is observed to be 1.16±0.10, a value similar to that observed for the ethene studies. Thus, the present studies with an alkane species appear to yield a higher pressure dependence than observed for either of the alkene species.

Fuel Concentration Studies

Recently Axelbaum and Law [8] have examined the effects of fuel concentration and temperature on soot formation in a co-flow flame environment. Based on the importance of these results, a similar series of experiments have recently been undertaken in our laboratory. In these studies, fuel concentration and temperature are varied by the addition of nitrogen or argon to the fuel flow. Because of the difference in the heat capacity of these species, flames of identical calculated temperature but different fuel concentrations can be achieved. In the present studies, flames burning ethene and propane have been examined. The ethene flames have been studied for a range of fuel flow rates and dilutions while a single fuel flow rate condition has been examined for the propane flame (see Table 1).

In order to quantitatively determine the effect of variation in fuel concentration, the

integrated soot volume fraction, F_v, was determined from the extinction measurements and is expressed as

$$-\frac{F_v}{k} = \int_o^D \ln\left(\frac{I}{I_o}\right) dy \qquad (3)$$

where k is a constant and y is the axis perpendicular to the path of the laser beam. This measurement provides a quantity proportional to the soot volume fraction at a particular height integrated across the entire flame. In evaluating the effect of fuel concentration, the maximum value of F_v/k along the axial position was used. Values for F_v/k are tabulated in Tables 1 and 2 along with the fuel species, fuel flow rate, fuel mole fraction and the calculated adiabatic flame temperature for each diluent condition for the flames studied.

In order to quantify the effect of fuel concentration on the amount of soot formed in the flame, F_v/k was taken to be proportional to $X_F{}^b$ for each temperature condition studied. From the observed differences in F_v/k for the nitrogen and argon dilution cases, a value for b could be obtained. For the flames of highest dilution (flames 1-4), b was equal to or exceeded 1. As the amount of dilution decreased (flames 5-10), b was observed to be 0.4 for the 4.9 cm^3/s fuel flow cases and 0.8 for the 6.58 cm^3/s fuel flow case. For the propane flame, b was also found to be 0.4. No systematic variation in the value of b was evident with respect to fuel flow rate. These observations in general reaffirm the earlier results of Axelbaum and Law with regard to the importance of concentration [8]. However, the deviation of b from unity indicates that other effects such as residence time or diffusion may also be important.

As an alternative approach to studying concentration effects, a 50% argon diluted propane or ethene flame at two atmospheres operating pressure was investigated and compared to appropriate undiluted flames at a pressure of one atmosphere. For these conditions, the initial molar fuel concentrations are the same for the flames at each pressure. The results for these studies are shown in Table 2. Clearly, the amount of soot formed increases in the two atmosphere flames indicating that effects in addition to the fuel concentration are enhancing the formation of soot as the operating pressure increases.

The above results are presently being further analyzed to assess the importance of residence time and diffusion on the observed concentration effects. Of particular interest is the importance of concentration versus temperature on the early particle inception region. This aspect of the study will likely require information on the gas phase species present in the flame.

REFERENCES

1. Dobbins, R.A., Santoro, R.J. and Semerjian, H.G., "Analysis of Light Scattering From Soot Using Optical Cross Sections for Aggregates", Twenty-Third Symposium (International) on Combustion, accepted for publication (1990).

2. Davis, R.W., Moore, E.F., Santoro, R.J. and Ness, J., "Isolation of Buoyancy Effects in Jet Diffusion Flames", presented at the Central States Section, The Combustion Institute, Cincinnato, OH, May 20-22, 1990.

3. Santoro, R.J., Yeh, T.T., Horvath, J.J. and Semerjian, H.G., Combustion Science and Technology, 53, 89 (1987).

4. Richardson, T.F. and Santoro, R. J., "Soot Growth in Diffusion Flames Burning Fuel Mixtures", 1988 Fall Technical Meeting of the Eastern States Section of the Combustion Institute, Clearwater Beach, FL, Dec. 5-7, 1988.

5. Santoro, R.J., "Fuel Structure and Pressure Effects on the Formation of Soot Particles in Diffusion Flames", Annual Report, Air Force Office of Scientific Research, AFOSR Contract AFOSR-87-0145, March 1989.

6. Flower, W.L. and Bowman, C.T., Twenty-first Symposium (International) on Combustion, The Combustion Institute, 1986, 1115-1124.

7. Schalla, R.L., Clark, T.P. and McDonald, G.E., NACA 1186 (1954).

8. Axelbaum, R.L. and Law, C.K., "Dilution and Temperature Effects on Soot Formation in the Co-Flow Flame", The Eastern Section of the Combustion Institute, Fall Technical Meeting, paper 60, Albany, NY, Oct. 30, 31 and Nov. 1, 1989.

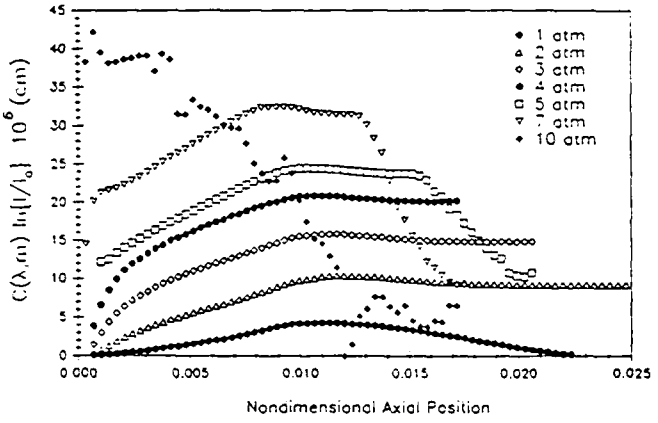

Figure 1. $C(\lambda,m)\ln(I/I_o)$ as a function of the non-dimensional position, η, for the ethene/air laminar diffusion flames for operating pressures between 1 and 10 atm. The non-dimensional axial position is given by $\eta=zD/Q)\ln(1+1/s)$, where z is the axial position, D is the diffusion coefficient ($0.156\ cm^2s^{-1}$), Q is the fuel flow rate ($3.9\ cm^3/s$) and s is the volume of air to the volume of fuel required for complete combustion. (s=14.28 for C_2H_4).

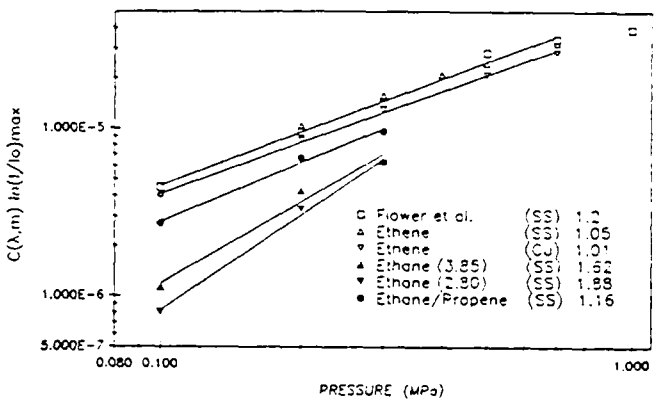

Figure 2. $C(\lambda,m)\ln(I/I_o)_{max}$ as a function of operating pressure for a series of ethene, ethane and ethane/propene laminar diffusion flames burning in air. Solid lines are fits to P^n

TABLE 1

Experiment #	Fuel (Q) (cm^3/s)	Diluent	X_{Fuel}	T_{ad} (K)	(F_v/k)	% of Pure $(F_{st}X)/(F_{st}X)_{Pure}$
1	C_2H_4(2.75)	N_2	0.50	2310	0.0244	46.7
2	C_2H_4(2.75)	Ar	0.37	2310	0.0155	29.6
3	C_2H_4(4.90)	N_2	0.50	2310	0.0429	51.8
4	C_2H_4(4.90)	Ar	0.37	2310	0.0312	37.7
5	C_2H_4(4.90)	N_2	0.74	2346	0.0722	87.2
6	C_2H_4(4.90)	Ar	0.64	2346	0.0672	81.2
7	C_2H_4(4.90)	N_2	0.64	2333	0.0602	72.7
8	C_2H_4(4.90)	Ar	0.52	2333	0.0556	67.2
9	C_2H_4(6.58)	N_2	0.64	2333	0.0781	74.5
10	C_2H_4(6.58)	Ar	0.52	2333	0.0660	63.0
11	C_2H_4(2.75)	--	1.00	2369	0.0522	100.0
12	C_2H_4(4.90)	--	1.00	2369	0.0828	100.0
13	C_2H_4(6.58)	--	1.00	2369	0.1047	100.0
14	C_3H_8(2.56)	N_2	0.61	2240	0.0392	79.8
15	C_3H_8(2.56)	Ar	0.50	2240	0.0362	73.7
16	C_3H_8(2.56)	--	1.00	2266	0.0491	100.0

TABLE 2

Experiment #	Fuel (Q) (cm^3/s)	Diluent	Pressure (atm)	X_{Fuel}	T_{ad} (K)	(F_v/k)
17	C_2H_4(3.85)	--	1	1.00	2369	0.0767
18	C_2H_4(3.85)	Ar	2	0.50	2351	0.0959
19	C_3H_8(2.56)	--	1	1.00	2250	0.0490
20	C_3H_8(2.56)	Ar	2	0.50	2258	0.0780

COMPUTER MODELING OF SOOT FORMATION COMPARING FREE RADICAL AND IONIC MECHANISMS

(AFOSR Grant No. 88–0072)

Principal Investigator: M. Frenklach

Fuel Science Program
Department of Materials Science and Engineering
The Pennsylvania State University
University Park, PA 16802

SUMMARY/OVERVIEW:

This is a part of a joint program between The Pennsylvania State University and AeroChem (Principal Investigator: Dr. H. F. Calcote) in which the main objective is to compare the relative importance of the free radical mechanism and the ionic mechanism of soot formation in flames. The approach undertaken is that of experimenting with chemical kinetic models. As we have continued working on the ionic mechanisms developed by AeroChem, the major accomplishments during the last year were: (1) A complete revision of our neutral mechanism; and (2) A detailed simulations, for the first time, of soot particle nucleation and growth in several different laminar premixed flames, in which surface growth and oxidation are described in terms of elementary chemical reactions of surface active sites. We were able, using a single reaction mechanism, to simulate quantitatively PAH profiles and soot particle characteristics determined experimentally in several different laminar premixed hydrocarbon flames. These results are detailed below.

TECHNICAL DISCUSSION

The computational model consists of three logical parts: (I) *initial PAH formation*, which includes a detailed chemical kinetic description of acetylene pyrolysis and oxidation, formation of the first aromatic ring, and its subsequent growth to a prescribed size; (II) *planar PAH growth*, comprised of replicating-type growth of PAHs beyond the prescribed size; and (III) *spherical particle formation and growth*, consisting of coagulation of PAHs formed in part (II) followed by the growth of the resulting particles by coagulation and surface reactions.

The reaction mechanism for pyrolysis and oxidation of small hydrocarbon molecules, responsible for the main flame structures, and reactions describing the formation and growth of PAHs was composed of data taken primarily from several recent sources.[1] The formation and growth of aromatics followed the basic reaction scheme of Frenklach and co-workers.[2] The formation reactions of the first aromatic ring and its key reactions were assigned the rate coefficients from the sources indicated below:

$n\text{–}C_4H_3 + C_2H_2 \rightarrow$ phenyl	Westmoreland *et al.* 1989	(1)
$n\text{–}C_4H_5 + C_2H_2 \rightarrow$ benzene + H	Westmoreland *et al.* 1989	(2)
arylH + H $\rightarrow$ aryl• + H_2	Kiefer *et al.* 1985	(3)

$$\text{aryl}\bullet + H \rightarrow \text{arylH} \qquad \text{Rao and Skinner 1988} \qquad (4)$$

$$\text{aryl}\bullet + C_2H_2 \rightarrow \text{aryl}\text{–}C_2H + H \qquad \text{Fahr and Stein 1989} \qquad (5)$$

$$\text{aryl}\bullet + O_2 \rightarrow \text{products} \qquad \text{Lin and Lin 1987} \qquad (6)$$

The chemical reaction mechanism, comprised of a total of 337 reactions and 70 species, was capable of predicting near-quantitatively the measured species profiles,[1] including those of aromatics, for three premixed laminar flames whose conditions are summarized in the following table:

Table 1. Flame conditions

No.	Composition in Argon	P (torr)	Cold gas velocity (cm/s)	Reference
1	46.5 % C_2H_2 – 48.5 % O_2	20	50	MIT group[3]
2	23.6 % C_2H_2 – 21.4 % O_2	90	20	Bockhorn *et al.*[4]
3	16.5 % C_2H_4 – 17.9 % O_2	760	7.8	Harris *et al.*[5]

The Sandia burner code[6] was used for the flame modeling, simulating PAH formation and growth up to coronene. The computed profiles of H, H_2, C_2H_2, O_2, OH, H_2O and of a prescribed-size PAH, A_ℓ, were then used as an input for the particle nucleation and growth simulation. Accomplished with an in-house kinetic code, several simultaneously occurring processes were modeled using a method of moments.[7] The first part of this model, *nucleation*, describes the planar growth of PAHs via the H-abstraction/C_2H_2-addition reaction sequence using the technique of chemical lumping.[7] This method provides a mathematically rigorous description of the growth process to an infinite size PAH, which can be schematically represented as

$$A_\ell \rightarrow A_{\ell+1} \rightarrow A_{\ell+2} \rightarrow \cdots \rightarrow A_\infty \,, \qquad (7)$$

where A_ℓ represents an aromatic species containing ℓ fused rings. The PAH species formed in (7) are then allowed to *coagulate*, that is, all the A_i's ($i = \ell, \ell+1,\ldots,\infty$) collide with each other forming dimers; the dimers, in turn, collide with A_i forming trimers or with other dimers forming tetramers; and so on. The coalescence reactions were treated as irreversible having sticking coefficients of unity. As the focus of this work is on very young, small particles, it was assumed that the coagulation dynamics is in the free-molecular regime.

Beginning with the dimers, the forming clusters were assumed to be "solid phase" and allowed to add and lose mass by surface reactions

$$C_{soot}\text{–}H + H \rightleftharpoons C_{soot}\bullet + H_2 \qquad (8)$$

$$C_{soot}\bullet + H \rightarrow C_{soot}\text{–}H \qquad (9)$$

$$C_{soot}\bullet + C_2H_2 \rightarrow C_{soot}\text{–}H + H \qquad (10)$$

$$C_{soot}\bullet + O_2 \rightarrow \text{products} \qquad (11)$$

$$C_{soot}\text{–}H + OH \rightarrow \text{products} \,, \qquad (12)$$

where C_{soot}–H represents an arm-chair site on the soot particle surface and $C_{soot}\bullet$ the corresponding radical. This mechanism is adopted based on the postulate that the H-abstraction/C_2H_2-addition (HACA) reaction sequence[2] is responsible for high-temperature growth of all forms of carbonaceous materials. Wieschnowsky *et al.*[4] also suggested that the HACA reactions "offer a key to the understanding of a number of phenomena" observed in their flame study. The particle dynamics — the evolution of soot particles undergoing simultaneous

nucleation, coagulation and surface reactions described above — was modeled by a method of moments.[7] This method does not require the assumption of a particle size distribution function (PSDF). The closure of the differential equations for the PSDF moments is accomplished by interpolation between the moments. The numerical integration of the moment equations took from 20 to 50 s on an IBM 3090/600S main-frame computer.

The two figures on the next page demonstrate some of the computational results for two flames: the graph on the left – flame 2 of Table 1, and the graph on the right – flame 3 of Table 1. Shown in these figures are soot particle number density, N, specific surface area, S, average soot particle diameter, d, and two scattering moments. It can be seen in these figures that the model predictions are in relatively close agreement with experiment for the initial, particle inception part of the flames. The reliability of our model is further supported by the facts that the computed net surface growth rate is in close agreement with that determined by Harris and Weiner (right–bottom) and that the predicted rate of soot oxidation by O_2 agrees well with the expression of Nagle and Strickland-Constable (left–bottom). Some of the modeling results are: (1) The computed rate of nucleation is balanced by the rate of coagulation throughout the particle inception zone, however, the nucleation rate decays more slowly with flame height than is usually deduced from experiment; (2) Particle inception is primarily determined by PAH coagulation, initiated and controlled by PAH coalescence into dimers; (3) While the average soot particle is computed to contain 10^3–10^5 carbon atoms, the corresponding average PAH size is only 20 to 50 carbon atoms. This indicates that the crystallites comprising incipient soot particles should be on the order of 7 to 12 Å; (4) The oxidation by OH and O_2 is quite insignificant in the post-flame zone; (5) The surface growth of soot mass is primarily determined by two processes: acetylene addition via the HACA reaction sequence, and PAH condensation on the particle surface. The relative contribution of each of these processes appears to change with experimental conditions. Thus, while the acetylene addition dominates surface growth in Flame 3, PAH condensation prevails in Flame 2. The main contribution of the PAH condensation occurs at the early stages of PAH coagulation; (6) The model predicts the classical structure of soot particles: a less dense particle core, composed of randomly oriented PAH oligomers, and a more dense concentrically-arranged particle shell; (7) Surface processes can be understood in terms of elementary chemical reactions of surface active sites. The number density of these sites is determined by the chemical environment.

REFERENCES

1. Wang, H. and Frenklach, M.: *Modeling of PAH Profiles in Premixed Flames.* Paper presented at the Fall Technical Meeting of the Eastern States Section of the Combustion Institute, Albany, New York, October 1989, Paper 12.
2. Frenklach, M., Clary, D.W., Gardiner, W.C., Jr., and Stein, S.E.: *Twentieth Symposium (International) on Combustion*, p. 887, The Combustion Institute, 1985.
3. Westmoreland, P.R., Dean, A.M., Howard, J.B. and Longwell, J.P.: *J. Phys. Chem.* **93**, 8171 (1989).
4. Wieschnowsky, U., Bockhorn, H. and Fetting, F.: *Twenty-Second Symposium (International) on Combustion*, p. 343, The Combustion Institute, 1989.
5. Harris, S.J., Weiner, A.M. and Blint, R.J.: *Combust. Flame* **72**, 91 (1988).
6. Kee, R. J., Grcar, J. F., Smooke, M. D., and Miller, J. A., Sandia Report No. SAND85–8240, December 1985.
7. Frenklach, M.: *Complex Chemical Reaction Systems, Mathematical Modelling and Simulation* (J. Warnatz and W. Jäger, Eds.), p. 2, Springer–Verlag, Berlin, 1987.

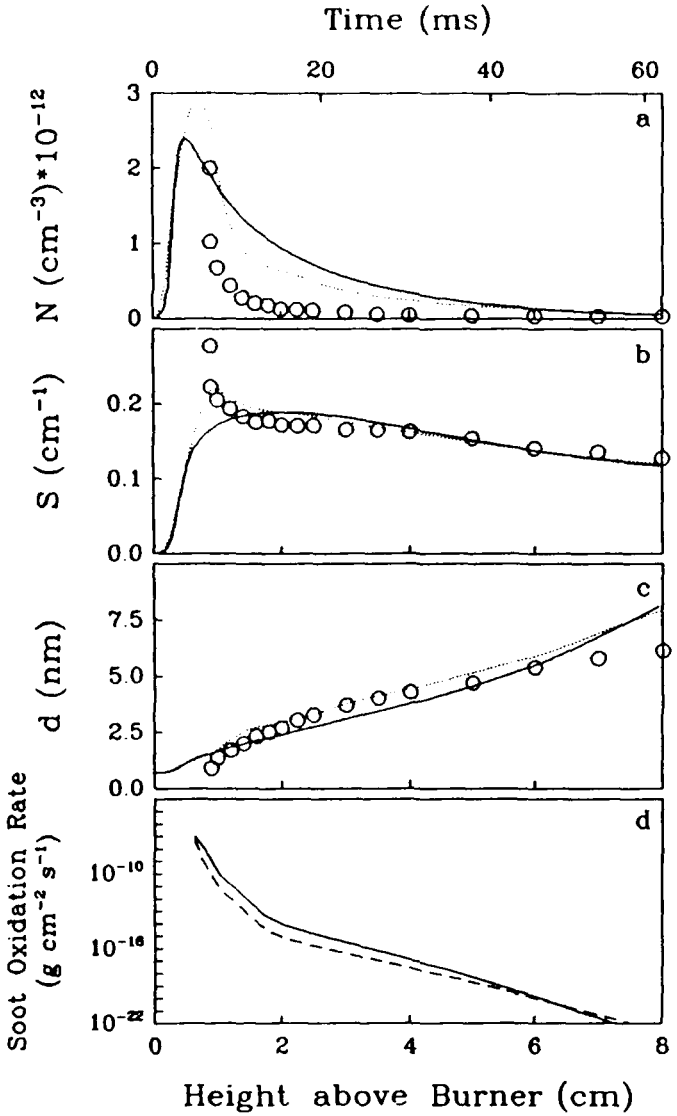
Time (ms)
0
20
40
60
a
b
c
d
N (cm^{-3})*10^{-12}
S (cm^{-1})
d (nm)
Soot Oxidation Rate
(g cm^{-2} s^{-1})
Height above Burner (cm)

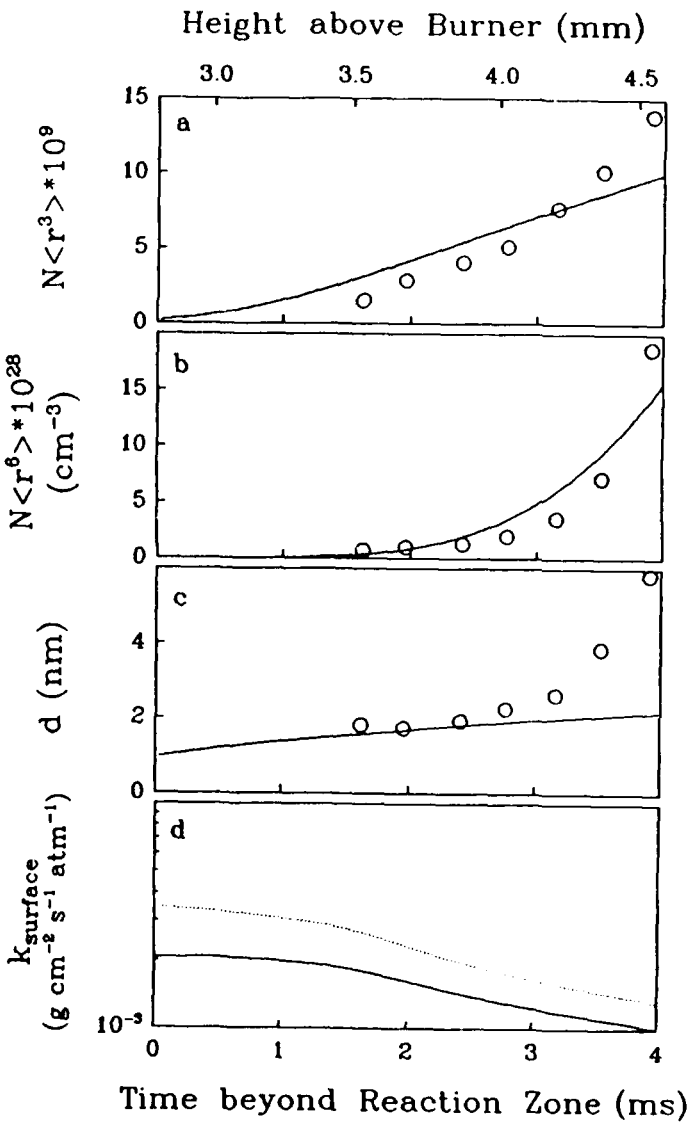
Height above Burner (mm)
3.0
3.5
4.0
4.5
a
b
c
d
N<r^3>*10^9
N<r^6>*10^{28}
(cm^{-3})
d (nm)
k$_{surface}$
(g cm^{-2} s^{-1} atm^{-1})
Time beyond Reaction Zone (ms)

COMPUTER MODELING OF SOOT FORMATION COMPARING FREE RADICAL AND IONIC MECHANISMS

(AFOSR Contract No. F49620-88-C-0007)

Principal Investigator: H. F. Calcote

AeroChem Research Laboratories, Inc.
P.O. Box 12
Princeton, NJ 08542

SUMMARY/OVERVIEW:

The main objective of a joint program between AeroChem and Penn State (Principal Investigator: Michael Frenklach) and Robert Brown at Iowa State (subcontractor) is to compare the relative importance of the free radical and ionic mechanisms of soot formation in flames. A detailed ionic mechanism is being developed and the necessary thermodynamic and reaction rate coefficients are being estimated at AeroChem to be run on the computer programs of Frenklach and Brown. The results should clarify the mechanism of soot formation in flames, account for the source of ions in flames, and lead to a simple mechanism of soot formation that can be incorporated into a more complex mechanism.

TECHNICAL DISCUSSION

During the last year, we have: further refined the detailed mechanism, especially the estimates of ion-molecule reactions; continued to improve the thermodynamic data base for both neutrals and ions; developed a dominant reaction pathway for ion-molecule reactions; interpreted the available neutral and ion data for the standard acetylene/oxygen flame in terms of rates of formation and destruction; and compared the reaction times required by the neutral and ionic mechanisms to add ten carbon atoms to a precursor species.

A limited number of computer runs, made by Frenklach, guided the development of the dominant reaction pathway. His program has no direct means of handling the non-Arrhenius temperature dependence of the ion-molecule reactions; he is improvising around this and a means of handling the charge balance and ion/electron diffusion. When these deficiencies are corrected we will test the ionic mechanism.

Brown is using a program he previously developed for ion formation in flames to which he has made some modifications to handle our ionic mechanism of soot formation. Ion/electron diffusion is incorporated into the program via the Poisson equation. Tests in a methane/air flame at 2.67 kPa demonstrate the importance of diffusion. His program also handles non-Arrhenius temperature dependence and a set of reactant species concentrations can be used as input data. Thus, the major neutral species can be calculated and the results used as input to the ionic mechanism. When experimental data are available they can be used. This eliminates the dependence of the ionic mechanism on the neutral mechanism (this has been a problem), and it makes it possible to extend the model to larger species by reducing the number of reactions and species required for a given computer run.

The present dominant path for ion-molecule reactions (recombination reactions are considered separately) is presented in Fig. 1. The first objective when computer runs are possible will be to reduce this set of reactions. It has already been reduced considerably by thermodynamic and concentration considerations. The different combinations of C and H refer to specific isomers. Each reaction rate coefficient was estimated at a series of temperatures by calculating the Langevin rate coefficient in the reaction direction for negative free energy. Then, using the equilibrium constant, the forward rate, i.e., toward increasing ion mass, was calculated. This assured realistic rates of reaction but produced non-Arrhenius temperature coefficients. The forward rates of ion-molecule reactions decrease with increasing temperature - as does soot production in a premixed flame.

A simple analysis was carried out to compare the rate of formation of large carbon species, which presumably lead to soot, by the neutral free radical mechanism and by the ionic mechanism (H. F. Calcote and D.G. Keil, "The Role of Ions in Soot Formation," Pure & Appl. Chem. 62, 815-824 (1990)). The number of neutrals or ions equal to the maximum number density of soot particles observed in the standard acetylene/oxygen flame were followed through a series of growth steps. Experimentally measured concentrations of both neutral and ionic species were used in the comparison. These experimental concentrations were combined with the rate coefficients for the growth of that species to the next larger species in the reaction sequence and a time was calculated for each step. Concentrations are not known for the free radicals, so the concentration for a radical was assumed equal to the concentration of the preceding stable species. The mechanism and times to add 10 carbon atoms for the free radical mechanism and 12 carbon atoms for the ionic mechanism are compared in Table I.

The total times required, considering forward times only, to add ten and twelve carbon atoms respectively are: 130 μs for the free radical mechanism and 18 μs for the ionic mechanism. The greater concentration of neutral species is balanced by the greater reaction rate coefficients for ion-molecule reactions and the fewer steps needed to add a specific number of carbon atoms to the growing species for the ionic mechanism than for the free radical mechanism. Also of importance is the fact that the concentration of neutral species falls rapidly with increasing mass while the ion concentration does not. Because reverse reactions are important, their times are also included in the table. They would appear to be a greater complication for the free radical mechanism than for the ionic reaction.

This analysis is no substitute for running a complete computer model, but it does indicate that the ionic model is a strong competitor to the free radical model.

Dr. Robert J. Gill has worked closely with the principal investigator on this program and his contribution is gratefully acknowledged.

FREE RADICAL MECHANISM	Time, μs		IONIC MECHANISM	Time, μs	
	Forward	Reverse		Forward	Reverse
$C_{10}H_8$			$H_9C_{11}^+$		
↓↑ $H\cdot - H_2$	0.34	0.06	↓↑ $C_2H_2 - H_2$	5.3	0.30
$C_{10}H_7\cdot$			$C_{13}H_9^+$		
↓ $C_2H_2 - H\cdot$	0.04	14	↓ C_4H_2	11	1,000
$C_{12}H_8$			$H_{11}C_{17}^+$		
↓↑ $H\cdot - H_2$	0.37	0.08	↓ $C_2H_2 - H_2$	1.3	160
$C_{12}H_7\cdot$			$C_{19}H_{11}^+$		
↓ $C_2H_2 - H\cdot$	0.64	2.0	↓ $C_2H_2 - H_2$	0.65	200
$C_{14}H_8$			$C_{21}H_{11}^+$		
↓↑ $H\cdot - H_2$	2.0	0.23			
$C_{14}H_7\cdot$			TOTAL FORWARD		
↓↑ $C_2H_2 - H\cdot$	20	0.0003	TIME	18 μs	
$C_{16}H_9\cdot$					
↓	0.0001	0.02			
$C_{16}H_9\cdot$					
↓ $C_2H_2 - H\cdot$	3.8	10,000			
$C_{18}H_{10}$					
↓ $H\cdot - H_2$	37	40			
$C_{18}H_9\cdot$					
↓ $C_2H_2 - H\cdot$	70	170			
$C_{20}H_{11}$					
TOTAL FORWARD					
TIME	130 μs				

TABLE I

Comparison of the times required to add ten carbon atoms by the free radical and the ionic mechanisms

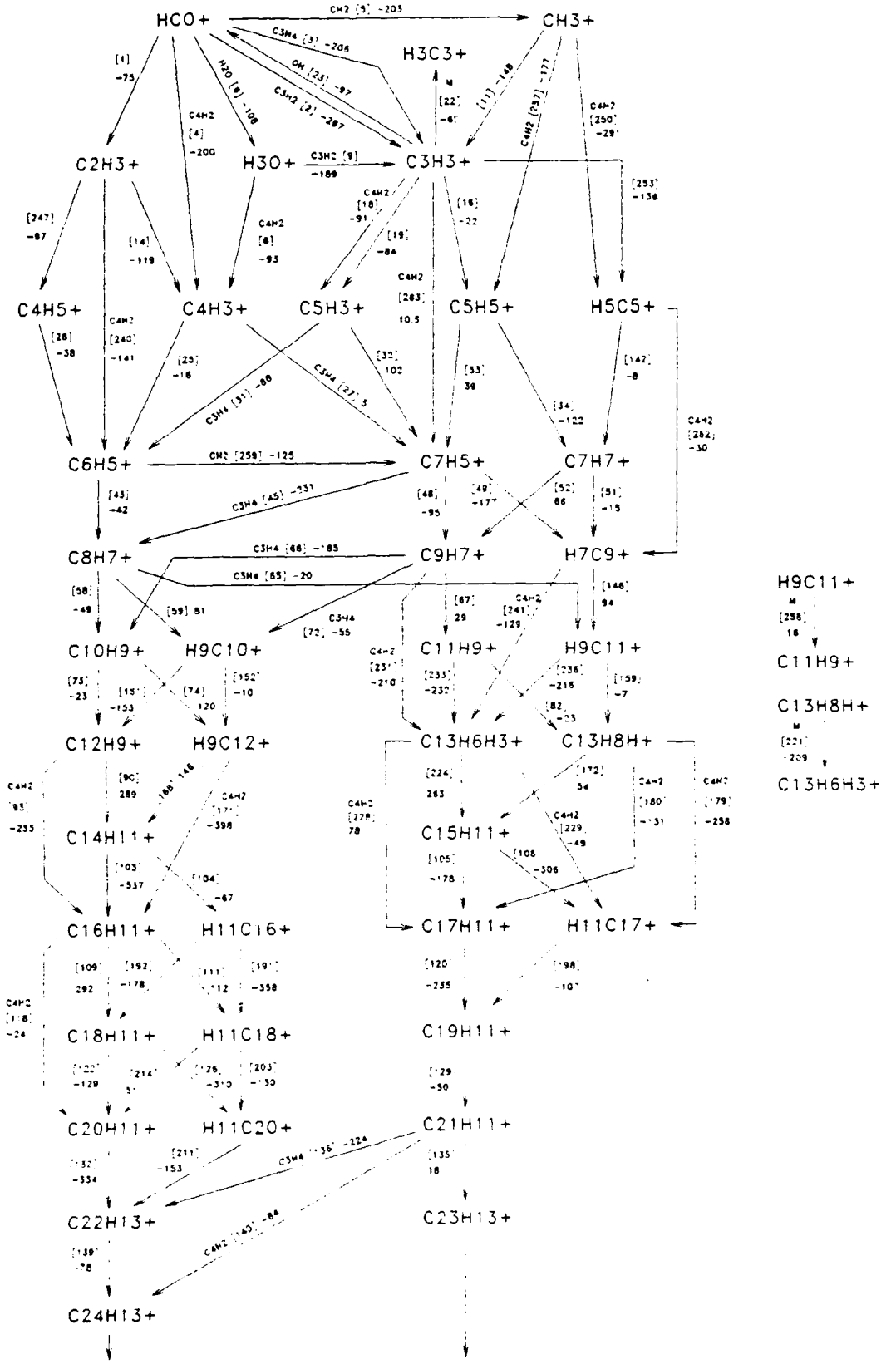

FIGURE 1 DOMINANT ION-MOLECULE REACTION PATHWAY
Reactions are with C_2H_2 unless noted otherwise. Numbers in brackets are the reaction numbers. Other numbers are ΔG_{rxn} at 1750 K.

A SYSTEMATIC APPROACH TO COMBUSTION MODEL REDUCTION AND LUMPING

(AFOSR Grant No. AFOSR-89-0070)
Principal Investigators: Herschel Rabitz*[‡] and Frederick L. Dryer**

*Department of Chemistry
**Department of Mechanical and Aerospace Engineering
Princeton University
Princeton, NJ 08544-1009

SUMMARY/OVERVIEW

This research is concerned with the development and application of new techniques for simplifying the complexity of chemical kinetic schemes arising particularly in combustion systems. Advanced techniques from sensitivity analysis, formal system lumping and Lie Group theory are being adapted for this purpose. The emphasis in this work is on the systematic aspects of model reduction and lumping including the assessment of whether a given system may be simplified successfully and the development of practical means for doing so.

TECHNICAL DISCUSSION:

Combustion phenomena inherently involve coupling of complex reactive and transport processes. The common goal in many current investigations is to develop comprehensive mathematical and computational models of combustion processes in various environments. These models would be used to provide a more fundamental understanding of combustion phenomena as well as allow for reliable engineering design studies. Therefore, a requirement is that the models be as complete and accurate as possible. This latter task will be an ongoing, iterative effort, but already the level of complexity of realistic models especially in higher spatial dimensions exceeds the capabilities of current or even foreseen computers. The recognition of this problem has led to the desire to lump or reduce the complexity of the models to a practical level yet at the same time retain their essential physical characteristics. Until recently, efforts along these lines have largely been based on the introduction of steady-state approximations, equilibrium approximations or the imposition of intuitively motivated empirical forms. These approaches have proved to be of limited utility, or generality, and typically lack any systematic structure.

In the present context, the term "reduced" refers to a decrease in the number of independent parameters (e.g., reaction rate constants) and the term "lumped" refers to a decrease in the number of dependent variables (e.g., species concentrations). Because the process of lumping inherently involves reduction, the size (number of species and reactions) of a lumped mechanism is smaller than that of a reduced mechanism.

---

‡ H.R. was partially supported through ONR Grant No. N00014-89-J-1939.

Mechanism reduction and lumping are important because they lead to further understanding of the controlling chemical and physical processes and to substantial savings in computational time. However, it is important to recognize that savings in computational time of simplified mechanisms is also coupled to numerical procedures. For example, further simplification of a reduced model to a lumped model by application of steady-state and partial equilibrium approximation does not always lead to a savings in computer time. Although a reduction in species concentrations is obtained, no change in the number of reaction rate constants is made. If the time consuming step of the numerical procedure is function evaluations rather than integration, then no gain is obtained with the lumped model. For example, we have shown recently, using the premixed flame code from Sandia National Laboratories, the CH_4/air example provided in the code manual and the associated simplified model by Peters et al.(Twenty-first Symposium on Combustion), that 97% of the computational time is used for function evaluations and less than 3% is used for Newton procedures including solution of linear algebraic systems. A second important point of reduced and lumped models are the domains of their validity. In particular, the methodology used to develop simplified models can result in models valid for one trajectory through operating parameter space or many.

Clearly, the problem of model simplification has many aspects, including the fact that combustion phenomena can occur under a variety of conditions each perhaps calling for an optimally distinct model. Three general approaches have been considered here based on (1) the introduction of linear projection lumping transformations, (2) application of advanced sensitivity analysis tools to identify and suggest reduced models and (3), the development of specialized Lie group techniques as a means to introduce fully nonlinear systems techniques. In each of these procedures, computational efficiencies are considered. Progress in these three areas is described below.

1. Lumping by Linear Transformation

A. A General Analysis of Approximate Lumping in Chemical Kinetics

A general analysis of approximate lumping based on linear transformations has been developed. This analysis can be applied to any reaction system with n species described by $dy/dt = f(y)$, where y is an n-dimensional vector in a desired region Ω and f(y) is an arbitrary n-dimensional function vector. Here we have considered lumping by means of a rectangular constant matrix M (i.e., $\hat{y} = My$, where M is a row-full rank matrix and $\hat{y}$ has dimension $\hat{n}$ not larger than n). The observer theory initiated by Luenberger was formally employed to obtain the kinetic equations and discuss the properties of the approximately lumped system. The approximately lumped kinetic equations have the same form $d\hat{y}/dt = Mf(\bar{M}\hat{y})$ as that for the exactly lumped ones, but depend on the choice of the generalized inverse $\bar{M}$ of M. The (1,2,3,4) inverse is a good choice of the generalized inverse of M. The equations to determine the approximate lumping matrices M has been developed. These equations can be solved by iteration. An approach for choosing suitable initial iteration values of the equations has been illustrated in several examples.

B. The Determination of Constrained Lumping Schemes for a Reaction System in the Whole Composition Space

Two new approaches to the determination of constrained lumping schemes have been developed. They are based on the property that the lumping schemes validated in the whole composition Y_n-space of y are only determined by the invariance of the subspace spanned by the row vectors of lumping matrix M with respect to the transpose of the Jacobian matrix $J^T(y)$ for the kinetic equations. We have proved that when a part of a lumping matrix M_G is given, each row of the part of the lumping matrix to be determined M_D is a certain linear combinations of a set of eigenvectors of a special symmetric matrix. This symmetric matrix is related to M_G^T and $A_k M_G^T$, where A_k are the basis matrices of $J^T(y)$. It has been shown that the appropriate lumping matrices containing M_G with different row number $\hat{n}(\hat{n}<n)$ and global minimum errors can be determined by an optimization method. Using the concept of the minimal invariant subspace of a constant matrix over a given subspace one can directly obtain the lumping matrices containing M_G with different $\hat{n}$. The accuracy of these lumping matrices was shown to be satisfactory in several sample calculations.

C. Determination of Constrained Lumping Schemes for Nonisothermal First-order Reaction Systems

The direct approach to determining the constrained lumping schemes summarized in paragraph B above has been applied to nonisothermal first-order reaction systems. The constant basis matrices of the transpose of the Jacobian matrix for the kinetic equations were replaced by a set of rate constant matrices at different temperatures which properly cover the desired temperature region. This approach allows for the consideration of a distribution of temperatures as well as directly incorporating an energy balance equation. As an illustration, the technique was successfully applied on a model for petroleum cracking.

2. Insights Into Lumping and Model Reduction Through Advanced Sensitivity Analysis Techniques

A. A Combined Stability-Sensitivity Analysis of Weak and Strong Ignition/ Reaction of Hydrogen/Oxygen Mixtures: Implications of Global Reactions and Rates

Stability and sensitivity analysis were used to examine the ignition/ reaction characteristics of dilute hydrogen-oxygen mixtures. The analysis confirms the existence of two distinct regions of ignition and fast reaction, previously labeled "weak" and "strong" ignition, both of which are located in the explosive pressure-temperature domain and separated by a region related to the "extended" classical second limit. The stability analysis is based on an eigenanalysis of the Green's function matrix of the governing kinetic equations. The magnitudes of the largest (and system controlling) eigenvalue allow the strengths (overall reaction rates) of the two processes to be quantified, giving a clear definition to the terms "weak" and "strong". The sensitivities of the largest eigenvalue to the reaction rate constants of the mechanism pinpoint the elementary steps controlling the two ignition processes and the subsequent reaction. The associated eigenvectors yield the direction of change in species concentrations and temperature during the course of reaction. The overall reactions are essentially global reactions of the mechanism. These vectors are found to be nearly constant during the induction

period of both "weak" and "strong" ignition, thus producing constant overall stoichiometric reactions. The subsequent reaction of major reactants associated with "weak" ignition also has a constant overall reaction, although, different from that for the induction period. However, the vector describing the reaction of major reactants associated with "strong" ignition is found never to be constant, but continuously changing.

B. The Effects of Thermal Coupling and Diffusion of the Mechanism of H_2 Oxidation in Steady, Premixed Laminar Flames

The work considered the question of why steady premixed laminar flames can be successfully described by highly reduced models, whereas the underlying mechanism is inherently complex. The calculations were performed on H_2-air systems. Sensitivity functions were evaluated and studied for diffusion-free situations, both isothermal and adiabatic, as well as for steady premixed flames. In the diffusion-free cases most reactions of a 38-step mechanism were shown to be influential in a distinct fashion. The form of sensitivity functions is, however, radically changed and rendered self-similar by simultaneous thermal coupling and diffusion that introduce strong nonlinear coupling among the variables. Due to self similarity, the mechanism can be reduced to 15 reactions while keeping the temperature profile and the mass fraction profiles of molecular species almost unchanged in flame calculations. Furthermore, there exists an invariant subspace in the space of kinetic parameters such that large parameter perturbations along any vector in this subspace result in relatively small changes in the computed flame properties. By giving mechanistic interpretation to such parameter perturbations, the model can be simplified in many ways. In particular, a sequence of models was constructed in a stoichiometric H_2-air flame problem that converge to a 9-step reduced mechanism with quasi steady state assumptions in radicals except H, thereby resulting in a two-step quasi-global model. All these approximations are inappropriate without the presence of molecular and thermal diffusion.

3. Development of Lie Group Techniques for Combustion Model Simplification

This research concerns the utilization of Lie Group techniques to investigate the simplification of kinetic equations. The approach is based on the ability of Lie methods to directly establish functional relationships determining the consequences of wide ranging variations in physical and chemical variables. Two key results have been achieved thus far: (1) Lie transformations can be established that preserve the global qualitative characteristics of a kinetic system (i.e., phase space structure), and (2) the methods can be applied to convert inherently nonlinear kinetic systems to linearized forms for practical solution (this approach is at least regionally global and quite distinct from traditional local linearization methods). The techniques involved here can be viewed as being global sensitivity analysis or a fully nonlinear generalization of the linear lumping matrix methods mentioned in section 1 above.

Simulation of Turbulent Combustion

AFOSR Contract No. AFOSR-ISSA-89-0025

Principal Investigators:

Howard R. Baum
Ronald G. Rehm

National Institute of Standards and Technology
Gaithersburg, Maryland 20899

SUMMARY/OVERVIEW:
A mathematical model of diffusion-controlled combustion in a turbulent flow dominated by large-scale eddy motion and including realistic hydrocarbon chemistry within a laminar flamelet model is described. This model significantly extends the research on diffusion-controlled combustion in a turbulent flow carried out previously by NIST for AFOSR and is consistent with a large-scale three-dimensional, time-dependent fire-driven flow simulation developed independently by NIST. The extensions involve finite-rate chemistry, the effects of realistic hydrocarbon chemistry within a laminar flamelet model and the effects of heat release upon the combustion model previously developed.

TECHNICAL DISCUSSION
The theoretical study of turbulent combustion including hydrocarbon chemistry has become a very active area of research in recent years. The problem is formidable because combustion is fundamentally transient, nonlinear, multidimensional and involves length and time scales which range over several orders of magnitude. It is extremely important in applications such as internal combustion engines, gas turbines, furnaces, and unwanted room fires.

Prediction of heat release and species transformation is the central issue in combustion science. Since the chief technical difficulty to making such predictions is the fact that the phenomena of interest are strongly coupled

over a range of five orders of magnitude in length and time, the processes have been analyzed in the present research program in three co-existing frames of reference. Each reference frame is a natural coordinate system for calculation of one or more processes at a given scale. Moreover, the solutions obtained in each coordinate system provide the information necessary to generate the coordinate system needed to describe the phenomena at the next smaller scale. At the largest scales the fluid flow is essentially nondissipative and is related to the geometry defining the flow configuration and global mixing and the fuel and oxidizer distributions. Combustion takes place on the intermediate scales associated with the diffusion of fuel and oxidizer into each other; it "rides on" the geometrical scale flow field and establishes the local environment which determines the rate at which the reactants disappear and heat is released. Finally, the smallest scales are determined by the details of the hydrocarbon chemistry; these scales are associated with species and temperature profiles in the chemical reaction zone.

The combustion process resolved on the scale of an individual fuel parcel has been the emphasis of the research efforts this year. The solution to the two-dimensional problem formulated by Marble has been completed, and has appeared in Combustion Science and Technology, 66, 4-6, p. 293 (1989). Research has also continued to determine the effects of heat release on the local velocity field. An "idealized" single step irreversible reaction model and a model treating the effects of real chemistry within the laminar flamelet approximation have been considered. The convection-diffusion equation for the mixture fraction and the mass conservation equation are analyzed using the experimental observation that specific volume is a piecewise linear function of mixture fraction. A Cole-Hopf transformation is used to reduce this equation to an incompressible form in terms of a new "pseudo mixture fraction" which can be related to all scalar properties using measured or idealized state relationships. Seven different fuels have been studied to determine these "state relationships". Sample results for two fuels, C_2H_2 and CH_4 are shown in the appended figure. Here the specific volume is shown as a function of the mixture fraction for each fuel for two values of the radiative heat loss fraction X_R. For all fuels, these relationships can be closely approximated by four straight line segments. A manuscript describing this work has been accepted for presentation at the Twenty Third International Symposium on Combustion, University of

Orleans, France, July 22-27, 1990.

Finally, an extension to the two-dimensional Marble problem which accounts for finite rate chemistry has been investigated, and a manuscript describing this work is under preparation. A brief description of this work follows. A two-dimensional model of a constant-density diffusion-controlled reaction with finite reaction-rate chemistry occurring between unmixed species initially occupying adjacent half-spaces has been formulated and analyzed. The chemical reaction term has been taken to be appropriate for an isothermal, bimolecular reaction for simplicity. An axisymmetric viscous vortex field satisfying the Navier-Stokes equations winds up the interface between the species as they diffuse together and react. The vortex is of the same form as that originally proposed by Marble. The diffusion rates for the two species are assumed constant and equal so that a mixture fraction or Schvab-Zeldovich dependent variable can be used. The resulting equation for the mixture fraction is linear and can be solved by noting that a Lagrangian coordinate system removes the convection and that the equation permits a global similarity solution. In a previous paper (the CST paper), the authors solved the mixture-fraction problem assuming a flame-sheet approximation both asymptotically for large Schmidt numbers and numerically. In the current work, the problem is solved when the reaction rate is finite. The solution for the mixture fraction is used to eliminate one of the species in the complete convection, diffusion, reaction problem for the two species, fuel and oxidizer. The single resulting nonlinear problem is also analyzed in a Lagrangian coordinate system. An additional transformation of independent variables to time, similarity variable and the distance normal to the interface between the fuel and oxidizer in Lagrangian coordinates is then made. This change results in a linear equation for the mixture fraction and a nonlinear equation for one of the species concentrations. In the limit of large Schmidt numbers, a simple expression for the mixture fraction (not found before) can be obtained and the nonlinear equation for the species concentration can also be substantially simplified. Asymptotic and numerical results show the competing influences of reaction, diffusion and convection on species consumption.

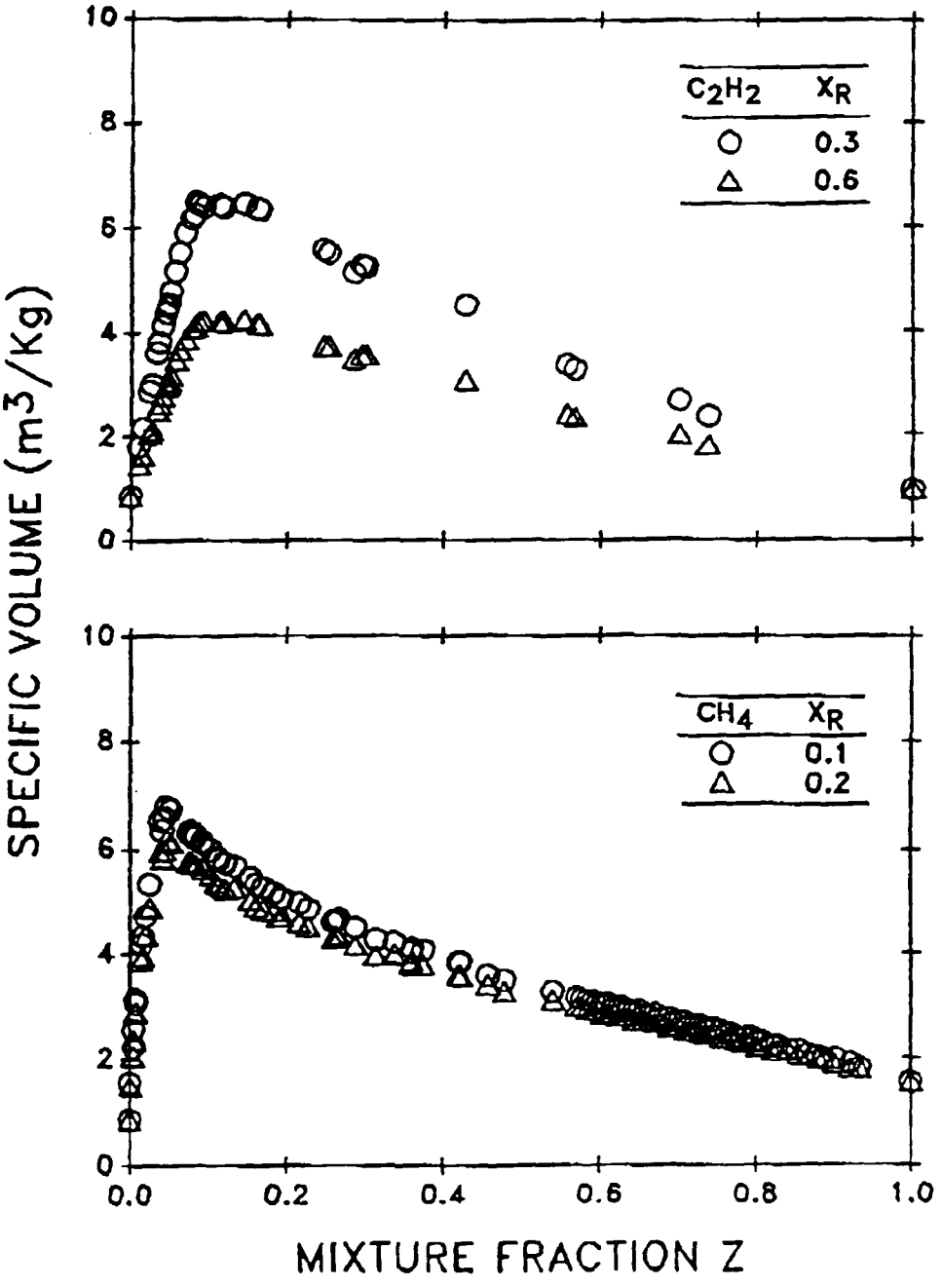

Specific Volume - Mixture Fraction Relationship as a Function of Radiative Heat Loss Fraction X_r

A STUDY OF MIXING AND COMBUSTION IN SUPERSONIC FLOWS

(AFOSR Contract No. 90-0151)

Principal Investigators: C. T. Bowman, R. K. Hanson, M. G. Mungal, and W. C. Reynolds

Department of Mechanical Engineering
Stanford University
Stanford, CA 94305-3032

SUMMARY/OVERVIEW:

An experimental and computational investigation of supersonic combustion flows is being conducted to gain a more fundamental understanding of mixing and chemical reaction in supersonic flows. The research effort comprises three interrelated elements: (1) an experimental study of mixing and combustion in a supersonic mixing layer; (2) development of laser-induced fluorescence techniques for time-resolved, two-dimensional imaging of species concentration, temperature and velocity; and (3) numerical simulations of compressible reacting flows.

TECHNICAL DISCUSSION:

Experiments on Mixing and Reaction in Supersonic Flow

Experimental investigations of supersonic mixing continued during the past year. Our facility, described in Ref. 1, consists of a high-speed stream of Mach number 2.2 to 1.5 and a low-speed stream of Mach number 0.5. Presently, both streams are unheated air. Convective Mach numbers range from 0.3 to 0.8. In order to visualize the flowfield in detail, without the limitations of spatial integration as is common in Toepler schlieren techniques, we have developed an alcohol visualization technique that allows the easy use of planar laser Mie scattering. Reference 2 provides a detailed account of the technique and only a brief summary is provided here. In this approach, finely atomized alcohol is injected well upstream of either the high-speed settling chamber or low-speed settling chamber and fully vaporizes before reaching the test section. High-speed seeding causes the condensation of a fine mist of particles which uniformly mark the high-speed stream and are then diluted by mixing with the low-speed stream. Low-speed seeding causes the fine mist to appear where the low-speed fluid mixes with the cold high-speed fluid, and so marks only the mixed fluid regions. In analogy with combustion studies these two approaches are referred to as the "passive scalar" and "product formation" modes, respectively.

Figure 1, using the "product formation" approach, summarizes one of our main findings to date. This photo shows side and plan view planar cuts of the layer at low convective Mach number and at a higher convective Mach number. The low convective Mach number case, representing low compressibility, reveals the classic Brown-Roshko structure consisting of generally two-dimensional roller structures, which span the test section, with a thin interconnecting braid region. This is to be contrasted with the higher compressibility case where the two-dimensional structures are not evident and the flow appears considerably more three-dimensional. Further details about these changes to the flow can be found in Ref. 3.

In addition, we have begun the final facility preparations that will allow combustion studies to begin this summer. Reacting experiments will be interpreted on the basis of our findings in the non-reacting case. Finally, in addition to the experimental work, we have developed a simplified flow model for a reacting supersonic mixing layer with full chemistry. This model, Ref. 4, which is based on the Broadwell-Breidenthal-Mungal model for incompressible layers, is being used to determine the range of experimental conditions to be employed in the reacting flow experiments.

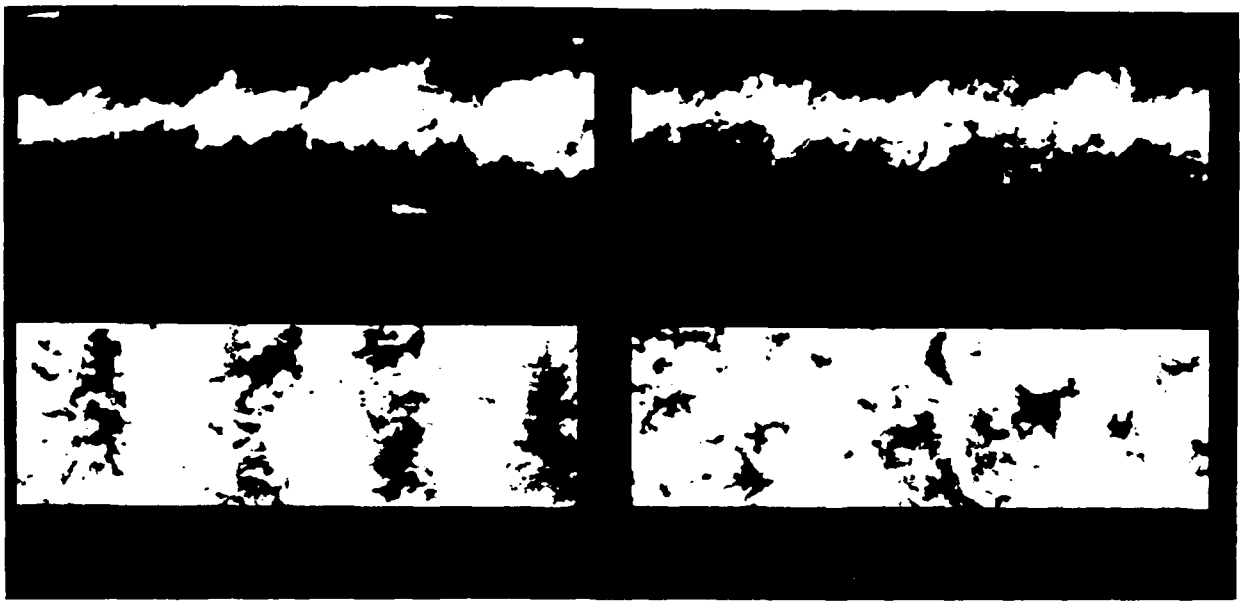

Figure 1. Side and plan views of compressible mixing layer. Left images $M_c = 0.3$, right images $M_c = 0.6$.

Development of Supersonic Flow Diagnostics

This research is aimed at establishing Planar Laser-Induced Fluorescence (PLIF) techniques for imaging in supersonic flowfields. Successful techniques will subsequently be applied in the supersonic mixing layer facility. Work during the past year has been in four areas: (1) supersonic flow facility development; (2) shock wave imaging; (3) temperature imaging; and (4) imaging in the supersonic mixing layer rig.

In order to provide useful test environments for investigating new PLIF imaging concepts, we have built several new flow facilities. During the past year, progress was made with three such facilities: (1) a 75 kW RF plasma-heated supersonic tunnel which can provide stagnation conditions of up to 4 atm and 5000 K (equilibrium temperature) in air; (2) a pressure-driven shock tube and tunnel which provides a wide range of flow conditions for a short duration: and (3) a small gas-fired rocket motor intended to provide a steady supersonic flow of combustion products. All three facilities are now operational, although refinements are needed in both the shock tunnel and rocket motor to meet all our research needs.

We have made good progress in solving the experimental problems associated with PLIF imaging in pulsed flow facilities with shock waves present. Work during the past year has emphasized imaging of NO using a tunable narrow-bandwidth ArF laser (193 nm). Spectroscopic codes were assembled which allow identification and selection of optimum molecular transitions, and these codes have been verified in controlled laboratory experiments. The ability to probe different transitions, particularly different vibrational levels, is critical to applications of PLIF in flows with vibrational nonequilibrium. The measurement strategy developed allows inference of vibrational temperature through ratios of PLIF signals for excitation from $v = 1$ and $v = 0$. Good agreement has been found between measured and computed vibrational temperatures for simple flows behind normal incident shocks; see Ref. 5. Current work is aimed at flows with 2- or 3-d characteristics, such as shown in Fig. 2, which are more difficult to calculate.

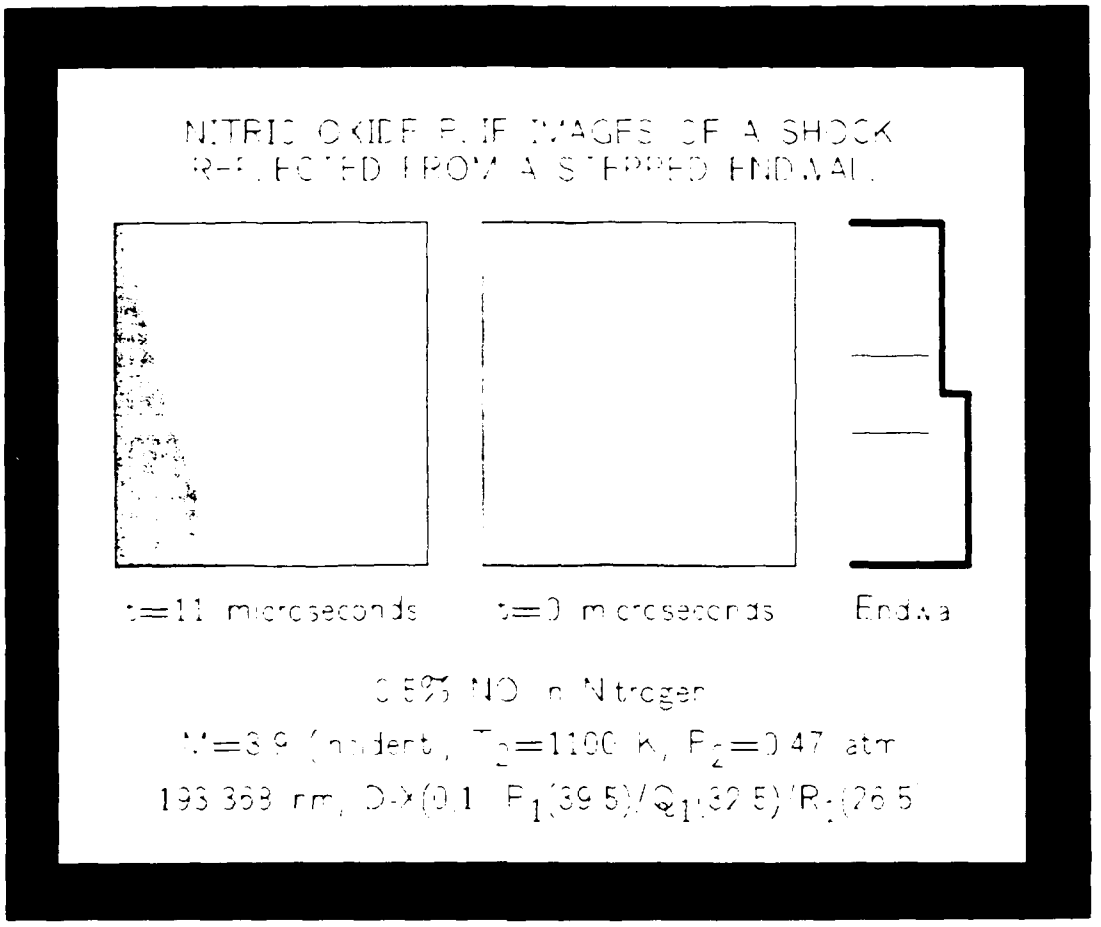

Figure 2. Single-shot PLIF images of NO in a shock tube.

In view of the importance of temperature as a variable in supersonic flows, we have explored temperature imaging strategies in both cold and hot flows. Using an underexpanded supersonic jet of N_2 seeded with a low level of NO, we have studied PLIF strategies for temperature based on both single and multiple laser wavelengths. When the mole fraction of the tracer is known, and the fluorescence signal is quenching dominated, single-shot PLIF imaging of temperature was found to work very well; see Ref. 6. In combustion flows, however, the preferred strategy is to utilize two separate laser wavelengths (probing two separate states) yielding two PLIF images whose ratio can be used for temperature. Measurements of this type are in progress in both subsonic and supersonic combustion flows (for two species: NO and OH).

During this past year, we made our first attempt to perform PLIF imaging in the supersonic mixing layer facility. Owing to limitations of the windows available, the measured species was I_2 (seeded into the low-speed stream). Problems associated with beaming the tunable dye laser from one lab to another were overcome, and the entire process of laser excitation, image data collection, data storage, and processing of PLIF data was successfully demonstrated. Window modifications needed to permit similar measurements with NO and OH are now in progress.

Stability and Numerical Simulation

This phase of the program is intended to provide fundamental understanding of reacting supersonic mixing layers and insight into their modeling from a combination of linear stability analyses and direct numerical simulation.

Our previous stability work showed that oblique waves dominate the flow for convective Mach number, $M_c = 0.6$. Analysis of a reacting compressible mixing layer has recently shown that heat release (with infinitely fast reaction rates) postpones the onset of dominance of oblique waves, in some cases to $M_c = 2.0$. New modes occur with heat release, and the physics can be easily understood in terms of the mean vorticity-density profiles in the flow.

Numerical simulations of the non-linear development with finite reaction rates is now being formulated. This work will draw heavily on related work in our laboratory supported by the NASA/Stanford Center for Turbulence Research.

Direct numerical simulations of homogeneous compressible turbulence subjected to mean shear have been completed. These are intended for use in developing models for the fine-scale turbulence in inhomogeneous flows, for example for Large Eddy Simulations. The simulations have revealed a number of interesting features. In particular, the flow appears to develop an RMS fluctuation Mach number of about 0.4, irrespective of the initial conditions, and a ratio of the dilitation dissipation to the solenoidal dissipation of about 10%. These numbers are in good agreement with recent models for compressible turbulence suggested by Zeman at CTR and Sarkar at NASA/Langley. New ideas for modeling other parameters have been suggested by the simulations and are being explored.

References

1. Clemens, N. T., Mungal, M. G., Berger, T. E. & Vandsburger, U., "Visualizations of the structure of the turbulent mixing layer under compressible conditions", AIAA-90-0500, Reno, NV, Jan. 1990.

2. Clemens, N. T. & Mungal, M. G., "A planar Mie scattering technique for visualizing supersonic mixing flows", submitted to Expts. Fluids, 1990.

3. Clemens, N. T. & Mungal, M. G., "Two- and three-dimensional effects in the supersonic mixing layer", AIAA-90-1978, Orlando, FL, July 1990.

4. Miller, M. F., Bowman, C. T., Miller, J. A., Kee, R. J., "A model for chemical reaction in a compressible mixing layer," Paper 89-110, Western States Section, The Combustion Institute, Oct. 1989.

5. McMillin, B. K., Lee, M. P., Palmer, J. L., Paul, P. H. and Hanson, R. K., "Planar Laser-Induced Fluorescence Imaging of Shock-Heated Flows in Vibrational Nonequilibrium," 1989 ASME, Winter Meeting, San Francisco, CA, Dec. 1989, in press.

6. Hanson, R. K., Chang, A. Y., Seitzman, J. M., Lee, M. P., Paul, P. H. and Battles, B. E., "Laser-Induced Fluorescence Diagnostics for Supersonic Flows," AIAA-90-0625, Reno, NV, Jan. 1990.

Theories of Turbulent Combustion in High Speed Flows

AFOSR GRANT NO. 89-0539A
Principal Investigator: K. N. C. Bray,
Engineering Department,
University of Cambridge,
Trumpington Street,
Cambridge, CB2 1PZ.

Summary/Overview

The objective of this research is to improve understanding of turbulent combustion in high speed flows. In a related program Libby and Williams [1] show that supersonic combustion of nonpremixed hydrogen and air under conditions of applied interest will typically occur in the reaction-sheet regime. The aim of the present research is to develop simple theoretical models of turbulent combustion which are applicable to this combustion regime. The results may help to enhance capabilities of reasonable computations of high-speed turbulent reacting flows.

Technical Discussion

The present research forms part of a collaborative program with Professors P. A. Libby and F. A. Williams of the University of California, San Diego.

Much progress has been made during the past decade in identifying processes which control the rate of burning in low Mach number turbulent flames. It is known that, at the high Damköhler numbers typical of practical systems, incomplete turbulent mixing leads to large fluctuations in scalar variables, and to conditions consistent with the reaction-sheet burning regime rather than the distributed-reaction regime. Laminar flamelet models [2, 3] then provide an appropriate description of mean burning rates while models based upon an assumed distributed-reaction flame

structure can lead to large errors. Another consequence of fluctuations in scalar variables is an additional transport mechanism [4], due to interactions between density fluctuations and pressure gradients, which can lead to counter-gradient turbulent transport.

Studies [1, 5, 6] of nonpremixed hydrogen-air combustion, for flight between altitudes of 20 and 70 km at Mach numbers from 1 to 25, with a combustion Mach number of one third of the flight Mach number, indicate conditions consistent with the reaction-sheet burning regime. Phenomena similar to those discussed above are therefore possible in high speed combustion.

The objective of the present research is to develop a theoretical model of nonpremixed turbulent combustion, in high speed flows, for application to the reaction-sheet burning regime.

Work currently in progress aims to extend conventional second-moment (Reynolds stress), presumed pdf closure methods for application to high speed flows. A variety of alternative simplifying assumptions are being explored. It is anticipated that, before the end of the first year of the grant, an initial model of a two-dimensional, high speed, turbulent, reacting shear layer will have been developed. This model will be used to assess differences between reaction-sheet and distributed-reaction heat release rates and also non-gradient transport processes.

References

1. P. A. Libby, F. A. Williams: Theories of Turbulent Combustion in High Speed Flows. Research Abstract, Grant AFOSR-89-0310: 15th March, 1990.

2. F. A. Williams: Combustion Theory, Second Edition, Benjamin/Cummings Co. Inc., 1985.

3. S. K. Liew, K. N. C. Bray, J. B. Moss: Combust. and Flame, 56, 199, 1984.

4. K. N. C. Bray, P. A. Libby, G. M. Masuya, J. B. Moss: Combust. Sci. and Tech. 25. 127, 1981.

5. E. Gutheil, F. A. Williams: "The Structure of Hydrogen-Air Counterflow Diffusion Flames", Western States Section, The Combustion Institute, Preprint 89-109, Livermore, CA, October, 1989.

6. E. Gutheil, F. A. Williams: "A Numerical and Asymptotic Investigation of Structures of Hydrogen-Air Diffusion Flames at Pressures and Temperatures of High-Speed Combustion". Twenty-Third Symp. (Int.) on Combustion. The Combustion Institute (submitted) 1990.

TURBULENT MIXING IN EXPONENTIAL TRANSVERSE JETS

(AFOSR Grant NO. 87-0366)

Principal Investigator: R.E. Breidenthal

Aeronautics and Astronautics
University of Washington
Seattle, WA 98195

SUMMARY/OVERVIEW:

Turbulent vortices are known to be controllable under external forcing in some cases. In this study we pursue the hypothesis that under exponential forcing, the entrainment and mixing rate of vortices can be influenced. A new, self-similar flow is sought, where the e-folding time scale of the acceleration controls the vortex rotation rate rather than the Lagrangian age of the vortex. Chemically reacting flow visualization in water reveals the structure of the vortices and the flame length in a transverse jet. The results indicate that this forcing can have a dramatic effect on the mixing rate, even in the far field, long after the acceleration is over.

TECHNICAL DISCUSSION:

All unforced free turbulent shear flows have large scale vortices which rotate once in a time interval about equal to their Lagrangian age. This follows since there are no other time scales available. Such vortices therefore rotate more slowly as they age. Irrotational fluid entrained and mixed into the vortices dilute their vorticity. Fluid with the opposite sign of vorticity also is entrained.

Under appropriate forcing, the rotation rate of the vortices need not decline with time. Sinusoidal forcing of the plane shear layer induces spectacular changes, where for a time the vortices do not grow (Oster and Wygnanski, 1982). Both the mass and momentum mixing rates vanish (Roberts, 1985). Does this always occur any time the forcing imposes a well-defined time scale on the flow, so that the vortex rotation rate does not decay?

In these experiments, a well-defined time scale is imposed using an exponential acceleration function on a transverse jet. The configuration is sketched in figure 1. A streamwise array of up to ten nozzles of exponentially increasing width inject one fluid into a crossflow of another fluid flowing in a water tunnel. The injection speed increased exponentially along the nozzle array, so that the ratio of the local nozzle width d_j to the local injection speed V_j was a constant time,

$$\tau_j \equiv \frac{d_j}{V_j}$$

This is compared with the time τ_e it takes for the crossflow to convect at speed U_∞ one e-folding distance x_e along the nozzle length,

$$\tau_e \equiv \frac{x_e}{U_\infty}$$

The ratio of these two times

$$\alpha \equiv \frac{\tau_j}{\tau_e} = \frac{d_j}{x_e} \frac{U_\infty}{V_j}$$

is an acceleration parameter indicating how many revolutions a vortex makes before the forcing increases the nozzle width and velocity by a factor of e.

Results for vortex growth are shown in figure 2 for several different conditions and nozzle configurations. The size of the longitudinal vortex normalized by the vortex separation is plotted as a function of the acceleration parameter α. As α increases, the vortices are reduced in size by about a factor of three in diameter or a factor of ten in cross sectional area. If all the mixed fluid resided within this vortex pair, the amount of mass mixing would be expected to be proportional to the vortex area. Acceleration strongly inhibits vortex growth.

The flame length of the exponential transverse jet is shown in figure 3. A standard acid-base reaction with disodium fluorescein was used. Here the flame length x_f, normalized by the e-folding length of the nozzle, is plotted as a function of α for several different values of the reaction equivalence ratio ϕ. For each value of ϕ, the flame length is a maximum near $\alpha = 1$. Therefore, x_f is independent of U_∞/V_j at its maximum. At large α, x_f appears to weakly depend on α, declining slowly with increasing α.

In contrast, the flame length of a conventional transverse jet is shown in figure 4. As the velocity ratio U_∞/V_j is increased, the flame length increases monotonically. This is expected in light of simple dilution arguments given by Broadwell and Breidenthal (1984).

The non-monotonic behavior of the exponential jet in figure 3 suggests that the manner of injection can have a strong far-field effect on the mixing and that something significant occurs when $\alpha \cong 1$.

The physical mechanism for this peculiar behavior is not yet clear. At large α, the acceleration inhibits the mixing in the near field, as shown in figure 2. At the same time, acceleration enhances the mixing in the far field, yielding a flame length which is nearly independent of U_∞. The isolation of the mixing rate from longitudinal pressure waves and their associated changes in velocity ratio U_∞/V_j may be desirable in certain combustion applications, where the inhibition of near field and control of far field mixing would inhibit combustion instabilities.

REFERENCES:

[1] Broadwell, J.E. and Breidenthal, R.E., 1984 "Structure and mixing of a transverse jet in incompressible flow", *J. Fluid Mech.*, Vol. 148, pp. 405-412.

[2] Roberts, F.A., 1985 "Effects of a periodic disturbance on structure and mixing in turbulent shear flows and wakes", Ph.D. thesis, California Institute of Technology.

[3] Oster, D. and Wygnanski, I., 1982 "The forced mixing layer between parallel streams", *J. Fluid Mech.*, Vol. 123, pp. 91-130.

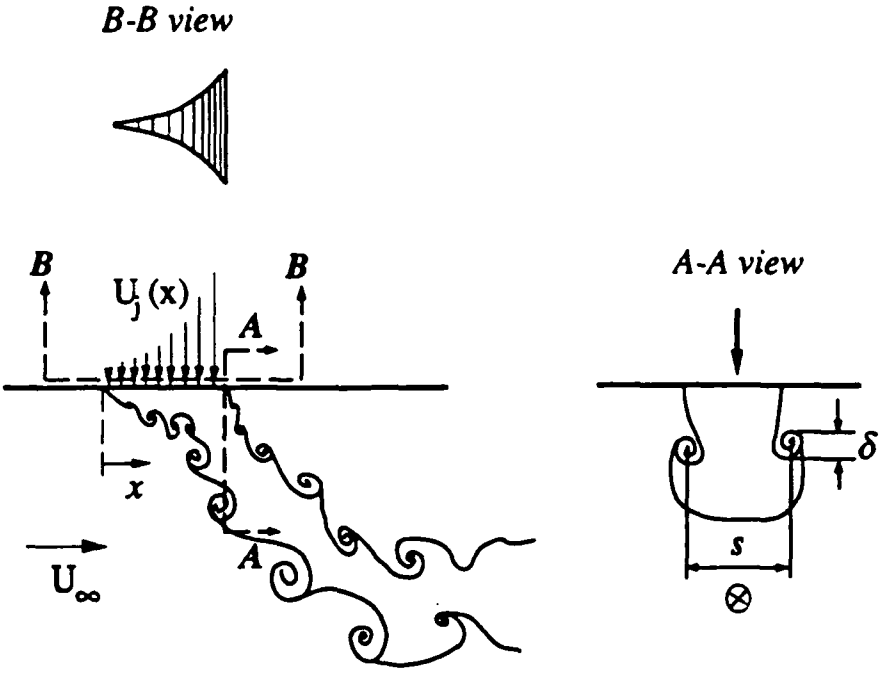

Figure 1 Flow geometry

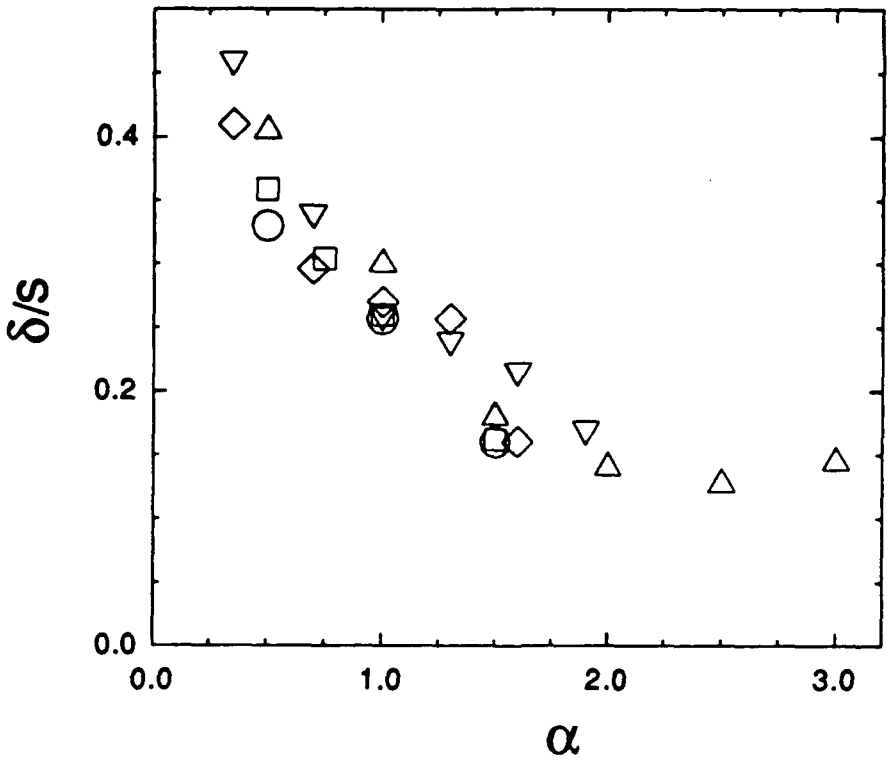

Figure 2 Size of the longitudinal vortices

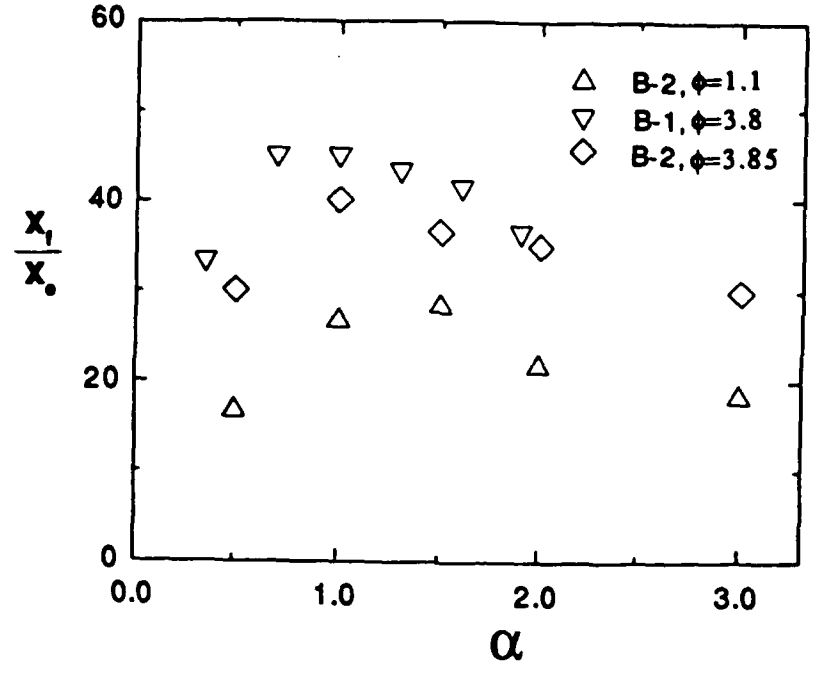

Figure 3 Flame length as a function of the acceleration parameter

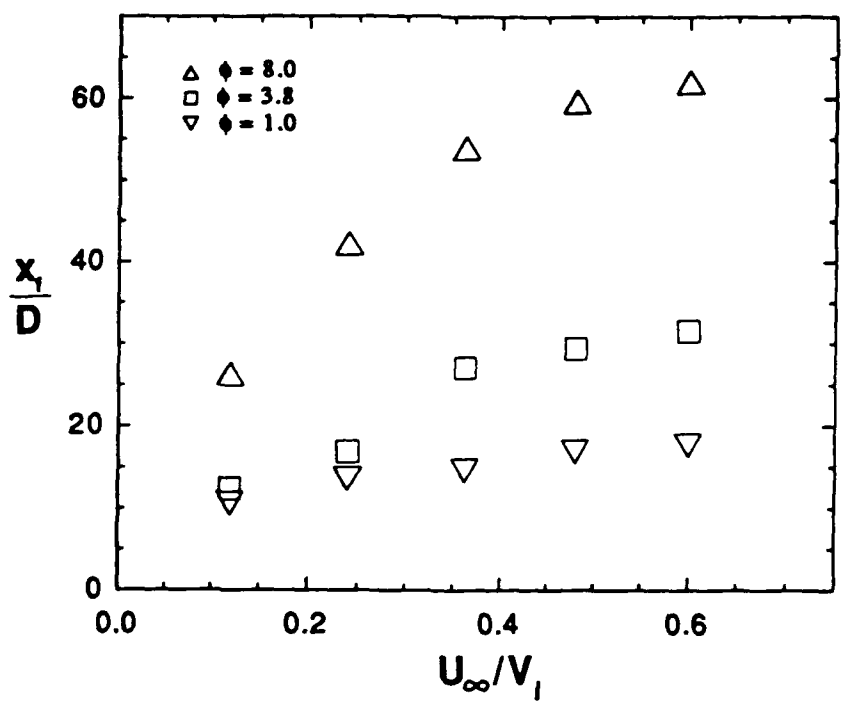

Figure 4 Flame length of a conventional transverse jet

LOCAL EXTINCTION MECHANISMS IN NON-PREMIXED TURBULENT COMBUSTION

AFOSR Contract No. F-49620-88-C-0066

Principal Investigators: S.M.Correa and A. Gulati

General Electric Corporate Research and Development Center

Schenectady, New York 12301

INTRODUCTION AND PRIOR RESULTS

This is an experimental and modeling study of turbulence-chemistry interactions in gaseous flames under conditions approaching blowoff. It builds on prior work on CO/H_2 jet flames under less severely strained conditions [1,2]. In the previous reporting period, we investigated a non-premixed turbulent jet flame, composed volumetrically of a 40% CO/10% H_2/50% N_2 mixture, in co-flowing air [3,4]. The flame was stabilized by a co-annular premixed pilot flame. Pointwise measurements of (i) temperature, mole fractions of major species, and mixture fraction ξ, by spontaneous Raman spectroscopy and (ii) velocity, by laser velocimetry, showed significant temperature decrements due to finite-rate chemistry effects but no evidence of localized extinction. A computational model for a jet flame under such conditions was developed. Combustion chemistry was represented by two-body shuffle reactions and three-body recombination reactions. The scalar dissipation rate field was examined for a critical value below which the two-body reactions were assumed to be in partial equilibrium and above which they were assumed to be frozen and the gas therefore unburned. The kinetics of the recombination reactions were activated for the former fraction of the gas. This approach was been implemented in a shear-layer finite-volume averaged Navier-Stokes model with k-ε/assumed shape probability density function (pdf) sub-models for turbulence.

It was concluded that local strain-induced extinction is not seen in the above CO/H_2-air flames, despite its relatively low critical strain of 950 s^{-1} in a Tsuji burner. This is because the reaction zones, centered on $\xi_s \simeq 0.43$, are too broad to interact with the straining scales [5,6]. H_2 and CH_4 flames have much narrower reaction zones, and CH_4 flames do indeed show localized extinction. Alkyl consumption of radicals may, however, provide a chemical (non-aerodynamic) explanation for extinction in the methane case [6]. Finally, higher strain rates were not attainable with pilot-flame stabilization, suggesting a need for bluff-body stabilization.

Work in the last year has proceeded from this background.

PROGRESS IN THE PAST YEAR. I: MODELING

Should turbulent flames be viewed as ensembles of strained laminar "flamelets" [5] or as broader "distributed zones" [6] of reacting species? The answer is not unique even in a given flame. To illustrate the range of interactions, chemical and fluid-mechanical scales have been compared for two types of air-breathing combustors. Diffusion flames have no intrinsic length scale, so time scales are used to compare mixing and chemistry. The physical picture to bear in mind is whether, at an interface between dissimilar reactants, turbulent straining occurs rapidly or slowly relative to the rates of important reactions.

Selected characteristic kinetic times were obtained from stirred reactor calculations, under conditions of (i) 0.1 atm. H_2-air combustion, 1 ms residence time, H_2 at 1100K, air at 800 K, equivalence ratio ϕ = 0.8, and (ii) 10 atm. CH_4-air combustion, 10 ms residence time, CH_4 at 300K, air at 610 K, and ϕ = 0.7, a stoichiometry representative of low-NO_x "head-end" conditions. The two cases approximate a hypothetical supersonic combustion ramjet ("scramjet") in the mid-Mach number range (10-15) and a methane-fueled gas turbine combustor, respectively, closely enough for the present purpose of extracting kinetic time scales.

The kinetic scheme, adopted from Reference 7, contains 25 species and 100 reactions for methane oxidation excluding C_2-chemistry. The "thermal" and "prompt" (alkyl species-plus-nitrogen) NO_x mechanisms are also

included because pollutant chemistry introduces additional time scales. Concentrations, density and temperature from each of the stirred reactor solutions were used to estimate characteristic times of the ten reactions selected in Table I. Characteristic chemical time scales are estimated as $\tau_c = 1./(k_f[X])$ where k_f is the reaction rate and [X] is the concentration of the more abundant reactant, with an additional concentration factor for three-body reactions. Time scales for selected reactions are shown in Table I.

Turbulence scales are estimated as follows. The integral time scale is given by $\tau_I = \lambda_I/u'$ where u' is the r.m.s. velocity fluctuation and λ_I is the integral length-scale. From the kinematic viscosity ν and the dissipation rate $\varepsilon = u'^3/\lambda_I$, the Kolmogorov time scale τ_K follows as $\tau_K = (\nu/\varepsilon)^{1/2}$. The relevance of the Kolmogorov time scale is worth attention. τ_K characterizes the intense turbulent straining associated with the smallest scales. Since the pdf for scalar dissipation is log-normally distributed, this (τ_K) process is highly intermittent and is experienced by only a small part of the flow at any given instant.

These estimates are applied to the two cases described above, with the following assumptions: (i) in the supersonic combustor, the mean axial velocity $<u>$ = 3000 m/s, u' = 300 m/s, λ_I = 0.002 m.; the latter follows from PLIF (planar laser-induced fluorescence) flow visualization of the mixing of jets injected behind a realistically-sized step into a supersonic crossflow [8] and (ii) the mean velocity $<u>$ = 100 m/s, u' = 10 m/s, λ_I = 0.005 m., being typical conditions in a turbine combustor. Turbulence time scales are shown in Table II.

Numerical values in Tables I and II may be used to compute the turbulent Damkohler numbers τ_I/τ_c and τ_K/τ_c, the latter also being an inverse Karlovitz number, and so to compare the turbulence and chemical scales:

(i) Scramjet: Due to the long chemical time scales (caused by the low static pressures), the reactions are slow relative to both the integral and Kolmogorov scales. The exceptions are the two-body oxyhydrogen reactions which are comparable to the integral scale. The recombination reaction time scales are comparable to the residence time, which is why there is a combustion efficiency issue in such devices. The ordering of time scales implies that partial equilibrium in the radical pool can be a useful simplifying assumption. In any event, it is unlikely that the flamelet model would be applicable. Flame broadening by finite-rate chemistry would destroy the laminar flamelet topology.

(ii) Turbine combustor: Here the oxyhydrogen shuffle reactions are fast compared with the turbulence, except for $O + H_2$, which is comparable to the Kolmogorov scale. Due to the higher density, the recombination reactions have sped up and are in between the two turbulence scales. The thermal NO_x and $CH_2 + N_2$ reactions are slow relative to both turbulence scales, but $CH + N_2$ is fast. Time scales for the $CH_4 + M$ and the $CO + OH$ reactions are comparable to the integral and Kolmogorov scales, respectively.

It is apparent that while some combustion reactions fall in the flamelet regime and some in the distributed regime, many important reactions fall in between. Turbulence-chemistry interactions occur in a greater variety of modes than accounted for by modern combustion theory. The simultaneous prediction of kinetically sensitive phenomena such as pollutants, flame stability and combustion efficiency, will require a new approach.

PROGRESS IN THE PAST YEAR. II: EXPERIMENTS

Since the turbulence in a pilot-stabilized non-premixed turbulent CO/H_2 jet flame was not intense enough to cause local extinction, axisymmetric bluff-body stabilization has been experimented with in the past year. Typical conditions and a schematic of the burner in the tunnel are shown in Figure 1. The joint Rayleigh-Raman diagnostic system is similar to that described previously [4]. A flashlamp-pumped dye laser, which provides pulses of ~ 1J in ~ 2 μs within a 0.2 nm bandpass at 488.0 nm at 1 Hz, is used to excite the scattering processes. Light from the 0.2 x 0.2 x 0.6 mm^3 scattering volume is collected by two lenses, separated in frequency by a 3/4 m polychromator and detected by eight photomultiplier tubes. Laser velocimetry is being used to measure the axial velocity. Raman data have been taken at x/d_{jet} = 1, 5, 10, 20, 40 and along the centerline for the 70% H_2/ 30% N_2 flame. A typical scattergram of data from all radial locations at x/d_{jet} = 5 is shown in Figure 2. Figure 3 presents the radial profile of the conventionally-averaged mean temperature at x/d_{jet} = 5. CH_4 flames will be measured next; required modifications to the Raman system are under way. Scattergrams of temperature versus mixture fraction, as well as other data, will be analyzed for turbulence-chemistry interactions. This will guide the formulation of new models.

REFERENCES

[1] Pope, S.B. and Correa, S.M., Twenty-first (International) Symposium on Combustion, The Combustion Institute, Pittsburgh, PA, p. 1341, 1986.

[2] Correa, S.M., Gulati, A. and Pope, S.B., Combust. Flame, 72, p. 159, 1988.

[3] Gulati, A. and Correa, S.M., AIAA Paper 87-1717, 21st Joint Propulsion Conference, San Diego, CA, 1987.

[4] Correa, S.M., and Gulati, A., Twenty-second Symposium (International) on Combustion, The Combustion Institute, Pittsburgh, PA, p. 599, 1988.

[5] Peters, N., "Laminar Flamelet Concepts in Turbulent Combustion," Twenty-First (International) Symposium on Combustion, The Combustion Institute, Pittsburgh, PA, p. 1231, 1987.

[6] Bilger, R.W., "The Structure of Turbulent Nonpremixed Flames," Twenty-Second (International) Symposium on Combustion, The Combustion Institute, Pittsburgh, PA, p. 475, 1988.

[7] Glarborg, P., Miller, J.A. and Kee, R.J., "Kinetic Modeling and Sensitivity Analysis of Nitrogen Oxide Formation in Well-Stirred Reactors," Comb. Flame, 65, p. 177, 1986.

[8] Correa, S.M., Warren, R.E., Gulati, A., Haller, F., and Kaiser, W.O., "Supersonic Sudden-Expansion Flow with Fluid Injection: an Experimental and Computational Study," Paper AIAA 89-0389, 1989.

Table I: Characteristic Time Scales of Selected Reactions in Two Combustors.

	Reactions	0.1 atm H_2 scramjet (τ_c, s.)	10 atm CH_4 combustor (τ_c, s.)
1.	$H + O_2 = OH + O$	3.49×10^{-5}	1.67×10^{-7}
2.	$O + H_2 = OH + H$	2.64×10^{-5}	1.81×10^{-5}
3.	$H + OH + M = H_2O + M$	1.59×10^{-3}	7.20×10^{-5}
4.	$N_2 + O = NO + N$	9.45×10^{4}	3.92×10^{-2}
5.	$CH_4 + M = CH_3 + H + M$	___	4.68×10^{-4}
6.	$CH_4 + OH = CH_3 + H_2O$	___	2.48×10^{-7}
7.	$CH_3 + OH = CH2 + H_2O$	___	1.85×10^{-6}
8.	$CO + OH = CO_2 + H$	___	2.22×10^{-5}
9.	$CH + N_2 = HCN + N$	___	3.43×10^{-6}
10.	$CH_2 + N_2 = HCN + NH$	___	0.20

Table II: Characteristic Turbulence Time Scales.

	u´ (m/s)	λ_I (m)	τ_I (s)	ϵ (m^2/s^3)	τ_K (s)
Scramjet combustor	300	0.002	6.67×10^{-6}	1.35×10^{10}	6.01×10^{-7}
Turbine combustor	10	0.005	5.0×10^{-4}	2.0×10^{5}	1.81×10^{-5}

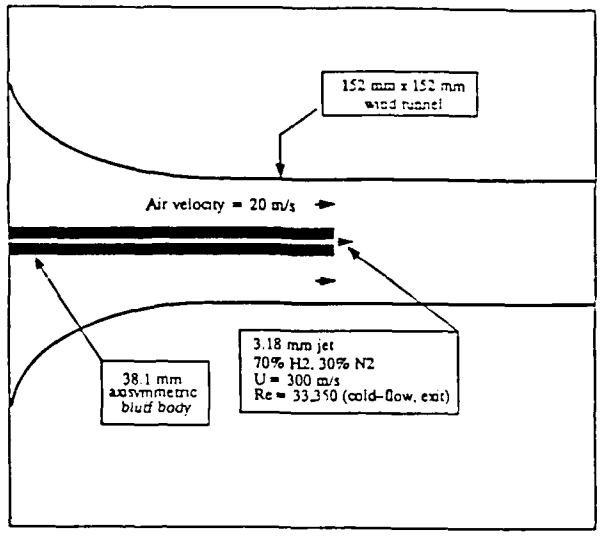

Figure 1. Schematic of bluff body combustor in tunnel (not to scale). Raman data at x/d_{jet} = 1, 5, 10, 20, 40 and along centerline.

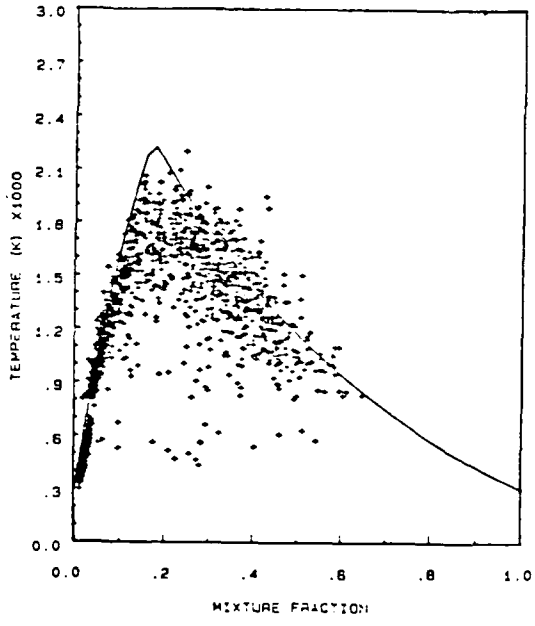

Figure 2. Raman temperature-mixture fraction scattergram at x/d_{jet} = 5.

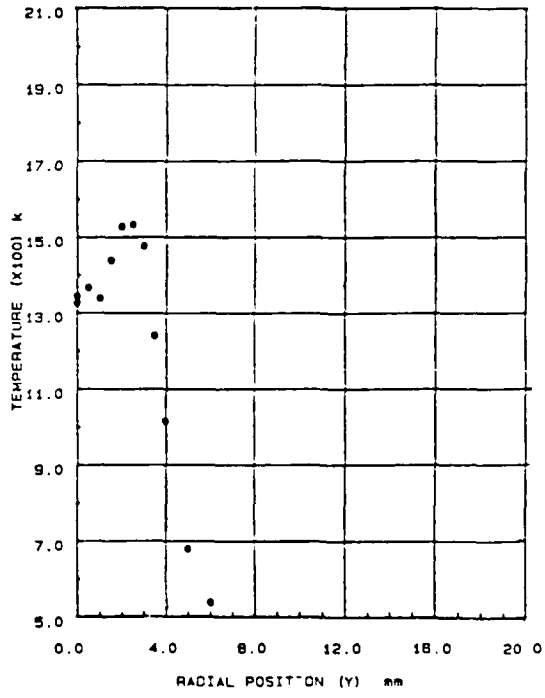

Figure 3. Mean temperature at x/d_{jet} = 5, from Raman data.

HIGH RESOLUTION MEASUREMENTS of STRAINED DIFFUSION LAYER STRUCTURE and EXTINCTION in TURBULENT FLOWS

AFOSR Grant No. 89-0541

Werner J.A. Dahm

Gas Dynamics Laboratories
Department of Aerospace Engineering
The University of Michigan
Ann Arbor, MI 48109-2140

Summary/Overview

The objective of this research is to experimentally study the fine scale structure within which the actual molecular mixing occurs in turbulent shear flows. Measurements of the local instantaneous molecular mixing rate field in turbulent flows have in the past been difficult to obtain due in part to *(i)* the necessity of resolving the finest molecular diffusion scales in the flow, and *(ii)* the need for simultaneously determining all three components of the scalar gradient field. Here we experimentally acquire fully resolved three- and four-dimensional laser induced fluorescence imaging measurements of the conserved scalar field $\zeta(\mathbf{x},t)$, with spatial and temporal resolution reaching the local strain-limited molecular diffusion scale of the flow, from which the corresponding molecular mixing rate field $(ReSc)^{-1}\nabla\zeta\cdot\nabla\zeta(\mathbf{x},t)$ can be determined. The resulting data volumes are numerically analyzed to directly determine details of the underlying fine scale structure associated with the molecular mixing process. A further element of this research relates this fine structure to the chemical reaction and local extinction processes in turbulent reacting flows. The combined results are aimed at developing a physically correct understanding for the fine scale structure of the molecular mixing and chemical reaction processes in turbulent reacting flows.

Technical Discussion

An understanding of the processes by which molecular mixing and chemical reactions occur in turbulent shear flows is central to the development of techniques for enhancing the rates of mixing and combustion in advanced airbreathing propulsion systems, and to the development of new theoretical and computational methods for assessing the complex phenomena at work in turbulent reacting flows. When the molecular mixing process is formulated in terms of a conserved scalar field $\zeta(\mathbf{x},t)$, the associated scalar energy dissipation rate per unit mass $(ReSc)^{-1}\nabla\zeta\cdot\nabla\zeta(\mathbf{x},t)$ gives the local instantaneous rate of molecular mixing throughout the flow. Here we experimentally obtain this molecular mixing rate field by measuring the conserved scalar field with sufficiently high resolution and signal quality to allow direct differentiation of the data to determine the scalar gradient field $\nabla\zeta(\mathbf{x},t)$ and the corresponding scalar dissipation rate field.

The experimental technique builds on our earlier work[1-3] in obtaining fully resolved three-dimensional spatio-temporal data volumes of the $Sc \gg 1$ scalar field in turbulent flows. In these earlier results, the molecular mixing rate was determined from the in-plane projection of the true scalar gradient vector field. The assumption of isotropy could then be combined with such measurements to reconstruct various statistical measures of the three-dimensional scalar gradient field[2-4]. The present study, however, involves fully four-dimensional measurements from which the true scalar gradient field and its temporal evolution can be directly determined to yield previously unobtainable details of the fine structure of mixing.

During the past year, the diagnostic technique has been developed for experimentally obtaining fully-resolved four-dimensional measurements of the conserved scalar field based on direct imaging of laser induced fluorescence in turbulent shear flows, and a first set of measurements has been obtained. As shown in Figure 1, each such four-dimensional spatio-temporal data space consists of a temporal succession of up to 256 three-dimensional spatial data volumes, each comprised of a succession of up to 256 two-dimensional spatial data planes, each of which consists of 256 × 256 individual data points. The experiment is designed so that the spatial separations Δx_1 and Δx_2 between adjacent pixels within each spatial data plane are considerably smaller than the local strain-limited molecular diffusion scale[5-8] of the scalar field. Though the laser beam thickness is generally larger than the spatial separation Δx_3 between successive parallel data planes, the resulting overlap between adjacent spatial planes allows a deconvolution, as shown in Figure 2, to yield an effective x_3-resolution controlled by the sweep separation Δx_3 which also resolves the local molecular diffusion scale of the flow. Similarly, the temporal separation between successive spatial data planes, Δt, and between successive spatial data volumes, ΔT, are smaller than the local strain-limited diffusion scale passage time. These resolution requirements place an upper limit on the Reynolds number (typically around 6,000) at which such fully-resolved four-dimensional measurements can currently be obtained. The resulting conserved scalar data are then simultaneously differentiable in all three spatial dimensions and in time, allowing detailed numerical analyses of the molecular mixing process.

As Figure 3 indicates, in order to meet these resolution requirements the present measurements are obtained in the fully-developed self-similar far field ($x/d^* = 230$) of an axisymmetric non-coflowing turbulent jet at Reynolds numbers based on δ and u, denoting the length and velocity scales characterizing the shear at that stage in the flow, ranging from 3,000 – 6,000. However, because as indicated the region in the flow which these measurements span is much smaller than the local flow width δ (typically $^1/_{20}\delta$), when scaled by the local outer variables $\delta(x)$, $u(x)$ and $\zeta(x)$ of the flow, the molecular mixing process within this four-dimensional data space should be largely generic to mixing in turbulent shear flows in general, and not just specific to this one particular flow. Results obtained to date support this conjecture.

Briefly, the diagnostic technique[9] is based on fully-resolved high-speed acquisition of successive 256 × 256 planar imaging of the laser induced fluorescence from a conserved scalar in the turbulent flow. Key elements of this imaging and data acquisition system are shown in Figure 3. A collimated laser beam is swept by a pair of very low inertia galvanometric mirror scanners, whose timing is slaved to the imaging array, in a raster pattern through the scalar field. The fluorescence from each sweep of the laser beam is imaged onto a photodiode array, driven by an externally generated clock producing variable pixel data rates up to 11 MHz, corresponding to continuous acquisition of up to 142 such spatial data planes per second. The fluorescence data from the array is then serially acquired through a programmable digital port interface, digitized to 8-bits digital resolution, and then ported into a 16 MB high-speed dual-ported data buffer from which it is continuously written to a 3.1 GB high-speed parallel transfer disk rank. The system can achieve a sustained overall data throughput rate to the disks, excluding all line and frame overhead cycles, of up to 9.3 MB/sec.

These data are currently being analyzed to discern the extent to which the true fine scale structure differs from that inferred from earlier lower-dimensional measurements. Results[10] show that essentially all of the molecular mixing appears to take place in relatively well-defined thin strained laminar diffusion layers. Thickness distributions and the internal structure of these layers are quantities of particular interest that are being determined from these data, and are being interpreted in the context of recent theoretical and numerical efforts[11-13] for modeling the fine scale mixing and reaction processes and their connection with the larger scales of the flow.

References

1. Dahm, W.J.A. & Buch, K.A. (1989) High-resolution three-dimensional spatio-temporal measurements of the conserved scalar field in turbulent shear flows. *Proc. 7th Symp. on Turbulent Shear Flows* v.1, pp.14.1.1-14.1.6; to appear in *Turbulent Shear Flows 7*, Springer Verlag (1990).

2. Dahm, W.J.A. & Buch, K.A. (1990) Fine scale structure of conserved scalar mixing in turbulent shear flows. Part I : Sc » 1. To be submitted to *Journal of Fluid Mechanics*.

3. Dahm, W.J.A. & Buch, K.A. (1990) Fine scale structure of conserved scalar mixing in turbulent shear flows. Part II : Sc ≈ 1. To be submitted to *Journal of Fluid Mechanics*.

4. Dahm, W.J.A. & Buch, K.A. (1989) Lognormality of the scalar dissipation pdf in turbulent flows. *Phys. Fluids A* **1** (7), 1290-1293.

5. Burgers, J.M. (1948) A mathematical model illustrating the theory of turbulence. *Adv. Appl. Mech.* **1**, 171-199.

6. Carrier, G.F., Fendell, F.E., & Marble, F.E. (1975) The effect of strain rate on diffusion flames. *SIAM J Appl. Math.* **28** (2), 463-500.

7. Corcos, G.M. & Sherman, F.S. (1976) Vorticity concentrations and the dynamics of unstable free shear layers. *J. Fluid Mech.* **73**, 241-264.

8. Corcos, G.M. & Sherman, F.S. (1984) The mixing layer: deterministic models of turbulent flow. Part 1. Introduction and the two-dimensional flow. *J. Fluid Mech.* **139**, 29-65.

9. Dahm, W.J.A., Southerland, K.B. & Buch, K.A. (1990) Four-dimensional laser induced fluorescence measurements of conserved scalar mixing in turbulent flows. To be presented at the *5th International Symposium on Application of Laser Techniques to Fluid Mechanics*, Lisbon, Portugal.

10. Dahm, W.J.A., Southerland, K.B. & Buch, K.A. (1990) Direct, high resolution, four-dimensional measurements of Sc » 1 molecular mixing in turbulent flows. To be presented at the *IUTAM Symposium on Fluid Mechanics of Stirring and Mixing*, La Jolla, CA.

11. Tryggvason, G. & Dahm, W.J.A. (1989) An integral method for mixing, chemical reactions, and extinction in unsteady strained diffusion layers. Submitted to *Combustion & Flame*.

12. Broadwell, J.E. (1987) A model of reactions in turbulent jets: Effects of Reynolds, Schmidt and Damköhler numbers. *Proc. US-France Joint Workshop on Turbulent Reactive Flows*, Rouen, France.

13. Broadwell, J.E. & Mungal, M.G. (1988) Molecular mixing and chemical reactions in turbulent shear layers. *Proc. 22nd Intl. Symp. on Comb.*, 579-587, The Combustion Institute.

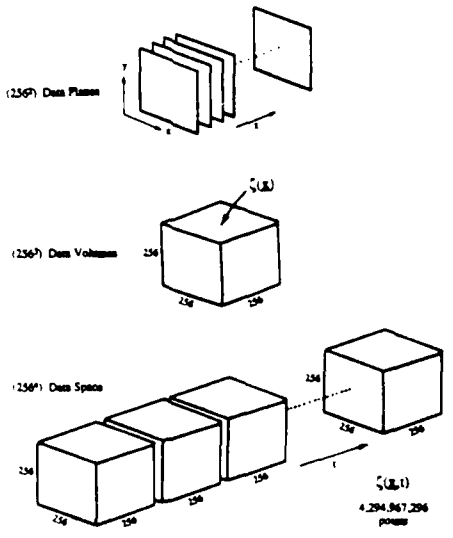

Fig. 1. Structure of the four-dimensional conserved scalar data space $\zeta(\mathbf{x},t)$ as a temporal sequence of up to 256 successive spatial data volumes, each consisting of a temporal sequence of up to 256 successive spatial data planes, each of which consists of 256 × 256 spatial data points. The resolution is sufficient to allow differentiation in all four directions, allowing the detailed fine scale structure of the molecular mixing rate field $(ReSc)^{-1}\nabla\zeta\cdot\nabla\zeta(\mathbf{x},t)$ to be directly determined.

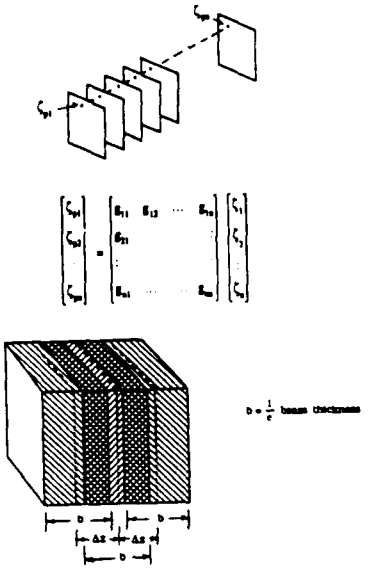

Fig. 2. Deconvolution between successive parallel spatial data planes to reduce the laser beam thickness resolution limitation, producing an effective x_3-resolution comparable to the planar separation distance.

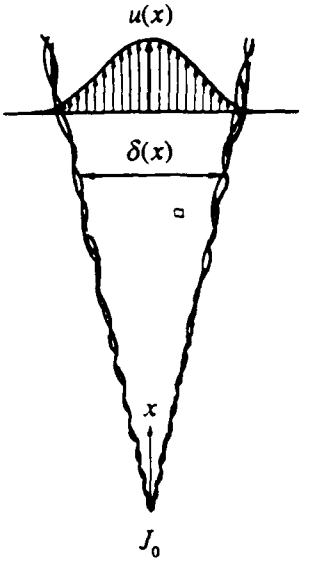

Fig. 3. Measurements are obtained in the fully-developed self-similar far field of an axisymmetric turbulent jet at $Re = 3000 - 6000$. The box shows the approximate size and location of the imaging region in the flow.

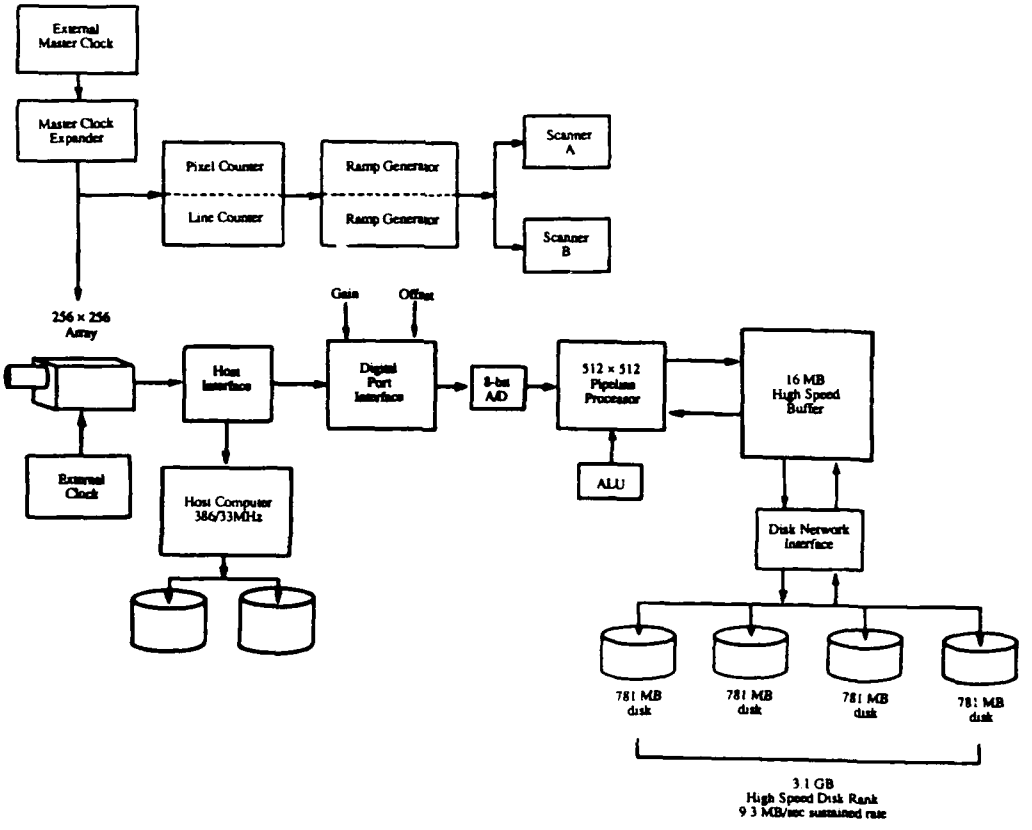

Fig. 4. Key elements of the imaging and data acquisition system assembled for these four-dimensional measurements. Two beam scanners slaved to the imaging array timing rapidly sweep the laser beam through the scalar field. The data acquisition system can sustain an overall data throughput rate to disk of up to 9.3 MB/sec for the full 3.1 GB disk capacity.

CHEMICAL REACTIONS in TURBULENT MIXING FLOWS

AFOSR Grant 88-0155

P. E. Dimotakis, J. E. Broadwell and A. Leonard

Graduate Aeronautical Laboratories
California Institute of Technology
Pasadena, California 91125

Summary/Overview

The purpose of this research is to conduct fundamental investigations of turbulent mixing, chemical reaction and combustion processes in turbulent, subsonic and supersonic flows. Our program is comprised of an experimental effort, an analytical modeling effort, a computational effort, and a diagnostics development and data-acquisition effort, the latter as dictated by specific needs of our experiments. Our approach is to carry out a series of detailed theoretical and experimental studies primarily in two, well-defined, fundamentally important flow fields: free shear layers and axisymmetric jets. The investigations of turbulent jet mixing are co-sponsored by the Gas Research Institute. To elucidate molecular transport effects, experiments and theory concern themselves with both liquids and gases. The computational studies are, at present, focused at fundamental issues pertaining to the computational simulation of both compressible and incompressible flows.

Technical discussion

Preliminary, non-reacting experiments are currently in progress in the new GALCIT Supersonic Shear Layer Combustion Facility. In these experiments, the flow is a 2-D, compressible mixing layer, with either N_2 or He in the high speed stream and N_2 in the low speed stream. The free stream Mach numbers are $M_1 = 1.5$ and $M_2 = 0.3$ respectively. Some of the preliminary results are discussed below with the aid of three side-view Schlieren photographs.

Figure 1 shows the basic form of the N_2/N_2 shear layer with negligible streamwise pressure gradient ($dp/dx \approx 0$). The shear layer forms a well-defined, linearly growing wedge that appears devoid of the coherent structures visible in incompressible shear layers. Similar observations were recently reported by Clemens *et al.* (1990). Two standing waves are clearly visible in the supersonic stream. One originates from a small surface bump at the nozzle/top guidewall junction, while the second comes from the splitter tip. Both waves have little apparent effect on the shear layer and gradually disappear downstream.

Figure 2 shows a N_2/N_2 shear layer in which the supersonic stream has been overexpanded, resulting in a strong oblique shock wave at the splitter tip. This wave, and its reflections, causes considerable deflection of the shear layer. It is noteworthy, however, that the growth rate is basically unchanged from that of the unperturbed flow (*cf.* Fig. 1).

The third photograph (Fig. 3) is representative of the He/N_2 shear layers. Immediately obvious is the complex, yet regular, wave system in the low speed flow. This represents a system of travelling oblique shocks and expansion waves, probably created by (unseen) shear layer turbulent structures that appear large and convect at speeds that are supersonic with respect to the low speed flow. The convective Mach number with respect to the low speed stream, of these structures, as inferred from the angles of their associated waves, lies in the range of $1.9 \leq M_{c2} \leq 2.2$. This can be compared to a value of $M_{c2} \approx 1.0$ based upon the standard shock-free models of the convection velocity (*cf.* Papamoschou & Roshko 1988, Papamoschou 1989, Dimotakis 1989). These traveling waves are reminiscent of those seen in supersonic jet flows, (*e.g.* Tam 1971) in which the waves originate from the supersonic shear layer in the vicinity of the jet exit. It should also be noted that the existence of these waves on only one side of the shear layer creates large asymmetries in the flow entrainment, with most of the growth occurring into the low speed side, and with M_{c1} in the low *subsonic* range ($M_{c1} \simeq 0.3$).

In support of the supersonic shear layer experiments, we have also been conducting linear stability analyses of compressible shear layers. During this last year, we have investigated the effect of upper/lower guidewalls on the stability of the flow. As had also been suggested by Tam & Hu (1989), we found (Zhuang *et al.* 1990) that bounded shear layers are more unstable at high Mach numbers compared to unbounded shear layers, and that two-dimensional disturbances have greater amplification rates than the oblique waves that are found to be the more unstable in unbounded flow.

We are proceeding with our experimental investigation of Reynolds number effects in the High Pressure Combustion Facility ($0.1 < p_0 < 10\,atm$). Specifically, a set of experiments is in progress which utilizes the F_2/NO chemical system, permitting very low adiabatic flame temperature rise ($\Delta T_f < 40\,K$) to be realized, to mitigate buoyancy effects, while allowing the turbulent flow/chemical processes to operate in the fast chemical kinetic rate regime. While these first experiments, which were conducted with $\Delta T_f \approx 26\,K$, in the Reynolds number range of $5{,}000 \leq Re \leq 100{,}000$, and a pressure range of $1 \leq p_0 \leq 5\,atm$, must be regarded as preliminary, they suggest a molecular mixing rate that increases with increasing Reynolds number, with a flame length that correspondingly decreases with increasing jet Reynolds number.

We are continuing our investigations of the fine scale turbulent structure in a liquid phase (high Schmidt number, Sc) axisymmetric jet. Conserved scalar measurements have been made in the range of Reynolds numbers from 3,000 to 24,000, both on the centerline and at several radial locations. A study has been conducted to examine the applicability of a (power-law) fractal description to the geometry of the iso-scalar surfaces in the jet, *e.g.* as suggested in Sreenivasan & Meneveau (1986). In contrast, we find that these surfaces *are not* characterized by a constant fractal dimension, and present a log-normal model of interface spacings that displays similar behavior to the experimental results. In addition, we find that this behavior persists throughout the entire range of scalar values. These results (Miller & Dimotakis 1989) were reported last summer at the *ASME Fluids Engineering Conference* (La Jolla, 10–12 July 1989). A more complete account of this work has been submitted for publication in the *Physics of Fluids*. Work currently in progress is aimed at extending the Reynolds number range that can be covered in our experiments to $Re \approx 100{,}000$. These studies are also intended to focus on the dependence of the scalar dissipation

(mixing rate) on Reynolds number, at these very high Schmidt numbers, and complement the gas-phase chemically reacting studies described above.

In other work, a major modeling effort supported in part by the present contract has been the development of a model for chemical reactions in a turbulent fuel jet that is based upon the ideas first put forward by Broadwell & Breidenthal (1982) for the shear layer. A refinement and clarification of these ideas is described in Broadwell & Mungal (1988) in which again the application is to reactions in a shear layer, in particular, to the $H_2/F_2/NO$ reaction studied experimentally by Mungal & Dimotakis (1984) and Mungal & Frieler (1988). The initial steps in the formulation of the jet model were put forth in Broadwell (1987). In collaboration with personnel of the Sandia National Laboratories, the picture of molecules mixing and chemical reaction is being put in the form of a numerical model. As an interim measure, a simpler version of the model in which the strained flame reactions are also assumed to be described by a perfectly-stirred reactor, has been formulated and applied to hydrogen and propane flames burning in air.

References

BROADWELL, J. E. [1987] "A Model for Reactions in Turbulent Jets: Effects of Reynolds, Schmidt, and Damköhler Numbers", US-France Workshop on Turbulent Reactive Flows (Rouen, France), 7–10 July 1987. Published: *Turbulent Reactive Flows*, (eds.) R. Borghi and S. N. B. Murthy *Lecture Notes in Engineering* **40** (Springer-Verlag, New York, 1989), 257–277.

BROADWELL, J. E. and BREIDENTHAL, R. E. [1982] "A Simple Model of Mixing and Chemical Reaction in a Turbulent Shear Layer", *J. Fluid Mech.* **125**, 397–410.

BROADWELL, J. E. and MUNGAL, M. G. [1988] "Molecular Mixing and Chemical Reactions in Turbulent Shear Layers", *22nd Symposium (International) on Combustion* (The Combustion Institute), 579–587.

CLEMENS, N. T., MUNGAL, M. G., BERGER, T. E. and VANDSBURGER, U. [1990] "Visualizations of the structure of the turbulent mixing layer under compressible conditions", 28^{th} *AIAA Aerospace Sciences Meeting*, 8–11 January 1989 (Reno, Nevada), Paper AIAA-90–0500.

DIMOTAKIS, P. E. [1989] "Turbulent Free Shear Layer Mixing and Combustion", 9^{th} ISABE (Athens, Greece), 3–9 September 1989.

MILLER, P. L. and DIMOTAKIS, P. E. [1989] "Stochastic Geometric Properties of Scalar Interfaces", *ASME Fluids Engineering Conference* (La Jolla, California), 10–12 July 1989, session on *Fractal Structures*. Submitted for publication in The *Phys. Fluids* .

MUNGAL, M. G. and DIMOTAKIS, P. E. [1984] "Mixing and combustion with low heat release in a turbulent mixing layer", *J. Fluid Mech.* **148**, 349-382.

MUNGAL, M. G. and FRIELER, C. E. [1988] "The Effects of Damköhler Number in a Turbulent Shear Layer", *Comb. & Flame* **71**, 23–34.

PAPAMOSCHOU, D. [1989] "Structure of the compressible turbulent shear layer", 27th *AIAA Aerospace Sciences Meeting*, 9–12 January 1989 (Reno, Nevada), AIAA Paper 89–0126.

PAPAMOSCHOU, D. and ROSHKO, A. [1988] "The Compressible Turbulent Shear Layer: An Experimental Study", *J. Fluid Mech.* **197**, 453–477.

SREENIVASAN, K. R. and MENEVEAU, C. [1986] "The Fractal Facets of Turbulence", *J. Fluid Mech.* **173**, 357–386.

TAM, C. K. W. [1971] "Directional acoustic radiation from a supersonic jet", *J. Fluid Mech.* **46**(4), 757–768.

TAM, C. K. W. and HU, F. Q. [1989] "The instability and acoustic wave modes of supersonic mixing layers inside a rectangular channel", *J. Fluid Mech.* **203**, 51–76.

ZHUANG, M., DIMOTAKIS, P. E. and KUBOTA, T. [1990] "The Effect of Walls on a Spatially Growing Supersonic Shear Layer", *Phys. Fluids* A **2**(4), 599–604.

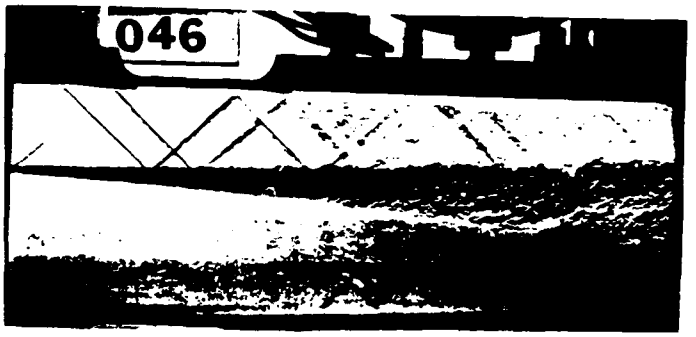

1

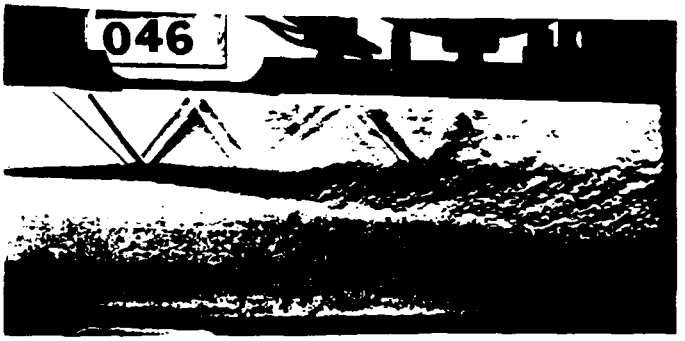

2

3

VORTEX SIMULATION OF TURBULENT COMBUSTION

(AFOSR Grant No. 89-0491)

Principal Investigator Ahmed F. Ghoniem

Department of Mechanical Engineering
Massachusetts Institute of Technology
Cambridge, MA 02139

SUMMARY/OVERVIEW

The objectives of this research are the development of accurate numerical methods for the simulation of the Navier-Stokes equations for chemically reacting flow at high Reynolds number and arbitrary Damkohler number, and the application of these methods to investigate the mechanisms of flow-combustion interactions. Lagrangian, grid-free methods are used to transport the vorticity and scalar gradient along particle trajectories, yielding adaptive solutions which are devoid of numerical diffusion. The focus of the work during the previous year was on extending the solution of the low-Mach-number compressible shear layer to spatially developing reacting flow and three-dimensional flow.

TECHNICAL REPORT

Solutions of the reacting compressible shear layer have been obtained for the premixed and the unpremixed cases [1,2] (incompressible solutions for the spatially developing case have also been obtained and analyzed [3,4]). In both cases, the flow was considered two-dimensional, and the roles of volumetric expansion and vorticity generation due to heat release were investigated in detail. In the premixed shear layer, vorticity generation plays an important role in the rate of growth of the shear layer by imparting a finite velocity on the large eddies in the direction of the heavier, reactant stream. Vorticity generation in the later stages leads to: (1) an asymmertic entrainment with a bias towards the lighter stream; and (2) the formation of a spotty structure with scales smaller than the nominal diameter of the original large structure. Apart from the effect of volumetric expansion due to energy release, the vorticity distribution in a premixed reacting shear layer strongly resembles that of a nonreacting shear layer with the same density ratio across the layer.

This observation was used in the study of the density effect on the structure of a three-dimensional nonreacting shear layer. It was found that while the spanwise vortex core is still driven in the direction of the heavier stream, the streamwise vortex structures appear at the midsections of the spanwise perturbation wavelength. The asymmertic entrainment persists since the strength of the baroclinic vorticity is different across the layer. Locally, however, asymmetric entrainment is enhanced or reversed by the density variation. This effect is currently under further investigation [5].

Including the effect of density variation on the vorticity field in three-dimensional flow prompted the formulation of grid-free schemes to account for vortex stretch by evaluating the velocity gradient using analytical differentiation of the velocity expression. Numerical experiments showed that, while using the transpose of the velocity gradient tensor in the evaluation of the stretch term can lead to an analytically conservative scheme, numerically, the scheme fails to capture the evolution of the streamwise vorticity accurately. Direct integration of the original form of the Navier-Stokes equation using the velocity gradient

tensor produced the most accurate results when the fundamental requirements of accurate vortex simulations were satisfied. Analysis was used to explain this unexpected behavior [6].

In the nonpremixed case, when the density is the same for both streams, baroclinic vorticity generation occurs on both sides of the products zone. Thus, its cumulative effect on the overall dynamics of the large eddies is much less pronounced than in the case of a premixed layer. In the results of the nonpremixed layer, we did not observe any substantial motion of the eddies or effect of vorticity generation on the internal structure of the eddies. This is despite the fact that linear stability analysis of a light fluid layer surrounded by heavier fluid on both sides shows that the growth rate here is less than that in the case when all fluid layers have the same density. The difference between the two cases lies in the fact that in the reacting flow simulation, the layer with lower density forms as vorticity rolls up. This result should be regarded as a warning that conclusions of nonreacting flow models should not be extended to reacting flows without first considering the role of the extra chemical time scale in the later.

In both the premixed and nonpremixed cases, we find that volumetric expansion has a profound effect on the rate of growth of the instability only when the initial perturbation is small. In both cases, if volumetric expansion, associated with the progress of the chemical reaction, proceeds before nonlinear rollup is initiated, vorticity is weakened by getting redistributed over a larger area. Here, as in the discussion of the effect of baroclinic vorticity generation, we emphasize that the ratio between the time scale of the chemical reaction and that of the transition of the instability into the nonlinear range plays a very important role. As exhibited by the numerical results, if the rollup process starts before substantial heat release has occurred, the growth of the large eddy proceeds in much the same way as in the nonreacting case. This conclusion also leaves the results of computations using zero rate chemical kinetic models in doubt since, in this case, thermal ignition delay times are not considered.

The numerical results in both cases were used to demonstrate the role of the large eddies in the development of the combustion process. Here we will review the results of the three dimensional case for the nonpremixed reaction [7]. It was found that, over a wide range of the Damkohler number, the distributions of product concentration and vorticity bear a strong resemblance, independent of that of the rate of reaction. Figure 1 depicts the product concentration and reacting rate on a section through the core normal to the streamwise direction for Damkohler number 0.1 and 10 (notice the complex distribution of product concentration which is consistent with the complex deformation of the spanwise core and the formation of the streamwise vorticity rods). The figure indicates that while the rate of reaction is highest within the cores of the eddies at low Damkohler number, it is highest on the outer edges of the eddies at high Damkohler number. In both cases, however, product concentration is maximum within the eddy cores where vorticity is highest. Similar conclusions can be drawn from figures 2 and 3 where both quantities, product concentration and reaction rate, are shown on a section normal to the spanwise direction at Damkohler number 0.1 and 10. These results suggest that the reaction zone structure approaches a distributed reaction at low Damkohler number and a reaction sheet at high Damkohler number.

REFERENCES

1. Ghoniem, A.F. and Krishnan, A., "Origin and manifestation of flow-combustion interactions in a premixed shear layer," Proceedings of the 22nd Symposium (International) on Combustion, The Combustion Institute, Pittsburgh, PA, 1988, pp. 665-675.

2. Ghoniem, A.F., Knio, O.M., and Krishnan, A., "Lagrangian simulation of the initial stages in a reacting jet," The 23rd Symposium (International) on Combustion, The Combustion Institute, July 1990, Orlean, France.

3. Ghoniem, A.F., and Heidarinejad, G., "Effect of Damkohler number on the reaction zone in a reacting shear layer," Combust. Flame, 1990, in press.
4. Ghoniem, A.F. and Heidarinejad, G., "Numerical study of scalar mixing and product formation in a shear layer," Combust. Sci. Tech., in press 1990.
5. Knio, O.M., and Ghoniem, A.F., "Variable density and asymmetric effects in three-dimensional shear layers," to be sumbitted for publication.
6. Knio, O.M., and Ghoniem, A.F., "Three-dimensional vortex simulation of roll-up and entrainment in a shear layer," J. Comput. Phys., 1990, in press.
7. Knio, O.M. and Ghoniem, A.F. "Three-dimensional vortex simulation of the reacting shear layer," the 28th AIAA Aerospace Sciences Meeting, Reno, NV, 1990, AIAA-90-0150

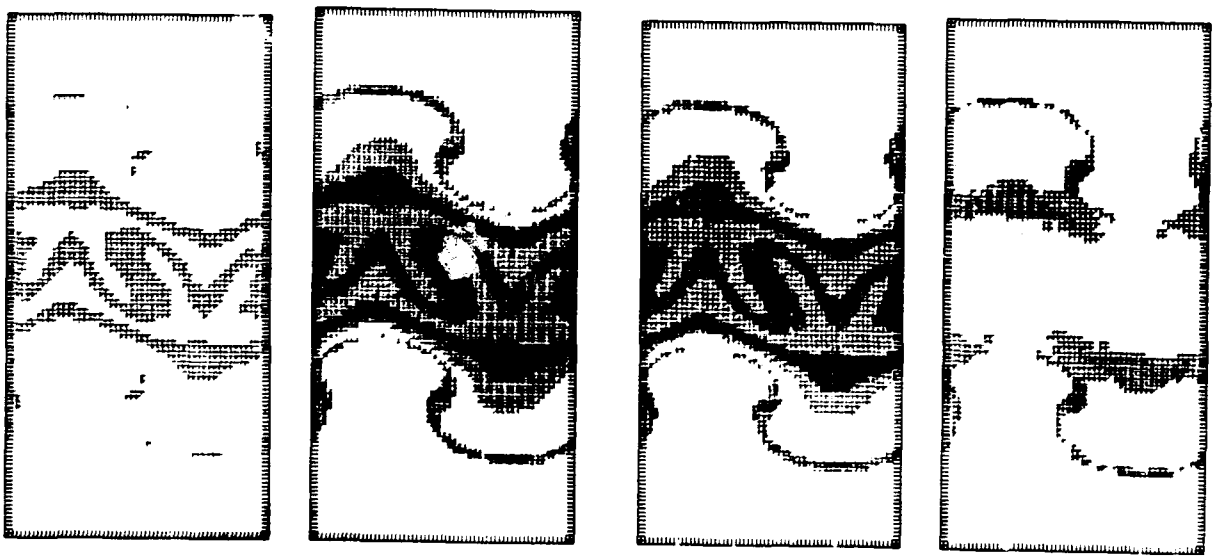

Figure 1. Distributions of product concentration, c, and reaction rate, W, plotted in a two-dimensional section normal to the streamwise direction and intersecting the spanwise core of reacting shear layers at low and high Damkohler numbers, Da = 0.1 and 10. Variables are shown in terms of shades of gray, darker areas corresponding to higher concentrations or reaction rates.

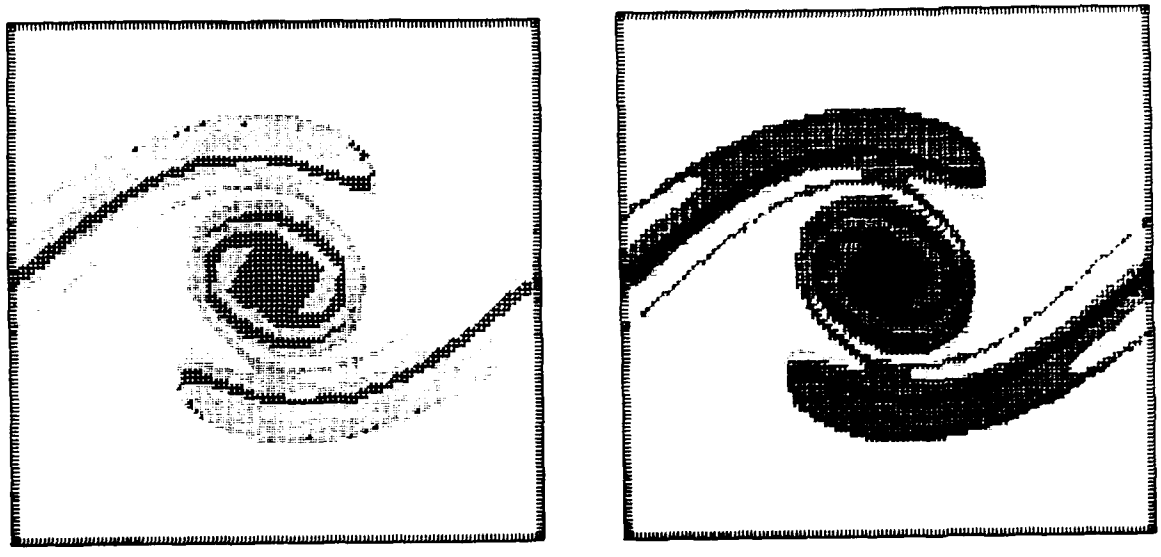

c W

Figure 2. Distributions of product concentration, c, and reaction rate, W, plotted in a two-dimensional section normal to the spanwise direction in a reacting shear layer at low Damkohler number, Da = 0.1.

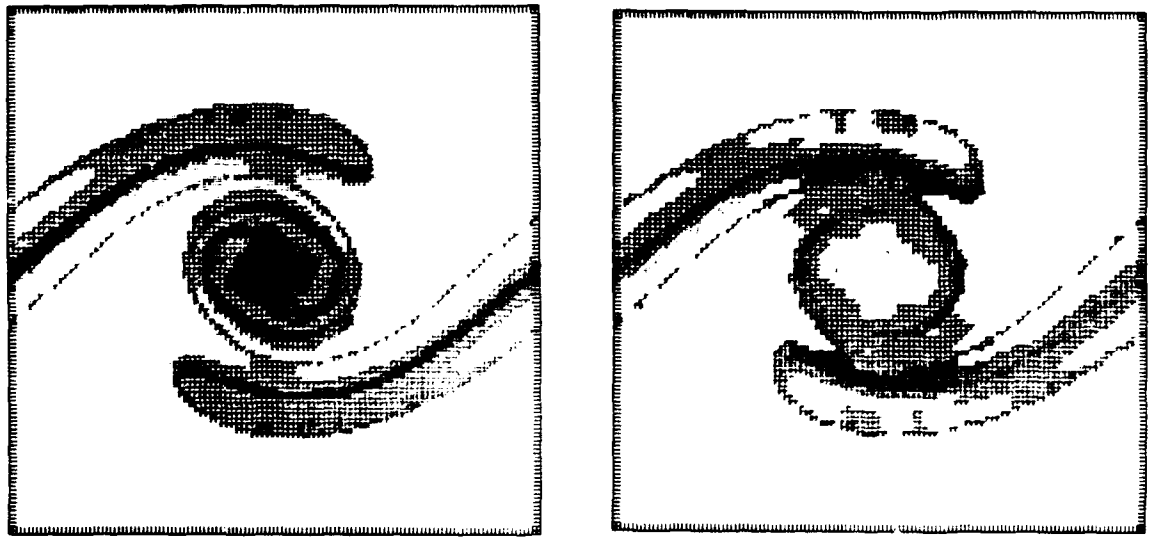

c W

Figure 3. Distributions of product concentration, c, and reaction rate, W, plotted in a two-dimensional section normal to the spanwise direction in a reacting shear layer at high Damkohler number, Da = 10.

CHEMICAL KINETIC AND AERODYNAMIC STRUCTURES OF FLAMES

(AFOSR Grant No. 89-0293)

Principal Investigator: Chung K. Law

Princeton University
Princeton, NJ 08544

SUMMARY/OVERVIEW:

The objective of the present program is to study the structure of laminar premixed and diffusion flames through (a) non-intrusive experimental determination in reduced and elevated pressure environments, (b) computational simulation using detailed flame and kinetic codes, and (c) asymptotic analysis for the reduced mechanisms. During the reporting period we have (1) experimentally and theoretically investigated the effects of dilution, pressure, and flow field on the extinction condition of methane/air/nitrogen diffusion flames; (2) extensively determined the laminar flame speeds of all of the C_2 hydrocarbons, namely ethane, ethylene, and acetylene, compared these values with the numerically calculated ones, and proposed a comprehensive C_2-mechanism; (3) experimentally and computationally studied the propagation of ultra-lean to moderately rich hydrogen flames and identified deficiencies in the low to intermediate temperature hydrogen oxidation kinetics; (4) experimentally studied the relative importance of fuel concentration dilution and flame temperature reduction on soot formation when inert is added to fuel; and (5) experimentally isolated the effects of dilution, temperature, and direct chemical participation when carbon dioxide and oxygen are used as additives.

TECHNICAL DISCUSSION:

1. Effects of Dilution, Pressure and Flow-Field on the Extinction Conditions of Methane-Air-Nitrogen Diffusion Flames

Velocity fields and extinction conditions for methane-air diffusion flames are measures for an opposed-flow nozzle type burner system and calculated by a numerical-integration routine for pressures form 0.25 to 2.5 atm and for dilutions having fixed stoichiometric mixture fractions with oxidizer-stream oxygen mass fractions from 0.233 to 0.190. Imposition of boundary conditions ranging from potential flow to plug flow reveals that changes on the order of a factor of two in the oxidizer-side strain rate at extinction, K_{ext}, can be produced by changes in opposed-flow burner design. It is shown that the maximum velocity gradient, however, which occurs on the fuel side of the main reaction zone, achieves a value at extinction, M_{ext}, that is relatively insensitive to the boundary conditions of the flow. Figure 1 compares the near extinction axial velocity profiles of experiments and of numerical calculations with potential flow and plug-flow boundary conditions of a typical flame. The exploded view illustrates the locations of the velocity gradients, K_{ext} and M_{ext}.

The present results explain differences found by different investigators on influences of dilution on extinction strain rates and show that most counterflow burners are closer to the plug-flow limit than to the potential

flow limit. Strain rates at extinction without dilution are shown to increase with increasing pressure over the above-stated range, contrary to previously observed behaviors with dilution at very high pressures. The behavior is explained as a consequence of decreasing peak radical concentration with increasing pressure.

2. Laminar Flame Speeds and Oxidation Kinetics of C_2-Hydrocarbons

Using the counterflow flame technique, laminar flame speeds of mixtures of ethane, ethylene, acetylene and propane with oxygen and nitrogen have been accurately determined over extensive lean-to-rich fuel concentration ranges and over the pressure range of 0.25 to 3 atm. These data are then compared with the numerically calculated values obtained by using the various kinetic schemes in the literature as well as one compiled in the present study. The present scheme yields close agreement with all of the experimental flame speeds except for diluted, rich acetylene flames, for which the calculated values are higher. Figure 2 compares the measured and calculated flame speeds of ethane, ethylene, and acetylene with air at 1 atmosphere. Close agreement is observed.

The relative importance and influence of the individual reactions on the flame speed and reaction mechanism are assessed and discussed with the aid of sensitivity analysis. The study also demonstrates that C_2 schemes validated through comparisons based on methane flame speeds may not be accurate enough for flame speed predictions of the C_2 fuels, and that the C_2 schemes developed through comparisons with the flame speeds of the C_2 fuels are rather insensitive to the details of the C_3 sub-mechanism. The importance of having accurate values of the thermophysical properties of radicals for flame simulation is also emphasized.

3. Burning Rates of Ultra-Lean to Moderately Rich $H_2/O_2/N_2$ Laminar Flames with Pressure Variations

In this investigation, the laminar flame speeds of $H_2/O_2/N_2$ mixtures have been experimentally determined in the fuel stoichiometric range of ultra-lean to moderately-rich, oxygen concentration range of 7.4 to 30 molar percent of the oxidizer, and pressure range of 0.2 to 2.25 atm. These results are then compared with the numerically-determined values obtained by using several existing H_2/O_2 kinetic schemes. Results show that, while these kinetic schemes accurately predict the propagation speeds of high-temperature flames, they substantially underpredict those of low temperature flames. Figure 3 shows comparisons between experimentally and numerically determined S_u^o for the atmospheric H_2/air mixtures, using a variety of kinetic schemes. The lack of agreement for the ultra lean flames is apparent.

Furthermore, while the experimental pressure exponents of the mass burning rates exhibit a minimum-point, parabola-like behavior with increasing pressure, indicating the initial, negative influence of the H-O_2 termination reaction and the subsequent availability of a positive channel which facilitates radical production, the calculated results fail to show the increasing trend in the pressure range investigated. It is suggested that existing kinetic schemes may require revision in the intermediate-temperature regime strongly influenced by the HO_2 and H_2O_2 chemistry.

4. Soot Formation and Inert Addition in Diffusion Flames

An experimental study has been conducted in coflow diffusion flames in order to identify the relative importance of fuel concentration dilution and

order to identify the relative importance of fuel concentration dilution and flame temperature reduction on soot formation when inert is added to fuel. Two different methodologies were used to isolate dilution and temperature effects, both involving substitution of inerts with different specific heats. To quantify the extent of soot reduction, laser-light extinction as well as smoke point measurements were made.

The results are in agreement with previous studies in counterflow flames and show that soot formation rates in the coflow flame behave nearly linearly with fuel concentration. Furthermore, while temperature exerts a strong influence of soot formation, dilution can also affect formation rates and smoke points when inerts are added to fuels. Figure 4 shows the integrated soot volume fraction as a function of the axial position for a coflow flame. Curve A is for a 100% C_2H_4 in the inner flow, curve B for 50%-C_2H_4/50%-N_2, while curve C also has 50%-C_2H_4/50%-N_2 except part of the N_2 in the oxidizer has been replaced with an equal amount of argon so that its temperature is the same as that of curve A. The closeness of curves B and C clearly demonstrates the importance of concentration dilution.

The study further shows that the relative importance of dilution and temperature depends on the extent of the addition. When moderate amounts of inert are added, the temperature reduction is typically very small so that the effect of dilution can be considerably greater than that of temperature. When large amounts of inert are added, temperature effects may dominate those of dilution although, in an absolute sense, dilution effects could still be important because fuel concentrations are low.

5. <u>The Influence of Carbon Dioxide and Oxygen as Additives on Soot Formation in Diffusion Flames</u>

A study of carbon dioxide and oxygen addition on soot formation has been performed such that the effects of dilution, temperature and direct chemical participation have been isolated for the additives on both the fuel and oxidizer sides. By measuring soot-inception limits in the counterflow flame and integrated soot volume fractions in the coflow flame, the influence of the additives on soot inception, growth and burnout has also been ascertained.

Results demonstrate that carbon dioxide, whether added to the fuel or oxidizer side, can suppress soot formation chemically. Figure 5 shows the systematically isolated effects of dilution, direct chemical, and thermal effects on soot suppression with CO_2 addition to C_2H_4 and C_3H_8.

The effect of oxygen addition is more complex. When added to the fuel side of an ethylene flame, the addition leads to an abrupt increase in the inception limit, indicating that the inception chemistry has been accelerated. The addition of propane, however, is initially suppressive and results in a significant reduction in the soot inception limit which is more than can be accounted for by dilution. The addition becomes promoting as the oxygen mole fraction approaches 40%. Finally, the effect of oxygen concentration on the oxidizer side, for both ethylene and propane flames, is almost totally thermal.

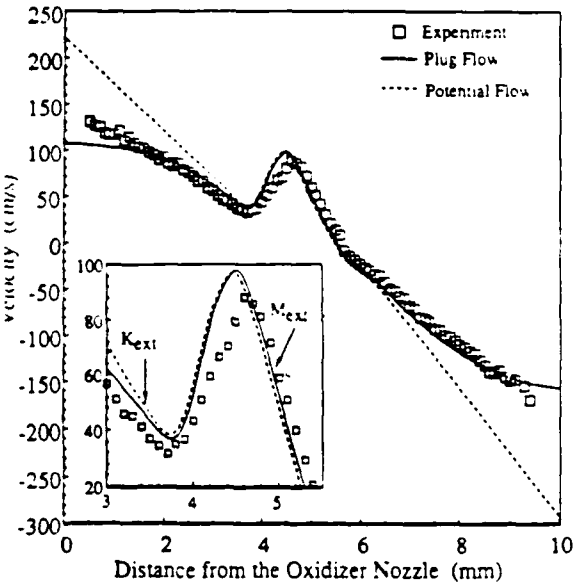

Figure 1

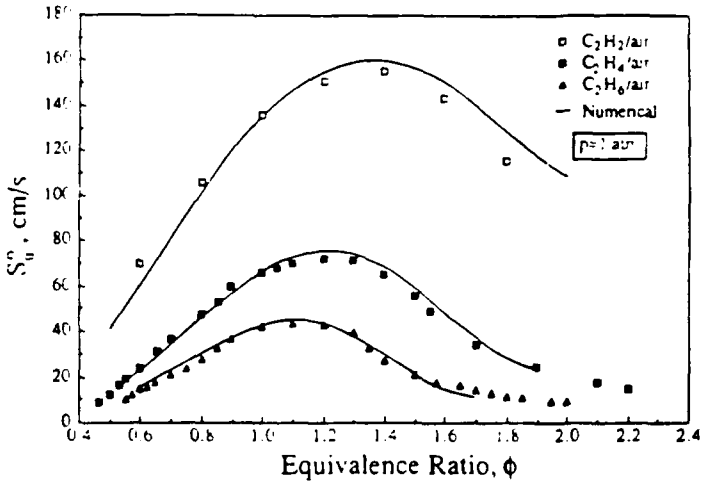

Figure 2

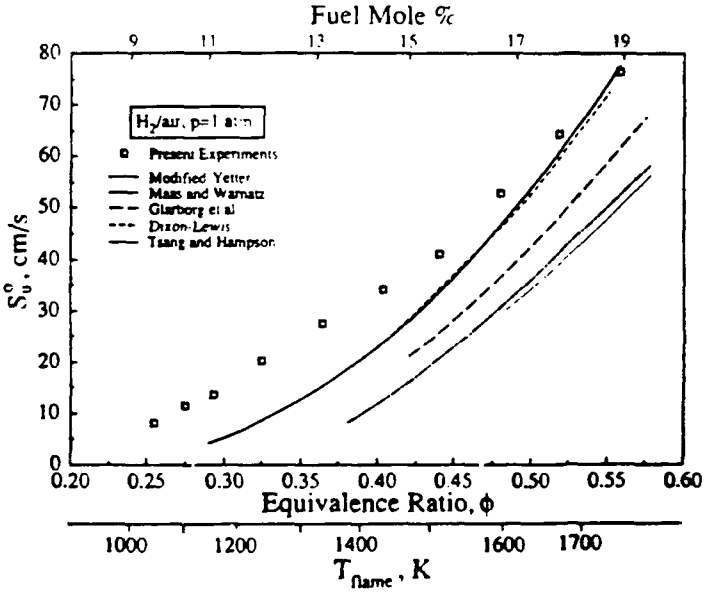

Figure 3

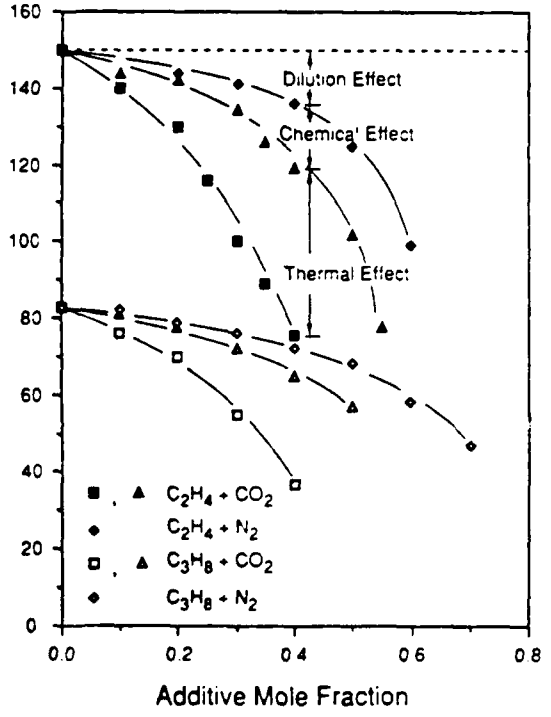

Figure 5

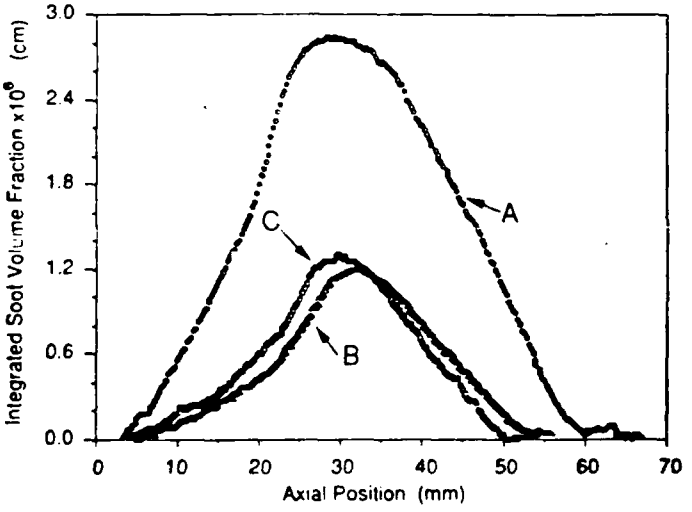

Figure 4

MIXING CONTROL IN SUPERSONIC SHEAR LAYERS

ONR Grant No. N00014-88-K-0242 (with AFOSR Contribution)

Principal Investigators: P. J. Morris*, D. K. McLaughlin* and G. S. Settles+.

Departments of Aerospace Engineering*
and Mechanical Engineering+
Penn State University
University Park, PA 16802

SUMMARY/OVERVIEW:

A combined experimental, analytical and computational program is underway to develop understanding of the mixing layer between two supersonic streams, with the ultimate objective to control and enhance the mixing. The experimental program involves both high Reynolds number studies of an axisymmetric shear layer and low Reynolds number studies of a two-dimensional shear layer. The analysis is based on the importance of large-scale coherent structures, modeled as instability waves, on the mixing process. The present interaction of the three phases of the research is developing the kind of understanding that will be necessary in the latter stages of the research as we pursue methods of mixing enhancement.

TECHNICAL DISCUSSION

To date, the majority of the experiments have been conducted on the unforced shear layer in both the low and high Reynolds number facilities. As expected, the large scale structures in the low Reynolds number shear layer are considerably more organized than the high Reynolds number counterpart. Preliminary comparisons with the developing models have shown promising results. More importantly the opportunities to make further advances are excellent.

Analysis and Computations (P. J. Morris)

The models that are being developed for the mixing process in high speed shear layers are based on the hypothesis that large scale coherent motions play a dominant role. This is known to be the case at lower speeds. In addition, our models make use of the close relationship between the observed properties of the large scale structures and predictions based on linear, inviscid stability theory. The large scale structures in the shear layer are modeled as instability waves. A model for the average development of the layer has been developed assuming that the initial conditions consist of a superposition of many instability waves of different frequencies and spanwise wavenumbers. A second model has been studied in which a single passage of a train of large scale structures is modeled as a superposition of a hierarchy of fixed frequency waves. These include the fundamental shedding frequency and its subharmonics.

These models have been implemented in both plane and axisymmetric shear layers. In both cases, both two- and three-dimensional instability waves are permitted. In the axisymmetric case these are the axisymmetric and helical structures. It is found that, in the axisymmetric case, as the convective Mach number increases, the helical motions dominate the flow development.

A careful examination has been conducted of the role of duct walls on the stability characteristics and growth of a two-dimensional shear layer. It has been shown that, for conditions typical of those used in current model experimental facilities, there are two types of instability waves. The first are the Kelvin-Helmholtz instabilities that are driven by the same physical mechanisms as those present in subsonic shear layers. These structures are predominantly three-dimensional at high Mach numbers. The second class are the supersonic instability waves that are primarily two-dimensional. They are driven by a coupling between the reflected Mach waves from the duct wall and the nearly periodic motions in the shear layer. In all the cases studied the maximum growth rates are associated with the Kelvin-Helmholtz instability. It has been shown that the choice of the ratio of the duct height to width has a significant influence on the growth of the three-dimensional instabilities. A technique for selecting the width-to-height ratio for maximum growth has been developed; and has been reported in the literature.

The effects of duct walls on the instability waves or large structures in ducted jets is also being studied using a boundary element method. The numerical technique has been validated for the case of a circular jet in a circular duct.

In the immediate future the calculations for the confined circular jet will be continued. In particular, we will be comparing the results with those for the two-dimensional geometries. It is hoped that this analysis will lead to predictions for optimum wall dimensions to maximize the jet growth rate. In addition, wave-packet calculations will be performed for the two-dimensional shear layer. These are important as the stability calculations have indicated that the most unstable motions in the supersonic shear layer are highly three-dimensional. The wave-packet calculations, in which the shear layer is excited at a single point with a pulse, should give us some guidance as to the nature of the structures one would expect to observe in the supersonic shear layer. Equivalent experiments in the low Reynolds shear layer facility will be conducted to assist in the modeling and to validate the predictions.

High Reynolds Number Experiments (G. S. Settles)

An axisymmetric compressible mixing layer is being used to study compressible turbulent mixing and the possibility of mixing enhancement and control by the manipulation of large-scale turbulent structures. This mixing layer is generated by injecting a gas stream through a cylindrical centerbody mounted along the axis of a supersonic wind tunnel test section. Primarily by varying the composition of the gas thus injected, the isentropic convective Mach number, M_c, may be varied from 0.08 to 1.5 in these experiments. This allows the study of a broad range of compressibility effects, while the axisymmetry of the mixing layer facilitates the observation of individual turbulent structures on the outer edge of the layer.

As reported previously, high-speed schlieren observations have been made, both as single frames and with a Cranz-Schardin camera which takes several consecutive frames with an interval in the microsecond range. A severe schlieren cutoff was required to reveal large-scale turbulent structure imbedded in finer-scale turbulence. A selection of such images is shown in the Figure. In general, "poorly-organized" large-scale structures are observed at the high Reynolds numbers of these experiments. It is clear that these structures are always highly inclined and that the inclination is always toward the high-speed side of the mixing layer.

In addition to these qualitative observations, quantitative data have been

obtained by optical deflectometry (wherein the deflection of a light beam by density gradients in the mixing layer is sensed and digitized at high speed). Spectra from single-point deflectometry experiments show a mixing layer containing a broad range of turbulent scales, with no obvious concentration of energy at any specific frequency. Two-point deflectometry, currently being developed, will allow us to make a better determination of coherent structures by way of spatial correlations.

An initial attempt to control this compressible mixing layer by acoustic excitation has been made. Flow-off sound pressure levels of about 110 dB over the frequency range of 5-25 kHz were tried with no noticeable effect on the shear layer. Among several possible reasons for this are: improper phasing, frequency too low, and inadequate dB level (presuming, of course, that it is possible to acoustically excite the mixing layer under any circumstances).

Finally, the axisymmetry-centerbody nozzle has been used to generate a Mach 3 airjet into still air (M_c = 1.1) for comparison with our helium/air case in the supersonic wind tunnel (M_c = 1.5). While having similar M_c values, these two cases differ in that the former has an outer subsonic flow while the latter is supersonic on both sides of the mixing layer. Thus, acoustic communication from downstream to upstream is inhibited in the latter case.

Initial schlieren results from these two cases are compared in the Figure. The only obvious difference thus far is the fact that there is more of an indicatio. of regular large-scale structure in the freejet case. Quantitative measurements are now under way.

In summary, it seems clear from these results that large-scale structures do exist even for $M_c > 1$. However, these are certainly dissimilar to those known in $M_c = 0$ mixing. This is a real failure of Morkovin's hypothesis, which opens many opportunities to learn more about this essentially-unknown aspect of turbulent mixing. Further details of this work have been submitted for presentation as an AIAA Paper.

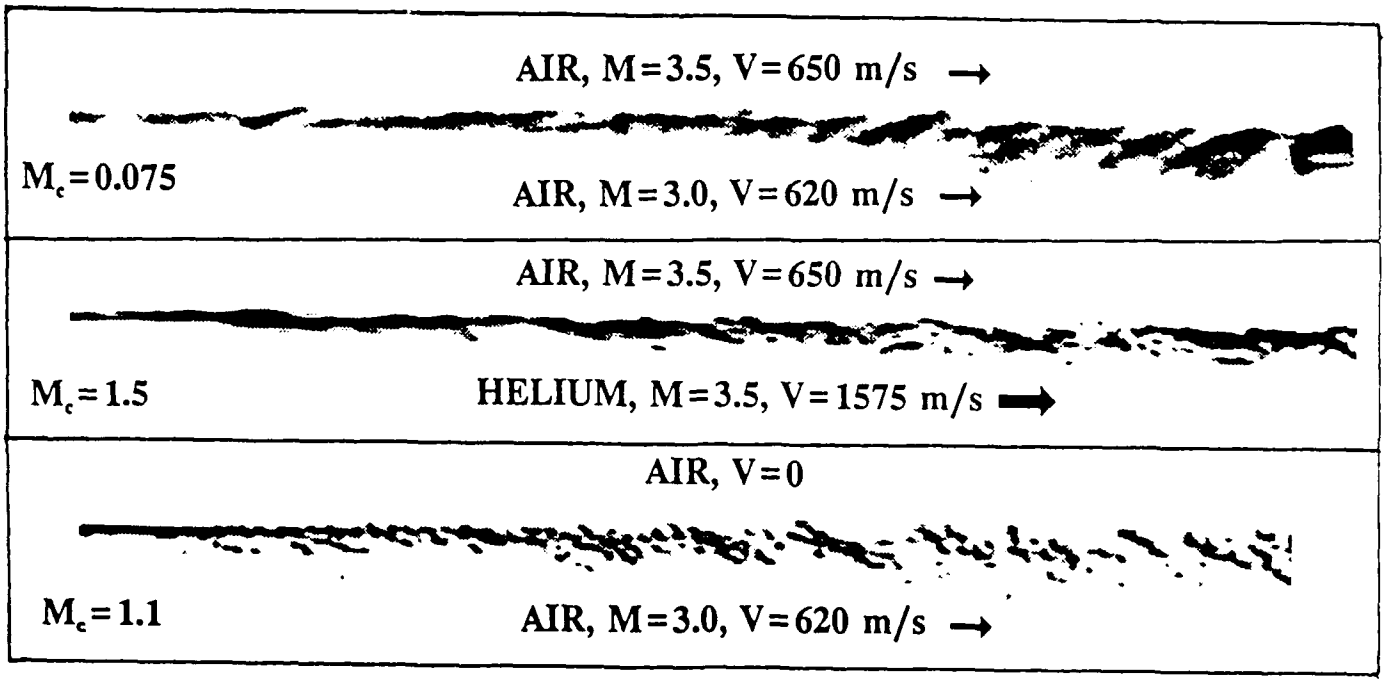

Low Reynold. Number Experiments (D. K. McLaughlin)

Since these experiments use a newly developed facility, a significant amount of time has been spend qualifying the facility. This has involved a series of pitot rake measurements together with schlieren photographs. A sample schlieren visualization is shown in the figure below. The lower stream is M = 3.0 and the upper stream is M = 1.5, with flow from left to right. The unit Reynolds number is Re = 1.7 x 10^6/meter and the total height of the channel is about 5cm.

At the conditions of this experiment, the Kelvin-Helmholtz instability grows rapidly beginning at the point where the two pictures are joined together (11.5cm downstream from the end of the splitter plate). The character of the instabilities is quite similar to some of the visualizations of the high Reynolds number shear layer performed by Settles and his student. However, as expected, the structures are much more "organized" in this low Reynolds number flow.

Preparations are underway for much more detailed investigations. These include hot-wire measurements over a broad range of operating conditions. Improvements to the diffuser will extend the high speed stream operating Mach number to M = 4, which together with a low speed stream of M = 1, will yield supersonic convective Mach numbers. Under these conditions we expect significant deviation from the structures previously measured in the incompressible shear layer.

As the hot-wire measurements proceed, development is also underway of the glow discharge excitation device. Once operational, this device will allow detailed measurements of the relative phase of the instability waves in the shear layer. This will become very important to our developing understanding at the higher convective Mach numbers where we expect significant components of oblique waves. Additionally, the glow discharge will allow us to measure the response to various configurations of artificial excitation, with the potential to produce enhanced mixing in the shear layer.

File: C:\wp50\papers\onrafosr.90 Date: 5/8/90

THE EFFECTS OF COMPRESSIBILITY ON A SUPERSONIC MIXING LAYER

AFOSR Contract No. F49620-88-C-0003

Principal Investigator: David Nixon

Nielsen Engineering & Research, Inc.
510 Clyde Avenue
Mountain View, CA 94043-2287

SUMMARY/OVERVIEW

The objective of the work is to identify the flow mechanisms that cause the decrease in spreading rate of supersonic mixing layers as the convective Mach number increases, and to suggest means of enhancing the mixing. A computer code has been used to simulate both time and space developing mixing layers to get some indication of the flow physics. To complement the numerical study a simple analysis has been developed that explains the variation of mixing rate with convective Mach number. The analysis seems to indicate that little can be done to enhance mixing as such, although the real problem of simultaneous mixing and combustion may be more amenable to control.

TECHNICAL DISCUSSION

In the past year the objective have been to extend and consolidate the simple theory developed in the first year of the contract and to see if it provides some insight into enhancement of mixing. This study was augmented by development of a computer code to simulate temporally and spatially developing mixing layers to gain insight into the physics of the flow.

At the end of the first year of the contract a simple theory had been developed for the spreading rate variation with convective Mach number. This theory is based on the transonic small disturbance equation

$$(\beta^2 - k\phi_x)\phi_{xx} + \phi_{yy} = M_c^2\phi_{tt} + 2M_c^2\phi_{xt} \tag{1}$$

where ϕ is a perturbation velocity potential, t is time nondimensionalized by c/U_c where c and U_c are characteristic length and convective velocity respectively, and M_c is the convective Mach number.

$$\beta^2 = 1 - M_c^2$$
$$k = (\gamma+1)M_c^2 \tag{2}$$

The theory relates the nondimensionalized compressible mixing, $\bar{m}$, to its value at incompressible ($M_c = 0$) speeds, $\bar{m}_i$, by

$$\frac{\bar{m}}{\bar{m}_i} = \left(\frac{\bar{m}_o}{\bar{m}_{oi}}\right)^2 \left[(RKE)_{oi} / (RKE) \right] \qquad (3)$$

where $\bar{m}_o$ is the nondimensional mixing associated with a rotational kinetic energy (RKE) of $(RKE)_o$ at a convective Mach number of M_c.

If $M_c << 1$, the Prandtl-Glauert equation ($k = 0$) may be used to evaluate the quantities in Equation (3) analytically and we obtain

$$\frac{\bar{m}}{\bar{m}_i} = \beta^3 / (1 - M_c^2/2) \qquad (4)$$

The results predicted by this theory show good agreement with experimental data, see Figure 1, especially for $M_c < 0.7$.

At the end of the first year of the contract it was concluded that mixing is reduced because the eddies decreased in size as M_c increases. In the last year we have concluded that this explanation is wrong and provided a simpler, more physical explanation for the phenomenon. The primary mechanism underlying the decrease is the attenuating effect compressibility has on the large scale structures' ability to deflect fluid away from the free streams and into the mixing layer. This is an irrotational effect; thus it is a completely different mechanism than the vorticity redistribution idea suggested by others.

Over the last year the theory has been consolidated, that is, fewer assumptions are made, and has been extended to include three-dimensional effects. A full description of the theory has been given in AIAA Paper 90-0706. A summary of the main findings is given below.

(a) No matter the size or number of spanwise vortices, the mixing will decrease with increasing M_c at the same rate. This indicates that two-dimensional eddy break up devices may not work.

(b) Streamwise vortices will not be affected by M_c to a first approximation and the mixing associated with these vortices is unchanged with M_c.

(c) If the hypothesis is made that large fluid mechanical structures, such as vortices, will deform to avoid shock waves, then the theory is greatly improved (Figure 1). The deformation may consist of vortex sweep, rather like a swept wing, or a bifurcation,

rather like the braids commonly seen in incompressible mixing layers. This hypothesis, if true, would have considerable implications in other fluid mechanics problems.

(d) Since the present theory is based on notions of irrotational flow it suggests that other studies based on vorticity redistribution arguments are erroneous. It may also be suggested that since the present theory is based on nonlinear finite disturbances, explanations of the phenomena based on linear stability theory are irrelevant. This latter viewpoint is corroborated by the fact that experimental data are taken a considerable distance downstream of the region where linear instability theories are valid.

(e) The main cause of the decrease in mixing as M_c increases is that an increasing amount of the energy in the two streams goes into compression of the fluid during entrainment, rather than being used to produce pure mixing. The only way to increase mixing is to accentuate streamwise vorticity and, if the hypothesis in (c) is valid, Nature is doing its best to achieve this goal.

In addition to the theory numerical simulations of both time and space evolving mixing layers have been performed. The code used is a modification of a fourth order accurate code developed at Nielsen Engineering & Research for impinging jet flows. These calculations were performed to get some insight into two-dimensional mixing layers; a typical example of such a calculation is shown in Figure 2. At present the numerical results are similar to those obtained by other investigators.

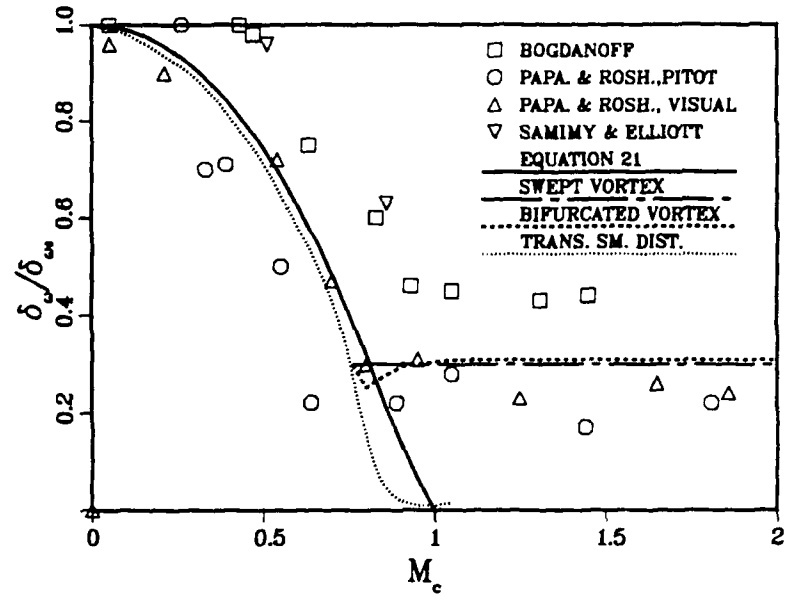

FIGURE 1. Experimentally measured layer growth rates compared to two– and three–dimensional theory.

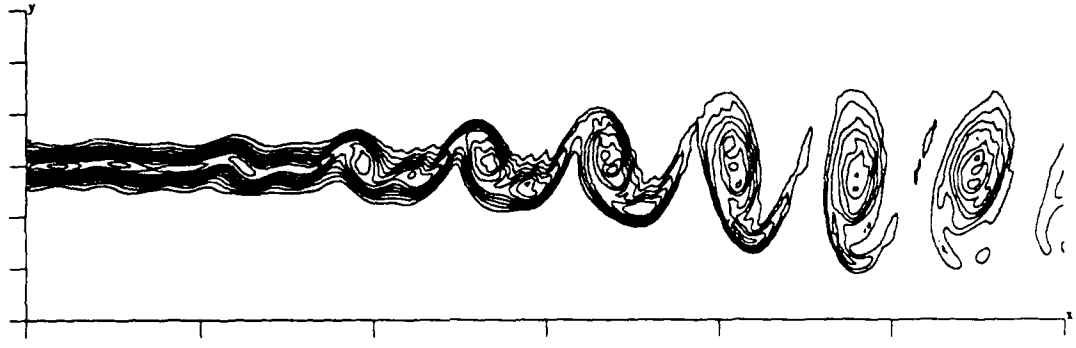

FIGURE 2. Vorticity contours in a two–dimensional mixing layer. $M_1 = 2.0$, $M_2 = 1.2$, $M_c = .4$.

NUMERICAL INVESTIGATION OF TURBULENT FLAME SHEETS

(AFOSR-88-0052)

Principal Investigator: Stephen B. Pope

Sibley School of Mechanical and Aerospace Engineering
Cornell University, Ithaca, NY 14853

SUMMARY

Direct numerical simulations of turbulence are being performed to study fundamental processes of turbulent combustion. In the flame-sheet regime of turbulent premixed combustion an important process is the stretching and bending of the surface by the turbulence. These processes have been studied for both material surfaces and propagating surfaces. Additional related work has been performed on material element deformation and on mapping closures for turbulent mixing. This work has revealed several important findings that are contrary to previous conjectures of long standing.

TECHNICAL DISCUSSION

Material Element Deformation

In Girimaji & Pope (1990) the previous studies of material surface elements is extended in two ways: first, additional important statistics are reported; and, second, material line and volume elements are also considered. The major findings are now itemized.

1. The growth rates of line and surface elements are significantly less (by a factor of about 3) than previous estimates (Monin & Yaglom 1975).

2. The smaller growth rates are due to the poor alignment between material elements and the turbulent straining motions. The lack of alignment is caused both by the action of vorticity to rotate the elements, and because the principal axes of the strain-rate rotate quite rapidly. In other words, contrary to conventional wisdom, we find that strain is fleeting rather than persistent.

3. An initially spherical infinitesimal volume element is deformed by the turbulent straining into an ellipsoid. The most probable shape of this ellipsoid is like a squashed cigar — one axis is extended, another equally compressed, while the third remains (approximately) unchanged.

Propagating Surfaces

The material surfaces considered previously (Pope et al. 1989) represent flame sheets only in special limits. In the context of premixed flames, the limit is $u_L/u_\eta \to 0$, where u_L is the laminar flame speed and u_η is the Kolmogorov velocity scale.

We have completed a study of propagating surfaces, with propagation speeds u_L of $u_L/u_\eta = 0, \frac{1}{4}, \frac{1}{2}, 1, 4, 8, 12, 16, 32$ (Girimaji 1990). The study of propagating surfaces ($u_L>0$) is much more difficult than that of material surfaces ($u_L=0$), because of cusp formation. That is, the curvature of a surface element can become infinite in finite time.

The first difficulty to be faced is to devise an accurate and stable numerical algorithm that can calculate the surface properties up to the point of cusp formation. This requires special consideration of the singularity (i.e. the cusps). Such an algorithm has been devised. It is second-order accurate, and reduces to an exact analytic solution as the singularity is approached.

Because of the formation of cusps, the time series of surface properties are finite in duration, and they are inherently non-stationary. Thus the second difficulty is the analysis of these time series — as compared to the stationary time series of arbitrarily long duration for material surfaces.

It is found, as expected, that the mean strain rate on a propagating surface decreases with u_L/u_η. For $u_L/u_\eta \leq 1$ the strain rate is close to that on a material surface (i.e. $u_L/u_\eta = 0$): for $u_L/u_\eta = 1$, it is just 7% less. But for $u_L/u_\eta = 4$ and 8, it is less by 35% and 75%, respectively. This information is needed in models of premixed turbulent combustion based on surface-to-volume concepts (e.g. Cant, Pope & Bray 1990).

A major finding — not entirely expected — is that cusps form in finite time for all propagation speeds $u_L > 0$, no matter how small. Starting from a plane surface at $t = 0$, we denote by $T_{1/2}$ the time at which half of the initial surface has experienced cusp formation. For $u_L/u_\eta = \frac{1}{4}$, 1, 4 we observe $T_{1/2}/\tau_\eta = 26, 10, 4$. For all u_L/u_η, the fraction of the initial surface that at time t has not experienced cusp formation is found to be $\exp(-ln(2)t/T_{1/2})$, to a good approximation for large t.

In considering surface propagation in a simple one-dimensional sinusoidal flow field, Ashurst, Sivashinsky and Yakhot (1988) concluded that cusps do not form if a parameter (equivalent to u_L/u_η) is less than unity. In view of this apparent disagreement we performed careful analytical and numerical studies of this flow. Our conclusion is that in fact cusps do form in finite time for all propagation speeds, no matter how small. An analytical upper bound has been obtained showing that the time to cusp formation varies as $(u_L/u_\eta)^{-1}$ (when this parameter is small).

Mapping Closures

For decades to come, direct numerical simulation will not be used as an engineering design tool for turbulent combustion devices, because the computation demands are way beyond reach. Instead, our philosophy is to use DNS to guide and test the development of statistical models that can be used as design tools. For turbulent combustion the most favorable statistical approach is the pdf method (see, e.g. Pope 1985, 1990).

In the pdf approach, while complex reactions can be treated without approximation, mixing — i.e. molecular diffusion processes — have to be modelled. For the last 15 years the development of a completely satisfactory mixing model has proved an allusive objective. Recently Kraichnan (1989) has proposed a completely new modelling methodology — mapping closures — which appear to be a breakthrough. As described in the following paragraphs, we have obtained an analytic solution to Kraichnan's model equations which are in spectacular agreement with our previous DNS results. First these DNS results are reviewed.

Eswaran & Pope (1988) (work supported by AFOSR 85-0083) performed direct numerical simulations of the decay of an inert passive scalar $\phi(\underline{x},t)$ in stationary, homogeneous, isotropic turbulence. The initial condition corresponds to blobs of scalar with $\phi \approx 1$ and an equal quantity of blobs with $\phi \approx -1$. Thus the initial pdf of ϕ, $f(\psi)$, corresponds, approximately, to the double-delta-function distribution.

$$f(\psi) = \frac{1}{2}[\delta(\psi+1) + \delta(\psi-1)] \,. \qquad (1)$$

The results show that the decay of the scalar variance depends on the size of the initial blobs (relative to the turbulence scales) — consistent with experimental observations. However, it is found that the shapes adopted by the pdf's are independent of blob size.

Kraichnan's model is conceptually simple, though technically difficult. The idea is to map the non-Gaussian scalar field $\phi(\underline{x},t)$ to a Gaussian field $\phi_o(\underline{x},t)$ by a mapping $Y(\bullet,t)$: i.e. $\phi_o(\underline{x},t) = Y(\phi[\underline{x},t],t)$. Gaussian closure approximation are then applied to the Gaussian field ϕ_o.

For the case of an inert passive scalar with the initial condition given by Eq. (1) we have obtained the following analytic solution to Kraichnan's model:

$$f(\psi;t) = \frac{1}{2}\Sigma \exp\{-\frac{1}{2}\psi_o^2(1-\Sigma^{-2})\} \,, \qquad (2)$$

where

$$\Sigma^{-2} = e^{t^*}-1 \,,$$

$$\psi_o = \sqrt{2}\ \Sigma\, \mathrm{erf}^{-1}(\psi) \,,$$

and t^* is normalized time. Figure 1b shows the pdf's according to Eq. (2) compared (Fig. 1a) to those from DNS. It may be seen that the agreement is remarkable. In spite of the considerable efforts of several workers over the past 15 years, no other models have come close to Kraichnan's in qualitative or quantitative performance.

REFERENCES

Ashurst, W.T., Sivashinsky, G.I. & Yakhot, V. (1988) Combust. Sci. Tech. 62, 273.

Cant, R.S., Pope, S.B. & Bray, K.N.C. (1990) "Modelling of flamelet surface-to-volume ratio in premixed turbulent combustion," Twenty-Third Symposium (International) on Combustion (to be published).

Eswaran, V. & Pope, S.B. (1988) Phys. Fluids 31, 506.

Girimaji, S.S. (1990) Ph.D. Thesis, Cornell University.

Girimaji, S.S. & Pope, S.B. (1990) "Material element deformation in isotropic turbulence," J. Fluid Mech., to be published.

Kraichnan, R.H. (1989) "Closures for probability distributions," Bull. Amer. Phys. Soc. 34, 2298.

Monin, A.S. & Yaglom, A.M. (1975) Statistical Fluid Mechanics, Vol. 2, MIT Press.

Pope, S.B. (1990) "Computations of turbulent combustion: progress and challenges," Twenty-Third Symposium (International) on Combustion (to be published).

Pope, S.B. (1985) Prog. Energy Combust. Sci., 11, 119.

Pope, S.B., Yeung, P.K. & Girimaji, S.S. (1989) Phys. Fluids A, 1, 2010.

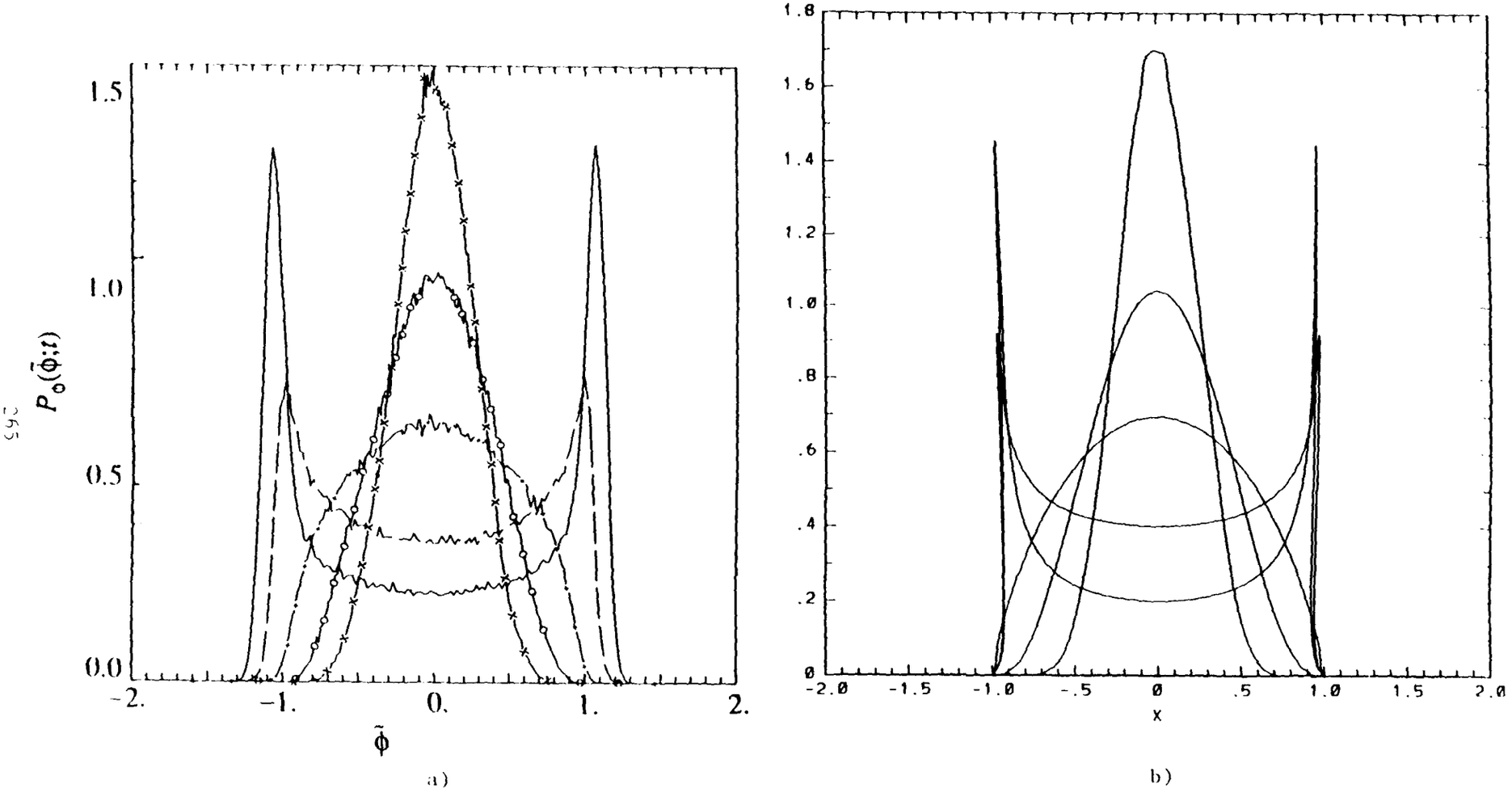

Fig. 1: Scalar pdf's from a) DNS, Eswaran & Pope (1988), b) Kraichnan's model, Eq. (2).

FLAME-TURBULENCE INTERACTIONS

(AFOSR Grant No. AFOSR-90-0025)

Principal Investigator: Domenic A. Santavicca

Department of Mechanical Engineering
Penn State University
University Park, PA 16802

SUMMARY/OVERVIEW:

The objective of this research is to obtain an improved understanding of flame-turbulence interactions in premixed turbulent flames. Experiments are continuing in a one-dimensional, freely propagating turbulent flame configuration and have recently been initiated in a single vortex-laminar flame configuration. LDV and PIV are used to characterize the velocity field and two-dimensional Mie scattering and laser induced fluorescence are used to characterize the flame structure. Of specific interest is the fractal nature of the flame structure, the effect of strain on flame propagation and extinction, and the mechanisms of flame generated turbulence. Such information will lead to a better understanding of the factors which determine the mass burning rate and flame-out limits of real combustors.

TECHNICAL DISCUSSION

The flame generated turbulence measurements in 1-D, freely propagating, stoichiometric, propane-air flames have been extended to include turbulence intensity conditions of 0.5 m/sec, 1.0 m/sec and 2.0 m/sec. In order to achieve these levels of turbulence, while maintaining uniform flow properties and high relative turbulence intensities, a new turbulence generator has been developed which is capable of operating at relative turbulence intensities approaching 100%. LDV measurements have been made at these new operating conditions of the ensemble averaged, parallel and normal (with respect to the mean flame front) velocity components, from which the mean velocities, turbulence intensities, energy spectra, and integral time scales have been calculated, in both the unburned and burned gases. The results which have been obtained at these new turbulence conditions continue to show significant increases in the normal component of the turbulence intensity and highly anistropic turbulence in the burned gases. The density weighted turbulent kinetic energy is found to increase across the flame at low turbulence levels, while it decreases at the high turbulence conditions. This is illustrated in Figures 1 and 2, which show the individual turbulence intensity components and the total turbulent kinetic energy, respectively, at the new turbulence conditions. Measurements of the integral length scale (from a two-point spatial correlation) and the Reynolds stress at the same conditions are in progress.

The flame structure measurements in 1-D, freely propagating, propane-air flames, which are made using two-dimensional Mie scattering from micron sized zirconium oxide particles, have been extended to study the effects of turbulent strain and preferential diffusion. Of specific interest is the effect on the overall flame structure in terms of the flame surface fractal dimension, which defines the distribution of flame surface scales, and the inner cut-off, which defines the smallest flame surface scale. We have previously shown that the fractal dimension of premixed turbulent flame surfaces can be predicted solely as a function of u'/s_l with the following heuristic relationship:

$$D_F = \frac{1}{1+u'/S_l} 2.05 + \frac{1}{1+S_l/u'} \; 2.35. \qquad (1)$$

In this expression the unstretched, adiabatic laminar flame speed is used, however, it is well known that turbulent strain and preferential diffusion can result in significant variations in the local laminar flame speed along the turbulent flame front. It is reasonable, therefore, to expect that turbulent strain and preferential diffusion will result in a change in the overall flame structure geometry, i.e. its fractal dimension. In order to investigate this, a series of two-dimensional flame structure measurements have been made at sets of operating conditions that have the same u'/S_l and include one case near the lean propagation limit, one case at stoichiometry and one case near the rich propagation limit. Such measurements have been made over a range of u'/S_l from 1 to 6. The measurements which have been obtained to date do not indicate that there is a significant effect of turbulent strain and preferential diffusion on the overall geometry of the flame surface, however, this is only based on 10 measurements per operating condition. We are continuing these measurements for the purpose of obtaining a statistically significant data set in order to resolve this important issue.

These same two-dimensional flame structure measurements are also being used to determine the minimum flame structure scale, the so-called inner cutoff. By reducing the laser sheet thickness, reducing the field of view, and increasing the camera resolution, these measurements were also intended to provide information on the inner cutoff. Unfortunately, because of the non-uniform particle size distribution, it is not possible to clearly identify the flame structure at small scales due to the presence of noise associated with the Mie scattering technique. This is illustrated in Figures 3 and 4. The fact that the small scale structure shown in Figure 3 is not a real feature of the flame surface is evidenced by the fact that the fractal dimension over this range of scales actually increases to a value of 2.5 (Figure 4) which is characteristic of random noise. Since knowledge of the smallest flame structure scale is essential in order to be able to predict the flame propagation rate, we are currently repeating these measurements using two-dimensional laser induced fluorescence from flame generated OH molecules. Preliminary measurements show no evidence of the small scale noise obtained with the Mie scattering

technique.

The results of this study of 1-D, freely propagating, premixed turbulent flames have provided valuable new information and insights regarding flame-turbulence interactions, however, interpretation of these results is limited by the fact that the LDV measurements are made at a single point and are averaged over many flame events, while the flame structure measurements are made over a two-dimensional plane at a given time. In order to better understand the actual interaction between the turbulent flow field and the turbulent flame surface, a two-dimensional velocimetry technique based on particle imaging velocimetry (PIV) has been recently developed for use in this study. The PIV technique will provide simultaneous measurements of the two-dimensional velocity field and the flame structure and thus provide direct evidence of the flame-turbulence interaction. To date, the PIV system has been assembled, made operational and successfully demonstrated on simulated data and on actual data from simple laminar flows. The PIV technique is currently being used to obtain preliminary measurements in non-reacting turbulent flows.

PUBLICATIONS

Videto, B. and Santavicca, D.A., "Flame-Turbulence Interactions in a Freely-Propagating, Premixed Flame", Combust. Sci. and Tech., Vol. 70, No. 1-3, p. 47 (1990)

North, G. L. and Santavicca, D. A., "The Fractal Nature of Premixed Turbulent Flames," accepted for publication in Combust. Sci. and Tech. (1990).

Santavicca, D. A., Liou, D.-Y. and North, G. L., "A Fractal Model of Turbulent Flame Kernel Growth", SAE Paper No. 900024 (1990).

Videto, B. and Santavicca, D. A., "A Turbulent Flow Reactor for Studying Turbulent Combustion Processes," submitted to Combust. Sci. and Tech. (May 1990)

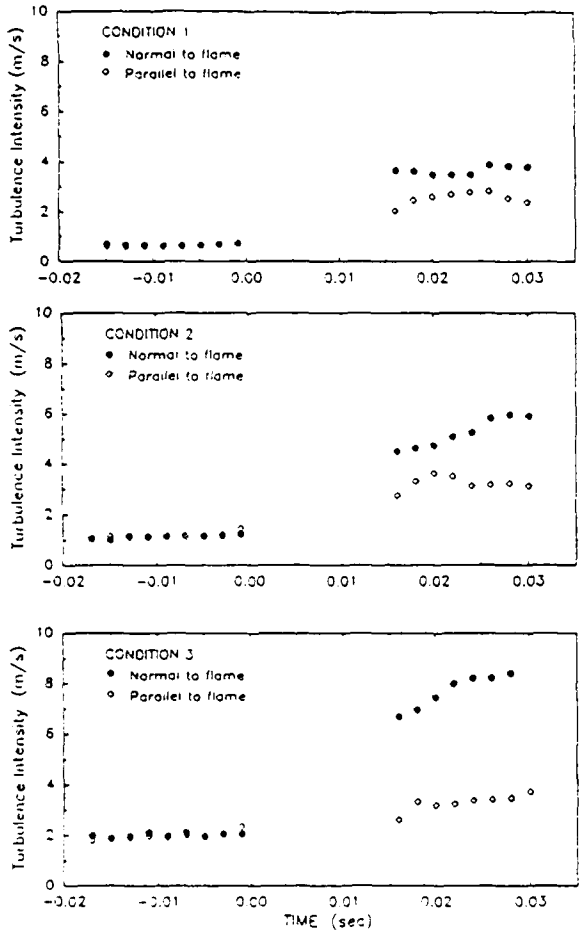

Figure 1. Parallel and normal components of the turbulence intensity before and after the turbulent flame zone.

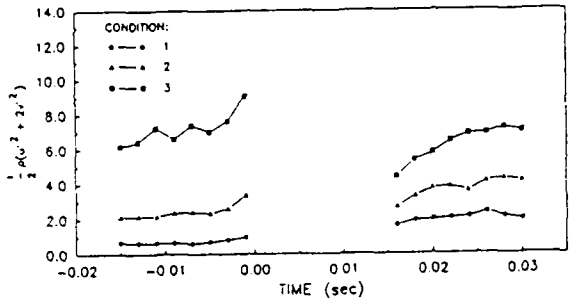

Figure 2. Density weighted turbulent kinetic energy before and after the turbulent flame zone.

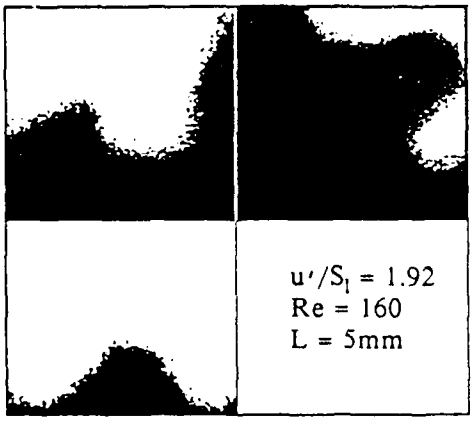

Figure 3. Two-dimensional Mie-scattering flame structure measurements (1 cm x 1 cm field of view)

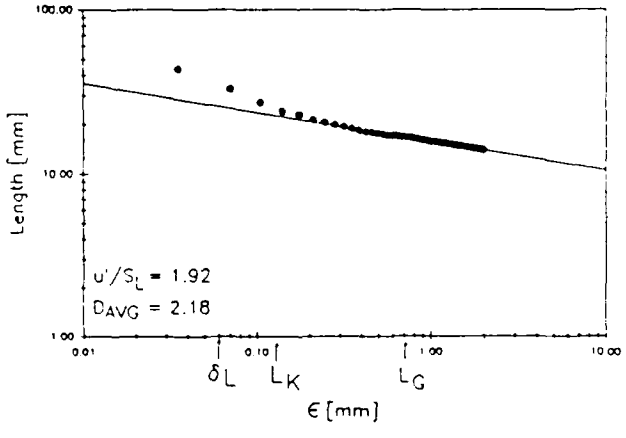

Figure 4. Fractal analysis of two-flame structure measurement.

THEORIES OF TURBULENT COMBUSTION IN HIGH SPEED FLOWS

(AFOSR Grant No. 89-0310)

Principal Investigators: P.A. Libby and F.A. Williams
Department of Applied Mechanics and Engineering Sciences
University of California, San Diego, La Jolla, CA 92093

SUMMARY/OVERVIEW

The objective of this research is to improve understanding of the chemical kinetics and fluid dynamics of turbulent combustion in high-speed flows. Supersonic combustion in hydrogen-air mixtures is being addressed by theoretical approaches that distinguish beween reaction-sheet and distributed-reaction regimes. The work seeks to identify effects of compressibility in turbulent combustion, methods for including compressibility in theoretical analyses, and reduced chemical-kinetic mechanisms appropriate for supersonic combustion. The results may help to enhance capabilities of reasonable computations of high-speed turbulent reacting flows.

TECHNICAL DISCUSSION

Research from a previous AFOSR grant, the publication of which is being supported by the present grant, is listed as the initial references [1-3].

In new work, attention has been focused first on nonpremixed hydrogen-air combustion [4,5], for flight between altitudes of 20 and 70 km and at Mach numbers from 1 to 25, with combustor Mach numbers about 1/3 flight Mach numbers. The Damköhler number D_ℓ, based on the integral turbulence scale and the overall premixed-flame combustion time, and the Reynolds number R_ℓ, based on the integral scale and the turbulence intensity, were estimated for this range of conditions and found to lie in the shaded, nearly triangular region in Fig. 1. This region is inconsistent with the distributed-reaction regime but consistent with the reaction-sheet regime. Therefore, attention was focused on determining structures of hydrogen-air diffusion flamelets that may be elements of the turbulent diffusion flames under these conditions.

Although not necessarily the only relevant structure, one flamelet of interest is the counterflow diffusion flame. The structure and extinction of counterflow diffusion flames of hydrogen and air were investigated for pressures from 0.5 to 10 atmospheres and for initial temperatures from 300 K to 1200 K. Numerical integrations were performed for air-side strain rates from 60 s^{-1} to extinction. The numerical results were compared with predictions of an asymptotic analysis that involved reduction to one-step chemistry through introduction of steady-state and partial-equilibrium approximations. Reasonable agreement was found for concentrations in the main reaction zone at low strain rates. Predicted extinction strain rates appear to be less than found in earlier numerical integrations but greater than experiment.

The computations began with a 21-step mechanism but found 8 of the steps to be relatively unimportant, so that a 13-step mechanism (among 8 species, H_2, O_2, H, O, OH, HO_2, H_2O_2 and H_2O) was obtained. Representative flame-structure results are shown in Figs. 2-5. The space coordinate x was selected for these plots because no mixture fraction was entirely unobjectionable. Shown in Fig. 2 are curves of mixture fraction based on O atoms, Z(O), H atoms, Z(H), nitrogen, Z(N), and enthalpy per unit mass, Z(h), the last of which agrees with Z(H) but does not yield linear profiles. Figure 2 shows the nonmonotonicity of the scalar dissipation at low strain rates and the reduction in peak temperature at high strain rate. Figure 3 shows profiles of major species and Fig. 4 of minor species for the same conditions. The O and OH profiles peak approximately where the temperature and H_2O profiles peak, while H peaks on the fuel side and HO_2 and H_2O_2 on the oxidizer side of this position for chemical-kinetic reasons. This behavior is consistent with predictions of an asymptotic analysis for large Damköhler numbers applied to a one-step mechanism derived from steady-state approximations for all minor species, and values of all mole fractions at the peak temperature, predicted from the asymptotics, agree with the results of the numerics within a factor of two. However, the steady states fail at temperatures below about 1000 K.

Figure 5 shows that increasing the pressure to 10 atm greatly decreases the peak values of most radical mole fractions but affects the OH peak little, also in agreement with asymptotic results. The peak temperature increases appreciably with pressure, approaching 2800 K at 10 atm, but profiles of scalar dissipation maintain about the same peaks. Figure 6 shows the dependence of the peak temperature on the strain rate for various pressures and ambient temperatures. Extinction events are seen for all conditions shown, except the air temperature of 1200 K. The extinction strain rate increases dramatically with increasing pressure but depends only slightly on fuel temperature. In general, extinction is absent when the air temperature exceeds roughly 1000 K at 1 atm, as would be expected from the chemical-kinetic crossover temperature between branching

and termination. The predicted extinction strain rate at 300 K and 1 atm, about 8000 s^{-1}, is nearly twice an experimentally reported value but is probably more realistic because of experimental difficulties. Although these results are quite helpful for defining flamelet structures, effects of turbulent scalar-dissipation variations through the flamelet, transient chemistry response and nonplanar flamelet structures need study.

In the application of flamelet models to turbulent flames it may be valid and certainly efficient to consider simplified descriptions of both the chemical kinetic and the fluid mechanical processes. Therefore as an effort complementary to that described earlier an analysis of hydrogen-air flames in counterflowing configurations with reduced chemical kinetic and simple transport descriptions is underway. Programs permitting the limiting cases of frozen and equilibrium as characterized by the flame sheet approximation are completed and incorporation of a reduced mechanism to deal with finite rate chemical effects is presently underway. The results of these simplified descriptions will be compared with the full calculations discussed earlier in order to assess the possible errors in applications to turbulent flames. In this same regard attention is being devoted to the special features associated with the incorporation of flamelet models into turbulent flames in high speed flows in particular with the influence of fluctuations of temperature and pressure in the two streams. A review which includes some comments on these studies is to appear as [6].

As a first step towards ascertaining influences of kinetic energy, compressibility and high Mach numbers in high speed combustion, a theoretical analysis of the inviscid flow between a porous plate and a parallel impermeable plate was performed for small values of the ratio of the plate separation distance to the lateral extent of the plates, for both planar and axisymmetric geometries [7]. The problem of computing the flow field was reduced to the solution of a single integral equation

$$\sqrt{\frac{\gamma-1}{\gamma}}\int_P^1 \left[\frac{X(P')}{X(P)}\right]^k \left(\frac{P'}{P}\right)^{1/\gamma}\left[1-\left(\frac{P}{P'}\right)^{(\gamma-1)/\gamma}\right]^{-1/2}\left[-\frac{dX(P')}{dP'}\right]dP' = 1\,,$$

which was accomplished numerically. The ratio of specific heats γ is a parameter of the solution, and parametric results are presented from $\gamma = 1.1$ to $\gamma = 1.67$ in Fig. 7. The flow exhibits choking at a critical value of the lateral extent of the plate, in the vicinity of which the Mach number approaches unity. The results are needed in providing external boundary-layer conditions for studying the flame structure in the viscous region between two counterflowing streams when compressibility is important. The choking limits the Mach number in the porous-plate experimental simulation, so other experimental configurations deserve consideration. Analysis of the viscous layer is needed to ascertain whether the flame is more robust at low Mach numbers, near the centerline, or at high Mach numbers, in the wings. Influences of large pressure fluctuations on the flame structure also need to be considered.

REFERENCES

1. S.C. Li, "Optical Measurement of Size Histories of Boron Particles in Ignition and Combustion Stages in a Flat-Flame Burner," Western-States and Canadian Sections, The Combustion Institute, Banff, Alberta, April 29-May 2, 1990.

2. S.C. Li and F.A. Williams, "Ignition and Combustion of Boron in Wet and Dry Atmospheres," Twenty-Third Symposium (International) on Combustion, The Combustion Institute, Pittsburgh, submitted, 1990.

3. S.C. Li, "Experimental and Theoretical Studies of Ignition and Combustion of Boron Particles in Wet and Dry Atmospheres," Ph.D. Thesis, Princeton University, 1990.

4. E. Gutheil and F.A. Williams, "The Structure of Hydrogen-Air Counterflow Diffusion Flames," Western States Section, The Combustion Institute, Preprint 89-109, Livermore, CA, October, 1989.

5. E. Gutheil and F.A. Williams, "A Numerical and Asymptotic Investigation of Structures of Hydrogen-Air Diffusion Flames at Pressures and Temperatures of High-Speed Combustion," Twenty-Third Symposium (International) on Combustion, The Combustion Institute, Pittsburgh, submitted, 1990.

6. P.A. Libby, "Comments on the Interaction of Turbulence and Chemical Kinetics," Proceedings of the ICASE/NASA Combustion Workshop, October 1989 (To appear).

7. G. Balakrishnan, A. Liñán and F.A. Williams, "Compressibility Effects in Counterflows," Western-States and Canadian Sections, The Combustion Institute, Banff, Alberta, April 29-May 2, 1990.

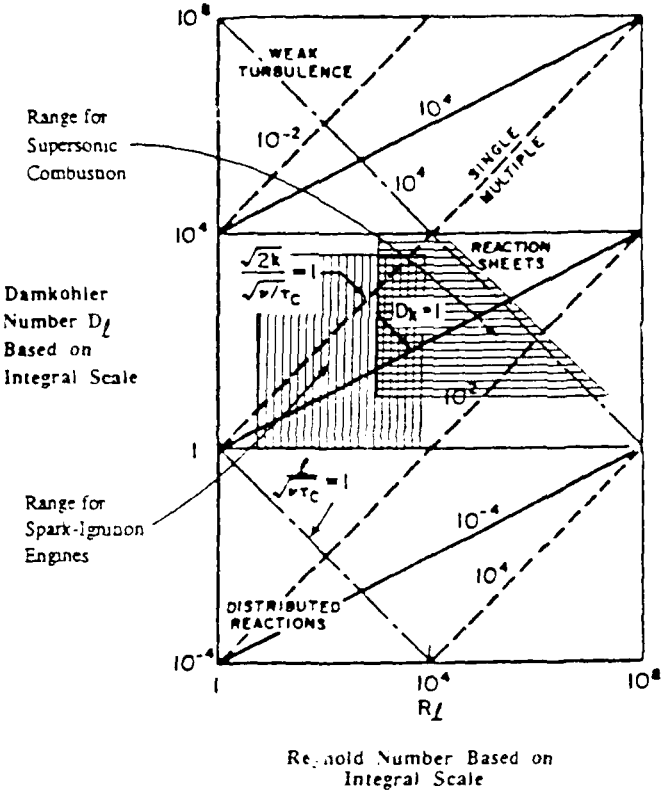

Fig. 1 Estimated range of Damköhler number and Reynolds number for turbulent combustion in high-speed flows.

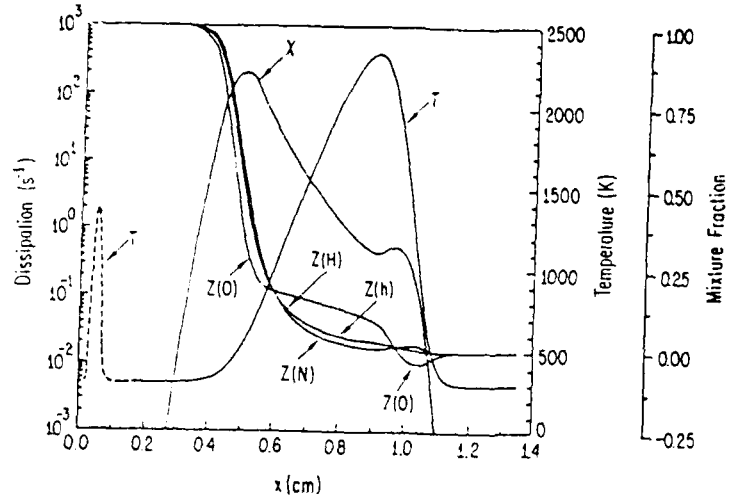

Fig. 2 Profiles of mixture fractions, Z, scalar dissipation, χ, and temperatures T at a strain rate of 60 s^{-1} (solid curves) and 8000 s^{-1} (dashed curves) at pressure p = 1 atm and boundary temperatures of 300 K.

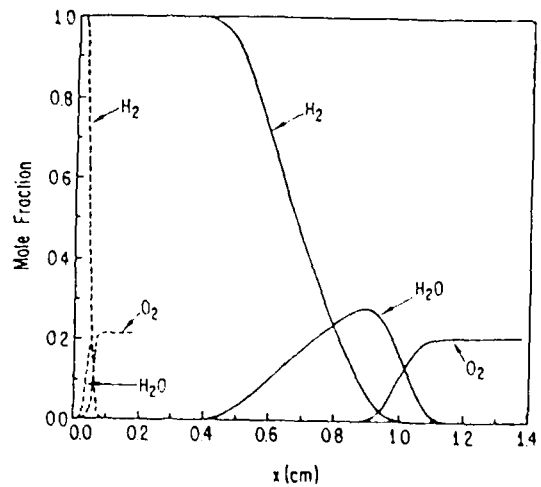

Fig. 3 Profiles of mole fractions of major species at a strain rate of 60 s^{-1} (solid curves) and 8000 s^{-1} (dashed curves) at p = 1 atm and boundary temperatures of 300 K.

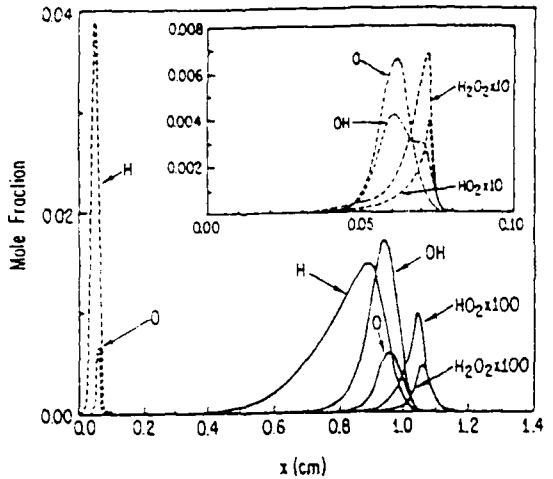

Fig. 4 Profiles of mole fractions of minor species at a strain rate of 60 s^{-1} (solid curves) and 8000 s^{-1} (dashed curves) at p = 1 atm and boundary temperatures of 300 K.

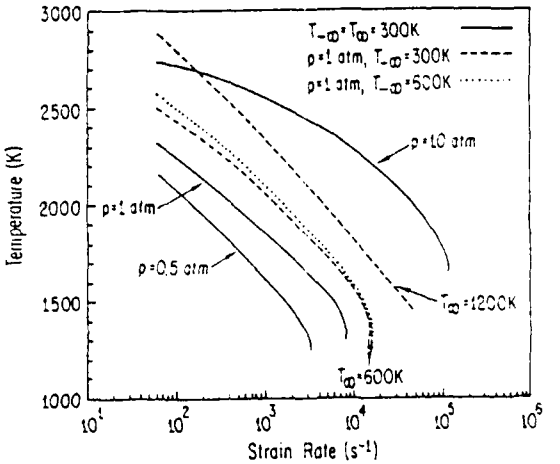

Fig. 6 The dependence of the maximum temperature on the strain rate for various pressures, fuel temperatures $T_{-\infty}$ and air temperatures T_∞.

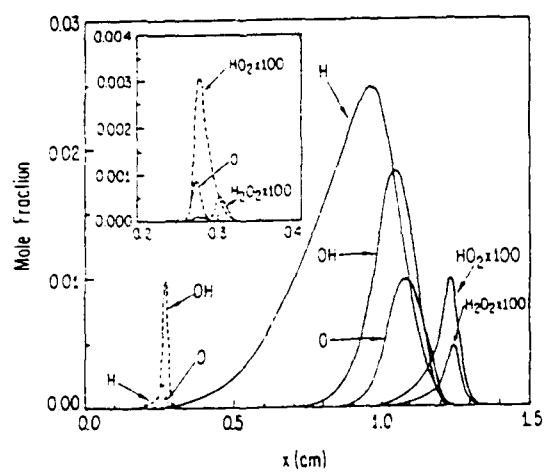

Fig. 5 Profiles of mole fractions of minor species at p = 0.5 atm (solid curves) and at p = 10 atm (dashed curves) for a strain rate of 60 s^{-1} and boundary temperatures of 300 K.

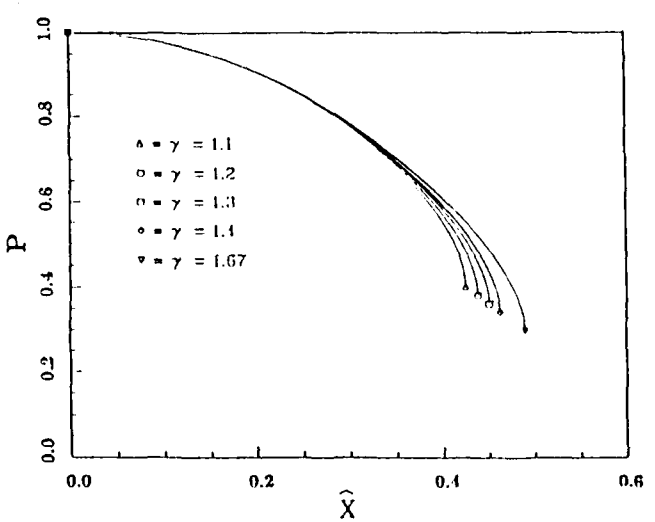

Fig. 7 Dependence of the pressure ratio P on the nondimensional lateral distance $X = \sqrt{\gamma}Mx/h$ (where M is injection Mach number and h plate separation distance) for various values of the ratio γ of specific heats, in the axisymmetric case (k = 1).

SHOCK INDUCED MIXING AND COMBUSTION IN A VORTEX

AFOSR Grants No. AFOSR-89-0413 and AFOSR-90-0188

Principal Investigator:

E. E. Zukoski
California Institute of Technology
Pasadena, California 91125

SUMMARY/OVERVIEW:

An experimental and computational study is being made of a novel technique to enhance the mixing and combustion in a supersonic flow between a jet of hydrogen and a co-flowing stream of air. Impinging oblique shocks are used to produce streamwise vorticity at the interface between the hydrogen jet and air which causes rapid distortion of the interface and rapid mixing of the hydrogen and air. Combustion in this type of vortex is being studied in a burner where combustion is initiated in the mixing layer between a premixed flow of fuel and air, and the hot products of combustion contained in a recirculation zone produced by a rearward facing step.

TECHNICAL DISCUSSION

1. SHOCK INDUCED MIXING INVESTIGATION

During the past year we have been studying shock induced mixing of helium and air in hypersonic flows, and combustion in a vortex produced at the interface between premixed fuel-air mixture and burned products of that mixture. In addition, we begun several new projects under a new grant which started on April 1, 1990 but have not progressed far enough on these new areas of research to report our progress here. Under the support of another grant we are also studying the application of the shock induced mixing ideas to a a fuel injector for a hypersonic combustion system. The injector will be studied in tests carried out in the high Reynolds number, Mach 6 wind tunnel at Langley Field, NASA.

Shock Induced Mixing Studies: Experimental work has concentrated on understanding the mixing produced by the passage of a shock over a cylinder of helium whose axis is parallel to the shock front. In the experiments discussed here the "cylinder" was a vertically directed laminar jet of helium and biacetyl dye which was injected into the test section of a 43 cm shock tube. Shocks with Mach numbers of 1.10 to 1.15 were produced in the shock tube and the flow produced after shock impingement on the jet were observed by viewing the fluorescence of the dye which was produced by passing a sheet of light from a pulsed dye laser perpendicular to the axis of the jet. In each experiment, the distortion of the helium cylinder could be observed with an exposure time of about 0.7 microseconds with an picture of the fluorescence obtained with an enhanced video camera. The distribution of the dye can be determined from the intensity measurement, and thus a good measure of the motion of the helium can also be determined.

This study was carried out by Dr. Jeff Jacobs for a range of Mach numbers and several positions in the jet which correspond to different initial distributions of helium and size of the cylinder. The apparatus allows study of the flow for several milliseconds after shock impingement. Jacobs primary efforts have been to understand the scaling of the interaction with initial size of the cylinder and the incident Mach number. The experiments to date show that the process is very reproducible and that we can successfully build up an accurate picture of the whole process by taking photographs of nominally identical experiments at different times after the start of the interaction.

Jacob's data show that within a few milliseconds after shock impingement about 70% of the original helium has been mixed with the surrounding air but that the remaining 30% develops into a stable pair of vortices. The low density helium gas at the center of these vortices is very stable and techniques to destabilize these vortices with additional shocks is being investigated. Computations suggest that this technique will produce substantial additional mixing.

We are also pursuing the development of a second technique for the production of helium cylinders in which the the helium gas is contained prior to shock impingement within a very thin plastic cylinder. The obvious problems here are to show that the cylinder does not affect the mixing process and to demonstrate that we can avoid spurious light signals generated by the scattering of the laser light from plastic surfaces which remain in the jet. The latter problem appears now to be a more serious than the former.

We have developed a calibration system which will allow us to determine the absolute concentration of the biacetyl dye from the enhanced video camera data in the presence of nonreproducible spatial and temporal variations of the intensity of the laser beam and variations in the initial concentration of the biacetyl dye. We are also in the process of resolving problems associated with the nonlinearity of the enhanced video camera, our primary diagnostic tool, which demonstrates strong nonlinearities at low light intensities.

Computational Program: The computations of shock induced mixing are being carried out with the FCT code supplied to us in two versions by J. Boris at NRL, Silver Springs Maryland. The aim of these calculations is to give guidance for the selection of parameters to be used in the experimental work and to allow us to determine approximately values of parameters such as vorticity which we can not measure in the experiments.

During the past year a number of calculations have been carried out on the San Diego Cray XMP using time made available by NSF. A matrix of the calculations which have been completed is given in the following tabulation. Much of this data is still in the process of being analyzed and some additional computations will be completed by June of 1990.

1. Geometry of helium mass has been varied to include: Single cylinders; single cylinders with sinusoidal perturbations of the radius; single ellipses with aspect ratios of 2 and 0.5; and two and three cylinder configurations.

2. The initial mass fraction of helium was 1.0 at the center and decreased smoothly to zero at the edge with maximum slope thicknesses of 0.05, 0.1, and 0.2 times the radius.

3. The ratio of channel height to cylinder radius was changed from 8 to 2 and a value of 4 was used in most calculations.

4. The Mach Number of the incident shock was 1.1, 1.2, or 2.0. and both incident and reflected shock interactions were studied.

5. Density ratio: In most calculations the density ratio of the gas within the fluid to that outside was that of helium to air, and in a few cases the density ratio was changed from 0.138 to 0.78.

Analysis of these computations has led to the development of several scaling procedures for prediction of the circulation produced by the impinging shock which include the effects of the density ratio and incident shock Mach number. Comparison with computational results is good and a comparison with previous experimental results is being carried out now.

We are also in the process of analyzing these data to determine which geometric configurations and parameter sets will produce the most rapid mixing. Qualitative measures of mixing can be obtained from the mixing produced by numerical diffusion, and by comparing the length of contours of a fixed helium mass fraction.

2. COMBUSTION IN A VORTEX

In a practical application, the enhanced mixing technique described above involves the generation of longitudinal vortices in the mixing layer between co-flowing hydrogen jets and the ambient air stream. Combustion will occur at the interface between the hydrogen jets and air as the vortices roll up and hence we have been interested in studying combustion in a vortex. The flow being studied now is that produced by vortices shed from a rearward facing step which forms the lower wall of a two dimensional combustion chamber and which acts as a flame holder for a premixed flow of fuel and air which passes over the step. Combustion occurs in the mixing layer formed downstream of the step between the unburnt fuel-air flow,which separates form the lip of the step, and products of combustion which recirculate behind the step. For certain sets of parameters, primarily gas speed and fuel-air ratio, natural interactions between the acoustic field within the combustion chamber system and the combustion process cause a regular shedding of vortices from the lip of the step at frequencies which range between 180 to 530 Hz. Acoustic forcing is also used to fix the frequency of shedding. We are studying the combustion within these vortices with a variety of experimental techniques which include pressure measurements through the combustion system, hot wire velocity measurements in the cold gas, and ionization probe delineations of regions of combustion.

Diagnostic techniques developed during the past year include the ability to obtain a digitized map of the intensity of chemiluminescence produced in the two dimensional premixed flame and 10 microseconds later a spark shadowgraph photographs of the density field. The exposure times for the shadowgraph and video camera photographs are about 1 and 10 microseconds which is short enough to give excellent time resolved photographs of the flow which contains velocities of about 30 m/s.

None of these techniques can be used to obtain photographs faster than about 30 per second so that they can not be used to map out the time history of one vortex. However, we can use a phase locking technique to obtain data from many vortices and build up a picture of the average history of the development of the combustion process. In this technique, the zero crossing of the pressure oscillation is measured and photographs are taken at a selected time delay later. Changing the time delay allows the whole cycle to be observed.

In addition, we have put into operation a two beam LDV which is being used to measure the velocity field of the flow as a function of position and time. The phase locking technique must be used here again so that data taken at different positions and times can be correlated.

Using these three techniques and continuous record of pressure, hot wire measurements of the cold gas speed at the flame holder lip and ionization probe measurements at several positions within the hot gas, we are now mapping the heat release pattern, as indicated by the chemiluminescence, the density field from the shadowgraph photographs and velocity field in the vortex.

Results obtained with these techniques show that the rate of combustion in the shear layer during the early stages of the growth of the vortex are relatively slow and are much more rapid after the vortex has grown large enough to impinge on the lower wall of the duct. The data also suggest that stretching of the interface between the hot products and the combustible mixture by the rapid growth of the vortex may inhibit combustion at the interface.

PAPERS:

Hendricks, Gavin J. and Marble, F.E., "Shock Enhancement of Supersonic Combustion Processes," accepted for presentation at the 26th Joint Propulsion Conference sponsored by the AIAA/SAE/ASME/ASEE.

ROCKET AND SPACE PROPULSION

Invitees

Mr. Robert Acree
AL/VSSC
Edwards AFB CA 93523-5000
(805)275-5598
AV525-5598

Dr George F. Adams
USA-BRL
AMXBR-I8D
Aberdeen Proving Gnd MD 21005-5006
(301)278-6168
(301)278-6783

Mr Ranney Adams
AL/PA
Edwards AFB CA 93523-5000
(805)275-5465
AV525-5465

Dr. Horst Adolph
Synthesis and Formulations Br
Naval Surface Weapons Center
10901 New Hampshire Avenue
Silver Spring MD 20903-5000

Dr William E Anderson
Aerojet Techsystems
P.O. Box 13222
Sacramento CA 95813
(916)355-6918

Mr. W. C. Andrepont
P.O. Box 431
858 W. Jackman
Suite 111
Lancaster CA 93534
(805)942-5098

Lt John L. Andreshak
AL/LKLR
Stop 24
Edwards AFB CA 93523-5000
(805)275-5194
AV525-5194

Mr Chris Andrews
AL/LSVE
Edwards AFB CA 93523-5000
(805)275-5766
AV 525-5766

Dr Ron Atkins
Naval Weapons Center
China Lake CA 93555-6001
(619)939-1630
AV437-1630

Dr Carl Aukerman
NASA/Lewis Research Center
21000 Brookpark Road
Cleveland OH 44135-3127
(216)433-2441

Dr William F Bailey
AFIT/ENP
Wright-Patterson AFB OH 45433-6583
(513)255-4498
AV785-4498

Dr Joseph D. Baum
SAIC
1710 Goodridge Drive
P.O. Box 1303,
McLean VA 22102
(703)827-4952

Dr Roger J. Becker
KL-462
Research Institute
University of Dayton
Dayton OH 45469
(513)229-3938

Mr Charles Beckman
AL/MKPA
Stop 24
Edwards AFB CA 93523-5000
(805)275-5487
AV525-5487

Dr Merrill Beckstead
Dept of Chemical Engineering
Brigham Young University
Provo UT 84602
(801)378-6239

Dr Robert Beddini
Univ of Illinois
AAE Department
104 South Mathews Avenue
Urbana IL 61801-2997
(217)333-4239

Dr Clifford Bedford
SRI International
Chemistry Laboratory
Menlo Park CA 94025
(415)859-4449

Dr S. J. Bennett
Adv Technology Projects Div
Morton Thiokol, Inc, Wasatch
Box 524
Brigham City UT 84302
(801)863-2980

Dr Greg Berry
Argonne National Laboratory
9700 South Class Avenue
Argonne IL 60439
(312)972-6160

Dr Oscar Biblarz
Department of Aeronautics
Naval Post Graduate School
Monterey CA 93943-5100
(408)646-2972
AV878-2972

Mr Robert A. Biggers
AL/XRX
Stop 24
Edwards AFB CA 93523-5000
(805)275-5241
AV525-5341

Dr S Binkley
Combustion Research Facility
Sandia National Laboratories
Livermore CA 94550

Dr Mitat A Birkan
AFOSR/NA
Bolling AFB DC 20332-6448
(202)767-4938
AV297-4938

Dr Fred S Blomshield
Code 3892,Propulsion
Research Branch
Naval Weapons Center
China Lake CA 93555
(619)939-3650
AV 437-3650

Dr Arthur Bracut
ARDC
LCWSL
Dover NJ 07801
(201)724-3788
AV880-3788

Dr Mel Branch
Mechanical Engineering Dept
University of Colorado
Boulder CO 80309-0427
(303)492-6318
(303)492-7151

Dr John E Brandenburg
Mission Research Corporation
8560 Cinderbed Road
Suite 700
Newington VA 22122
(703)339-6500

Dr Tom Brill
University of Delaware
Department of Chemistry
Newark DE 19716
(302)451-2466

Dr Bruce M. Broline
PO Box 3999
M/S 82-23
Boeing Aerospace
Seattle WA 98042
(206)773-5846

Dr Robert S. Brown
United Technologies Corp
Chemical Systems Division
P. O. Box 49028
San Jose CA 95161-9028
(408)778-4680

Dr James T. Bryant
Naval Weapons Center
China Lake CA 93555-6001
(619)939-7206
AV437-7206

Dr Rodney L Burton
Dept. of Aero. And Astro. Engg
University Of Illinois-UC
101 Transportation Building
Urbana IL 61801-2997
(217)333-2651

Mr David Byers
NASA Lewis Research Center
MS 500-219
21000 Prookpark Road
Cleveland OH 44135-3127
(216)433-2447

Dr George Caledonia
Physical Sciences Inc
20 New England Business Center
Andover MA 01810
(617)475-9030

Dr David Campbell
AL/DYC
Stop 24
Edwards AFB CA 93523-5000

Dr Robert Carrol
Pratt&Whitney
P.O. Box 109600
West Palm Beach FL 33410-9600
(407)796-2889

Dr Robert Cassel
Naval Sea Systems Command
Code 62D
Washington DC 20362
(202)692-8635

Dr Robert J. Cattolica
Sandia National Laboratories
Division 9351
Livermore CA 94550

Dr Leonard Caveny
OSD/SDIO/IST
Pentagon
Washington DC 20301-7100
(202)693-1530

Dr Yunus Ali Cengel
University of Nevada-Reno
Dept of Mechanical Engg
Reno NV 89557-0030

Dr May Chan
Naval Weapons Center
China Lake CA 93555-6001
(619)939-7519
AV437-7519

Dr Franklin R Chang-Diaz
Lyndon B Johnson Space Center
Code CB
Houston TX 77058
(713)483-2714

Dr Robert Chapman
AL/LKLR
Stop 24
Edwards AFB CA 93523-5000
(805)275-5416
AV525-5416

Dr Malcolm Chase
Center for Chemical Physics
National Inst of Stds & Tech
Building 222, Room A158
Gaithersburg MD 20899
(301)975-2526

Dr Fan-Bill Cheung
Penn State University
208 Mechanical Engineering
University Park PA 16802
(814)863-4281
FAX 865-3389

Dr Peck Cho
Dept. of Mechanical Engg.
College of Engineering
Michigan Technological Univ.
Houghton MI 49931

Dr Won-Ho Choe
214 Nuclear Engineering Lab
University of Illinois
103 South Goodwin Avenue
Urbana IL 61801
(217)333-2821

Dr Edgar Choueiri
Department of Mechanical And
Aerospace Engineering
Princeton University
Princeton NJ 08544-5263
(609)452-5221

Dr Karl Christe
Rocketdyne Division
Rockwell International
6633 Canoga Ave
Canoga Park CA 91304
(818)710-3268

Dr T. J. Chung
University of Alabama
Huntsville AL 35801
(205)895-6394

Dr George M. Clark
Aerojet Tactical Systems
PO Box 13400
Building 0525
Sacramento CA 95813
(916)988-6919

Dr William Clark
Naval Weapons Center
Code 3895
China Lake CA 93555-6001

Dr Norman Cohen
Aerospace Corporation
PO Box 92957
M/S 747
Los Angeles CA 90045
(213)648-7427

Dr Norman S. Cohen
Professional Services
141 Channing St
Redlands CA 92373
(714)792-8807

Dr Ronald Cohen
The Aerospace Corporation
PO Box 92957
Mail Stop M5-754
Los Angeles CA 90009
(213)336-5946

Dr Cliff Coon
Lawrence Livermore National
Laboratories
Livermore CA 94550
(415)422-6311

Cpt Edward N. Coppola
AL/MKPA
Stop 24
Edwards AFB CA 93523-5000
(805)275-5534
AV525-5534

Mr Robert Corley
AL/DYC
Stop 24
Edwards AFB CA 93523-5000
(805)275-5353
AV525-5353

Dr L. Cottle
RARDE, Fort Halstead
Knockholt
Matternrks Kent UK

Dr George B Cox Jr
United Technologies
Pratt-Whitney
P.O. Box 109600
West Palm Beach FL 33410-9600
(407)796-2887
FAX 796-5825

Dr F E C Culick
Engrg and Appl Sci Dept
California Institute of
Technology
Pasadena CA 91125
(818)356-4470

Dr C L Dailey
TRW Space and Technology Group
Applied Technology Division
One Space Park
Redondo Beach CA 90278
(213)536-1874

Dr John W Daily
University of Colorado
Engineering Center ME 1-13
Campus Box 427
Boulder CO 80309-0427
(303)492-7110

Dr B R Daniel
School of Aerospace Rngrg
Georgia Institute of
Technology
Atlanta GA 30332

Dr William D Deininger
Jet Propulsion Laboratory
California Inst. of Technology
4800 Oak Grove Drive
Pasadena CA 91109
(818)354-7765

Mr S T Demetriades
STD Research Corp
P.O. Box C
Arcadia CA 91006
(818)357-2311

Dr Gregory M Dobbs
United Technologies Res. Ctr.
MS 129-90 Silver Lane
East Hartford CT 06108
(203)727-7145
FAX 727-7669

Dr Joel Dubow
Materials Science
Univ of Utah
2008B Mechanical Engrg Bldg
Salt Lake City UT 84112
(801)581-8388

Dr. J. T. Edwards
AL/DYCR
Stop 24
Edwards AFB CA 93523-5000
(805)275-5656
AV525-5656

Dr John Eisch
Department of Chemistry
State University of New York
Binghamton NY 13901
(607)798-3994

Dr William J Escher
NASA Headquarters
Code RP
Washington DC 20546
(202)453-9111

Dr James J Fang
Rockwell/Rocketdyne Division
6633 Canoga Park
Canoga Park CA 91303
(818)718-3728
FAX 718-3600

Mrs Karen Farner
AL/RKLB
Edwards AFB CA 93523-5000

Dr Allan J Ferrenberg
Manager, Advanced Comb. Device
Rocketdyne Div, Rockwell Int.
Mail Stop IR06,6633 Canoga Ave
Canoga Park CA 91303
(818)718-3713

Dr John Fischer
Code 3853
Naval Weapons Center
China Lake CA 93555-6001
(619)939-1641
AV437-1641

Dr J. E. Flanagan
Rocketdyne
6633 Canoga
Canoga Park CA 91304
(818)710-2466

Dr Gary Flandro
School of Aerospace Engg.
Georgia Institute of Tech.
Atlanta GA 30332-0420
(404)853-9160

Dr Jim Fong
Aerojet Tech Systems
P O Box 13222
Sacramento CA 95813

Dr Arthur Fontijn
Chemical & Environmental
Engineering Department
Rensselaer Polytechnic Inst.
Troy NY 12180-3590
(518)276-6508

Dr Milt Frankel
Rocketdyne
6633 Canoga Avenue
Canoga Park CA 91304
(818)710-4803
(818)710-5088

Dr R A Frederick
Sverdrup Technology, Inc
Mail Stop 900
Arnold AFB TN 37389-9998
(615)454-3130

Dr Sheilah K. Fultz
Naval Weapons Center
China Lake CA 93555-6001
(619)939-7521
AV437-7521

Mr Robert Geisler
AL/YS
Edwards AFB CA 93523-5000
(805)275-5230
AV525-5230

Dr Eugene Gerber
Univ of Dayton Research Institute
KL465
Dayton OH 45419
(513)229-3221

Dr. Robert Ghirardelli
U.S. Army Research Office
P.O. Box 12211
Research Triangle Pk NC 27709-2211
(919)549-0641
AV935-3331

Lt Col Fred T Gilliam
EOARD
Box 14
FPO NY 09510-0200
AV235-4505

Dr David Golden
SRI International
333 Ravenswood Avenue
Menlo Park CA 94025-3696
(415)859-0811

Dr B. B. Goshgarian
AL/MKPB
Stop 24
Edwards AFB CA 93523-5000
(805)275-5183
AV525-5183

Dr William H Graham
Morton Thiokol, Inc
Huntsville Division
Huntsville AL 35807-7501
(205)882-8397

Dr Alten Grandt
Department of Aeronautics and Astronautics
Purdue University
West Lafayette IN 47907

Mr Eugene Haberman
AL/MK
Stop 24
Edwards AFB CA 93523-5000
(805)275-5420
AV525-5420

Dr V E Haloulakos
Advanced Propulsion
McDonnell Douglas
5301 Bolsa Avenue
Huntington Beach CA 92647

Dr Elmer Hansen
Department of Mechanical Engineering
University of Florida
Gainesville FL 32611
(904)392-0802

Dr Kenneth Harstad
Jet Propulsion Laboratory
4800 Oak Grove Drive
Pasadena CA 91109

Dr David Hastings
Department of Aeronautics and Astronautics
Massachusetts Inst of Tech
Cambridge MA 02139

Ms Sharon L Hasty
John Hopkins Univ/APL
CPIA
John Hopkins Road
Laurel MD 20707
(301)992-7306

Dr Donald J Hautman
United Technologies Res. Ctr.
East Hartford CT 06108
(203)727-7424

Dr Clark Hawk
AL/LR
Stop 24
Edwards AFB CA 93523-5000
(805)275-6530
AV525-6530

Dr Helmut W Hellwig
AFOSR/CC
Bolling AFB DC 20332-6448
(202)767-5017
AV297-5017

Dr Alan Hersh
Hersh Acoustical Engineering
9545 Cozycroft Avenue
Chatsworth CA 91311
(818)998-8311
FAX 341-0978

Dr Rich Hollins
Naval Weapons Center
China Lake CA 93555-6001
(619)939-1650
AV437-1650

Dr H R Jacobs
Mechanical Engg Bldg, 208
Penn State University
University Park PA 16802
(814)863-2519
FAX 865-3389

Dr J.I. Jagoda
Aerospace Engineering Dept
Georgia Institute of
Technology
Atlanta GA 30329
(404)894-3060

Dr Donald Jassowski
Aerojet Technical Systems Co
PO Box 13222
Sacramento CA 95813
(916)355-2849

Dr S M Jeng
University of Tennessee
Space Institute
Tullahoma TN 37388

Dr Robert Jensen
Rockwell/Rocketdyne Division
6633 Canoga Ave
Canoga Park CA 91303
(818)718-3730
FAX 718-3600

Dr Abraham Kadish
Earth and Space Sciences Div.
Atmospheric Sciences Group
Mail Stop D466, LANL
Los Alamos NM 87545

Dr Jordin Kare
Building 197, Room 1020
Lawrence Livermore Nat'l Lab
P O Box 808
Livermore CA 94550
(415)423-8300

Dr David R Kassoy
Dept of Mechanical Engineering
University of Colorado at
Boulder, Campus Box 427
Boulder CO 80309
(303)492-2991
(303)492-7694

Dr Myron Kaufman
Department of Chemistry
Emory University
Atlanta GA 30322
(404)727-6619

Dr Dennis Keefer
University of Tennessee
Space Institute
Tullahoma TN 37388
(615)455-0631

Dr Philip Kessel
AL/LSCF
Edwards AFB CA 93523-5000

Dr Sue Kim
California State University
6000 J Street
Sacramento CA 95819
(916)454-6712

Dr David King
Mail Stop 125-224
Jet Propulsion Laboratory
4800 Oak Grove Drive
Pasadena CA 91103
(818)354-3315

Dr Merrill K. King
Atlantic Research Corp
5390 Cherokee Ave
Alexandria VA 22312
(703)642-4217

Mr Mark D Kleim
Nasa Lewis Research Center
21000 Brookbark Rd
MS 510-219
Cleveland OH 44135

Dr Kenneth Kolouko
Morton Thiokol
Wasatch Division
P.O. Box 524
Brigham City UT 84302
(801)863-4220

Dr James J. Komar
Atlantic Research Corp
5390 Cherokee Avenue
Alexandria VA 23312
(703)642-4473

Dr Herman Krier
Dept of Mechanical and
Industrial Engineering
University of Illinois
Urbana IL 61801
(217)333-0529

Prof M Kristiansen
P.W. Horn Professor
Dept of Electrical Engg,MS3102
Texas Tech University
Lubbock TX 79409-4439
(806)792-3007

Dr Warren A. Krueger
167 Alvana Street, NW16-160
Massachusetts Institute of
Technology
Cambridge MA 02139
(617)253-0236

Dr Al Kudlach
AL/RKLA
Edwards AFB CA 93523-5000
(805)275-5248
AV 525-5248

Dr Kenneth K Kuo
Penn State University
208 Mechanical Engineering
University Park PA 16802
(814)863-6741
FAX 863-3203

Dr Bill Larson
AL/LSVF
Edwards AFB CA 93523-5000
(805)275-5657
AV525-5657

Dr Miller Layton
AL/LKLR
Stop 24
Edwards AFB CA 93523-5000

Dr Joel L Lebowitz
Rutgers-The State University
Department of Mathematics
Hill Center-Busch Campus
New Brunswick NJ 08903
(201)932-3117

Dr Ja H Lee
NASA Langley Research Center
M/S493
Hampton VA 23665
(804)864-4332

Mr Edward L Lee
Special Projects Leader
P.O. Box 808,L-368
LLNL-University of California
Livermore CA 94550
(415)422-1316

Mr Jay Levine
AL/LSCF
Edwards AFB CA 93523-5000
(805)275-5366
AV 525-5366

Dr P Y Liang
Advanced Combustion Devices
Rocketdyne Div, Rockwell Int.
6633 Canoga Avenue
Canoga Park CA 91303

Dr George A. Lo
Lockheed Palo Alto Research
Laboratory
3251 Hanover St, 8204-93-50
Palo Alto CA 94304
(415)424-2514

Dr Geoffrey Main
School of Mechanical Engrg
Georgia Institute of
Technology
Atlanta GA 30332-0420
(404)894-3242
(404)951-8058

Dr David M. Mann
Army Research Office
P.O. Box 12211
Research Triangle Pk NC 27709-2211
(919)549-0641
AV935-3331

Professor Alan P Marchand
Dept of Chemistry
North Texas State Univ
NTSU Station, Box 13767
Denton TX 76203-5068
(817)565-3823

Dr Stephen B Margolis
Combustion Research Facility
Sandia National Laboratories
Livermore CA 94550
(415)294-

Dr Manuel Martinez-Sanchez
Aeronautics and Astronautics
Massachusetts Inst of Tech
Building 37-401
Cambridge MA 02139
(617)253-5613

Dr Peter Mattern
Combustion Sciences
Sandia National Laboratories
Livermore CA 94550

Dr Jyotirmoy Mazumder
Department of Mechanical and
Industrial Engineering
University of Illinois
Urbana IL 61801
(217)333-1964

Dr John McVey
Rasor Associates, Inc
253 Humboldt Court
Sunnyvale CA 94086
(408)734-1622

Dr Franklin Mead
AL/LKVE
Edwards AFB CA 93523-5000
(805)275-5540
AV525-5540

Dr Carl F. Melius
Sandia National Laboratories
Livermore CA 94550
(415)294-2650

Dr Charles L. Merkle
205 ME
Pennsylvania State University
University Park PA 16802
(814)863-1501
FAX 865-3389

Dr Claude Merrill
AL/MKPL
Stop 24
Edwards AFB CA 93523-5000
(805)275-5169
AV525-5169

Dr Michael M. Micci
233 Hammond Building
Pennsylvania State University
University Park Pa 16802
(814)863-0043

Dr Richard S. Miller
Office of Naval Research
Mechanics Division, Code 432
800 North Quincy Street
Arlington VA 22217-5000
(202)696-4403

Dr Charles Mitchell
Dept. of Mechanical Engineerin
Colorado State University
Fort Collins CO 80523
(303)491-6654

Mr T S Mogstad
McDonnell Douglas Astr.Co-West
Design And Tech. Center
Huntington Beach CA 92647
(714)896-3437

Dr. Robert Moriarty
University of Illinois
(Chicago Circle)
Department of Chemistry
Chicago IL 60680
(312)996-2364

Dr Marlow D. Moser
AL/DYCC
Stop 24
Edwards AFB CA 93523-5000
(805)275-5442
AV525-5442

Dr Kenneth G Moses
Plasma Technology Division
JAYCOR
3547 Voyager Street, Suite 104
Torrance CA 90503-1667
(213)542-3800

Dr Philip Muntz
Dept. of Aerospace Engineering
University of Southern
California
Los Angeles CA 90089

Dr S N B Murthy
Dept of Mechanical Engineering
Purdue University
West Lafayette IN 47907
(317)494-1509
(317)494-5639

Dr Jeffrey Muss
Aerojet Techsystems
P.O. Box 13222
Sacramento CA 95813
(916)355-3663

Dr Thong V Nguyen
Aerojet Techsystems
P.O. Box 13222
Sacramento CA 95813
(916)355-3664

Dr Gary R. Nickerson
Software&Engineering Assoc.
1000 E. William St., Suite 200
Carson City NV 89701
(702)882-1966

Mr Randy T Nishiyama
R/E/WPS
US Dept of Commerce
NOAA, 325 Broadway
Boulder CO 80303-3328

Dr Douglas B. Olson
AeroChem Research Laboratories
Inc.
P. O. Box 12
Princeton NJ 08542
(609)921-7070

Col Arthur L Pavel
AFOSR/CD
Bolling AFB DC 20332-6448
(202)767-5018
AV297-5018

Dr Don Penn
AL/RKLB
Edwards AFB CA 93523-5000

Dr Subhash Narang
Chemistry Laboratory
SRI International
333 Ravenswood Avenue
Menlo Park CA 94025-3696

Dr Jim Nichols
AL/RKLB
Edwards AFB CA 93523-5000
(805)275-5249
AV 525-5249

Dr Arnold T. Nielsen
Naval Weapons Center
China Lake CA 93555-6001
(619)939-1614
AV437-1614

Col James R Nunn
AL/CC
Edwards AFB CA 93523-5000

Dr Tae-Woo Park
AL/TODP
Stop 24
Edwards AFB CA 93523-5000
(805)275-5196
AV525-5196

Ms Dorothy L Pecker
The John Hopkins Univ/APL
John Hopkins Rd
Laurel MD 20707

Dr Jerry L Pieper
Aerojet Techsystems
P.O. Box 13222
Sacramento CA 95813
(916)355-3087

Dr Leanne Pitchford
GTE Laboratories
40 Sylvan Road
Waltham MA 02254
(617)466-2704

Dr Robert L Poeschel
Plasma Physics Department
Hughes Research Laboratories
3011 Malibu Canyon Road
Malibu CA 90265
(213)317-5443

Dr Dimos Poulikakos
University of Illinois
(Chicago Circle)
Dept. of Mechanical Engg.
Chicago IL 60680
(312)996-5239

Dr Edward Price
School of Aerospace Engrg
Georgia Institute of
Technology
Atlanta GA 30332-0420
(404)894-3063

Dr Richard Priem
Priem Consultants
13533 Mohawk Trail
Cleveland OH 44130
(216)845-1083

Dr Andrej Przekwas
CFD Research Corporation
3313 Bob Wallace Ave,Suite 205
Huntsville AL 35805
(205)536-6576

Dr Lawrence P Quinn
AL/DYC
Edwards AFB CA 93523-5000
(805)275-5353
AV 525-5353

Dr Frederick H Reardon
Cal State U.-Sacramento
Dept of Mechanical Engineering
6000 J Street
Sacramento CA 95616
(916)278-6727

Dr Russell Reed
Naval Weapons Center
China Lake CA 93555-6001
(619)939-7296
AV437-7296

Dr Robert A Rhein
Research Chemist
Code 3244
Naval Weapons Center
China Lake CA 93555-6001
(619)939-7392
AV 437-7310

Dr J W Rich
Department of Mechanical
Engineering
The Ohio State University
Columbus OH 43212-1194
(614)292-6309

Dr Frank Roberto
AL/MKP
Stop 24
Edwards AFB CA 93523-5000
(805)275-5430
AV525-5430

Dr Stephen Rodgers
AL/LKLR
Stop 24
Edwards AFB CA 93523-5000
(805)275-5416
AV525-5416

Mr Wayne Roe
AL/XRX
Stop 24
Edwards AFB CA 93523-5000
(805)275-5206
AV525-5206

Dr David Rosen
Physical Sciences Inc.
Dascomb Research Park
Andover MA 01810
(617)475-9030

Dr S D Rosenberg
P O Box 13222
Sacramento CA 95813
(916)355-2609

Dr Thomas J Rosfjord
United Technologies Res.Ctr.
East Hartford CT 06108
(203)727-7418

Dr David S Ross
Director,Physical Organic Chem
SRI International
333 Ravenswood Avenue
Menlo Park CA 94025-3696
(415)859-2430

Dr Gabriel Roy
ONR Code 1132 P
Arlington VA 22217
(202)696-4405

Dr Kevin Rudolph
Martin Marietta Corporation
Mail Stop S8071
PO Box 179
Denver CO 80201
(303)977-3681

Lt Jim Rymarcsuk
AL/RKLB
Edwards AFB CA 93523-5000
(805)275-5542
AV 525-5542

Dr Mark Salita
Morton Thiokol/Wasatch Div
MS 280B
PO Box 524
Brigham City UT 84302
(801)863-2163

Dr. Michael J. Salkind
President
Ohio Aerospace Institute
2001 Aerospace Parkway
Brookpark OH 44142
(216)891-2100

Dr Robert J Santoro
Penn State University
208 Mechanical Emgineering
University Park PA 16802
(814)863-1285
FAX 865-3389

Dr Robert Schmitt
Chemistry Lab
SRI International
333 Ravenswood Avenue
Menlo Park CA 94025-3696
(415)859-5579

Dr Keith Schofield
Quantum Institute
University of California,
Santa Barbara
Santa Barbara CA 93106

Dr Herbert Schrade
Institut Fur Raumfahrtantriabe
Universitat Stuttgart
Pfaffenwaldring 31
D-7000 Stuttgart GE
7116-852-383
or 375

Dr Gary I. Sega
Aerospace Corp
P.O. Box 92957
MS/747
Los Angeles CA 90004
(213)648-6501

Maj Scott A Shackelford
F J Seiler Research Laboratory
United States Air Force Acad
Colorado Springs CO 80840
(719)472-2655

Dr R Shoureshi
School of Mechanical
Engineering
Purdue University
West Lafayette IN 47907
(317)494-5639

Dr Bill Sirigano
College of Engineering
University of California
Irvine CA 92717
(714)856-6002

Lt Col LaRell Smith
EOARD/LRC
Box 14
FPO NY 09510-0200
AV235-4505

Dr Warren Strahle
School of Aerospace Engrg
Georgia Institute of
Technology
Atlanta GA 30332
(404)894-3032

Dr. Mostafa Talukder
AL/LKLR
Edwards AFB CA 93523-5000
(805)275-5416
AV525-5416

Professor William C Trogler
Department of Chemistry
University of California, San
Diego
LaJolla CA 92093
(619)452-6175

Dr Pam Sherretz
Naval Weapons Center
China Lake CA 93555-6001
(619)939-7392
AV437-7392

Prof Jean'ne M. Shreeve
Dept of Chemistry
University of Idaho
Moscow ID 83843
(208)885-6552

Ms Elizabeth Slimak
AL/LSCF
Edwards AFB CA 93523-5000

Dr Ronald Spores
AL/LSVE
Edwards AFB CA 93523-5000
(805)275-5766
AV 525-5766

Dr V V Subramaniam
Department of Mechanical
Engineering
The Ohio State University
Columbus OH 43212-1194
(614)292-6096

Dr James Tien
Case Western Reserve
University
Glennan Building, Room 415
Cleveland OH 44106
(216)368-4581

Dr Wing Tsang
National Institute of Standard
and Technology
Chemical Kinetics Division
Gaithersburg MD 20899
(301)975-3507

Dr Peter Turchi
Aero/Astro Engineering
328 CAE Building
Ohio State University
Columbus OH 43210
(614)292-2691

Dr Robert Vondra
PO Box 596
Wrightwood CA 92397
(619)249-3451

Dr R H Woodward Waesche
Atlantic Research Corporation
7511 Wellington Road
Gainesville VA 22065

Dr Peter Wayner
Dept of Chemical and
Environmental Engineering
Rensselaer Polytechnic Inst
Troy NY 12180-3590
(518)276-6199

Dr Jim Weber
Rocketdyne Division
Rockwell International Corp.
6633 Canoga Ave
Canoga Park CA 91303
(818)710-5558

Dr Rodney Willer
Morton Thiokol Inc
Elkton Division
P.O. Box 241
Elkton MD 21921
(301)398-3000
(301)398-4440

Dr D O Woolery
Rocketdyne
6633 Canoga Avenue
Canoga Park CA 91304

Mr Gary L. Vogt
AL/DYCR
Stop 24
Edwards AFB CA 93523-5000
(805)275-5258
AV525-5258

Dr Nzoo Vu
Naval Weapons Center
China Lake CA 93555-6001
(916)939-7392
AV437-7392

Dr Richard Walker
Aerojet Techsystems
P.O. Box 13222
Sacramento CA 95813
(916)355-2694

Dr David P Weaver
AL/DYCR
Edwards AFB CA 93523-5000
(805)275-5657
AV525-5657

Dr Richard Weiss
AL/CA
Edwards AFB CA 93523-5000
(805)275-5622
AV525-5622

Dr W S Williamson
Plasma Physics Department
Hughes Research Laboratories
3011 Malibu Canyon Road
Malibu CA 90265
(213)317-5443

Dr Ted F. Yang
Massachusetts Institute of
Technology
167 Albany Street
Cambridge MA 02139
(617)253-8453

Dr Vigor Yang
Department of Mechanical Engineering
Pennsylvania State University
University Park PA 16802
(814)863-1502
FAX 865-3389

Dr Thomas M York
AERO/ASTRO Engineering
328 CAE Building
Ohio State University
Columbus OH 43210
(614)292-2691

Dr Ben T. Zinn
School of Aerospace Engrg
Georgia Institute of Technology
Atlanta GA 30332
(404)894-3033

Cpt Joseph Zirrolli
FJSRL/NC
United States Air Force Academy
Colorado Springs CO 80840
(303)472-2655

Mr Robert L Zurawski
Program Manager
Propulsion Technology Programs
NASA HQA, OAST-MAIL CODE RP
Washington DC 20546
(202)453-2261

DIAGNOSTICS IN REACTING MEDIA

Invitees

Mr. Leonard Angello
Electric Power Research Institute
3412 Hillview Avenue
Palo Alto CA 94303
(415)855-2873

Dr. W. D. Bachalo
Aerometrics, Inc.
894 Ross Drive
Unit 105
Sunnyvale CA 94089
(408)745-0321

Dr Edward J Beiting
Aerophysics Lab, Prop Env Sc
The Aerospace Corporation
P O Box 92957, M5/754
Los Angeles CA 90009-2957
(213)336-7035

Dr William K Bischel
Coherent, Inc.
3210 Porter Drive
Palo Alto CA 94304
(415)858-7639

Dr. Richard K. Chang
Electrical Engineering Dept.
P. O. Box 2157, Yale Station
Yale University
New Haven CT 06520
(203)432-4272

Dr. Wai K. Cheng
Department of Mechanical Engineering
MIT
Cambridge MA 02139
(617)253-4531

Dr. David R. Crosley
Molecular Physics Department
SRI International
333 Ravenswood Avenue
Menlo Park CA 94025-3696
(415)326-6200

Dr. John W. Daily
Center for Combustion Research
Mechanical Engineering Dept
University of Colorado
Boulder CO 80309
(303)492-7110

Dr. Gregory Dobbs
United Technologies Research Center - Mail Stop 90
Silver Lane
East Hartford CT 06108
(203)727-7145

Dr. A. C. Eckbreth
United Technologies Research Center
Silver Lane
East Hartford CT 06108
(203)727-7269

Dr Thomas Ehlert
Department of Chemistry
Marquette University
Milwaukee WI 53233
(414)288-7066

Dr Peter Erbland
AFSC/NAT
Wright-Patterson AFB OH 45433-6503
(513)255-3196
(513)255-9757

Dr Gregory N Faris
SRI International
333 Ravenswood Avenue
Menlo Park CA 94025
(415)859-4131

Dr. Richard Field
U. S. Army Armament RD Center
DRSMC-LCA-G(D)
Building 382-S
Dover NJ 07801
(201)724-5844
(201)724-5682

Dr. Bish Ganguly
WRDC/POOC-3
Wright-Patterson AFB OH 45433-6563
(513)255-2923
AV785-2923

Dr. Alan Garscadden
WRDC/POOC-3
Wright-Patterson AFB OH 45433-6563
(513)255-2923
AV785-2923

Dr. Larry P. Goss
Research Applications Division
Systems Research Labs, Inc.
2800 Indian Ripple Road
Dayton OH 45440-3696
(513)252-2706

Dr. R. K. Hanson
Department of Mechanical Engineering
Stanford University
Stanford CA 94305-3032
(415)723-1745

Dr. D. L. Hartley
Combustion Sciences
Sandia National Laboratories
Livermore CA 94550

Dr. L. Hesselink
Department of Aeronautics and Astronautics
Stanford University
Stanford CA 94305-3032
(415)723-3466

Dr. E. D. Hirleman
Department of Mechanical and Aerospace Engineering
Arizona State University
Tempe AZ 85287
(602)965-3895

Dr. Donald J. Holve
Insitec
28 Bobbie Court
Danville CA 94526
(415)837-1330

Dr David Huestis
SRI International
333 Ravenswood Avenue
Menlo Park CA 94025
(415)859-3464

Dr Thomas K Ishii
Department of Electrical Engineering
Marquette University
Milwaukee WI 53233
(414)288-1593

Dr Jay B Jeffries
SRI International
333 Ravenswood Avenue
Menlo Park CA 94025
(415)859-6431

Dr. Roman Kuc
Department of Electrical Engineering
Yale University
New Haven CT 06520
(203)432-4891

Dr. Marshall B. Long
Department of Mechanical Engineering
Yale University
New Haven CT 06520
(203)432-4229

Dr. Bruce G. MacDonald
Research Applications Division
Systems Research Labs, Inc.
2800 Indian Ripple Road
Dayton OH 45440-3696
(513)252-2706

Dr T E Parker
Physical Sciences
20 New England Business Center
Andover MA 01810
(508)689-3232

Dr. Timothy Parr
Naval Weapons Center
Code 3893
China Lake CA 93555
(619)939-2521

Dr. S. S. Penner
Dept. Of. Appl. Mech. and
Engrg. Sci.
University of California
La Jolla CA 92093
(619)534-4284

Dr Emil Pfender
Department of Mechanical Engrg
125 Mechanical Engineering
The University of Minnesota
Minneapolis MN 55455

Dr. John P. Renie
Department of Mechanical and
Industrial Engineering
University of Illinois
Urbana IL 61801
(217)333-6199

Dr Won B Roh
Department of Engrg Physics
Air Force Institute of
Teechnology
Wright-Patterson AFB OH 45433-6583

Dr Gregory P Smith
Department of Chem Kinetics
SRI International
333 Ravenswood Avenue
Menlo Park CA 94025
(415)859-3496

Dr. Alan C. Stanton
Southwest Sciences, Inc.
1570 Pacheco Street
Suite E-11
Santa Fe NM 87501
(505)984-1322

Dr. James D. Trolinger
MetroLaser
18006 Skypark Circle
Suite 108
Irvine CA 92714-6428
(714)553-0688

Dr. John A. Vanderhoff
Ballistic Research Laboratory
DRSMC-BLI(A)
Aberdeen Proving Ground MD 21005
(301)278-6642

Dr. James F. Verdieck
Rockwell International
Rocketdyne Div, M/S FA26
6633 Canoga Avenue
Canoga Park CA 91303
(818)700-4709

Dr. Joda Wormhoudt
Aerodyne Research, Inc.
45 Manning Road
Manning Park Research Center
Billerica MA 01821-3976
(508)663-9500

AFOSR/ONR CONTRACTORS MEETING ON COMBUSTION

Invitees

Dr Griffin Y Anderson
NASA Langley Research Center
M/S 168
Hampton VA 23665
(804)864-3772

Dr. Scott L. Anderson
Department of Chemistry
State University of New York
Stony Brook NY 11794-3400
(516)632-7915

Dr K Annamalai
Mechanical Engineering Dept
Texas AM University
College Station TX 77843-3123

Dr Kurt Annen
Aerodyne Research, Inc.
45 Manning Road
Manning Park Research Center
Billerica MA 01821-3976
(508)663-9500

Dr Simon H Bauer
Department of Chemistry
Cornell University
Ithaca NY 14853-1301

Dr. S. L. Baughcum
Spectra Technology
2755 Northrup Way
Bellevue WA 98004-1495
(206)828-3517

Dr. H. R. Baum
National Institute of
Standards and Technology
Center for Fire Research
Gaithersburg MD 20899
(301)975-6668

Dr John Bdzil
Los Alamos National Laboratory
Los Alamos NM 87545

Dr. H. L. Beach
NASA Langley Research Center
MS 168
Hampton VA 23665-5225
(804)864-3772
(804)864-2658

Dr. Josette Bellan
Applied Technologies Section
Jet Propulsion Laboratory
4800 Oak Grove Drive
Pasadena CA 91109
(818)354-6959

Dr. Paul A. Bonczyk
United Technologies Research
Center
Silver Lane
East Hartford CT 06108
(203)727-7162

Dr Kevin G Bowcutt
Rockwell International
Mail Code NA40
12214 Lakewood Boulevard
Downey CA 90241
(213)420-0317

Dr. C. T. Bowman
Department of Mechanical
Engineering
Stanford University
Stanford CA 94305-3032
(415)723-1745

Dr K N C Bray
University of Cambridge
Department of Engineering
Trumpington Street
Cambridge CB2 1PZ, England UK
0223 332744
0223 337733

Dr Robert E Breidenthal
Department of Aeronautics a
Astronautics
University of Washington, FS10
Seattle WA 98195
(206)545-1098

Dr Kenneth Brezinsky
Department of Mechanical and
Aerospace Engineering
Princeton University
Princeton NJ 08544-5263
(609)258-5225

Dr. J. E. Broadwell
Graduate Aeronautical Labs
California Irstitute of
Technology
Pasadena CA 91125

Dr Garry L Brown
Aeronautical Research Labs
506 Lorimer St, Fishermen's Bn
Box 4331, P. O.
Melbourne, Victoria AUSTRALIA 3
03-647-7511

Dr R C Brown
Aerodyne Research, Inc.
45 Manning Road
Manning Park Research Center
Billerica MA 01821-3976
(508)663-9500

Lt Col Larry W Burggraf
AFOSR/NC
Bolling AFB DC 20332-6448
(202)767-4960
AV297-4960

Dr Dennis Bushnell
NASA Langley Research Center
Mail Stop 168
Hampton VA 23665
(804)864-4546

Dr Ron Butler
WRDC/POSF
Wright-Patterson AFB OH 45433-6563

Dr. T. D. Butler
Group T-3
Los Alamos National Labo tory
Los Alamos NM 87545
(505)667-4156

Dr. H. F. Calcote
AeroChem Research Laboratories
Inc.
P. O. Box 12
Princeton NJ 08542
(609)921-7070

Dr. B. J. Cantwell
Department of Mechanical
Engineering
Stanford University
Stanford CA 94305-3032
(415)723-4825

Dr. T Charalampopoulos
Mechanical Engineering Dept.
Louisiana State University
Baton Rouge LA 70803
(504)388-5792
(504)388-5799

Capt Wayne Chepren
HQ AFESC/RDV
Tyndall AFB FL 32403-6001
(904)283-4234
AV523-4234

Dr. Robert E. Childs
Nielsen Engineering and
Research, Inc.
510 Clyde Avenue
Mountain View CA 94043-2287
(415)968-9457

Dr M-S Chou
Building R1, Room 1044
TRW Space and Technology Group
One Space Park
Redondo Beach CA 90278
(213)535-4321

Mr Steven Clouser
Research and Technology Group
Naval Air Propulsion Center
Trenton NJ 08628
(609)896-5752
AV442-7752

Mr Stephen Corda
Applied Physics Laboratory
Johns Hopkins University
Johns Hopkins Road
Laurel MD 20707-6099
(301)953-5000
Ext 4654

Dr C Criner
Mach I, Inc
346 East Church Road
King of Prussia PA 19406
(803)292-3345

Dr. E. T. Curran
WRDC/CA-P
Wright-Patterson AFB OH 45433-6563
(513)255-2246
AV785-2246

Dr Norman A Chigier
Department of Mechnanical
Engineering
Carnegie-Mellon University
Pittsburgh PA 15213
(412)578-2498

Dr S Y Cho
Department of Mechanical and
Aerospace Engineering
Princeton University
Princeton NJ 08544-5263

Mr. R. W. Claus
NASA Lewis Research Center
21000 Brookpark Road
Cleveland OH 44135-3127
(216)433-5869

Dr. M. B. Colket
United Technologies Research
Center
Silver Lane
East Hartford CT 06108
(203)727-7481

Dr. S. M. Correa
General Electric - Corporate
Research and Development
P. O. Box 8
Schenectady NY 12301
(518)387-5853

Dr Clayton T Crowe
Department of Mechanical
Engineering
Washington State University
Pullman WA 99164-2920
(509)335-3214

Dr Eli K Dabora
Mechanical Engineering Dept
University of Connecticut
Box U-139 ME
Storrs CT 06268
(203)486-2415
(203)486-2189

Dr Werner J A Dahm
Department of Aerospace
Engineering
The University of Michigan
Ann Arbor MI 48109-2140
(313)764-4318

Lt Col Larry P Davis
AFOSR/NC
Bolling AFB DC 20332-6448
(202)767-4963
AV297-4963

Dr George S Deiwert
NASA Ames Research Center
MS 230-2
Moffett Field CA 94035
(415)604-6198

Dr. R. W. Dibble
Department of Mechanical Eng
6159 Etcheverry Hall
University of California
Berkeley CA 94720
(415)642-4901
FAX -6163

Dr. P. E. Dimotakis
Graduate Aeronautical Labs
California Institute of
Technology
Pasadena CA 91125
(818)356-4456

Mr Lee G Dodge
Southwest Research Institute
P O Drawer 28510
San Antonio TX 78284
(512)684-5111
Ext 3251

Dr David Dolling
Department of Aerospace Engrg
and Engineering Mechanics
University of Texas at Austin
Austin TX 78712
(512)471-4470
(512)471-7593

Capt Randy Drabczuk
AFATL/SAH
Eglin AFB FL 32542-5434
AV872-0360
(904)882-0360

Dr. M. C. Drake
Physical Chemistry Department
General Motors Research Labs
Twelve Mile and Mound Roads
Warren MI 48090-9055

Dr. Fredrick L. Dryer
Department of Mechanical and
Aerospace Engineering
Princeton University
Princeton NJ 08544-5263
(609)258-5206

Dr C Dutton
Department of Mechanical and
Industrial Engineering
University of Illinois
Urbana IL 61801

Dr. H. A. Dwyer
Department of Mechanical
Engineering
University of California
Davis CA 95616

Dr Raymond B Edelman
WC 70
Rocketdyne
6633 Canoga Avenue
Canoga Park CA 91304
(805)371-7196

Ms Charlotte Eigel
WRDC/POSF
Wright-Patterson AFB OH 45433-6563
(513)255-5106
AV785-5106

Dr Phillip Emmerman
Harry Diamond Laboratories
Attn. SLCHD-ST-RD
2800 Powder Mill Road
Adelphi MD 20783-1197
(301)394-3000

Dr. K. C. Ernst
Pratt and Whitney Aircraft
Group
Government Products Division
West Palm Beach FL 33402

Mr John R Facey
Code RP
NASA
400 Maryland Avenue, S W
Washington DC 20546
(202)453-2854

Dr. G. M. Faeth
Department of Aerospace
Engineering
University of Michigan
Ann Arbor MI 48109-2140
(313)764-7202

Dr. Francis E. Fendell
TRW Space and Technology Group
Building R1, Room 1022
One Space Park
Redondo Beach CA 90278
(213)812-0327

Dr Michael Frenklach
202 Academic Projects Building
The Pennsylvania State
University
University Park PA 16802
(814)865-4392

Mr Jack Fultz
WRDC/POPR
Wright-Patterson AFB OH 45433-6563
(513)255-2175
AV785-2175

Dr David E Fyfe
Laboratory for Computational
Physics
Naval Research Laboratory
Washington DC 20375
(202)767-6583
AV297-6583

Dr Alon Gany
Department of Aeronautical Eng
Technion-Israel Institute of
Technology
32000 Haifa, ISRAEL
04-292308

Dr. A. F. Ghoniem
Department of Mechanical
Engineering
MIT
Cambridge MA 02139
(617)253-2295

Mr. R. Giffen
General Electric Company
Aircraft Engine Group
Neumann Way
Cincinnati OH 45215

Dr. P. Givi
Department of Mechanical
and Aerospace Engineering
State University of New York
Buffalo NY 14260

Dr. Irvin Glassman
Department of Mechanical and
Aerospace Engineering
Princeton University
Princeton NJ 08544-5263
(609)258-5199

Dr A D Gosman
Department of Mechanical Engrg
Imperial College of Science
and Technology
London WS7 2BX UK

Dr Frederick C Gouldin
Department of Mechanical and Aerospace Engineering
Cornell University
Ithaca NY 14853-1301

Dr F Grinstein
Laboratory for Computational Physics
Naval Research Laboratory
Washington DC 20375
(202)767-

Dr William Grosshandler
National Science Foundation
Chemical and Process Eng. Div.
1800 G Street, N. W.
Washington DC 20550
(202)357-9606

Dr Ephraim Gutmark
Research Department
Code 3892
Naval Weapons Center
China Lake CA 93555-6001
(619)939-3745
AV437-3745

Dr Robert J Hansen
Office of Naval Research
Code 1215
800 North Quincy Street
Arlington VA 22217-5000
(202)696-4715

Lt Col George K Haritos
AFOSR/NA
Bolling AFB DC 20332-6448
(202)767-4987
AV297-4987

Dr Stephen J Harris
Physical Chemistry Department
General Motors Research Labs
30500 Mound Road
Warren MI 48090-9055
(313)986-1305

Dr James C Hermanson
Propulsion Technology
United Technologies Research Center
East Hartford CT 06108

Mr Norman Hirsch
WRDC/POPR
Wright-Patterson AFB OH 45433-6563
(513)255-2175
AV785-2175

Mr Robert E Holland
United Technologies Chemical Systems Division
P O Box 49028
San Jose CA 95161-9028
(408)224-7656

Mr. Dale A. Hudson
WRDC/POTC
Wright-Patterson AFB OH 45433-6563
(513)255-5974
AV785-5974

Dr A K M F Hussain
Department of Mechanical Engineering
University of Houston
Houston TX 77004
(713)749-4444

Dr. T. A. Jackson
WRDC/POSF
Wright-Patterson AFB OH 45433-6563
(513)255-6462
AV785-6462

Mr Gordon E Jensen
United Technologies Chemical Systems Division
P O Box 49028
San Jose CA 95161-9028
(408)365-5552

Dr Sheridan C Johnston
Combustion Sciences
Sandia National Laboratories
Livermore CA 94550
(415)294-2138

Dr. W-H Jou
M/S 7K-06
P. O. Box 3707
Seattle WA 98124-2207
(206)865-6102

Dr. Ann R. Karagozian
Mechanical, Aerospace and
Nuclear Engineering Department
University of California, LA
Los Angeles CA 90024
(213)825-5653

Dr. Arnold A. Kelly
Department of Mechanical and
Aerospace Engineering
Princeton University
Princeton NJ 08544-5263
(609)258-5221

Dr. John T. Kelly
Altex Technologies Corporation
650 Nuttman Road
Suite 114
Santa Clara CA 95054
(408)980-8610

Dr Ian M Kennedy
Mechanical Engineering Dept
University of California,
Davis
Davis CA 95616
(916)752-2796

Mr. M. Kenworthy
General Electric Company
Aircraft Engine Group
Neumann Way
Cincinnati OH 45215

Dr. J. A. Kezerle
Gas Research Institute
8600 West Bryn Mawr Avenue
Chicago IL 60631
(312)399-8331

Dr. G. B. King
Department of Mechanical
Engineering
Purdue University
West Lafayette IN 47907
(317)494-2713

Mr. R. Kirby
Garrett Turbine Engine Company
111 South 34th Street
P. O. Box 5217
Phoenix AZ 85010

Dr Charles E Kolb
Aerodyne Research, Inc.
45 Manning Road
Manning Park Research Center
Billerica MA 01821-3976
(508)663-9500

Dr Wolfgang Kollmann
Mechanical Engineering Dept
University of California,
Davis
Davis CA 95616
(916)752-1452

Dr C R Krishna
Department of Nuclear Energy
Brookhaven National Laboratory
Upton NY 11973

Mr David Kruczynski
Attn SLCBR-IBA
Interior Ballistics Division
Ballistic Research Laboratory
Aberdeen Proving Ground MD 21005-506
(301)278-6202
AV298-6202

Dr Kenneth K Kuo
Department of Mechanical Engineering
Pennsylvania State University
University Park PA 16802
(814)865-6741

Lt James LaCasse
AFATL/SAH
Eglin AFB FL 32542-5434
(904)882-0207
AV872-0207

Dr. Marshall Lapp
High Temperature Interfaces Division
Sandia National Laboratories
Livermore CA 94550
(415)294-2435

Dr. John C. Larue
Department of Mechanical Engineering
University of California
Irvine CA 92717

Dr. A. Laufer
Office of Energy Research
U. S. Department of Energy
1000 Independence Avenue, N.W.
Washington DC 20585
(202)353-5820

Dr. N. M. Laurendeau
Department of Mechanical Engineering
Purdue University
West Lafayette IN 47907
(317)494-2713

Dr. Moshe Lavid
ML Energia, Inc.
P. O. Box 1468
Princeton NJ 08540
(609)799-7970

Dr. C. K. Law
Department of Mechanical and Aerospace Engineering
Princeton University
Princeton NJ 08544-5263
(609)258-5271

Dr Stan Lawton
McDonnell Douglas Research Lab
McDonnell Douglas Corporation
PO Box 516
St Louis MO 63166-0516
(314)233-2547

Dr J Carl Leader
McDonnell Douglas Research Lab
McDonnell Douglas Corporation
PO Box 516
St Louis MO 63166-0516
(314)232-4687

Dr C C Lee
Environmental Protection Agency
Cincinnati OH 45268
(513)569-7520

Dr Spiro Lekoudis
Office of Naval Research
Mechanics Division, Code 432
800 North Quincy Street
Arlington VA 22217-5000
(202)696-4406

Dr. Anthony Leonard
Graduate Aeronautical Labs
California Institute of Technology
Pasadena CA 91125
(818)356-4465

Dr. R. S. Levine
National Institute of Standards and Technology
Center for Fire Research
Gaithersburg MD 20899
(301)921-3845

Dr. Erwin A. Lezberg
NASA Lewis Research Center
21000 Brookpark Road
Cleveland OH 44135-3127
(216)433-5884

Dr. P. A. Libby
Dept. Of. Appl. Mech. and
Engrg. Sci.
University of California
La Jolla CA 92093
(619)534-3168

Dr. Wilbert Lick
Department of Mechanical and
Environmental Engineering
University of California
Santa Barbara CA 93106

Dr. Hans W. Liepmann
Graduate Aeronautical Labs
California Institute of
Technology
Pasadena CA 91125
(818)356-4535

Dr. F. E. Lytle
Department of Chemistry
Purdue University
West Lafayette IN 47907
(317)494-5261

Dr Andrej Macek
National Institute of
Standards and Technology
Physics Building, B-312
Gaithersburg MD 20899
(301)975-2610

Dr James Madson
McDonnell Douglas Research Lab
McDonnell Douglas Corporation
PO Box 516
St Louis MO 63166-0516

Dr. Edward T. Mahefkey
WRDC/POOC-5
Wright-Patterson AFB OH 45433-6563
(513)255-6241
AV785-6241

Dr Oscar Manley
US Department of Energy
Office of Energy Research
1000 Independence Avenue, SW
Washington DC 20585

Dr. Nagi N. Mansour
Computational Fluid Mechanics
Branch, RFT 202A-1
NASA Ames Research Center
Moffett Field CA 94035
(415)604-6420

Dr. F. E. Marble
Engrg. and Appl. Sci. Dept.
California Institute of
Technology
Pasadena CA 91125
(818)356-4784

Dr John C Marek
NASA Lewis Research Center
21000 Brookpark Road
Cleveland OH 44135-3127

Mr. C. R. Martel
WRDC/POSF
Wright-Patterson AFB OH 45433-6563
(513)255-7431
AV785-7431

Dr Bruce Masson
AFWL/ARDF
Kirtland AFB NM 87117-6008
(505)844-0208
AV244-0208

Dr. James McDonald
Code 6110
Naval Research Laboratory
Chemistry Division
Washington DC 20375
(202)767-3340
AV297-3340

Dr James McMichael
AFOSR/NA
Bolling AFB DC 20332-6448
(202)767-4936
AV297-4936

Dr. Lynn A. Melton
Programs in Chemistry
University of Texas, Dallas
P. O. Box 668
Richardson TX 75080
(214)690-2913

Dr D L Mingori
Mechanical, Aerospace and
Nuclear Engineering Dept
University of California
Los Angeles CA 90024
(213)825-1265

Dr Parviz Moin
Center for Turbulence Research
Stanford University
Stanford CA 94305-3032
(415)725-2081

Dr Peter A Monkewitz
Mechanical, Aerospace and
Nuclear Engineering Dept
University of California
Los Angeles CA 90024
(213)825-5217

Dr. E. J. Mularz
Aviation Res. and Tech. Activ.
NASA Lewis Res. Ctr., MS 5-11
21000 Brookpark Road
Cleveland OH 44135-3127
(216)433-5850

Dr D K McLaughlin
233 Hammond Building
Pennsylvania State University
University Park PA 16802
(814)865-2569

Dr A M Mellor
Mech Matls Eng Department
Station B, Box 6019
Vanderbilt University
Nashville TN 37235
(615)343-6214

Dr. R. Metcalfe
Department of Mechanical
Engineering
University of Houston
Houston TX 77004
(713)749-2439

Dr. Andrzej W Miziolek
Ignition and Combustion Branch
Interior Ballistics Division
Ballistic Research Laboratory
Aberdeen Proving Gnd MD 21005-506
(301)278-6157

Dr. H. Mongia
General Motors Corporation
Allison Gas Turbine Operations
P. O. Box 420
Indianapolis IN 46206-0420
(317)242-5945

Dr P J Morris
233-L Hammond Building
Pennsylvania State University
University Park PA 16802
(814)863-0157

Dr. M. G. Mungal
Department of Mechanical
Engineering
Stanford University
Stanford CA 94305-3032
(415)725-2019

Dr Arje Nachman
AFOSR/NM
Bolling AFB DC 20332-6448
(202)767-5028
AV297-5028

Dr. Abdollah Nejad
WRDC/POPT
Wright-Patterson AFB OH 45433-6563
(513)255-9991
AV785-9991

Dr Herbert Nelson
Code 6110, Chemistry Division
Naval Research Laboratory
Washington DC 20375
(202)767-3686

Dr. David Nixon
Nielsen Engineering and
Research, Inc.
510 Clyde Avenue
Mountain View CA 94043-2287
(415)968-9457

Dr. G. B. Northam
NASA Langley Research Center
MS 168
Hampton VA 23665-5225
(804)864-6248

Dr. R. C. Oldenborg
Chemistry Division
Los Alamos National Laboratory
Los Alamos NM 87545
(505)667-2096
(505)667-3758

Dr. A. K. Oppenheim
Department of Mechanical
Engineering
University of California
Berkeley CA 94720
(415)642-0211

Dr. E. S. Oran
Laboratory for Computational
Physics
Naval Research Laboratory
Washington DC 20375
(202)767-2960

Dr Simon Ostrach
Case Western Reserve Univ
Department of Mechanical and
Aerospace Engineering
Cleveland OH 44106

Dr Richard B Peterson
Department of Mechanical
Engineering
Oregon State University
Corvallis OR 97331-6001
(503)754-2567

Dr. W. M. Pitts
National Institute of
Standards and Technology
Center for Fire Research
Gaithersburg MD 20899
(301)975-6486

Dr. Robert W. Pitz
Department of Mechanical and
Materials Engineering
Vanderbilt University
Nashville TN 37235
(615)322-0209

Dr. S. B. Pope
Department of Mechanical and
Aerospace Engineering
Cornell University
Ithaca NY 14853-1301
(607)255-4314

Dr. C. L. Proctor II
Department of Mechanical
Engineering
University of Florida
Gainesville FL 32611
(904)392-7555

Dr. Herschel Rabitz
Department of Chemistry
Princeton University
Princeton NJ 08544-5263
(609)258-3917

Dr Saad Ragab
Engrg Sci Mechanics Dept
Virginia Polytechnic Institute
and State University
Blacksburg VA 24061
(703)231-5950

Dr. S. R. Ray
National Institute of
Standards and Technology
Center for Chemical Engrg
Gaithersburg MD 20899

Dr. R. G. Rehm
National Institute of
Standards and Technology
Center for Fire Research
Gaithersburg MD 20899

Dr M Renksizbulut
Department of Mechanical
Engineering
University of Waterloo
Waterloo, Ontario CN N2L 3G1
(519)885-1211
Ext 3977

Dr David Reuss
Fluid Mechanics Department
General Motors Research Labs
30500 Mound Road
Warren MI 48090-9055
(313)986-0029

Dr. W. C. Reynolds
Department of Mechanical
Engineering
Stanford University
Stanford CA 94305-3032
(415)723-3840

Dr James J Riley
Mechanical Engineering Dept
University of Washington
Seattle WA 98195
(206)543-5347

Dr Michael Roco
National Science Foundation
Chemical and Thermal Syst Div
1800 G Street, N W
Washington DC 20550
(202)357-9606

Dr. U. S. Rohatgi
Department of Nuclear Energy
Brookhaven National Laboratory
Upton NY 11973
(516)282-2475

Dr. W. M. Roquemore
WRDC/POSF
Wright-Patterson AFB OH 45433-6563
(513)255-6813
AV785-6813

Dr. Anatol Roshko
Graduate Aeronautical Labs
California Institute of
Technology
Pasadena CA 91125
(818)356-4484

Dr. D. E. Rosner
Department of Chemical
Engineering
Yale University
New Haven CT 06520
(203)432-4391

Dr John Ross
Department of Chemistry
Stanford University
Stanford CA 94305-3032
(415)723-9203

Dr Gabriel Roy
Office of Naval Research
Mechanics Division, Code 1132
800 North Quincy Street
Arlington VA 22217-5000
(202)696-4405

Dr Leonidas Sakell
AFOSR/NA
Bolling AFB DC 20332-6448
(202)767-4935
AV297-4935

Dr. G. S. Samuelsen
Department of Mechanical Engineering
University of California
Irvine CA 92717
(714)856-5468

Dr. B. R. Sanders
Thermofluids Division, 8363
Combustion Research Facility
Sandia National Laboratories
Livermore CA 94550
(415)294-3113

Dr Lakshmi Sankar
School of Aerospace Engrg
Georgia Institute of Technology
Atlanta GA 30332
(404)894-3014

Dr. R. J. Santoro
Department of Mechanical Engineering
Pennsylvania State University
University Park PA 16801
(814)863-1285

Dr Klaus Schadow
Naval Weapons Center
Code 3892
China Lake CA 93555-6001
(619)939-6532
AV437-6532

Mr Kurt Sacksteder
NASA Lewis Research Center
MS 500-217
21000 Brookpark Road
Cleveland OH 44135
(216)433-2857

Dr Mohammad Samimy
Ohio State University
Mechanical Engineering Dept
206 West 18th Street
Columbus OH 43210-1107
(614)422-6988

Mr. John Sanborn
Garrett Turbine Engine Company
111 South 34th Street
P. O. Box 5217
Phoenix AZ 85010
(602)231-2588

Dr. J. J. Sangiovanni
United Technologies Research Center
Silver Lane
East Hartford CT 06108
(203)727-7328

Dr. Domenic Santavicca
Department of Mechanical Engineering
Pennsylvania State University
University Park PA 16802
(814)863-1863

Mr William Scallion
NASA Langley Research Center
Mail Stop 408
Hampton VA 23665
(804)864-5235

Dr. John W. Schaefer
Energy and Environmental Div.
Acurex Corporation
555 Clyde Ave., P. O. Box 7555
Mountain View CA 94039

Dr W H Schofield
Aeronautical Research Labs
506 Lorimer St, Fishermen's Bn
Box 4331, P O
Melbourne, Victoria AUSTRALIA 3001

Dr. D. J. Seery
United Technologies Research
Center
Silver Lane
East Hartford CT 06108

Dr. H. G. Semerjian
National Institute of
Standards and Technology
Center for Chemical Engrg
Gaithersburg MD 20899
(301)975-2609

Dr C Senior
PSI Technology Company
Research Park
P O Box 3100
Andover MA 01810
(508)475-9030

Dr. K. Seshadri
Dept. Of. Appl. Mech. and
Engrg. Sci.
University of California
La Jolla CA 92093
(619)534-4876

Dr G S Settles
309 Mechanical Engrg Building
Pennsylvania State University
University Park PA 16802
(814)863-1504

Dr Robert W Shaw
Division of Chemical and
Biological Sciences
U S Army Research Office
Research Triangle Park NC 27709-2211
(919)549-0641

Mr. Harold C. Simmons
Parker Hannifin Corporation
Gas Turbine Fuel Systems Div.
17325 Euclid Avenue
Cleveland OH 44143
(216)531-3000
Ext 2309

Dr. W. A. Sirignano
School of Engineering
University of California
Irvine CA 92717
(714)856-6002

Dr Bernard Spielvogel
U S Army Research Office
P O Box 12211
Research Triangle Park NC 27709-221

Dr F Dee Stevenson
Office of Basic Energy Science
U. S. Department of Energy
1000 Independence Avenue, N W
Washington DC 20585

Dr David S Stewart
Department of Theoretical and
Applied Mechanics
University of Illinois
Urbana IL 61801

Dr Anthony Strawa
NASA Ames Research Center
MS 230-2
Moffett Field CA 94035
(415)604-3437

Dr. F. D. Stull
WRDC/POPS
Wright-Patterson AFB OH 45433-6563
(513)255-5210
AV785-5210

Dr B Sturtevant
Engrg and Appl Sci Dept
California Institute of
Technology
Pasadena CA 91125

Dr G Sullins
Applied Physics Laboratory
Johns Hopkins University
Johns Hopkins Road
Laurel MD 20707-6099
(301)953-5000

Dr. Dexter Sutterfield
National Institute for
Petroleum and Energy Research
Post Office Box 2128
Bartlesville OK 74005
(918)337-4251

Dr. L. Talbot
Department of Mechanical
Engineering
University of California
Berkeley CA 94720
(415)642-6780

Dr Christopher Tam
Department of Mathematics
Florida State University
Tallahasee FL 32306-3027
(904)644-2455

Julian M. Tishkoff
AFOSR/NA
Bolling AFB DC 20332-6448
(202)767-0465
AV297-0465

Dr. T. Y. Toong
Department of Mechanical
Engineering
MIT
Cambridge MA 02139
(617)253-3358

Dr Michael Trenary
Department of Chemistry
The University of Illinois
Chicago IL 60680

Dr Timothy R Troutt
Department of Mechanical
Engineering
Washington State University
Pullman WA 99164-2920

Dr Allen J Twarowski
Rockwell International Sci Ctr
1049 Camino dos Rios
P O Box 1085
Thousand Oaks CA 91360
(805)373-4576

Dr. C. J. Ultee
United Technologies Research
Center
Silver Lane
East Hartford CT 06108

Dr A D Vakili
University of Tennessee
Space Institute
Tullahoma TN 37388

Dr Earl VanLandingham
National Aeronautics Space
Administration, Code RB
400 Maryland Avenue, SW
Washington DC 20546
(202)453-2847

Dr. S. P. Vanka
Department of Mechanical
and Industrial Engrg
University of Illinois
Urbana IL 61801

Dr. P. J. Waltrup
Applied Physics Laboratory
Johns Hopkins University
Johns Hopkins Road
Laurel MD 20707-6099
(301)953-5000
Ext. 4186

Dr. C. K. Westbrook
Lawrence Livermore National Laboratories
P. O. Box 808
Livermore CA 94550

Dr James Whitelaw
Department of Mechanical Engrg
Imperial College of Science and Technology
London SW7 2BX UK

Dr. Forman A. Williams
Department of Applied Mech and Engineering Science
University of California
La Jolla CA 92093
(619)534-5492

Dr Michael Winter
Propulsion Science
United Technologies Research Center
East Hartford CT 06108
(203)727-7805

Dr. Francis Wodarczyk
AFOSR/NC
Bolling AFB DC 20332-6448
(202)767-4960
AV297-4960

Dr J M Wu
University of Tennessee
Space Institute
Tullahoma TN 37388

Dr Richard A Yetter
Department of Mechanical and Aerospace Engineering
Princeton University
Princeton NJ 08544-5263

Mr Fred Zarlingo
Code 3246
Naval Weapons Center
China Lake CA 93555-6001
(619)939-7395
AV437-7395

Dr. E. E. Zukoski
Engrg. and Appl. Sci. Dept.
California Institute of Technology
Pasadena CA 91125
(818)356-4785